TRANSACTIONS
OF THE ASME
Series E

Journal of APPLIED MECHANICS

March 1960

DYNAMICS • VIBRATIONS • ELASTICITY • LUBRICATION AND WEAR
RHEOLOGY • FRACTURES • STRUCTURES • HYDRAULICS • AERODYNAMICS
INTERNAL FLOW • MECHANICAL PROPERTIES OF METALS • THERMODYNAMICS
TURBULENCE • HEAT TRANSFER • COMPUTING DEVICES AND METHODS
BOUNDARY LAYERS • AEROELASTICITY • EXPERIMENTAL STRESS ANALYSIS

Published Quarterly by
THE AMERICAN SOCIETY OF MECHANICAL ENGINEERS

TRANSACTIONS
OF THE ASME
Series E

EDITORIAL DEPARTMENT

Editor, J. J. JAKLITSCH, JR.
Consulting Editor, LEO BLODGETT
Art Editor, HENRY BALFOUR
Production, HILDA K. WILGUS

APPLIED MECHANICS DIVISION

Chairman, S. B. BATDORF
Secretary, A. M. WAHL
Technical Editor, D. C. DRUCKER
Technical Editor, J. KESTIN
Honorary Editor, JOHN M. LESSELLS

OFFICERS OF THE ASME

President, W. L. CISLER
Secretary, O. B. SCHIER, II
Treasurer, E. J. KATES
Assistant Treasurer, H. J. BAUER

PUBLICATIONS COMMITTEE

Chairman, B. G. A. SKROTZKI
HENDLEY N. BLACKMON
R. D. MINDLIN
MARTIN GOLAND
VITO L. SALERNO

Junior Representatives
A. S. GOLDSTEIN
J. W. FOLLANSBEE

REGIONAL ADVISORY BOARD

Region I, H. M. ROGERS, JR.
Region II, GLENN R. FRYLING
Region III, F. J. HEINZE
Region IV, FRANCIS C. SMITH
Region V, H. M. CATHER
Region VI, C. R. EAPLE
Region VII, M. T. UBBENHAUER
Region VIII, CARL J. ECKHARDT

Published quarterly by The American Society of Mechanical Engineers. Publication office at 20th and Northampton Streets, Easton, Pa. The editorial department is located at the headquarters of the Society, 29 West Thirty-Ninth Street, New York 18, N. Y. Cable address, "Mechanize," New York. Price $3.00 a copy, $10.00 annually; to members, $1.50 a copy, $5.00 annually. Add 50 cents for postage to all countries outside the United States and Canada. Changes of address must be received at Society headquarters seven weeks before they are to be effective on the mailing list. Please send old as well as new address. . . By-Law: The Society shall not be responsible for statements or opinions advanced in papers or . . . printed in its publications (B13, Par. 4). . . Second-Class mail privileges authorized at Easton, Penna. This publication is authorized to be mailed at the special rates of postage prescribed by Section 132.122.

© Copyright, 1960, by The American Society of Mechanical Engineers. Reprints from this publication may be made on condition that full credit be given the TRANSACTIONS of the ASME, Series E—Journal of Applied Mechanics and the author, and that date of publication be stated.

TRANSACTIONS OF THE ASME
Indexed by the Engineering Index, Inc.

Journal of APPLIED MECHANICS

VOLUME 27 • SERIES E • NUMBER 1

March 1960

CONTENTS

TECHNICAL PAPERS

1 **A Theory of Lubrication With Turbulent Flow and Its Application to Slider Bearings**
L. N. Tao

5 **Effect of the Wall on Two-Phase Turbulent Motion**
S. L. Soo and C. L. Tien

16 **The Melting of Finite Slabs**
T. R. Goodman and J. J. Shea

25 **Heat-Exchanger Tube-Sheet Design—3. U-Tube and Bayonet-Tube Sheets**
Karl A. Gardner

34 **Mechanics of the Sheet-Bending Process**
B. W. Shaffer and E. E. Ungar

41 **Relaxation of a Cylinder on a Rigid Shaft**
E. A. Davis

45 **Strain-Hardening Solutions to Axisymmetric Disks and Tubes**
Nicholas Perrone

54 **Effect of Shear Deformations on the Bending of Rectangular Plates**
V. L. Salerno and M. A. Goldberg

59 **Plastic Stress Concentration at a Circular Hole in an Infinite Sheet Subjected to Equal Biaxial Tension**
Bernard Budiansky and O. L. Mangasarian

65 **Stresses in the Plastic Range Around a Normally Loaded Circular Hole in an Infinite Sheet**
O. L. Mangasarian

74 **On a Dynamical Saint Venant Principle**
B. A. Boley

79 **Correlation of Theoretical and Photothermoelastic Results on Thermal Stresses in Idealized Wing Structures**
Herbert Tramposch and George Gerard

87 **Stresses in a Circular Cylinder Having an Infinite Row of Spherical Cavities Under Tension**
Akira Atsumi

93 **Transient Thermal Stresses in a Semi-Infinite Slab**
W. Jaunzemis and E. Sternberg

104 **On Stress-Strain Relations and Strain-Energy Expressions in the Theory of Thin Elastic Shells**
J. K. Knowles and Eric Reissner

107 **On the Effect of Shear on Plastic Deformation of Beams Under Transverse Impact Loading**
B. Karunes and E. T. Onat

111 **The Half-Space Under Pressure Distributed Over an Elliptical Portion of Its Plane Boundary**
H. Deresiewicz

120 **Earth Motion Beneath a Prescribed Boundary Displacement**
R. C. Geldmacher, J. W. Dunkin, and R. L. Anderson

125 **On the Elastic Bending of Columns Due to Dynamic Axial Forces Including Effects of Axial Inertia**
Eugene Sevin

132 **Dominance of Shear Stresses in Early Stages of Impulsive Motion of Beams**
H. H. Bleich and R. Shaw

139 **The Elastic-Plastic Response of Thin Spherical Shells to Internal Blast Loading**
W. E. Baker

CONTENTS

145 **Axially Symmetric Waves in Elastic Rods**
R. D. Mindlin and H. D. McNiven

152 **Vibrations and Waves in Elastic Bars of Rectangular Cross Section**
R. D. Mindlin and E. A. Fox

159 **Subharmonic Oscillations of a Pendulum**
Richard Skalak and M. I. Yarymovych

165 **Plane-Stress Unloading Waves Emanating From a Suddenly Punched Hole in a Stretched Elastic Plate**
Julius Miklowitz

172 **Plastic-Wave Propagation Effects in Transverse Impact of Membranes**
B. Karunes and E. T. Onat

177 **The Motion and Loading of a Hinged Ramp Which Supports a Sliding Mass**
B. Saelman

182 **An Analytical Method for Locating the Burmester Points for Five Infinitesimally Separated Positions of the Coupler Plane of a Four-Bar Mechanism**
J. C. Wolford

187 **Steady-State Undamped Vibrations of a Class of Nonlinear Discrete Systems**
P. R. Sethna

196 **A Unified Criterion for the Degree of Constraint of Plane Kinematic Chains**
B. Paul

201 **Approximate Synthesis of Spatial Linkages**
J. Denavit and R. S. Hartenberg

BRIEF NOTES

Buckling and Deflection of Isosceles-Triangular Plates 207
L. S. Han

The Creep Deflection of a Rivet in Double Shear 208
L. N. Tao

Torsion of Prismatical Rods With Isosceles-Triangle Cross Sections 209
H. D. Conway

210 Buckling of a Beam on a Number of Elastic Restraints
J. P. Ellington

211 The Second Approximation for Buckling Loads
M. M. Abbassi

DISCUSSION

213 Discussion of previously published papers by *S. J. Kline and P. W. Runstadler; J. H. Baltrukonis; J. Modrey; A. Dornig; E. W. Gaylord; B. Paul; W. F. Stokey and C. F. Zorowski; R. M. Rosenberg and C. P. Atkinson*

BOOK REVIEWS

Dynamics of Framed Structures 221
Introduction to Plasticity 221
Engineering Thermodynamics 221
Heat and Mass Transfer 222

TRANSACTIONS OF THE ASME Series C

Journal of HEAT TRANSFER

Vol. 82 • Series C • No. 1

CONTENTS FOR FEBRUARY, 1960

1 Radiant Interchange Within an Enclosure, by J. T. Bevans and R. V. Dunkle. (59—HT-4)

20 Numerical Solutions to an Inverse Problem of Heat Conduction for Simple Shapes, by G. Stolz, Jr. (59—SA-20)

27 Effect of Thermocouple Cavity on Heat Sink Temperature, by J. V. Beck and H. Hurwicz. (59—HT-20)

37 Freezing of a Growing Liquid Column, by G. Horvay. (59—HT-11)

48 Measurement of the Thermal Conductivities of Gases at High Temperatures, by R. G. Vines. (59—HT-2)

53 Laminar Transfer From Isothermal Spanwise Strips on a Flat Plate, by H. H. Sogin. (59—HT-1)

64 Spectral Characteristics of Fabrics From 1 to 23 Microns, by R. V. Dunkle, F. Ehrenburg, and J. T. Gier. (59—HT-9)

Technical Briefs

71 The Effect of Vapor Drag on Rotating Condensation, by E. M. Sparrow and J. L. Gregg.

73 Radiation Fin Effectiveness, by J. G. Bartas and W. H. Sellers.

75 A Tabulation of the Function $\exp X^2 \operatorname{erfc} X$, by J. E. Sunderland and R. J. Grosh.

TRANSACTIONS OF THE ASME
Series A

Journal of
ENGINEERING FOR POWER
Volume 82 • Series A • Number 1

CONTENTS FOR JANUARY, 1960

1 Development of a Three-Stage Liquid-Cooled Gas Turbine, by Sumner Alpert, R. E. Grey, and W. O. Flaschar. (59—GTP-1)
10 Effect of Ambient and Fuel Pressure on Spray Drop Size, by S. M. DeCorso. (59—GTP-3)
19 Presentation of a Blade-Design Method for Axial-Flow Turbines, Including Design and Test Results of a Typical Axial-Flow Stage, by F. Baumgartner and R. Amsler. (59—GTP-4)
27 The Basic Heat Transfer and Flow Friction Characteristics of Six Compact High-Performance Heat Transfer Surfaces, by W. M. Kays. (59—GTP-2)
35 Metallurgical Evaluation of Superheater-Tube Alloys After Six-Months' Exposure at Temperatures of 1100 to 1500 F, by C. L. Clark, J. J. B. Rutherford, A. B. Wilder, and M. A. Cordovi. (59—Pwr-1)
68 Blast-Furnace-Gas Cleaning for Iron and Ferromanganese Production, by J. S. Mackay and J. F. Kearns.
73 Influence Coefficients for Open-Crown Hemispheres, by G. D. Galletly. (59—SA-4)

TRANSACTIONS OF THE ASME
Series B

Journal of
ENGINEERING FOR INDUSTRY
Volume 82 • Series B • Number 1

CONTENTS FOR FEBRUARY, 1960

1 Design and Analysis of Welded Pressure-Vessel Skirt Supports, by N. A. Weil and J. J. Murphy. (58—A-153)
15 Static Testing High-Pressure Piping Components, by T. G. Moore and E. J. Opersteny.
23 Tire Testing, by J. W. Hanneil. (59—SA-48)
29 Nomographic Synthesis of Generator Linkages, by D. P. Adams. (59—SA-11)
41 The Effect of Presetting Helical Compression Springs, by T. J. Atterbury and W. B. Diboll, Jr. (59—SA-12)
47 A Quantitative Investigation of the Factors Which Influence the Fatigue Life of a V-Belt, by S. M. Marco, W. L. Starkey, and K. G. Hornung. (59—SA-18)
60 Edge Influence Coefficients for Toroidal Shells of Positive Gaussian Curvature, by G. D. Galletly. (59—Pet-2)
69 Edge Influence Coefficients for Toroidal Shells of Negative Gaussian Curvature, by G. D. Galletly. (59—Pet-3)
76 The Influence of Surface Residual Stress on Fatigue Limit of Titanium, by E. C. Reed and J. A. Viens. (59—Prod-1)
79 Shear-Zone Size, Compressive Stress, and Shear Strain in Metal-Cutting and Their Effects on Mean Shear-Flow Stress, by Dimitri Kececioglu. (59—Prod-3)

TRANSACTIONS OF THE ASME
Series D

Journal of
BASIC ENGINEERING
Vol. 82 • Series D • No. 1

CONTENTS FOR MARCH, 1960

1 Cavitation Effect on the Discharge Coefficient of the Sharp-Edged Orifice Plate, by F. Numachi, M. Yamabe, and R. Ōba. (58—A-93)
12 Measurement of Oil-Film Thickness Between Disks by Electrical Conductivity, by S. I. El-Sisi and G. S. A. Shawki. (58—A-253)
19 Performance Characteristics of Lubricating Oil Film Between Rotating Disks, by S. I. El-Sisi and G. S. A. Shawki. (58—A-254)
29 The Measurement of Oil-Film Thickness in Gear Teeth, by I. O. MacConochie and A. Cameron. (58—A-142)
35 A New Approach to Linear Filtering and Prediction Problems, by R. E. Kalman. (59—IRD-11)
46 Shannon's Theory and Feedback Systems, by S. S. L. Chang. (59—IRD-12)
51 Dynamic Response and Control of Multipass Heat Exchangers, by M. Masubuchi. (59—IRD-6)
66 Bang-Bang Versus Linear Control of a Second-Order Rate-Type Servomotor, by P. F. Meyfarth. (59—IRD-13)
73 The Design and Analysis of a Servovalve With Flow Feedback, by E. Bahniuk and S.-Y. Lee. (59—IRD-3)
81 A Thermocouple System for Measuring Turbine-Inlet Temperatures, by M. E. Ihnat and W. C. Hagel. (59—IRD-1)
87 Estimating the Roots of the Characteristic Determinant for Multicoupled Systems, by S. Lees, H. D. Felsenthal, and E. M. Goldberg. (59—IRD-2)
96 Human Body as an Inconstant Heat Source and Its Relation to Determination of Clothes Insulation, Part I, by A. S. Iberall. (59—IRD-7)
103 Human Body as an Inconstant Heat Source and Its Relation to Clothes Insulation, Part 2, by A. S. Iberall. (59—IRD-8)
113 Some General Considerations in Process Optimization, by G. E. P. Box.
120 Ejector-Nozzle Flow and Thrust, by H. E. Weber. (59—Hyd-5)
131 Pressure Losses in Smooth Pipe Bends, by H. Itō. (59—Hyd-4)
144 Discharge Coefficients and Steady-State Flow Forces for Hydraulic Poppet Valves, by J. A. Stone. (59—Hyd-18)
155 Crossover Systems Between the Stages of Centrifugal Compressors, by G. O. Ellis. (59—Hyd-3)
169 The Inception of Cavitation on Isolated Surface Irregularities, by J. W. Holl. (59—Hyd-12)
184 Indentation of Metals by Cavitation, by W. H. Wheeler. (59—Hyd-15)
195 A Shock-Tube Technique to Determine Steady-Flow Losses of Orifices and Other Duct Elements, by G. Rudinger. (59—Hyd-13)
201 Separation Prediction for Conical Diffusers, by J. M. Robertson and H. R. Fraser. (59—Hyd-14)
210 Unsteady Transfer of Momentum and Heat Between Concentric Cylinders, by C.-S. Yih. (59—Hyd-17)
217 Chamber Dimension Effects on Induced Flow and Frictional Resistance of Enclosed Rotating Disks, by J. W. Daily and R. E. Nece. (59—Hyd-9)
233 On the Three-Dimensional Turbulent Boundary Layer Generated by Secondary Flow, by J. P. Johnston. (59—Hyd-6)
249 Addendum to a previously published paper by B. Sternlicht.

L. N. TAO
Associate Professor,
Department of Mechanics,
Illinois Institute of Technology,
Chicago, Ill.
Assoc. Mem. ASME

A Theory of Lubrication With Turbulent Flow and Its Application to Slider Bearings

The governing equation of turbulent lubrication in three dimensions, equivalent to the Reynolds equation of laminar lubrication, is derived. The problem of a slider bearing with no side leakage is then analyzed. An exact solution is found in closed form. Bearing characteristics are also established. It is found that the Reynolds number is an important parameter in the problem of turbulent lubrication. Furthermore, it is shown that the laminar lubrication may be considered as the special case of the present study. A numerical example is also included.

In most bearings the lubricant flow is laminar and hence governed by the Reynolds equation of hydrodynamic lubrication. However, the problem of lubrication with turbulent flow is becoming inevitable as a result of the trend toward high-speed operation and low-viscosity lubricants. Some recent experiments [1, 2, 3][1] have demonstrated the existence of this turbulent flow.

It is only recently that the analytical studies of this problem have appeared. For journal bearings, because of the complexities of the problem, only a special case, the bearing of very "short" length, has been studied [4]. For slider bearings, Chou and Saibel [5] investigated those with no side leakage. They attacked the problem by means of Prandtl's mixing-length concept and the assumption that the inertia effect is negligible, and found an approximate solution which is applicable only when the ratio of inlet and outlet film thicknesses is less than 2. Physically, this restriction is not realistic.

In the present paper, by employing a semiempirical theory the governing equation of turbulent lubrication in three dimensions, equivalent to the Reynolds equation of laminar lubrication, is derived. For simplicity, the basic equation is applied to slider bearings with no side leakage. An exact solution is found in closed form. Bearing characteristics are then established. It is found that the Reynolds number of the flow is an important parameter in the problem of turbulent lubrication. Furthermore, it is shown that the laminar problem may be considered as the special case of the present study. A numerical example is also included to show the relative magnitudes.

Governing Equation

The principal feature of turbulent flow is that the turbulent fluctuations are random in nature. For engineering applications we may assume that the instantaneous velocity may be resolved into two components; namely, the mean velocity components and turbulent-perturbation velocity components which are zero in average. When these velocity components are substituted into the Navier-Stokes equations, it is found that the number of unknowns is larger than the number of equations. Hence these equations are insufficient to determine the unknowns. However, when the problem is only the determination of the mean velocity distribution, it can be solved by using some semiempirical theories, partially substantiated by experiments. In the present analysis the Blasius' law of friction with the velocity profile of fractional power is used in place of the linear relation of Newton's law of viscous shear as the flow becomes turbulent.

Because of the thinness of the oil film, we may assume that the pressure and velocity are uniform over a section. In other words, the pressure and velocity at a section may be taken to be the average value of the section. We shall further assume that the inertia effect may be ignored. This leads to the implication that the pressure and velocity at a local section are independent of those at other sections as if it were a region between two parallel plates of proper film thickness.

Both assumptions are justifiable in the Reynolds equation of laminar lubrication. In this study of turbulent lubrication, it seems that the second assumption on the inertia effect might not be well justified owing to the high Reynolds number involved. However, this is not the case. It is well known that in the laminar range the ratio of inertia force to viscous force is of the order

$$\frac{\text{Inertia force}}{\text{Viscous force}} = 0\left(\mathbf{R}\frac{h}{l}\right) \tag{1}$$

where l is a physical linear dimension such as the length of the bearing. By the adoption of Blasius' law of friction in place of the linear stress-strain rate relationship, it can be easily verified that

$$\frac{\text{Inertia force}}{\text{Viscous force}} = 0\left(\mathbf{R}^n\frac{h}{l}\right) \tag{2}$$

This expression is in agreement with that for the laminar case where $n = 1$. For fully developed turbulent flow the exponent n is small; i.e., between 0 (extremely high Reynolds number) and 0.25 (smooth walls). This indicates that for a Reynolds number of 10,000 in turbulent flow the ratio will have, at most, the same order as that of $\mathbf{R} = 10$ in the laminar case. Hence, the assumption of ignoring the inertia effect in bearings with turbulent flow is justifiable.

Based on these two assumptions and the application of Blasius' law of friction,

[1] Numbers in brackets designate References at end of paper.

Contributed by the Applied Mechanics Division and presented at the Annual Meeting, Atlantic City, N. J., November 29–December 4, 1959, of The American Society of Mechanical Engineers.

Discussion of this paper should be addressed to the Secretary, ASME, 29 West 39th Street, New York, N. Y., and will be accepted until April 10, 1960, for publication at a later date. Discussion received after the closing date will be returned.

Note: Statements and opinions advanced in papers are to be understood as individual expressions of their authors and not those of the Society. Manuscript received by ASME Applied Mechanics Division, December 18, 1958. Paper No. 59--A-26.

$$\lambda = C\left(\frac{\nu}{2hq_s}\right)^n = -\nabla p \frac{2h}{\rho}\frac{2}{q_s^2} \tag{3}$$

where λ is the friction factor, C and n are experimentally determined constants, and q_s is the velocity in the direction of a streamline, the velocity vector $\mathbf{q}$ in the film due to the pressure gradient is then

$$\mathbf{q} = \nabla p|\nabla p|^{\frac{n-1}{2-n}} K^{\frac{1}{2-n}} h^{\frac{1+n}{2-n}}, \quad K = \frac{2^{2+n}}{C\nu^n\rho} \tag{4}$$

The dragging effect due to the relative motion U of the surfaces can be obtained from the velocity distribution of a Couette flow [6]

$$\frac{u}{U} = 1 + \frac{2t+1-s}{2t}\xi + \frac{s-1}{2t}\xi^{2t+1} \tag{5}$$

where s and t are experimentally determined constants and ξ is a nondimensional length measured from the mid-section with boundaries of the walls at $\xi = \pm 1$. By integration the mean flow of the section is found to be $Uh/2$.

Applying the continuity equation of a steady flow to the lubricant film, we immediately get

$$\operatorname{div}\left[|\nabla p|^{\frac{n-1}{2-n}} \nabla p\, K^{\frac{1}{2-n}} h^{\frac{3}{2-n}}\right] = -\frac{U}{2}\frac{\partial h}{\partial x} \tag{6}$$

where x is taken in the direction of relative motion. This equation is consistent with the Reynolds equation for laminar flow. In that case, $n = 1$, $C = 96$; Equation (6) is reduced to

$$\frac{\partial}{\partial x}\left[\frac{h^3}{12\mu}\frac{\partial p}{\partial x}\right] + \frac{\partial}{\partial z}\left[\frac{h^3}{12\mu}\frac{\partial p}{\partial z}\right] = -\frac{U}{2}\frac{\partial h}{\partial x} \tag{7}$$

Slider Bearings With No Side Leakage

For plane slider bearings with no side leakage, the pressure is a function of x only and the film thickness may be expressed as

$$h = \alpha x \tag{8}$$

The governing equation, Equation (6), is reduced to

$$\frac{U}{2}\frac{dh}{dx} \pm \frac{d}{dx}\left[\left(\pm\frac{dp}{dx}\right)^{\frac{1}{2-n}} K^{\frac{1}{2-n}} h^{\frac{3}{2-n}}\right] = 0 \tag{9}$$

where the first and second signs are for $dp/dx \gtrless 0$, respectively.

Let h_m be the value of h at $dp/dx = 0$ and x_m the location of this point. With boundary conditions $p = 0$ at two ends $x = a$ and $x = b$, we may proceed to obtain the pressure distribution. Direct integrations of Equation (9) give

$$\frac{dp}{dx} = \left(\frac{U}{2}\right)^{2-n}\frac{1}{K}\frac{(h_m - h)^{2-n}}{h^3} \qquad a \le x \le x_m \tag{10a}$$

$$\frac{dp}{dx} = -\left(\frac{U}{2}\right)^{2-n}\frac{1}{K}\frac{(h - h_m)^{2-n}}{h^3} \qquad x_m \le x \le b \tag{10b}$$

Using the substitutions of

$$\zeta = 1 - \frac{x}{x_m} \quad \text{when} \quad a \le x \le x_m \tag{11a}$$

$$\eta = 1 - \frac{x_m}{x} \quad \text{when} \quad x_m \le x \le b \tag{11b}$$

and integrating Equations (10a), and (10b), we have

$$p = \left(\frac{U}{2}\right)^{2-n}\frac{1}{K}\frac{1}{\alpha^{1+n}x_m^{\,n}}\int_{\zeta}^{\zeta_a}\zeta^{2-n}(1-\zeta)^{-2}d\zeta$$

$$= \left(\frac{U}{2}\right)^{2-n}\frac{1}{K}\frac{1}{\alpha^{1+n}x_m^{\,n}}[B_{\zeta_a}(3-n,-2) - B_{\zeta}(3-n,-2)] \qquad a \le x \le x_m \tag{12a}$$

$$p = \left(\frac{U}{2}\right)^{2-n}\frac{1}{K}\frac{1}{\alpha^{1+n}x_m^{\,n}}\int_{\eta}^{\eta_b}\eta^{2-n}(1-\eta)^{n-1}d\eta$$

$$= \left(\frac{U}{2}\right)^{2-n}\frac{1}{K}\frac{1}{\alpha^{1+n}x_m^{\,n}}[B_{\eta_b}(3-n,n) - B_{\eta}(3-n,n)] \qquad x_m \le x \le b \tag{12b}$$

where ζ_a and η_b are values of ζ at $x = a$ and η at $x = b$, respectively, and $B_x(s,t)$ is the incomplete beta function (see Appendix).

Introducing a Reynolds number based upon the average film thickness

$$\mathbf{R} = U\bar{h}/\nu, \quad \bar{h} = \alpha(a+b)/2 \tag{13}$$

and rearranging Equations (12a) and (12b), we have

$$p = \frac{\mu U}{a+b}\,\mathbf{R}^{1-n}\left(\frac{a+b}{2x_m}\right)^n\frac{C}{8\alpha^2}$$

$$[B_{\zeta_a}(3-n,-2) - B_{\zeta}(3-n,-2)] \quad a \le x \le x_m \tag{14a}$$

$$p = \frac{\mu U}{a+b}\,\mathbf{R}^{1-n}\left(\frac{a+b}{2x_m}\right)^n\frac{C}{8\alpha^2}$$

$$[B_{\eta_b}(3-n,n) - B_{\eta}(3-n,n)] \quad x_m \le x \le b \tag{14b}$$

In these two equations, x_m has to be found. By the matching of Equations (14a) and (14b) at $x = x_m$, i.e.,

$$B_{\zeta_a}(3-n,-2) = B_{\eta_b}(3-n,n) \tag{15}$$

and the relation

$$(1-\zeta_a)(1-\eta_b) = \frac{a}{b} \tag{16}$$

ζ_a and η_b, consequently x_m, can be determined. Hence the pressure distribution of a slider bearing with no side leakage is completely determined.

Bearing Characteristics

Load Capacity. The load capacity per unit width of a bearing may be found by the integration of the pressure force

$$W = \int_a^b p\,dx = -\int_a^b \frac{dp}{dx}\,x\,dx \tag{17}$$

The last expression is obtained from integration by parts and conditions $p = 0$ at $x = a$ and $x = b$. Again, the substitutions of ζ and η in Equation (17) give

$$W = \left(\frac{U}{2}\right)^{2-n}\frac{x_m^{\,1-n}}{\alpha^{1+n}K}\left[\int_0^{\eta_b}\eta^{2-n}(1-\eta)^{n-2}\,d\eta - \int_0^{\zeta_a}\zeta^{2-n}(1-\zeta)^{-2}\,d\zeta\right] = \mu U(\mathbf{R})^{1-n}\left(\frac{2x_m}{a+b}\right)^{1-n}\frac{C}{16\alpha^2}$$

$$[B_{\eta_b}(3-n,n-1) - B_{\zeta_a}(3-n,-1)] \tag{18}$$

Center of Pressure. The position of the center of pressure is obtainable by taking the moment about the origin of the co-ordinates. Integration by parts leads to

$$\bar{x} = \frac{1}{W}\int_a^b px\,dx = -\frac{1}{2W}\int_a^b \frac{dp}{dx}\,x^2dx \tag{19}$$

Substitutions of ζ and η give

$$\bar{x} = \frac{1}{2W}\left(\frac{U}{2}\right)^{2-n}\frac{x_m^{2+n}}{\alpha^{1+n}K}\left[\int_0^{\eta_b}\eta^{2-n}(1-\eta)^{n-1}d\eta - \int_0^{\zeta_a}\zeta^{2-n}(1-\zeta)^{-1}d\zeta\right]$$

$$= \frac{x_m}{2}\,\frac{B_{\eta_b}(3-n, n-2) - B_{\zeta_a}(3-n, 0)}{B_{\eta_b}(3-n, n-1) - B_{\zeta_a}(3-n, -1)} \tag{20}$$

Frictional Force and Power Loss. We assume that the shear stress at the wall is the sum of those contributed by the pressure gradient and by the relative motion of bearing surfaces. The shear stress due to the pressure gradient is obtainable from the momentum consideration,

$$\tau = -\frac{h}{2}\frac{dp}{dx} \tag{21}$$

and the shear stress due to the relative motion of bearing surfaces may be found from the commonly used expression

$$\tau = C_f\frac{\rho U^2}{2}, \quad C_f = M\mathrm{R}_h^m \tag{22}$$

where C_f is the coefficient of friction, $\mathrm{R}_h = Uh/\nu$ is the local Reynolds number, and M and m are experimentally determined constants. However, as mentioned by Pai [6], the constants M and m have not been determined definitely.

The frictional force per unit width acting on the bearing may be found by the integration of the shear force,

$$F = \frac{\rho U^2}{2}\int_a^b M\mathrm{R}_h^m dx - \int_a^b \frac{h}{2}\frac{dp}{dx}\,dx$$

$$= \frac{\rho U^2}{2}\mathrm{R}^m\left(\frac{2}{a+b}\right)^m M\,\frac{b^{1+m} - a^{1+m}}{1+m} + \frac{W\alpha}{2} \tag{23}$$

The power loss is the product of F and U,

$$H = FU = \frac{\rho U^3}{2}\mathrm{R}^m\left(\frac{2}{a+b}\right)^m M\,\frac{b^{1+m} - a^{1+m}}{1+m} + \frac{WU\alpha}{2} \tag{24}$$

Special Case of Laminar Flow

Another feature of the present analysis is that the derived equations may also be used for the flow in the laminar viscous shear range. In that case the constants in Equations (3) and (20) are $n = 1$, $C = 96$ and $m = -1$, $M = 2$. Recall the recurrence formula and the degenerated cases of incomplete beta functions (see Appendix),

$$\begin{aligned} B_z(s+1, t) &= B_z(s, t) - B_z(s, t+1) \\ B_z(s, -s) &= z^s(1-z)^{-s}/s \\ B_z(s, 1) &= z^s/s \\ B_z(1, 0) &= -\log(1-z) \end{aligned} \tag{25}$$

we obtain

$$p = \left(\frac{U}{2}\right)\frac{1}{K}\,\frac{1}{\alpha^2 x_m}\,[B_{\zeta_a}(2, -2) - B_\zeta(2, -2)]$$

$$= \left(\frac{U}{2}\right)\frac{1}{K}\,\frac{1}{\alpha^2 x_m}\,[B_{\eta_b}(2, 1) - B_\eta(2, 1)] \tag{26}$$

with x_m evaluated from

$$B_{\zeta_a}(2, -2) = B_{\eta_b}(2, 1)$$

$$(1 - \zeta_a)(1 - \eta_b) = \frac{a}{b} \tag{27}$$

i.e.,

$$x_m = \frac{2ab}{a+b} \tag{28}$$

Hence

$$p = \frac{6\mu U}{\alpha^2(a+b)}\left[\frac{a+b}{x} - \frac{ab}{x^2} - 1\right] \tag{29}$$

Similarly, the load capacity W, the center of pressure $\bar{x}$, and the frictional force F are

$$W = \frac{6\mu U}{\alpha^2}\left[\log\frac{b}{a} - 2\,\frac{b-a}{b+a}\right] \tag{30}$$

$$\bar{x} = \frac{1}{2}\,\frac{b^2 - a^2 - 2ab\log(b/a)}{(b+a)\log(b/a) - 2(b-a)} \tag{31}$$

$$F = \frac{\mu U}{\alpha}\left[4\log\frac{b}{a} - \frac{2(b-a)}{a+b}\right] \tag{32}$$

These formulas are identical to those given for laminar lubrication [7].

Numerical Example

In applying the derived formulas to a slider bearing operated in the turbulent regime with no side leakage, we take a bearing of $h_b/h_a = 2$, $\alpha = 0.001$, and $\mathrm{R} = 10{,}000$. And the constants in Equation (3) are established from the adoption of a velocity profile of one-seventh power; $C = 0.326$, $n = 0.25$.

The pressure distribution in the form of p/p_{max} is then found and plotted in Fig. 1. For the purpose of comparison, Fig. 1 also includes the pressure distribution of laminar lubrication and their respective positions of maximum pressure and centers of pressure. It is seen from Fig. 1 that the turbulent case has a flatter pressure-distribution curve. This indicates that for equal p_{max} in both regimes, turbulent lubrication will have a larger load capacity.

In addition, the maximum pressures, load, capacities, and centers of pressure of these two regimes are tabulated in Table 1. However, the frictional force is not given, since the constants M and m in Equation (22), as mentioned previously, have not been determined definitely.

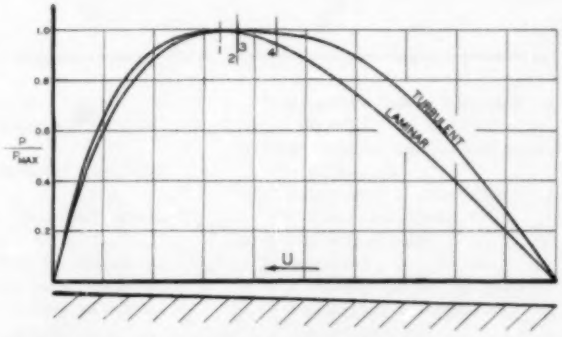

Fig. 1 Pressure distributions and locations of P_{max} and $\bar{x}$; $h_b/h_a = 2$, $\alpha = 0.001$. Laminar flow: maximum pressure, 1; center of pressure, 2. Turbulent flow: maximum pressure, 3; center of pressure, 4.

Table 1

	Laminar	Turbulent
$p_{max}(a+b)/\mu U$	7.50×10^5	7.92×10^5
$W/\mu U$	1.589×10^5	1.863×10^5
$\bar{x}/a$	1.365	1.445

The values in Table 1 are in dimensionless forms. A larger value of $p_{max}(a+b)/\mu U$ or $W/\mu U$ in turbulent lubrication does not necessarily mean a larger value of p_{max} or W. For turbulent lubrication, the Reynolds number of the lubricant flow must be above the critical value. This may be achieved by either a high-speed operation of the bearing or a low-viscosity lubricant in the bearing. However, these two effects are pointing in two different directions. The turbulent lubrication of a high-speed bearing will have a higher p_{max} and also a larger W than the laminar case of low-speed operation. On the other hand, the turbulent lubrication of using a low-viscosity lubricant will show a lower p_{max} and a smaller W than that of high-viscosity lubricant. This differs from the conclusion of Chou and Saibel [5].

References

1 D. F. Wilcock, "Turbulence in High-Speed Journal Bearings," TRANS. ASME, vol. 72, 1950, pp. 825–834.

2 S. Abramovitz, "Turbulence in a Tilting-Pad Thrust Bearing," TRANS. ASME, vol. 78, 1956, pp. 7–12.

3 M. I. Smith and D. D. Fuller, "Journal-Bearing Operation at Superlaminar Speed," TRANS. ASME, vol. 78, 1956, pp. 469–474.

4 L. N. Tao, "A Theory of Lubrication in Short Journal Bearings With Turbulent Flow," TRANS. ASME, vol. 80, 1958, pp. 1734–1740.

5 Y. T. Chou and E. Saibel, "The Effect of Turbulence on Slider-Bearing Lubrication," JOURNAL OF APPLIED MECHANICS, vol. 26, TRANS. ASME (Series E), vol. 81, 1959, pp. 122–126.

6 S. I. Pai, "On Turbulent Flow Between Parallel Plates," JOURNAL OF APPLIED MECHANICS, vol. 20, TRANS. ASME, vol. 75, 1953, pp. 109–114.

7 A. G. M. Michell, "Lubrication," Blackie and Son Limited, London, England, 1950.

8 A. Erdélyi, Editor, "Higher Transcendental Founctins. Vol. I," McGraw-Hill Book Company, Inc., New York, N. Y., 1953.

APPENDIX

Incomplete Beta Functions

The incomplete beta function [8] is defined by the integral

$$B_z(s, t) = \int_0^z u^{s-1}(1-u)^{t-1}\,du \qquad |z| < 1 \tag{33}$$

Expressing Equation (33) in terms of hypergeometric function $F(a, b; c; z)$, we have

$$B_z(s, t) = s^{-1}z^s F(s, 1-t; s+1; z) \tag{34}$$

For $|z| < 1$, $F(a, b; c; z)$ is defined for all finite values of s and t with the exception that s is a negative integer.

Hence the incomplete beta function is defined for all values of t and Re $(s) > 0$.

By the use of the recurrence formula of the hypergeometric function, we have

$$B_z(s+1, t) = B_z(s, t) - B_z(s, t+1) \tag{35}$$

Furthermore, from the degenerated cases of hypergeometric functions [8]

$$\begin{aligned} F(a, b; b; z) &= (1-z)^{-a} \\ F(a, 0; c; z) &= 1 \\ zF(1, 1; 2; z) &= -\log(1-z) \end{aligned} \tag{36}$$

we obtain

$$\begin{aligned} B_z(s, -s) &= z^s(1-z)^{-s}/s \\ B_z(s, 1) &= z^s/s \\ B_z(1, 0) &= -\log(1-z) \end{aligned} \tag{37}$$

S. L. SOO
Professor of Mechanical Engineering,
University of Illinois, Urbana, Ill.
Mem. ASME

C. L. TIEN
Assistant Professor
of Mechanical Engineering,
University of California,
Berkeley, Calif.

Effect of the Wall on Two-Phase Turbulent Motion

Stationary solution on the effect of a wall on two-phase (solid particles in gas) turbulent motion shows that the intensity of motion of solid particles is affected by the presence of the wall and the distribution of turbulent intensity of the stream near the wall. The intensity of motion of solid particles can be significantly higher than the turbulence intensity of the mean stream. These modifications are consequences of Bernoulli force acting between the wall and the particle.

Analytical studies published [1, 2][1] on the momentum transfer in two-phase turbulent motion were made only on particle motion in an isotropic infinite turbulent field. While the results attained were adequate for the understanding of the case where the main stream turbulent motion (nearly isotropic) predominates, experimental results [3] have shown significant contribution of wall interference. For duct flow at moderate turbulence level (say, at duct Reynolds number of the order of 50,000), the variation of the properties of turbulence of the stream [4, 5, 6] is sufficient to render main stream consideration alone unrealistic. It was shown that in spite of greater inertia of the solid particles, the intensity of particle motion may be much greater than the intensity of the mean stream. This can be expected because of the increase of stream intensity toward the wall. The measured particle diffusivity was smaller than the eddy diffusivity of the mean stream because of reduced mixing toward the wall.

While experiments can be carried out without the complication of shear flow, for instance, behind a grid in a wind tunnel, some understanding of the wall interference on two-phase turbulent motion is needed because a wall is ever present in almost any physical applications. This is particularly significant when treating transport processes other than momentum transfer. In the heat-transfer process from a wall to a two-phase stream, for example, the particle motion near the wall affects predominantly this rate process. This type of two-phase flow is also involved in propulsion devices where the transfer surface is allowed to erode in order that a high temperature can be used to achieve the best possible performance.

In the following, motion of a single spherical solid particle near the wall of a turbulent fluid is considered. The analysis consists of the basic equation of motion of wall interferences on a two-phase turbulent field, and solution of the equation including only significant contributions for the stationary case.

Fundamental Considerations

The simplified system adopted for this study consists of a spherical solid particle in a semi-infinite body of turbulent fluid bounded by an infinite wall, Fig. 1. The solid particle is taken to be much smaller than the size of eddy or microscale of stream turbulence, so that it is under the influence of only a single fluctuating velocity at all times. Description of the character of stream motion is based on [4], [5], and [6] for the distribution of intensities and scales of turbulence. The stream, especially at near the wall, is anisotropic and nonhomogeneous, but the concept of local isotropy [7] is accepted as a basic constraint. The turbulence is fully developed so that intermittency [6] can be neglected.

The motion of a particle in a fluid bounded by an infinite fixed wall can be treated by extending the method due to Stokes [8]. Assuming potential motion for particle-wall interaction, the motion of a sphere moving perpendicularly to a wall is identical to the case where two identical spheres are moving along the line connecting the centers. The kinetic energy of the fluid is

$$2T_y = {}^2/_3\pi\rho a^3\left(1 + {}^3/_8\frac{a^3}{y^3}\right)\dot{y}^2, \qquad (1)$$

[1] Numbers in brackets designate References at end of paper.

Presented at the West Coast Conference of the Applied Mechanics Division, Stanford, Calif., September 9–11, 1959, of THE AMERICAN SOCIETY OF MECHANICAL ENGINEERS.

Discussion of this paper should be addressed to the Secretary, ASME, 29 West 39th Street, New York, N. Y., and will be accepted until April 10, 1960, for publication at a later date. Discussion received after the closing date will be returned.

NOTE: Statements and opinions advanced in papers are to be understood as individual expressions of their authors and not those of the Society. Manuscript received by ASME Applied Mechanics Division, December 31, 1958. Paper No. 59-APMW-18.

Nomenclature

A, B = reduced mass functions as defined after Equation (3)
A_n = amplitude of nth harmonic of velocity fluctuation
a = radius of solid particle
b = parametric time coefficient [t^{-1}] as defined after Equation (13)
c = dimensionless constant as defined after Equation (13)
ϵ = reduced volume as defined after Equation (13)
D = eddy diffusivity
D_p = particle diffusivity
F = force
θ_n = angle of phase lag of velocity of particle
f = Lagrangian statistical power spectrum
K = two-phase flow parameter relating Reynolds number, scale and density as defined by Equation (29)
l = Lagrangian scale of turbulence of fluid stream
l_m = molecular mean free path of fluid
l_p = Lagrangian scale of turbulence of particle
λ = Lagrangian microscale of stream turbulence
μ = viscosity of fluid
n = frequency
ν = kinematic viscosity of fluid
R = Lagrangian correlation of stream motion

(*Continued on next page*)

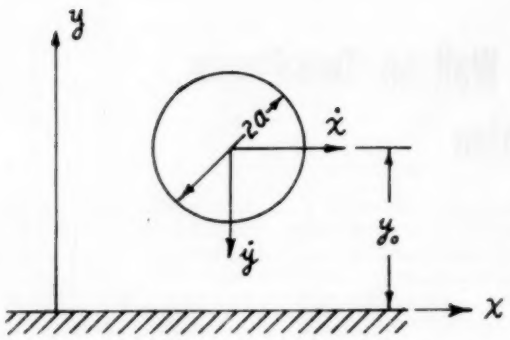

Fig. 1 Co-ordinate system of a sphere moving near a wall

where ρ is the density of the fluid. For a sphere moving parallel to the wall, the kinetic energy of the fluid is

$$2T_a = {}^2/_3\pi\rho a^3\left(1 + {}^3/_{16}\frac{a^3}{y^3}\right)\dot{x}^2 \tag{2}$$

In general, for a spherical particle moving in a fluid as shown in Fig. 1, the total kinetic energy of the system can be represented by

$$T = {}^1/_2(A\dot{x}^2 + B\dot{y}^2) \tag{3}$$

where

$$A = {}^4/_3\pi\rho_p a^3 + {}^2/_3\pi\rho a^3\left(1 + {}^3/_{16}\frac{a^3}{y^3}\right),$$

$$B = {}^4/_3\pi\rho_p a^3 + {}^2/_3\pi\rho a^3\left(1 + {}^3/_8\frac{a^3}{y^3}\right),$$

and ρ_p is the density of the spherical particle. Assuming holonomic motion, the Lagrange equation for the system based on generalized space co-ordinate x_i and velocity $\dot{x}_i$ gives for generalized external force F_i:

$$F_i = \frac{d}{dt}\left(\frac{\partial T}{\partial \dot{x}_i}\right) - \left(\frac{\partial T}{\partial x_i}\right) \tag{4}$$

Hence

$$F_x = \frac{d}{dt}A\dot{x} = {}^4/_3\pi a^3(\rho_p + {}^1/_2\rho)\ddot{x} + {}^1/_3\pi\rho\frac{a^3}{y^4}(\dot{y}\dot{x} - 3\dot{x}\dot{y}), \tag{5}$$

and

$$F_y = \frac{d}{dt}(B\dot{y}) - {}^1/_2\dot{x}^2\frac{\partial A}{\partial y} - {}^1/_2\dot{y}^2\frac{\partial B}{\partial y}$$

$$= {}^4/_3\pi a^3(\rho_p + {}^1/_2\rho)\ddot{y} + {}^1/_4\pi\rho\frac{a^3}{y^4}(y\ddot{y} - {}^3/_2\dot{y}^2 + {}^3/_4\dot{x}^2) \tag{6}$$

These are components of the generalized Bernoulli force.

The forces acting on the spherical particle in a turbulent field consist of:

(*a*) Forces due to potential field such as gravitational (buoyancy), thermal, and electrostatic field. Only gravity is considered here.

(*b*) Viscous drag following Stokes' approximation

$$F_1 = 6\pi a\mu(\dot{x}_i - u_i) \tag{7}$$

with u_i as the velocity of the sphere. This is valid for particle Reynolds number $2(\dot{x}_i - u_i)a/\nu \ll 1$ and Knudsen number much smaller than one or $l_m/a \ll 1$, l_m being the mean free path of the fluid.

(*c*) Fluid resistance due to relative acceleration of the particle [2]

$$F_2 = 6\pi a_\mu\left[\frac{a}{(\pi\nu)^{1/2}}\int_{-\infty}^{t}\frac{[\ddot{x}_i - \dot{u}_i(\tau)]}{(t-\tau)^{1/2}}\,d\tau\right] \tag{8}$$

For sinusoidal motion $u \sim \sin\omega t$, where ω is the angular velocity of the fluctuation, the ratio of F_2/F_1 is of the order $a\omega^{1/2}\nu^{-1/2}$.

(*d*) Fluid inertia which gives rise to the apparent mass consideration [9]. This is due to the pressure gradient induced by the acceleration of the fluid in addition to the pressure force of $2\pi a^3\rho_p u$.

(*e*) Forces due to spin of the sphere. This force, which tends to give rise to the Magnus effect, is small when the particle diameter is small compared to the characteristic length of the turbulent eddies. Summing up,

$$F_i = {}^4/_3\pi a^3 g(\rho_p - \rho) + 6\pi a_\mu(\dot{x}_i - u_i) + 6\pi a_\mu\left[\frac{a}{\sqrt{(\pi\nu)}}\int_{-\infty}^{t}\frac{(\ddot{x}_i - \dot{u}_i)}{\sqrt{t-\tau}}\,d\tau\right] \tag{9}$$

($i = x, y$), which, when combined with Equations (5) and (6) and follow a similar treatment as in [10], gives

$${}^4/_3\pi a^3\rho_p\ddot{x} = -6\pi a\mu(\dot{x} - u) - 6\pi a\mu\left[\frac{a}{\sqrt{\pi\nu}}\int_{-\infty}^{t}\frac{\ddot{x} - \dot{u}}{\sqrt{t-\tau}}\,d\tau\right] - {}^2/_3\pi\rho a^3(\ddot{x} - \dot{u}) - {}^1/_3\pi\rho\frac{a^3}{y^4}[y(\ddot{x} - \dot{u}) - 3(\dot{x} - u)(\dot{y} - v)] + {}^4/_3\pi a^3\rho\dot{u} \tag{10}$$

$${}^4/_3\pi a^3\rho_p\ddot{y} = -{}^4/_3\pi a^3 g(\rho_p - \rho) - 6\pi a\mu(\dot{y} - v) - 6\pi a\mu\left[\frac{a}{\sqrt{\pi\nu}}\int_{-\infty}^{t}\frac{(\ddot{y} - \dot{v})}{\sqrt{t-\tau}}\,d\tau\right] - {}^2/_3\pi\rho a^3(\ddot{y} - \dot{v}) - {}^1/_4\pi\rho\frac{a^3}{y^4}[y(\ddot{y} - \dot{v}) - {}^3/_2(\dot{y} - \dot{v})^2 + {}^3/_4(\dot{x} - u)^2] + {}^4/_3\pi a^3\rho\dot{v} \tag{11}$$

Equations (10) and (11) are the basic equations of motion of the system.

Nomenclature

R' = Lagrangian correlation of particle motion
ρ = density of fluid stream
ρ_p = density of solid particle
T = kinetic energy
t, τ = time
u = velocity of solid particle in x-direction
v = velocity of solid particle in y-direction
$\sqrt{\langle v^2\rangle}$ = intensity of fluid stream turbulence
ω = circular frequency
η = defined as $d\eta = \sqrt{\langle v^2\rangle}\,dt$
x = co-ordinate parallel to the solid wall
y = co-ordinate normal to the solid wall
y_0 = distance of particle from the wall
$\cdot\ \cdot\cdot$, $,\ ,\cdot\cdot$ = first, second, .. , derivatives with respect to time

Subscripts

p = solid particle
1, 2 = as defined

Forward Subscripts

0, 1, = order of perturbation

Stationary Solution

The solution of Equations (10) and (11), the basic equation of motion of the system together with the statistical prescriptions of the turbulent field is obviously a formidable task. To develop some understanding of the property of the system, a stationary (i.e., without considering the probability for a particle to be at a certain state at any time, but considering what would happen if it is there) solution is attempted here, together with simplifications from order-of-magnitude considerations.

The force due to relative accelerations of the particle may be neglected from considering the ratio of F_2/F_1 in the previous section. The second-order product of the relative velocity can be neglected as necessitated by the Stoke's approximation for drag; i.e., the relative velocity must be small. The buoyancy force, giving only a constant lift, is also neglected here. The basic equations become

$$\ddot{x} + b(\dot{x} - u) + \epsilon \frac{1}{y^2}(\ddot{x} - \dot{u}) = c\dot{u}, \tag{12}$$

$$\ddot{y} + b(\dot{y} - v) + \epsilon \frac{1}{y^2}(\ddot{y} - \dot{v}) = c\dot{v}, \tag{13}$$

where

$$b = \frac{9\mu}{2a^2\left(\rho_p + \frac{\rho}{2}\right)},$$

$$c = \tfrac{3}{2}\frac{\rho}{\left(\rho_p + \frac{\rho}{2}\right)},$$

and

$$\epsilon = \tfrac{3}{16}\frac{\rho a^2}{\left(\rho_p + \frac{\rho}{2}\right)}$$

In order to compare with the experimental results of [3], the order of magnitude of terms in Equations (12) and (13) were calculated for the case of a two-phase stream consisting of air and glass beads of the order of 100 microns diam, as well as the case in which air is replaced by water to visualize the range of validity of such considerations. The data are presented in Table 1, showing the order of magnitude of all quantities involved. It is clearly indicated that, in almost all cases, the term $c\dot{u}$ and $c\dot{v}$ can be neglected, and that ϵ is a small quantity. The latter suggests solution of Equations (12) and (13) in the following form:

$$\ddot{x} + b(\dot{x} - u) + \epsilon(\ddot{x} - \dot{u})/y^3 = 0 \tag{14}$$

$$\ddot{y} + b(\dot{y} - v) + \epsilon(\ddot{y} - \dot{v})/y^3 = 0 \tag{15}$$

by a series expansion in terms of ϵ. The small order of magnitude of ϵ, as well as the fact that y must be greater than the thickness of the laminar sublayer, only the zeroth and the first perturbation of the following would be adequate

$$y = {}_0y + \epsilon({}_1y) + \epsilon^2({}_2y) + \ldots \tag{16}$$

due to quick convergence.

Substitution of Equation (16) into Equation (15) gives

$$({}_0\ddot{y}) + b({}_0\dot{y}) = bv \tag{17}$$

$$({}_1\ddot{y}) + b({}_1\dot{y}) = \frac{\dot{v} - ({}_0\ddot{y})}{({}_0y)^3} \tag{18}$$

with v given by the concept of spectrum

$$v = \Sigma A_n \sin 2\pi n t \tag{19}$$

It can be seen that Equation (17) is identical to the equation of motion in the absence of wall interference [1]. Its solution can be expressed as:

$${}_0y = y_0 + \sum\left(\frac{-1}{2\pi n}\right)\frac{A_n}{\left[1 + \left(\frac{2\pi n}{b}\right)^2\right]^{1/2}}\cos(2\pi n t - \theta_1) \tag{20}$$

and

$$\theta_1 = \tan^{-1}\left(\frac{2\pi n}{b}\right) \tag{21}$$

The solution to Equation (18) can be expressed as (Appendix 1):

$${}_1y = \sum\frac{1}{y_0^3}\frac{-A_n}{b\left[1 + \left(\frac{2\pi n}{b}\right)^2\right]^{1/2}}\cos(2\pi n t + \theta_2) + \sum\frac{1}{y_0^3}\frac{A_n}{b\left[1 + \left(\frac{2\pi n}{b}\right)^2\right]}\cos(2\pi n t - \theta_3) \tag{22}$$

where

$$\theta_3 = \tan^{-1}\left(\frac{b}{2\pi n}\right) \tag{23}$$

$$\theta_2 = \tan^{-1}\left\{\frac{2\pi n}{b} - \tfrac{1}{2}\left(\frac{b}{2\pi n}\right)\left[1 + \left(\frac{2\pi n}{b}\right)^2\right]\right\} \tag{24}$$

Based on the Lagrangian power spectrum $f(n)$ of the fluid phase, where

$$\tfrac{1}{2}A_n^2 = \langle v^2\rangle f(n)dn \tag{25}$$

where $\langle v^2\rangle$ is the mean squared velocity of the stream, the intensities and correlations of the spherical particle can be evaluated. When there is no wall interference

$$\langle {}_0v_p^2\rangle = \langle {}_0\dot{y}^2\rangle = \langle v^2\rangle\int_0^\infty\frac{f(n)dn}{1 + \left(\frac{2\pi n}{b}\right)^2} \tag{26}$$

The Lagrangian power spectrum $f(n)$ can be approximated by [1]

$$f(n) = \frac{2\sqrt{\pi}\lambda}{\sqrt{\langle v^2\rangle}}e^{-\pi^2\lambda^2 n^2/\langle v^2\rangle} \tag{27}$[3]$$

---

[3] Alternately, $f(n) = \dfrac{4l}{\sqrt{\langle v^2\rangle}}\, e^{-4\pi l^2 n^2/\langle v^2\rangle}$, where l is the Lagrangian scale of stream turbulence.

Table 1 Table of order of magnitudes

(Based on glass beads of the order of 100 micron diam in air [3] or water)

	Air	Water
ρ, pcf	10^{-3}	10
ρ_p, pcf	10^2	10^2
a, ft	10^{-4}	10^{-4}
μ, lb/ft-sec	10^{-5}	10^{-3}
b	10	10^3
c	10^{-4}	10^{-1}
ϵ	10^{-17}	10^{-14}
$\dot{y}$, fps	10^0	10^0
$\dot{x}$, fps	10	10^1
$\ddot{x}$	10^2	10^2
$b(\dot{x} - u)$	10^2	10^3
$\epsilon(\ddot{x} - \dot{u})/y^3$	$10^{-15}/y^3$	$10^{-14}/y^3$
$c\dot{u}$	10^{-3}	10^{-1}
$\ddot{y}$	10	10^2
$b(\dot{y} - \dot{v})$	10	10^2
$\epsilon(\ddot{y} - \dot{v})/y^3$	$10^{-16}/y^3$	$10^{-15}/y^3$
$c\dot{v}$	10^{-4}	10^{-2}

where λ is the Lagrangian microscale. The foregoing spectrum function is a Fourier transform of the Lagrangian correlation of the fluid turbulence based on the approximation $R = e^{-\eta^2/\lambda^2}$. This, as shown in [1], gives close approximation especially in the low wave-number range. Based on Equation (27), the zero-order of particle intensity can be shown to be:

$$\frac{\langle {}_0v_p^2\rangle}{\langle v^2\rangle} = \sqrt{\pi}\, e^{1/K^2}\,\mathrm{erfc}\left(\frac{1}{K}\right)\Big/K, \tag{28}$$

where

$$K^2 = \frac{4\langle v^2\rangle}{\lambda^2 b^2} = {}^2/_{\overline{R}e}\left(\frac{a}{\lambda}\right)\frac{\left(\rho_p + \dfrac{\rho}{2}\right)}{\rho} \tag{29}$$

(Appendix 2). Considering wall interference, for

$$\dot{y} \cong {}_0\dot{y} + \epsilon_1\dot{y} \tag{30}$$

$$\dot{y}^2 \cong {}_0\dot{y}^2 + 2\epsilon {}_0\dot{y}_1\dot{y}, \tag{31}$$

and

$$\langle {v_p}^2\rangle = \langle \dot{y}^2\rangle = \langle {}_0\dot{y}^2\rangle + 2\epsilon\,\langle {}_0\dot{y}_1\dot{y}\rangle, \tag{32}$$

we have (Appendix 3)

$$\frac{\langle {v_p}^2\rangle}{\langle v^2\rangle} = \frac{\sqrt{\pi}}{K}\left[1 - \frac{2\epsilon}{{y_0}^3}\left({}^1/_2 + \frac{1}{K^2}\right)\right]e^{1/K^2}\,\mathrm{erfc}\left(\frac{1}{K}\right) + \frac{2\epsilon}{{y_0}^3K^2} \tag{33}$$

This relation and Equation (28) were plotted as shown in Fig. 2, in terms of $(\langle v^2\rangle - \langle {v_p}^2\rangle)/\langle v^2\rangle$.

Similarly, Equation (14) can be solved with the approximation:

$$x = ({}_0x) + \epsilon({}_1x), \tag{34}$$

leading to

$$({}_0\ddot{x}) + b({}_0\dot{x}) = bu, \tag{35}$$

$$({}_1\ddot{x}) + b({}_1\dot{x}) = \frac{\dot{u} - ({}_0\ddot{x})}{({}_0y)^3} \tag{36}$$

Using similar spectrum approximation, for ${}_0y = \text{const} = y_0$, we get a similar solution as Equation (33):

$$\frac{\langle {u_p}^2\rangle}{\langle u^2\rangle} = \frac{\sqrt{\pi}}{K}\left[1 - \frac{2\epsilon}{{y_0}^3}\left({}^1/_2 + \frac{1}{K^2}\right)\right]e^{1/K^2}\,\mathrm{erfc}\left(\frac{1}{K}\right) - \frac{2\epsilon}{{y_0}^3K^2} \tag{37}$$

(note the difference in sign of the last term, and that the K in Equations (33) and (37) are in general different).

The Lagrangian correlation coefficients of the particle motion can be evaluated according to:

$$R_y' = \frac{\langle \dot{y}\dot{y}_\tau\rangle}{\langle \dot{y}^2\rangle} \cong \frac{\langle [({}_0\dot{y}) + \epsilon({}_1\dot{y})][({}_0\dot{y})_\tau + \epsilon({}_1\dot{y})_\tau]\rangle}{\langle \dot{y}^2\rangle} \cong \frac{\langle ({}_0\dot{y})({}_0\dot{y})_\tau\rangle + \epsilon\langle ({}_0\dot{y})_\tau({}_1\dot{y})\rangle + \epsilon\langle ({}_0\dot{y})({}_1\dot{y})_\tau\rangle}{\langle \dot{y}^2\rangle} \tag{38}$$

where

$$\dot{y} = \dot{y}(t), \quad \text{and} \quad \dot{y}_\tau = \dot{y}(t+\tau)$$

We get

$$R_y' \cong \frac{\displaystyle\int_0^\infty \left[1 - \frac{2\epsilon}{{y_0}^3}\,\frac{\left(\dfrac{2\pi n}{b}\right)^2}{1 + \left(\dfrac{2\pi n}{b}\right)^2}\right]\frac{f(n)}{1 + \left(\dfrac{2\pi n}{b}\right)^2}\cos 2\pi n\,\frac{\eta}{\sqrt{\langle v^2\rangle}}\,dn}{\displaystyle\int_0^\infty \left[1 - \frac{2\epsilon}{{y_0}^3}\,\frac{\left(\dfrac{2\pi n}{b}\right)^2}{1 + \left(\dfrac{2\pi n}{b}\right)^2}\right]\frac{f(n)}{1 + \left(\dfrac{2\pi n}{b}\right)^2}\,dn} \tag{39}$$

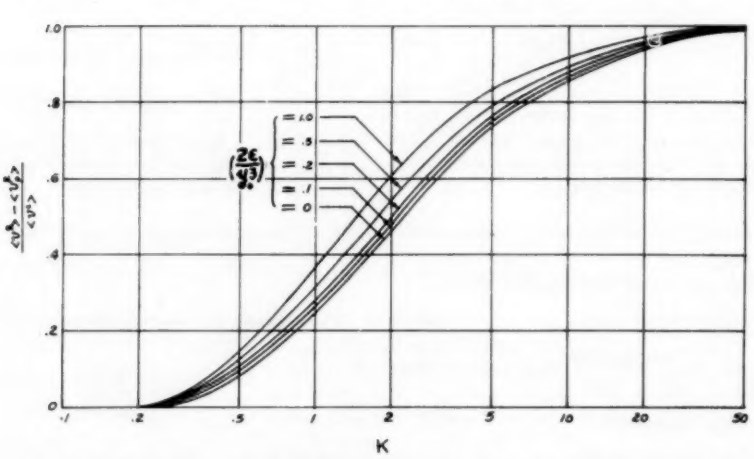

Fig. 2 Deviation of local intensity of motion of a particle from that of the stream at various distances from the wall

where η is defined by $d\eta = \sqrt{\langle v^2 \rangle} dt$ and for nondecaying turbulence $\eta = \sqrt{\langle v^2 \rangle} t$. Equation (39) gives, for large y_0, i.e., without wall interference (Appendix 4),

$$ {}_0R_y' = \frac{1}{2 \operatorname{erfc}\left(\frac{1}{K}\right)} \left\{ e^{-2\eta/K\lambda} \left[2 - \operatorname{erfc}\left(\frac{\eta}{\lambda} - \frac{1}{K}\right)\right] + e^{2\eta/K\lambda} \operatorname{erfc}\left(\frac{\eta}{\lambda} + \frac{1}{K}\right)\right\} \quad (40) $$

(Fig. 3) and with wall interference,

$$ R_y' = {}_0R_y' \frac{\langle v_p' v_p'' \rangle}{\langle v_p'^2 \rangle} - \frac{2\epsilon}{y_0^2} \Phi\left(K_1 \frac{\eta}{\lambda}\right) \frac{\langle v^2 \rangle}{\langle v_p'^2 \rangle} \quad (41) $$

The function Φ is given in Appendix 5. Fig. 4 (*a*), (*b*), and (*c*) shows the effect of $2\epsilon/y_0^2$.

It can be shown further that the diffusivity of the particle is identical to the eddy diffusivity of the stream, or

$$ \frac{D_p}{D} = 1 = \frac{l_p}{l} \sqrt{\frac{\langle v_p'^2 \rangle}{\langle v^2 \rangle}} \quad (42) $$

(Appendix 6), where l_p and l are the scales of turbulence of the particle and the stream.

Discussion

The foregoing analysis shows that, based on local stream intensity, contribution of wall interference actually reduces the intensity of motion of solid particles such that the local quantity of $[\langle v^2 \rangle - \langle v_p'^2 \rangle]/\langle v^2 \rangle$ is less than 1 but greater than zero, Fig. 2. The local value of $\langle v^2 \rangle$ or $\langle u^2 \rangle$ varies with the distance from the wall as shown in Fig. 5, according to Laufer [4]. In Fig. 5, y_0 is the distance from the wall while r_0 is the duct radius. When corrected to the mean stream condition, assuming constant eddy diffusivity [11] in the stream, the relation in Fig. 2 can be expressed as in Figs. 6 and 7, showing the intensity that a particle at various values of y_0/r_0 tends to attain. These figures show that at low-stream Reynolds numbers a particle moving across the turbulence field is constantly accelerated and decelerated by the changing stream turbulence and wall interaction as well as by the constant turbulence intensity in the middle portion of the stream, resulting in high particle intensity in the middle portion of the stream as presented in [3]. This effect is more pronounced for low duct Reynolds numbers than high duct Reynolds numbers.

The analysis was shown to be valid when the particle diffusivity is of similar order of the eddy diffusivity of the stream; i.e., for very small particles. The eddy diffusivity has been reported to be sensibly constant over the duct height. The present analysis indicates that the effect of the wall on the particle diffusivity is

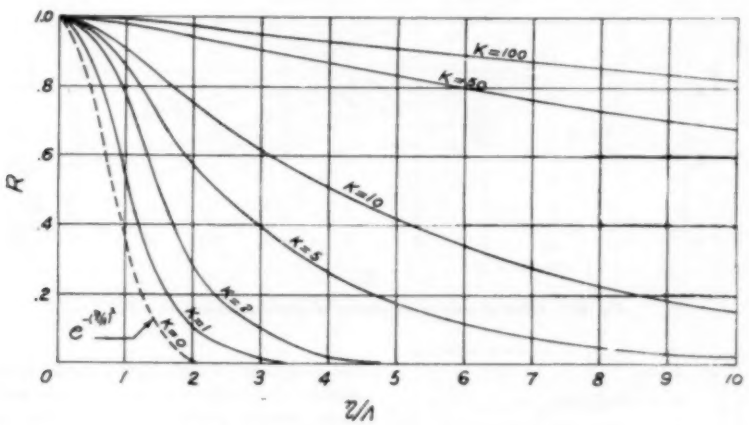

Fig. 3 Correlation of particle motion in mean stream

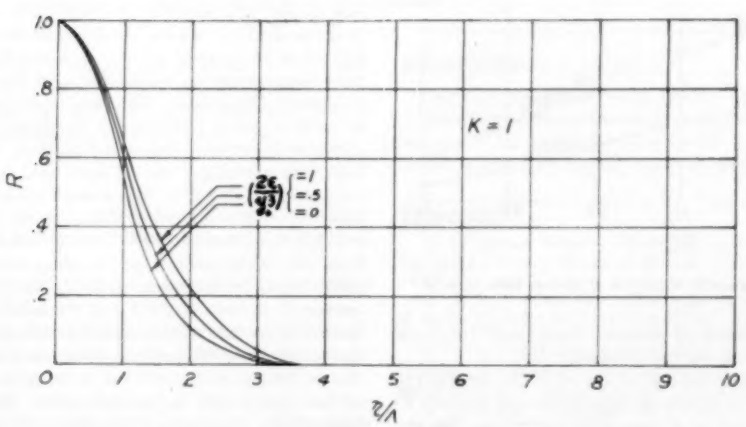

Fig. 4(a) Effect of wall on correlation of particle motion; $K = 1$

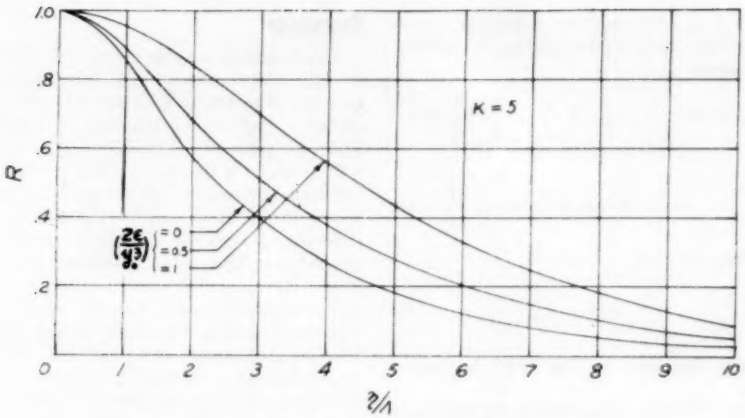

Fig. 4(b) Effect of wall on correlation of particle motion; $K = 5$

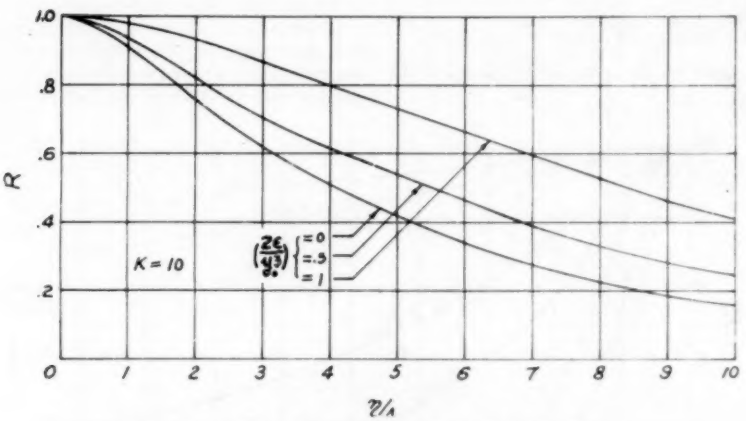

Fig. 4(c) Effect of wall on correlation of particle motion; $K = 10$

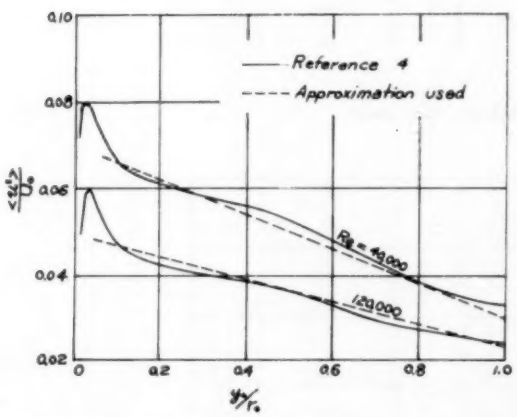

Fig. 5 Variation of intensity of motion of stream from wall [4]

secondary. The probability of particle-stream encounter is the basic mechanism affecting particle diffusivity [12].

In the immediate neighborhood of the wall, the intensity of turbulence of the fluid decreases sharply to zero at the wall together with a sharp gradient of mean fluid velocity. The contribution of the reduced fluid turbulence can be accounted for by the foregoing solution, giving rise to reduced turbulence in the motion of solid particles to zero at the wall. However, the sharp mean velocity gradient of fluid motion gives rise to significant spinning motion of the solid particles. In other words, item (*e*) in the section "Fundamental Considerations," should not be neglected. Qualitatively, the spinning motion of the solid particles due to the fluid velocity gradient leads to the motion due to Magnus effect, i.e., a force is induced by the spin, causing the solid particle to move away as it approaches the wall. This effect is more pronounced for particles smaller than the boundary-layer thickness. Statistically, while some solid particles hit the wall as a result of random motion, a significant portion of the solid particles is turned away before reaching it. This explains the fact that a straight run of duct used in the pneumatic conveyance of solids suffers only a small amount of wear over a long time.

When heat is transferred from a wall at higher temperature than that of the mean of the two-phase stream, the solid particles receive heat by radiation, while the fluid receives heat by convection from both the wall and the solid particles. Greater intensity of particle motion near the wall gives greater amount of convection from the particles, resulting in a lower temperature of the particles near the wall than in the mean stream. The amount of heat transferred is therefore higher than it would be if the main-stream properties were used. On the other hand, if the wall is at a lower temperature, the particles near the wall are

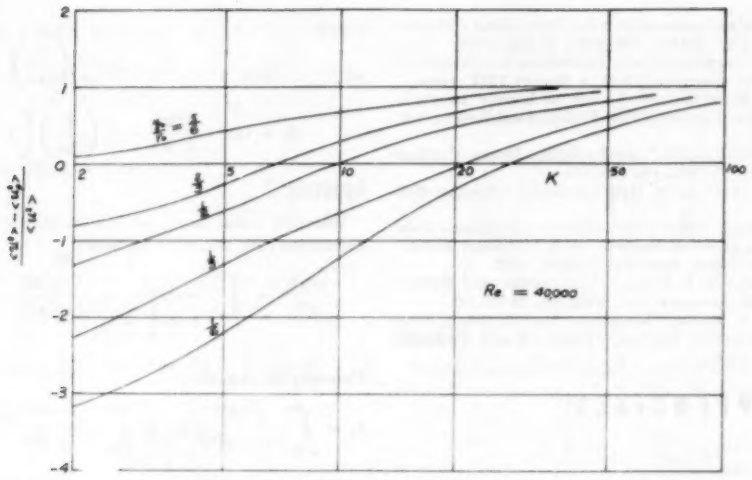

Fig. 6 Deviation of intensity of motion of a particle from that of the mean stream at various distances from wall at duct Reynolds number of 40,000

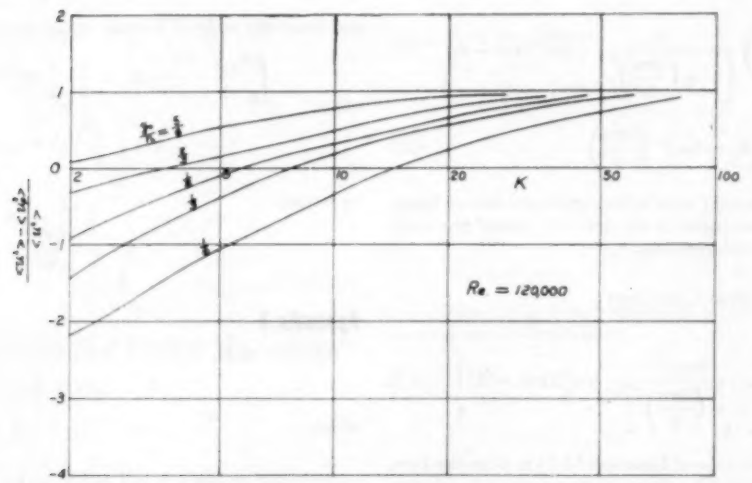

Fig. 7 Deviation of intensity of motion of a particle from that of the mean stream at various distances from wall at duct Reynolds number of 120,000

cooled by convection to the stream and radiation to the wall. In addition, heat is transferred by radiation from the particles in the mean stream, resulting in a still greater heat-transfer rate than if only the mean-stream properties were used.

Conclusions

1 The presence of the wall affects the intensity of motion of the particles in the mean stream of a two-phase duct flow significantly.

2 The particle diffusivity is not significantly affected by the wall.

3 The intensity of particle motion increases toward the wall. The scale of turbulence of particle motion decreases toward the wall.

4 The effect of the wall on the mean stream is more predominating for low duct Reynolds numbers than for high Reynolds numbers.

Acknowledgment

This work was sponsored by Project SQUID which is supported by the Office of Naval Research, Department of the Navy, under contract Nonr 1858 (25) NR-098-038. Reproduction in full or in part is permitted for any use of the United States Government.

References

1 S. L. Soo, "Statistical Properties of Momentum Transfer in Two-Phase Flow," *Chemical Engineering Science*, vol. 5, 1956, pp. 57–67.

2 J. L. Lumley, "Some Problems Connected With the Motion of Small Particles in Turbulent Fluid," PhD thesis in Aeronautics, The Johns Hopkins University, Baltimore, Md., 1957.

3 S. L. Soo and H. K. Ihrig, Jr., "Experimental Determination of Statistical Properties of Two-Phase Turbulent Motion," Project Squid Technical Report PR-82-P, August, 1958.

4 J. Laufer, "Investigation of Turbulent Flow in a Two-Dimensional Channel," NACA Report 1053, 1951.

5 D. R. Chapman and R. H. Kester, "Turbulent Boundary

Layer and Skin Friction Measurements in Axial Flow Along Cylinder at Mach Number 0.5 to 3.6," NACA TN 3097, March, 1954.
6 P. S. Klebanoff, "Characteristics of Turbulence in a Boundary Layer With Zero Pressure Gradient," NACA Report 1247, 1955.
7 G. K. Batchler, "Kolmogoroff's Theory of Locally Isotropic Turbulence," *Proceedings of The Cambridge Philosophical Society*, vol. 43, 1949, p. 533.
8 H. Lamb, "Hydrodynamics," sixth edition, Dover Publications, Inc., New York, N. Y., 1932, pp. 130–134.
9 A. B. Basset, "A Treatise in Hydrodynamics," George Bell and Sons, 1888.
10 C. M. Tchen, "Mean Value and Correlation Problems Connected With the Motion of Small Particles in a Turbulent Fluid," Dissertation, Delft, The Hague Martinus Nijhoff, 1947.
11 T. K. Sherwood and R. L. Pigford, "Absorption and Extraction," McGraw-Hill Book Company, Inc., 1952, pp. 38–40, 60.
12 S. L. Soo and R. L. Peskin, "Statistical Distribution of Solid Phase in Two-Phase Turbulent Motion," Project Squid Technical Report, PR-80-R, May, 1958.

APPENDIXES[3]

Appendix 1

Solution of Equation (18):

$$ {}_1\ddot{y} + b_1\dot{y} = \frac{\dot{v} - {}_0\ddot{y}}{{}_0y^2} \tag{18}$$

where

$$ {}_0y = y_0 + \sum \left(\frac{-1}{2\pi n}\right) \frac{A_n}{\left[1 + \left(\frac{2\pi n}{b}\right)^2\right]^{1/2}} \cos(2\pi nt - \theta_1) \tag{20}$$

$$ \theta_1 = \tan^{-1}\left(\frac{2\pi n}{b}\right) \tag{21}$$

Since, in general, the second term in the right-hand side of Equation (20) is small as compared to the first (i.e., initial position), only the first term is considered in ${}_0y$:[3]

$$ {}_1\ddot{y} + b_1\dot{y} = \frac{1}{{y_0}^2}\left\{\sum (2\pi n)A_n \cos 2\pi nt - \sum \frac{2\pi nA_n}{\left[1 + \left(\frac{2\pi n}{b}\right)^2\right]^{1/2}} \cos(2\pi nt - \theta_1)\right\} \tag{A.1}$$

The complementary solution of Equation (A.1) is of no use here, because it vanishes in obtaining the mean-square particle velocity. The particular solution of Equation (A.1) is the sum of the following two equations

$$ {}_1\ddot{y} + b_1\dot{y} = \frac{1}{{y_0}^2} \sum (2\pi n)A_n \cos 2\pi nt \tag{A.2}$$

$$ {}_1\ddot{y} + b_1\dot{y} = -\sum \frac{2\pi nA_n}{\left[1 + \left(\frac{2\pi n}{b}\right)^2\right]^{1/2}} \cos(2\pi nt - \theta_1) \tag{A.3}$$

and it is:

$$ {}_1y = \sum \frac{1}{{y_0}^2} \frac{-A_n}{b\left[1 + \left(\frac{2\pi n}{b}\right)^2\right]^{1/2}} \cos(2\pi nt + \theta_2) + \sum \frac{1}{{y_0}^2} \frac{A_n}{b\left[1 + \left(\frac{2\pi n}{b}\right)^2\right]} \cos(2\pi nt - \theta_2) \tag{22}$$

where

$$ \theta_2 = \tan^{-1}\left(\frac{b}{2\pi n}\right) \tag{23}$$

$$ \theta_2 = \tan^{-1}\left\{\frac{2\pi n}{b} - \frac{1}{2}\left(\frac{b}{2\pi n}\right)\left[1 + \left(\frac{2\pi n}{b}\right)^2\right]\right\} \tag{24}$$

Appendix 2

Intensity ratio $\langle {}_0v_p{}^2\rangle/\langle v^2\rangle$ (without wall interference): From Equations (26) and (27) we have

$$ \frac{\langle {}_0v_p{}^2\rangle}{\langle v^2\rangle} = \int_0^\infty \frac{1}{1 + \left(\frac{2\pi n}{b}\right)^2} \frac{2\sqrt{\pi}\lambda}{\sqrt{\langle v^2\rangle}} e^{-\lambda^2\pi^2n^2/\langle v^2\rangle}\, dn \tag{A.4}$$

Considering the integral:

$$ I_1 = \int_0^\infty \frac{e^{-\alpha^2n^2}}{1 + \beta^2n^2}\, dn = \int_0^\infty \frac{e^{-\alpha^2n}}{1 + \beta^2n} \frac{dn}{\sqrt{n}} = \frac{\pi}{2\beta} \int_0^\infty \frac{\frac{1}{\beta} e^{-\alpha^2n}}{\pi\sqrt{n}\left(\frac{1}{\beta^2} + n\right)}\, dn \tag{A.5}$$

and from the table of Laplace transforms,[4] we have

$$ \int_0^\infty \frac{e^{-\alpha^2n^2}}{1 + \beta^2n^2}\, dn = \frac{\pi}{2} \frac{1}{\beta} e^{\alpha^2/\beta^2} \operatorname{erfc}\left(\frac{\alpha}{\beta}\right) \tag{A.6}$$

$$ \frac{\langle {}_0v_p{}^2\rangle}{\langle v^2\rangle} = \sqrt{\pi}\left(\frac{1}{K}\right) e^{1/K^2} \operatorname{erfc}\left(\frac{1}{K}\right) \tag{28}$$

by letting

$$ K^2 = \frac{4\langle v^2\rangle}{\lambda^2b^2} \tag{29}$$

Appendix 3

Intensity ratio, $\langle v_p{}^2\rangle/\langle v^2\rangle$ (with wall interference):

$$ \langle v_p{}^2\rangle = \langle {}_0\dot{y}^2\rangle + 2\epsilon\langle {}_0\dot{y}_1\dot{y}\rangle \tag{32}$$

where

$$ \langle {}_0\dot{y}^2\rangle = \langle {}_0v_p{}^2\rangle = \langle v^2\rangle \sqrt{\pi}\left(\frac{1}{K}\right) e^{1/K^2} \operatorname{erfc}\left(\frac{1}{K}\right) \tag{28}$$

and from Equation (20) and Equation (22):

$$ \langle {}_0\dot{y}_1\dot{y}\rangle = \lim_{l\to\infty} \frac{1}{2l} \int_{-l}^{l} {}_0\dot{y}_1\dot{y}\, dt = \sum_m \sum_n \frac{1}{{y_0}^2}\left(\frac{2\pi m}{b}\right) \frac{A_nA_m}{\left[1 + \left(\frac{2\pi n}{b}\right)^2\right]^{1/2}\left[1 + \left(\frac{2\pi m}{b}\right)^2\right]^{1/2}} \left[\lim_{l\to\infty} \frac{1}{2l} \int_{-l}^{l} \sin(2\pi nt - \theta_1)\sin(2\pi mt + \theta_2)dt\right] - \sum_m \sum_n \frac{1}{{y_0}^2}\left(\frac{2\pi m}{b}\right) \frac{A_nA_m}{\left[1 + \left(\frac{2\pi n}{b}\right)^2\right]^{1/2}\left[1 + \left(\frac{2\pi m}{b}\right)^2\right]} \left[\lim_{l\to\infty} \frac{1}{2l} \int_{-l}^{l} \sin(2\pi nt - \theta_1)\sin(2\pi mt - \theta_2)dt\right] \tag{A.7}$$

[3] The Appendixes are by C. L. Tien.

[4] R. V. Churchill, "Modern Operational Method in Engineering," McGraw-Hill Book Company, Inc., New York, N. Y., 1944, Appendix 4, formula III.

It can be easily shown that for all values of m and n:

$$\int_{-l}^{l} \sin(2\pi nt - \theta_1) \sin(2\pi mt + \theta_2)dt = 0 \qquad (A.8)$$

and

$$\int_{-l}^{l} \sin(2\pi nt - \theta_1) \sin(2\pi mt - \theta_2)dt = \begin{cases} 0 & \text{for } m \neq n \\ \dfrac{l\left(\dfrac{2\pi n}{b}\right)}{\left[1 + \left(\dfrac{2\pi n}{b}\right)^2\right]^{1/2}} & \text{for } m = n \end{cases} \qquad (A.9)$$

With Equations (A.8) and (A.9), Equation (A.7) becomes:

$$\langle \dot{y}_1 \dot{y} \rangle = -\sum_n \frac{1}{2y_0^2}\left(\frac{2\pi n}{b}\right)^2 \frac{A_n^2}{\left[1 + \left(\frac{2\pi n}{b}\right)^2\right]^2}$$

$$= -\langle v^2 \rangle \int_0^\infty \frac{1}{y_0^2}\left(\frac{2\pi n}{b}\right)^2 \frac{f(n)}{\left[1 + \left(\frac{2\pi n}{b}\right)^2\right]^2} dn$$

$$= -\langle v^2 \rangle \int_0^\infty \frac{1}{y^2}\left(\frac{2\pi n}{b}\right)^2 \frac{1}{\left[1 + \left(\frac{2\pi n}{b}\right)^2\right]^2} \frac{2\sqrt{\pi}\lambda}{\sqrt{\langle v^2 \rangle}} e^{-\lambda^2\pi^2 n^2/\langle v^2 \rangle} dn \qquad (A.10)$$

Considering the integral:

$$I_4 = \int_0^\infty \frac{n^2 e^{-\alpha^2 n^2}}{(1 + \beta^2 n^2)^2} dn = \frac{1}{\beta^2}\int_0^\infty \frac{e^{-\alpha^2 n^2}}{1 + \beta^2 n^2} dn - \frac{1}{\beta^2}\int_0^\infty \frac{e^{-\alpha^2 n^2}}{(1 + \beta^2 n^2)^2} dn \qquad (A.11)$$

and evaluating the second integral in the right side by successive integration by parts:

$$\int_0^\infty \frac{e^{-\alpha^2 n^2}}{(1 + \beta^2 n^2)^2} dn = \int_0^\infty \left[\frac{n}{2(1 + \beta^2 n^2)} + \frac{1}{2\beta}\tan^{-1}\beta n\right] 2\alpha^2 n e^{-\alpha^2 n^2} dn$$

$$= \alpha^2 \int_0^\infty \frac{n^2 e^{-\alpha^2 n^2}}{1 + \beta^2 n^2} dn + \frac{\alpha^2}{\beta^2}\int_0^\infty n e^{-\alpha^2 n^2}\tan^{-1}\beta n\, dn$$

$$= \alpha^2 \int_0^\infty \left(\frac{n}{\beta^2} - \frac{1}{\beta^2}\tan^{-1}\beta n\right) 2\alpha^2 n e^{-\alpha^2 n^2} dn + \frac{\alpha^2}{\beta^2}\int_0^\infty n e^{-\alpha^2 n^2}\tan^{-1}\beta n\, dn$$

$$= \frac{2\alpha^4}{\beta^2}\int_0^\infty n^2 e^{-\alpha^2 n^2} dn + \left(\frac{\alpha^2}{\beta^2} - \frac{2\alpha^4}{\beta^2}\right)\int_0^\infty n e^{-\alpha^2 n^2}\tan^{-1}\beta n\, dn$$

$$= \frac{\alpha\sqrt{\pi}}{2\beta^2} - \frac{\pi}{2\beta}\left(\tfrac{1}{2} - \frac{\alpha^2}{\beta^2}\right) e^{\alpha^2/\beta^2}\operatorname{erfc}\left(\frac{\alpha}{\beta}\right) \qquad (A.12)$$

Equation (A.11) becomes

$$I_2 = -\frac{\alpha\sqrt{\pi}}{2\beta^4} + \frac{\pi}{2\beta^3}\left(\tfrac{1}{2} + \frac{\alpha^2}{\beta^2}\right) e^{\alpha^2/\beta^2}\operatorname{erfc}\left(\frac{\alpha}{\beta}\right) \qquad (A.13)$$

With Equation (A.12), Equation (A.9) can be expressed as

$$\langle \dot{y}_1 \dot{y} \rangle = -\langle v^2 \rangle \left(\frac{1}{y_0^2}\right)\left(\frac{1}{K}\right)\left[\sqrt{\pi}\left(\tfrac{1}{2} + \frac{1}{K^2}\right) e^{1/K^2}\operatorname{erfc}\left(\frac{1}{K}\right) - \frac{1}{K}\right] \qquad (A.14)$$

Hence, from Equation (32);

$$\frac{\langle v_p^2 \rangle}{\langle v^2 \rangle} = \frac{\sqrt{\pi}}{K}\left[1 - \frac{2\epsilon}{y_0^2}\left(\tfrac{1}{2} + \frac{1}{K^2}\right)\right] e^{1/K^2}\operatorname{erfc}\left(\frac{1}{K}\right) + \frac{2\epsilon}{y_0^2 K^2} \qquad (33)$$

Appendix 4

Correlation coefficient, ${}_0R_y'$ (without wall interference): Without wall interference, i.e., $\epsilon = 0$, Equation (39) is given as

$$R_y' = {}_0R_y' = \frac{\displaystyle\int_0^\infty \frac{f(n)}{1 + \left(\frac{2\pi n}{b}\right)^2}\cos 2\pi n \frac{\eta}{\sqrt{\langle v^2 \rangle}} dn}{\displaystyle\int_0^\infty \frac{f(n)}{1 + \left(\frac{2\pi n}{b}\right)^2} dn} \qquad (A.15)$$

Considering the integral:

$$I_3 = \int_0^\infty \frac{e^{-\alpha^2 n^2}}{1 + \beta^2 n^2}\cos\gamma n\, dn = \frac{1}{\beta}\int_0^\infty \frac{e^{-\alpha_1^2 n^2}}{1 + n^2}\cos\gamma_1 n\, dn \qquad (A.16)$$

where

$$\alpha_1 = \frac{\alpha}{\beta}, \quad \gamma_1 = \frac{\gamma}{\beta}$$

and differentiating it with respect to γ_1, the following differential equation can be established:

$$\frac{d^2 I_3}{d\gamma_1^2} - \frac{dI_3}{d\gamma_1} = -\frac{1}{\beta}\int_0^\infty e^{-\alpha_1^2 n^2}\cos\gamma_1 n\, dn = -\frac{\sqrt{\pi}}{2\alpha} e^{-\gamma_1/4\alpha_1^2} \qquad (A.17)$$

The solution will be

$$I_3 = c_1 e^{-\gamma_1} + c_2 e^{\gamma_1} + I_{3p} \qquad (A.18)$$

By variation of parameter method:

$$I_{3p} = \int_0^{\gamma_1} K(\gamma_1, t) f(t) dt \qquad (A.19)$$

where

$$f(t) = -\frac{\sqrt{\pi}}{2\alpha} e^{-\gamma_1/4\alpha_1^2}$$

$$K(\gamma_1, t) = \frac{\phi_1(t)\phi_2(\gamma_1) - \phi_1(\gamma_1)\phi_2(t)}{W(\phi_1, \phi_2)(t)} = \tfrac{1}{2}(e^{-t}e^{\gamma_1} - e^t e^{-\gamma_1})$$

$\phi_1(t)$ and $\phi_2(t)$ are two linearly independent solutions of the homogeneous equation

$$W(\phi_1, \phi_2)(t) = \begin{vmatrix} \phi_1 & \phi_2 \\ \phi_1' & \phi_2' \end{vmatrix}(t) = \begin{vmatrix} e^{-t} & e^t \\ -e^{-t} & e^t \end{vmatrix} = 2$$

or

$$I_{3p} = {}^1/_2 \int_0^{\gamma_1} (e^{-t}e^{\gamma_1} - e^t e^{-\gamma_1}) \left(-\frac{\sqrt{\pi}}{2\alpha} e^{-t^2/4\alpha^2} \right) dt \quad \text{(A.20)}$$

Neglecting the constant coefficients of $e^{-\gamma_1}$, e^{γ_1}, since they are included in the complementary solution, we get

$$I_{3p} = -\frac{\pi}{4\beta} e^{\alpha_1^2} \left[e^{\gamma_1} \operatorname{erf} \left(\frac{\gamma_1}{2\alpha_1} + \alpha_1 \right) - e^{-\gamma_1} \operatorname{erf} \left(\frac{\gamma_1}{2\alpha_1} - \alpha_1 \right) \right] \quad \text{(A.21)}$$

Applying the boundary conditions:

$$I_3 = \int_0^\infty \frac{e^{-\alpha^2 n^2}}{1 + \beta^2 n^2} dn = \frac{\pi}{2\beta} e^{\alpha^2/\beta^2} \operatorname{erfc} \left(\frac{\alpha}{\beta} \right) \quad \text{(A.22)}$$

as $\gamma \to 0$ $\quad \beta = 0$ i.e., $\gamma_1 \to 0$

$$I_3 = 0 \quad \text{(A.23)}$$

as $\gamma \to \infty$ $\quad \beta$ finite, i.e., $\gamma_1 \to \infty$

the constants c_1, c_2 can be determined, and the solution will be:

$$I_3 = \frac{\pi}{4\beta} e^{\alpha^2/\beta^2} \left\{ e^{-\gamma/\beta} \left[2 - \operatorname{erfc} \left(\frac{\gamma}{2\alpha} - \frac{\alpha}{\beta} \right) \right] + e^{\gamma/\beta} \operatorname{erfc} \left(\frac{\gamma}{2\alpha} + \frac{\alpha}{\beta} \right) \right\} \quad \text{(A.24)}$$

With Equations (27), (A.6), and (A.24), Equation (A.15) can be easily shown as follows:

$${}_0R_y' = \frac{1}{2 \operatorname{erfc} \left(\frac{1}{K} \right)} \left\{ e^{-2\eta/K\lambda} \left[2 - \operatorname{erfc} \left(\frac{\eta}{\lambda} - \frac{1}{K} \right) \right] + e^{2\eta/K\lambda} \operatorname{erfc} \left(\frac{\eta}{\lambda} + \frac{1}{K} \right) \right\} \quad \text{(40)}$$

Appendix 5

Correlation coefficient, R_y' (with wall interference):

$$R_y' \cong \frac{\displaystyle\int_0^\infty \left[1 - \frac{2\epsilon}{y_0^3} \frac{\left(\frac{2\pi n}{b}\right)^2}{1 + \left(\frac{2\gamma n}{b}\right)^2} \right] \frac{f(n)}{1 + \left(\frac{2\pi n}{b}\right)^2} \cos 2\pi n \frac{\eta}{\sqrt{\langle v^2 \rangle}} \, dn}{\displaystyle\int_0^\infty \left[1 - \frac{2\epsilon}{y_0^3} \frac{\left(\frac{2\pi n}{b}\right)^2}{1 + \left(\frac{2\pi n}{b}\right)^2} \right] \frac{f(n)}{1 + \left(\frac{2\pi n}{b}\right)^2} dn} \quad \text{(39)}$$

The denominator in Equation (39) is $\langle v^2 \rangle / \langle v_p^2 \rangle$ and also let

$$\Phi \left(K, \frac{\eta}{\lambda} \right) = \int_0^\infty \frac{\left(\frac{2\pi n}{b}\right)^2 f(n)}{\left[1 + \left(\frac{2\pi n}{b}\right)^2 \right]^2} \cos 2\pi n \frac{\eta}{\sqrt{\langle v^2 \rangle}} \, dn \quad \text{(A.25)}$$

therefore

$$R_y' = \left\{ \left[{}_0R_y' \frac{\langle v_p^2 \rangle}{\langle v^2 \rangle} \right] - \frac{2\epsilon}{y_0^3} \Phi \left(K, \frac{\eta}{\lambda} \right) \right\} \frac{\langle v^2 \rangle}{\langle v_p^2 \rangle} = {}_0R_y' \frac{\langle v_p^2 \rangle}{\langle v_p^2 \rangle} - \frac{2\epsilon}{y_0^3} \Phi \left(K, \frac{\eta}{\lambda} \right) \frac{\langle v^2 \rangle}{\langle v_p^2 \rangle} \quad \text{(41)}$$

The expression, $\Phi(K, \eta/\lambda)$ can be obtained by considering the integral:

$$I_4 = \int_0^\infty \frac{n^2 e^{-\alpha^2 n^2}}{(1 + \beta^2 n^2)^2} \cos \gamma n \, dn \quad \text{(A.26)}$$

Following the same method in Appendix 4,

$$\frac{d^2 I_4}{d\gamma_1^2} - I_4 = \frac{1}{\beta^2} \frac{d^2 I_3}{d\gamma_1^2} = \frac{1}{\beta^2} I_3 - \frac{\sqrt{\pi}}{2\alpha\beta^2} e^{-\gamma_1^2/4\alpha^2} \quad \text{(A.27)}$$

with the boundary conditions:

$$I_4 = \frac{1}{\beta^2} \int_0^\infty \frac{n^2 e^{-\alpha_1^2 n^2}}{(1 + n^2)^2} dn = -\frac{2\sqrt{\pi}}{2\beta^3} + \frac{\pi}{2\beta^3} (\alpha_1^2 + {}^1/_2) e^{\alpha_1^2} \operatorname{erfc} \alpha_1 \quad \text{(A.28)}$$

as $\gamma \to 0$ $\quad \beta \neq 0$, i.e., $\gamma_1 \to 0$

$$I_4 = 0 \quad \text{(A.29)}$$

as $\gamma \to \infty$ $\quad \beta$ finite, i.e., $\gamma_1 \to \infty$

it can be shown,

$$I_4 = \frac{\sqrt{\pi}}{2\beta^2} \frac{\beta}{\alpha} e^{\alpha^2/\beta^2 + \gamma/\beta} \Phi_1 \left(\frac{\alpha}{\beta}, \frac{\gamma}{2\alpha} \right) - \frac{\sqrt{\pi}}{2\beta^2} \frac{\beta}{\alpha} e^{\alpha^2/\beta^2} - \gamma/\beta \, \Phi_2 \left(\frac{\alpha}{\beta}, \frac{\gamma}{2\alpha} \right) \quad \text{(A.30)}$$

where

$$\Phi_1 \left(\frac{\alpha}{\beta}, \frac{\gamma}{2\alpha} \right) = \frac{\sqrt{\pi}}{2} \frac{\alpha}{\beta} \left[{}^1/_2 \operatorname{erfc} \left(\frac{\gamma}{2\alpha} + \frac{\alpha}{\beta} \right) - \frac{\alpha}{\beta} \operatorname{ierfc} \left(\frac{\gamma}{2\alpha} + \frac{\alpha}{\beta} \right) \right] \quad \text{(A.31)}$$

$$\Phi_2 \left(\frac{\alpha}{\beta}, \frac{\gamma}{2\alpha} \right) = \frac{\sqrt{\pi}}{2} \frac{\alpha}{\beta} \left[\frac{\gamma}{\beta} + {}^1/_2 \operatorname{erfc} \left(\frac{\gamma}{2\alpha} - \frac{\alpha}{\beta} \right) + \frac{\alpha}{\beta} \operatorname{ierfc} \left(\frac{\gamma}{2\alpha} - \frac{\alpha}{\beta} \right) - \left(2 \frac{\alpha^2}{\beta^2} + 1 \right) \right] \quad \text{(A.32)}$$

From Equations (A.25), (27), and (A.30)

$$\Phi \left(K, \frac{\eta}{\lambda} \right) = e^{1/K^2 + 2\eta/K\lambda} \Phi_1 \left(K, \frac{\lambda}{\eta} \right) + e^{1/K^2 - 2\eta K/K\lambda} \Phi_2 \left(K, \frac{\eta}{\lambda} \right) \quad \text{(A.33)}$$

where

$$\Phi_1 \left(K, \frac{\lambda}{\eta} \right) = \frac{\sqrt{\pi}}{2K} \left[{}^1/_2 \operatorname{erfc} \left(\frac{\lambda}{\eta} + \frac{1}{K} \right) - \frac{1}{K} \operatorname{ierfc} \left(\frac{\eta}{\lambda} + \frac{1}{K} \right) \right] \quad \text{(A.34)}$$

$$\Phi_2 \left(K, \frac{\eta}{\lambda} \right) = \frac{\sqrt{\pi}}{2K} \left[\frac{2\eta}{K\lambda} + {}^1/_2 \operatorname{erfc} \left(\frac{\eta}{\lambda} - \frac{1}{K} \right) + \frac{1}{K} \operatorname{ierfc} \left(\frac{\lambda}{\eta} - \frac{1}{K} \right) - \left(\frac{2}{K^2} + 1 \right) \right] \quad \text{(A.35)}$$

Appendix 6

Diffusivity ratio, D_p/D (with or without wall interference): From Einstein's equation of diffusivity:

$$\frac{D_p}{D} = \frac{l_p}{l}\sqrt{\frac{\langle v_p^2\rangle}{\langle v^2\rangle}} \tag{A.36}$$

where by definition,

$$l = \int_0^\infty e^{-\eta^2/\lambda^2}d\eta = \frac{\sqrt{\pi}}{2}\lambda \tag{A.37}$$

$$l_p = \int_0^\infty R\eta' d\eta' = \lambda\sqrt{\frac{\langle v_p^2\rangle}{\langle v^2\rangle}}\int_0^\infty R\eta'\, d\left(\frac{\eta}{\lambda}\right) \tag{A.38}$$

with Equation (41),

$$l_p = \lambda\sqrt{\frac{\langle v_p^2\rangle}{\langle v^2\rangle}}\left\{\frac{\langle v'^2_p\rangle}{\langle v_p^2\rangle}\int_0^\infty R_y' d\left(\frac{\eta}{\lambda}\right) - \frac{2\epsilon}{y_0^2}\frac{\langle v^2\rangle}{\langle v_p^2\rangle}\int_0^\infty \Phi\left(K,\frac{\eta}{\lambda}\right)d\left(\frac{\eta}{\lambda}\right)\right\} \tag{A.39}$$

it can be easily shown that, from Equation (40):

$$\int_0^\infty {}_0R_y' d\left(\frac{\eta}{\lambda}\right) = \frac{1}{2\text{erfc}\left(\frac{1}{K}\right)}\int_0^\infty \left\{e^{-2\eta/K\lambda}\left[2 - \text{erfc}\left(\frac{\eta}{\lambda} - \frac{1}{K}\right)\right] + e^{2\eta/K\lambda}\,\text{erfc}\left(\frac{\eta}{\lambda} + \frac{1}{K}\right)\right\} d\left(\frac{\eta}{\lambda}\right) = \frac{1}{2\text{erfc}\left(\frac{1}{K}\right)} Ke^{-1/K^2} \tag{A.40}$$

and from Equations (A.33), (A.34), and (A.35):

$$\int_0^\infty \Phi\left(K,\frac{\eta}{\lambda}\right)d\left(\frac{\eta}{\lambda}\right) = \int_0^\infty e^{1/K^2+2\eta/K\lambda}\Phi_1\left(K,\frac{\eta}{\lambda}\right)d\left(\frac{\eta}{\lambda}\right) + \int_0^\infty e^{1/K^2-2\eta/K\lambda}\Phi_2\left(K,\frac{\eta}{\lambda}\right)d\left(\frac{\eta}{\lambda}\right) = 0 \tag{A.41}$$

So, with Equation (28),

$$l_p = \frac{\sqrt{\pi}}{2}\lambda\sqrt{\frac{\langle v_p^2\rangle}{\langle v^2\rangle}} \tag{A.42}$$

Combining Equations (A.37) and (A.42),

$$\frac{l_p}{l} = \sqrt{\frac{\langle v^2\rangle}{\langle v_p^2\rangle}} \tag{A.43}$$

or from Equation (A.35),

$$\frac{D_p}{D} = \frac{l_p}{l}\sqrt{\frac{\langle v_p^2\rangle}{\langle v^2\rangle}} = 1 \tag{A.44}$$

THEODORE R. GOODMAN
Senior Engineer,
Allied Research Associates, Inc.,
Boston, Mass.

JOHN J. SHEA
Staff Engineer,
Allied Research Associates, Inc.,
Boston, Mass.

The Melting of Finite Slabs[1]

An approximate method, known as the heat-balance integral, is used to determine the melting rate of a finite slab which is initially at a uniform temperature below the melting point. The slab is acted upon by a constant heat input at one face and has its other face either insulated or kept at its initial temperature. The first three terms of series solutions in an intrinsically small parameter are obtained for the time histories of melting and the temperature distribution in the slab.

ONE-DIMENSIONAL heat conduction in a solid finite slab is a familiar and elementary example of a linear boundary-value problem and readily yields its solution to any of the elegant methods available for treating such problems. If, however, a sufficiently strong heat flux is applied at one end of an initially solid slab, the slab begins to melt. The linearity of the problem now disappears and the classical solutions are no longer applicable. Indeed, no general analytical method is known which will provide an exact solution to heat-conduction problems involving a moving boundary such as the melt line, the location of which is unknown a priori and is in fact required as part of the solution. The "heat-balance integral" method of Goodman[2] is an approximate analytical method which has been applied successfully to certain melting problems of this type.

The purpose of this paper is to apply the heat-balance integral method to the following melting problems: A constant heat flux is applied at one face of a finite slab which is initially at some uniform temperature below the melting point; the other face of the slab is either insulated or kept at its initial temperature. Eventually the slab begins to melt. The problem is to determine how the melting propagates and how the temperature is distributed in the melted and unmelted portions of the slab.

The heat-balance integral method is introduced in Section 1 and illustrated by determining the temperature distribution in the slab at the instant melting starts; i.e., by determining the initial conditions for the melting problem. The melting problem is then stated in Section 2, both exactly and with the heat-balance integral approximation. The approximate problem is solved in Section 3 and the results are displayed and discussed in succeeding sections.

1 The Heat-Balance Integral Approximation

While the heat-balance integral method is potentially applicable to more general heat-transfer problems, only one-dimensional problems are treated in this paper. For such problems, the method consists of:

(*a*) Assuming that the temperature distribution depends on the space variable in some particular fashion consistent with the boundary conditions; e.g., the temperature might be assumed to be a polynomial or a finite trigonometric series in the space variable.

(*b*) Substituting the assumed form of the temperature distribution into the heat-conduction equation and integrating with respect to the space variable over the appropriate interval to obtain the heat-balance integral, i.e., the resulting ordinary differential equation with time as the independent variable.

(*c*) Solving the heat-balance integral to obtain the time dependence of the temperature distribution and of whatever moving boundaries are present.

Although the heat-balance integral method is particularly convenient in nonlinear melting problems, it is equally applicable to linear problems, and will be employed in this section to determine the temperature distribution in the slab before melting starts. The solution to this linear problem provides the initial conditions for the nonlinear melting problem.

Consider a homogeneous solid slab bounded by the planes $x = 0$ and $x = l$, as shown in Fig. 1. Beginning at time $t = 0$, a constant flux H is applied at the face $x = 0$; initially, the temperature, u_2, of the slab is $-V$ (the temperature scale is chosen so that the melting-point temperature is 0). The temperature distribution must satisfy the heat-conduction equation,

$$\kappa_2 \frac{\partial^2 u_2}{\partial x^2} = \frac{\partial u_2}{\partial t} \qquad 0 < x < l, \quad t > 0 \tag{1}$$

and the boundary condition

$$k_2 \frac{\partial u_2}{\partial x} = -H \qquad x = 0, \quad t > 0 \tag{2}$$

where κ_2 and k_2 are the thermal diffusivity and conductivity, respectively, of the solid.

Ignoring for the moment whatever boundary condition is prescribed at $x = l$, one can make the following observation: Since the mechanism of heat conduction is diffusion, the effect of the excitation H at $x = 0$ is not immediately felt throughout the slab, but rather is confined, for early times, to some region extending from $x = 0$ to, say, $x = \delta$ where $\delta(t)$ is less than l and bounds the region containing significant thermal gradients at time t. This qualitative observation can be made the basis of an analytic technique by postulating the existence of a function $\delta(t)$ such that

$$u_2 = -V \qquad x = \delta, \quad t > 0 \tag{3}$$

$$\frac{\partial u_2}{\partial x} = 0 \qquad x = \delta, \quad t > 0 \tag{4}$$

[1] This research was supported by the United States Air Force through the Air Force Office of Scientific Research of the Air Research and Development Command, under Contract No. AF 49(638)-347. Reproduction in whole or in part is permitted for any purpose of the United States Government.

[2] T. R. Goodman, "The Heat-Balance Integral and Its Application to Problems Involving a Change of Phase," TRANS. ASME, vol. 80, 1958, pp. 335–342.

Presented at the West Coast Conference of the Applied Mechanics Division, Stanford, Calif., September 9–11, 1959, of THE AMERICAN SOCIETY OF MECHANICAL ENGINEERS.

Discussion of this paper should be addressed to the Secretary, ASME, 29 West 39th Street, New York, N. Y., and will be accepted until April 10, 1960, for publication at a later date. Discussion received after the closing date will be returned.

NOTE: Statements and opinions advanced in papers are to be understood as individual expressions of their authors and not those of the Society. Manuscript received at ASME Applied Mechanics Division, December 17, 1958. Paper No. 59—APMW-11.

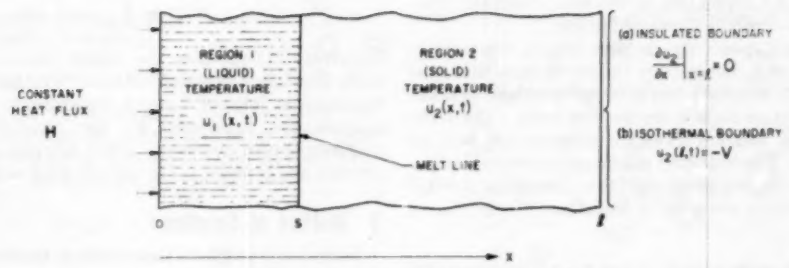

Fig. 1 Schematic representation of melting problem

$$\delta = 0 \qquad t = 0 \tag{5}$$

The function $\delta(t)$ is called the thermal-layer thickness and is analogous to the boundary-layer thickness in fluid mechanics.

The heat-balance integral method now provides an approximate solution to the problem of determining $u_2(x, t)$ and $\delta(t)$ so as to satisfy Equations (1) through (5). Assume that $u_2(x, t)$ is of the form

$$u_2(x, t) = a(t) + b(t)x + c(t)x^2 \tag{6}$$

Substitution of the boundary conditions, Equations (2) through (4), into Equation (6) gives

$$u_2(x, t) = -V + \frac{H}{2k_2\delta}(\delta - x)^2 \tag{7}$$

Integration of the heat-conduction equation, Equation (1), over x from 0 to δ [by Equations (3) and (4), this is equivalent to integration from 0 to l] provides

$$\kappa_2\left[\frac{\partial u_2}{\partial x}(\delta, t) - \frac{\partial u_2}{\partial x}(0, t)\right] = \frac{d}{dt}(\theta_2 + V\delta) \tag{8}$$

where

$$\theta_2(t) = \int_0^{\delta(t)} u_2(x, t)dx \tag{9}$$

$$= -V\delta + \frac{H\delta^2}{6k_2}, \text{ by Equation (7)} \tag{10}$$

Substitution of Equation (7) into Equation (8) gives

$$\frac{d}{dt}(\delta^2 H) = 6\kappa_2 H \tag{11}$$

This differential equation, together with its initial condition, Equation (5), is integrated directly as

$$\delta(t) = (6\kappa_2 t)^{1/2} \tag{12}$$

For sufficiently early times, the temperature is given by Equations (7) and (12). However, this solution is invalid as soon as either of the following critical times is reached: the time t_m when melting begins at the face $x = 0$, i.e., $u_2(0, t_m) = 0$; and the time t_δ when δ reaches l. From Equation (7), it is clear that $t_\delta \leq t_m$ whenever $\alpha\ (= Hl/2k_2V) \leq 1$. The present paper restricts itself to problems for which $\alpha \leq 1$; the methods used here are equally applicable, however, if $\alpha > 1$.

As soon as δ reaches l, it becomes necessary to specify the boundary condition at $x = l$. This paper considers the two boundary conditions:

$$(a)\ \frac{\partial u_2}{\partial x} = 0;\ (b)\ u_2 = -V \qquad x = l,\ t > t_\delta \tag{13}$$

where here, and below, the letters (a) and (b) appearing in the equation number refer to the problems with insulated and isothermal boundary, respectively. The problem now is to determine the temperature $u_2(x, t)$ so as to satisfy the heat-conduction equation, Equation (1), and the boundary conditions, Equations (2) and (13), along with the initial condition

$$u_2(x, t) = -V + \frac{Hl}{2k_2}\left(1 - \frac{x}{l}\right)^2 \quad 0 \leq x \leq l, \quad t = t_\delta = \frac{l^2}{6\kappa_2} \tag{14}$$

The temperature u_2 is again assumed to be quadratic in x. In a manner perfectly analogous to that described in the foregoing, the heat-balance integral is derived and solved, with the results that

$$u_2(x, t) = -V + \frac{Hl}{2k_2}\left(1 - \frac{x}{l}\right)^2 \qquad t_\delta < t < t_m$$
$$+ \frac{H}{k_2}\frac{\kappa_2}{l}(t - t_\delta) \tag{15a}$$

$$u_2(x, t) = -V + \frac{Hl}{k_2}\left(1 - \frac{x}{l}\right) \qquad t_\delta < t < t_m$$
$$- \frac{Hl}{2k_2}\left(1 - \frac{x^2}{l^2}\right)\exp\left\{-\frac{3\kappa_2}{l^2}(t - t_\delta)\right\} \tag{15b}$$

Setting $u_2\ (x = 0, t)$, as given by Equation (15), equal to zero, gives t_m, the time when melting begins, as

$$t_m = \frac{l^2}{\kappa_2}\left(\frac{1}{6} + \frac{1 - \alpha}{2\alpha}\right) \tag{16a}$$

$$t_m = \frac{l^2}{\kappa_2}\left(\frac{1}{6} + \frac{1}{3}\log\frac{\alpha}{2\alpha - 1}\right) \tag{16b}$$

Similarly, the temperature distribution at $t = t_m$ is given by

$$u_2(x, t = t_m) = -\frac{Hl}{2k_2}\left[1 - \left(1 - \frac{x}{l}\right)^2\right] \tag{17a}$$

$$u_2(x, t = t_m) = -V\left(\frac{x}{l}\right)^2 + \frac{Hl}{k_2}\left(\frac{x^2}{l^2} - \frac{x}{l}\right) \tag{17b}$$

It should be noted that, according to Equation (16b), the slab with isothermal end will never begin to melt unless $\alpha > 1/2$.

2 Statement of the Melting Problem

At any instant after melting starts, the slab consists of distinct liquid and solid portions containing melted and unmelted material and designated Regions 1 and 2, respectively. The interface between these two regions is called the melt line and is specified by the function $s(t)$ which gives the thickness of Region 1 at time t. The problem is to determine the thickness of melt and the temperature distributions in Regions 1 and 2, so as to satisfy the heat-

conduction equation in both regions, as well as the boundary conditions. The slab geometry is illustrated in Fig. 1.

The equations which specify the problem exactly are summarized in the following text, and embody the conventions that subscripts 1 and 2 refer to Regions 1 and 2, respectively, and that the origin of the temperature scale is the melting point. The basic heat-conduction equations are given by Equation (1) and its analog for Region 1. The boundary conditions at the ends of the slab are expressed by Equations (2) and (13). The initial ($t = t_m$) conditions of the problem are given by Equation (17) and the requirement that

$$u_1 = 0; \; s = 0 \qquad t = t_m \tag{18}$$

The conditions at the melt line are specified as follows:

$$u_1 = 0 = u_2 \qquad x = s, \; t > t_m \tag{19}$$

$$k_1 \frac{\partial u_1}{\partial x} - k_2 \frac{\partial u_2}{\partial x} = -\rho_2 L \frac{ds}{dt} \qquad x = s, \; t > t_m \tag{20}$$

where

ρ = density
L = latent heat of melting

Equation (19) requires simply that the temperature at the melt line be equal to the melting temperature. Equation (20) couples the temperature distributions in the two regions by requiring that the thermal energy transmitted across the melt line be reduced by the amount necessary to produce melting.

The heat-balance integral approximation is now introduced, as in the preceding Section. The temperature distributions in both the melted and unmelted portions of the slab are assumed to be quadratic in x. Exactly as before, the heat-balance integral method leads to ordinary differential equations. For the slab with insulated end, these equations take the form

$$\rho_2 L \frac{ds}{dt} + \frac{k_1}{\kappa_1} \frac{d\theta_1}{dt} + \frac{k_2}{\kappa_2} \frac{d\theta_2}{dt} = H \tag{21a}$$

$$\theta_1 = s^2 \left(\frac{H}{2k_1} - \frac{1}{3\kappa_1} \frac{d\theta_1}{dt} \right) \tag{22a}$$

$$\theta_2 = -\frac{(l - s)^2}{3\kappa_2} \frac{d\theta_2}{dt} \tag{23a}$$

with the initial conditions

$$s(t_m) = 0; \quad \theta_1(t_m) = 0; \quad \theta_2(t_m) = -\frac{Hl^2}{3k_2} \tag{24a}$$

For the slab with isothermal end, the analogous system is

$$\rho_2 L \frac{ds}{dt} + \frac{k_1}{\kappa_1} \frac{d\theta_1}{dt} + \frac{1}{2} \frac{k_2}{\kappa_2} \frac{d\theta_2}{dt} + \frac{k_2 V}{l - s} = H \tag{21b}$$

$$\theta_1 = s^2 \left(\frac{H}{2k_1} - \frac{1}{3\kappa_1} \frac{d\theta_1}{dt} \right) \tag{22b}$$

$$\theta_2 = -\frac{V}{2} (l - s) - \frac{(l - s)^2}{12\kappa_2} \frac{d\theta_2}{dt} \tag{23b}$$

$$s(t_m) = 0; \quad \theta_1(t_m) = 0; \quad \theta_2(t_m) = -\frac{Vl}{3} - \frac{Hl^2}{6k_2} \tag{24b}$$

The quantities θ_1 and θ_2 appearing in both systems are defined as follows:

$$\theta_1(t) = \int_0^{s(t)} u_1(x, t) dx \tag{25}$$

$$\theta_2(t) = \int_{s(t)}^{l} u_2(x, t) dx \tag{26}$$

Equation (21) specifies the energy balance at the melt line, while Equations (22) and (23) are "averaged" heat-conduction equations in Regions 1 and 2, respectively. Despite the great simplification introduced by the heat-balance integral, the problems remain nonlinear. Their solution is thus not straightforward and is presented in the following section.

3 Method of Solution

Each of the problems formulated in the foregoing has been reduced to a system of three simultaneous ordinary differential equations. In each system, however, two of the three equations are coupled nonlinearly, and therefore the system is not readily soluble. In problems of this type, if no transformation can be found which reduces the equations to some integrable form, it is a standard approach to assume a solution in the form of a power series in powers of some small parameter. This series is substituted into the original equation to obtain equations for the coefficients in the series. It is to be hoped that these equations are simpler than the original and that the resulting series converges. It is clear that the choice of the parameter with which to expand has a decisive effect upon both the equations for the coefficients and upon the convergence of the series. In the problems at hand, the parameter $\alpha = Hl/2k_2V$ seems a natural choice, since, by definition of the problem, it lies between 0 and 1. (For the slab with isothermal end, the stronger restriction $1/2 < \alpha < 1$ holds.) The consequences of this choice are presented in succeeding paragraphs.

Before proceeding further, it is expedient to nondimensionalize the equations so that meaning can be attached to the "smallness" of the small parameter in which a power-series expansion is made. The new variables are defined as follows:

$$\sigma = s/l \tag{27}$$

$$w = \frac{k_1 \kappa_2 \theta_1}{k_2 \kappa_1 V l} \tag{28}$$

$$v = \frac{\theta_2}{Vl} \tag{29}$$

$$\tau = (\kappa_2/l^2)(t - t_m) \tag{30}$$

The following parameters are introduced:

$$\alpha = \frac{Hl}{2k_2V} \tag{31}$$

$$\mu = \frac{k_2 V}{\kappa_2 \rho_2 L} \tag{32}$$

$$\nu = \kappa_1/\kappa_2 \tag{33}$$

Slab With Insulated End. In terms of the dimensionless quantities introduced in the foregoing, Equations (21*a*) through (24*a*) take the form

$$\frac{d\sigma}{d\tau} + \mu \frac{dw}{d\tau} + \mu \frac{dv}{d\tau} = 2\mu\alpha \tag{34}$$

$$\frac{\sigma^2}{3} \frac{dw}{d\tau} = \alpha\sigma^2 - \nu w \tag{35}$$

$$(1 - \sigma)^2 \frac{dv}{d\tau} = -3v \tag{36}$$

$$\sigma(\tau = 0) = 0; \; w(\tau = 0) = 0; \; v(\tau = 0) = -2\alpha/3 \tag{37}$$

The assumption can now be made that the functions $\sigma(\tau)$, $w(\tau)$, and $v(\tau)$ admit expansions of the form

$$f(\alpha, \mu, \nu, \tau) = f_0(\mu, \nu, \tau) + \alpha f_1(\mu, \nu, \tau) + \alpha^2 f_2(\mu, \nu, \tau) + \ . \ .$$

When these expansions are substituted into Equations (34) through (37) it is found that the approximations of every order are given by first-order linear equations and hence are readily obtained. The "zeroth" order solution is given simply by

$$\sigma_0 = 0 = w_0 = 0 = v_0$$

This is, of course, intuitively plausible, since $\alpha = 0$ corresponds to no temperature rise whatsoever in the slab. The first-order solution is obtained straightforwardly and is well behaved. Similarly, the second-order solution is obtained straightforwardly, but unfortunately is not well behaved. It is found that $v_2(\tau)$ contains terms of the form $\tau e^{-3\tau}$ and $\tau^2 e^{-3\tau}$. The effect of these terms is to produce "humps" in the plot of v_2 versus τ and also, for sufficiently large τ, in the plot of v versus τ, so that v overshoots zero and then dies away to zero through positive values. Since v is intrinsically negative, it is clear that the presence of these terms invalidates the entire solution. On the other hand, since the assumption of a solution in the form of a power series in α is plausible, and since the first-order approximations are reasonable, it is proper to ask how to continue the expansion to higher order approximations while avoiding undesirable terms of the type just discovered.

The question just posed is answered by having recourse to Lighthill's method for "rendering approximate solutions uniformly valid."[1] The essence of Lighthill's method is the assumption that the independent variable of a problem can be expanded in a power series of exactly the same form as that assumed for the dependent variables. (This of course necessitates the introduction of a new independent variable.) The higher-order approximations in the expansion of the original independent variable are now so chosen as to eliminate undesirable terms in the higher-order approximations of the dependent variables. This inevitably vague description will now be illustrated by applying the method to the present problem.

A new independent variable T is introduced and the assumption made that the former independent variable τ admits an expansion of the form

$$\tau(\alpha, \mu, \nu, T) = T + \alpha\tau_1(\mu, \nu, T) + \alpha^2\tau_2(\mu, \nu, T) + \ . \ . \ .$$

Similar expansions are assumed for σ, w, and v. The problem expressed by Equations (34) through (36) can now be restated:

$$\frac{d\sigma}{dT} + \mu \frac{dw}{dT} + \mu \frac{dv}{dT} = 2\mu\alpha \frac{d\tau}{dT} \tag{38}$$

$$\frac{\sigma^2}{3} \frac{dw}{dT} = (\alpha\sigma^2 - \nu w) \frac{d\tau}{dT} \tag{39}$$

$$\frac{(1 - \sigma)^2}{3} \frac{dv}{dT} = -v \frac{d\tau}{dT} \tag{40}$$

The initial conditions cannot be rewritten directly; however, if the functions $\tau_i(T)$ are so chosen that $\tau_i(T = 0) = 0$, $i \geq 1$, it is easily shown that the initial conditions (Equation 37) become

$$\sigma(T = 0) = 0; \ w(T = 0) = 0; \ v(T = 0) = -2\alpha/3 \tag{41}$$

When the expansions for τ, σ, w, and v are introduced into Equations (38) through (40), one obtains a system of first-order linear equations for the approximations of each order. The zeroth order solution is given directly, as in the foregoing, by

$$\sigma_0(T) = 0 = w_0(T) = 0 = v_0(T) \tag{42}$$

The first-order solution is likewise given directly as

$$\sigma_1(T) = 2\mu T + \frac{2\mu}{3} [e^{-3T} - 1] \tag{43}$$

$$w_1(T) = 0 \tag{44}$$

$$v_1(T) = -(2/3)e^{-3T} \tag{45}$$

The equations for the second-order approximations now become

$$\frac{d\sigma_2}{dT} + \mu \frac{dw_2}{dT} + \mu \frac{dv_2}{dT} = 2\mu \frac{d\tau_1}{dT} \tag{46}$$

$$w_2 = 0 \tag{47}$$

$$\frac{dv_2}{dT} + 3v_2 = 2\sigma_1 \frac{dv_1}{dT} - 3v_1 \frac{d\tau_1}{dT} = 2e^{-3T} \left[4\mu \left(T - \frac{1}{3} + \frac{1}{3} e^{-3T} \right) + \frac{d\tau_1}{dT} \right] \tag{48}$$

If the right-hand side of Equation (48) were free of terms of the form e^{-3T} and Te^{-3T}, then v_2 would no longer contain the undesirable terms, Te^{-3T} and T^2e^{-3T}. Thus it is clear that τ_1 should be chosen so that

$$\frac{d\tau_1}{dT} + 4\mu(T - 1/3) = 0 \tag{49}$$

or

$$\tau_1 = -2\mu(T^2 - 2/3T) \tag{50}$$

With this choice of τ_1, the solution of Equations (46) and (48) becomes

$$\sigma_2 = -4\mu^2(T^2 - 2/3T) - \frac{8\mu^2}{9} (e^{-3T} - e^{-6T}) \tag{51}$$

$$v_2 = \frac{8\mu}{9} (e^{-3T} - e^{-6T}) \tag{52}$$

It is clear from Equation (52) that v_2 now behaves properly as a function of T; it is equally well behaved as a function of τ. Thus the Lighthill method has succeeded in removing the undesirable terms in the original expansion.

The equations for the third-order approximations are derived and solved in a perfectly analogous manner. The choice of τ_2 is dictated to be

$$\tau_2 = 4\mu^2[(T - 1/3)^2 + 2/9(T + 1/3)(e^{-3T} - 1) + 1/27] \tag{53}$$

The corresponding third-order approximations are

$$v_3 = \frac{4\mu^2}{27} (-9e^{-3T} + 20e^{-6T} - 11e^{-9T}) \tag{54}$$

$$\sigma_3 = 2\mu\tau_2 - \frac{\mu}{\nu} \sigma_1^2 - \mu v_3 \tag{55}$$

$$w_3 = \frac{\sigma_1^3}{\nu} \tag{56}$$

By proceeding in this fashion, the approximations of any order can be determined. The significance of these results is discussed in Section 4.

Slab With Isothermal End. The problem is defined by Equations (21*b*) through (24*b*). These equations have the steady-state solu-

[1] M. J. Lighthill, "On a Technique for Rendering Approximate Solutions to Physical Problems Uniformly Valid," *Philosophical Magazine*, vol. 40, seventh series, 1949, pp. 1179–1201.

tion given, in terms of the dimensionless quantities introduced in the foregoing, as

$$\sigma = 1 - \frac{1}{2\alpha} \tag{57}$$

$$w = \frac{\alpha}{\nu}\left(1 - \frac{1}{2\alpha}\right)^2 \tag{58}$$

$$v = -1/4\alpha \tag{59}$$

This steady-state solution is also a valid steady solution of the exact boundary-value problem. It represents a linear temperature distribution in both the liquid and solid portions of the slab and is equivalent to the trivial geometric problem of passing a straight line of given slope through a given point.

By definition of the problem, α is restricted to lie between 1/2 and 1; hence the steady-state value of σ, i.e., $1 - (1/2\alpha)$, must lie between 0 and 1/2. Denote this steady-state value by ϵ,

$$\epsilon = 1 - (1/2\alpha) \tag{60}$$

Since σ is at most of order ϵ, the choice of ϵ, rather than α, is suggested for the small parameter in which to form power-series expansions. In terms of ϵ, the governing Equations (21*b*) through (24*b*) become

$$\frac{d\sigma}{d\tau} + \mu\frac{dw}{d\tau} + \frac{\mu}{2}\frac{dv}{d\tau} + \mu(1 + \sigma + \sigma^2 + \ldots) = \mu(1 + \epsilon + \epsilon^2 + \ldots) \tag{61}$$

$$\nu w = \frac{\sigma^2}{6}\left[3(1 + \epsilon + \epsilon^2 + \ldots) - 2\frac{dw}{d\tau}\right] \tag{62}$$

$$v = -\frac{(1-\sigma)}{2} - \frac{(1-\sigma)^2}{12}\frac{dv}{d\tau} \tag{63}$$

$$\sigma(\tau = 0) = 0;\ w(\tau = 0) = 0;\ v(\tau = 0) = -1/6\,[3 + \epsilon + \epsilon^2 + \ldots] \tag{64}$$

If σ, w, and v are now assumed to be power series in ϵ, difficulties arise similar to those encountered in the preceding subsection (Slab With Insulated End). In the second-order approximation for v, terms appear which again cause v to become positive before approaching its steady-state value. Since a solution containing such terms is invalid, it is again necessary to circumvent this difficulty.

Although Lighthill's method employed in the foregoing is equally applicable to this problem, a more direct and intuitive approach is used here; the results obtained are equivalent to those which Lighthill's method would provide. In essence, the present method assumes that the solution consists of the steady-state solution minus exponential terms of the form $Ae^{\lambda\tau}$, which approach zero as τ increases and which have initial values that combine to satisfy the initial conditions. In order for a solution of this form to satisfy the differential equations, it is necessary that the exponents λ be functions of ϵ and, in particular, power series in ϵ with coefficients depending on μ and ν only. Thus it is assumed that, to the second order in ϵ,

$$\sigma = \epsilon[1 + S_1e^{\lambda_1\tau} + S_2e^{\lambda_2\tau}] + \epsilon^2[S_3e^{\lambda_1\tau} + S_4e^{\lambda_2\tau} + S_5e^{2\lambda_1\tau} + S_6e^{2\lambda_2\tau} + S_7e^{(\lambda_1+\lambda_2)\tau}] \tag{65}$$

$$w = \epsilon w_1 + \epsilon^2 w_2 \tag{66}$$

$$v = -1/2 + \epsilon[1/2 + V_1e^{\lambda_1\tau} + V_2e^{\lambda_2\tau}] + \epsilon^2[V_3e^{\lambda_1\tau} + V_4e^{\lambda_2\tau} + V_5e^{2\lambda_1\tau} + V_6e^{2\lambda_2\tau} + V_7e^{(\lambda_1+\lambda_2)\tau}] \tag{67}$$

where

$$\lambda_i = \lambda_{i0} + \epsilon\lambda_{i1} + \epsilon^2\lambda_{i2} + \ldots,\ i = 1, 2 \tag{68}$$

and S_j, V_j, and λ_{ij} depend only on μ and ν.

The motivation for this representation is given in the Appendix; analytic expressions for the various parameters in the solution are likewise to be found in the Appendix. The significance of these results is discussed in the next section.

4 Discussion of Results

Slab With Insulated End. By means of the heat-balance integral and Lighthill's method for rendering approximate solutions uniformly valid, the melting problem for a finite slab with insulated boundary has been reduced to determining σ (the dimensionless melt thickness), τ (the dimensionless time), w and v (the dimensionless integrals of the temperature over Regions 1 and 2, respectively) as functions of the independent variable T and the parameters α, μ, and ν. The solution to this problem, as given in the preceding section, may be summarized as follows: The dimensionless time τ is given [Equations (50) and (53)] as

$$\tau = T + \alpha\mu\frac{\tau_1}{\mu}(T) + (\alpha\mu)^2\frac{\tau_2}{\mu^2}(T) \tag{69}$$

and is thus a function only of T and $\alpha\mu$. The dimensionless integral v of the temperature in the solid portion of the slab is given [Equations (45), (52), and (54)] as

$$v = \alpha\left[v_1(T) + \alpha\mu\frac{v_2}{\mu}(T) + (\alpha\mu)^2\frac{v_3}{\mu^2}(T)\right] \tag{70}$$

so that v/α is a function only of T and $\alpha\mu$. Similarly, w, the dimensionless integral of the temperature over the liquid portion of the slab is given [Equations (44), (47), and (56)] as

$$w = \frac{\alpha(\alpha\mu)^2}{\nu}\left[\frac{\sigma_1}{\mu}(T)\right]^2 \tag{71}$$

Finally, σ, the dimensionless thickness of melt, is given [Equations (43), (51), and (55)] as

$$\sigma = \alpha\mu\frac{\sigma_1}{\mu}(T) + (\alpha\mu)^2\frac{\sigma_2}{\mu^2}(T) + (\alpha\mu)^2\frac{\sigma_3}{\mu^2}(\nu, T) \tag{72}$$

and is thus a function only of T, $\alpha\mu$, and ν. By means of Equation (69), it is possible to obtain σ, w, and v as functions of the physically meaningful variable τ, rather than the artificially introduced variable T.

It should be noted that the parameter ν appears only in the third-order approximations to σ and w and that the parameter μ appears only in the combination $\alpha\mu$. Thus it is implicit in these results (and indeed can be verified by substitution into the governing differential equations) that if the new variables $v' = v/\alpha$ and $w' = w/\alpha$ be introduced, then the solution depends only on the two parameters $\alpha\mu$ and ν. This has not been done here, however, since α is small (relative to 1) by definition of the problem, whereas $\alpha\mu$ is not intrinsically small.

While the regions of convergence of these series are undetermined, some general comments can be made about their convergence. For these comments to be meaningful, it should be borne in mind that the parameter α is restricted to lie between 0 and 1, while, for metals at least, ν lies between 0 and 1, and μ between 0 and 5, roughly, depending on the initial temperature of the slab. The series for τ and σ are both quite similar to alternating power series in the "small" variable $\alpha\mu$ T; the exponential terms in the expansion for τ and σ are essential, yet have little over-all effect. Consequently, for early times, i.e., $T \ll 1$, the series can be expected to converge for relatively large $\alpha\mu$. However, for large T and, in particular, for T large enough that $\sigma(T) =$

1, the series must be applied cautiously. Thus approximations of odd order must be retained in the series expansion for σ and τ since both of these functions are necessarily positive and yet are given by "alternating" series; consequently, in order to extend the third-order approximations found in the foregoing, it is necessary to obtain both the fourth and fifth-order approximations. Moreover, for T of order 1, the series can be expected to converge only for relatively small $\alpha\mu$; in fact, it has been found that for T this large, the solution may behave pathologically unless $\alpha\mu \leq \nu/2$. These restrictions on σ and τ are the critical requirements for the solution as a whole; whenever σ and τ are well behaved, the series for v converges satisfactorily, since it is simply a sum of pure exponential terms.

Fig. 2 is a plot of σ versus τ for $\alpha\mu = 0.15$ and for $\nu = 0.3$, 0.6, and 1.0, corresponding, respectively, to iron, aluminum, and the commonly idealized material which has the same diffusivity in its solid and liquid phases. It is clear from this figure that for small $\alpha\mu$, the propagation of melting is relatively insensitive to ν. Fig. 3 illustrates the dependence of melting upon $\alpha\mu$ by displaying σ versus τ for $\nu = 0.6$ and $\alpha\mu = 0.15$, 0.3, and 0.4. The parameter $\alpha\mu$ is restricted to these small values in order to show the full propagation of melting until the entire slab is molten. Fig. 3 bears out the intuitively obvious fact that the slab melts more quickly for larger $\alpha\mu$, since larger $\alpha\mu$ represents less resistance to melting. Fig. 4 gives the dependence upon $\alpha\mu$ and ν of the time required to melt the entire slab. It is significant that this time is not altered appreciably by changing ν from 0.6 to 1.0.

It is of interest to recover the temperature distributions from the solution as just given. The temperature distributions, $u_1(x, t)$ and $u_2(x, t)$, in the liquid and solid portions of the slab, respectively, are given by

$$u_1(x, t) = V \frac{k_2}{k_1}\left[\frac{\alpha\sigma}{2}\left(1 - 3\frac{x/l}{\sigma}\right)\left(1 - \frac{x/l}{\sigma}\right) + \frac{3\nu}{2}\frac{w}{\sigma}\left(1 + \frac{x/l}{\sigma}\right)\left(1 - \frac{x/l}{\sigma}\right)\right] 0 \leq x/l \leq \sigma, t \geq t_m \quad (73)$$

$$u_2(x, t) = \tfrac{1}{2}V\frac{v}{1 - v}\left[1 - \left(\frac{1 - x/l}{1 - \sigma}\right)^2\right] \sigma \leq x/l \leq 1, t \geq t_m \quad (74)$$

The time dependence of u_1 and u_2 is expressed by the time dependence of σ, w, and v, as given in Equations (70) through (72). By means of these equations, it is thus possible to determine the temperature at any point of the slab at any instant after melting starts. Fig. 5 presents the time variation of the temperature at the insulated boundary, $x = l$, for $\nu = 0.6$ and $\alpha\mu = 0.15$, 0.3, and 0.4. It is clear from this figure that the temperature of the solid portion of the slab is quickly raised to the melting point and that the heat subsequently applied is free only to produce melting and to raise the temperature in the molten portion of the slab. This result suggests employing the assumption that the solid portion of the slab is at the melting temperature from the outset; presumably the results so obtained are valid save for a relatively small translation of the time origin. This is precisely the assumption made by Goodman[3] to determine the melting of a semi-infinite solid.

Slab With Isothermal End. Just as for the slab with insulated end, the heat-balance integral has reduced the melting problem for the slab with isothermal end to determining the dimensionless variables σ, w, and v as functions of τ, the dimensionless time, and of the parameters ϵ, μ, and ν. The solution to this problem is given by Equations (65) through (68); the detailed form of the solution is given in the Appendix. In essence, the complete solution consists of the steady-state solution minus terms of the form $Ae^{\lambda\tau}$ where A depends only on μ and ν, and λ is an infinite series in ϵ with coefficients depending only on μ and ν. The steady-state solution represents simply a linear temperature distribution in both the liquid and solid portions of the slab; the significance of the solution presented here is that it specifies how much time is required to establish the steady heat flow.

The ideal solution to the problem would, for any ν between 0 and 1, converge for every ϵ between 0 and 0.5, and every μ between 0 and 5, say. However, it is clear that a solution of the form described in the preceding paragraph is valid only if none of the exponential terms diverges, i.e., only if every λ is negative; otherwise, there is no steady-state solution. It is shown in the

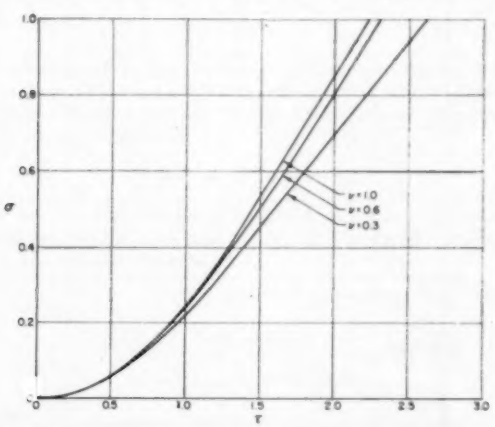

Fig. 2 Thickness of melt versus time, for $\alpha\mu = 0.15$ and various values of ν

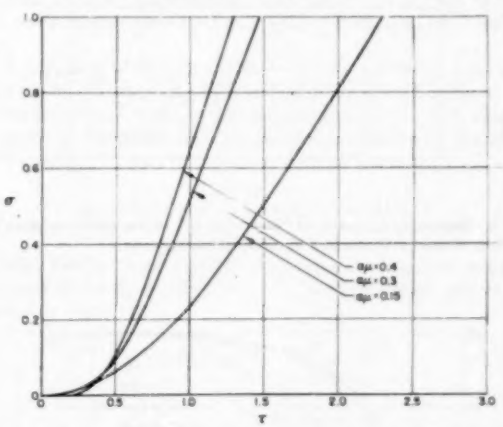

Fig. 3 Thickness of melt versus time, for $\nu = 0.6$ and various values of $\alpha\mu$

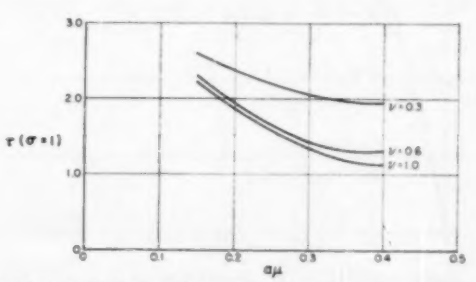

Fig. 4 Time required to melt the entire slab versus $\alpha\mu$, for various values of ν

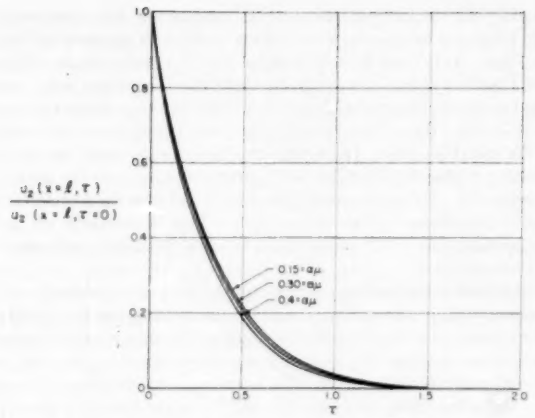

Fig. 5 Temperature at face $x = l$ versus time, for $\nu = 0.6$

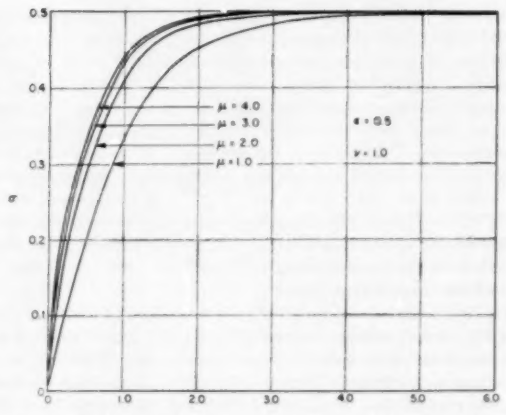

Fig. 8 Thickness of melt versus time, for various values of μ

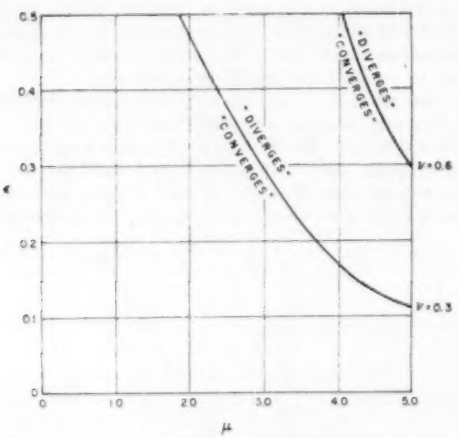

Fig. 6 Region, in $\varepsilon\mu$ space, of "convergence" of the series solution for melting of slab with one end at constant temperature

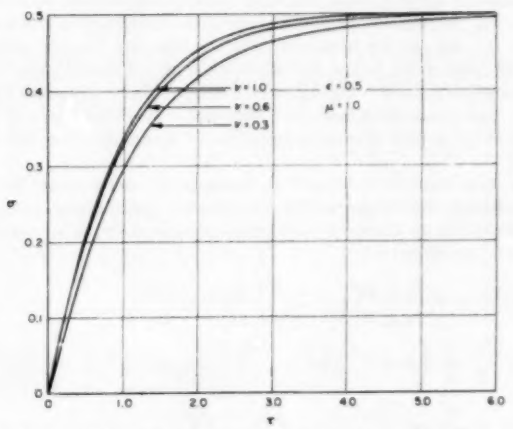

Fig. 9 Thickness of melt versus time, for various values of ν

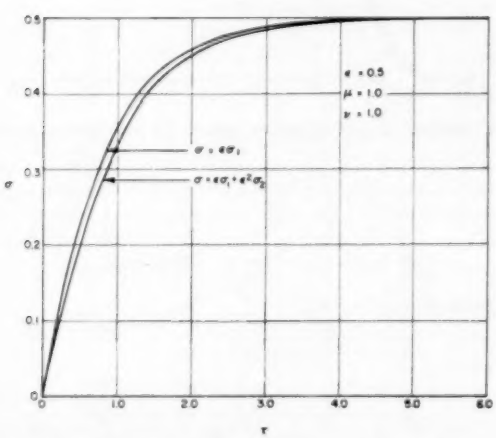

Fig. 7 Comparison of first and second-order solutions for thickness of melt of a slab with one end at constant temperature

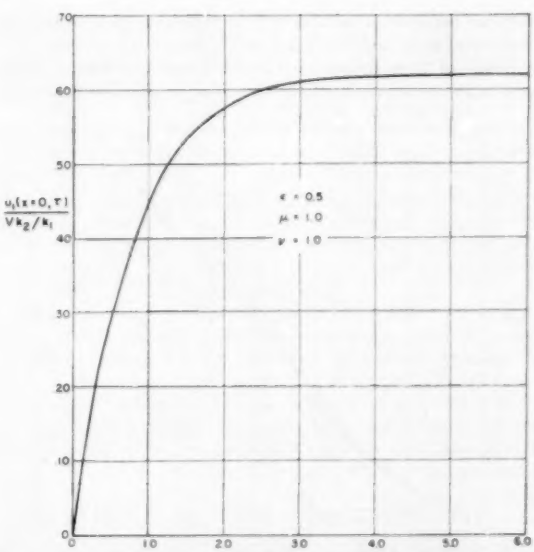

Fig. 10 Temperature at face $x = 0$ versus time

Appendix that this requirement can be expressed as a functional relationship between ϵ, μ, and ν. For a given ν, this functional relationship defines a region in $\epsilon\mu$ space outside of which region the series cannot be valid. As just mentioned, if the solution were ideal, then for every ν the corresponding region would contain the rectangle defined by the lines $\epsilon = 0$, $\epsilon = 0.5$, $\mu = 0$, $\mu = 5$. However, as Fig. 6 shows, the solution presented here is not ideal. This figure displays, for $\nu = 0.3$ and $\nu = 0.6$, the region to which the solution must be restricted (for $\nu = 1.0$, the entire rectangle is acceptable); in each instance, this region is the entire rectangle less a portion corresponding to simultaneously large μ and ϵ.

The restriction of μ and ϵ to their appropriate region is obviously a necessary condition for the convergence of the solution. Surprisingly, however, this restriction has been found to be a very reliable sufficient condition (no proof is offered for this statement, other than experience with specific computations for many combinations of parameter values). For example, Fig. 7 displays both the first and second-order approximations to σ for $\epsilon = 0.5$, $\mu = 1.0$, $\nu = 1.0$. The agreement shown in this figure between the first and second-order approximations is characteristic of (ϵ, μ) pairs chosen within the appropriate region of Fig. 6.

Fig. 8 is a plot of σ versus τ for $\epsilon = 0.5$, $\nu = 1.0$, and $\mu = 1, 2, 3, 4$; it is again clear that larger μ corresponds to faster melting. Similarly, Fig. 9 displays the time history of melting for $\epsilon = 0.5$, $\mu = 1.0$ and $\nu = 0.3$, 0.6, and 1.0. Again, the melting is not significantly affected by changing ν from 0.6 to 1.0.

The temperature distributions, u_1 and u_2, in the liquid and solid portions of the slab, respectively, can be expressed in terms of the solution just described. The expression for u_1 is formally the same as that given in Equation (73) for the slab with insulated end, while u_2 is given by

$$u_2(x, t) = -V\left[\frac{(x/l) - \sigma}{1 - \sigma}\right]\left[\frac{3(x/l) - 2 - \sigma}{1 - \sigma} - 6\,\frac{1 - x/l}{(1 - \sigma)^2}\,v\right] \quad \sigma \le x/l \le 1, t \ge t_m \tag{75}$$

These equations, together with Equations (65) through (68), make it possible to determine the temperature at any point of the slab at any instant after melting starts. Thus Fig. 10 presents the time history of the temperature at the face $x = 0$.

APPENDIX

The melting problem for the slab with insulated end has been reduced to solving Equations (61) through (64). When expansions of the form

$$f(\epsilon, \mu, \nu, \tau) = f_0(\mu, \nu, \tau) + \epsilon f_1(\mu, \nu, \tau) + \epsilon^2 f_2(\mu, \nu, \tau) + \ldots$$

are substituted into these equations for σ, w, and v, it is found that the approximations of every order are given by simple linear differential equations and are thus readily obtained. The zeroth-order solution is given by

$$\sigma_0 = 0; \quad w_0 = 0; \quad v_0 = -1/2 \tag{76}$$

This solution corresponds, as it should, to a linear temperature distribution in the solid, with no melting whatsoever. The first-order solution is found to be

$$\sigma = 1 + S_1 e^{\lambda_{10}\tau} + S_2 e^{\lambda_{20}\tau} \tag{77}$$

$$w_1 = 0 \tag{78}$$

$$v_1 = 1/2 + V_1 e^{\lambda_{10}\tau} + V_2 e^{\lambda_{20}\tau} \tag{79}$$

where

$$\lambda_{10,20} = -2(\mu + 3) \pm 2(\mu^2 + 3\mu + 9)^{1/2} \tag{80}$$

$$S_1 = -\frac{\lambda_{20}}{\lambda_{20} - \lambda_{10}}, \quad S_2 = \frac{\lambda_{10}}{\lambda_{20} - \lambda_{10}} \tag{81}$$

$$V_1 = -1/2\,\frac{\lambda_{20} + 3}{\lambda_{20} - \lambda_{10}}, \quad V_2 = 1/2\,\frac{\lambda_{10} + 3}{\lambda_{20} - \lambda_{10}} \tag{82}$$

The differential operator which specifies σ_2 and v_2 turns out to be precisely the same operator which specified σ_1 and v_1; it thus has the same eigenvalues; viz., λ_{10} and λ_{20}. However, the right-hand sides of the equations for σ_2 and v_2 contain terms of the form $Ae^{\lambda_{10}\tau}$ and $Be^{\lambda_{20}\tau}$. The solution for σ_2 and v_2 accordingly contains terms of the form $A\tau e^{\lambda_{10}\tau}$ and $B\tau e^{\lambda_{20}\tau}$. For reasons discussed in Section 3, the presence of such terms is most undesirable. The outlook becomes even darker when one notes that this phenomenon is repeated at every order of approximation. For every $n \ge 2$, the differential operator specifying σ_n and v_n is the same as that specifying σ_1 and v_1, while the right-hand sides of the equations for σ_n and v_n contain terms of the form $\tau^m e^{\lambda_{10}\tau}$ and $\tau^m e^{\lambda_{20}\tau}$.

The dilemma of finding a new solution which retains the zeroth and first-order approximations of the old solution, and which yet avoids the latter's embarrassing higher-order approximations, is resolved by a stratagem identical in spirit to Lighthill's method employed in Section 3. The method again involves introducing greater generality into the assumed form of the solution and then using the freedom associated with this generality to eliminate undesirable terms. In particular, the method assumes that the transient solution to Equations (61) through (64) is characterized by two eigenvalues, λ_1 and λ_2, which, to the first order in ϵ are independent of ϵ and are, in fact, equal to λ_{10} and λ_{20} as given in the foregoing. The crucial assumption is then made that the eigenvalues are simply infinite series in ϵ with coefficients depending only on μ and ν. Thus it is assumed that σ, w, v, λ_1, and λ_2 have the second-order expansions displayed in Equations (65) through (68.)

Substitution of these expansions into the governing equations [Equations (61) through (64)], and equating of coefficients of like terms in each equation provide λ_{i0}, S_i, and V_i, $i = 1, 2$, exactly as given in Equations (80) through (82). Moreover, Equation (62) gives

$$w_1 = 0; \quad w_2 = \frac{1}{2\nu}\,[1 + S_1 e^{\lambda_{10}\tau} + S_2 e^{\lambda_{20}\tau}]^2 \tag{83}$$

Finally, twelve linear algebraic equations are obtained, relating λ_{11}, λ_{21} and the S_j, V_j, $3 \le j \le 7$. These equations can be inverted to obtain:

$$\lambda_{11} = 2\lambda_{10} + \frac{\mu}{\nu}\,\frac{\lambda_{10}(\lambda_{10} + 12)}{\lambda_{20} - \lambda_{10}} \tag{84}$$

$$\lambda_{21} = 2\lambda_{20} - \frac{\mu}{\nu}\,\frac{\lambda_{20}(\lambda_{20} + 12)}{\lambda_{20} - \lambda_{10}} \tag{85}$$

$$V_3 = \frac{12\mu(2\lambda_{20} + \lambda_{10} + 6) - 12(\lambda_{20}^2 - \lambda_{10}^2)}{(\lambda_{10} + 12)(\lambda_{20} - \lambda_{10})(2\lambda_{20} - \lambda_{10})} - \frac{6\mu}{\nu}\,\frac{\lambda_{20}^2(2\lambda_{20} + \lambda_{10}) - \lambda_{10}^2(2\lambda_{20} - \lambda_{10})}{(\lambda_{20} - \lambda_{10})^2(2\lambda_{20} - \lambda_{10})} \tag{86}$$

$$S_3 = \frac{\lambda_{10} + 12}{6}\,V_3 - \frac{\mu}{\nu}\,\frac{\lambda_{10}\lambda_{20}}{(\lambda_{20} - \lambda_{10})^2} \tag{87}$$

$$V_4 = \frac{12\mu(2\lambda_{10} + \lambda_{20} + 6) + 12(\lambda_{20}^2 - \lambda_{10}^2)}{(\lambda_{20} + 12)(\lambda_{20} - \lambda_{10})(2\lambda_{10} - \lambda_{20})} + \frac{6\mu}{\nu}\,\frac{\lambda_{10}^2(2\lambda_{10} + \lambda_{20}) - \lambda_{20}^2(2\lambda_{10} - \lambda_{20})}{(\lambda_{20} - \lambda_{10})^2(2\lambda_{10} - \lambda_{20})} \tag{88}$$

$$S_4 = \frac{\lambda_{20} + 12}{6} V_4 - \frac{\mu}{\nu} \frac{\lambda_{10}\lambda_{20}}{(\lambda_{20} - \lambda_{10})^2} \quad (89)$$

$$V_5 = \left[\frac{12}{\lambda_{10} + 12} + \frac{\lambda_{20}/2}{2\lambda_{10} - \lambda_{20}} - \frac{\mu}{\nu} \frac{6}{2\lambda_{10} - \lambda_{20}} \right] S_1^2 \quad (90)$$

$$S_5 = \left[1 + \frac{2(\lambda_{10} + \mu)}{2\lambda_{10} - \lambda_{20}} - \frac{\mu}{\nu} \frac{2(\lambda_{10} + 6)}{2\lambda_{10} - \lambda_{20}} \right] S_1^2 \quad (91)$$

$$V_6 = \left[\frac{12}{\lambda_{20} + 12} + \frac{\lambda_{10}/2}{2\lambda_{20} - \lambda_{10}} - \frac{\mu}{\nu} \frac{6}{2\lambda_{20} - \lambda_{10}} \right] S_2^2 \quad (92)$$

$$S_6 = \left[1 + \frac{2(\lambda_{20} + \mu)}{2\lambda_{20} - \lambda_{10}} - \frac{\mu}{\nu} \frac{2(\lambda_{20} + 6)}{2\lambda_{20} - \lambda_{10}} \right] S_2^2 \quad (93)$$

$$V_7 = \frac{2}{(\lambda_{20} - \lambda_{10})^2} \left[6\mu + \frac{2(\lambda_{10} + \lambda_{20} + \mu)(\lambda_{10} + \lambda_{20} + 2\mu)}{\mu} + \frac{6\mu}{\nu} \frac{\lambda_{10} + \lambda_{20}}{(\lambda_{20} - \lambda_{10})^2} \right] S_1 S_2 \quad (94)$$

$$S_7 = -\frac{2}{(\lambda_{20} - \lambda_{10})^2} \left[4\mu^2 + (\lambda_{10} + \lambda_{20})(\lambda_{10} + \lambda_{20} + 2\mu) - \frac{\mu}{\nu} \frac{4\mu(\lambda_{17} + \lambda_{20})}{(\lambda_{20} - \lambda_{10})^2} \right] S_1 S_2 \quad (95)$$

Each of these twelve quantities can be written in the form, $f_1(\mu) + (1/\nu) f_2(\mu)$; thus if each $f_1(\mu)$ and $f_2(\mu)$ be tabulated, the task of finding the value of any of the twelve quantities for given μ and ν is trivial.

Finally, it should be noted that the condition $\lambda_1 = 0$ can be written [Equations (68) and (84)] as

$$\epsilon(\lambda_1 = 0) = -\frac{1}{2 + \frac{\mu}{\nu} \frac{\lambda_{10} + 12}{\lambda_{20} - \lambda_{10}}} \quad (96)$$

For given ν, the right-hand side of this equation is a function only of μ. The analogous expression for the condition $\lambda_2 = 0$ is

$$\epsilon(\lambda_2 = 0) = -\frac{1}{2 - \frac{\mu}{\nu} \frac{\lambda_{20} + 12}{\lambda_{20} - \lambda_{10}}} \quad (97)$$

It is clear that, for given μ and ν, the solutions for σ and v are invalid for any ϵ greater than either of these two critical values. Thus, for given ν, a plot versus μ of the minimum of these critical values defines a boundary of the "convergence region" discussed in Section 4; the boundaries of Fig. 6 are in fact so determined.

Heat-Exchanger Tube-Sheet Design—3. U-Tube and Bayonet-Tube Sheets

KARL A. GARDNER[1]
Chief Engineer,
The Griscom-Russell Company,
Massillon, Ohio
Mem. ASME

Tube sheets of U-tube and bayonet-tube exchangers differ from those of floating-head exchangers in that they receive no external support from the staying or column action of the tubes. The strengthening effect of tube-bending reaction is here investigated, evaluated quantitatively, and presented in the form of simple design factors. These factors are functions of a parameter u_a, a measure of the relative "barreling" rigidity of the tube bundle as compared to the flexural rigidity of the tube sheet. With stiff tubes and flexible tube sheets (high u_a) the reinforcement due to tube bending is considerable and, in the central region of the tube sheet, the deflection and curvature are essentially independent of any tube-sheet property. At low u_a the benefit gained is negligible.

In two previous papers [1, 2][2] an attempt was made to formulate rational design methods for heat-exchanger tube sheets of the "floating" and "fixed" types. In both cases it was shown that the two tube sheets of an exchanger are mutually self-supporting through interaction with the tubes fixed into them, and that the nature of this support is that of an elastic foundation. Although the bending of the tubes due to the bending of the tube sheet was recognized from the standpoint of possible damage to the tubes themselves, reactive effects tending to reduce bending of the tube sheets were deliberately ignored as negligible. It is the purpose of this paper to investigate the quantitative effects of this reactive bending on the tube sheets of exchangers having no other means of resisting deflection; i.e., of U-tube and bayonet-tube exchangers.

Miller [3], in a paper combining a review of the author's first work [1], an independent derivation of the fixed tube-sheet equations of the second [2], and a proposed empirical method for estimation of flexural and ligament efficiencies, stated clearly the assumption implicit in the author's previous work:

"The deflection of the tube plate is small, and hence the angular distortion of the tube ends due to the bending of the tube plate can be neglected."

This paper makes this assumption unnecessary.

Unpublished work by the author in 1951 and 1952, of which this paper is a partial outcome, led to solution of the equations for U-tube, floating head, and fixed tube-sheet exchangers with appreciable reactive tube bending. Unfortunately for the author's hopes of original publication, the solutions to the latter two types were published in Russia by Yakovlev [4] in 1954, although not abstracted here until 1957. Galletly [5], while this paper was in the process of review, also called attention to Yakovlev's work in a brief comment on reference [23] of this paper. Although Yakovlev did not cover U-tube exchangers, credit must go to him for the first published discussion of the nature of the interaction between bending tube and tube sheet.

The tubes of a heat exchanger are customarily held in position relative to one another by support plates, or pairs of semisupport plates, with close-fitting holes drilled on the same layout as the

[1] Currently, Vice-President-Engineering, Yuba Consolidated Industries, Palo Alto, Calif.

[2] Numbers in brackets designate References at end of paper.

Contributed by the Applied Mechanics Division and presented at the Annual Meeting, Atlantic City, N. J., November 29–December 4, 1959, of The American Society of Mechanical Engineers.

Discussion of this paper should be addressed to the Secretary, ASME, 29 West 39th Street, New York, N. Y., and will be accepted until April 10, 1960, for publication at a later date. Discussion received after the closing date will be returned.

Note: Statements and opinions advanced in papers are to be understood as individual expressions of their authors and not those of the Society. Manuscript received by ASME Applied Mechanics Division, March 26, 1958; final draft received June 24, 1959. Paper No. 59—A-81.

Nomenclature

a = radius of tube sheet over which hydrostatic pressure acts, in.

A, B, C = arbitrary constants

d = outside diameter of tube, in.

D = flexural rigidity = $Eh^3\eta_m/12(1 - \nu_0^2)$, in-lb

E = modulus of elasticity of tube-sheet material, psi

E_T = modulus of elasticity of tube material, psi

F_w, F_θ, F_M, F_Q, F_q = dimensionless multipliers for obtaining maximum deflection, slope, radial bending moment, shear, and effective pressure for tube sheets

F_* = factor relating tube bending moment to tube-sheet slope

h = tube-sheet thickness, in.

$I_0(u)$, $I_1(u)$ = modified Bessel functions of first kind, of orders 0 and 1, of argument u

I_T = moment of inertia of tube cross section with respect to a diameter = $\pi[d^4 - (d - 2t)^4]/64$, in.^{4}

$K_0(u)$ = modified Bessel function of second kind and zero order of argument u

L = tube-bundle length, in.

M = bending moment, in-lb/in.

M' = reactive bending moment due to M_T of all tubes lying at radius r, in-lb/in.

M_a = radial bending moment at radius a, in-lb/in.

M_T = tube bending moment at junction with tube sheet, in-lb/tube

n = number of tube-support plates

N = total number of tubes in bundle

(*Continued on next page*)

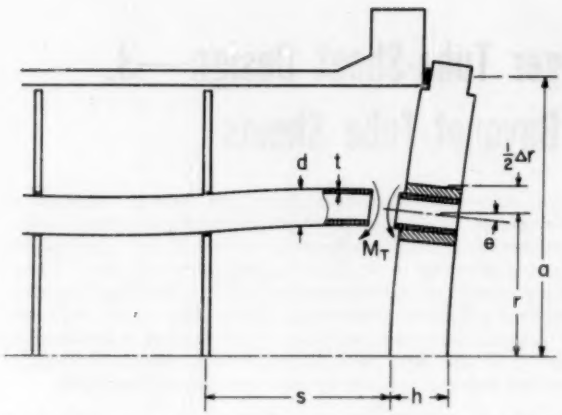

Fig. 1 Diagrammatic section of bayonet-tube heat exchanger showing nature of interaction between bending tube and tube sheet

tube sheets. The maximum spacing of these supports from the tube sheets and from each other is normally about 60 tube diameters. For heat-transfer reasons, however, intermediate baffles are introduced to provide desired flow paths and velocities, and their spacing is usually considerably less than the maximum. The result of this construction in a bayonet-tube bundle is that the tubes, instead of bristling out normal to the loaded tube-sheet surface, are constrained by the baffles to practically zero deflection from their unloaded position at regular intervals along the tube length, Fig. 1. The effect on U-tubes is for all practical purposes the same.

Method of Attack

The following analysis is limited to circular tube sheets supported only at the periphery. The nomenclature and fundamental assumptions of the author's two previous papers [1, 2] are repeated here for convenience and are equally valid in the present discussion:

1 The median deflection surface of a uniformly perforated plate under load may be considered congruent to that of a homogeneous plate of the same radius, identically loaded, whose flexural rigidity D is a fraction η_w of that of the undrilled plate.

2 The tube-sheet element associated with a single tube may be considered of differential size compared to the whole tube-sheet area and, hence, the external forces exerted on the latter by the tubes may be treated as continuously varying.

3 The entire surface of the tube sheet over which the pressure acts may be treated as uniformly perforated.

Table 1 Effect of baffles and support plates on tube-end bending moments

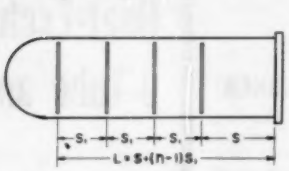

S_1/S \ F_n	1	2	3 OR MORE
0	—	4.00	4.00
0.2	—	3.83	3.83
0.4	—	3.69	3.70
0.6	—	3.59	3.60
0.8	—	3.52	3.53
1.0	3.00	3.43	3.46

$$M_T = -F_n \frac{E_T I_T}{S}\theta \quad ; \quad F_n = 2\left[(1-\tfrac{S_1}{S}) + \sqrt{1+\tfrac{S_1}{S}+(\tfrac{S_1}{S})^2}\,\right]$$

The bending moment M_T at the end of a tube fixed into a tube sheet, and passing through regularly spaced points of zero deflection, may be expressed in terms of tube (and tube sheet) slope thus:

$$M_T = -F_n \frac{E_T I_T}{s}\theta \tag{1}$$

where F_n is given in Table 1. This equation and a similar table were given in reference [1] for exchangers in which both ends of the tubes were fixed into tube sheets. Yakovlev's [4] expression for M_T ignores the presence of the baffles as far as the author can tell.

In an annular ring of radius r and width Δr there are $N_r = (2\pi r \Delta r N/\pi a^2)$ tubes, each contributing a moment M_T in accordance with equation (1). The effect is that of an externally applied radial bending moment, M_r', at radius r, thus:

$$M_r' = \frac{-N_r E_T I_T F_n}{2\pi r s}\theta \tag{2}$$

or

$$M_r' = \frac{-N E_T I_T F_n \Delta r}{\pi a^2 s}\theta \qquad \text{in-lb/in.} \tag{2a}$$

Inasmuch as there is no tangential component to this applied moment, it may be considered due simply to the distributed couple of an externally applied shear Q_T with moment arm Δr. From equation (2a), then,

Nomenclature

N_a = number of tubes in outermost circle
N_r = number of tubes lying on circle whose radius is r
p = hydrostatic pressure, psi
P = tube pitch (spacing), in.
q = effective pressure at radius r, psi
Q = shear, lb per in.
Q_T = reactive shear due to tube bending, lb per in.
r = radius, in.
s = span from tube sheet to nearest support, in.
t = tube-wall thickness, in.
u = δr, dimensionless
w = tube sheet deflection, in.
δ = $(NE_T I_T F_n/\pi a^2 D)^{1/2}$, in^{-1}
Δr = increment of radius, in.
η_w = flexural efficiency
η_σ = ligament efficiency for normal or bending stresses
η_τ = ligament efficiency for shear
θ = tube sheet (or tube end) slope at radius r, radians
κ = $(aM_a/D\theta_a)$, dimensionless
λ = parameter defined by Equation (32), dimensionless
ν_0 = Poisson's ratio for tube-sheet material
ν = effective Poisson's ratio for perforated plate
σ = tube-sheet stress, psi
σ_{Tb} = tube bending stress, psi
τ = tube-sheet shear stress, psi

Subscripts

a = at outside radius a
c = clamped
r = radial
ss = simply supported
t = tangential
T = tube

$$Q_T = -\delta^2 D\theta \tag{3}$$

where

$$\delta = \left(\frac{NE_T I_T F_n}{\pi a^2 s D}\right)^{1/4} \tag{4}$$

It may be concluded then that the effect of the tube-bending reaction on a hydrostatically loaded tube sheet is that of a shear directly proportional to the slope of the tube sheet at the radius under consideration.

Substitution of the resultant net shear $(Q - Q_T)$, in which Q is the equivalent hydrostatic component, into the fundamental equation for the deflection of symmetrically loaded circular plates yields

$$\frac{d}{dr}\left[\frac{1}{r}\frac{d}{dr}\left(r\frac{dw}{dr}\right)\right] = \frac{Q}{D} + \delta^2\frac{dw}{dr} \tag{5}$$

as the differential equation for the deflection of a tube sheet with reactive tube bending. Since bayonet tubes and U-tubes can exert no thrust on the face of the tube sheet, the equivalent hydrostatic pressure in this case equals the actual pressure p and the corresponding shear is simply $Q = pr/2$. With this substitution and a change of variable a single integration of equation (5) gives

$$u^2\frac{d^2w}{du^2} + u\frac{dw}{du} - u^2w = \frac{pa^4}{D}\frac{1}{u_a^4}\left(\frac{u^4}{4} + Bu^2\right) \tag{5a}$$

the left-hand member of which is a form of Bessel's equation. In this,

$$u = \delta r \tag{6}$$

$$u_a = \delta a \tag{6a}$$

The solution is

$$w = \frac{pa^4}{D}\frac{1}{u_a^4}\left[\frac{A}{2}I_0(u) - (B+1) - \frac{u^2}{4} + CK_0(u)\right] \tag{7}$$

where A, B, and C are constants of integration.

Taking cognizance of the conditions that the deflection at the periphery equals zero, and can only be finite at the center if C equals zero, equation (7) and its first derivative may be restated in the form

$$w = \frac{pa^4}{D}\frac{1}{2u_a^4}\left\{\frac{(u_a^2 - u^2)}{2} - A[I_0(u_a) - I_0(u)]\right\} \tag{8}$$

$$\frac{dw}{dr} = \frac{pa^3}{D}\frac{-1}{2u_a^3}[u - AI_1(u)] \tag{9}$$

where A remains to be determined by the condition of peripheral restraint.

The foregoing equation, substituted into the appropriate expressions for bending moment, shear, and local equivalent pressure for circular plates, results in

$$M_r = D\left[\frac{d^2w}{dr^2} + \frac{\nu}{r}\frac{dw}{dr}\right]$$

$$= pa^2\frac{-1}{2u_a^2}\left\{(1+\nu) - A\left[I_0(u) - \frac{(1-\nu)}{u}I_1(u)\right]\right\} \tag{10}$$

$$M_t = D\left[\nu\frac{d^2w}{dr^2} + \frac{1}{r}\frac{dw}{dr}\right]$$

$$= pa^2\frac{-1}{2u_a^2}\left\{(1+\nu) - A\left[\nu I_0(u) + \frac{(1-\nu)}{u}I_1(u)\right]\right\} \tag{11}$$

$$Q_r = D\left[\frac{d^3w}{dr^3} + \frac{1}{r}\frac{d^2w}{dr^2} - \frac{1}{r^2}\frac{dw}{dr}\right] = pa\frac{A}{2u_a}I_1(u) \tag{12}$$

$$q = D\left[\frac{d^4w}{dr^4} + \frac{2}{r}\frac{d^3w}{dr^3} - \frac{1}{r^2}\frac{d^2w}{dr^2} + \frac{1}{r^3}\frac{dw}{dr}\right]$$

$$= p\frac{A}{2}I_0(u) \tag{13}$$

Of these, the last is of academic interest only since it represents the artificial distribution of hydrostatic pressure necessary to produce the same deflection of the tube sheet as actually brought about by combined reactive tube bending and uniform pressure. It should be noted also that the radial bending moment M_r is always greater than or equal to the tangential bending moment M_t, regardless of the values of A or ν.

To the extent, however, that maximum deflection, slope, radial bending, or shear may be governing factors in tube-sheet design, equations (8, 9, 10, 12) remain of interest.

Boundary Restraint

The arbitrary constant A may be determined from the relation between radial bending moment and slope at the tube-sheet boundary. In previous works [1, 2] the author has used the *ratio* of these two values as a convenient parameter to set the bounds of peripheral restraint between simply supported and clamped conditions. Bagnell [6] was the first to call to the author's attention the shortcomings of this device, which serves very well for its intended purpose of delimiting the field of interest, but not for specific conditions within this field. Yakovlev [4] appears to have been the first to publish a thorough discussion on this subject, although a limited publication of the author's [7] dealt with it at approximately the same time. The results of the latter were published (in unrecognizable form) in the TEMA Standards 1954 Addenda [8] and the FHMA (Feedwater Heater Manufacturers' Association) Standards of 1953 [9], in the paragraphs dealing with integral tube sheets.

More recently and more forcefully, Yu [10] has called attention to the deficiencies of the author's earlier approach in a paper which deals in detail with a more general and appropriate treatment of boundary restraint. Reference should be made to his paper and the subsequent discussion [11] for details. Since the author's present aim is the presentation of equations generally applicable to U-tube tube sheets regardless of boundary restraint, he nevertheless confines attention here, for illustrative purposes, to simply supported and clamped tube sheets.

Division of equation (10) by equation (9), substituting the peripheral value u_a, gives an expression for A in the form

$$A = \frac{u_a}{I_1(u_a)}\left\{\frac{\kappa - (1+\nu)}{\kappa - \left[\dfrac{u_a I_0(u_a)}{I_1(u_a)} - (1-\nu)\right]}\right\} \tag{14}$$

where

$$\kappa = \frac{aM_a}{D\theta_a} \tag{15}$$

and in which κ is a dimensionless expression for the ratio of radial bending moment to slope just referred to. Study of Yu's paper [10] will show that the general expression for A is considerably more complicated than this.

Clamped tube sheets are characterized by $\theta_a = 0$ and $\kappa_a = \infty$, from which, with equation (14),

$$A_c = \frac{u_a}{I_1(u_a)} \tag{16}$$

Simply supported tube sheets with reactive tube bending are not, however, characterized by $M_a = 0$, as is the case for simply supported plates in general. As a matter of fact, it might very well be stated that there is no such thing as a simply supported tube sheet because any peripheral slope entails an edge bending moment due to the reaction of the outermost ring of tubes. With the clear understanding then that the term "simply supported" applies to the *system, tube sheet-tube bundle*, and not to the tube sheet as such, equations (2, 4, 6*a*, 15) provide the appropriate value of κ_{aa} as

$$\kappa_{aa} = -\frac{N_a}{2N} u_a^2 \tag{17}$$

where N_a is the number of tubes in the outermost circle. N_a/N is given quite closely by $2\sqrt{(\pi/N)}$ so, to a good approximation,

$$\kappa_{aa} = -\left(\frac{\pi}{N}\right)^{1/2} u_a^2 \tag{17a}$$

This with equation (14) is sufficient to determine

$$A_{aa} = \frac{u_a}{I_1(u_a)} \left\{ \frac{\left(\frac{\pi}{N}\right)^{1/2} u_a^2 + (1+\nu)}{\left(\frac{\pi}{N}\right)^{1/2} u_a^2 + \left[\frac{u_a I_0(u_a)}{I_1(u_a)} - (1-\nu)\right]} \right\} \tag{18}$$

Yu's method [10] might equally well be used to evaluate A in more general form by the addition of a term in K_T paralleling his K_s, and with $\theta_T = 0$ (Yu's nomenclature, with subscript T referring to tube-bending reaction).

Design Equations

In previous papers the author [1, 2], and Miller in somewhat different style [3], have reduced the problems of tube sheet design to use of simple multipliers and characteristic terms in the hydrostatic pressure p, the flexural rigidity D, and powers of the effective radius a. The author's preferred presentation is of the form:

$$w_{max} = \frac{pa^4}{D} F_w \tag{19}$$

$$\theta_{max} = \frac{pa^3}{D} F_\theta \tag{20}$$

$$M_{max} = pa^2 F_M \tag{21}$$

$$Q_{max} = pa F_Q \tag{22}$$

$$q_{max} = p F_q \tag{23}$$

where the evaluation of the F's is apparent from equations (8, 9, 10, 12, 13) once the critical radii (those at which the maxima occur) are determined. For deflection, this is at the center; for moment, at either center or edge; for shear, at the edge; and for slope, at the edge or near the edge, depending on the peripheral restraint.

The foregoing mode of presentation assumes in effect that all unknown properties of perforated plates may be accounted for in the parameter u_a, in terms of which the various F are evaluated, and that the design factors themselves are immutable functions of u_a alone. It was first used by the author on the basis that D was the only property affected by tube-sheet perforation, and that $\nu = 0.3$ as for solid plates. Subsequent use of the procedure [2] was influenced by Malkin's work [12] which indicated that, although both D and ν were affected by drilling, the latter varied only from 0.282 to 0.333 for customary tube spacings; thus the customary mean value for ν of 0.3 appeared to introduce no significant error in the design factors.

Since 1952, however, a considerable literature on equivalent perforated-plate properties has developed, in which Miller [3], Malkin [11, 12, 13, 16, 20], Horvay [13, 14, 15, 16, 17, 18, 20], Duncan [11, 19, 21], and Yu [11] have been prime contributors. A distinction has been drawn between thin plates, in which torsion of the tube-sheet ligaments plays a significant role [12, 15], and thick tube sheets in which deformations are more nearly analogous to those of perforated sheets in a state of plane stress [17, 20]. It appears that thick-plate considerations apply to most shell-and-tube-exchanger tube sheets and that, for customary tube pitches, the effective Poisson ratios are on the order of 0.45 to 0.55. Although Horvay [18] has suggested that the author's previous results are not seriously affected thereby, the fact remains that they are at least open to question.

In view of the foregoing, the design factors presented in this paper are based on an effective Poisson ratio of 0.5. They are intended for customary tube layouts in which the tube-sheet-thickness/minimum-ligament-thickness ratio exceeds 3.

A Royal-Precision LGP-30 digital computer was programmed by the author to solve equations (8, 9, 10, 12) in dimensionless form (f_w, f_θ, f_M, and f_Q) at unit intervals of u_a, $0.1u_a^2$ intervals of κ, and 0.2 intervals of u/u_a (i.e., r/a), and to tabulate the results.

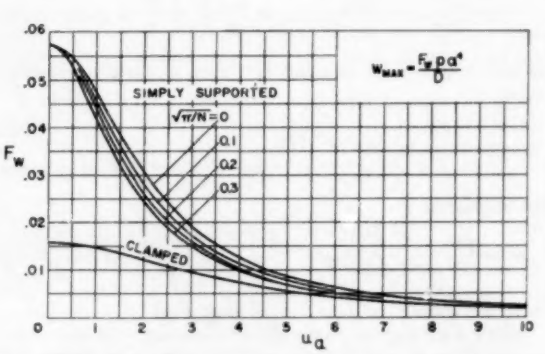

Fig. 2 Variation of maximum tube-sheet deflection factor with parameter u_a defined by equations (4) and (6)

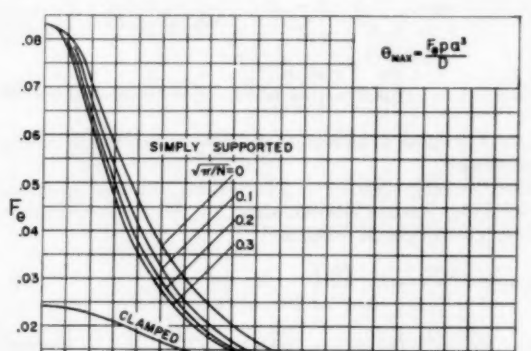

Fig. 3 Variation of maximum tube-sheet (and tube-end) slope factor with parameter u_a, defined by equations (4) and (6)

Table 2 Design factors for U-tube sheets simply supported and clamped

	$F_w = \frac{D w_{max}}{pa^4}$					$F_\theta = \frac{-D\theta_{max}}{pa^3}$					$F_M = \frac{M_{r\,max}}{pa^2}$					$F_Q = \frac{Q_{max}}{pa}$				
$(\pi/N)^{1/2}$	0	0.1	0.2	0.3	∞ [a]	0	0.1	0.2	0.3	∞ [a]	0	0.1	0.2	0.3	∞ [a]	0	0.1	0.2	0.3	∞ [a]
u_a																				
0	0.0573	0.0573	0.0573	0.0573	0.0156	0.0833	0.0833	0.0833	0.0833	0.0241	0.219	0.219	0.219	0.219	0.125	0.500	0.500	0.500	0.500	0.500
0.5	0.0544	0.0538	0.0532	0.0526	0.0154	0.0808	0.0807	0.0793	0.0783	0.0236	0.207	0.205	0.203	0.202	0.124	0.480	0.481	0.481	0.481	0.500
1.0	0.0471	0.0453	0.0438	0.0423	0.0146	0.0712	0.0676	0.0649	0.0624	0.0225	0.178	0.173	0.169	0.165	0.120	0.431	0.435	0.438	0.441	0.500
1.5	0.0385	0.0360	0.0339	0.0322	0.0135	0.0582	0.0536	0.0500	0.0471	0.0209	0.144	0.137	0.132	0.128	0.115	0.372	0.385	0.395	0.404	0.500
2.0	0.0306	0.0280	0.0260	0.0244	0.0122	0.0566	0.0416	0.0381	0.0355	0.0188	0.113	0.107	0.102	0.0982	0.108	0.317	0.343	0.363	0.379	0.500
3.0	0.0193	0.0171	0.0158	0.0148	0.0096	0.0301	0.0256	0.0233	0.0217	0.0149	0.0685	0.0648	0.0625	0.0608	0.0947	0.234	0.292	0.330	0.356	0.500
4.0	0.0126	0.0112	0.0103	0.0098	0.0074	0.0203	0.0169	0.0155	0.0146	0.0116	0.0434	0.0417	0.0407	0.0442	0.0823	0.182	0.270	0.321	0.353	0.500
5.0	0.0087	0.0077	0.0072	0.0069	0.0057	0.0141	0.0118	0.0109	0.0106	0.0077	0.0291	0.0284	0.0356	0.0428	0.0719	0.147	0.263	0.322	0.357	0.500
6.0	0.0063	0.0056	0.0053	0.0051	0.0044	0.0106	0.0088	0.0082	0.0079	0.0067	0.0206	0.0236	0.0345	0.0407	0.0636	0.123	0.264	0.328	0.364	0.500
7.0	0.0048	0.0043	0.0041	0.0039	0.0035	0.0080	0.0069	0.0066	0.0063	0.0055	0.0152	0.0233	0.0330	0.0383	0.0568	0.106	0.267	0.335	0.372	0.500
8.0	0.0037	0.0033	0.0032	0.0031	0.0029	0.0064	0.0054	0.0052	0.0051	0.0046	0.0117	0.0227	0.0314	0.0361	0.0512	0.093	0.273	0.343	0.380	0.500
9.0	0.0030	0.0027	0.0026	0.0025	0.0024	0.0051	0.0044	0.0043	0.0042	0.0037	0.0093	0.0220	0.0299	0.0339	0.0466	0.083	0.280	0.351	0.387	0.500
10.0	0.0024	0.0022	0.0021	0.0021	0.0020	0.0043	0.0036	0.0035	0.0034	0.0032	0.0075	0.0213	0.0284	0.0320	0.0427	0.075	0.287	0.358	0.393	0.500

[a] Values in columns headed ∞ are those for clamped edges.

The values of F_w, F_M, and F_Q given in Table 2 and Figs. 2, 3, and 4 were taken from the lines of the LGP-30 tabulation for $u = 0$ or $u = u_a$ (center or edge), whichever was greater in absolute value. The values of F_θ in Table 2 and Fig. 5 were determined from the maxima on graphs of $(D\theta/pa^3)$ versus r/a. These design factors may be used with equations (19, 20, 21, 22) to determine maximum deflection, slope, bending moment, and shear, respectively. The last three of these are normally of less interest than the maxima of tube bending stress, tube-sheet bending stress, and shear stress. These latter are given by

$$(\sigma_{TA})_{max} = 6(1 - \nu^2)F_\theta F_a p \left(\frac{d}{s}\right)\left(\frac{E_T}{\eta_\sigma E}\right)\left(\frac{a}{h}\right)^2 \quad (24)$$

$$= p\left(\frac{\pi d a^2}{2NI_T}\right) u_a^2 F_\theta \quad (24a)$$

$$(\sigma_r)_{max} = \frac{6F_M p}{\eta_\sigma}\left(\frac{a}{h}\right)^2 \quad (25)$$

$$\tau_{max} = p\,\frac{F_\theta}{\eta_\tau}\left(\frac{a}{h}\right) \text{ (through centers of outermost tubes)} \quad (26)$$

or

$$\tau_{max} = \frac{p}{2}\left(\frac{a}{h}\right) \text{ (just beyond outermost tubes)} \quad (26a)$$

where η_σ and η_τ are the tube-sheet-ligament efficiencies for radial bending stress and for shear stress, which would normally be assumed identical for plane-stress problems. This identity remains to be demonstrated, however.

It should be borne in mind that the ligament efficiencies are not functions of the tube-sheet geometry alone but depend also upon the nature of loading. Horvay [17] presents reciprocal ligament efficiencies in terms of the ratio of principal stresses. There is an assumption implicit in the F_M-values, then, that the quotient, M_r/η_σ, has its maximum at the same radius as M_r itself. This point requires further investigation, but time and space do not permit it here.

Discussion of Design Factors

The design factors of Figs. 2, 3, 4, and 5 may be represented by the well-known circular plate values as small u_a; i.e., for tube sheets whose flexural rigidity is very high compared to that of the tube bundle. For very stiff tube bundles and flexible tube sheets on the other hand, u_a becomes large and advantage may be taken of the asymptotic Bessel-function expressions to simplify the design factor equations. Both limiting conditions are covered by Table 3.

No further remarks are indicated for the design factors at low u_a, but there are several noteworthy features of the factors for large u_a. Bearing in mind that

$$u_a = \left(\frac{NE_T I_T F_a}{\pi s D}\right)^{1/2} \quad (6a)$$

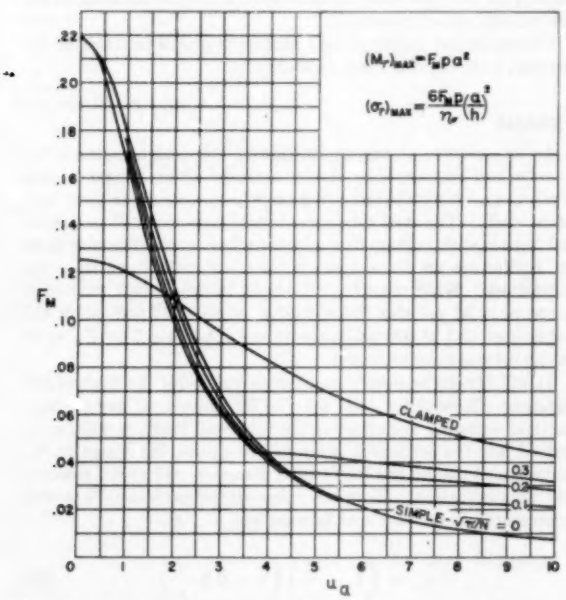

Fig. 4 Variation of maximum radial bending-moment factor with parameter u_a, defined by equations (4) and (6)

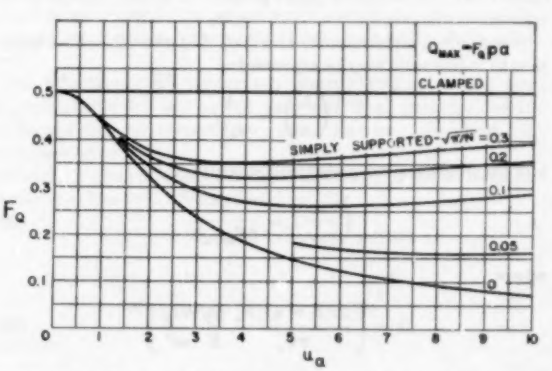

Fig. 5 Variation of maximum tube-sheet shear factor with parameter u_a, defined by equations (4) and (6)

Table 3 Limiting design factors

Factor	$u_a = 0$ Simple	$u_a = 0$ Clamped	$u_a \to \infty$ Simple	$u_a \to \infty$ Clamped
$F_w = \frac{Dw_{max}}{pa^4}$	$\frac{(5+\nu)}{64(1+\nu)}$	$1/64$	$\frac{1}{4u_a^2}\left(1-\frac{2\psi}{u_a^2}\right)^a$	$\frac{1}{4u_a^2}\left(1-\frac{2}{u_a}\right)$
$F_\theta = \frac{D\theta_{max}}{pa^3}$	$\frac{-1}{8(1+\nu)}$	$\frac{-\sqrt{3}}{72}$	$\frac{-1}{2u_a^2}\left[1-\frac{1}{u_a}(1+\ln\psi)\right]^a$	$\frac{-1}{2u_a^2}\left[1-\frac{1}{u_a}(1+\ln u_a)\right]$
$F_{M,b} = \frac{M_0}{pa^2}$	$\frac{-(3+\nu)}{16}$	$\frac{-(1+\nu)}{16}$	$\frac{-(1+\nu)}{2u_a^2}$	$\frac{-(1+\nu)}{2u_a^2}$
$F_{M,a} = \frac{M_a}{pa^2}$	0	$1/8$	$\frac{1}{2u_a^2}[\psi-(1+\nu)]^a$	$\frac{1}{2u_a^2}[u_a-(1+\nu)]$
$F_Q = \frac{Q_{max}}{pa}$	$1/2$	$1/2$	$\frac{\psi}{2u_a}$	$1/2$

[a] $\psi = \left[\frac{\left(\frac{\pi}{N}\right)^{1/2}u_a^2+(1+\nu)}{\left(\frac{\pi}{N}\right)^{1/2}u_a+1}\right]$.

i.e., that u_a is inversely proportional to $\sqrt{D}$, or to $h\sqrt{h}$, the following observations may be made as to the properties of tube sheets *at large* u_a:

1 ***Deflection.*** The maximum tube-sheet deflection is essentially independent of any property of the tube sheet or of its peripheral restraint.

2 ***Bending.*** The center tube-sheet bending stress, which may be the maximum in simply supported tube sheets, *increases directly with the thickness.* The edge bending stress in clamped tube sheets increases inversely as the *square root* of the thickness. The edge bending stress in simply supported tube sheets is not so readily simplified; however, in the range of $5 < u_a < 15$ it increases approximately as the inverse *square* of the thickness, as with ordinary plates.

3 ***Shear.*** The shear through the outermost tube ligaments for clamped tube sheets is given by $pa/2$, as for ordinary plates; for simply supported tube sheets, however, it may be considerably less, depending upon the tube count.

Since u_a increases with decreasing h, item 2 gives rise to the interesting possibility of thinning down a simply supported U-tube sheet to improve its load-carrying ability, which is quite the reverse of customary procedure. The reason for this behavior is to be found under item 1. Near the center of the tube sheet deflections, slopes, and curvatures are independent of any tube-sheet property. Increasing or decreasing its thickness therefore has no effect on the radius of curvature in this region since, as long as u_a remains large, it is governed only by the flexural rigidity of the tube bundle. It follows that the surface fiber stress is increased in direct proportion to the increase in the tube-sheet thickness.

Noting from equations (4) and (6*a*) that the tube-sheet thickness to radius ratio may be expressed as

$$\left(\frac{h}{a}\right) = \frac{\lambda}{u_a^{3/4}} \tag{27}$$

and the dimensionless pressure/stress ratio as

$$\left(\frac{p}{\eta_\sigma \sigma}\right) = \frac{\lambda^3}{6F_M u_a^{3/4}} \tag{28}$$

where

$$\lambda = \left[\frac{12(1-\nu_0^2)F_w}{\pi\eta_w}\frac{E_T}{E}\frac{NI_T}{sa^3}\right]^{1/3} \tag{20}$$

it is possible to express the content of the preceding paragraph graphically by plotting

$$u_a^{-3/4} = (h/a)/\lambda \text{ versus } (6F_M u_a^{3/4})^{-1} = (p/\eta_\sigma\sigma)/\lambda^3$$

This is done in Fig. 6. For simply supported tube sheets, and for given values of $(p/\eta_\sigma\sigma)$ and λ, there may be either one or two values of (h/a) which just use up the allowable stress, as shown in the following example. If the value of the abscissa lies to the left of the knee of the tube-sheet-center stress curve, there is only *one* answer—that governed by edge bending. If it lies to the right of the knee of the center stress curve, but to the left of the intersection of the latter with the appropriate edge stress curve, there are two answers—one governed by edge bending and one governed by the upper branch of the center stress curve. If the value of the abscissa lies to the right of the aforesaid intersection, there is again only *one* answer—that corresponding to the upper branch of the center stress curve. In the former cases, however, other considerations such as shear or tube bending stress may become limiting and render useless the lower values of (h/a) based on tube-sheet bending stress alone. The dual choice in the second case amounts, in effect, either to designing for the tube sheet itself to absorb most of the load, or for the tubes to absorb most of it.

Charts similar to Fig. 6 may also be prepared in terms of deflection, tube bending stress, or shear.

Example

As an example of the application of the design methods for U-tube and bayonet-tube sheets, consider an exchanger having 1260 $^3/_4$-in. 16-BWG steel tubes on $^{15}/_{16}$-in. triangular pitch in a 35-in. shell. The steel tube sheet is held between shell and channel flanges with narrow ring gaskets whose mean diameter is 36 in. Baffles are on 23-in. spacing from each other and from the tube sheet. What must the tube-sheet thickness be if the design pressure is 50 psi and the allowable stress is 17,500 psi in the tube sheet and 15,000 psi in the tubes? Assume $E = E_T = 29 \times 10^6$ psi and simple support.

It will first be necessary to estimate values for the flexural and ligament efficiencies η_w and η_σ. In the absence of any rigorous method assessing the effect of the tube wall itself, it will be assumed that the arithmetic mean of two values, one based on the outside and one on the inside tube diameter, will give a reasonable approximation. Horvay's plane stress method [17] is well represented in the region of interest by

$$\eta_w = \left(1-\frac{d}{p}\right)\left(1-0.3\frac{d}{p}\right) \tag{30}$$

On this basis

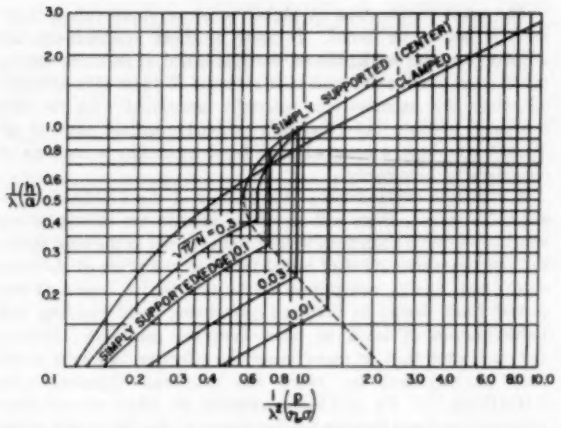

Fig. 6 Dependence of tube-sheet thickness/radius ratio on pressure/stress ratio for U-tube and bayonet-tube exchangers, as limited by tube-sheet bending stress

$$\eta_a = {}^1/_2[(0.2 \times 0.76) + (0.339 \times 0.802)] = 0.211$$

In the same region Horvay's ratio of solid-plate stress to maximum ligament stress ranges from 0.2 at $d/p = 0.8$, to 0.33 at $d/p = 0.66$, yielding a mean value of $\eta_\sigma = 0.27$.[3]

With these approximations, equation (32) gives

$$\lambda = \left[\frac{12 \times 0.91 \times 3.46}{\pi \times 0.211} \times \frac{1260 \times 0.00264}{23(18)^3}\right]^{1/3} = 0.1122$$

where 0.00264 is the moment of inertia of the tube section.

$$\left(\frac{p}{\eta_\sigma \sigma}\right) = \frac{50}{0.27 \times 17{,}500} = 0.0106$$

$$\frac{1}{\lambda^3}\left(\frac{P}{\eta_\sigma \sigma}\right) = \frac{0.0106}{(0.1122)^3} = 0.842$$

$$\left(\frac{\pi}{N}\right)^{1/2} = \left(\frac{\pi}{1260}\right)^{1/2} = 0.05$$

Entering Fig. 6 with these values,

$$\frac{1}{\lambda}\left(\frac{h}{a}\right) = 0.266 \text{ or } 0.91$$

and

$$h = 0.1122 \times 18 \times (0.266 \text{ or } 0.91) = 0.537 \text{ in. or } 1.84 \text{ in.}$$

Either thickness is therefore satisfactory as far as tube-sheet bending stress is concerned. The values of u_a are

$$u_a = [\lambda/(h/a)]^{3/2} = (1/0.266)^{3/2} = 7.3$$

or

$$= (1/0.91)^{3/2} = 1.154$$

The tube bending stress is next investigated, using equation (24a) and Fig. 3

$$\sigma_{T_b} = 50\left[\frac{\pi \times 0.75\,(18)^3}{2 \times 1260 \times 0.00264}\right] \times (7.3)^2 \times 0.0069 = 37{,}900 \text{ psi}$$

or

$$\sigma_{T_b} = \left(\frac{1.154}{7.3}\right)^2\left(\frac{0.065}{0.0069}\right) \times 37{,}900 = 8920 \text{ psi}$$

Obviously the thinned tube sheet is incapable of protecting the tubes from excessive stresses and, although these stresses are only half the allowable value at the greater tube-sheet thickness, no intermediate thickness can be used without exceeding the permissible tube-sheet bending stress.

The shear stress in and just beyond the outermost row of tubes is computed from equations (26) and (26a) and Fig. 5, thus:

$$\tau = \frac{50}{0.27}\left(\frac{18}{0.537}\right) \times 0.163 = 1015 \text{ psi (in ligaments)}$$

$$\tau = 50\left(\frac{18}{0.537}\right) \times 0.5 = 849 \text{ psi (at gasket)}$$

Actually it is inconsistent to use the 18-in. radius in both these equations since the tube-center radius must be at least a tube radius less than a. However, it is a conservative simplification in accord with the assumptions made in the derivation. At the larger tube-sheet thickness,

$$\tau = \left(\frac{50}{0.27}\right)\left(\frac{18}{1.84}\right) \times 0.42 = 760 \text{ psi (in ligaments)}$$

If the construction is such that tube-sheet deflection may relax a partition gasket, this may be checked from equation (19) and Fig. 2, after calculating

$$D = \frac{29 \times 10^6(0.537)^3}{12 \times 0.91} \times 0.211 = 8.70 \times 10^4$$

or

$$D = 8.70 \times 10^4\left(\frac{1.84}{0.537}\right)^3 = 3.5 \times 10^6$$

Then

$$w_{max} = \frac{50 \times (18)^4}{8.70 \times 10^4} \times 0.0041 = 0.248 \text{ in.}$$

or

$$w_{max} = \frac{50 \times (18)^4}{3.5 \times 10^6} \times 0.0435 = 0.0652 \text{ in.}$$

Certainly the thinner tube-sheet deflection would not be acceptable, with or without a partition gasket. Since the ratio of deflection to thickness (0.248/0.537 = 0.46) is high, the basic equations used to derive it are not strictly applicable; there would no doubt be an appreciable tension in the mid-plane of the tube sheet.

The deflection of the thicker tube sheet (0.065 in.) would also be unacceptable for any except very soft thick gaskets, and it would probably be necessary to use a heavier tube sheet for this reason alone.

Finally, a comparison with the well-known TEMA formula [8] will be of interest. From this

$$(h/a) = 1.25\,(50/17500)^{1/3} = 0.0669$$

or

$$h = 0.0669 \times 18 = 1.21 \text{ in.}$$

Therefore,

$$u_a = (0.1122/0.0669)^{3/2} = 2.18$$

$$F_M = 0.100 \text{ and } F_\theta = 0.040$$

[3] See reference [17] for discussion on the effect of the ratio of principal stresses on η_σ. The values cited are for equal principal stresses.

$$\sigma = \frac{6 \times 0.100 \times 50}{0.27\,(0.0669)^2} = 24{,}800 \text{ psi}$$

$$\sigma_{Tb} = 37{,}900\left(\frac{2.18}{7.3}\right)^2\left(\frac{0.040}{0.0069}\right) = 19{,}600 \text{ psi}$$

A ligament efficiency of $(24.8 \times 0.27/17.5) = 0.38$ would thus be required to justify the TEMA formula under the conditions of the present example. However, if the tube-bending reaction were ignored entirely, the calculated tube-sheet bending stress would be

$$\sigma = \frac{6 \times 0.219 \times 50}{0.27 \times (0.0669)^2} = 54{,}500 \text{ psi}$$

and the value of η_σ would have to be 0.83 to justify the TEMA thickness. In the low pressure region at least, the present analysis goes a long way toward explaining the success of TEMA tube sheets—but in terms of tube-bending reaction rather than high apparent ligament efficiencies.

It may be verified readily that the foregoing partial explanation of high apparent ligament efficiencies is *not* valid for higher ratios of pressure to allowable stress.

Summary and Conclusions

Investigation of the effect on tube-sheet deflection of the distributed reactive bending of the tubes leads to the conclusion that the tube sheet behaves as though subjected to a distributed reactive shear proportional to its slope [equations (3) and (5)]. Solution of the deflection equation on this basis for U-tube and bayonet-tube sheets leads to derived equations for maximum slope, bending moment and shear and, from these, for tube-sheet bending stress, tube-sheet shear stress, and tube bending stress, equations (19, 20, 21, 22, 25, 26, 24). These are presented in terms of design factors defined in Tables 2 and 3, whose numerical values are given in Table 2 and Figs. 2, 3, 4, and 5. The factors themselves (F_w, F_θ, F_M and F_Q) are functions of two parameters: u_a, a measure of the "barreling" rigidity of the tube bundle relative to the flexural rigidity of the tube sheet, and $(\pi/N)^{1/4}$, a measure of the tube concentration in the outermost ring of tubes. The latter effect is shown to remove the tube sheet *per se* from the category of simply supported plates, even though the system of tube sheet and tube bundle may itself be simply supported.

At sufficiently high values of u_a the central tube-sheet deflections, and hence curvatures, are independent of any property of the tube sheet, and depend only on the tube-bundle properties. As a consequence, the central bending stresses *decrease* with decreasing tube-sheet thickness and required thicknesses tend to be determined by permissible *tube* bending stresses.

At small values of u_a, on the other hand, the tubes have no influence and tube-sheet stresses are determined by the customary equations for symmetrically loaded circular plates, modified as required to distinguish perforated from solid plates.

This paper purports to throw no additional light on the quantitative effects of boundary restraint intermediate between clamped and simply supported conditions. No contribution to the properties of perforated plates is attempted, although a complete bibliography on the subject is included.

The conclusions to be drawn from the foregoing results are by no means clear. The exceptionally high apparent ligament efficiencies demanded by the TEMA tube-sheet formulas are justified to some extent at low values of the pressure/stress ratio by tube-bending reaction.

The same justification at higher pressure/stress ratios, however, is not to be found. In spite of these uncertainties the TEMA formulas work; the author has heard of no more than a dozen cases of difficulty with tube sheets in 22 years of experience. Although this experience is naturally associated with his own company, it does nevertheless vicariously include that of all TEMA members, among whom tube-sheet design is an item of considerable importance.

A complete explanation of the success of the TEMA U-tube-sheet design equations will no doubt involve the strengthening effect of the tube wall, both within and external to the tube sheet; the reactive shear effect of radial forces in the plane of the tube sheet; and, finally, recognition of the fact that a degree of empirical limit design is involved permitting local yielding and redistribution of loads in more favorable patterns. Horvay [22] indicates that in many cases the effective ligament width may be increased by twice the tube-wall thickness plus $1.10(t/h)(dt)^{1/2}$. Yu [23] has considered the effect of mid-plane forces on fixed and floating-head-exchanger tube sheets and shows it to be identical to reactive tube bending in its effect on deflection; and Conway [24], in a "brief note" entirely unrelated to tube-sheet design, derives an equation for a plate subjected to mid-plane force which is identical in form to equation (5) of this paper.

Acknowledgment

The author expresses his appreciation to Mr. R. E. Riley[4] for his assistance in checking the mathematics and reviewing the paper, to Dr. G. Horvay[5] for present and past helpfulness in bringing new references to his attention, and to Mr. O. W. Heimberger[6] for permission to publish this paper.

References

1 K. A. Gardner, "Heat-Exchanger Tube-Sheet Design," JOURNAL OF APPLIED MECHANICS, vol. 15, TRANS. ASME, vol. 70, 1948, p. A-377.

2 K. A. Gardner, "Heat-Exchanger Tube-Sheet Design—2: Fixed Tube Sheets," JOURNAL OF APPLIED MECHANICS, vol. 19, TRANS. ASME, vol. 74, 1952, p. 159.

3 K. A. G. Miller, "Design of Tube Plates in Heat Exchangers," *Proceedings of The Institution of Mechanical Engineers*, series B, vol. 1, 1952, pp. 215–231.

4 Yu V. Yakovlev, "On the Design of Heat Transfer Apparatus," Trudi Kharkovskovo Aviatsionnovo Instituta, 1954, pp. 133–148.

5 G. D. Galletly, "Circular Plates on a Generalized Elastic Foundation," JOURNAL OF APPLIED MECHANICS, vol. 26, TRANS. ASME, vol. 81, 1959, series E, p. 297.

6 E. J. Bagnell, personal communication, 1953.

7 K. A. Gardner, communication to TEMA and BHMA, January, 1958.

8 "Standards of Tubular Exchanger Manufacturers Association—1954 Addenda," New York, N. Y., 1954.

9 "Standards of Bleeder Heater Manufacturers Association," New York, N. Y., 1953.

10 Yi-Yuan Yu, "Rational Analysis of Heat-Exchanger Tube-Sheet Stresses," JOURNAL OF APPLIED MECHANICS, vol. 23, TRANS. ASME, vol. 78, 1956, pp. 468–473.

11 Discussion of [10], JOURNAL OF APPLIED MECHANICS, vol. 24, TRANS. ASME, vol. 79, 1957, p. 315.

12 I. Malkin, "Notes on a Theoretical Basis for the Design of Tube Sheets of Triangular Layout," TRANS. ASME, vol. 74, 1952, pp. 387–396.

13 Discussion of [12], TRANS. ASME, vol. 74, 1952, pp. 395–396.

---

[4] Engineer, The Griscom-Russell Company, Massillon, Ohio.

[5] Metallurgy and Ceramics Research Department, The General Electric Company, Schenectady, N. Y.

[6] Vice-President-Engineering, The Griscom-Russell Company, Massillon, Ohio.

14 G. Horvay, "Thermal Stresses in Perforated Plates," Proceedings of the First U. S. National Congress of Applied Mechanics, Chicago, Ill., 1951, p. 247.

15 G. Horvay, "Bending of Honeycombs and of Perforated Plates," JOURNAL OF APPLIED MECANICS, vol. 19, TRANS. ASME, vol. 74, 1952, p. 122.

16 Discussion of [15], JOURNAL OF APPLIED MECHANICS, vol. 19, Trans. ASME, vol. 74, 1952, p. 405.

17 G. Horvay, "The Plane Stress Problem in Perforated Plates," JOURNAL OF APPLIED MECHANICS, vol. 19, TRANS. ASME, vol. 74, 1952, p. 355.

18 G. Horvay, Discussion of reference [2], JOURNAL OF APPLIED MECHANICS, vol. 19, TRANS. ASME, vol. 74, 1952, p. 372.

19 J. P. Duncan, "The Structural Efficiency of Tube-Plates for Heat Exchangers," *Proceedings of The Institution of Mechanical Engineers*, vol. 169, 1955, pp. 789–802.

20 Discussion of [19], ibid., pp. 803–810.

21 J. P. Duncan, "Rational Design of Stayed Tubes Plates," *Engineering*, London, England, October 12 and 26, 1956.

22 G. Horvay, "Massachusetts Institute of Technology Lectures—Problems of Stress Analysis," June 26, 27, and 28, 1957.

23 Yi-Yuan Yu, "Axisymmetrical Bending of Circular Plates Under Simultaneous Action of Lateral Load, Force in the Middle Plane, and Elastic Foundation," JOURNAL OF APPLIED MECHANICS, vol. 24, TRANS. ASME, vol. 79, 1957, pp. 141–143.

24 H. D. Conway, "Note on Way's Large-Deflection Solution for the Uniformly Loaded and Clamped Circular Plates," JOURNAL OF APPLIED MECHANICS, vol. 24, TRANS. ASME, vol. 79, 1957, pp. 151–152.

BERNARD W. SHAFFER
Professor of Mechanical Engineering, New York University, New York, N. Y. Mem. ASME

ERIC E. UNGAR[2]
Senior Engineering Scientist, Bolt, Beranek and Newman, Inc., Cambridge, Mass. Assoc. Mem. ASME

Mechanics of the Sheet-Bending Process[1]

Two sets of expressions are obtained for residual stresses and deformations resulting from bending processes in which initially flat sheets are permanently deformed to sheets having finite radii of curvature. One of these sets applies for sheets whose concave surfaces have radii of curvature under load which are greater than 0.84 times the sheet thickness, and is associated with a residual plastic zone in the interior of the sheet. The other set applies whenever the afore-mentioned radii of curvature are less than 0.84 times the sheet thickness, and is associated with residual plastic zones in the bar interior and near the concave boundary of the sheet.

SHEET BENDING is a fabricating process in which initially flat sheets are permanently deformed into intricate shapes by the use of plate rolls or dies. The sheet is subject to a complex history of loading intimately related to the fabricating process. When the load-application device is released, the sheet tends to return to its initial shape—a phenomenon which is called springback. The springback deformation must be taken into consideration by deforming the sheet initially to an extent beyond that which is finally required, by an amount usually determined from experience or experimental data.

Mathematical analysis of the problem is obviously complex, and the general problem has not yet been analyzed successfully. However, a number of investigators [1–6][3] have studied the behavior of a sheet bent into a circular arc, the simplest kind of configuration encountered in the sheet-bending process. Even though deformation of the sheet to this geometry actually requires a complex system of loads between the dies and the sheet, the afore-mentioned analyses are based on the assumption of strains which vary linearly with the thickness co-ordinate only, a condition which also corresponds to that obtained when pure moments are applied to the ends of the sheet. Accordingly, unloading may be considered to correspond to the release of such end moments.

Hill [2] and Lubahn and Sachs [3] have independently performed mathematical analysis of the initial deformation process, based on the assumptions of perfectly plastic materials in plane strain. Schroeder [4] and Gardiner [5], on the other hand, have analyzed the springback effect by taking into consideration only circumferential stresses and by assuming that the neutral axis remains fixed at the center of the sheet. Even though Alexander [6] has considered the residual-stress problem under special conditions, it appears not to have been investigated fully as yet.

Since Shaffer and House [7] have shown that the radial stress reaches significant levels in the interior of a fully plastic wide curved bar, and that the neutral axis of such a bar shifts during elastic-plastic bending, it appears that the problem should be reexamined, with a view toward eliminating the assumptions used in the afore-mentioned springback analyses. This, as well as the evaluation of the residual stresses, is the intent of the present paper.

For purposes of the subsequent analysis, it is assumed that the bending moment initially applied to the sheet is sufficiently intense to cause the elastic region to disappear completely, so that the two plastic zones formed during elastic-plastic bending [7] meet at a surface which represents the degenerate elastic zone. Theoretically, such a fully plastic bending moment applied to a perfectly plastic material may be approached as closely as desired but can be attained only with infinitely large displacements [8]. Practically, however, real materials exhibit a certain amount of strain-hardening so that the fully plastic moment is attained with finite displacements, and the assumption of a completely plastic state of stress during initial loading is a reasonable one.

Basic Considerations

An initially flat wide sheet of thickness h and made of a perfectly plastic material is subjected to an edge moment M per unit width, of sufficient intensity to bend the sheet to a shape whose concave surface has a radius of curvature a. The sheet is assumed wide enough so that the anticlastic curvature is negligible (except near the ends) and a typical strip of the sheet may be analyzed as a problem of plane strain [9]. A perfectly plastic material is one which obeys Hooke's law up to the yield point of the material, and does not work-harden within the plastic range.

It has been shown that the sheet is the same thickness before and after the bending process, if upon loading the sheet is fully within the plastic range [8]. The radius of curvature of the convex surface, therefore, is $(a + h)$ if the concave surface has a radius of curvature a, and h denotes the thickness of the sheet. The geometry of a bent sheet is indicated in Fig. 1, where the letters θ and r denote the circumferential and radial co-ordinates, and σ_r and σ_θ stand for the normal stresses in the radial and circumferential directions, respectively.

The stress components in the bent sheet under load satisfy the equation of equilibrium [2, 3]

$$\frac{d\sigma_r}{dr} = \frac{\sigma_\theta - \sigma_r}{r} \tag{1}$$

---

[1] The results presented in this paper were obtained in the course of research sponsored by the Office of Ordnance Research, Department of the Army (Ordnance Corps), under Contract No. DA-30-069-ORD-1398, with New York University.

[2] Formerly, Assistant Professor of Mechanical Engineering, New York University, New York, N. Y.

[3] Numbers in brackets designate References at end of paper.

Contributed by the Applied Mechanics Division and presented at the Annual Meeting, Atlantic City, N. J., November 29–December 4, 1959, of THE AMERICAN SOCIETY OF MECHANICAL ENGINEERS.

Discussion of this paper should be addressed to the Secretary, ASME, 29 West 39th Street, New York, N. Y., and will be accepted until April 10, 1960, for publication at a later date. Discussion received after the closing date will be returned.

NOTE: Statements and opinions advanced in papers are to be understood as individual expressions of their authors and not those of the Society. Manuscript received by ASME Applied Mechanics Division, May 2, 1958. Paper No. 59—A-35.

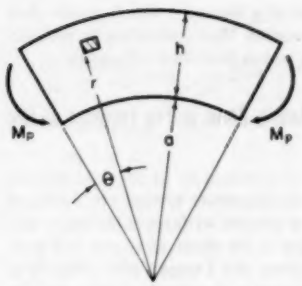

Fig. 1(a) Geometry of the bent sheet showing the applied edge moment M_p

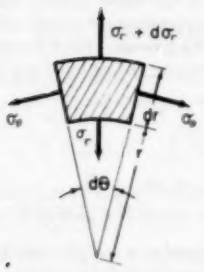

Fig. 1(b) Stresses on a typical element

and the Tresca yield condition. For the sheet-bending problem, the Tresca yield condition may be expressed as

$$\sigma_\theta - \sigma_r = 2k \quad \text{when} \quad \sigma_\theta > \sigma_r \tag{2a}$$

$$\sigma_r - \sigma_\theta = 2k \quad \text{when} \quad \sigma_r > \sigma_\theta \tag{2b}$$

where k is the yield stress of the material in simple shear, or as

$$\sigma_\theta' - \sigma_r' = +1 \quad \text{when} \quad \sigma_\theta > \sigma_r \tag{3a}$$

$$\sigma_\theta' - \sigma_r' = -1 \quad \text{when} \quad \sigma_r > \sigma_\theta \tag{3b}$$

if dimensionless stress parameters are introduced which are defined as

$$\sigma_r' = \sigma_r/2k, \quad \sigma_\theta' = \sigma_\theta/2k \tag{4}$$

In the bent sheet under load $\sigma_\theta > \sigma_r$ in the region $c \leq r \leq a + h$ while $\sigma_r > \sigma_\theta$ in the region $a \leq r \leq c$. The stress components are therefore given by the expressions

$$\sigma_{r_p}' = -\log \frac{r}{a}, \quad \sigma_{\theta_p}' = -\left[1 + \log \frac{r}{a}\right] \quad \text{for} \quad a \leq r \leq c;$$

$$\sigma_{r_p}' = -\log \frac{a+h}{r}, \quad \sigma_{\theta_p}' = 1 - \log \frac{a+h}{r} \quad \text{for} \quad c \leq r \leq a + h; \tag{5}$$

where log refers to the natural logarithm and the subscript p has been appended to the stress symbols to indicate the fully plastic loading condition. The radius c of the neutral surface, determined from the additional requirement that σ_r be continuous at this surface because of equilibrium considerations, is given by the relationship [2, 3]

$$c^2 = a\,(a + h) \tag{6}$$

The bending moment per unit width required to produce the foregoing stress distribution is

$$M_p = \int_a^{a+h} \sigma_\theta r\, dr = \frac{k}{2} h^2, \tag{7}$$

where h denotes the thickness of the sheet.

Unloading of the sheet from its deformed position may be viewed analytically as caused by additional application of an unloading bending moment M, which is of the same magnitude as the loading moment M_p, but opposite in direction. Radial sections are known to remain plane during the unloading process, and cylindrical surfaces to remain cylindrical [10]. The displacement components u (in the radial direction) and v (in the circumferential direction), measured from the deformed position of the sheet before release of the edge moment, are given by the expressions [8, 10]

$$2G\frac{u}{r} = -\frac{A'}{r^2} - B', \quad 2G\frac{v}{r} = 2B'\theta \tag{8}$$

where A' and B' are constants, and G is the shear modulus of the sheet material. From the foregoing, one finds the rotation of radial planes as

$$\Delta\theta = \frac{\partial v}{\partial r} = \frac{B'\theta}{G} \tag{9}$$

Initially, the unloading process may be assumed to be entirely elastic; the validity of this assumption is discussed subsequently. Thus the unloading stress components may be calculated by combining Equations (8) with the strain-displacement expressions [11, 12]

$$\epsilon_r = \frac{\partial u}{\partial r}, \quad \epsilon_\theta = \frac{u}{r} + \frac{1}{r}\frac{\partial v}{\partial \theta} \tag{10}$$

and the elastic stress-strain relation for plane strain

$$\sigma_r = \sigma_z + 2G\epsilon_r, \qquad \sigma_\theta = \sigma_z + 2G\epsilon_\theta \tag{11}$$

to obtain

$$\sigma_r = \frac{A'}{r^2} - B' + \sigma_z, \quad \sigma_\theta = -\frac{A'}{r^2} + B' + \sigma_z \tag{12}$$

Elastic unloading stresses, however, must satisfy the conditions of equilibrium and compatibility, and must therefore be of the form [7]

$$\sigma_{r_e}' = \frac{A}{r^2} + B(1 + \log r^2) + C$$

$$\sigma_{\theta_e}' = -\frac{A}{r^2} + B(3 + \log r^2) + C \tag{13}$$

where A, B, C are undetermined constants and the stress parameters defined by Equations (4) have been written with subscript e to denote elastic stresses. The unprimed constants are related to the primed constants of Equations (12) as

$$A' = 2kA, \quad B' = 2kB, \quad \sigma_z = 2k[B(2 + \log r^2) + C], \tag{14}$$

as found by comparison of Equations (12) and (13).

It is demonstrated subsequently that plastic flow may occur during the unloading process, thereby giving rise to a situation in which elastic unloading occurs in two regions separated by a plastic region. Since the condition that planes remain plane is independent of the state of stress existing in the sheet [10], the displacements in both regions which are unloading elastically must obey Equations (8) and maintain a constant value of $\Delta\theta/\theta$ throughout the entire sheet. Thus, according to Equation (9), the constant B' (and thus the constant B) must have the same value in both elastic zones. In addition, continuity of the displacements at the two elastic-plastic boundaries require the constant A' of Equations (8) (and thus the constant A) also to have the same value in both elastic regions. The displacement cri-

teria, however, place no restriction on the constant C, and it may possess a different value in each of the two elastic zones.

Examination of the Elastic Unloading Assumption

If one assumes that unloading occurs elastically, one may obtain the residual stresses by subtracting the unloading stress components from those induced during the loading process. For this unloading condition, one can evaluate the constants appearing in Equation (13) by making use of the appropriate boundary conditions, and writing the unloading stress components as [7]

$$\sigma_{r_e}' = \frac{M}{N}\left\{\left[1-\left(\frac{a+h}{r}\right)^2\right]\log\left(\frac{a+h}{a}\right) + \left[\left(\frac{a+h}{a}\right)^2-1\right]\log\left(\frac{a+h}{r}\right)\right\} \tag{15}$$

$$\sigma_{\theta_e}' = \frac{M}{N}\left\{\left[1+\left(\frac{a+h}{r}\right)^2\right]\log\left(\frac{a+h}{a}\right) + \left[\left(\frac{a+h}{a}\right)^2-1\right]\left[\log\left(\frac{a+h}{r}\right)-1\right]\right\}$$

where

$$N = \frac{k}{2}(a+h)^3\left[\left(\frac{a+h}{a}-\frac{a}{a+h}\right)^2 - \left(2\log\frac{a+h}{a}\right)^2\right] \tag{16}$$

and M is the unloading bending moment, defined as positive when it is directed opposite to M_p, shown in Fig. 1. The corresponding residual stresses are given by the expressions

$$\sigma_r' = \sigma_{r_p}' + \sigma_{r_e}', \quad \sigma_\theta' = \sigma_{\theta_p}' + \sigma_{\theta_e}', \tag{17}$$

where σ_{r_p}' and σ_{θ_p}', the plastic components of the dimensionless stresses, are described in Equations (5).

Elastic unloading occurs until the residual-stress distribution satisfies one of the yield conditions of Equation (3). A check of the residual state of stress described by Equations (17) reveals that

$$\sigma_\theta' - \sigma_r' = -1+\beta \quad a \le r \le c \tag{18a}$$

$$\sigma_\theta' - \sigma_r' = +1+\beta \quad c \le r \le a+h \tag{18b}$$

where

$$\beta = \sigma_{\theta_e}' - \sigma_{r_e}' = \frac{M}{N}\left[1-\left(\frac{a+h}{a}\right)^2 + 2\left(\frac{a+h}{r}\right)^2\log\left(\frac{a+h}{a}\right)\right] \tag{19}$$

Thus, according to Equations (3), elastic unloading occurs within the range $a \le r \le c$ as long as β is positive in this region, and within $c \le r \le a+h$ as long as β is negative in this region.

Since the unloading bending moment M is positive by definition and N is shown to be positive in the Appendix, inspection of Equation (19) reveals that the function β decreases monotonically as r increases. If r_y denotes the value of r for which β is equal to zero, one finds

$$\left(\frac{r_y}{a+h}\right)^2 = \frac{2a^2}{(a+h)^2-a^2}\log\left(\frac{a+h}{a}\right) \tag{20}$$

As demonstrated in the Appendix, the radius r_y is less than the radius of the neutral surface c for all values of $h > 0$. Thus, in the region $r_y \le r \le c$, β is negative and the right-hand side of Equation (18a) exceeds the yield condition expressed by Equation (3b), thereby implying the existence of a region in which plastic flow occurs. Obviously, the assumption that unloading is entirely elastic leads to a contradiction and is therefore untenable.

Residual Stresses With a Plastic Zone in the Interior of the Sheet

As a consequence of the results obtained in the previous section, one is led to investigate a residual-stress system consisting of elastic regions at the convex and concave surfaces of the sheet, and of a plastic region in the interior of the sheet, as shown in Fig. 2. Stresses in the plastic region obey the Tresca yield criterion of Equation (3b), whereas the stresses in the elastic regions may be found by superimposing the stress expressions for elastic unloading on those induced during the loading process. The corresponding residual-stress system is thus given by the expressions

$$\begin{aligned}
&\sigma_r' = \sigma_{r_p}' + \sigma_{r_e}', && \sigma_\theta' = \sigma_{\theta_p}' + \sigma_{\theta_e}', && a \le r \le t_0;\\
&\sigma_r' = \sigma_{r_{p-}}', && \sigma_\theta' = \sigma_{\theta_{p-}}', && t_0 \le r \le c;\\
&\sigma_r' = \sigma_{r_p}' + \sigma_{r_e}' + H, && \sigma_\theta' = \sigma_{\theta_p}' + \sigma_{\theta_e}' + H, && c \le r \le a+h;
\end{aligned} \tag{21}$$

where the stress parameters with subscript p are given by Equations (5) and those with subscripts e are given by Equations (13). The constant H was added to the last two of Equations (21) in keeping with the earlier conclusion that the stress components in two elastic regions separated by a plastic region may differ by a constant. The radius t_0 denotes the radial co-ordinate of one of the elastic-plastic boundaries of the residual-stress system. The stresses with subscript $p-$ are those which occur in the plastic region in which yield criterion (3b) applies. They must satisfy the equilibrium Equation (1) in addition to the yield condition (3b), and are thus given by the expressions

$$\sigma_{r_{p-}}' = -\log\left(\frac{D_1 r}{a+h}\right), \quad \sigma_{\theta_{p-}}' = -\left[1+\log\left(\frac{D_1 r}{a+h}\right)\right] \tag{22}$$

where D_1 is an undetermined constant. (The constant of integration was chosen to be $-\log(D_1/a+h)$, for convenience.)

The constants appearing in Equation (21) may be determined from the boundary conditions. Equilibrium demands that σ_r vanish at the boundary surfaces $r = a$ and $r = a+h$, and be continuous at the elastic-plastic boundaries $r = t_0$ and $r = c$, prescribed by Equation (6). Satisfaction of the yield criterion at the elastic-plastic boundary $r = t_0$ requires that σ_θ also be continuous there. These boundary conditions result in five relations among the parameters which may be reduced to

$$\begin{aligned}
&B = A/t_0^2\\
&C = -B(1+\log a^2) - A/a^2\\
&\log D_1 = (B+1)\log\left(1+\frac{h}{a}\right) - \frac{A(h/a)}{a^2\left(1+\frac{h}{a}\right)^2}\\
&-H = \frac{A}{a^2\left(1+\frac{h}{a}\right)^2} + B\left[1+\log a^2\left(1+\frac{h}{a}\right)^2\right] + C\\
&1+\log\left[\left(\frac{t_0}{a}\right)^2\left(1+\frac{h}{a}\right)\right] = \left(\frac{t_0}{a}\right)^2\left[1+\frac{(h/a)}{\left(1+\frac{h}{a}\right)^2}\right]
\end{aligned} \tag{23}$$

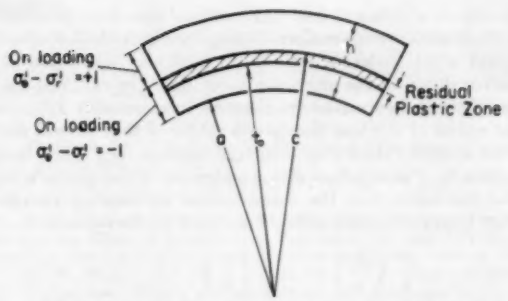

Fig. 2 Residual-stress zone in sheet with $a > 0.84h$

Furthermore, when the bending moment is completely released, equilibrium of the residual-stress system requires

$$\int_a^{a+h} \sigma_\theta r\, dr = 0 \tag{24}$$

Substitution of Equations (21) and (23) into the foregoing results in the following additional relationship between the parameters

$$\left[\frac{(t_0/a)}{1+(h/a)}\right]^2 \left[1 + 3\frac{h}{a} + \left(\frac{h}{a}\right)^2\right] - 2 + \left(\frac{a}{t_0}\right)^2 \left[1 - \frac{h}{a} - \left(\frac{h}{a}\right)^2\right] = \frac{h^2}{2A} \tag{25}$$

and substitution of the same equations into the relation

$$\int_a^{a+h} \sigma_\theta\, dr = 0, \tag{26}$$

which expresses equilibrium of the stress system with a zero resultant circumferential force, shows that the latter condition is identically satisfied.

Equations (23) and (25) constitute a system of six equations from which one may compute the six unknown parameters A, B, C, D_1, H, and t_0. Unfortunately, these equations are transcendental and so complex that they cannot be solved explicitly. Of course, numerical solutions may be obtained for any particular problem.

The solution described by Equation (21), with its constants evaluated from Equations (23) and (25), can represent the residual-stress distribution correctly only as long as it leads to no contradictions. Numerical calculations show that no contradictions arise as long as $a/h > 0.84$ (or $h/a < 1.19$). However, the yield criterion expressed by Equation (3b) is satisfied at the boundary $r = a$ whenever $a/h < 0.84$. Under these conditions, the foregoing solution is no longer applicable, and one must seek another solution which takes the additional yielding into account.

Residual Stresses With Plastic Zones in the Sheet Interior and at the Concave Surface

The results obtained in the previous section lead one to investigate a system of residual stresses which is similar to the one described in Equations (21), but which has an additional plastic zone in the region $a \le r \le t_i$ within which the yield criterion of Equation (3b) is satisfied. With the positions of the residual plastic zones and their boundaries as shown in Fig. 3, the stress system is described by the set of equations

$$\begin{aligned}
&\sigma_r' = \sigma_{r\mathfrak{p}+}', && \sigma_\theta' = \sigma_{\theta\mathfrak{p}+}' && a \le r \le t_i;\\
&\sigma_r' = \sigma_{r\mathfrak{p}}' + \sigma_{r_0}', && \sigma_\theta' = \sigma_{\theta\mathfrak{p}}' + \sigma_{\theta_0}' && t_i \le r \le t_0;\\
&\sigma_r' = \sigma_{r\mathfrak{p}-}', && \sigma_\theta' = \sigma_{\theta\mathfrak{p}-}' && t_0 \le r \le c;\\
&\sigma_r' = \sigma_{r\mathfrak{p}}' + \sigma_{r_0}' + H, && \sigma_\theta' = \sigma_{\theta\mathfrak{p}}' + \sigma_{\theta_0}' + H && t_0 \le r \le a+h;
\end{aligned} \tag{27}$$

where the terms on the right-hand side of each expression are described in Equations (5), (13), and (22), and where

$$\sigma_{r\mathfrak{p}+}' = \log\left(\frac{D_3 r}{a+h}\right), \quad \sigma_{\theta\mathfrak{p}+}' = 1 + \log\left(\frac{D_3 r}{a+h}\right) \tag{28}$$

The latter expression may be obtained from simultaneous solution of the equation of equilibrium (1) and the yield criterion of Equation (3a), in terms of a constant of integration D_3.

The boundary conditions that σ_r vanish at $r = a$ and $r = b$ and be continuous at $r = t_i$, $r = t_0$ and $r = c$, and that σ_θ be continuous at $r = t_i$ and $r = t_0$, provide the following relationships among the constants appearing in the stress and displacement equations:

$$\begin{aligned}
A &= \frac{a^2(t_0/a)^2(t_i/a)^2}{(t_i/a)^2 - (t_0/a)^2}\\
B &= A/t_0^2\\
C &= 2\log(t_i/a) - (A/t_i^2) - B(1 + 2\log t_i)\\
\log D_1 &= (B+1)\log\left(1+\frac{h}{a}\right) - \frac{A(h/a)}{a^2\left(1+\frac{h}{a}\right)^2}\\
D_2 &= 1 + (h/a)\\
-H &= \frac{A}{a^2\left(1+\frac{h}{a}\right)^2} + B\left[1 + 2\log a\left(1+\frac{h}{a}\right)\right] + C\\
1 + \log\left[\left(1+\frac{h}{a}\right)\left(\frac{t_0}{a}\right)^2\right] &= \frac{(h/a)(t_0/a)^2}{\left(1+\frac{h}{a}\right)^2} + \frac{(t_0/a)^2}{(t_i/a)^2}\left[1 + 2\log\frac{t_i}{a}\right]
\end{aligned} \tag{29}$$

Furthermore, the moment equilibrium requirement of Equation (24) imposes the added condition

$$\frac{(h/a)}{\left(1+\frac{h}{a}\right)^2} - \frac{\left(\frac{h}{a}\right)\left(1+\frac{h}{a}\right)}{(t_0/a)^4} = \left[\left(\frac{a}{t_0}\right)^2 - \left(\frac{a}{t_i}\right)^2\right]\left[1 + \frac{(h/a)^2 - 2}{2(t_0/a)^2} + 2\log\frac{t_i}{a}\right] \tag{30}$$

and one may verify that the equilibrium condition of Equation (26) is identically satisfied.

Equations (29) and (30) are a set of eight equations containing eight unknowns A, B, D, D_1, D_2, H, t_i, and t_0, and may be solved

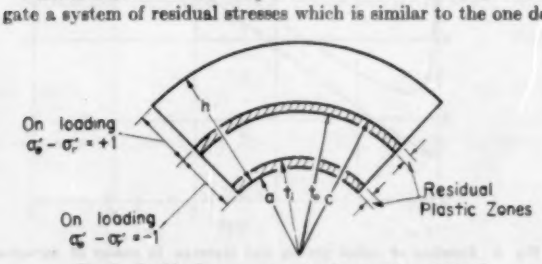

Fig. 3 Residual-stress zones in sheet with $a < 0.84h$

numerically in any given problem. One may also verify numerically that the solution described in the present section is tenable only when the ratio a/h is less than 0.84.

Springback Calculations

It has been demonstrated that in pure bending of a wide curved bar or sheet, made of an incompressible perfectly plastic material, the displacements in the elastic and in the plastic regions obey the same relationships [10]. Thus the displacements throughout the sheet may be studied by observing the behavior of only the elastic zone.

The displacement components during unloading are given by Equations (8) and (9). The constants A' and B' appearing in these equations are related through Equation (14) to the constants appearing in the unloading stress equations which are applicable in the elastic region of the residual-stress system; the latter constants being given by Equations (23) and (25), when $a/h > 0.84$ and by Equations (29) and (30) when $a/h < 0.84$.

The rotation of radial sections of the sheet in springback and the corresponding change of the radius of curvature of the concave surface of the sheet are of particular interest. The aforementioned rotation $\Delta\theta$ may be computed from Equation (9), which may be converted to the dimensionless form

$$\frac{G}{k}\left(\frac{\Delta\theta}{\theta}\right) = 2B \tag{9a}$$

by use of Equation (14). The change Δa which the radius of curvature a experiences in springback may, in view of Equations (8) and (14), be expressed in the dimensionless form

$$\frac{G}{k}\left(\frac{\Delta a}{a}\right) = \frac{G}{k}\left[\frac{u}{r}\right]_{r=a} = -\left[\frac{A}{a^2} + B\right] \tag{31}$$

The manner in which these dimensionless quantities vary with a/h is shown in Fig. 4.

Concluding Remarks

In the actual sheet-bending process, a bending moment is applied to an initially flat sheet until a radius of curvature is obtained which is slightly smaller than that finally desired. Upon release of the bending moment, the sheet springs back toward the original flat position, but retains some permanent deformation.

It has been found that a completely elastic residual-stress state does not occur in sheet bending, in contrast to the conditions observed in most other plastic-flow analyses. This phenomenon may be ascribed to the fact that in sheet bending the neutral surface is at a position during plastic loading which is different from that which it occupies during the elastic unloading process. The portion of the sheet between the two positions of the neutral surface is subject to stresses which are of the same algebraic sign during loading and unloading, thus causing the persistence of a residual plastic region in the interior of the sheet. The relative size of the plastic zone decreases as a/h increases, but remains finite within the range of applicability of the solution.

The range of applicability is limited by the requirement that a fully plastic stress state be developed during the initial bending process. This condition may be assumed to be sufficiently closely approximated when the ratio of radius of curvature to wall thickness is small enough so that the strains developed in the outer fiber of the sheet are at least of the order of 15 to 20 times the yield strain of the material. (This corresponds to a/h ratios between 25 and 30 for mild steel.) For bending not falling within this limit, one may wish to apply the analysis recently published by Alexander [6].

The results of springback calculations, summarized in Fig. 4, can be used to evaluate the radius to which a sheet must be bent in order to obtain a desired final radius of curvature provided the technological process conforms closely enough to the mathematical model which underlies the present analysis. Inspection of the curves shown in the afore-mentioned figure reveals that the dimensionless deformation parameters increase with a/h, except for values of a/h less than about 0.3; and that for a/h greater than about 0.7 these deformation parameters vary nearly linearly with a/h. Examination of a complete set of curves leads one to the conclusion that the dimensionless deformation parameters may be approximated within 5 per cent by the expressions

$$\left.\begin{aligned} \frac{G}{k}\left(\frac{\Delta\theta}{\theta}\right) &\approx -\frac{3}{2}\left(\frac{a}{h}\right) \\ \frac{G}{k}\left(\frac{\Delta a}{a}\right) &\approx \frac{3}{2}\left(\frac{a}{h}\right) + \frac{3}{4} \end{aligned}\right\} \quad \frac{a}{h} > 10 \tag{32}$$

and

$$\begin{aligned} \frac{G}{k}\left(\frac{\Delta\theta}{\theta}\right) &\approx -\left[\frac{3}{2}\left(\frac{a}{h} + \frac{1}{2}\right)\right] \qquad \frac{a}{h} \leq 10 \\ \frac{G}{k}\left(\frac{\Delta a}{a}\right) &\approx \frac{3}{2}\left(\frac{a}{h} + 1\right) \qquad 1.7 < \frac{a}{h} \leq 10 \end{aligned} \tag{33}$$

These equations may be used for approximating purposes only. The more accurate expressions are contained in the previous sections of the paper.

It may be of interest to note that the results of the present paper for sheets whose radii of curvature under load are greater than 0.84 times the sheet thickness agree with some of the observations of Shanley [1]; namely, (*a*) that less springback occurs with materials of lower yield strength than with materials of higher yield strength, (*b*) that for the same yield strength less springback occurs for materials of higher Young's modulus than with materials of lower Young's modulus. (*c*) that springback is not affected if both G and k are changed, provided the ratio G/k is held constant, and (*d*) that for the same radius of bend less springback occurs for thicker sheets than for thin ones.

The previous observations also remain valid for sheets whose radii of curvature under load are less than 0.84 times the sheet thickness. The apparent reversal of the $(G/k)(\Delta a/a)$ versus a/h curve, shown in Fig. 4, is due to the decrease in a (which appears in the denominator of the ordinate) as the origin is approached, and is not due to any changes in the springback characteristics of sheets whose a/h ratios are very small.

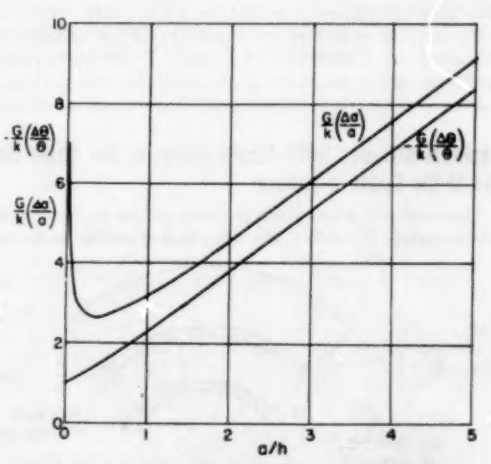

Fig. 4 Rotation of radial planes and increase in radius of curvature during springback

References

1 F. R. Shanley, "Elastic Theory in Sheet Metal Forming Problems," *Journal of the Aeronautical Sciences*, vol. 9, 1942, pp. 313–333.

2 R. Hill, "The Mathematical Theory of Plasticity," Oxford University Press, London, England, 1950, pp. 287–294.

3 J. D. Lubahn and G. Sachs, "Bending of an Ideal Plastic Metal," TRANS. ASME, vol. 72, 1950, pp. 201–208.

4 W. Schroeder, "Mechanics of Sheet-Metal Bending," TRANS. ASME, vol. 65, 1943, pp. 817–827.

5 F. J. Gardiner, "The Spring Back of Metals," TRANS. ASME, vol. 79, 1957, pp. 1–9.

6 J. M. Alexander, "An Analysis of the Plastic Bending of Wide Plate, and the Effect of Stretching on Transverse Residual Stresses," *Proceedings, Institution of Mechanical Engineers*, vol. 173, 1959, p. 73.

7 B. W. Shaffer and R. N. House, Jr., "The Elastic-Plastic Stress Distribution Within a Wide Curved Bar Subjected to Pure Bending," JOURNAL OF APPLIED MECHANICS, vol. 22, TRANS. ASME, vol. 77, 1955, pp. 305–310.

8 B. W. Shaffer and R. N. House, Jr., "Displacements in a Wide Curved Bar Subjected to Pure Elastic-Plastic Bending," JOURNAL OF APPLIED MECHANICS, vol. 24, TRANS. ASME, vol. 79, 1957, pp. 447–452.

9 G. Gerard, "Notes on Beams and Plates," *Journal of the Aeronautical Sciences*, vol. 19, 1952, pp. 207–208.

10 B. W. Shaffer and R. N. House, Jr., "The Significance of Zero Shear Stress in the Pure Bending of a Wide Curved Bar," *Journal of the Aeronautical Sciences*, vol. 24, 1957, pp. 307–308.

11 S. Timoshenko and J. N. Goodier, "Theory of Elasticity," McGraw-Hill Book Company, Inc., New York, N. Y., 1951.

12 Chi-Teh Wang, "Applied Elasticity," McGraw-Hill Book Company, Inc., New York, N. Y., 1953, chapter 3.

APPENDIX

Proofs of Inequality Relationships

Consider a function

$$F(J) = J - \frac{1}{J} - 2 \log J, \tag{34}$$

where $J \geq 1$. The function and its first derivative are seen to vanish at $J = 1$. Furthermore, since the second derivative is always positive for $J \geq 1$, the first derivative and $F(J)$ itself is also positive. Thus

$$J - \frac{1}{J} \geq 2 \log J \tag{35}$$

and

$$\left[J - \frac{1}{J}\right]^2 \geq (2 \log J)^2 \tag{36}$$

By comparing the previous expression with Equation (16), it is apparent that

$$N = \frac{k}{2}(a+h)^2 \left[\left(\frac{a+h}{a} - \frac{a}{a+h}\right)^2 - \left(2 \log \frac{a+h}{h}\right)^2\right] \geq 0 \tag{37}$$

One also may determine from Equation (35) that

$$J^2 - 1 \geq 2J \log J \tag{38}$$

and hence,

$$\frac{2 \log J}{J^2 - 1} \leq \frac{1}{J} \tag{39}$$

Comparing this result with Equation (20), it is apparent that

$$\left[\frac{r_y}{a+h}\right]^2 = \frac{2 \log \left(\frac{a+h}{a}\right)}{\left(\frac{a+h}{a}\right)^2 - 1} \leq \frac{a}{a+h} \tag{40}$$

Since, in view of Equation (6),

$$\frac{a}{a+h} = \left[\frac{c}{a+h}\right]^2 \tag{41}$$

one arrives at the conclusion that

$$r_y \leq c \tag{42}$$

Applicability of Equations (21) and (27)

According to Equations (21) and (22) the difference in residual-stress components associated with an interior plastic zone may be expressed as

$$\begin{aligned} \sigma_\theta' - \sigma_r' &= -1 + 2A\left[\frac{1}{t_0^2} - \frac{1}{r^2}\right] \quad a \leq r \leq t_0 \\ \sigma_\theta' - \sigma_r' &= 1 + 2A\left[\frac{1}{t_0^2} - \frac{1}{r^2}\right] \quad c \leq r \leq a+h \end{aligned} \tag{43}$$

Calculations based on Equations (23) and (25) show that the constant A is always negative. Thus, since $r < t_0$ within the region $a \leq r < t_0$, the term $(1/t_0^2 - 1/r^2)$ is also negative, making it impossible for the yield criterion of Equation (3*b*) to be satisfied within this region. Similarly, since $r > t_0$ in $c \leq r \leq a+h$, the yield criterion cannot be satisfied within this second region.

However, yield condition (3*a*) can be satisfied if

$$(-A)\left[\frac{1}{r^2} - \frac{1}{t_0^2}\right] \geq 1, \quad a \leq r \leq t_0 \tag{44}$$

and yield criterion (3*b*) can be satisfied if

$$(-A)\left[\frac{1}{t_0^2} - \frac{1}{r^2}\right] \geq 1, \quad c \leq r \leq a+h \tag{45}$$

The first of these relationships is most likely to be satisfied at the smallest permissible value of r, or $r = a$, for which it becomes

$$(-A)\left[\frac{1}{a^2} - \frac{1}{t_0^2}\right] \geq 1, \tag{46}$$

whereas the second of the foregoing relationships is most likely to be satisfied at the largest value of r, or $r = a+h$, where it reduces to

$$(-A)\left[\left(\frac{a+h}{t_0}\right)^2 - 1\right] \geq 1 \tag{47}$$

Calculations based on Equations (21), (23), and (25) indicate that Equation (46) is satisfied for $a/h < 0.84$ but not for $a/h > 0.84$, and Equation (47) is never satisfied. Thus Equations (21) represent an acceptable stress distribution whenever $a/h > 0.84$, but a plastic zone forms at the concave boundary surface when $a/h < 0.84$.

Similarly, from Equations (27), one may calculate

$$\begin{aligned} \sigma_\theta' - \sigma_r' &= -1 + 2A\left[\frac{1}{t_0^2} - \frac{1}{r^2}\right] \quad t_i \leq r \leq t_0 \\ \sigma_\theta' - \sigma_r' &= +1 + 2A\left[\frac{1}{t_0^2} - \frac{1}{r^2}\right] \quad c \leq r \leq a+h \end{aligned} \tag{48}$$

In view of the first of Equations (29), one finds that $(\sigma_\theta' - \sigma_r')$ varies monotonically from -1 to $+1$ as r varies from t_0 to t_i, so that neither of the yield criteria of Equations (3) can be satisfied within $t_i < r < t_0$.

The first of Equations (29) indicates that A is negative, so that the yield criterion of Equation (3*a*) cannot be satisfied in the

region $c \leq r \leq a + h$, since $t_0 \leq c \leq r$, and $(1/t_0^2 - 1/r^2)$ is positive in this region. Satisfaction of criterion (3*b*), on the other hand, requires that

$$(-A)\left[\frac{1}{t_0^2} - \frac{1}{r^2}\right] \geq 1, \tag{49}$$

which is most likely to be satisfied at the largest value of r, or at $r = a + h$, where it reduces to

$$(-A)\left[\frac{1}{t_0^2} - \frac{1}{(a+h)^2}\right] \geq 1 \tag{50}$$

Calculations based on Equations (27), (29), and (30) indicate that this condition is not satisfied for $a/h < 0.84$, and that no solutions consistent with the problem may be obtained for $a/h > 0.84$, from which it is evident that Equations (27) represent an acceptable stress distribution for sheets with $a/h < 0.84$ only.

E. A. DAVIS
Advisory Engineer,
Mechanics Department,
Research Laboratories,
Westinghouse Electric Corporation,
Pittsburgh, Pa.
Mem. ASME

Relaxation of a Cylinder on a Rigid Shaft

Equations are developed for the radial and tangential stresses in a cylinder that has been shrunk on a rigid shaft. The analysis is made for a material having elastic properties and behaving according to a power-function speed-effect law.

In a previous paper[1] the author attempted to solve the problem of relaxation in a state of combined stress. At that time the only solution obtained was that for an ideal viscoelastic material. The stress distributions, according to that solution, were the original elastic distributions multiplied by a decaying function of the time. In the present paper an attempt is made to extend the problem to a more realistic material where the plastic strain rates are proportional to the nth power of the stresses. The present problem of a shrink-fit cylinder on a rigid shaft differs from that of the rolled-in tube only in the boundary conditions.

A solution to the plane-stress problem, or the relaxation of a thin disk on a rigid shaft, has still not been obtained. The general problem of plane strain with any arbitrary value of Poisson's ratio also remains unsolved. It has been possible, however, to describe the behavior of the incompressible cylinder under the condition of constant total tangential strain at the bore.

Development of Equations

As in the previous paper, it will be convenient to use the variables u and v rather than the radial and tangential stresses σ_r and σ_θ.

$$u = \sigma_\theta + \sigma_r \qquad v = \sigma_\theta - \sigma_r \tag{1}$$

The equilibrium equation with these variables becomes

$$r^2 \frac{\partial u}{\partial r} = \frac{\partial (r^3 v)}{\partial r} \tag{2}$$

The compatibility equation must be based upon a consideration of the total strain ϵ

$$r \frac{\partial \epsilon_\theta}{\partial r} + \epsilon_\theta - \epsilon_r = 0 \tag{3}$$

where ϵ is the sum of the elastic strain ϵ' and the plastic strain ϵ''

$$\epsilon = \epsilon' + \epsilon'' \tag{4}$$

The relationships between the stresses and the elastic strain rates for an incompressible material ($\nu = 0.5$) in a state of plane strain are given by

$$\frac{\partial \epsilon_\theta'}{\partial t} = \frac{3}{4E}\left(\frac{\partial \sigma_\theta}{\partial t} - \frac{\partial \sigma_r}{\partial t}\right) = \frac{3}{4E}\frac{\partial v}{\partial t} \tag{5}$$

$$\frac{\partial \epsilon_r'}{\partial t} = \frac{3}{4E}\left(\frac{\partial \sigma_r}{\partial t} - \frac{\partial \sigma_\theta}{\partial t}\right) = -\frac{3}{4E}\frac{\partial v}{\partial t} \tag{6}$$

The corresponding relationships for the plastic strain rates are given by

$$\frac{\partial \epsilon_\theta''}{\partial t} = \frac{3\psi}{4}(\sigma_\theta - \sigma_r) = \frac{3\psi}{4} v \tag{7}$$

$$\frac{\partial \epsilon_r''}{\partial t} = \frac{3\psi}{4}(\sigma_r - \sigma_\theta) = -\frac{3\psi}{4} v \tag{8}$$

where ψ is a function of the stresses which determines the speed-effect law.

These expressions for the strain rates can be substituted in Equation (3) if it is first differentiated with respect to the time t. The resulting differential equation can be written as

$$\frac{1}{E}\frac{\partial\left(r^2 \dfrac{\partial v}{\partial t}\right)}{\partial r} + \frac{\partial (r^2 \psi v)}{\partial r} = 0 \tag{9}$$

This expression can be integrated with respect to r immediately:

$$\frac{\partial v}{\partial t} + E\psi v = \frac{E}{r^2} f_1(t) \tag{10}$$

where $f_1(t)$ is an unknown function of the time.

The speed-effect function ψ, introduced in Equations (7) and (8), will be a function of the variable v if it is assumed that for the plastic properties the maximum shearing-strain rate $\partial\gamma_{max}/\partial t_{max}$ is a function of the maximum shearing stress τ_{max}

$$\frac{\partial \gamma_{max}}{\partial t} = f(\tau_{max}) \tag{11}$$

For a cylinder with inside radius a and outer radius b the boundary conditions are that at $t = 0$, the strains are all elastic, and the stresses follow the elastic distribution, and that at any time the radial stress is zero at the outer radius $r = b$:

$$\text{At} \quad t = 0, \quad r = r \qquad u = 2c_1, \quad v = 2c_1 \frac{b^2}{r^2} \tag{12}$$

$$\text{At} \quad t = t, \quad r = b \qquad u = v \tag{13}$$

where $2c_1$ is the value of σ_θ at $r = b$ and $t = 0$.

In order to make this a relaxation problem the additional boundary condition of constant radial displacement at the bore must be imposed. The radial displacement will remain constant

[1] E. A. Davis, "Relaxation of Stress in a Heat-Exchanger Tube of Ideal Material," TRANS. ASME, vol. 74, 1952, pp. 381–385.

Contributed by the Applied Mechanics Division and presented at the Annual Meeting, Atlantic City, N. J., November 29–December 4, 1959, of THE AMERICAN SOCIETY OF MECHANICAL ENGINEERS.

Discussion of this paper should be addressed to the Secretary, ASME, 29 West 39th Street, New York, N. Y., and will be accepted until April 10, 1960, for publication at a later date. Discussion received after the closing date will be returned.

NOTE: Statements and opinions advanced in papers are to be understood as individual expressions of their authors and not those of the Society. Manuscript received by ASME Applied Mechanics Division, December 15, 1958. Paper No. 59—A-31.

with time if the tangential strain rate is zero, hence the boundary condition can be written for $r = a$ as

$$\frac{\partial \epsilon_\theta}{\partial t} = \frac{\partial \epsilon_\theta'}{\partial t} + \frac{\partial \epsilon_\theta''}{\partial t} = \frac{3}{4E}\frac{\partial v}{\partial t} + \frac{3\psi}{4}v = 0 \qquad (14)$$

Since Equation (10) must hold at all points, including $r = a$, we see that the function of time $f(t)$ in this equation must be set equal to zero. The differential equation to be considered as the compatibility equation then becomes

$$\frac{\partial v}{\partial t} + E\psi v = 0 \qquad (10a)$$

In the plane-stress problem and in all plane-strain problems dealing with compressible material the compatibility equation will contain the variable u, and these problems become complex because of the necessity of solving the compatibility and the equilibrium equations simultaneously. In the present problem Equation (10a) can be integrated independently if reasonable forms are chosen for the function ψ. The equilibrium equation can then be used to obtain the expression for the variable u.

It should be noted here that Equation (14) was required to hold only at $r = a$, but since it does not contain the variable r explicitly, it could hold also for any value of r. This is a consequence of the assumptions of incompressibility and plane strain, for a cylinder of such material when once deformed by the process of obtaining a shrink fit will remain in that deformed position indefinitely and there will be no change in the radial displacement at any radius as relaxation takes place.

Equation (11) will be satisfied if the speed-effect function ψ is taken as a power function of the variable v,

$$\psi = Av^n \qquad (15)$$

where n can have any value greater than zero. If n were taken as zero, we would be dealing again with a viscoelastic material. Equation (10) can now be written as

$$\frac{dv}{v^{n+1}} = -EA\,dt \qquad (16)$$

from which

$$v = \frac{2c_1b^2}{(K_1t + r^{2n})^{1/n}} \qquad (17)$$

where

$$K_1 = EAn(2c_1b^2)^n$$

The variable v and hence the maximum shearing stress τ_{max} is thus determined for any allowable value of n. The variable u, or the sum of the radial and tangential stresses, can be determined by substituting Equation (17) in Equation (2)

$$\frac{\partial(r^2v)}{\partial r} = r^2\frac{\partial u}{\partial r} = \frac{4c_1b^2K_1tr}{(K_1t + r^{2n})^{\frac{n+1}{n}}}$$

from which the variable u becomes

$$u = 4c_1b^2K_1t\int \frac{dr}{r(K_1t + r^{2n})^{\frac{n+1}{n}}} + f(t) \qquad (18)$$

This can be integrated readily for $n = 1$ or $n = 2$ and can be evaluated graphically for other values of n. The function of time $f(t)$ can be determined from the boundary condition that $u = v$ at $r = b$.

For the case where $n = 1$ Equation (17) becomes

$$v = \frac{2c_1b^2}{K_1t + r^2} \qquad (17a)$$

and Equation (18) becomes

$$u = 4c_1b^2K_1t\int \frac{dr}{r(K_1t + r^2)^2} + f(t) \qquad (18a)$$

where $K_1 = 2EAc_1b^2$ in both expressions. By integrating Equation (18a) we obtain for the variable u

$$u = \frac{2c_1b^2}{K_1t + r^2} + \frac{2c_1b^2}{K_1t}\ln\frac{r^2(K_1t + b^2)}{b^2(K_1t + r^2)} \qquad (19)$$

This expression approaches the value $2c_1$ as t approaches zero.

For the case where $n = 2$ the expressions for v and u become

$$v = \frac{2c_1b^2}{(K_1t + r^4)^{1/2}} \qquad (17b)$$

$$u = 4c_1b^2K_1t\int \frac{dr}{r(K_1t + r^4)^{3/2}} + f(t) \qquad (18b)$$

The expression for u can be obtained from integral tables by making the transformation $y = r^2$

$$u = \frac{2c_1b^2}{(K_1t + r^4)^{1/2}} + \frac{2c_1b^2}{(K_1t)^{1/2}}\ln\frac{r^2[(K_1t)^{1/2} + (K_1t + b^4)^{1/2}]}{b^2[(K_1t)^{1/2} + (K_1t + r^4)^{1/2}]} \qquad (20)$$

where $K_1 = 2EA(2c_1b^2)^2$.

This expression also converges to the value $2c_1$ when $t = 0$.

Relaxation Under Uniaxial Tension

In order to compare, if possible, the expressions just developed for the state of combined stress with the results of uniaxial tension tests, it will be necessary to derive the expression for the decrease of stress in pure tension from the fundamental assumption expressed in Equation (11). This fundamental law, expressed in terms of Equations (7), (8), and (15) can be written as

$$\frac{\partial \gamma_{max}}{\partial t} = 3A(2)^n\tau_{max}^{n+1} \qquad (21)$$

For uniaxial tension $\gamma_{max} = (3/2)\epsilon''$ and $\tau_{max} = \sigma/2$ and Equation (21) becomes

$$\frac{\partial \epsilon''}{\partial t} = A\sigma^{n+1} \qquad (22)$$

The differential equation for relaxation in pure tension then becomes

$$\frac{1}{E}\frac{\partial \sigma}{\partial t} + A\sigma^{n+1} = 0 \qquad (23)$$

from which

$$\sigma = \frac{\sigma^*}{[(\sigma^*)^nEAnt + 1]^{1/n}} \qquad (24)$$

where σ^* is the stress at $t = 0$. This expression can then be used to evaluate the constants A and n if uniaxial relaxation test data are available.

Determination of Constants

Relaxation curves for a Cr-Mo-Va bolting steel at 950 F and under uniaxial tension are shown by the solid lines in Fig. 1. The elastic modulus of this material at this temperature is 23 ×

10^6 psi. The constants A and n will be determined by choosing a value of n and finding the value of A that will make the curve for $\sigma^* = 34{,}400$ pass through the point $\sigma = 31{,}000$ psi at $t = 1$ hr. Curves for $n = 1, 2, 4, 6, 8$, and 10 that pass through this point are plotted as dashed curves in Fig. 1. The best fit is obtained when $n = 10$, and the value of the constant A for this case is $A = 3.40 \times 10^{-54}$.

In Fig. 2 curves using these values of the constants are plotted for the three values of initial stress used in the tests. The three theoretical curves soon approach each other, and the long-time relaxation behavior, according to this theory, is independent of the initial stress.

It should be pointed out that the agreement between the theoretical curves and the actual test-data curves is not very good. This is as should be expected, for it is known that the decrease in stress during a relaxation test is affected by strain-hardening and by recovery as well as by the speed-effect relation which is the only factor considered in the present theoretical curves. The value of n evaluated from the relaxation test is greater than would have been obtained from minimum-creep-rate data taken from creep tests. This is the result of trying to neglect the effect of strain-hardening which does not appear in the minimum-creep-rate data, but which has a large influence in the primary-creep stage and in the relaxation test. However, the problem of relaxation under combined stress is complicated to the extent that the speed-effect factor can be analyzed only under special cases.

Relaxation of Cylinder

The stress distribution in a cylinder as expressed by Equations (17) and (18) can now be evaluated for various values of the exponent n. A cylinder with an inside radius of $a = 1$ in. and an outside radius of $b = 4$ in. will be considered. The elastic modulus is $E = 2.33 \times 10^7$ psi and a value of 2000 psi has been chosen for the constant c_3. The other constants as determined by the theoretical curves in Fig. 1 are given in the following table:

n	1	2	10
A	1.385×10^{-13}	4.21×10^{-13}	3.40×10^{-54}
K_1	0.2065	0.804	915

For the case where $n = 1$ the variables u and v and hence the stress distributions are obtained from Equations (17a) and (19). The radial and tangential stresses for various values of time are plotted in Fig. 3.

Similar curves for the case where $n = 2$, obtained from Equations (17b) and (20) are shown in Fig. 4.

For the case where $n = 10$ the variable v can be evaluated from Equation (17). Curves of the variable v, and hence curves proportional to the maximum shearing stress τ_{max}, are plotted in Fig. 5.

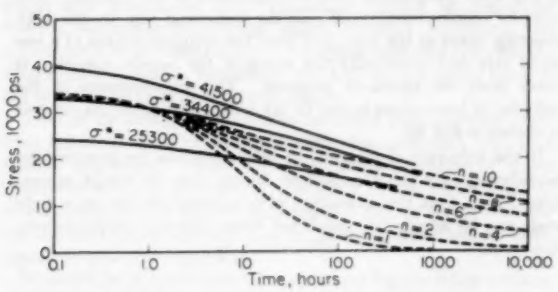

Fig. 1 Relaxation in uniaxial tension, experimental and theoretical

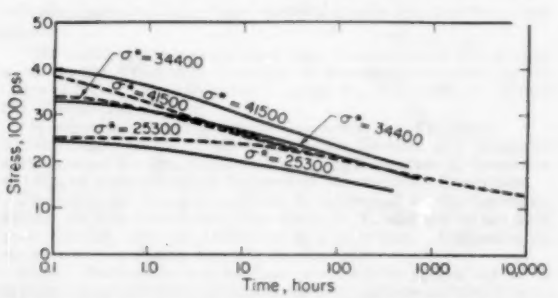

Fig. 2 Comparison of theoretical and experimental relaxation in uniaxial tension

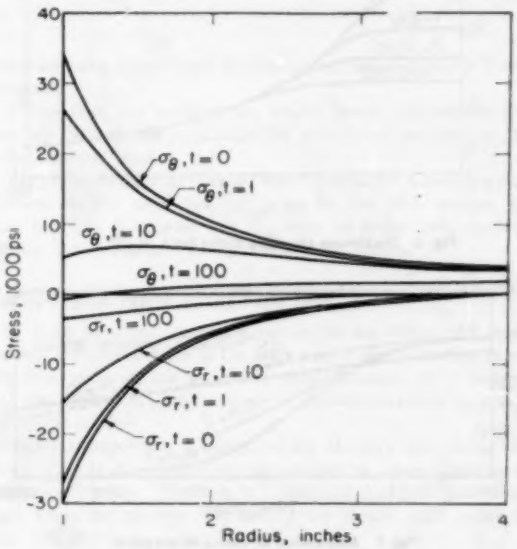

Fig. 3 Radial and tangential stresses for $n = 1$

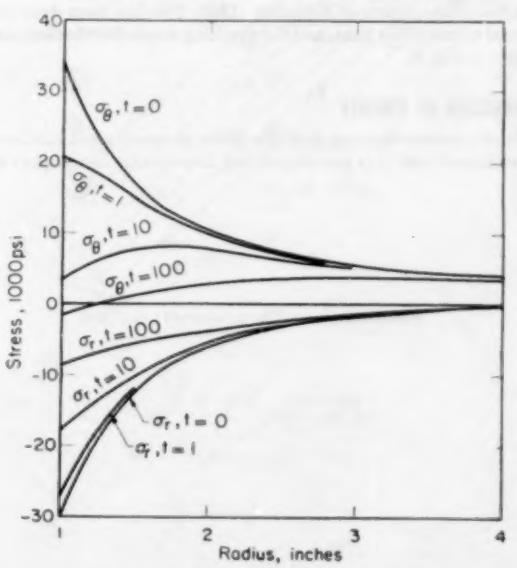

Fig. 4 Radial and tangential stresses for $n = 2$

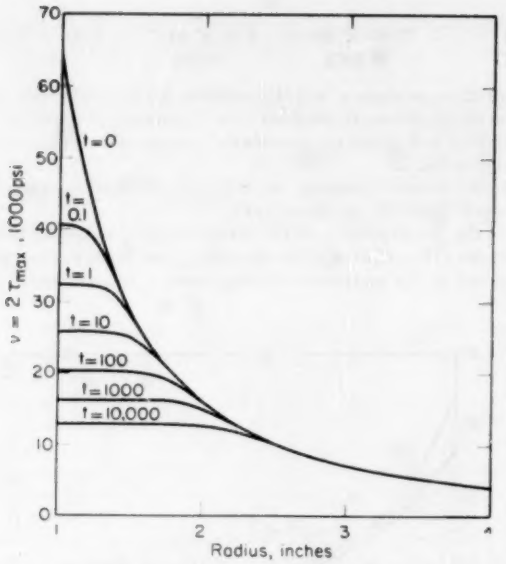

Fig. 5 Maximum shearing stress for $n = 10$

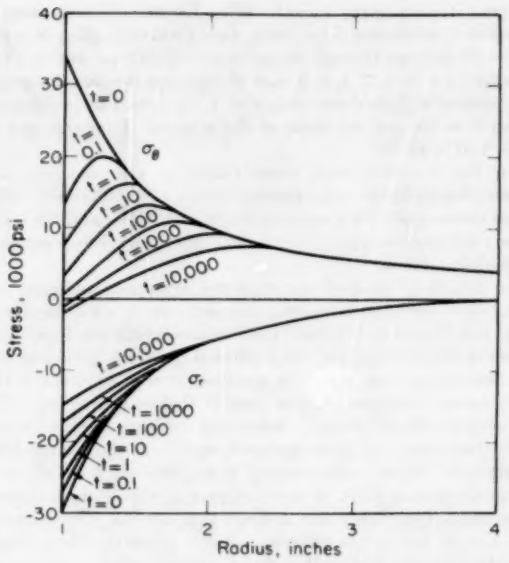

Fig. 6 Radial and tangential stresses for $n = 10$

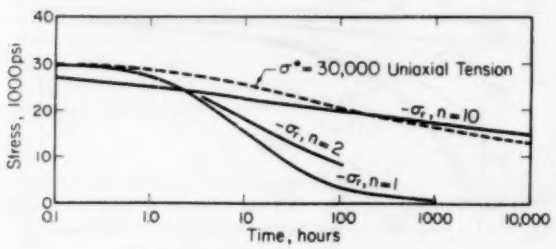

Fig. 7 Relaxation of shrink-fit pressure

The variable u for $n = 10$ must be obtained by numerical or graphical integration of Equation (18). This has been done for several values of the time, and the resulting stress distributions are shown in Fig. 6.

Discussion of Results

In the present analysis only the factor of speed effect has been investigated, and it is not known just how serious the absence of strain-hardening and recovery factors might be. The present analysis does, however, shed some light upon the effect of combined stress on relaxation and should give designers some help in applying the results of uniaxial tension tests to the combined stress problem. Fig. 7 shows how the shrink-fit pressure or the radial stress at $r = a$ decreases with time for three different values of the exponent n. The initial radial stress was 30,000 psi in each case. A curve showing how a uniaxial tension specimen would relax when $n = 10$ and $A = 3.40 \times 10^{-44}$ has been plotted in Fig. 7 for comparison with the relaxation of the cylinder. The cylinder relaxes more rapidly at the beginning due to the high shearing stress at the bore, but later the cylinder relaxes at a less rapid rate and eventually the stress in the tensile specimen is lower than the shrink-fit pressure. This improvement in the cylinder at later times is due to the redistribution of the stresses as shown in Fig. 6.

If the behavior of material in relaxation can be analyzed by considering only the speed-effect factor, then it would appear from Fig. 7 that the relaxation of a cylinder shrunk on a rigid shaft can be adequately predicted from uniaxial tension-relaxation data.

NICHOLAS PERRONE
Assistant Professor,
Engineering Science Department,
Pratt Institute, Brooklyn, N. Y.
Assoc. Mem. ASME

Strain-Hardening Solutions to Axisymmetric Disks and Tubes[1]

Solutions are obtained for annular disks and tubes made of a linearly strain-hardened material, loaded by a uniform tensile load on the outer boundary. The strain-hardening is assumed to follow a kinematic hardening flow law. In addition, a second solution for tubes which accounts for finite deformation is determined. Some numerical comparisons are made with existing isotropic hardening solutions.

PROBLEMS concerned with disks and tubes with axial symmetry probably constitute the simplest examples of multiaxial stress states. Consequently, these problems have received considerable attention in the past. In the field of perfect plasticity the solutions to axisymmetric disk and tube problems now occupy a classical portion of the literature [1, 2, 3].[2] However, in strain-hardening plasticity such is not the case. This is not surprising in view of the fact that at this stage there is no theory of strain-hardening which has yet been verified by extensive experimental agreement.

One of the most promising theories of strain-hardening was only recently proposed by Hodge [4]. His linear theory is mathematically feasible and yet sufficiently flexible to cause hope for reasonable experimental agreement. In fact, the generality of his theory is exhibited in that it includes two earlier theories, isotropic and kinematic hardening, as limiting cases.

In isotropic hardening the strength properties increase simultaneously in all directions, or in other terms the yield curve expands uniformly about its origin. On the other hand, in kinematic hardening the yield curve maintains its original size and shape and experiences only translatory motion in the stress space. Kinematic hardening, unlike isotropic hardening, accounts for a Bauschinger effect. According to recent experiments conducted by Naghdi, Essenburg, and Koff [5] kinematic hardening seems to be the more realistic theory.

Most of the existing solutions to hardened tube and disk problems were obtained for isotropic hardening materials. To give specific examples: Nadai has solved some problems of tubes loaded by internal pressure for a material which yields initially in accordance with the Mises criterion [3]; Hodge has determined the solution for an annular disk of an initially Tresca material loaded by external tension [6].

It would be of interest to have solutions for the other extreme of Hodge's general linear hardening theory [4]; namely, kinematic hardening. Hence in the present work some solutions to tubes and annular disks under external tensile loadings have been obtained using a kinematic hardening law for an initially Tresca material.

In the first two sections the elastic-plastic plane-stress flow laws are derived and applied in the solution of an annular disk under external tension.

The plane-strain flow laws are developed and applied to a tube problem in the next two sections. In the fifth section the tube problem is treated for the case of finite deformations. Finally, the results are discussed in the last section.

Elastic-Plastic Plane-Stress Flow Laws

In order to obtain accurate values for the stress and strain states in a material prior to the fully plastic condition it is necessary to consider elastic as well as plastic strains. It is assumed that the total strain may always be decomposed into an elastic and plastic portion.

The elastic portion is governed by Hooke's law, while the plastic part of the strain will be assumed to obey a kinematic hardening flow law. Further, it is assumed that plastic flow can begin when the stresses first satisfy the Tresca yield criterion, Figs. 1(*a*) and (*b*).

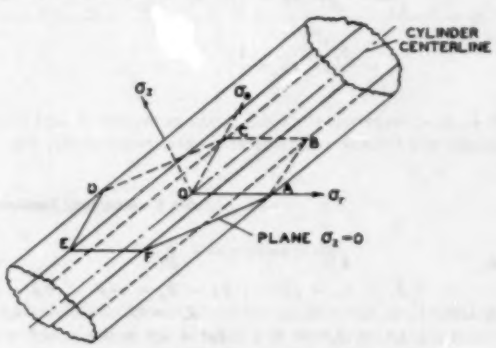

Fig. 1(a) Perspective of Tresca yield surface

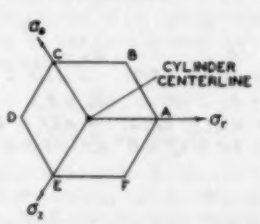

Fig. 1(b) End view of yield cylinder

---

[1] The results of the present paper were obtained in the course of research at the Polytechnic Institute of Brooklyn, sponsored by the Office of Naval Research under Contract No. Nonr 839(14), Project No. NR 064-167.

[2] Numbers in brackets designate References at end of paper.

Contributed by the Applied Mechanics Division and presented at the Annual Meeting, Atlantic City, N. J., November 29–December 4, 1959, of THE AMERICAN SOCIETY OF MECHANICAL ENGINEERS.

Discussion of this paper should be addressed to the Secretary, ASME, 29 West 39th Street, New York, N. Y., and will be accepted until April 10, 1960, for publication at a later date. Discussion received after the closing date will be returned.

NOTE: Statements and opinions advanced in papers are to be understood as individual expressions of their authors and not those of the Society. Manuscript received by ASME Applied Mechanics Division, December 19, 1958. Paper No. 59—A-29.

A kinematic hardening material is one for which the yield surface retains its size and shape, but translates in each stress direction in proportion to the hardening that occurs [7, 8, 9]. Consequently, the yield surface can be thought of as being replaced by a rigid frame which can experience motion when acted upon by a frictionless pin representing the stress state of the material. Frame motion can be correlated with plastic straining. Alternatively the kinematic hardening material can be thought of as being a special case of Hodge's general linear-hardening theory [4]. The physical interpretation of the hardening process may then be regarded as superfluous.

In either event the kinematic hardening flow laws for an initially Tresca material, Figs. 1(*a*) and (*b*), in an $r - \vartheta - z$ principal space may be found [4, 9] and are listed in Table 1 for all possible plastic regimes. Stress and strain components are given by $\bar{\sigma}$ and $\bar{\epsilon}$ terms, respectively, with appropriate subscripts. Dots denote differentiation with respect to time, p superscripts refer to the plastic portion of the strain rate, and c is the hardening rate.

Upon differentiating Hooke's law with respect to time the elastic-strain-rate components are obviously given as:

$$\dot{\epsilon}_r^e = \frac{1}{E}\,[\dot{\bar{\sigma}}_r - \nu(\dot{\bar{\sigma}}_\vartheta + \dot{\bar{\sigma}}_z)],$$

$$\dot{\epsilon}_\vartheta^e = \frac{1}{E}\,[\dot{\bar{\sigma}}_\vartheta - \nu(\dot{\bar{\sigma}}_z + \dot{\bar{\sigma}}_r)], \qquad (1)$$

$$\dot{\epsilon}_z^e = \frac{1}{E}\,[\dot{\bar{\sigma}}_z - \nu(\dot{\bar{\sigma}}_r + \dot{\bar{\sigma}}_\vartheta)],$$

where E is Young's modulus, ν Poisson's ratio, and e superscripts refer to the elastic portion of the total strain rate.

To facilitate a nondimensional portrayal of the flow laws the following dimensionless quantities are introduced:

$$\varphi = Y/E, \quad \rho = E/c',$$

$$\epsilon_r = \frac{\dot{\bar{\epsilon}}_r}{\varphi}, \quad \epsilon_\vartheta = \frac{\dot{\bar{\epsilon}}_\vartheta}{\varphi}, \quad \epsilon_z = \frac{\dot{\bar{\epsilon}}_z}{\varphi}, \qquad (2)$$

$$\sigma_r = \frac{\dot{\bar{\sigma}}_r}{Y}, \quad \sigma_\vartheta = \frac{\dot{\bar{\sigma}}_\vartheta}{Y}, \quad \sigma_z = \frac{\dot{\bar{\sigma}}_z}{Y},$$

where $\dot{\bar{\epsilon}}_r$, $\dot{\bar{\epsilon}}_\vartheta$, $\dot{\bar{\epsilon}}_z$ represent the total strain rates, and Y and c' are the tensile yield stress and hardening rate, respectively, Fig. 2.

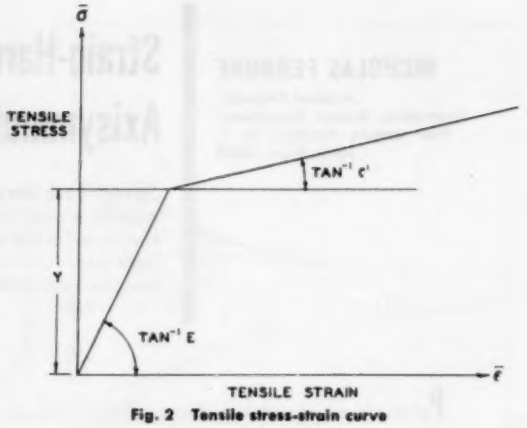

Fig. 2 Tensile stress-strain curve

The hardening rate c is related to c' by the expression [9],

$$c = \frac{4}{3}\,c'$$

The elastic-plastic-rate flow laws can be determined for any plastic regime by adding the elastic strain rates of Equations (1) to the pertinent plastic strain rate of Table 1. (To account for the plane-stress condition, σ_z and $\dot{\sigma}_z$, the stress and stress rate in the third direction must be set equal to zero.)

The flow laws may be integrated for each regime, provided the stress point goes from the elastic interior directly to the regime in question. It is only necessary to employ appropriate elastic stresses and strains as initial conditions. The integrated flow laws for three regimes of eventual interest are:

$$C: \quad \epsilon_r = \sigma_r(1+\rho) - \sigma_\vartheta\left(\nu + \frac{\rho}{2}\right) + \frac{\rho}{2},$$

$$\epsilon_\vartheta = \sigma_\vartheta(1+\rho) - \sigma_r\left(\nu + \frac{\rho}{2}\right) - \rho,$$

$$\epsilon_z = -(\sigma_r + \sigma_\vartheta)\left(\nu + \frac{\rho}{2}\right) + \frac{\rho}{2};$$

$$BC: \quad \epsilon_r = \sigma_r - \nu\sigma_\vartheta,$$

$$\epsilon_\vartheta = -\nu\sigma_r + \sigma_\vartheta\left(1 + \frac{3}{4}\,\rho\right) - \frac{3}{4}\,\rho, \qquad (3)$$

Table 1 Kinematic hardening flow laws—maximum shear stress

		FACES					
Face		*AB*	*BC*	*CD*	*DE*	*EF*	*FA*
Flow law		$\dot{\bar{\sigma}}_r - \dot{\bar{\sigma}}_z = c\dot{\epsilon}_r^p$ $\dot{\epsilon}_\vartheta^p = 0$ $\dot{\epsilon}_r^p + \dot{\epsilon}_z^p = 0$	$\dot{\bar{\sigma}}_\vartheta - \dot{\bar{\sigma}}_z = c\dot{\epsilon}_\vartheta^p$ $\dot{\epsilon}_r^p = 0$ $\dot{\epsilon}_\vartheta^p + \dot{\epsilon}_z^p = 0$	$\dot{\bar{\sigma}}_\vartheta - \dot{\bar{\sigma}}_r = c\dot{\epsilon}_\vartheta^p$ $\dot{\epsilon}_z^p = 0$ $\dot{\epsilon}_r^p + \dot{\epsilon}_\vartheta^p = 0$	$\dot{\bar{\sigma}}_z - \dot{\bar{\sigma}}_r = c\dot{\epsilon}_z^p$ $\dot{\epsilon}_\vartheta^p = 0$ $\dot{\epsilon}_r^p + \dot{\epsilon}_z^p = 0$	$\dot{\bar{\sigma}}_z - \dot{\bar{\sigma}}_\vartheta = c\dot{\epsilon}_z^p$ $\dot{\epsilon}_r^p = 0$ $\dot{\epsilon}_\vartheta^p + \dot{\epsilon}_z^p = 0$	$\dot{\bar{\sigma}}_r - \dot{\bar{\sigma}}_\vartheta = c\dot{\epsilon}_r^p$ $\dot{\epsilon}_z^p = 0$ $\dot{\epsilon}_r^p + \dot{\epsilon}_\vartheta^p = 0$
		EDGES					
Edge		*A*	*B*	*C*	*D*	*E*	*F*
Flow law		$\dot{\bar{\sigma}}_\vartheta - \dot{\bar{\sigma}}_r = c(\dot{\epsilon}_\vartheta^p + \dot{\epsilon}_z^p/2)$ $\dot{\bar{\sigma}}_z - \dot{\bar{\sigma}}_r = c(\dot{\epsilon}_z^p + \dot{\epsilon}_\vartheta^p/2)$ $\dot{\epsilon}_r^p + \dot{\epsilon}_\vartheta^p + \dot{\epsilon}_z^p = 0$	$\dot{\bar{\sigma}}_\vartheta - \dot{\bar{\sigma}}_z = c(\dot{\epsilon}_\vartheta^p + \dot{\epsilon}_r^p/2)$ $\dot{\bar{\sigma}}_r - \dot{\bar{\sigma}}_z = c(\dot{\epsilon}_r^p + \dot{\epsilon}_\vartheta^p/2)$ $\dot{\epsilon}_r^p + \dot{\epsilon}_\vartheta^p + \dot{\epsilon}_z^p = 0$	$\dot{\bar{\sigma}}_z - \dot{\bar{\sigma}}_\vartheta = c(\dot{\epsilon}_z^p + \dot{\epsilon}_r^p/2)$ $\dot{\bar{\sigma}}_r - \dot{\bar{\sigma}}_\vartheta = c(\dot{\epsilon}_r^p + \dot{\epsilon}_z^p/2)$ $\dot{\epsilon}_r^p + \dot{\epsilon}_\vartheta^p + \dot{\epsilon}_z^p = 0$	$\dot{\bar{\sigma}}_\vartheta - \dot{\bar{\sigma}}_r = c(\dot{\epsilon}_\vartheta^p + \dot{\epsilon}_z^p/2)$ $\dot{\bar{\sigma}}_z - \dot{\bar{\sigma}}_r = c(\dot{\epsilon}_z^p + \dot{\epsilon}_\vartheta^p/2)$ $\dot{\epsilon}_r^p + \dot{\epsilon}_\vartheta^p + \dot{\epsilon}_z^p = 0$	$\dot{\bar{\sigma}}_\vartheta - \dot{\bar{\sigma}}_z = c(\dot{\epsilon}_\vartheta^p + \dot{\epsilon}_r^p/2)$ $\dot{\bar{\sigma}}_r - \dot{\bar{\sigma}}_z = c(\dot{\epsilon}_r^p + \dot{\epsilon}_\vartheta^p/2)$ $\dot{\epsilon}_r^p + \dot{\epsilon}_\vartheta^p + \dot{\epsilon}_z^p = 0$	$\dot{\bar{\sigma}}_z - \dot{\bar{\sigma}}_\vartheta = c(\dot{\epsilon}_z^p + \dot{\epsilon}_r^p/2)$ $\dot{\bar{\sigma}}_r - \dot{\bar{\sigma}}_\vartheta = c(\dot{\epsilon}_r^p + \dot{\epsilon}_z^p/2)$ $\dot{\epsilon}_r^p + \dot{\epsilon}_\vartheta^p + \dot{\epsilon}_z^p = 0$
Strain rates	$\dot{\epsilon}_r^p$	+	+	−	−	−	+
	$\dot{\epsilon}_\vartheta^p$	−	+	+	+	−	−
	$\dot{\epsilon}_z^p$	−	−	−	+	+	+

$$\epsilon_z = -\nu\sigma_r - \sigma_\theta\left(\nu + \frac{3}{4}\rho\right) + \frac{3}{4}\rho;$$

B:

$$\epsilon_r = \sigma_r(1+\rho) - \sigma_\theta\left(\nu + \frac{\rho}{2}\right) - \frac{\rho}{2},$$

$$\epsilon_\theta = \sigma_\theta(1+\rho) - \sigma_r\left(\nu + \frac{\rho}{2}\right) - \frac{\rho}{2},$$

$$\epsilon_z = -(\sigma_r + \sigma_\theta)\left(\nu + \frac{\rho}{2}\right) + \rho$$

If necessary, the flow laws for regimes E, EF, and F can also be obtained from the foregoing equations through the use of symmetry considerations.

Equations (3) are bound by the rather strong restriction that any given portion of material can experience plastic flow from one and only one of the various regimes. However, Hodge has shown that for a rigid-plastic material this restriction can be partially removed [4]. In particular, he has demonstrated that the material can go from a side regime to an adjacent corner without explicitly introducing transitional stresses and strains. He calls such stress-point travels, regular progressions. It can be shown that the present elastic-plastic material enjoys the same degree of generality [10].

Annular Disk—External Tension

As an application of the previously developed plane-stress flow laws, a thin annular disk of constant thickness h under a uniform external tensile loading per unit area, $\bar{p}$ is considered. Let a and b be the inner and outer radii, respectively, r and ϑ a suitable cylindrical co-ordinate system, and $\bar{u}$ the radial displacement of a particle.

For convenience, the following dimensionless parameters are chosen, Fig. 3:

$$P = \frac{\bar{p}}{Y}, \quad \mu = \frac{b}{a},$$

$$\xi = \frac{r}{a}, \quad u = \frac{\bar{u}}{a\varphi}, \tag{4}$$

where $\varphi = Y/E$.

Obviously, from axial symmetry, it is clear that the radial and tangential directions are always the principal directions. Hence the flow laws developed in the preceding sections are applicable.

The strain displacement and equilibrium expression may be determined readily (see [11], for example) and are given as

$$\epsilon_r = \partial u/\partial\xi, \quad \epsilon_\theta = u/\xi \tag{5a}$$

$$\xi\sigma_{r,\xi} + \sigma_r - \sigma_\theta = 0 \tag{5b}$$

where comma subscripts denote differentiations.

For brevity, only the qualitative nature of the solution for all load ranges is discussed. Complete analytical details are available in reference [10].

Under small loads the entire disk will experience elastic stresses only. The complete elastic solution is well known [11] and results in a 45-deg straight-line stress profile, Fig. 4.

For loads in excess of the maximum elastic load which is $(\mu^2 - 1)/(2\mu^2)$ a plastic ring will form starting at the inner free boundary. In view of the dividing lines between different flow regimes, Fig. 4, a reasonable choice of elastic-plastic profile would be

$$\begin{aligned} &1 \le \xi \le \alpha, \quad \text{corner } C, \\ &\alpha \le \xi \le \beta, \quad \text{side } BC, \\ &\beta \le \xi \le \mu, \quad \text{elastic} \end{aligned} \tag{6}$$

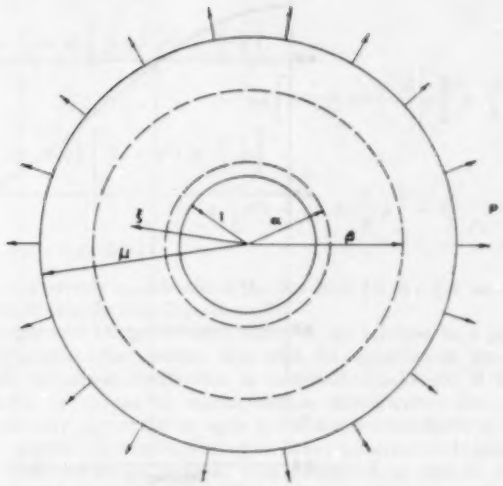

Fig. 3 Annular disk—external tensile loading

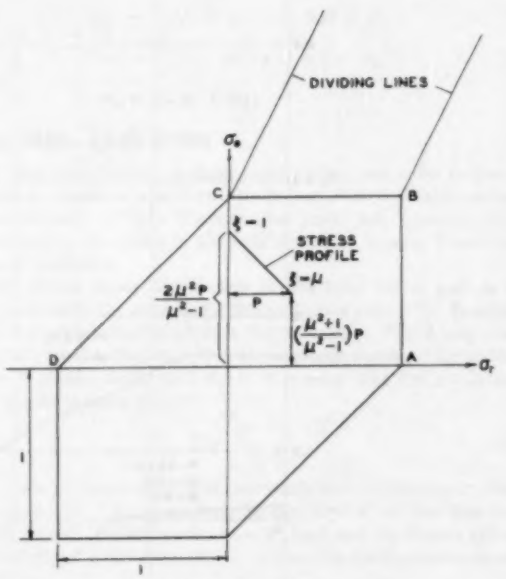

Fig. 4 Elastic stress profile

The complete solution is found for this as well as forthcoming stages by evaluating the constants of integration which arise in the simultaneous solution of (3) and (5) such that all continuity and boundary conditions are satisfied.

The elastic-plastic solution of (6) applies until the load is such that β equals μ, Fig. 3. For the next stage fully plastic flow ensues in the following manner:

$$\begin{aligned} &1 \le \xi \le \alpha \quad \text{corner } C, \\ &\alpha \le \xi \le \mu \quad \text{side } BC \end{aligned}$$

This second stage is valid up to the load for which the stress profile just touches the dividing line between corner B and side BC, Fig. 4; that is, until the outermost material first begins to flow from corner B. Thereafter, the following stress profile turns

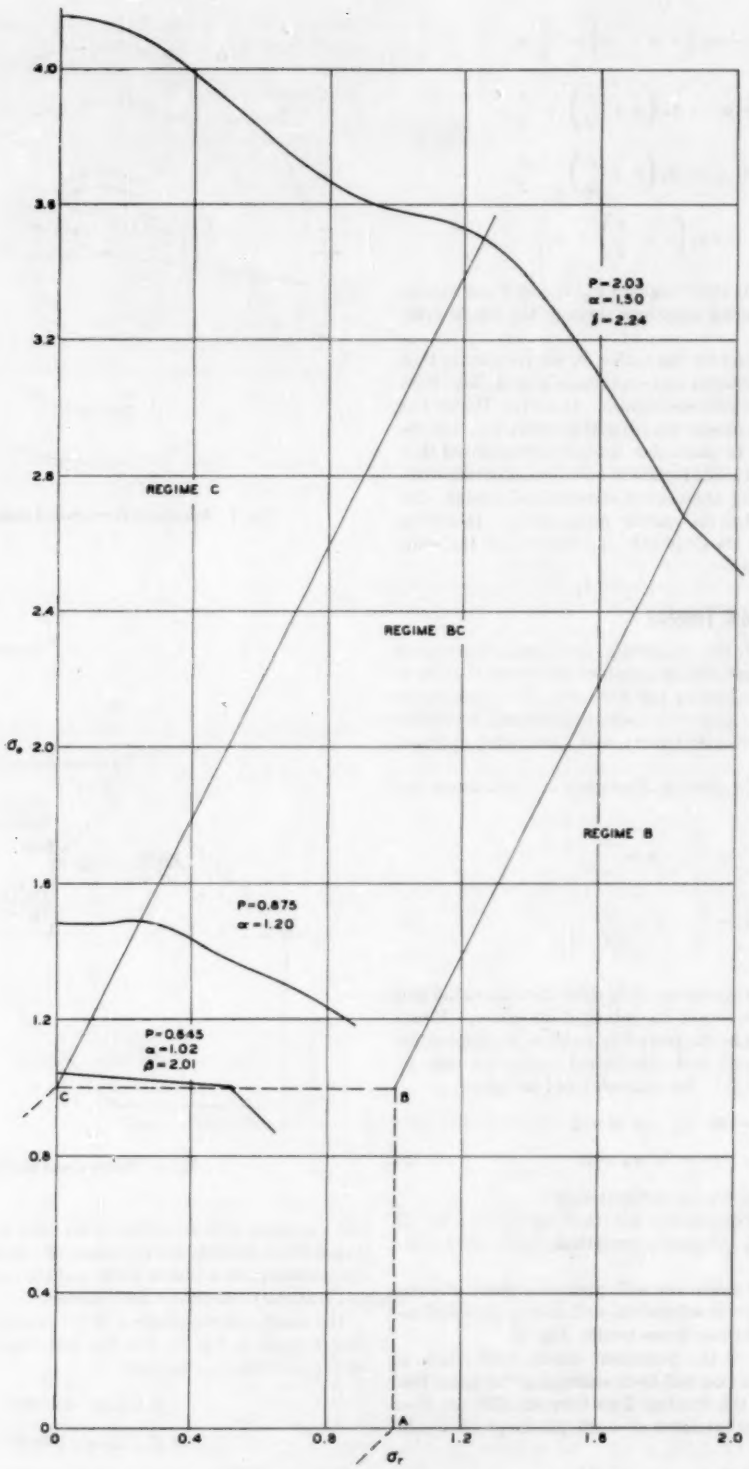

Fig. 5 Annular disk—stress profiles

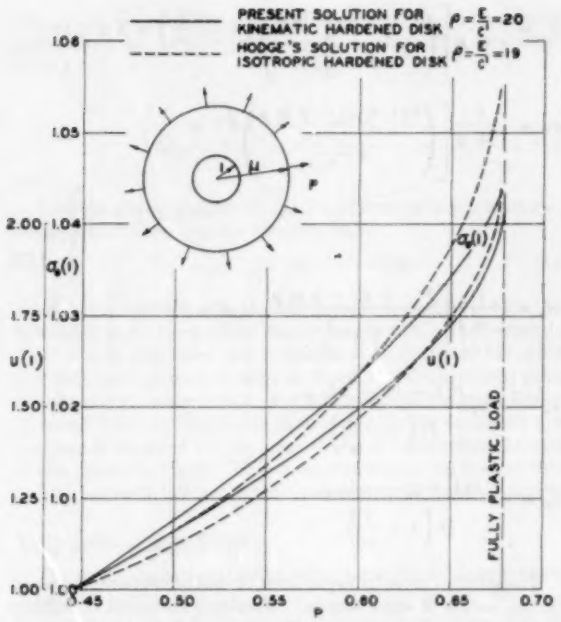

Fig. 6 Comparison of elastic-plastic solutions

out to be the correct one for the final stage of solution:

$$1 \leq \xi \leq \alpha, \quad \text{corner } C,$$
$$\alpha \leq \xi \leq \gamma, \quad \text{side } BC,$$
$$\gamma \leq \xi \leq \mu, \quad \text{corner } B$$

A numerical example is solved by making use of the afore-mentioned general solution [10]. The following parameters were chosen:

$$\mu = 3, \quad \rho = 20, \quad \nu = 0.3$$

Typical stress profiles for each of the three different stages of solution were calculated and are shown in Fig. 5. Some pertinent curves for the elastic-plastic solution, that is, for $P < 0.679$, are given in Fig. 6. Shown in the same figure for comparison are curves which have been taken from Hodge's solution to the same problem [6]. Hodge's solution was found for a completely incompressible material which obeys an isotropic hardening law. Although his hardening ratio ρ was slightly different, the difference was small enough to allow an intelligent comparison.

Elastic-Plastic Plane-Strain Flow Laws

The remainder of the paper will be primarily concerned with the contrasting problem, plane strain. In the problems to be treated it will be assumed that the strain in the third, or z-direction, will be zero at all times and places. As long as the Tresca yield condition is utilized, such an assumption implies that plastic flow can only occur from faces CD or FA, Fig. 1, independently of whether a perfectly plastic or a strain-hardening material is being considered. However, it should be stipulated that the hardening must be such that all faces move parallel to their original positions. This condition is satisfied by all cases of Hodge's general linear hardening theory [4].

The integrated plane-strain flow laws for face CD can be found by using Equations (1) and Table 1 in the same manner as before. These flow laws are

$$CD: \quad \epsilon_r = \sigma_r\left[(1-\nu^2)+\frac{3}{4}\rho\right] - \sigma_\theta\left[\nu(1+\nu)+\frac{3}{4}\rho\right]+\frac{3}{4}\rho,$$
$$\epsilon_\theta = \sigma_\theta\left[(1-\nu^2)+\frac{3}{4}\rho\right] - \sigma_r\left[\nu(1+\nu)+\frac{3}{4}\rho\right]-\frac{3}{4}\rho,$$
$$\sigma_z = \nu(\sigma_r+\sigma_\theta) \tag{7}$$

From symmetry considerations the flow laws for face FA can be obtained directly from Equations (7).

Prager and Hodge [1] have noted in the solution to a perfectly-plastic tube problem that, with the exception of the σ_z stress, the stress distribution is essentially unchanged if the material is treated as incompressible throughout. The σ_z stresses also were shown to agree well if a correction factor of 2ν were applied. It is probable that similar conclusions would apply if a strain-hardening material were considered, so that in the present analysis the material will be assumed to be incompressible throughout. For an incompressible material Equations (7) reduce to:

$$CD: \quad \epsilon_r = {}^3/_4[(1+\rho)(\sigma_r-\sigma_\theta)+\rho],$$
$$\epsilon_\theta = \frac{3}{4}[(1+\rho)(\sigma_\theta-\sigma_r)-\rho], \tag{8}$$
$$\sigma_z = {}^1/_2(\sigma_r+\sigma_\theta)$$

Long Tube—Small Strains

A long tube having an inner radius unity and outer radius μ loaded by means of a uniform tensile load P on the outer surface is considered. [P is a dimensionless load; see Equation (4).] Assuming ϵ_z, the strain in the axial direction, is zero, Equations (8) are applicable.

The elastic stress distribution in the tube for σ_r and σ_θ is still essentially the same as for the analogous disk [11]. In addition, a σ_z stress must arise such that ϵ_z vanish. Fig. 4 may now be interpreted as the projection of the elastic-stress profile on the $\sigma_z = 0$ plane. From that figure it is clear that the maximum elastic load is again given by

$$P = \frac{\mu^2-1}{2\mu^2} \tag{9}$$

For loads in excess of (9) the innermost material begins to flow from face CD. This is not surprising in view of the fact that the profile actually lies above the $\sigma_z = 0$ plane and the Tresca cylinder is oblique to this same plane. Hence the elastic-plastic stress profile is

$$1 < \xi < \beta, \quad \text{face } CD,$$
$$\beta < \xi < \mu, \quad \text{elastic}$$

The simultaneous satisfaction of the equilibrium conditions (5b) and flow laws (8) as well as all continuity and boundary conditions leads to the following elastic-plastic solution:

$$0 \leq \xi \leq \beta \begin{cases} \sigma_r = \dfrac{1}{1+\rho}\left[\dfrac{\beta^2}{2}\left(1-\dfrac{1}{\xi^2}\right)+\rho\ln\xi\right], \\ \sigma_\theta = \dfrac{1}{1+\rho}\left[\dfrac{\beta^2}{2}\left(1+\dfrac{1}{\xi^2}\right)+\rho(\ln\xi+1)\right], \\ \sigma_z = \dfrac{1}{1+\rho}\left[\dfrac{\beta^2}{2}+\rho(\ln\xi+{}^1/_2)\right], \\ \epsilon_r = -{}^3/_4\dfrac{\beta^2}{\xi^2}, \quad \epsilon_\theta = {}^3/_4\dfrac{\beta^2}{\xi^2}, \quad \epsilon_z = 0; \end{cases} \tag{10a}$$

$$\beta \leq \xi \leq \mu \begin{cases} \sigma_r = -\dfrac{\beta^2}{2\xi^2} + \dfrac{\rho(2\ln\beta + 1) + \beta^2}{2(1+\rho)}, \\ \sigma_\vartheta = \dfrac{\beta^2}{2\xi^2} + \dfrac{\rho(2\ln\beta + 1) + \beta^2}{2(1+\rho)}, \\ \sigma_z = \dfrac{\rho(2\ln\beta + 1) + \beta^2}{2(1+\rho)}, \\ \epsilon_r = -\dfrac{3}{4}\dfrac{\beta^2}{\xi^2}, \quad \epsilon_\vartheta = \dfrac{3}{4}\dfrac{\beta^2}{\xi^2}, \quad \epsilon_z = 0; \end{cases} \tag{10b}$$

$$P = \frac{\beta^2}{2}\left(\frac{1}{1+\rho} - \frac{1}{\mu^2}\right) + \frac{\rho}{1+\rho}(1/2 + \ln\beta) \tag{10c}$$

Obviously, the solution is given in implicit form since β is related to the load via Equation (10c). Equations (10) remain valid until the load is such that $\beta = \mu$. This maximum elastic-plastic load can be obtained directly from Equation (10c):

$$P = \frac{\mu^2 - 1 + 2\rho\ln\mu}{2(1+\rho)} \tag{11}$$

For loads in excess of (11) the fully plastic solution may be found readily by using Equations (8) in the equilibrium condition (5*b*) and enforcing the appropriate boundary conditions. The resulting fully plastic solution is given by the following equations:

$$\sigma_r = \frac{1}{1+\rho}\left[\left(\frac{P(1+\rho) - \ln\mu}{1 - \frac{1}{\mu^2}}\right)\left(1 - \frac{1}{\xi^2}\right) + \rho\ln\xi\right],$$

$$\sigma_\vartheta = \frac{1}{1+\rho}\left[\left(\frac{P(1+\rho) - \rho\ln\mu}{1 - \frac{1}{\mu^2}}\right)\left(1 + \frac{1}{\xi^2}\right) + \rho(\ln\xi + 1)\right], \tag{12}$$

$$\sigma_z = \frac{1}{1+\rho}\left[\frac{P(1+\rho) - \rho\ln\mu}{1 - \frac{1}{\mu^2}} + \rho(\ln\xi + 1/3)\right],$$

$$\epsilon_r = -3/2\,\frac{P(1+\rho) - \rho\ln\mu}{\xi^2\left(1 - \frac{1}{\mu^2}\right)},$$

$$\epsilon_\vartheta = 3/2\,\frac{P(1+\rho) - \rho\ln\mu}{\xi^2\left(1 - \frac{1}{\mu^2}\right)}$$

The solution given by Equations (12) has been essentially based on the notion of small strains. Therefore its extent of validity is bound by this restriction. One way of introducing this restriction is to specify that only a certain multiple of the maximum elastic strain is permissible; let n be this multiple. Since the maximum strains in the present case occur at the inner boundary, it can be shown via Equations (4) and (5*a*) that this restriction on the strains reduces to

$$\epsilon_\vartheta(1) \leq n$$

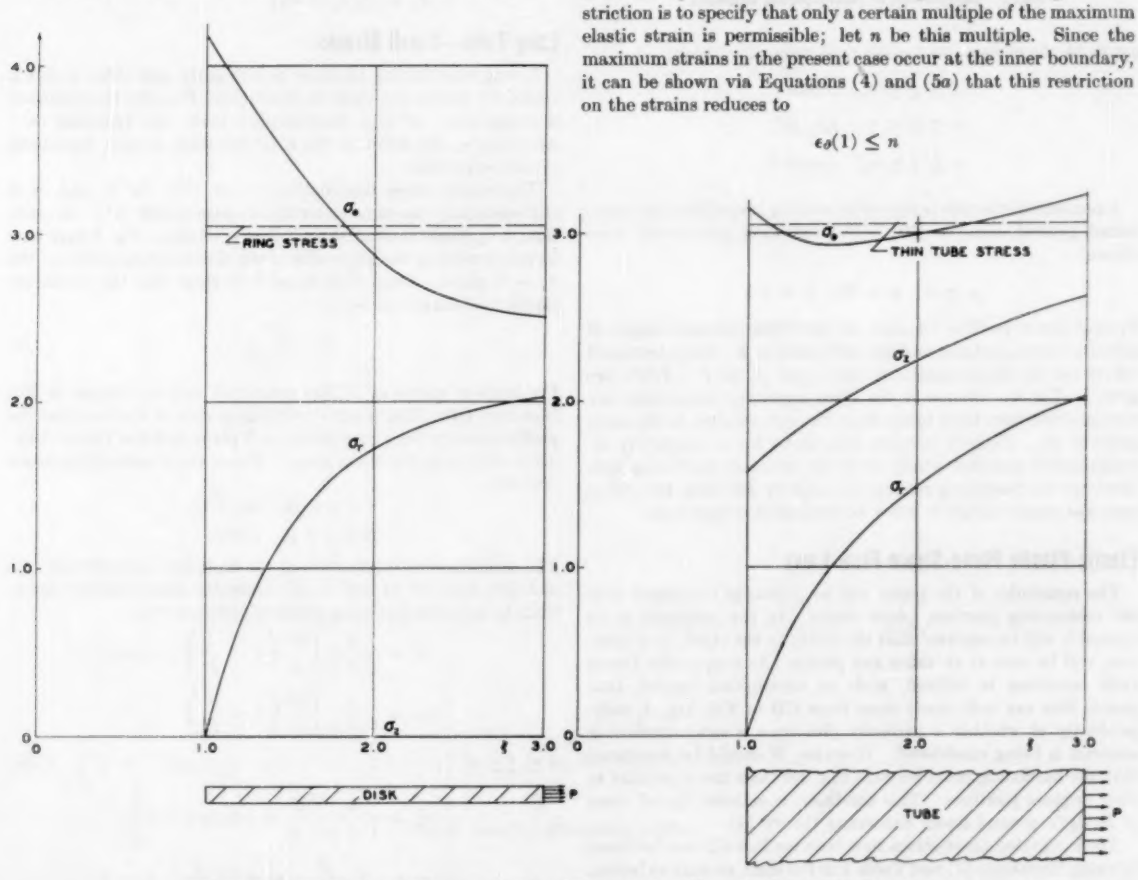

Fig. 7 Stress distribution in kinematic hardened disk and tube; $b/a = 3$; $E/\sigma' = 20$ $P/ = 2.03$

Using this condition in the last of Equations (12), the maximum permissible load for which those equations are valid is determined to be:

$$P_{\max} = \frac{{}^2/_3\left(1 - \frac{1}{\mu^3}\right)n + \rho \ln \mu}{1 + \rho} \tag{13}$$

Based on the general solution in the present section, a numerical example was solved for the following case:

$$\mu = 3, \quad \rho = 20, \quad P = 2.03 \tag{14}$$

From Equations (9) and (11), the maximum elastic load for (14) is 0.445 and the lowest fully plastic load is 1.23. Consequently, for $P = 2.03$ the entire tube is plastic and Equations (12) apply. For that load all stresses are calculated and the complete stress distribution shown in Fig. 7. From the section, "Annular Disk—External Tension," the stress distribution for the analogous disk problem is obtained for the same choice of parameters (14) and is also shown in Fig. 7. The stress distribution for a short tube should probably fall somewhere between the two sets of results.

Long Tube—Large Strains

The preceding section was based on a small strain assumption. When this assumption is violated, say for loads greater than $P_{\max}$ of Equation (13), a more accurate analysis is required. For the same problem, namely, the long tube under external tension, such as analysis will be undertaken.

In the large strain problem it turns out to be more convenient to use dimensional geometric variables while still retaining the same dimensionless load variable P. Let a_0 and b_0 be the original inner and outer tube radii, respectively, and a and b their subsequent values after finite deformations. The initial and current distances of any particle from the tube axis are taken as r_0 and r, respectively; the displacement of a particle is denoted by $\hat{u}$.

For analytical expedience the material is considered as rigid-plastic; hence elastic strains are nonexistent. The complete flow laws are therefore given by Table 1. In particular, for side CD the flow laws are given by

$$\dot{\sigma}_\theta - \dot{\sigma}_r = \frac{4}{3\varphi\rho}\,\hat{\epsilon}_\theta, \tag{15a}$$

$$\hat{\epsilon}_r + \hat{\epsilon}_\theta = 0, \tag{15b}$$

where

$$\hat{\epsilon}_r = \frac{\partial \hat{u}}{\partial r}, \quad \hat{\epsilon}_\theta = \frac{\hat{u}}{r},$$

and r is an Eulerian co-ordinate. Dots will be interpreted as meaning differentiation with respect to a, the inner radius. The validity of this step is ascertained *a posteriori*, since a is eventually shown to be a monotonically increasing function, and hence can represent a "time" parameter.

Although infinitesimal strain expressions are used, finite deformation can be considered in the present analysis because the strains are always defined with respect to the deformed state; that is, current or Eulerian co-ordinates are employed [1].

Equation (15*b*) is identical to the corresponding equation for a perfectly plastic material. Therefore Prager and Hodge's integration of that equation still holds and is reproduced here [1]:

$$r = (r_0^2 + a^2 - a_0^2)^{1/2}, \tag{16a}$$

$$\hat{u} = \frac{dr}{da} = \frac{a}{r} \tag{16b}$$

If use is made of Equations (16), Equation (15*a*) can be integrated with respect to a to yield

$$\sigma_\theta - \sigma_r = \frac{1}{1+\rho}\left[\frac{b_0^2}{r_0^2} + \rho\right] + \frac{4}{3\varphi\rho}\ln\left(\frac{r}{r_0}\right) \tag{17}$$

As initial conditions (at "time" $a = a_0$) it was assumed $\sigma_\theta - \sigma_r$ was continuous with the fully plastic solution, Equation (10*a*) with $\beta = \mu$. In light of the rigid-plastic assumption that is being made, this is the best that could be done in the way of continuity. If the equilibrium equation (5*b*) is solved in conjunction with the integrated flow law (17), wherein r_0 terms have been eliminated via Equation (16*a*), the final solution which accounts for all boundary conditions is

$$\sigma_r = \frac{\lambda}{2(1+\rho)(\eta-1)}\ln\left[\left(\frac{r}{a}\right)\left(\frac{a_0}{r_0}\right)\right] + \frac{\rho}{1+\rho}\ln\left(\frac{r}{a}\right) + \frac{1}{3\varphi\rho}\sum_{i=1,2,3}^{\infty}\frac{1}{i^i}\left[1 - \left(\frac{a^2}{r^2}\right)^i\right]\left(\frac{\eta-1}{\eta}\right)^i, \tag{18a}$$

$$\sigma_\theta = \sigma_r + \frac{1}{1+\rho}\left(\frac{b_0^2}{r_0^2} + \rho\right) + \frac{4}{3\varphi\rho}\ln\left(\frac{r}{r_0}\right), \tag{18b}$$

$$P = \frac{\lambda}{2(1+\rho)(\eta-1)}\ln\left(\frac{\lambda\eta}{\lambda+\eta-1}\right) + \frac{\rho}{2(1+\rho)}\ln\left(\frac{\lambda+\eta-1}{\eta}\right) + \frac{1}{3\varphi\rho}\sum_{i=1,2,3}^{\infty}\frac{1}{i^i}\left[1 - \left(\frac{\eta}{\lambda+\eta-1}\right)^i\right]\left(\frac{\eta-1}{\eta}\right)^i, \tag{18c}$$

where

$$\lambda = \frac{b_0^2}{a_0^2}, \quad \eta = \frac{a^2}{a_0^2}$$

At $\eta = 1$, or $a = a_0$, Equation (18*c*) reduces to the fully plastic load, Equation (11).

The solution of Equations (18) is actually given in implicit form. Once a load P is specified the corresponding value of η is determined from Equation (18*c*). This value of η in turn should be used in Equations (18*a*) and (18*b*) to arrive at the stress distribution for P.

A perfectly plastic material can be thought of as being the limiting case of a strain-hardened material. In the present situation this would occur when $\rho = \infty$. By letting ρ approach infinity Equation (18*c*) becomes

$$P = {}^1/_2 \ln\left(\frac{\lambda+\eta-1}{\eta}\right), \tag{19}$$

which coincides with a perfectly plastic solution to a similar problem by Prager and Hodge [1]. In their problem internal pressure, rather than external tension, was applied. The coincidence of the two results is not surprising in view of the fact that an incompressible material is being considered. Evidently, it makes little difference whether the material is pulled out from the outside or pushed out from the inside.

Moreover, Prager and Hodge found that the pressure required to initiate plastic flow was greater than any subsequent pressure which would sustain the flow. This implies that the fully plastic configuration is unstable. Equation (19) gives evidence that the same instability would occur for the tube under external tension. To find the minimum amount of strain-hardening which will give rise to an initially stable configuration, Equation (18*c*) can be differentiated once with respect to η, and solved for ρ with $\eta = 1$. The resulting maximum value of ρ is given by

$$\rho_{max} = B + \left(B^2 + \frac{2}{3\varphi}\right)^{1/2} \tag{20}$$

where

$$B = \frac{1}{3\varphi} - \frac{\lambda + 1}{4}$$

(It should be recalled that ρ varies inversely with hardening rate; $\rho = E/c'$.) It can be shown that for $\rho < \rho_{max}$

$$\frac{dP}{d\eta} > 0$$

From Equation (20) a curve of ρ_{max} as a function of the ratio of radii, b_0/a_0 is drawn in Fig. 8 for a material specified by

$$\varphi = Y/E = 0.005$$

Also, a curve of ρ_{max} for isotropic hardened disks is determined from Hodge's solution [6] and is shown in the same figure.

Further numerical results have been calculated for the following case:

$$\frac{b_0}{a_0} = 3, \quad \rho = 19, \quad \varphi = 0.005. \tag{21}$$

For this numerical example some stress and deflection comparisons between Hodge's disk solution and the present tube solution are shown in Fig. 9. It should be noted that the load in the figure has been further nondimensionalized with respect to the fully plastic load associated with each problem.

Discussion of Results

In the present work some solutions are obtained for strain-hardened tubes and disks under external tension. A kinematic hardening material is utilized. This represents one extreme of Hodge's general linear hardening theory [4]; isotropic hardening represents the other extreme.

The disk solution given in the section "Annular Disk—External Tension," is considerably more complicated than an isotropic hardening solution to the same problem by Hodge [6]. In the present solution flow occurs at first from two regimes, C and BC, Fig. 4, and later from three regimes, C, BC, and B; whereas in his solution flow occurred from only one regime BC for all loads. Despite the decided qualitative difference between the two solutions, a quantitative comparison of the elastic-plastic solutions shows fairly good agreement, Fig. 6. This is somewhat surprising, especially in view of the slightly different hardening ratios which were used and the different assumptions made as to elastic compressibility. The agreement is probably due to the fact that no more than about 1 per cent of the entire disk flowed from corner C in the elastic-plastic stage so that, in effect, the qualitative difference did not manifest itself numerically. Therefore the slight disagreement which occurs in Fig. 6 can be attributed to the differences in compressibility assumptions and hardening ratios.

It was assumed implicitly in the disk solution that the thickness of the disk was constant. This assumption was reasonably well satisfied in the numerical example considered for loads up to about twice the fully plastic load.

Since disk solutions have now been obtained for both extremes of Hodge's general linear hardening theory [4], it is probable that solutions for any intermediate case can be found.

It might be noted also that the disk solutions appear to be qualitatively and quantitatively analogous to a kinematic hardening solution for an annular plate with a uniform moment along its outer edge [12].[3]

It is encouraging to note that the tube solution, Equations

[3] In that paper "complete hardening" was used to denote what has been called "kinematic hardening" here.

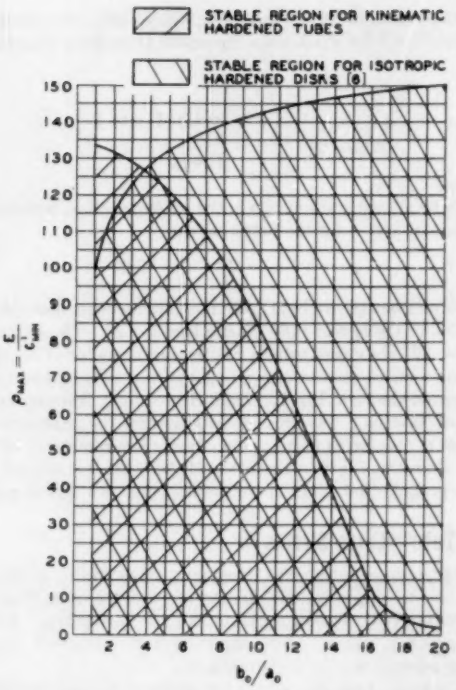

Fig. 8 Chart of minimum stable hardening rates for tubes and disks under external tension — $Y/E = 0.005$

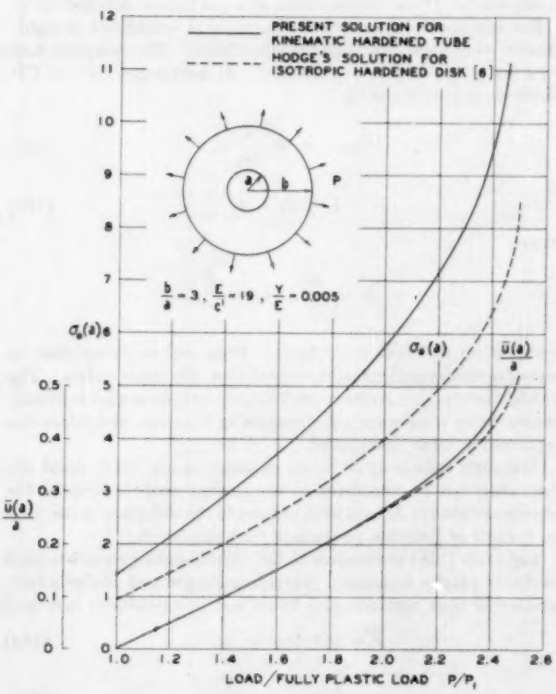
PRESENT SOLUTION FOR KINEMATIC HARDENED TUBE
HODGE'S SOLUTION FOR ISOTROPIC HARDENED DISK [6]
$\frac{b}{a} = 3, \frac{E}{c'} = 19, \frac{Y}{E} = 0.005$
$\sigma_0(a)$
$\frac{\bar{u}(a)}{a}$
LOAD/FULLY PLASTIC LOAD P/P_f

Fig. 9 Comparison of tube and disk solutions for finite deformations

(10), reduces to the correct perfectly plastic one when $\rho = \infty$. On the other hand, for a similar problem solved with a power law governing the hardening, Nadai [3] mentioned that in the perfectly plastic case his solution did not reduce to the correct one.

In Fig. 7, the stress distribution in a geometrically similar tube and disk are compared for the same load. Obviously, the σ_r-stresses compare very well, whereas the σ_θ-distributions compare less favorably. Of course, because of the difference in the physical problems the σ_z should not compare well. It might be of some interest to compare σ_θ stresses with those which evolve from a ring or thin-tube analysis. These are given by broken lines in Fig. 7. Evidently, for the disk the ring stress only gives a measure of the average stress. However, the thin-tube stress gives a very good estimate of the actual σ_θ-distributions; the maximum deviation is about 3 per cent.

A chart giving the minimum stable hardening rates for tubes and disks in Fig. 8 is in accord with what one would intuitively expect. As b_0/a_0 takes on higher values, the minimum fully plastic load for tubes increases rapidly, Equation (11), whereas for disks it increases at a much slower rate. Consequently, for increasing b_0/a_0 the minimum stable hardening rate (the reciprocal of ρ_{max}) increases sharply for tubes and actually decreases slightly for disks, Fig. 8.

In Fig. 9 a comparison between the present kinematic hardening tube solution (preceding section) and Hodge's isotropically hardened disk [6] is presented. Both solutions are for finite deformations. While the stresses give only a fair comparison, remarkable agreement is evident with the deformations. The results for a short tube should probably fall somewhere between the two sets of curves.

References

1 W. Prager and P. G. Hodge, Jr., "Theory of Perfectly Plastic Solids," John Wiley & Sons, Inc., New York, N. Y., 1951.

2 R. Hill, "The Mathematical Theory of Plasticity," Oxford University Press, 1950.

3 A. Nadai, "Theory of Flow and Fracture of Solids," vol. 1 McGraw-Hill Book Company, Inc., New York, N. Y., 1950.

4 P. G. Hodge, Jr., "A General Theory of Piecewise Linear Plasticity Based on Maximum Shear," *Journal of the Mechanics and Physics of Solids*, vol. 5, 1957, pp. 242–260.

5 P. M. Naghdi, F. Essenburg, and W. Koff, "An Experimental Study of Initial and Subsequent Yield Surfaces of Plasticity," Journal of Applied Mechanics, vol. 25, Trans. ASME, vol. 80, 1958, pp. 201–209.

6 P. G. Hodge, Jr., "The Effect of Strain Hardening in an Annular Slab," JOURNAL OF APPLIED MECHANICS, vol. 20, TRANS. ASME, vol. 75, 1953, pp. 530–536.

7 W. Prager, "The Theory of Plasticity: A Survey of Recent Achievements," *Proceedings of The Institution of Mechanical Engineers*, vol. 169, 1955, pp. 41–57.

8 W. Prager, "A New Method of Analyzing Stresses and Strains in Work Hardening Plastic Solids," JOURNAL OF APPLIED MECHANICS, vol. 23, TRANS. ASME, vol. 78, 1956, pp. 493–496.

9 N. Perrone and P. G. Hodge, Jr., "Applications of a Consistent Theory for Strain Hardening Plastic Solids," PIBAL Report No. 403, Polytechnic Institute of Brooklyn, Brooklyn, N. Y., 1957.

10 N. Perrone, "Strain Hardening Solutions to Axisymmetric Disks and Tubes," PIBAL Report No. 478, Polytechnic Institute of Brooklyn, Brooklyn, N. Y., 1958.

11 S. Timoshenko and J. N. Goodier, "Theory of Elasticity," McGraw-Hill Book Company, Inc., New York, N. Y., 1951.

12 N. Perrone and P. G. Hodge, Jr., "Strain-Hardening Solutions to Plate Problems," JOURNAL OF APPLIED MECHANICS, vol. 26, TRANS. ASME, series E, vol. 81, 1959, pp. 276–284.

Effect of Shear Deformations on the Bending of Rectangular Plates

V. L. SALERNO[1]
Consulting Engineer,
Grumman Aircraft Engineering Corporation,
Bethpage, Long Island, N. Y.
Mem. ASME

M. A. GOLDBERG
Research Engineer,
Grumman Aircraft Engineering Corporation,
Bethpage, Long Island, N. Y.

The three partial differential equations derived by Dr. E. Reissner[2,3] have been reduced to a fourth-order partial differential equation resembling that of the classical plate theory and to a second-order differential equation for determining a stress function. The general solution for the two partial differential equations has been applied to a simply supported plate with a constant load p and to a plate with two opposite edges simply supported and the other two edges free. Numerical calculations have been made for the simply supported plate and the results compared with those of classical theory. The calculations for a wide range of parameters indicate that the deviation is small.

THE field equations governing the bending of plates when shear deformations are included have been developed in detail by E. Reissner.[2,3] Employing this theory Reissner treated several examples of technical importance.[2,3] Problems concerning rectangular plates sustaining a load $p(x, y)$, in which shear deformations are considered, do not appear to have been treated in recent literature. In the present paper, Reissner's theory is applied to a simply supported plate with a constant load p and to a plate with two opposite edges simply supported and the other two edges free.

General Theory

Reissner showed that the solution to problems of this type depends upon a system of linear partial differential equations involving the deflection w and the two resultant shear forces, V_x and V_y. The required system of equations is

$$V_x - \frac{h^2}{10}\nabla^2 V_x + \frac{h^2}{10(1-\nu)}\frac{\partial p}{\partial x} = -D\frac{\partial \nabla^2 w}{\partial x} \quad (1a)$$

$$V_y - \frac{h^2}{10}\nabla^2 V_y + \frac{h^2}{10(1-\nu)}\frac{\partial p}{\partial y} = -D\frac{\partial \nabla^2 w}{\partial y} \quad (1b)$$

$$\frac{\partial V_x}{\partial x} + \frac{\partial V_y}{\partial y} = -p \quad (1c)$$

where D is the flexural rigidity,

$$D = \frac{Eh^3}{12(1-\nu^2)}$$

h is the thickness of the plate, and the sign convention employed is shown in Fig. 1. Associated with Equations (1) are the modified stress resultants

$$M_x - \frac{h^2}{5}\frac{\partial V_x}{\partial x} + \frac{\nu h^2}{10(1-\nu)}p = -D\left(\frac{\partial^2 w}{\partial x^2} + \nu\frac{\partial^2 w}{\partial y^2}\right) \quad (2a)$$

$$M_y - \frac{h^2}{5}\frac{\partial V_y}{\partial y} + \frac{\nu h^2}{10(1-\nu)}p = -D\left(\frac{\partial^2 w}{\partial y^2} + \nu\frac{\partial^2 w}{\partial x^2}\right) \quad (2b)$$

$$H_{xy} - \frac{h^2}{10}\left(\frac{\partial V_x}{\partial y} + \frac{\partial V_y}{\partial x}\right) = -(1-\nu)D\frac{\partial^2 w}{\partial x \partial y} \quad (2c)$$

Reissner demonstrated that, for the case $p = 0$, a stress function can be introduced to yield a solution to the homogeneous system of Equations (1). A particular integral must then be found to account for the loading function, $p(x, y)$. In the present paper a particular integral for an arbitrary choice of $p(x, y)$ is given. First, V_x and V_y are eliminated from Equations (1). This is accomplished by differentiating (1a) with respect to x, (1b) with respect to y, adding the results and employing (1c) to simplify and obtain

$$D\nabla^4 w = p - \frac{kh^2}{10}\nabla^2 p \quad (3)$$

where

$$k = \frac{2-\nu}{1-\nu}$$

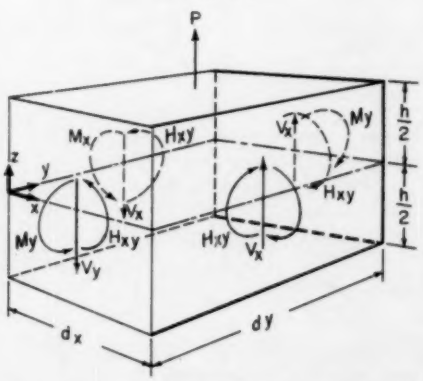

Fig. 1 Rectangular plate element with forces and moments

[1] Dean, School of Engineering and Science, Fairleigh Dickinson University, Teaneck, N. J.

[2] E. Reissner, "The Effect of Transverse Shear Deformation on the Bending of Elastic Plates," JOURNAL OF APPLIED MECHANICS, vol. 12, TRANS. ASME, vol. 67, 1945, pp. A69–A77.

[3] E. Reissner, "On Bending of Elastic Plates," *Quarterly of Applied Mathematics*, vol. 5, 1947, pp. 55–68.

Contributed by the Applied Mechanics Division and presented at the Annual Meeting, Atlantic City, N. J., November 29–December 4, 1959, of THE AMERICAN SOCIETY OF MECHANICAL ENGINEERS.

Discussion of this paper should be addressed to the Secretary, ASME, 29 West 39th Street, New York, N. Y., and will be accepted until April 10, 1960, for publication at a later date. Discussion received after the closing date will be returned.

NOTE: Statements and opinions advanced in papers are to be understood as individual expressions of their authors and not those of the Society. Manuscript received by ASME Applied Mechanics Division, October 27, 1958. Paper No. 59—A-66.

It is readily seen that particular integrals to (1) are given by

$$V_{x1} = -D\frac{\partial \nabla^2 w}{\partial x} - \frac{kh^2}{10}\frac{\partial p}{\partial x} \tag{4a}$$

$$V_{y1} = -D\frac{\partial \nabla^2 w}{\partial y} - \frac{kh^2}{10}\frac{\partial p}{\partial y} \tag{4b}$$

and with

$$V_x = V_{x1} + V_{x2} \tag{5a}$$

$$V_y = V_{y1} + V_{y2} \tag{5b}$$

then V_{x2} and V_{y2} must satisfy the homogeneous system of equations. The homogeneous equations will be satisfied[2,3] by

$$V_{x2} = \frac{\partial \phi}{\partial y} \tag{6a}$$

$$V_{y2} = \frac{-\partial \phi}{\partial x} \tag{6b}$$

where the stress function ϕ is governed by the equation

$$\nabla^2 \phi - \frac{10}{h^2}\phi = 0 \tag{7}$$

In Cartesian co-ordinates, the solution to (7) is

$$\phi = (C_1 \sin qx + C_2 \cos qx)\cosh \eta y + (C_3 \sin qx + C_4 \cos qx)\sinh \eta y \tag{8}$$

where q is the separation constant and

$$\eta^2 = \frac{10}{h^2} + q^2$$

Hence the form of the resultant vertical shears are completely determined by Equations (6) and (7) in terms of the deflection function w of the plate, namely,

$$V_x = -D\frac{\partial \nabla^2 w}{\partial x} - \frac{kh^2}{10}\frac{\partial p}{\partial x} + \eta[(C_1 \sin qx + C_2 \cos qx)\sinh \eta y + (C_3 \sin qx + C_4 \cos qx)\cosh \eta y] \tag{9a}$$

$$V_y = -D\frac{\partial \nabla^2 w}{\partial y} - \frac{kh^2}{10}\frac{\partial p}{\partial y} - q[(C_1 \cos qx - C_2 \sin qx)\cosh \eta y + (C_3 \cos qx - C_4 \sin qx)\sinh \eta y] \tag{9b}$$

The problem thus reduces to the solution of Equation (3) subject to either stress or displacement boundary conditions.[2,3]

Uniformly Loaded Rectangular Plate Simply Supported on All Edges

The analysis is now specialized by considering a simply supported rectangular plate having a uniform load p, Fig. 2. As a consequence of the constant load, terms multiplied by derivatives of the load in the general field Equations (1) to (9) are zero.

The usual solution assumed for w is either a double Fourier series or the Levy solution.[4] Neither solution, in its original form, appears to have the required flexibility to satisfy the following two requirements:

1 At a simply supported edge the curvature should reflect the effects of shear, that is, $w_{xx} \neq 0$.

[4] S. Timoshenko, "Theory of Plates and Shells," McGraw-Hill Book Company, Inc., New York, N. Y., 1940.

2 The solution for an infinite plate should be obtainable from a finite plate when one dimension of the finite plate is permitted to increase without limit.

With the foregoing conditions in view, we construct a modified Levy-type solution in the form

$$w = \frac{p}{24D}\sum_{1,3,5\ldots}^{\infty}\left[\frac{96}{a\mu^5}Y(y)\sin \mu x + \frac{6kh^2}{5}(ax - x^2)\right] \tag{10a}$$

where

$$\mu = \frac{m\pi}{a};\quad m = 1, 3, 5\ldots \tag{10b}$$

Equation (10a) yields the solution for an infinite plate, by letting $Y = 1$.

In anticipation of subsequent use we note that the Fourier-series expansion for $(x^2 - ax)$ in the interval $0 \leq x \leq a$ is

$$x^2 - ax = -\frac{8}{a}\sum_{1,3,5\ldots}^{\infty}\frac{1}{\mu^3}\sin \mu x \tag{11}$$

Substituting (10a) into (3), and making use of (11) leads to the differential equation governing $Y(y)$; namely,

$$\frac{d^4Y}{dy^4} - 2\mu^2\frac{d^2Y}{dy^2} + \mu^4 Y = \mu^4 \tag{12}$$

The complete solution in even functions of the argument is

$$Y = C_5 \cosh \mu y + C_6\, \mu y \sinh \mu y + 1 \tag{13}$$

Consequently, the form of the deflection shape w is given by (10a) and (13). The Laplacian and its derivatives are obtained from (10a) and used in (9) to yield the shear resultants,

$$V_x = -\frac{4p}{a}\sum_{1,3,5\ldots}^{\infty}\frac{1}{\mu^4}\left[\frac{d^3Y}{dy^3} - \mu^2 Y\right]\cos \mu x + \Sigma \eta C_4 \cos qx \cosh \eta y \tag{14a}$$

$$V_y = -\frac{4p}{a}\sum_{1,3,5\ldots}^{\infty}\frac{1}{\mu^5}\left[\frac{d^3Y}{dy^3} - \mu^2\frac{dY}{dy}\right]\sin \mu x + \Sigma q C_4 \sin qx \sinh \eta y \tag{14b}$$

where the symmetry of loading and axes requires

$$C_1 = C_2 = C_3 = 0 \tag{14c}$$

The development by E. Reissner[2,3] indicates that three

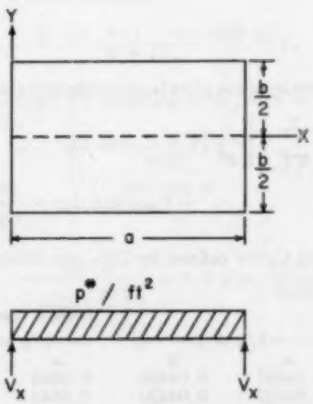

Fig. 2 Co-ordinate axes for simply supported rectangular plate

boundary conditions can be satisfied along each edge. For the simply supported plate, the obvious conditions are

$$w = 0 \text{ along all edges} \tag{15a}$$

$$M_s = 0 \text{ along all edges} \tag{15b}$$

The third boundary condition is

$$\frac{\partial w}{\partial s} - \frac{12(1+\nu)}{5Eh} V_s = 0 \text{ along all edges} \tag{15c}$$

which states that there is to be no rotation of the edges in the direction of the edges.

Before calculating the constants of integration, it is observed that all even derivatives, with respect to x, of the first term of (10a), evaluated at $x = 0$ and a, will be zero. All the derivatives of y, evaluated at $x = 0$ and a, will likewise be zero.

Consequently, conditions (15a) and (15b) are automatically satisfied by virtue of the form of (10a). Equation (15c) implies that $V_y = 0$ along the x edges, from which we find

$$q = \frac{m\pi}{a} = \mu \tag{16}$$

Proceeding to evaluate the coefficients along the y edges, we have, from (10a),

$$C_3 \cosh \alpha_m + C_4 \alpha_m \sinh \alpha_m + 1 + \frac{kh^2\mu^2}{10} = 0 \tag{17a}$$

where

$$\alpha_m = \frac{\mu b}{2} \tag{17b}$$

Substituting (10a) and (14a) into (15c) with x corresponding to s leads to

$$2C_4 \cosh \alpha_m - \frac{a\mu^2}{4p} C_4 \eta \cosh\left(\frac{\eta b}{2}\right) - 1 = 0 \tag{18}$$

From the vanishing of M_y at $y = \pm b/2$ we obtain, after making use of (17a) and (18) then collecting terms,

$$C_3 = {}^1/_2 \cosh \alpha_m \tag{19}$$

Substituting (19) into (17a) and (18), respectively, yields

$$C_4 = -\frac{1}{\cosh \alpha_m}\left[1 + \frac{kh^2\mu^2}{10} + \frac{\alpha_m \tanh \alpha_m}{2}\right] \tag{20a}$$

and

$$C_4 = 0 \tag{20b}$$

The deflection of the plate is now completely determined and is

$$w = \frac{4p}{aD} \sum_{1,3,5\ldots}^{\infty} \left[\frac{1}{\mu^5}(1 + C_3 \cosh \mu y + C_4 \mu y \sinh \mu y) + \frac{kh^2}{10\mu^3}\right] \sin \mu x \tag{21}$$

where C_3 and C_4 are defined by (19) and (20a), respectively.

Numerical Calculations

The maximum deflection occurs at the point $x = a/2$, $y = 0$ and is

$$w_{max} = \frac{4p}{aD} \sum_{1,3,5\ldots}^{\infty} \left[\frac{(1 + C_3)}{\mu^5} + \frac{kh^2}{10\mu^3}\right](-1)^{\frac{m-1}{2}} \tag{22a}$$

The maximum deflection consists of a term representing the classical solution and another representing the increase in deflection due to shear deformations. The second term contains the thickness of the plate h as a multiplier and is given by

$$(\Delta w)_{max} = \alpha' \frac{pa^4}{Eh^3}\left(\frac{h}{a}\right)^2 \tag{22b}$$

where

$$\alpha' = 0.34220 \sum_{1,3,5\ldots}^{\infty} \frac{(-1)^{\frac{m-1}{2}}}{m^3}\left(1 - \frac{1}{\cosh \alpha_m}\right) \tag{22c}$$

Numerical factors associated with uniformly loaded and simply supported plates are given by Timoshenko.[6] The coefficient α of the expression

$$w_{max} = \alpha \frac{pa^4}{Eh^3} \tag{23a}$$

is given[3] for various values of (b/a). The corresponding expression for the deflection modified to include the effect of shear is

$$\bar{w}_{max} = \bar{\alpha} \frac{pa^4}{Eh^3} \tag{23b}$$

where

$$\bar{\alpha} = \alpha + \left(\frac{h}{a}\right)^2 \alpha' \tag{23c}$$

Table 1 gives the deflection coefficient α and $\bar{\alpha}$ for various values of h/a and b/a.

It is noted that the maximum deflection due to shear deformations increases with increase of h/a and b/a. For the ranges chosen in the foregoing, the maximum percentage of deviation from classical theory is by about 4.4 at $h/a = 0.100$ and $b/a = 1$ (square plate).

The shear forces V_x and V_y are given by (14a) and (14b). For the simply supported plate with a uniform load we have that $C_4 = 0$. Therefore, for this problem the shear resultants are independent of the thickness and are the same as for the classical theory.

The equations for the bending moments are given by (2a) and (2b). Substitution of the derivatives of w, V_x, and V_y and expansion of the constant load p into a Fourier series leads to expressions for the bending moments M_x and M_y. Each moment consists of two parts; the first represents the classical solution, and the second the portion dependent upon the thickness of the plate h. The increment of moment $(\Delta M)_{max}$, which is due to the plate-thickness effect and occurs at the center of the plate, is

[6] Reference, footnote 4, p. 133.

Table 1 Coefficients α and $\bar{\alpha}$ for various values of h/a and b/a

	$b/a = 1$		$b/a = 1.5$		$b/a = 2$		$b/a = 5$		$b/a = \infty$	
h/a	α	$\bar{\alpha}$	α	$\bar{\alpha}$	α	$\bar{\alpha}$	α	$\bar{\alpha}$	α	$\bar{\alpha}$
0.005	0.04437	0.04438	0.0843	0.0843	0.1106	0.1106	0.1416	0.1416	0.1422	0.1422
0.010	0.04437	0.04439	0.0843	0.0843	0.1106	0.1106	0.1416	0.1420	0.1422	0.1422
0.050	0.04437	0.04486	0.0843	0.0850	0.1106	0.1114	0.1416	0.1424	0.1422	0.1430
0.100	0.04437	0.04632	0.0843	0.0870	0.1106	0.1136	0.1416	0.1449	0.1422	0.1455

Table 2 Coefficients β and $\bar{\beta}$ for various values of h/a and b/a

	$b/a = 1$		$b/a = 1.5$		$b/a = 2$		$b/a = 5$	
h/a	β	$\bar{\beta}$	β	$\bar{\beta}$	β	$\bar{\beta}$	β	$\bar{\beta}$
0.005	0.0479	0.0479	0.0812	0.0812	0.1189	0.1189	0.1246	0.1246
0.010	0.0479	0.0479	0.0812	0.0812	0.1189	0.1189	0.1246	0.1246
0.050	0.0479	0.0479	0.0812	0.0812	0.1189	0.1189	0.1246	0.1246
0.100	0.0479	0.0481	0.0812	0.0813	0.1189	0.1189	0.1246	0.1246

Table 3 Coefficients β_1 and $\bar{\beta}_1$ for various values of h/a and b/a

	$b/a = 1$		$b/a = 1.5$		$b/a = 2$		$b/a = 5$	
h/a	β_1	$\bar{\beta}_1$	β_1	$\bar{\beta}_1$	β_1	$\bar{\beta}_1$	β_1	$\bar{\beta}_1$
0.005	0.0479	0.0479	0.0499	0.0499	0.0464	0.0464	0.0375	0.0375
0.010	0.0479	0.0479	0.0499	0.0499	0.0464	0.0464	0.0375	0.0375
0.050	0.0479	0.0479	0.0499	0.0450	0.0464	0.0465	0.0375	0.0376
0.100	0.0479	0.0481	0.0499	0.0502	0.0464	0.0467	0.0375	0.0378

$$(\Delta M_x)_{max} = \beta' pa^2 \left(\frac{h}{a}\right)^2 \tag{24a}$$

where

$$\beta' = 0.12732 \sum_{1,3,5\ldots}^{\infty} \frac{(-1)^{\frac{m-1}{2}}}{m} \frac{\nu}{\cosh \alpha_m} \tag{24b}$$

The values of the coefficient β for the maximum value of M_x are given[5] in the form

$$(M_x)_{max} = \beta pa^2 \tag{25a}$$

The revised maximum bending moment may be expressed as

$$(\bar{M}_x)_{max} = \bar{\beta} pa^2 \tag{25b}$$

where

$$\bar{\beta} = \beta + \beta' \left(\frac{h}{a}\right)^2 \tag{25c}$$

The values of β and $\bar{\beta}$ for several values of b/a and h/a with Poisson's ratio equal to 0.3 are tabulated in Table 2.

The increment of moment $(\Delta M_y)_{max}$, which is due to the thickness effect h and occurs at the center of the plate, is

$$(\Delta M_y)_{max} = \beta_1' pa^2 \left(\frac{h}{a}\right)^2 \tag{26a}$$

where

$$\beta_1' = 0.12732 \sum_{1,3,5\ldots}^{\infty} \frac{(-1)^{\frac{m-1}{2}}}{m} \nu \left(1 - \frac{1}{\cosh \alpha_m}\right) \tag{26b}$$

The values of the coefficient β_1 for the maximum value of M_y are given[5] as

$$(M_y)_{max} = \beta_1 pa^2 \tag{27a}$$

The revised maximum bending moment may be expressed as

$$(M_y)_{max} = \bar{\beta}_1 pa^2 \tag{27b}$$

where

$$\bar{\beta}_1 = \beta_1 + \beta_1' \left(\frac{h}{a}\right)^2 \tag{27c}$$

The values of β_1 and $\bar{\beta}_1$, for several values of b/a and h/a with Poisson's ratio equal to 0.3 are tabulated in Table 3.

The largest deviation of the maximum bending moment from the $(M_x)_{max}$ and $(M_y)_{max}$ of classical theory is about 0.8 per cent, the moments containing the thickness effect being larger than those of classical theory.

Uniformly Loaded Rectangular Plate Simply Supported at Two Opposite Edges and Free at the Other Two Edges

The quality of the Levy method, which admits solutions for a plate simply supported at two opposite edges and various boundary conditions at the other two edges, is not altered by the introduction of the shear deformation. Consequently, the solution to this problem can be obtained readily by making use of the development for a plate simply supported on all its edges.

The deflection function w and the associated shear resultants are given by Equations (10) and (14), respectively. Along the x edges the boundary conditions (15) are still valid, while at the y edges only (15b) remains unaltered. At $y = \pm b/2$ Equations (15a) and (15b) are replaced by

$$V_y = 0 \tag{28a}$$

$$H_{xy} = 0 \tag{28b}$$

respectively.

Proceeding to evaluate the constants C_4, C_5, and C_6, we first substitute Equation (14b) into (28a) which yields

$$C_4 = \frac{8p}{a\mu^2} \frac{\sinh \alpha}{\sinh\left(\frac{\eta b}{2}\right)} C_6 \tag{29}$$

provided that $q = \mu$.

Substituting Equations (10), (14a), and (14b) into (28b) and using (29) leads to the relationship

$$C_5 = \frac{[1 + \nu - (1 - \nu)\alpha \coth \alpha]}{1 - \nu} C_6 \tag{30}$$

Finally, we have from the vanishing of M_y at $y = \pm b/2$, after using (29) and (30)

$$C_6 = \frac{\nu h^2 \eta^2}{10K \cosh \alpha} \tag{31a}$$

where

$$K = \frac{2\mu^2 h^2}{5}\left[1 - \frac{\eta \tanh \alpha}{\mu \tanh\left(\frac{\eta b}{2}\right)}\right] + 3 + \nu - \frac{2\alpha(1 - \nu)}{\sinh 2\alpha} \tag{31b}$$

The deflection of the plate is now completely determined and is given by (10) with C_5 and C_6 recorded in the foregoing.

It is to be noted that for this case the shear resultants are not identical with those given by the classical theory. This is evidenced by the nonvanishing of C_4, Equation (29).

No supporting numerical computations for this case have been included in this paper.

Edge Reactions

Reissner[2,3] indicated that concentrated reactions will not occur at the corners of the plate. This can be easily shown as follows.

From the sign convention given in Fig. 1, the edge reactions are

$$R_x + R_y = \int_{-b/2}^{b/2} [V_x(a, y) - V_x(0, y)]dy + \int_0^a [V_y(x, b/2) - V_y(x, -b/2)]dx \quad (32)$$

or

$$R_x + R_y = \int_0^a \int_{-b/2}^{b/2} \left[\frac{\partial V_x}{\partial x} + \frac{\partial V_y}{\partial y}\right] dx\, dy \quad (33)$$

Substituting (10) in the foregoing we have

$$R_x + R_y = -\int_0^a \int_{-b/2}^{b/2} p\, dx\, dy \quad (34)$$

which is free of any additional terms representing corner reactions.

Acknowledgments

The authors wish to acknowledge the assistance rendered by Mrs. R. Fortunato in checking, Mrs. Mildred Sudwischer in typing, and Mr. Joseph Sarno in editorial matters.

BERNARD BUDIANSKY
Associate Professor of Structural Mechanics, Division of Engineering and Applied Physics, Harvard University, Cambridge, Mass. Mem. ASME

O. L. MANGASARIAN
Shell Development Company, Emeryville, Calif.

Plastic Stress Concentration at a Circular Hole in an Infinite Sheet Subjected to Equal Biaxial Tension

With the use of J_2 deformation theory, the stress-concentration factor at a circular hole in an infinite sheet of strain-hardening material subjected to equal biaxial tension at infinity is found for a variety of representative materials. The analysis exploits a transformation which permits the calculation of the stress-concentration factor without determining the stress distribution in the sheet. Subsequent calculations reveal that, for a monotonically increasing applied stress, the stress history at all points in the sheet is nearly radial.

The well-known solution of plane elasticity for the stresses around a circular hole in an infinite sheet subjected to biaxial stresses σ_∞ at infinity, Fig. 1, gives a circumferential stress σ_θ at the hole equal to twice the applied stress; thus the elastic stress-concentration factor is $K = 2$. The present paper considers the problem of determining the plastic stress-concentration factor that occurs in a sheet of strain-hardening material when the applied stress is increased (monotonically) to values sufficiently high to produce plastic deformation. The usual assumptions of generalized plane stress are made, with strains assumed small and changes in the plate thickness neglected. The analysis is based on the simple deformation theory of plasticity, and numerical results are obtained for a representative variety of materials, each of which is characterized by a particular uniaxial stress-strain curve of the Ramberg-Osgood type [1].[1] The use of deformation theory can be justified by examination of the results in the light of a recent reassessment of deformation theories [2].

An important feature of the present analysis is the exploitation of a transformation which eliminates the space variable from explicit consideration, and thereby permits the calculation of stress-concentration factors without the need for a detailed calculation of the spatial stress distribution. (A similar transformation was recently used by Weir [3] in a creep problem.) The present problem has been considered by Wu [4] for only two specific materials, with changes in plate thickness and finite straining taken into account; for the infinitesimal strain case, the procedure of this paper is considerably less complicated than Wu's approach, and furthermore it may be applied to a variety of materials by changing a single parameter.

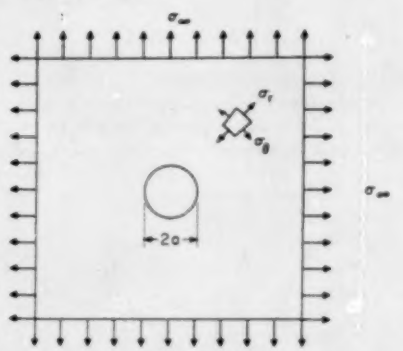

Fig. 1 Circular hole in an infinite sheet subjected to biaxial tension

[1] Numbers in brackets designate References at end of paper.

Presented at the West Coast Conference of the Applied Mechanics Division, Stanford, Calif., September 9–11, 1959, of The American Society of Mechanical Engineers.

Discussion of this paper should be addressed to the Secretary, ASME, 29 West 39th Street, New York, N. Y., and will be accepted until April 10, 1960, for publication at a later date. Discussion received after the closing date will be returned.

Note: Statements and opinions advanced in papers are to be understood as individual expressions of their authors and not those of the Society. Manuscripts received by ASME Applied Mechanics Division, December 29, 1958. Paper No. 59—APMW-16.

Nomenclature

r = radial distance from center of hole
σ_r = normal stress in radial direction
σ_θ = normal stress in tangential direction
u = displacement in radial direction
ϵ_r = normal strain in radial direction
ϵ_θ = normal strain in tangential direction
ν = Poisson's ratio
$\bar{\sigma}$ = effective stress $= (\sigma_r^2 + \sigma_\theta^2 - \sigma_r\sigma_\theta)^{1/2}$
E = Young's modulus
$E_s(\bar{\sigma})$ = secant modulus of uniaxial stress-strain curve at effective stress $\bar{\sigma}$
σ_∞ = the value of σ_r and σ_θ at infinity
a = radius of hole
$\zeta = (a/r)^2$ = nondimensional space variable
$s_r = \sigma_r/\sigma_\infty$ = nondimensional radial stress
$s_\theta = \sigma_\theta/\sigma_\infty$ = nondimensional tangential stress
$\bar{s} = \bar{\sigma}/\sigma_\infty$ = nondimensional effective stress
K = stress-concentration factor at hole $= \sigma_{\theta\text{hole}}/\sigma_\infty$
n = parameter in Ramberg-Osgood relation
σ_1 = nominal yield stress (stress at which $E_s = 0.7E$)
λ = loading parameter (σ_∞/σ_1)
$A = 7/3\lambda^{n-1}$
$z = (\bar{s}^2 - 1)^{1/2}/\bar{s}$
ϵ_1 = nominal yield strain (strain at which $E_s = 0.7E$)

Basic Equations

The radial and circumferential stresses σ_r and σ_θ must satisfy the equilibrium equation

$$\sigma_\theta = \frac{d}{dr}(r\sigma_r) \tag{1}$$

and the corresponding strains ϵ_r and ϵ_θ given by

$$\begin{aligned} \epsilon_r &= du/dr \\ \epsilon_\theta &= u/r \end{aligned} \tag{2}$$

in terms of the radial displacement u must satisfy the compatibility equation

$$\epsilon_r = \frac{d}{dr}(r\epsilon_\theta) \tag{3}$$

The shearing stresses and strains $\tau_{r\theta}$ and $\gamma_{r\theta}$ are zero by symmetry.

According to the simple deformation theory of plasticity (Nadai's law, J_2 deformation theory) the strains are related to the stresses by

$$\begin{aligned} \epsilon_r &= \frac{1}{E}[\sigma_r - \nu\sigma_\theta] + \left[\frac{1}{E_s(\bar{\sigma})} - \frac{1}{E}\right]\left[\sigma_r - \frac{1}{2}\sigma_\theta\right] \\ \epsilon_\theta &= \frac{1}{E}[\sigma_\theta - \nu\sigma_r] + \left[\frac{1}{E_s(\bar{\sigma})} - \frac{1}{E}\right]\left[\sigma_\theta - \frac{1}{2}\sigma_r\right] \end{aligned} \tag{4}$$

where $E_s(\bar{\sigma})$ is the secant modulus of the uniaxial stress-strain curve at the effective stress given by

$$\bar{\sigma} = (\sigma_r^2 + \sigma_\theta^2 - \sigma_r\sigma_\theta)^{1/2} \tag{5}$$

The boundary conditions are:

$$\sigma_r = \sigma_\theta = \sigma_\infty \quad \text{at} \quad r = \infty \tag{6a}$$

$$\sigma_r = 0 \quad \text{at} \quad r = a \tag{6b}$$

By the extended Michell theorem [5] the solution for the stresses is independent of the elastic Poisson's ratio ν; consequently, as far as the determination of the stresses is concerned, an immediate gain in simplicity without loss of generality is achieved by setting $\nu = 1/2$ in the stress-strain relations (4) and using the following resulting relations

$$\begin{aligned} \epsilon_r &= \frac{1}{E_s}\left[\sigma_r - \frac{1}{2}\sigma_\theta\right] \\ \epsilon_\theta &= \frac{1}{E_s}\left[\sigma_\theta - \frac{1}{2}\sigma_r\right] \end{aligned} \tag{7}$$

Once the stresses are found, the correct strains may then be calculated from (4) with the use of the appropriate value of Poisson's ratio.

Elimination of the Space Variable

With the introduction of the nondimensional quantities

$$\begin{aligned} \zeta &= \left(\frac{a}{r}\right)^2 \quad s_r = \frac{\sigma_r}{\sigma_\infty} \quad s_\theta = \frac{\sigma_\theta}{\sigma_\infty} \\ \bar{s} &= \frac{\bar{\sigma}}{\sigma_\infty} = (s_r^2 + s_\theta^2 - s_r s_\theta)^{1/2} \end{aligned} \tag{8}$$

the governing equations (1), (3), and (7) become

$$s_r - s_\theta - 2\zeta\frac{ds_r}{d\zeta} = 0 \tag{9}$$

$$\epsilon_r - \epsilon_\theta + 2\zeta\frac{d\epsilon_\theta}{d\zeta} = 0 \tag{10}$$

$$\begin{aligned} \epsilon_r &= \frac{\sigma_\infty}{E_s}(s_r - {}^1\!/_2\, s_\theta) \\ \epsilon_\theta &= \frac{\sigma_\infty}{E_s}(s_\theta - {}^1\!/_2\, s_r) \end{aligned} \tag{11}$$

where now E_s depends on $(\sigma_\infty \bar{s})$. Substitution of the stress-strain relation (11) into the compatibility equation (10) gives

$$\frac{3}{2E_s}(s_r - s_\theta) + 2\zeta\frac{d}{d\zeta}\left[\frac{1}{E_s}(s_\theta - {}^1\!/_2\, s_r)\right] = 0 \tag{12}$$

Next, using the equilibrium equation (9) in the first term of (12) gives

$$\zeta\left(\frac{3}{E_s}\right)\frac{ds_r}{d\zeta} + \zeta\frac{d}{d\zeta}\left[\frac{1}{E_s}(2s_\theta - s_r)\right] = 0 \tag{13}$$

Now, with the tentative assumption that $\bar{s}$ is a monotonic function of ζ, division of (13) by $(d\bar{s}/d\zeta)$ and cancellation of the common factor ζ gives

$$\frac{3}{E_s}\frac{ds_r}{d\bar{s}} + \frac{d}{d\bar{s}}\left[\frac{1}{E_s}(2s_\theta - s_r)\right] = 0 \tag{14}$$

Since E_s depends only on $(\sigma_\infty \bar{s})$, equation (14) constitutes a first-order linear differential equation for s_θ and s_r as functions of $\bar{s}$. The additional equations needed for the determination of $s_r(\bar{s})$ and $s_\theta(\bar{s})$ are the quadratic algebraic relation, from (8),

$$\bar{s}^2 = s_r^2 + s_\theta^2 - s_r s_\theta \tag{15}$$

and the initial conditions, corresponding to the stress state (6a) at infinity in the physical plane

$$s_r = s_\theta = 1 \quad \text{at} \quad \bar{s} = 1 \tag{16}$$

The condition (6b) at the hole then serves to determine the stress-concentration factor K. At the hole, $s_r = 0$ and $s_\theta = \bar{s} = K$. Hence K is the root of

$$s_\theta(K) = K \tag{17}$$

or, equivalently, of

$$s_r(K) = 0 \tag{18}$$

It is remarkable that, subject to the validity of the assumption concerning the monotonicity of $\bar{s}(\zeta)$, the stress at the hole is determinable without the detailed calculation of the dependence of s_r and s_θ on the space variable ζ. Once $s_r(\bar{s})$ and $s_\theta(\bar{s})$ are determined, the spatial variation of the stress can be calculated, and the monotonicity of $\bar{s}$ verified, by use of the equilibrium equation (9).

Introduction of the Ramberg-Osgood Relation

An explicit formula for the dependence of E_s on $\bar{\sigma}$ (or $\sigma_\infty \bar{s}$) may be introduced by the use of the Ramberg-Osgood equation for the uniaxial stress-strain curve

$$\epsilon = \frac{\sigma}{E}\left[1 + \frac{3}{7}\left(\frac{\sigma}{\sigma_1}\right)^{n-1}\right] \tag{19}$$

Here σ_1 is a nominal yield stress; as seen from the formula derived from (19)

$$\frac{1}{E_s} = \frac{1}{E}\left[1 + \frac{3}{7}\left(\frac{\sigma}{\sigma_1}\right)^{n-1}\right], \tag{20}$$

the value of the secant modulus at $\sigma = \sigma_1$ is 70 per cent of the elastic modulus E. The dependence of the shape of the stress-strain curve on the parameter n is exhibited in Fig. 2, which presents plots of $(E\epsilon/\sigma_1)$ versus (σ/σ_1) for several values of n.

With the introduction of the loading parameter $\lambda = \sigma_\infty/\sigma_1$, the formula for $1/E_s$ to be used in the differential equation (14) becomes

$$\frac{1}{E_s} = \frac{1}{E}\left[1 + \frac{3}{7}\lambda^{n-1}\,\mathfrak{z}^{n-1}\right] \tag{21}$$

It is convenient to introduce into the problem the further transformations

$$\xi = {}^1/_2(s_\theta + s_r)$$
$$\eta = {}^1/_2(s_\theta - s_r) \tag{22}$$

The governing equations (14) and (15) then become

$$[A + \mathfrak{z}^{n-1}]\frac{d\xi}{d\mathfrak{z}} + \frac{n-1}{4}\mathfrak{z}^{n-2}(\xi + 3\eta) = 0 \tag{23}$$

$$\mathfrak{z}^2 = \xi^2 + 3\eta^2 \tag{24}$$

where $A = 7/(3\lambda^{n-1})$. The initial condition (16) becomes

$$\xi(1) = 1 \quad \eta(1) = 0 \tag{25}$$

and the condition (17), (18) at the hole (for the determination of K) gives

$$\xi(K) = \eta(K) = K/2 \tag{26}$$

Solution for the Stress-Concentration Factor

Limiting Cases ($\lambda = 0, \infty$). Purely elastic behavior should correspond to the case $\lambda = 0$; in fact, for this case, A becomes infinite and the differential equation (23) degenerates into

$$\frac{d\xi}{d\mathfrak{z}} = 0$$

and the complete solution is

$$\xi = 1$$

and

$$\eta = \left(\frac{\mathfrak{z}^2 - 1}{3}\right)^{1/2}$$

Consequently, condition (26) yields $K = 2$, the elastic stress-concentration factor.

At the other extreme, λ very large corresponds to the situation where elastic strains are negligible compared to plastic strains. For λ infinite, A vanishes and the resulting system of equations is susceptible to an exact solution.

With $A = 0$, (23) becomes

$$\mathfrak{z}\frac{d\xi}{d\mathfrak{z}} + \frac{n-1}{4}(\xi + 3\eta) = 0 \tag{27}$$

The parametric representation, due to Nadai [6],

$$\left.\begin{aligned}\xi &= \mathfrak{z}\cos\theta \\ \eta &= \frac{\mathfrak{z}}{\sqrt{3}}\sin\theta\end{aligned}\right\} \tag{28}$$

automatically satisfies equation (24), and when substituted in (27) gives

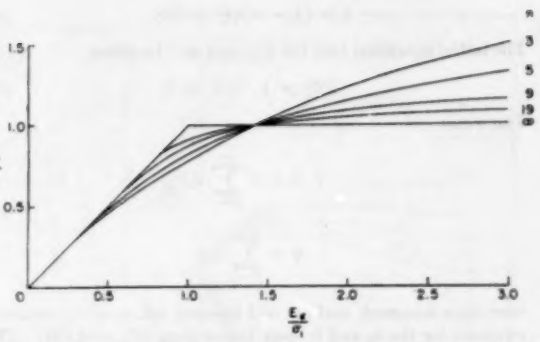

Fig. 2 Nondimensional Ramberg-Osgood stress-strain curves

$$\frac{d\mathfrak{z}}{\mathfrak{z}} = \frac{4\sin\theta\,d\theta}{(n+3)\cos\theta + (n-1)\sqrt{3}\sin\theta} \tag{29}$$

With the use of the initial condition $\mathfrak{z} = 1$ at $\theta = 0$ (corresponding to the conditions at infinity in the physical plane), the foregoing equation is easily integrated to give

$$\mathfrak{z} = \left[\frac{e^{\frac{\sqrt{3}(n-1)\theta}{n+3}}}{\cos\theta + \frac{\sqrt{3}(n-1)}{n+3}\sin\theta}\right]^{(n+3)/(n^2+3)} \tag{30}$$

The condition (26) at the hole corresponds to $\mathfrak{z} = K$ and $\theta = \pi/3$. Upon substitution of this condition in (30), the stress-concentration factor

$$K = \left[\left(\frac{n+3}{2n}\right)^{\frac{n+3}{n^2+3}}\right] e^{\left[\frac{\pi(n-1)}{\sqrt{3}(n^2+3)}\right]} \tag{31}$$

is immediately obtained. It is worthy of note that this limiting value of K for λ approaching infinity is precisely the stress-concentration factor associated with a material having a uniaxial stress-strain curve that obeys a pure power law of the form $\epsilon = K\sigma^n$. When a power law is used, the stress distribution, as was shown by Ilyushin [7], varies linearly with the applied loading, with stresses at various points in the plate retaining a constant ratio to each other; thus for a power law, the stress-concentration factor is independent of the applied stress. In the present problem, with a Ramberg-Osgood law, the stress-concentration factor varies from the elastic value to the power-law value as λ varies from zero to infinity. (It should be remarked that allowing λ to become infinite is not, of course, consistent with the assumption of small strains; nevertheless, the case $\lambda = \infty$ does provide a useful asymptotic result.) The transition for intermediate values of λ is obtained from the solution described next.

General Case (λ **Finite**). For arbitrary λ (or A), the system (23), (24) was solved by a power-series technique briefly described as follows.[3]

With the new independent variable

$$z = \frac{(\mathfrak{z}^2 - 1)^{1/2}}{\mathfrak{z}} \tag{32}$$

the equations (23), (24) become

$$[1 - z^2]\left[A(1 - z^2)^{\frac{n-1}{2}} + 1\right]\frac{d\xi}{dz} + \frac{(n-1)z}{4}(\xi + 3\eta) = 0 \tag{33}$$

[3] An alternative procedure, developed subsequently and used in [8] on another problem, is actually preferable to the one used here.

$$1 = (1 - z^2)(\xi^2 + 3\eta^2) \tag{34}$$

The initial condition (25) for $\xi(z)$ and $\eta(z)$ becomes

$$\xi(0) = 1 \quad \eta(0) = 0 \tag{35}$$

The series

$$\xi = 1 + \sum_{i=1}^{\infty} a_i z^i$$
$$\eta = \sum_{i=1}^{\infty} b_i z^i \tag{36}$$

were then assumed, and for odd integral values of n, recurrence relations for the a_i and b_i were found from (33) and (34). (The introduction of the variable z, although seemingly complicating, was made in order to obtain a power series with adequate rate of convergence.) For each given value of A, the power series for ξ and η were calculated on a Univac I digital computer, and the condition (26) $\xi = \eta = K/2$ was used to determine the stress-concentration factor. Depending on A, from fifteen to forty terms in the power series were found to be needed for satisfactory convergence as measured by the repeatability of the result for K when additional terms were added. As checks, the K's for $A = 0$ and $A = \infty$ were calculated by the power-series method and were found to agree to six and three significant figures, respectively, with the exact analytic results.

Numerical Results. Calculations were made for values of $n = 3$, 5, 9, and 19; the results for K are shown in Fig. 3 as plots of K versus $\lambda = \sigma_\infty/\sigma_1$ for λ less than 1, and versus $1/\lambda$ for λ greater than 1. The end points of these curves correspond to the elastic and power-law solutions; the calculations for the curves were made at intervals of 0.1 on the horizontal axis. Also shown in this figure is the limiting result for $n = \infty$, corresponding to ideal plasticity, with a sharp yield stress at σ_1. For this case, the sheet is elastic until the stress at the hole reaches the value of σ_1 at $\lambda = 1/2$; thereafter the stress at the hole remains at the value σ_1. The curve of K versus λ is therefore the hyperbola $K = 1/\lambda$ for $1/2 \leq \lambda \leq 1$, and terminates abruptly at $\lambda = 1$, since σ_∞ cannot exceed σ_1 for the ideally plastic case. The dashed lines in Fig. 3 connect points of constant $(\epsilon_\theta)_{hole}/\epsilon_1$, where ϵ_1 is the nominal yield strain associated with σ_1; that is, $\epsilon_1 = (10/7)(\sigma_1/E)$. Since the stress state at the hole is uniaxial, $(\epsilon_\theta)_{hole}/\epsilon_1$ is obtained from the Ramberg-Osgood relation (19) as

$$(\epsilon_\theta)_{hole}/\epsilon_1 = 0.7\lambda K + 0.3(\lambda K)^n$$

These dashed lines may be used to assess, at least qualitatively, the validity of the small-strain assumption made at the outset of the analysis. For example, with $n = 19$ and $\lambda = 1.11$, $(\epsilon_\theta)_{hole}/\epsilon_1$ is seen to be less than 10. Thus for $\epsilon_1 = 0.0025$ (characteristic of some aluminum alloys) ϵ_θ at the hole is less than 2.5 per cent, and so it would be presumed that the small-strain assumption has not been grossly violated. It is obvious that the lower the nominal yield strain ϵ_1 of the material, the larger are the values of λ that may be reached before the strains become "large."

Fig. 4 shows, for the same values of n, how the circumferential stress at the hole varies with the applied stress at infinity.

Spatial Stress Distribution

The well-known elastic distribution of stresses, corresponding to $\lambda = 0$, is given by

$$\sigma_\theta/\sigma_\infty = 1 + \zeta$$
$$\sigma_r/\sigma_\infty = 1 - \zeta \tag{37}$$

The stress distribution for λ approaching infinity can be found in closed form in terms of the parameter θ previously introduced.

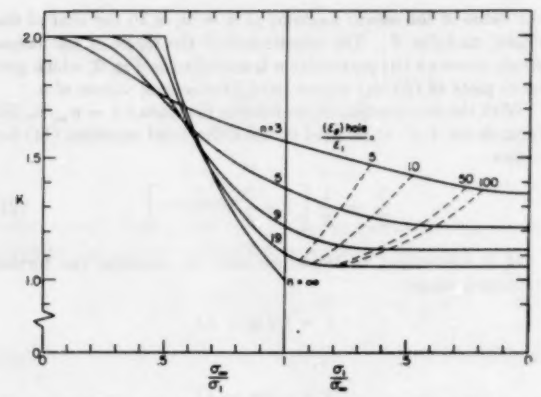

Fig. 3 Variation of stress-concentration factor with applied stress

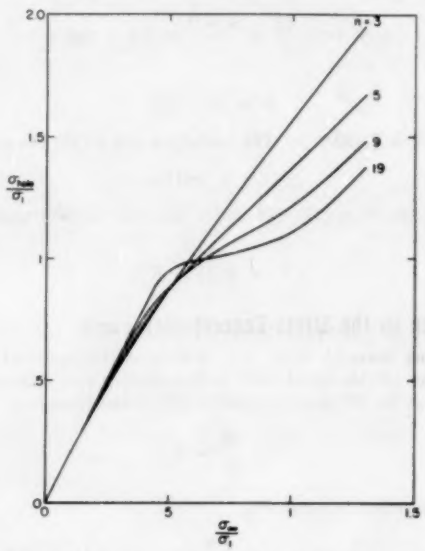

Fig. 4 Variation of stress at hole with applied stress

The equation of equilibrium (9) written in terms of the variables ξ and η (22) is

$$\eta + \zeta \frac{d}{d\zeta}(\xi - \eta) = 0 \tag{38}$$

or

$$\frac{d\zeta}{\zeta} = \frac{d\eta}{\eta} - \frac{d\xi}{\eta}$$

With the transformation (28) this becomes

$$\frac{d\zeta}{\zeta} = \frac{d(\bar{s}\sin\theta)}{\bar{s}\sin\theta} - \frac{\sqrt{3}\,d(\bar{s}\cos\theta)}{\bar{s}\sin\theta}$$
$$= \sqrt{3}\,d\theta + \frac{d(\bar{s}\sin\theta)}{\bar{s}\sin\theta} - \sqrt{3}\cot\theta\,\frac{d\bar{s}}{\bar{s}}$$

Substitution for $d\bar{s}/\bar{s}$ from (29) gives

$$\frac{d\zeta}{\zeta} = \sqrt{3}\,d\theta + \frac{d(\bar{s}\sin\theta)}{\bar{s}\sin\theta} - \frac{4}{n-1}\,\frac{d\theta}{\dfrac{n+3}{\sqrt{3}(n-1)} + \tan\theta}$$

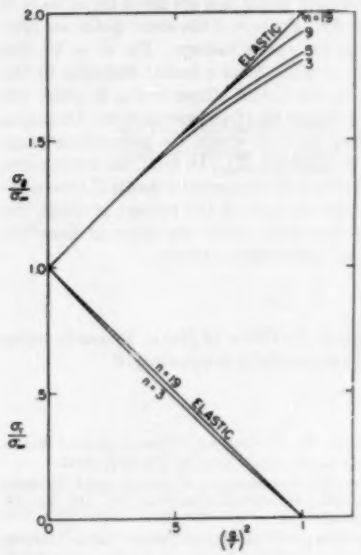

Fig. 5 Spatial stress distribution for $\sigma_\infty/\sigma_1 = 0.4$

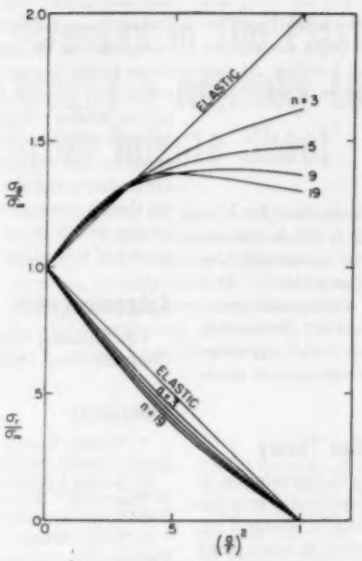

Fig. 6 Spatial stress distribution for $\sigma_\infty/\sigma_1 = 0.8$

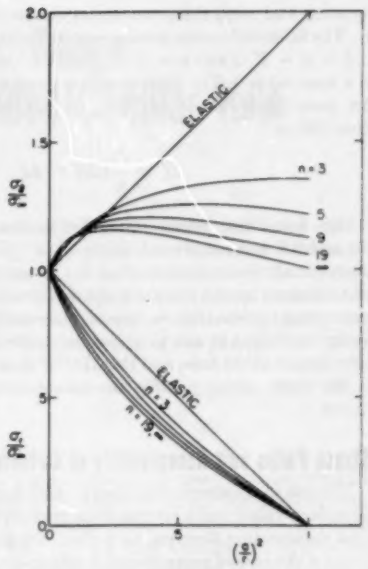

Fig. 7 Spatial stress distribution for $\sigma_\infty/\sigma_1 = \infty$ or power-law solution

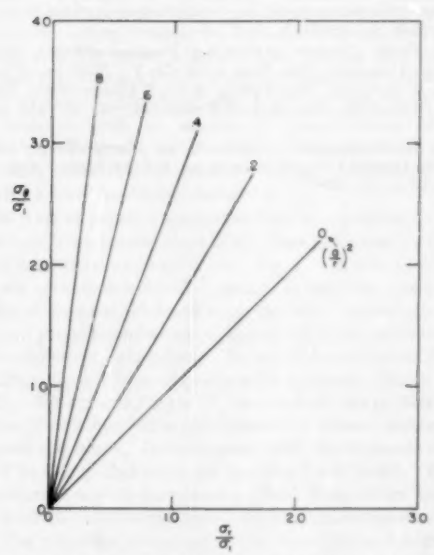

Fig. 8 Stress history at fixed points in the sheet for $n = 3$

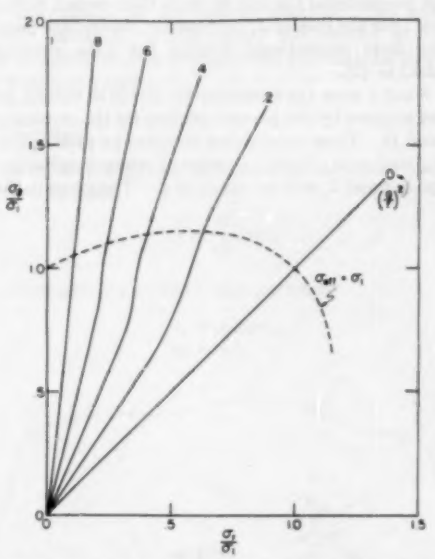

Fig. 9 Stress history at fixed points in the sheet for $n = 19$

With the use of the conditions at the hole $\bar{s} = K$, $\theta = \pi/3$, and $\zeta = 1$, integration and subsequent substitution for $\bar{s}$ and K from (30) and (31), respectively, provide

$$\zeta = \frac{2}{\sqrt{3}} e^{\left[\frac{\sqrt{3}(n^2-1)}{n^2+3}\left(\theta-\frac{\pi}{3}\right)\right]} \left[\frac{(n+3)\cos\theta + \sqrt{3}(n-1)\sin\theta}{2n}\right]^{\frac{-4n}{n^2+3}\sin\theta} \quad (39)$$

Thus the expressions (39), (30), and (28) completely determine the stress distribution in the sheet through the parameter $\theta (0 \leq \theta \leq \pi/3)$. Fig. 7 shows the stress distribution for the several values of n. These curves may be interpreted in either of two ways. They may be considered as the asymptotic stress distributions in a Ramberg-Osgood sheet as the loading parameter λ approaches infinity, or they may be regarded as the stress-distribution curves for a material with a pure power law. The curve labeled $n = \infty$ in Fig. 7 corresponds to a rigid, ideally plastic material and was obtained from the analytic results of Nadai [6]. It is interesting to note the continuous transition of the curves for finite n to Nadai's result for $n = \infty$.

The spatial stress distribution for arbitrary λ was obtained by replacing the equilibrium equation (38) by a finite-difference

equation and using the power-series representation (36) for ξ and η. The finite-difference process was started at the hole where $\zeta = 1$, $\xi = \eta = K/2$ and $z = [1 - (1/K^2)]^{1/2}$, and finite decrements in z were taken. The corresponding changes in ξ and η, $\Delta\xi$ and $\Delta\eta$, were calculated from (36), and the change in ζ was found from (38) as

$$\Delta\zeta = \frac{\zeta}{\eta}(\Delta\eta - \Delta\xi)$$

Figs. 5 and 6 depict the stress distribution in the sheet for $\lambda = 0.4$ and 0.8 and for several values of n. (Fig. 7, which was obtained analytically as described in the previous paragraph, also was obtained by the present numerical process, as a check.) It is interesting to note that σ_θ does not necessarily attain a maximum at the hole; but it can be shown numerically that $\bar{\sigma}$ does attain a maximum at the hole, and that $\Delta\bar{\sigma}/\Delta\zeta$ does not vanish anywhere in the sheet, which justifies the monotonicity assumption made earlier.

Stress Paths and Acceptability of Deformation Theory

The use of a deformation theory of plasticity in the solution of boundary-value problems has often been criticized on the grounds that deformation theories, as a class, are physically unsound except for the case of proportional loading; i.e., when at every point the stress components remain in constant ratio. It is shown in [2] however, that this stigma need not be attached to the use of a deformation theory as long as it leads to results that do not deviate from proportional loading by more than certain fairly liberal amounts. For the case of J_2 deformation theory, the permissible deviation from proportional loading has been quantitatively established in [2].

Figs. 8 and 9 show the stress-history curves at various points in the sheet as given by the present solution for the extreme cases of $n = 3$ and 19. These curves were obtained by picking the values of σ_r/σ_∞ and $\sigma_\theta/\sigma_\infty$ from a number of stress-distribution curves like Figs. 5, 6 and 7, at fixed values of ζ. The stress paths at the hole and infinity are obviously radial and are given by $\sigma_r/\sigma_\theta = 0$ and $\sigma_r/\sigma_\theta = 1$, respectively. For $n = 3$ the stress paths are very nearly radial throughout the entire history. For $n = 19$, the stress paths depart only slightly from a radial direction in the range $\bar{\sigma} < \sigma_1$ bounded by the dotted ellipse in Fig. 9, where the plastic strains are still quite small. In any event, the deviations from proportional loading are well within the permissible range given by the criterion of reference [2]. In fact, the stress paths are so nearly radial that it may be conjectured that if J_2 incremental theory were used in the solution of the present problem, the results would in all likelihood be nearly the same as those obtained in this paper by J_2 deformation theory.

Acknowledgment

The financial support of the Office of Naval Research under Contract Nonr 1866(02) is gratefully acknowledged.

References

1 Walter Ramberg and W. R. Osgood, "Description of Stress-Strain Curves by Three Parameters," NACA TN 902, 1943.

2 Bernard Budiansky, "A Reassessment of Deformation Theories of Plasticity," JOURNAL OF APPLIED MECHANICS, vol. 26, TRANS. ASME, vol. 81, 1959, pp. 259–264.

3 C. D. Weir, "The Creep of the Thick Tubes Under Internal Pressure," JOURNAL OF APPLIED MECHANICS, vol. 24, TRANS. ASME, vol. 79, 1957, pp. 464–466.

4 M. H. Lee Wu, "Analysis of Plane-Stress Problems With Axial Symmetry in Strain-Hardening Range," NACA TR 1021, 1951.

5 Bernard Budiansky, "Extension of Michell's Theorem to Problems of Plasticity and Creep," *Quarterly of Applied Mathematics*, vol. 16, 1958, pp. 307–309.

6 A. Nadai, "Theory of Flow and Fracture of Solids," McGraw-Hill Book Company, Inc., New York, N. Y., 1950, pp. 472–481.

7 A. A. Ilyushin, "The Theory of Small Elastic-Plastic Deformations," *Prikladnaia Matematika i Mekhanika*, vol. 10, 1946, pp. 347–356.

8 O. L. Mangasarian, "Stresses in the Plastic Range Around a Normally Loaded Circular Hole in an Infinite Sheet," this issue of the JOURNAL, pp. 65–73.

Stresses in the Plastic Range Around a Normally Loaded Circular Hole in an Infinite Sheet[1]

O. L. MANGASARIAN
Shell Development Company, Emeryville, Calif.

The stresses in the plastic range around a normally loaded circular hole in an infinite sheet are found numerically on the basis of both J_2 deformation and incremental theories. The results of deformation theory are quantitatively assessed in the light of a criterion, recently developed by Budiansky, for the acceptability of deformation theories. The criterion is completely satisfied. Moreover, the results obtained by using these two different theories of plasticity do not differ greatly despite the fact that the stress paths are far from being radial.

A NUMBER of authors have treated the finite expansion of a circular hole in an infinite sheet for both ideally plastic and work-hardening materials. Most of these authors neglect elastic deformations that occur in the plastic range; i.e., they consider the material to be a rigid plastic material. Taylor [1][2] considered a rigid perfectly plastic material, using Tresca's yield condition and the flow rule associated with Mises' yield condition. Hill [2] also considered a nonstrain-hardening material. Prager [3] used Tresca's yield condition and its associated flow rule on a rigid work-hardening material to obtain a solution for a restricted finite value of the pressure at the hole. Hodge and Sankaranarayanan [4] extended Prager's work to include all values of the internal pressure. Alexander and Ford [5] have used Mises' yield condition and the associated Prandtl-Reuss relations. (The work of Alexander and Ford is the only one based on flow theory that takes into account the elastic components of the strains for a work-hardening material.)

In the present paper, a similar problem is considered. A finite circular hole in an infinite sheet of constant thickness is subjected to a uniform load normal to its wall, Fig. 1. Only small displacements are contemplated. The change in the hole size and the variation of the sheet thickness are neglected. However, both the elastic and plastic components of strain are taken into consideration everywhere in the analysis. Nadai [6] has obtained the general solution for this type of problem for an elastic, ideally plastic material. Winzer and Prager [7] have solved this problem using J_2 deformation theory and a pure power-law relation between uniaxial stress and strain. In the present work, two separate theories are used to set up and solve the problem numerically. Each of J_2 deformation and J_2 incremental (flow) theories are used, together with the Ramberg-Osgood [8] uniaxial stress-strain relation. The solutions are obtained on the Univac I high-speed digital computer.

The present analysis, like a preceding one [9], exploits a very useful transformation that eliminates the space variable from the explicit problem temporarily, thereby permitting a straightforward calculation of a universal stress-history curve for every point in the sheet. (Weir [10] has used a similar transformation on a creep problem.) The geometric similarity of the problem is utilized directly in simplifying the incremental theory solution.

The results of J_2 deformation theory are quantitatively assessed in the light of a criterion recently developed by Budiansky [11] for the acceptability of deformation theories. The criterion is completely satisfied. Furthermore, the results of the two theories do not differ greatly despite the fact that the stress paths are far from being radial.

Basic Equations

The radial and tangential stresses σ_r and σ_θ must satisfy the equilibrium equation

$$\sigma_\theta = \frac{d}{dr}(r\sigma_r) \tag{1}$$

and the corresponding strains ϵ_r and ϵ_θ given by

$$\left.\begin{aligned}\epsilon_r &= du/dr \\ \epsilon_\theta &= u/r\end{aligned}\right\} \tag{2}$$

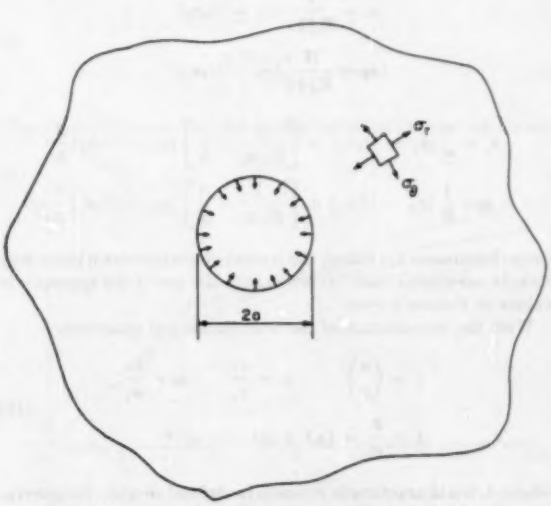

Fig. 1 Infinite sheet with a normally loaded circular hole

[1] The results presented in this paper are based upon a thesis submitted to Harvard University in partial fulfillment of the requirements for the degree of Doctor of Philosophy.

[2] Numbers in brackets designate References at end of paper.

Contributed by the Applied Mechanics Division and presented at the Annual Meeting, Atlantic City, N. J., November 29–December 4, 1959, of THE AMERICAN SOCIETY OF MECHANICAL ENGINEERS.

Discussion of this paper should be addressed to the Secretary, ASME, 29 West 39th Street, New York, N. Y., and will be accepted until April 10, 1960, for publication at a later date. Discussion received after the closing date will be returned.

NOTE: Statements and opinions advanced in papers are to be understood as individual expressions of their authors and not those of the Society. Manuscript received by ASME Applied Mechanics Division, January 23, 1959. Paper No. 59—A-130.

in terms of the radial displacement u must satisfy the compatibility equation

$$\epsilon_r = \frac{d}{dr}(r\epsilon_\theta) \tag{3}$$

The shearing stresses and strains $\tau_{r\theta}$ and $\gamma_{r\theta}$ are zero by symmetry.

According to J_2 deformation theory of plasticity, the strains are related to the stresses by

$$\begin{aligned}\epsilon_r &= \frac{1}{E}[\sigma_r - \nu\sigma_\theta] + \left[\frac{1}{E_s(\bar\sigma)} - \frac{1}{E}\right][\sigma_r - {}^1/_2\sigma_\theta] \\ \epsilon_\theta &= \frac{1}{E}[\sigma_\theta - \nu\sigma_r] + \left[\frac{1}{E_s(\bar\sigma)} - \frac{1}{E}\right][\sigma_\theta - {}^1/_2\sigma_r]\end{aligned} \tag{4}$$

where $E_s(\bar\sigma)$ is the secant modulus of the uniaxial stress-strain curve at the effective stress defined by

$$\bar\sigma = (\sigma_r^2 + \sigma_\theta^2 - \sigma_r\sigma_\theta)^{1/2} \tag{5}$$

According to J_2 incremental theory of plasticity, the strain rates are related to the stresses and stress rates by

$$\begin{aligned}\dot\epsilon_r &= \frac{1}{E}[\dot\sigma_r - \nu\dot\sigma_\theta] + \left[\frac{1}{E_t(\bar\sigma)} - \frac{1}{E}\right]\frac{\dot{\bar\sigma}}{\bar\sigma}[\sigma_r - {}^1/_2\sigma_\theta] \\ \dot\epsilon_\theta &= \frac{1}{E}[\dot\sigma_\theta - \nu\dot\sigma_r] + \left[\frac{1}{E_t(\bar\sigma)} - \frac{1}{E}\right]\frac{\dot{\bar\sigma}}{\bar\sigma}[\sigma_\theta - {}^1/_2\sigma_r]\end{aligned} \tag{6}$$

where dots denote differentiation with respect to some monotonic quantity such as time, and $E_t(\bar\sigma)$ is the tangent modulus of the uniaxial stress-strain curve at the effective stress $\bar\sigma$ defined by (5).

The boundary conditions on the problem are

$$\sigma_r = \sigma_\theta = 0 \qquad \text{at} \qquad r = \infty \tag{7a}$$

$$\sigma_r = \sigma_a \qquad \text{at} \qquad r = a \tag{7b}$$

By the extended Michell theorem [12] the solution for the stresses is independent of the elastic Poisson's ratio ν; consequently, as far as the determination of the stresses is concerned, an immediate gain in simplicity without loss of accuracy is achieved by setting $\nu = 1/2$ in the stress-strain relations (4) and (6) and using the following resulting relations:

$$\begin{aligned}\epsilon_r &= \frac{1}{E_s(\bar\sigma)}[\sigma_r - {}^1/_2\sigma_\theta] \\ \epsilon_\theta &= \frac{1}{E_s(\bar\sigma)}[\sigma_\theta - {}^1/_2\sigma_r]\end{aligned} \tag{8}$$

$$\begin{aligned}\dot\epsilon_r &= \frac{1}{E}[\dot\sigma_r - {}^1/_2\dot\sigma_\theta] + \left[\frac{1}{E_t(\bar\sigma)} - \frac{1}{E}\right][\sigma_r - {}^1/_2\sigma_\theta]\frac{\dot{\bar\sigma}}{\bar\sigma} \\ \dot\epsilon_\theta &= \frac{1}{E}[\dot\sigma_\theta - {}^1/_2\dot\sigma_r] + \left[\frac{1}{E_t(\bar\sigma)} - \frac{1}{E}\right][\sigma_\theta - {}^1/_2\sigma_r]\frac{\dot{\bar\sigma}}{\bar\sigma}\end{aligned} \tag{9}$$

Once the stresses are found, the correct strains or strain rates may then be calculated from (4) or (6) with the use of the appropriate values of Poisson's ratio.

With the introduction of the nondimensional quantities

$$\begin{aligned}\zeta &= \left(\frac{a}{r}\right)^2 \qquad s_r = \frac{\sigma_r}{\sigma_1} \qquad s_\theta = \frac{\sigma_\theta}{\sigma_1} \\ \bar s &= \frac{\bar\sigma}{\sigma_1} = (s_r^2 + s_\theta^2 - s_r s_\theta)^{1/2}\end{aligned} \tag{10}$$

where σ_1 is a characteristic stress to be defined shortly, the governing equations (1), (3), (8), and (9) become

$$s_r - s_\theta - 2\zeta\frac{ds_r}{d\zeta} = 0 \tag{11}$$

$$\epsilon_r - \epsilon_\theta + 2\zeta\frac{d\epsilon_\theta}{d\zeta} = 0 \tag{12}$$

$$\begin{aligned}\epsilon_r &= \frac{\sigma_1}{E_s}(s_r - {}^1/_2 s_\theta) \\ \epsilon_\theta &= \frac{\sigma_1}{E_s}(s_\theta - {}^1/_2 s_r)\end{aligned} \tag{13}$$

$$\begin{aligned}\dot\epsilon_r &= \frac{\sigma_1}{E}[\dot s_r - {}^1/_2\dot s_\theta] + \sigma_1\left[\frac{1}{E_t} - \frac{1}{E}\right][s_r - {}^1/_2 s_\theta]\frac{\dot{\bar s}}{\bar s} \\ \dot\epsilon_\theta &= \frac{\sigma_1}{E}[\dot s_\theta - {}^1/_2\dot s_r] + \sigma_1\left[\frac{1}{E_t} - \frac{1}{E}\right][s_\theta - {}^1/_2 s_r]\frac{\dot{\bar s}}{\bar s}\end{aligned} \tag{14}$$

where now E_s and E_t depend on $(\sigma_1\bar s)$.

Analysis Based on J_2 Deformation Theory

Elimination of the Space Variable. The governing equations for J_2 deformation theory are equations (11), (12), and (13) subject to the boundary conditions (7). Substitution of the stress strain relation (13) in the compatibility equation (12) gives

$$\frac{3}{2E_s}(s_r - s_\theta) + 2\zeta\frac{d}{d\zeta}\left[\frac{1}{E_s}(s_\theta - {}^1/_2 s_r)\right] = 0 \tag{15}$$

Substituting in the first term of (15) from the equilibrium equation (11) gives

$$\zeta\frac{3}{E_s}\frac{ds_r}{d\zeta} + \zeta\frac{d}{d\zeta}\left[\frac{1}{E_s}(2s_\theta - s_r)\right] = 0 \tag{16}$$

Now, with the tentative assumption that $\bar s$ is a monotonic function of ζ (this assumption can be easily verified *a posteriori* by the numerical results), division of (16) by $(d\bar s/d\zeta)$ and cancellation of the common factor ζ gives

$$\frac{3}{E_s}\frac{ds_r}{d\bar s} + \frac{d}{d\bar s}\left[\frac{1}{E_s}(2s_\theta - s_r)\right] = 0 \tag{17}$$

Since E_s depends only on $(\sigma_1\bar s)$, equation (17) is a linear, first-order differential equation for s_θ and s_r as functions of $\bar s$. The additional equations needed for the determination of $s_r(\bar s)$ and $s_\theta(\bar s)$ are the algebraic relation from (10)

$$\bar s^2 = s_r^2 + s_\theta^2 - s_r s_\theta \tag{18}$$

and the initial conditions (7a) corresponding to the stress state at infinity in the physical plane

$$s_r = s_\theta = 0 \qquad \text{at} \qquad \bar s = 0 \tag{19}$$

The condition (7b) at the hole is satisfied by terminating the solution to the system (17), (18), (19) at a value of $\bar s$ such that $s_r = \sigma_a/\sigma_1$. Since σ_a can take on any real value, any stress state which is a solution of the system (17), (18), (19) is a permissible stress state at the hole. In other words, subject to the monotonicity assumption of $\bar s$, the solution of (17), (18), (19) may be regarded as depicting the stress history at the hole, or for that matter, the stress history at any point in the sheet, since the hole can be imagined to extend over to any such point. Thus all points in the sheet undergo identical stress history, and the problem is said to have geometrical similarity.

The space variable ζ, temporarily removed from the problem, may be reintroduced through the equilibrium equation (11) once the universal stress-history relation between s_r and s_θ is obtained by solving the system (17), (18), (19).

Introduction of the Ramberg-Osgood Relation. An explicit formula for the dependence of E_s on $\bar{\sigma}$ (or $\sigma_1\bar{s}$) may be introduced by the use of the Ramberg-Osgood [8] equation for the uniaxial stress-strain curve

$$\epsilon = \frac{\sigma}{E}\left[1 + \frac{3}{7}\left(\frac{\sigma}{\sigma_1}\right)^{n-1}\right] \tag{20}$$

where σ_1 is the characteristic stress referred to earlier in (10), and which is known as the nominal yield stress of the material. As seen from the formula derived from (20)

$$\frac{1}{E_s} = \frac{1}{E}\left[1 + \frac{3}{7}\left(\frac{\sigma}{\sigma_1}\right)^{n-1}\right] \tag{21}$$

the value of the secant modulus at $\sigma = \sigma_1$ is 70 per cent of the elastic modulus E. The dependence of the shape of the stress-strain curve on the parameter n is exhibited in Fig. 2, which presents plots of (σ/σ_1) versus $(E\epsilon/\sigma_1)$ for several values of n. Evaluation of the expression (21) at $\bar{\sigma}$

$$\frac{1}{E_s(\bar{\sigma})} = \frac{1}{E}\left[1 + \frac{3}{7}\bar{s}^{n-1}\right],$$

and substitution in (17) gives

$$2(7 + 3\bar{s}^{n-1})\left(\frac{ds_\theta}{d\bar{s}} + \frac{ds_r}{d\bar{s}}\right) + 3(n-1)\bar{s}^{n-2}(2s_\theta - s_r) = 0 \tag{22}$$

Limiting Cases as Boundary Conditions. As the effective stress $\bar{s}$ approaches zero, the stresses become elastic. The elastic solution is well known and may be written as

$$\frac{s_r}{\bar{s}} = \pm\frac{1}{\sqrt{3}} \qquad \frac{s_\theta}{\bar{s}} = \mp\frac{1}{\sqrt{3}}$$

(The second set of signs represents a compressive radial stress at the hole. Because a change in sign of the load merely changes the sign of the stresses, the second set of signs will be neglected throughout.) It can be seen easily that the foregoing elastic solution satisfies the equation

$$\frac{ds_\theta}{d\bar{s}} + \frac{ds_r}{d\bar{s}} = 0$$

which is obtained from (22) by letting $\bar{s}$ approach zero.

Since the stresses approach zero at infinity in the sheet, elastic behavior must prevail there and thus the condition (19) may be equivalently written as

$$\bar{s} = 0 \qquad \frac{s_r}{\bar{s}} = \frac{1}{\sqrt{3}} \qquad \frac{s_\theta}{\bar{s}} = -\frac{1}{\sqrt{3}} \tag{23}$$

As $\bar{s}$ becomes very large, the second term on the right-hand side of the Ramberg-Osgood equation (21) dominates and the relation behaves like a power law. Winzer and Prager [7] have obtained the solution for a pure power law which may be writtten as follows

$$\frac{s_r}{\bar{s}} = \frac{2n}{[3(n^2+3)]^{1/2}} \qquad \frac{s_\theta}{\bar{s}} = \frac{n-3}{[3(n^2+3)]^{1/2}} \tag{24}$$

This again can be shown to satisfy the equation

$$2\bar{s}\left(\frac{ds_\theta}{d\bar{s}} + \frac{ds_r}{d\bar{s}}\right) + (n-1)(2s_\theta - s_r) = 0$$

which is obtained from (22) by letting $\bar{s}$ approach infinity. (It should be remarked that allowing $\bar{s}$ to approach infinity is not, of course, consistent with the intrinsic assumption of small strains; nevertheless the case $\bar{s} = \infty$ does provide a useful asymptotic result.) The result (24) may be utilized in the present problem as a condition that the solution must satisfy for very large stresses and may be written as

$$\bar{s} = \infty \qquad \frac{s_r}{\bar{s}} = \frac{2n}{[3(n^2+3)]^{1/2}} \qquad \frac{s_\theta}{\bar{s}} = \frac{n-3}{[3(n^2+3)]^{1/2}} \tag{25}$$

To recapitulate, equations (22) and (18) must be solved subject to the conditions (23) and (25) in order to obtain the universal stress-history curve relating s_r and s_θ through $\bar{s}$. Because (22) is a first-order equation, a singular point may be associated with one of the conditions (23) or (25). As a matter of fact, the subsequent numerical work shows that any solution of the systems (22), (23) inevitably satisfies the condition (25).

Transformations. The parametric representation due to Nadai [6]

$$\frac{s_r}{\bar{s}} = \frac{2}{\sqrt{3}}\sin\left(\theta + \frac{\pi}{6}\right)$$
$$\frac{s_\theta}{\bar{s}} = \frac{2}{\sqrt{3}}\sin\left(\theta - \frac{\pi}{6}\right) \tag{26}$$

automatically satisfies the algebraic equation (18), and when substituted into (22) gives

$$4\bar{s}(7 + 3\bar{s}^{n-1})\frac{d\theta}{d\bar{s}} + (3n\bar{s}^{n-1} + 9\bar{s}^{n-1} + 28)\tan\theta - 3\sqrt{3}(n-1)\bar{s}^{n-1} = 0 \tag{27}$$

The transformation

$$x = \frac{3\bar{s}^{n-1}}{7 + 3\bar{s}^{n-1}} \tag{28}$$

conveniently confines the limits of the variable x into the range $0 \le x \le 1$, and the transformation

$$y = \tan\theta \tag{29}$$

gets rid of trigonometric functions. With these transformations, the differential equation (27) becomes

$$\frac{dx}{dy} = \frac{4(n-1)x(1-x)}{[1+y^2][\sqrt{3}(n-1)x - (nx - x + 4)y]} \tag{30}$$

and the boundary conditions (23) and (25) become

$$y = 0 \qquad x = 0 \tag{31}$$

$$y = \frac{\sqrt{3}(n-1)}{n+3} \qquad x = 1 \tag{32}$$

Equation (30) is an Abel differential equation as listed by Kamke

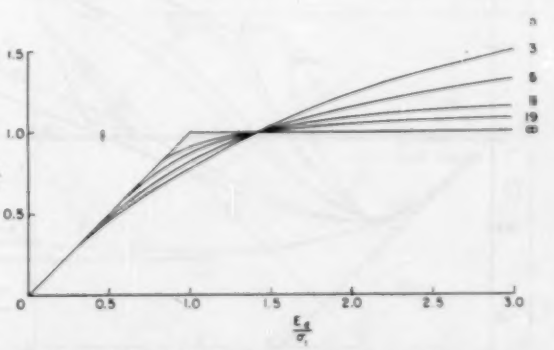

Fig. 2 Nondimensional Ramberg-Osgood stress-strain curves

[13]. No analytical solution seems feasible, but a numerical solution can be easily obtained.

For values of n shown in Fig. 2, equation (30) was solved on the Univac I digital computer by a first-order process of finite differences and obtaining three-figure accuracy. The solution was started at the regular point $y = 0$, $x = 0$ and inevitably terminated at the point $y = \sqrt{3}(n-1)/(n+3)$, $x = 1$, which can be rigorously shown to be a nodal point. Once the $x - y$ relation was obtained, the stresses s_r and s_θ were obtained by transforming back into the original variables as follows:

$$s_r = \left[\frac{7}{3}\frac{x}{1-x}\right]^{\frac{1}{n-1}}(1+y^2)^{-1/2}\left[y + \frac{1}{\sqrt{3}}\right] \tag{33}$$

$$s_\theta = \left[\frac{7}{3}\frac{x}{1-x}\right]^{\frac{1}{n-1}}(1+y^2)^{-1/2}\left[y - \frac{1}{\sqrt{3}}\right] \tag{34}$$

Fig. 3 depicts in solid lines the universal stress-history curves for values of $n = 3, 5, 9$, and 19 obtained numerically. The curve for $n = \infty$ was obtained from the exact analytic results of Nadai [6] for an ideally plastic material. It is interesting to note the continuous transition from the numerically obtained curves for finite n to Nadai's result for $n = \infty$. Also of interest is to note that near the origin, where the stresses are small, the stress-history curves are tangent to the elastic asymptote $s_\theta/s_r = -1$. For large values of the stresses, the curves approach the radial path $s_\theta/s_r = (n-3)/2n$ of the power-law solution. The fact that the stress paths are radial for a power-law relation is, of course, to be expected from Ilyushin's theorem [14]

Spatial Stress Distribution. Applying the transformations (26), (28), and (29) to the equilibrium equation (11) gives the following equation that relates the space variable ζ to the $x-y$ variables:

$$\frac{1}{\zeta}\frac{d\zeta}{dx} = \frac{\sqrt{3}y+1}{(n-1)x(1-x)} + \frac{\sqrt{3}-y}{1+y^2}\frac{dy}{dx} \tag{35}$$

At the hole

$$\zeta = 1 \qquad y = y_a \qquad x = x_a$$

$$0 < y_a < \frac{\sqrt{3}(n-1)}{n+3} \qquad 0 < x_a < 1 \tag{36}$$

The relation (36) serves as the initial condition for (35). By picking a valid pair of x_a and y_a [valid means lying on the integral curve of equation (30)] an initial condition is provided for (35) which can then be integrated numerically with the use of the integral curve $x-y$ of (30). Once the relation between ζ, x, and y is obtained, equations (33) and (34) provide the relation between the stresses s_r, s_θ, and the space variable ζ.

The transformation

$$g(y) = \log\left[\zeta\left(\frac{1-x}{x}\right)^{\frac{1}{n-1}}\right] \tag{37}$$

when used on (35) gives

$$\frac{dg}{dy} = \frac{\sqrt{3}y}{(n-1)x(1-x)}\frac{dx}{dy} + \frac{\sqrt{3}-y}{1+y^2} \tag{38}$$

thus eliminating the singularity at $x = 0$, $y = 0$. The initial condition (36) becomes

$$g(y_a) = \log\left[\frac{1-x_a}{x_a}\right]^{\frac{1}{n-1}} \qquad 0 < x_a < 1 \tag{39}$$

Since the dependent variable g appears only in differential form in (38), any other function defined as

$$\bar{g} = g + \text{const}$$

satisfies the same differential equation, and in particular does the function $\bar{g}(y)$ defined as

$$\bar{g}(y) = g(y) - g(0) \tag{40}$$

In other words, $\bar{g}(y)$ satisfies the differential equation

$$\frac{d\bar{g}}{dy} = \frac{\sqrt{3}y}{(n-1)x(1-x)}\frac{dx}{dy} + \frac{\sqrt{3}-y}{1+y^2} \tag{41}$$

subject to the initial condition

$$\bar{g} = 0 \qquad \text{at} \qquad y = 0 \qquad x = 0 \tag{42}$$

The system (41), (42) can easily be solved numerically in conjunction with the system (30), (31). As a matter of fact, $\bar{g}(y)$ defines another universal curve from which the space variable ζ can be determined from

$$\zeta = \frac{\left[\frac{x}{1-x}\right]^{\frac{1}{n-1}} e^{\bar{g}(y)}}{\left[\frac{x_a}{1-x_a}\right]^{\frac{1}{n-1}} e^{\bar{g}(y_a)}} \equiv \frac{\bar{\zeta}(x, y)}{\bar{\zeta}(x_a, y_a)} \tag{43}$$

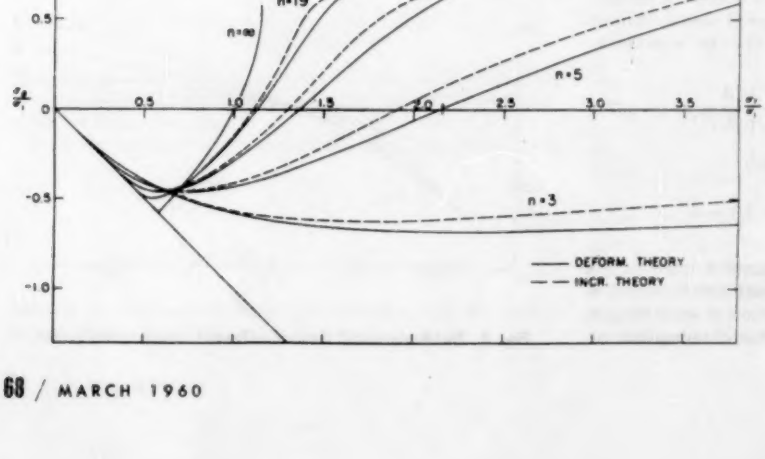

Fig. 3 Universal stress history curves for $n = 3, 5, 9, 19, \infty$

where the definition of $\bar{\zeta}(x, y)$ is obvious. It is now seen that the complete solution to the problem, for *any* load at the hole, reduces to finding two universal curves, the $x-y$ and $\varrho-y$ curves. From the $x-y$ curve, any pair of values x_a, y_a may be picked to give the desired radial stress at the hole, and the stress distribution within the sheet is found by using equations (33), (34), and (43) with $0 < x < x_a$, $0 < y < y_a$.

With the use of a first-order process of finite differences, the system (41), (42) was solved numerically for the $\beta(y)$ relation with

$$0 < y < \frac{\sqrt{3}(n-1)}{n+3}.$$

The $\bar{\zeta}(x, y)$ was calculated by using

$$\bar{\zeta}(x, y) = \left[\frac{x}{1-x}\right]^{\frac{1}{n-1}} e^{\beta(y)} \tag{44}$$

The ζ-curve for any desired radial stress at the hole was then calculated from the relation (43). The final numerical results consisted of a tabulation of $\bar{\zeta}$, s_r, s_θ. By picking any desired s_r for the load at the hole, the stress distribution in the sheet was obtained from $\zeta = \bar{\zeta}/(\bar{\zeta})_{\text{hole}}$, with, of course, $0 \leq \bar{\zeta} \leq (\bar{\zeta})_{\text{hole}}$.

The solid curves in Figs. 4 to 7 show the radial and tangential stress distribution in the sheet for $n = 3$ and 19 for various loads at the hole.

Analysis Based on J_2 Incremental Theory

Stress-Strain Relations. The stress-strain relations for J_2 incremental theory are given in (14). By using these relations, a new independent variable, time, is introduced into the problem thus complicating it considerably. However, the similarity property may be invoked here to minimize this complication.

Since each point in the sheet undergoes an identical stress history, the incremental effect at such a point, denoted by dots in (14), that results from varying time by an infinitesimal amount dt may be achieved by moving an infinitesimal distance $kd\zeta$ in the sheet. The factor k is, of course, some function of ζ and t. Therefore the dots in (14) may be replaced by total derivatives with respect to ζ (the k drops out because the expression is homogeneous in the dots) and the following expressions are obtained for stress-strain relations:

$$\begin{aligned}
\frac{d\epsilon_r}{d\zeta} &= \frac{\sigma_i}{E}\left[\frac{ds_r}{d\zeta} - \tfrac{1}{2}\frac{ds_\theta}{d\zeta}\right] + \sigma_i\left[\frac{1}{E_i} - \frac{1}{E}\right][s_r - \tfrac{1}{2}s_\theta]\frac{1}{3}\frac{d\bar{s}}{d\zeta} \\
\frac{d\epsilon_\theta}{d\zeta} &= \frac{\sigma_i}{E}\left[\frac{ds_\theta}{d\zeta} - \tfrac{1}{2}\frac{ds_r}{d\zeta}\right] + \sigma_i\left[\frac{1}{E_i} - \frac{1}{E}\right][s_\theta - \tfrac{1}{2}s_r]\frac{1}{3}\frac{d\bar{s}}{d\zeta}
\end{aligned} \tag{45}$$

Thus the independent variable time has been eliminated from the problem.

The dependence of E_i on $\bar{\sigma}$ must be specified in order to make an explicit solution possible. Once again, the Ramberg-Osgood relation (20) will be used to provide such a relation. (It

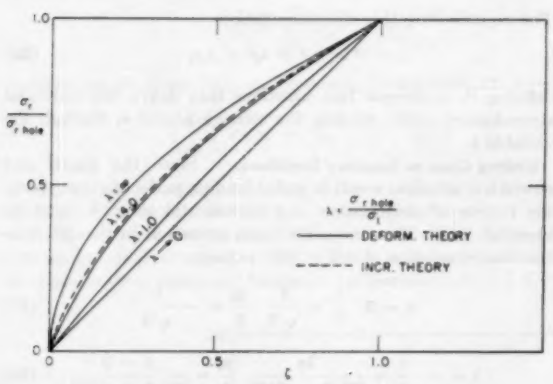

Fig. 4 $\sigma_r/\sigma_{r\,hole}$ versus ζ for $n = 3$

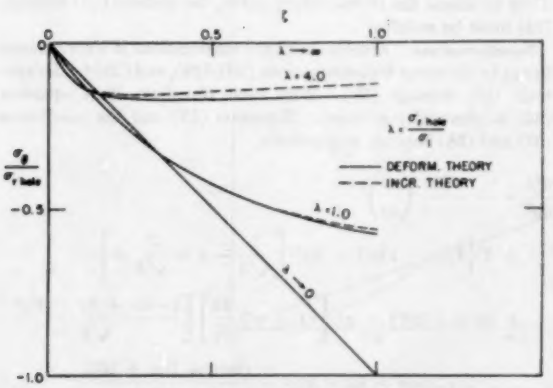

Fig. 5 $\sigma\theta/\sigma_{r\,hole}$ versus ζ for $n = 3$

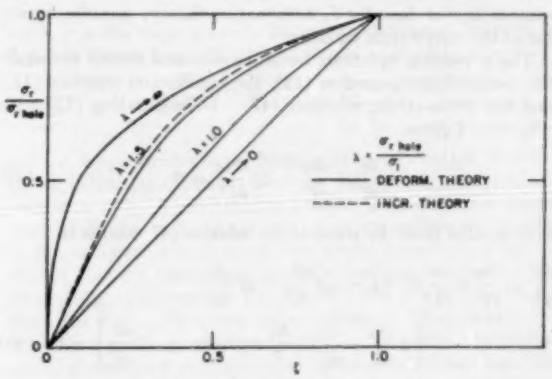

Fig. 6 $\sigma_r/\sigma_{r\,hole}$ versus ζ for $n = 19$

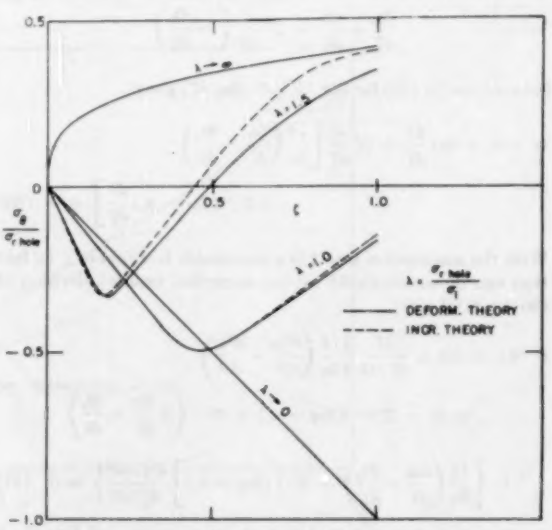

Fig. 7 $\sigma\theta/\sigma_{r\,hole}$ versus ζ for $n = 19$

should be remarked, that the use of the Ramberg-Osgood relation is not intrinsic to the method of solution of either J_2 deformation or incremental theory; any other monotonic stress-strain relation could have been used.) From (20)

$$\frac{1}{E_t} = \frac{d\epsilon}{d\sigma} = \frac{1}{E}\left[1 + \frac{3n}{7}\left(\frac{\sigma}{\sigma_1}\right)^{n-1}\right]$$

Thus

$$\frac{1}{E_t(\bar{\sigma})} = \frac{1}{E}\left[1 + \frac{3n}{7}\,\bar{s}^{n-1}\right] \tag{46}$$

Substituting (46) into (45) gives

$$\begin{aligned}\frac{d\epsilon_r}{d\zeta} &= \frac{\sigma_1}{E}\left[\frac{ds_r}{d\zeta} - {}^1/_2\frac{ds_\theta}{d\zeta}\right] + \frac{\sigma_1}{E}\frac{3n}{7}\,\bar{s}^{n-2}\,[s_r - {}^1/_2 s_\theta]\,\frac{d\bar{s}}{d\zeta}\\ \frac{d\epsilon_\theta}{d\zeta} &= \frac{\sigma_1}{E}\left[\frac{ds_\theta}{d\zeta} - {}^1/_2\frac{ds_r}{d\zeta}\right] + \frac{\sigma_1}{E}\frac{3n}{7}\,\bar{s}^{n-2}\,[s_\theta - {}^1/_2 s_r]\,\frac{d\bar{s}}{d\zeta}\end{aligned} \tag{47}$$

Setting up the Governing Equations. As in the analysis for J_2 deformation theory, the goal here will be to obtain a single differential equation, independent of the space variable ζ, that will define the universal stress-history curve. Once this relation is obtained, the space variable can be reintroduced in the same manner as was done for J_2 deformation theory; namely, by the use of the equilibrium equation.

The governing equations for J_2 incremental theory are again the compatibility equation (12), the equilibrium equation (11), and the stress-strain relations (47). Differentiating (12) with respect to ζ gives

$$\frac{d\epsilon_r}{d\zeta} + \frac{d\epsilon_\theta}{d\zeta} + 2\zeta\frac{d^2\epsilon_\theta}{d\zeta^2} = 0 \tag{48}$$

Substitution from the stress-strain relation (47) results in

$$\begin{aligned}\frac{ds_r}{d\zeta} + \frac{ds_\theta}{d\zeta} + \frac{3n}{7}\,\bar{s}^{n-2}(s_r + s_\theta)\frac{d\bar{s}}{d\zeta} + 2\zeta\frac{d}{d\zeta}\\ \left[2\frac{ds_\theta}{d\zeta} - \frac{ds_r}{d\zeta} + \frac{3n}{7}\,\bar{s}^{n-2}\,(2s_\theta - s_r)\frac{d\bar{s}}{d\zeta}\right] = 0\end{aligned} \tag{49}$$

Differentiating (11) with respect to ζ gives

$$\frac{ds_r}{d\zeta} + \frac{ds_\theta}{d\zeta} = 2\zeta\frac{d}{d\zeta}\left(-\frac{ds_r}{d\zeta}\right)$$

Substitution in (49) for $(ds_r/d\zeta) + (ds_\theta/d\zeta)$ gives

$$\begin{aligned}\bar{s}^{n-2}(s_r + s_\theta)\frac{d\bar{s}}{d\zeta} + 2\zeta\frac{d}{d\zeta}\left[\frac{14}{3n}\left(\frac{ds_\theta}{d\zeta} - \frac{ds_r}{d\zeta}\right)\right.\\ \left. + \bar{s}^{n-2}(2s_\theta - s_r)\frac{d\bar{s}}{d\zeta}\right] = 0\end{aligned} \tag{50}$$

With the assumption that $\bar{s}$ is a monotonic function of ζ (a fact that can be corroborated by the numerical results), division of (50) by $d\bar{s}/d\zeta$ gives

$$\begin{aligned}\bar{s}^{n-2}(s_r + s_\theta) + \frac{2\zeta}{d\zeta/d\bar{s}}\left\{\frac{14}{3n}\left(\frac{d^2s_\theta}{d\bar{s}^2} - \frac{d^2s_r}{d\bar{s}^2}\right)\right.\\ + (n-2)\bar{s}^{n-3}(2s_\theta - s_r) + \bar{s}^{n-2}\left(2\frac{ds_\theta}{d\bar{s}} - \frac{ds_r}{d\bar{s}}\right)\\ \left. - \left[\frac{14}{3n}\left(\frac{ds_\theta}{d\bar{s}} - \frac{ds_r}{d\bar{s}}\right) + \bar{s}^{n-2}\,(2s_\theta - s_r)\right]\frac{d^2\zeta/d\bar{s}^2}{d\zeta/d\bar{s}}\right\} = 0\end{aligned} \tag{51}$$

The variable ζ appears in two places in equation (51) in the form of $\zeta/(d\zeta/d\bar{s})$ and $(d^2\zeta/d\bar{s}^2)/(d\zeta/d\bar{s})$. In what follows, these two expressions will be replaced by ones that do not involve ζ explicitly.

Division of (11) by $d\zeta/d\bar{s}$ gives

$$(s_r - s_\theta)\frac{d\zeta}{d\bar{s}} - 2\zeta\frac{ds_r}{d\bar{s}} = 0 \tag{52}$$

or

$$2\zeta/(d\zeta/d\bar{s}) = (s_r - s_\theta)/(ds_r/d\bar{s}) \tag{53}$$

Differentiating (52) with respect to $\bar{s}$ and substituting from (53) gives

$$\frac{d^2\zeta/d\bar{s}^2}{d\zeta/d\bar{s}} = \frac{(ds_r/d\bar{s}) + (ds_\theta/d\bar{s})}{s_r - s_\theta} + \frac{(d^2s_r/d\bar{s}^2)}{(ds_r/d\bar{s})} \tag{54}$$

Substitution of (53) and (54) into (51) eliminates ζ from the problem temporarily and gives

$$\begin{aligned}\frac{1}{s_r - s_\theta}\left\{\frac{14}{3n}\left[\left(\frac{ds_r}{d\bar{s}}\right)^2 - \left(\frac{ds_\theta}{d\bar{s}}\right)^2\right] + \bar{s}^{n-2}(2s_r - s_\theta)\frac{ds_r}{d\bar{s}}\right.\\ \left. + \bar{s}^{n-2}(s_r - 2s_\theta)\frac{ds_\theta}{d\bar{s}}\right\}\frac{ds_r}{d\bar{s}} + \frac{14}{3n}\left(\frac{d^2s_\theta}{d\bar{s}^2}\frac{ds_r}{d\bar{s}} - \frac{d^2s_r}{d\bar{s}^2}\frac{ds_\theta}{d\bar{s}}\right)\\ + (n-2)\bar{s}^{n-3}(2s_\theta - s_r)\frac{ds_r}{d\bar{s}} + \bar{s}^{n-2}\left(2\frac{ds_\theta}{d\bar{s}} - \frac{ds_r}{d\bar{s}}\right)\frac{ds_r}{d\bar{s}}\\ + \bar{s}^{n-1}(s_r - 2s_\theta)\frac{d^2s_r}{d\bar{s}^2} = 0\end{aligned} \tag{55}$$

This equation together with the relation

$$\bar{s}^2 = s_r^2 + s_\theta^2 - s_r s_\theta \tag{56}$$

defining $\bar{s}^2$, constitute two equations that define the universal stress-history curve relating the stresses s_r and s_θ through the variable $\bar{s}$.

Limiting Cases as Boundary Conditions. Since the elastic and power-law solutions result in radial loading paths in stress space, the results of deformation and incremental theories must be identical [15]. Thus the same limits prevail as in the deformation-theory solution of this paper; namely,

$$\bar{s} = 0 \quad \frac{s_r}{\bar{s}} = \frac{1}{\sqrt{3}} \quad \frac{s_\theta}{\bar{s}} = -\frac{1}{\sqrt{3}} \tag{57}$$

$$\bar{s} = \infty \quad \frac{s_r}{\bar{s}} = \frac{2n}{[3(n^2+3)]^{1/2}} \quad \frac{s_\theta}{\bar{s}} = \frac{n-3}{[3(n^2+3)]^{1/2}} \tag{58}$$

Thus to obtain the stress-history curve, the systems (55) through (58) must be satisfied.

Transformations. From numerical considerations it is convenient to apply the same transformations (26), (28), and (29) to the systems (55) through (58). With these transformations equation (56) is identically satisfied. Equation (55) and the conditions (57) and (58) become, respectively,

$$\begin{aligned}\frac{d^2x}{dy^2} = -\frac{2}{1-x}\left(\frac{dx}{dy}\right)^2\\ + T\left\{4[(n-1)x(1-x)]^3\left[\frac{1}{\sqrt{3}} - y + \frac{2}{\sqrt{3}}\,y^2\right]\right.\\ + (n-1)^2x^3(1-x)\left[(1+y^2)\frac{dx}{dy}\right]\left[\frac{(-nx+4x-4)y^3}{\sqrt{3}}\right.\\ \left. + (3nx + 8x - 8)y^2 - \frac{(9nx - 16x + 16)y}{\sqrt{3}}\right.\end{aligned}$$

$$+ (3n - 4)x + 4\Big]$$

$$+ \frac{(n-1)x}{\sqrt{3}}\left[(1+y^2)\frac{dx}{dy}\right]^2 [\sqrt{3}(-nx + 4x - 4)y^3 + (-5nx + 8x + 4n)y^2 + \sqrt{3}(7nx - 8x + 8)y + (3n - 4)x + 4(n+1)]$$

$$+ \frac{1}{1-x}\left[(1+y^2)\frac{dx}{dy}\right]^3 \left[y^2[(n-1)(n+4)x + 4] + \frac{y}{\sqrt{3}}[-2(n-1)(n-2)x + 4] - (n-1)nx\right]\Bigg\} \quad (59)$$

$$y = 0 \qquad x = 0 \quad (60)$$

$$y = \frac{\sqrt{3}(n-1)}{n+3} \qquad x = 1 \quad (61)$$

where

$$T = \{(n-1)^2(1+y^2)^2x^2(1-x)\}^{-1} \left\{x\left[\frac{n-4}{\sqrt{3}}y^2 - 2ny + \frac{3n-4}{\sqrt{3}}\right] + \frac{4}{\sqrt{3}}[y^2+1]\right\}^{-1}$$

Equation (59) is a second-order differential equation. However, the condition (60) alone is sufficient to determine the solution completely, if x is assumed to be an analytic function of y at the origin. (This assumption may be justified on physical grounds since the origin corresponds to pure elastic behavior where no singularities are anticipated as evidenced by the deformation theory solution.) The assumption of

$$x = \sum_{i=1}^{\infty} b_i y^i$$

satisfies the condition (60) and when substituted into (59) gives

$$\left(\frac{dx}{dy}\right)_0 \equiv b_1 = \frac{4}{\sqrt{3}}\frac{n}{n-1} \quad (62)$$

It may be noted that the foregoing $(dx/dy)_0$ is identical with the corresponding term for the deformation theory solution.

With the conditions (60) and (62) a first-order finite-difference process was used on equation (59) to obtain a numerical solution accurate to three significant figures for the parameter $n = 3, 5, 9,$ and 19. The solution inevitably passed through the point (61), which is thus suspected to be a singular point. Once the $x - y$ curve was obtained, the remainder of the problem was solved in exactly the same manner as the deformation theory solution, since the transformations are the same in both cases.

Figs. 3 through 7 depict the results of incremental theory in dashed lines in distinction from the solid curves of deformation theory. Where the results of the two theories coincide, the curves are shown in one solid line. It should be noted here that, for ideal plasticity ($n = \infty$), the stresses are statically determinate and thus the results are independent of the stress-strain law used. Hence the single solid curve for $n = \infty$ in Fig. 3 was obtained from Nadai's results.

Discussion and Comparison of Results

Assessment of Deformation Theory Results. In a recent paper Budiansky [11] showed "that deformation theories of plasticity may be used for a range of loading paths other than proportional loading without violation of general requirements for the physical soundness of plasticity theory." These general requirements for physical soundness of the theory were taken to be Drucker's work-hardening postulates [16]. For the case of biaxial stress, Budiansky showed that if

$$\gamma \leq \tan^{-1}\sqrt{n} \quad (63)$$

where γ is the angle between the radius vector and the tangent vector to the loading path in the ξ versus $\sqrt{3}\eta$ plane where

$$\xi = \frac{\varepsilon_r + \varepsilon_\theta}{2}, \qquad \eta = \frac{\varepsilon_r - \varepsilon_\theta}{2}$$

and n is the parameter of the Ramberg-Osgood relation, then the use of deformation theory does not violate any of Drucker's postulates. Figs. 8 and 9 exhibit ξ versus $\sqrt{3}\eta$ curves for the extreme cases of $n = 3$ and 19; the maximum permissible γ given by (63) is noted in each figure. By actual inspection, it can be verified that the foregoing criterion is nowhere violated by the stress paths. (The same is true for the cases of $n = 5$ and 9 for which the $\xi - \sqrt{3}\eta$ curves are not shown.) Thus, despite the fact that the stress paths are far from being radial, the fundamental postulates of plasticity have nowhere been violated and the solution obtained with deformation theory is just as acceptable as the solution obtained by incremental theory (which of course

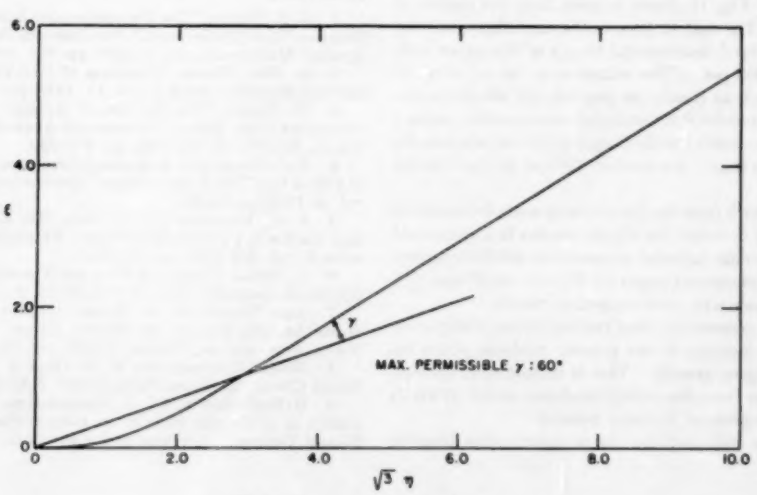

Fig. 8 ξ versus $\sqrt{3}\,\eta$ for $n = 3$

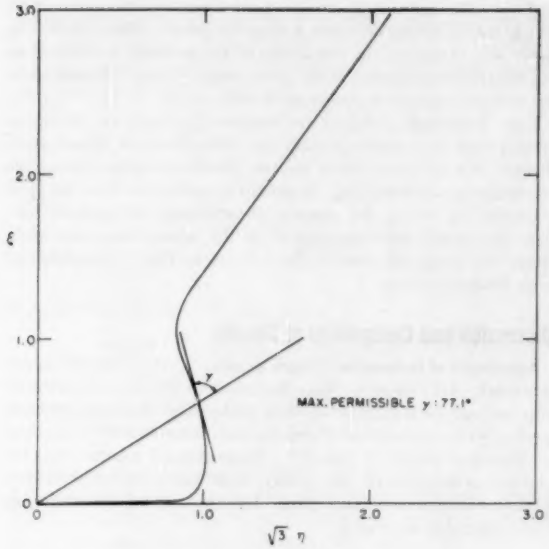

Fig. 9 ξ versus $\sqrt{3}\,\eta$ for $n = 19$

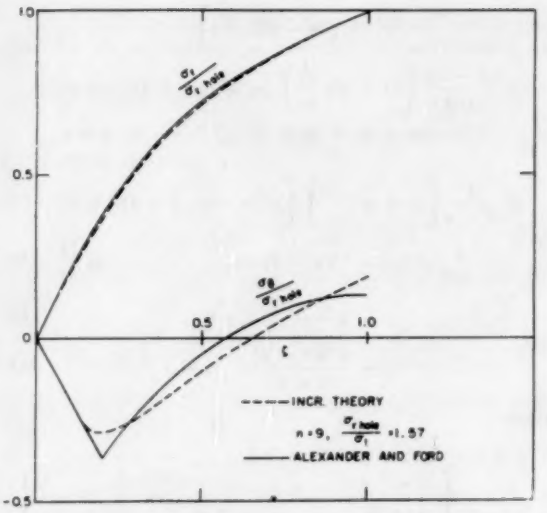

Fig. 10 Results of Alexander and Ford and of incremental theory

took considerably more labor and luck to obtain—luck because of the similarity nature of the problem that made a straightforward numerical procedure feasible).

Comparison With Previous Work. Since in most of the previous work, the elastic components of the strains are neglected, comparisons shall be made only with analyses that do not neglect the elastic strains.

Alexander and Ford [5] used a theory which is essentially equivalent to the incremental theory of this paper. They treated the problem using Mises' yield condition and the associated Prandtl-Reuss relations for a specific uniaxial stress-strain curve with a Young's modulus of 30,150,000 psi. By a numerical trial-and-error method, they solved four simultaneous, nonlinear, ordinary, differential equations. Since Alexander and Ford take into account the thickening of the sheet (which is neglected in this paper), their solution is taken only for the region where the thickening is negligible; i.e., the hole is assumed to extend over the thickened region. Fig. 10 shows in solid lines the results of Alexander and Ford. The dashed lines in the same figure are the results obtained from the J_2 incremental theory of this paper with $n = 9$ and $\sigma_1 = 35{,}000$ psi. (The values of n and σ_1 were, of course, picked to match as closely as possible the Ramberg-Osgood curve to the Alexander-Ford uniaxial stress-strain curve.) The results agree quite closely for the bigger of the two stresses σ_r, and differ by not more than 7 per cent of the load at the hole for σ_θ.

The only previous work done on this problem with deformation theory that takes into account the elastic strains is a numerical calculation for one specific uniaxial stress-strain relation carried out in the previously mentioned paper by Winzer and Prager [7]. No comparisons are made with their numerical results.

Final Remarks. It is noteworthy that the use of two completely different theories of plasticity in the present problem yields results that do not disagree greatly. This is remarkable, because the stress paths are far from the radial condition under which J_2 deformation and incremental theories coincide.

Many authors have criticized the use of deformation theories for any problem in which the loading path departed from a radial direction. However, from the present work, it is seen that such a path may depart significantly from a radial direction without violating anywhere the fundamental postulates of work-hardening plasticity. The relative simplicity of J_2 deformation theory in comparison with J_2 incremental theory should certainly recommend its use on problems that hitherto have been unassailable with incremental theory. The results of any analysis based on deformation theory should, however, be subjected to Budiansky's acceptability criterion.

Acknowledgments

The author wishes to thank Prof. Bernard Budiansky for suggesting this problem and for valuable help in its preparation. He is also grateful to the Office of Naval Research for financial support under Contract Nonr 1866(02).

References

1 G. I. Taylor, "The Formation and Enlargement of a Circular Hole in a Thin Plastic Sheet," *The Quarterly Journal of Mechanics and Applied Mathematics*, vol. 1, 1948, pp. 103–124.

2 R. Hill, "Plastic Distortion of Non-Uniform Sheets," *Philosophical Magazine*, series 7, vol. 11, 1949, pp. 971–983.

3 W. Prager, "On the Use of Singular Yield Conditions and Associated Flow Rules," JOURNAL OF APPLIED MECHANICS, vol. 20, TRANS. ASME, vol. 75, 1953, pp. 317–320.

4 P. G. Hodge and R. Sankaranarayanan, "On Finite Expansion of a Hole in a Thin Infinite Plate," *Quarterly of Applied Mathematics*, vol. 16, 1958, pp. 73–80.

5 J. M. Alexander and H. Ford, "On Expanding a Hole From Zero Radius in a Thin Infinite Plate," *Proceedings of the Royal Society*, series A, vol. 226, 1954, pp. 543–561.

6 A. Nadai, "Theory of Flow and Fracture of Solids," McGraw-Hill Book Company, Inc., New York, N. Y., 1950, pp. 472–481.

7 Alice Winzer and W. Prager, "On the Use of Power Laws in Stress Analysis Beyond the Elastic Range," JOURNAL OF APPLIED MECHANICS, vol. 14, TRANS. ASME, vol. 69, 1947, pp. A281–A284.

8 Walter Ramberg and W. R. Osgood, "Description of Stress-Strain Curves by Three Parameters," NACA TN 902, 1943.

9 B. Budiansky and O. L. Mangasarian, "Plastic Stress Concentration at a Circular Hole in an Infinite Sheet Subjected to Equal Biaxial Tension," this issue of the JOURNAL, pp. 59–64.

10 C. D. Weir, "The Creep of the Thick Tubes Under Internal Pressure," JOURNAL OF APPLIED MECHANICS, vol. 24, TRANS. ASME, vol. 79, 1957, pp. 464–466.

11 Bernard Budiansky, "A Reassessment of Deformation Theories of Plasticity," JOURNAL OF APPLIED MECHANICS, vol. 26, TRANS. ASME, vol. 81, 1959, series E, pp. 259–264.

12 Bernard Budiansky, "Extension of Michell's Theorem to Problems of Plasticity and Creep," *Quarterly of Applied Mathematics*, vol. 16, 1958, pp. 307–309.

13 E. Kamke, "Differentialgleichungen Lösung Methoden und Lösungen," vol. 1, Chelsea Publishing Company, 1948, pp. 24–26.

14 A. A. Ilyushin, "The Theory of Small Elastic-Plastic Deformations," *Prikladnaia Mathematika i Mekhanika*, vol. 10, 1946, pp. 347–356.

15 A. A. Ilyushin, "Relation Between the Theory of Saint-Venant-Levy-Mises and the Theory of Small Elastic-Plastic Deformations," *Prikladnaia Mathematika i Mekhanika*, vol. 9, 1945, pp. 207–218.

16 D. C. Drucker, "A More Fundamental Approach to Plastic Stress-Strain Relations," Proceedings of the First U. S. National Congress for Applied Mechanics, ASME, 1951, pp. 487–491.

APPENDIX

Limitations of the Results. The present work, besides neglecting time and temperature effects, is limited by the intrinsic assumption that the magnitude of the strains must be small. Thus before considering the results of the present work for a specific material, the magnitude of the strains should be investigated. The following approximate procedure is recommended to obtain a measure of the magnitude of strains involved in the problem.

Since, for most materials, Poisson's ratio varies about 1/3, orders of magnitude will be preserved if ν is taken to be 1/2. Furthermore, since the results of deformation and incremental theories are not very different, the expressions (8) may be used to calculate the order of magnitude of the strains at the hole. These should not exceed a few per cent if the present results are to be consistent with the implicit assumption of small strains. In general, it may be said that the lower the ratio σ_1/E for a given material, the bigger are the permissible loads at the hole that do not produce large strains.

B. A. BOLEY
Professor of Civil Engineering,
Institute of Flight Structures,
Columbia University,
New York, N. Y.

On a Dynamical Saint Venant Principle[1]

The dynamic behavior of a simple mechanical model composed of two Timoshenko beams connected by springs is studied. The accuracy of a quasi-static solution and of Saint Venant's principle is studied for various rates of load application.

Consider the class of dynamical problems of elasticity with the following properties:

(i) The body is initially undeformed and at rest.

(ii) Boundary tractions $T_i(P, t)$, $i = 1, 2, 3$, at a surface point P at a time t are prescribed as

$$T_i(P, t) = \begin{cases} f(t)F_i(P) \text{ for } P \text{ in } S^* \\ 0 \text{ for } P \text{ in } (S - S^*) \end{cases} \tag{1}$$

where S^* is a (small) portion of the total surface S. The function $f(t)$ will be taken to be dimensionless, and will be assumed to approach a constant value as $t \to \infty$, and thus a steady-state condition is approached for large times.

(iii) Saint Venant's principle holds in the corresponding static problem, i.e., one satisfying the static equations of elasticity theory under prescribed surface tractions given by

$$T_i(P) = \begin{cases} F_i(P) \quad \text{for } P \text{ in } S^* \\ 0 \text{ for } P \text{ in } (S - S^*) \end{cases} \tag{2}$$

We will denote by u_i and σ_{ij} the displacement and stress components, respectively, in the dynamic case, and by $u_i^{(0)}$ and $\sigma_{ij}^{(0)}$ those in the static case of (iii). We now wish to consider under what conditions, for problems of the type just described, Saint Venant's principle will hold in the dynamic case.

A discussion given elsewhere [1][2] indicated that Saint Venant's principle is a general property of elliptic boundary-value problems, and could not be expected to hold in general in problems of the hyperbolic type, such as, for example, those of the dynamical theory of elasticity. If the loading is applied sufficiently slowly, however, then it is intuitively clear the the static solution will be a good approximation to the dynamic one; i.e., that we may then set

$$\begin{aligned} u_i(Q, t) &= f(t)u_i^{(0)}(Q) \\ \sigma_{ij}(Q, t) &= f(t)\sigma_{ij}^{(0)}(Q) \end{aligned} \tag{3}$$

where Q is a generic point in the body. The condition that the body be initially undeformed will be satisfied if $f(0) = 0$; that requiring that it be initially at rest will be violated unless $\dot{f}(0) = 0$. If equations (3) hold in good approximation, then of course Saint Venant's principle holds in the dynamic case. We may therefore restate our problem as that of the determination of the error committed, in any one problem, by use of equations (3) in place of the actual dynamic solution. In other words, for the type of problems considered here, the question of the validity of Saint Venant's principle in dynamical problems is part of the larger question of how slowly loads must be applied before a quasi-static solution of the type (3) can be considered satisfactory.

We can answer this question in a general way by noting that a natural time-scale for any one problem is provided by the natural periods of vibration of the body; thus, for example, if the variation in $f(t)$ occurs in a time which is long compared with the longest natural period of the structure, then equations (3) will hold in good approximation. For a more detailed quantitative answer, we must consider each structure and each loading history on its own merits, as was done for a simple structural model in [2]; this model will now be discussed briefly.

Old Model

For convenience, the model of reference [2] is reproduced in Fig. 1; the equations governing the axial displacements under self-equilibrating axial loads are

$$a_1^2 \frac{\partial^2 u}{\partial x^2} - \frac{\partial^2 u}{\partial t^2} - \frac{3k_s}{\rho b h} u = 0 \tag{4}$$

$$v = -2u$$

where

$$a_1 = (E/\rho)^{1/2} \tag{4a}$$

The modulus k_s of the springs, which resist relative axial motions of the bars, was taken to be

$$k_s = Gb/h \tag{4b}$$

The natural periods of vibration t_n of a free-free rod governed by equations (4) are given by

$$\frac{a_1 t_n}{H} = \frac{2\pi}{\left[\left(\frac{3n\pi h}{L}\right)^2 + \frac{27G}{E}\right]^{1/2}} \tag{5}$$

or, for the semi-infinite rod considered in [2], by

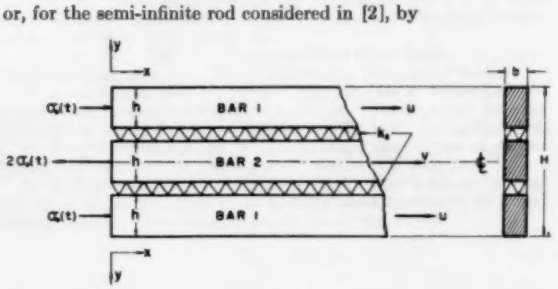

Fig. 1

---

[1] This work is part of a project sponsored by the Office of Naval Research.

[2] Numbers in brackets designate References at end of paper.

Contributed by the Applied Mechanics Division and presented at the Annual Meeting, Atlantic City, N. J., November 29–December 4, 1959, of The American Society of Mechanical Engineers.

Discussion of this paper should be addressed to the Secretary, ASME, 29 West 39th Street, New York, N. Y., and will be accepted until April 10, 1960, for publication at a later date. Discussion received after the closing date will be returned.

Note: Statements and opinions advanced in papers are to be understood as individual expressions of their authors and not those of the Society. Manuscript received by ASME Applied Mechanics Division, February 11, 1959. Paper No. 59—A-61.

$$\frac{a_1 t_0}{H} = 2\pi \left(\frac{E}{27G}\right)^{1/2} \approx 1.95 \tag{5a}$$

This, a symmetric thickness-shear mode of vibration, is the only one exhibited by this model. For the example considered in [2], for which the applied load is given by

$$\sigma(t) = \begin{cases} \sigma_0(t/t_0) & 0 \le t \le t_0 \\ \sigma_0 & t \ge t_0 \end{cases} \tag{6}$$

where t_0 and σ_0 are constants, it follows that the quasi-static solution, and therefore Saint Venant's principle, will hold if

$$\frac{a_1 t_0}{H} \gg 2\pi \left(\frac{E}{27G}\right)^{1/2} \tag{7}$$

This result is certainly in agreement with those of Fig. 4 of reference [2], but for more specific conclusions a detailed analysis such as that carried out in that reference is necessary.

We now turn to a different structural model than that discussed previously, one whose behavior more closely resembles that of a solid bar. In the case of the model of Fig. 1, it is clear from the form of equation (4) that all disturbance discontinuities travel, unchanged in magnitude, with a velocity a_1, while in a rod different types of discontinuities are propagated with different velocities; furthermore, it has already been noted that only one thickness-shear mode of vibration arises in this model. In order to obtain a structure with the desired properties, we can (aside of course from considering the elasticity equations describing the actual rod) either study an approximate theory of rod behavior [3], or construct a suitable physical model. The latter course was selected in this work, though for further improvements the contrary choice would no doubt be more profitable.

New Model

The structural model to be studied is shown in Fig. 2; it consists of two Timoshenko beams connected by distributed springs of modulus k_N which resist relative transverse displacements of the beams. Only symmetrical disturbances will be admitted; the governing equations are then, for each beam,

$$EI\frac{\partial^2 \psi}{\partial x^2} + k'AG\left(\frac{\partial y}{\partial x} - \psi\right) - \rho I\frac{\partial^2 \psi}{\partial t^2} = 0$$
$$k'AG\left(\frac{\partial^2 y}{\partial x^2} - \frac{\partial \psi}{\partial x}\right) - k_N y - \rho A\frac{\partial^2 y}{\partial t^2} = 0 \tag{8}$$

The usual notation (cf. reference [4] or [6]) is employed in these equations. With the dimensionless variables

$$y_1 = y/r;\quad x_1 = x/r;\quad t_1 = a_1 t/r;\quad \gamma = E/k'G;\quad K = k_N r^2/AE \tag{9}$$

where $r = (I/A)^{1/2} = h/\sqrt{12}$ is the radius of gyration of each bar of the model, equations (8) assume the form

$$\psi'' + \frac{1}{\gamma}(y_1' - \psi) - \ddot{\psi} = 0$$
$$\frac{1}{\gamma}(y_1'' - \psi') - Ky_1 - \ddot{y}_1 = 0 \tag{10}$$

where primes and dots represent derivatives with respect to x_1 and t_1, respectively. Elimination of ψ from equations (10) gives a single equation for y_1 as

$$y_1'''' + \ddot{y}_1 - (1+\gamma)y_1''\ddot{} + \gamma y_1\ddot{}\ddot{} + K(y_1 - y_1''\gamma + y_1\ddot{}\gamma) = 0 \tag{10a}$$

The natural periods of the first thickness-shear and thickness-stretch modes of vibrations of a structure governed by equations (10) are, respectively, given by

$$\frac{a_1 t_0}{H} = \frac{\pi\gamma}{h}\sqrt{\gamma} \approx 1.62 \quad \text{thickness-shear}$$
$$\frac{a_1 t_0}{H} = \pi\frac{r}{h\sqrt{K}} \approx 2.08 \quad \text{thickness-stretch} \tag{11}$$

where the numerical values correspond to:

$$\gamma = 3.2 \quad \text{and} \quad K = 0.19 \tag{11a}$$

These were chosen so that the two natural periods just given agree with the corresponding correct values for these periods on the basis of the theory of plane stress; the exact values in question are

$$\frac{a_1 t_0}{H} = (E/G)^{1/2} = 1.61 \quad \text{thickness-shear}$$
$$\frac{a_1 t_0}{H} = \frac{2}{(1-\nu^2)^{1/2}} = 2.10 \quad \text{thickness-stretch} \tag{11b}$$

with $\nu = 0.3$.

Solutions will now be obtained for the cases of a prescribed moment applied at $x = 0$, and of a prescribed velocity applied there. The time variation of these applied quantities will be taken to be of the ramp-type described by equation (6); thus for $t_0 = 0$ the loads are suddenly applied and for $t_0 \gg t_n$, where t_n is given by equations (11), the solution approaches the static one. The static and dynamic solutions are discussed in that order; in this presentation only the principal results are given, and most of the details of derivation are omitted.

Static Solution

The static solution for the structure of Fig. 2 under end-moments M_0 gives the following expression for the bending moment M and shear force Q at any point x:

$$\frac{M}{M_0} = e^{-x_1\left(\frac{K\gamma}{4}+\frac{\sqrt{K}}{2}\right)^{1/2}}\left\{\cos\left[x_1\left(-\frac{K\gamma}{4}+\frac{\sqrt{K}}{2}\right)^{1/2}\right] + \frac{1}{\left(\frac{4}{K\gamma^2}-1\right)^{1/2}}\sin\left[x_1\left(-\frac{K\gamma}{4}+\frac{\sqrt{K}}{2}\right)^{1/2}\right]\right\} \tag{12}$$

$$\frac{Q_r}{M_0} = -e^{-x_1\left(\frac{K\gamma}{4}+\frac{\sqrt{K}}{2}\right)^{1/2}}\left\{\frac{\cos\left[x_1\left(-\frac{K\gamma}{4}+\frac{\sqrt{K}}{2}\right)^{1/2}\right]}{\left(\frac{2}{\sqrt{K}}+\gamma\right)^{1/2}} + \frac{\sin\left[x_1\left(-\frac{K\gamma}{4}+\frac{\sqrt{K}}{2}\right)^{1/2}\right]}{\left(\frac{2}{\sqrt{K}}-\gamma\right)^{1/2}}\right\}$$

The displacement y_1 and the bending slope ψ due to an applied displacement at $x = 0$ equal to $(v_0 I)$ are

$$\frac{y_1 r}{v_0 I} = e^{-x_1\left(\frac{K\gamma}{4}+\frac{\sqrt{K}}{2}\right)^{1/2}}\left\{\cos\left[x_1\left(-\frac{K\gamma}{4}+\frac{\sqrt{K}}{2}\right)^{1/2}\right]\right.$$

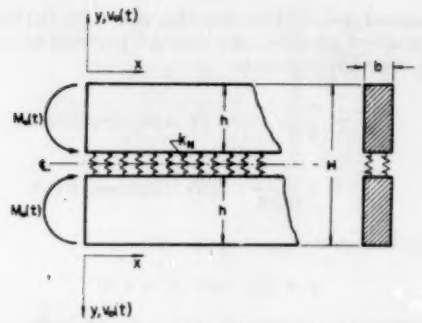

Fig. 2

$$-\frac{1}{\left(\frac{4}{K\gamma^2}-1\right)^{1/2}}\sin\left[x_1\left(-\frac{K\gamma}{4}+\frac{\sqrt{K}}{2}\right)^{1/2}\right]\Bigg\}$$

$$\frac{\psi_r}{v_0 t} = -e^{-x_1\left(\frac{K\gamma}{4}+\frac{\sqrt{K}}{2}\right)^{1/2}}\left\{\frac{\cos\left[x_1\left(-\frac{K\gamma}{4}+\frac{\sqrt{K}}{2}\right)^{1/2}\right]}{\left(\frac{2}{\sqrt{K}}+\gamma\right)^{1/2}}\right. \tag{13}$$

$$\left.+\frac{\sin\left[x_1\left(-\frac{K\gamma}{4}+\frac{\sqrt{K}}{2}\right)^{1/2}\right]}{\left(\frac{2}{\sqrt{K}}-\gamma\right)^{1/2}}\right\}$$

The exponential in the foregoing equations, with the values of equations (11*a*), is equal to $\exp(-2.107\,x/h)$. The following remarks about the static solution follow from these results:

(*a*) The effect of the disturbance decays rapidly with distance, so that Saint Venant's principle holds.

(*b*) The shear force due to an applied moment and the rotation due to an applied velocity are identical; this reciprocity will be seen to be preserved in the dynamic case.

(*c*) The stated solutions have the same form (i.e., damped oscillatory) as the solutions determined by Horvay by the variational method for a rectangular strip under self-equilibrating end loads [5].[3] Horvay finds that the axial stresses in such a strip, under parabolically distributed normal end-tractions, vary approximately as

$$g(x) = e^{-\alpha x}\left(\cos\beta x + \frac{\alpha}{\beta}\sin\beta x\right) \tag{14}$$

where $\alpha = 2.075$ and $\beta = 1.143$ (the exact value of the decay constant α is 2.1061). The value of the exponent is thus in good agreement with the approximate one previously quoted; the arguments of the trigonometric terms, however, differ somewhat more, the approximate one being about $(0.890\,x_1)$.

Dynamic Solution

The dynamic solution corresponding to a suddenly applied moment or velocity was obtained by means of Fourier sine and cosine transforms in the manner outlined in [6]. The notation

$$Y(p, t_1) = \sqrt{\frac{2}{\pi}}\int_0^\infty y_1(x_1, t_1)\sin px_1\,dx_1$$
$$\Psi(p, t_1) = \sqrt{\frac{2}{\pi}}\int_0^\infty \psi(x_1, t_1)\cos px_1\,dx_1 \tag{15}$$

will be used. The sine transform of the first of (10) and the cosine transform of the second of (10) are

$$\ddot{\Psi} + \left(p^2 + \frac{1}{\gamma}\right)\Psi - \frac{p}{\gamma}Y = \sqrt{\frac{2}{\pi}}\left[-\frac{y_1(0, t_1)}{\gamma} - \psi'(0, t_1)\right]$$
$$\ddot{Y} + \left(\frac{p^2}{\gamma} + K\right)Y - \frac{p}{\gamma}\Psi = \sqrt{\frac{2}{\pi}}\frac{p}{\gamma}\,y_1(0, t_1) \tag{16}$$

The solution of equations (16) for a structure initially undeformed and at rest must satisfy the conditions

$$Y(p, 0) = \dot{Y}(p, 0) = \Psi(p, 0) = \dot{\Psi}(p, 0) = 0 \tag{16a}$$

For a moment M_0 suddenly applied, i.e., with

$$y_1(0, t_1) = 0;\ \psi'(0, t_1) = \frac{M_0 r}{EI} \tag{17a}$$

the solution is

$$Y(p, t_1) = -\sqrt{\frac{2}{\pi}}\frac{M_0 r}{EI}\left(\frac{p}{p^4 + p^2K\gamma + K}\right)\left\{1 + \frac{\lambda_2^2\cos\lambda_1 t_1 - \lambda_1^2\cos\lambda_2 t_1}{\lambda_1^2 - \lambda_2^2}\right\}$$

$$\Psi(p, t_1) = -\sqrt{\frac{2}{\pi}}\frac{M_0 r}{EI}\left(\frac{p}{p^4 + p^2K\gamma + K}\right)\left\{p + \frac{K\gamma}{p} + \frac{\lambda_1^2(p^2 + K\gamma - \lambda_1^2\gamma)\cos\lambda_1 t - \lambda_1^2(p^2 + K\gamma - \lambda_2^2\gamma)\cos\lambda_2 t}{p(\lambda_1^2 - \lambda_2^2)}\right\} \tag{17b}$$

For a velocity v_0 suddenly applied, i.e., with

$$y_1(0, t_1) = v_0 t/r = \frac{v_0 t_1}{a_1};\ \psi'(0, t_1) = 0 \tag{18a}$$

the solution is

$$\frac{Y(p, t_1)}{(v_0/a_1)} = \frac{\sqrt{2/\pi}\,p}{p^4 + p^2K\gamma + K}\left\{p^2 t_1 + \frac{\lambda_2^2(\lambda_1^2 - p^2)\dfrac{\sin\lambda_1 t_1}{\lambda_1} - \lambda_1^2(\lambda_2^2 - p^2)\dfrac{\sin\lambda_2 t_1}{\lambda_2}}{\lambda_2^2 - \lambda_1^2}\right\}$$

$$\frac{\Psi(p, t_1)}{(v_0/a_1)} = \frac{\sqrt{2/\pi}}{p^4 + p^2K\gamma + K}\left\{-Kt_1 + \frac{(\lambda_2^2/\lambda_1)(K - \lambda_1^2)\sin\lambda_1 t_1 - (\lambda_1^2/\lambda_2)(K - \lambda_2^2)\sin\lambda_2 t_1}{\lambda_2^2 - \lambda_1^2}\right\} \tag{18b}$$

In all these formulas the notation

$$\lambda_{1,2}^2 = \frac{p^2(1 + \gamma) + K\gamma + 1}{2\gamma} \mp \{[p^2(\gamma - 1) - K\gamma + 1]^2 + 4p^2\}^{1/2} \tag{19}$$

is used. We note the following relations:

$$\frac{M(x_1, t_1)r}{EI} = \psi'(x_1, t_1) = -\sqrt{\frac{2}{\pi}}\int_0^\infty p\Psi\sin px_1 dp$$
$$\frac{Q(x_1, t_1)}{k'AG} = \psi - y_1' = \sqrt{\frac{2}{\pi}}\int_0^\infty (\Psi - pY)\cos px_1 dp \tag{20}$$

[3] The author is indebted to Dr. G. Horvay for pointing out these similarities between the above numerical values.

and the following identities:

$$U_1(x,t) = \frac{2}{\pi}\int_0^\infty \frac{1-\cos pt}{p}\sin px\,dp = \begin{Bmatrix} 1 \text{ for } t > x \\ 1/2 \text{ for } t = x \\ 0 \text{ for } t < x \end{Bmatrix} \tag{21a}$$

$$U_2(x,t) = \frac{2}{\pi}\int_0^\infty \frac{\cos(pt/\sqrt{\gamma}) - \cos pt}{p^2}\cos px\,dp$$

$$= \begin{Bmatrix} \left(\frac{1}{\sqrt{\gamma}} - 1\right) t \text{ for } x \le \frac{t}{\sqrt{\gamma}} \\ x - t \text{ for } \frac{t}{\sqrt{\gamma}} \le x \le t \\ 0 \text{ for } x \ge t \end{Bmatrix} \tag{21b}$$

With the aid of these we can easily get the desired results by means of the technique of [6]. The bending moment and shear force due to a suddenly applied moment are

$$\frac{M}{M_0} = U_1(x_1,t_1) + \frac{2}{\pi}\int_0^\infty \left\{\frac{\cos pt}{p} - \frac{1}{p^4 + p^2K\gamma + K}\left[\frac{K}{p} + \frac{p\lambda_2^2(p^2 + K\gamma - \lambda_1^2\gamma)\cos\lambda_1 t_1 - p\lambda_1^2(p^2 + K\gamma - \lambda_2^2\gamma)\cos\lambda_2 t}{\lambda_2^2 - \lambda_1^2}\right]\right\}\sin px_1 dp \tag{22a}$$

$$\frac{Qr}{M_0} = \frac{U_2(x_1,t_1)}{1-\gamma} + \frac{2}{\pi}\int_0^\infty \left\{\frac{\cos pt_1 - \cos pt_1/\sqrt{\gamma}}{p^2(1-\gamma)} + \frac{1}{p^4 + p^2K\gamma + K}\left[-K + \frac{\lambda_2^2(\lambda_1^2 - K)\cos\lambda_1 t_1 - \lambda_1^2(\lambda_2^2 - K)\cos\lambda_2 t_1}{\lambda_1^2 - \lambda_2^2}\right]\right\}\cos px_1 dp \tag{22b}$$

The velocity and the rate of change of rotation due to a suddenly applied velocity are

$$\frac{\dot{y}_1}{v_0/a_1} = U_1\left(\frac{t_1}{\sqrt{\gamma}}, x_1\right) + \frac{2}{\pi}\int_0^\infty \left\{\frac{\cos pt/\sqrt{\gamma}}{p} + \frac{p}{p^4 + p^2K\gamma + K}\left[-\left(\frac{p^2K\gamma + K}{p^2}\right) + \frac{\lambda_2^2(\lambda_1^2 - p^2)\cos\lambda_1 t_1 - \lambda_1^2(\lambda_2^2 - p^2)\cos\lambda_2 t_1}{\lambda_2^2 - \lambda_1^2}\right]\right\}\sin px_1 dp \tag{23a}$$

$$\frac{\dot{\psi}}{v_0/a_1} = \left(\frac{Qr}{M_0}\right) \text{ of equation (22b)} \tag{23b}$$

The results corresponding to an applied moment or velocity with ramp-type time variation are obtained from the ones just given by means of Duhamel's theorem.

Plots (not presented here) were made from equations (22) and (23), showing the variations of the various quantities on the left-hand side with time at various points along the structure. From these plots, the maximum value of the disturbance experienced at any one point was noted [2]; curves showing the variation of these maxima with distance from the loaded end were plotted and are shown in Figs. 3, 4, and 5. The entire procedure was repeated for different values of the time t_0 characterizing the ramp time-variation, i.e., $(a_1t_0/H) = 0.25, 0.50, \infty$; curves showing the maxima observed at each point in these cases are also shown in Fig. 3, 4, and 5. Some comments on these results follow.

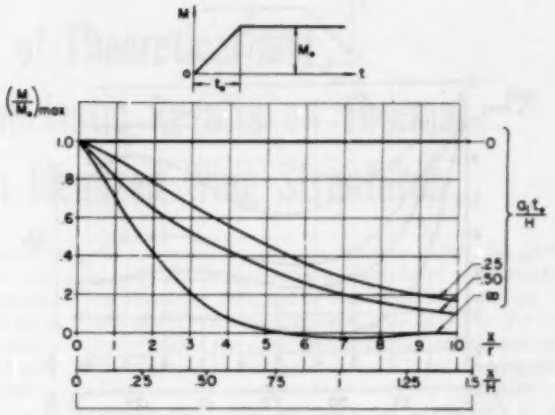

Fig. 3

Discussion

(*a*) In the structure of Fig. 2, discontinuities in bending moment and rotation are propagated unchanged with a velocity a_1, and discontinuities in velocity and shear force are propagated unchanged with a velocity

$$a_2 = \left(\frac{Gk'}{\rho}\right)^{1/2} \tag{24}$$

The reciprocal relation noted earlier in the discussion of the static solution holds in the dynamic case. These results are typical of Timoshenko beams [4, 7] and will not be discussed further here.

(*b*) In all cases the static solution is approached as $t_0 \to \infty$ and Saint Venant's principle holds in better and better approximation as t_0 becomes larger.

(*c*) The curves of Fig. 3 are almost the same as those of Fig. 4 of [2], allowance being made for the different scale employed in the two figures. This is reasonable since in both cases the diffusion of normal end-loads is studied.

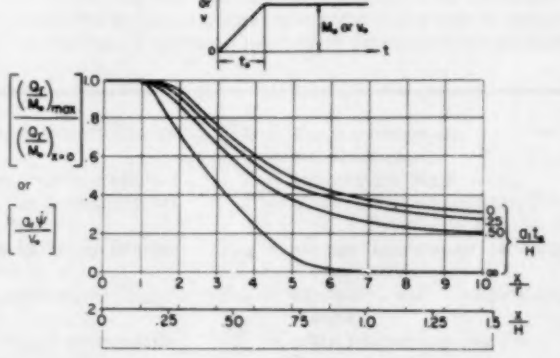

Fig. 4

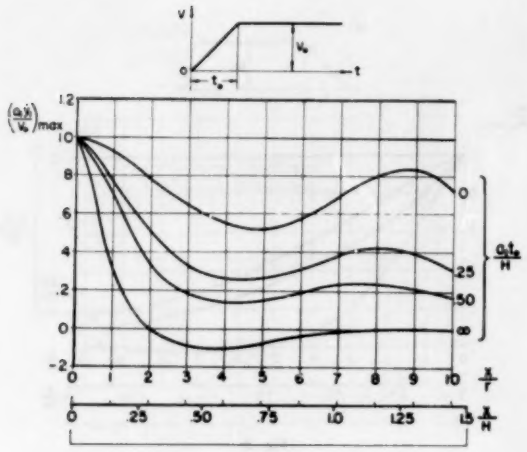

Fig. 5

(d) A markedly different type of behavior is exhibited by the curves of Fig. 3, 4, and 5. It is convenient to classify the various ordinates of these figures according to the velocity with which discontinuities in the quantities plotted travel along the beam. Thus we may denote as of type (ij) results pertaining to the variation of a quantity, in which jumps travel with velocity a_i, due to the application of a quantity, in which jumps travel with velocity a_j. Fig. 3 is then of type (11), Fig. 4 of type (12) = (21), and Fig. 5 of type (22). In type (11), for suddenly applied loads, the maximum experienced is the same at all points; as more gradual loads are considered, a comparatively rapid reduction in the maximum experienced is observed. In type (12) = (21) the effect of suddenly applied loads is less severe than in type (11), but the reduction for gradually applied loads is less rapid. In type (22), it is still less rapid, and in addition an oscillatory behavior is noted.

References

1 B. A. Boley, "Some Observations on Saint-Venant's Principle," Proc. Third U. S. National Congress of Applied Mechanics, ASME, 1958, pp. 259–264.

2 B. A. Boley, "The Application of Saint-Venant's Principle in Dynamical Problems," JOURNAL OF APPLIED MECHANICS, vol. 22, TRANS. ASME, vol. 77, 1955, pp. 204–206.

3 R. D. Mindlin and G. Herrmann, "A One-Dimensional Theory of Compressional Waves in an Elastic Rod," Proc. First U. S. National Congress of Applied Mechanics, ASME, 1952, pp. 187–191; Proc. of the Second U. S. National Congress of Applied Mechanics, ASME, 1955, p. 233.

4 B. A. Boley and C. C. Chao, "Some Solutions of the Timoshenko Beam Equations," JOURNAL OF APPLIED MECHANICS, vol. 22, TRANS. ASME, vol. 77, 1955, pp. 579–586.

5 G. Horvay, "The End Problem of Rectangular Strips," JOURNAL OF APPLIED MECHANICS, vol. 20, TRANS. ASME, vol. 75, 1953, pp. 87–94.

6 B. A. Boley, "On the Use of Sine Transforms in Timoshenko-Beam Impact Problems," JOURNAL OF APPLIED MECHANICS, vol. 24, TRANS. ASME, vol. 79, 1957, pp. 152–153.

7 B. A. Boley and C. C. Chao, "An Approximate Analysis of Timoshenko Beams Under Dynamic Loads," JOURNAL OF APPLIED MECHANICS, vol. 25, TRANS. ASME, vol. 80, 1958, pp. 31–36.

Correlation of Theoretical and Photothermoelastic Results on Thermal Stresses in Idealized Wing Structures[1]

HERBERT TRAMPOSCH
Engineering Scientist,
Research Division,
College of Engineering,
New York University,
New York, N. Y.
Mem. ASME

GEORGE GERARD
Associate Director,
Research Division,
College of Engineering,
New York University,
New York, N. Y.
Mem. ASME

After a rather complete exploratory program described in previous papers, the photothermoelastic method was applied to the experimental evaluation of thermal-stress theories. The new technique was correlated with several theories which analyzed the transient thermal stresses in idealized wing structures of high-speed aircraft. Various theories were investigated which represented the same idealized wing models and differed from each other only in the simplifying assumptions regarding the temperature distributions in skin and webs. The theories were evaluated by duplicating the boundary and initial conditions on plastic models and then by correlating the theories with the observed fringe orders in nondimensional form. A significant general conclusion was reached after correlating the available theories and experimental results. Owing to simplifying assumptions concerning the thermal behavior in the flanges, thermal stresses predicted by the available theories are all higher than the experimental observation. In some cases the discrepancy is as great as 30 per cent.

In previous investigations the potentialities of the photothermoelastic technique to obtain thermal stresses have been explored [1].[2] Also, the physical and optical properties of various plastics that may be useful for photothermoelastic studies have been investigated [2].

In the present investigation, it is first demonstrated by means of simple cemented models that the photothermoelastic technique yields reliable thermal-stress results. The technique is then used to obtain transient thermal stresses in built-up models which are representative of idealized wing structures subject to aerodynamic heating.

[1] Sponsored by United States Air Force through the Office of Scientific Research, Air Research and Development Command, Contract No. AF-18(600)-1471.

[2] Numbers in brackets designate References at end of paper.

Contributed by the Applied Mechanics Division and presented at the Annual Meeting, Atlantic City, N. J., November 29–December 4, 1959, of The American Society of Mechanical Engineers.

Discussion of this paper should be addressed to the Secretary, ASME, 29 West 39th Street, New York, N. Y., and will be accepted until April 10, 1960, for publication at a later date. Discussion received after the closing date will be returned.

Note: Statements and opinions advanced in papers are to be understood as individual expressions of their authors and not those of the Society. Manuscript received by ASME Applied Mechanics Division, October 9, 1958. Paper No. 59—A-36.

1 I-BEAM INVESTIGATION

Four long I-beam models were studied having the same height, flange thickness, and length but differing from each other either in the web thickness or the flange width. The investigation was concerned only with the center portion of the long beam and there only with the web in which plane-stress conditions existed. Here the thermal stresses could be analyzed by the photothermoelastic method and correlated with the stresses calculated from the measured temperature distribution of the cross section.

Experimental Equipment

Temperatures in the model were sensed by seven thermocouples which were connected by a switching unit to the vertical deflection circuit of a high-gain cathode-ray oscilloscope. In the horizontal direction, the electron beam was moved by means of a conventional voltage-divider network. The two circuits were synchronized mechanically and the result was a series of points on the oscilloscope screen which were photographed. A complete description of the temperature recording scheme is presented in [3].

The seven thermocouples were cemented along the center line of the model cross section at $^1/_4$-in. intervals. Each was constructed from 0.005-in-diam copper and constantan duplex wire by carbon-arc welding. The over-all accuracy of the temperature measure-

Nomenclature

a = length ratio, $a = t_s/w$
A = area, sq in.
b = width of flange, in.
B = Biot number, $B = ht_s/k$
c = specific heat, Btu/lb-deg F
C_1, C_2 = constants, Equation (2)
D = diffusivity, $D = k/\rho c$, sq in/hr
E = modulus of elasticity, psi
f = area ratio, total flange area to web area
h = heat-transfer coefficient, Btu/hr-sq ft-deg F
h_{avg} = average heat-transfer coefficient over the test period, Btu/hr-sq ft-deg F
k = thermal conductivity, Btu/hr-sq ft-deg F/in.
K = constant, Equation (10)
L = beam length, in.
t = dimension normal to x-co-ordinate, in.
t_s = flange thickness, in.
t_w = web thickness, in.
T = temperature, deg F
$\bar{T}$ = dimensionless temperature, $\bar{T} = (T - T_i)/(T_{aw} - T_i)$
T_{avg} = average temperature of beam cross section
T_{aw} = adiabatic wall temperature, deg F
T_i = initial temperature, deg F

(*Continued on next page*)

Table 1 Model dimensions, in.

Model	Flange width	Flange thickness	Web Height	Web Thickness	Beam length	Flange area / Web area
1	1 1/4	1/4	1 1/2	1/4	4 1/2	2.5
2	1 1/4	1/4	1 1/2	3/16	4 1/2	3.3
3	1 1/4	1/4	1 1/2	1/8	4 1/2	5
4	2 1/2	1/4	1 1/2	1/8	4 1/2	10

ments was estimatedto be within ±3 deg F of the true value.

The fringe pattern of the model was photographed in the same manner as described in [1]. The model was placed in the field of a circular polariscope with a white-light source and a 5 × 7-in. view camera. The second stage of the polariscope, consisting of the second quarter-wave plate, analyzer, and narrow-band interference filter at 5461 Ångstrom units, was mounted as a unit on the shutter of the camera.

I-Beam Models. Four models were machined from flat 1/4-in-thick plates of epoxy resin Hysol 6000-OP to the dimensions given in Table 1. This material was found to be highly suitable for use in photothermoelastic investigations as discussed in [2]. The plates were cemented to form the I-beams using Hysol 2030 mixed with Hardner "C" in the proportion of 4:1 and cured at 140 F for 1 hr. Thermocouples were installed using the same cement and curing cycle.

Thermal Loading. The thermal loading was produced by placing the top and bottom surfaces of the model in contact with two flat slabs of dry ice which were slightly larger than the flange area and approximately 1 in. thick. One slab was placed on a support upon which the model was lowered at time zero, and a second slab of dry ice was placed simultaneously on top of the model. Fig. 1 shows the arrangement just before the dry ice was placed in contact with the surfaces.

The measured temperature distribution over the cross section indicated the web and flange temperatures as well as the temperature gradient normal to the flange surfaces contacting the dry ice. This gradient, together with the known dry-ice temperature and the thermal conductivity of the material, were sufficient to calculate the heat-transfer coefficient used in nondimensionalizing the experimental results. The following formula of one-dimensional heat flow was applied in which T is the temperature at the surface:

$$h = \frac{-k(dT/dx)}{T_{sw} - T} \tag{1}$$

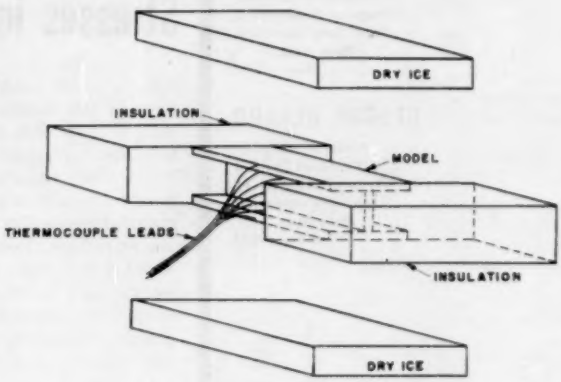

Fig. 1 Thermal-loading scheme

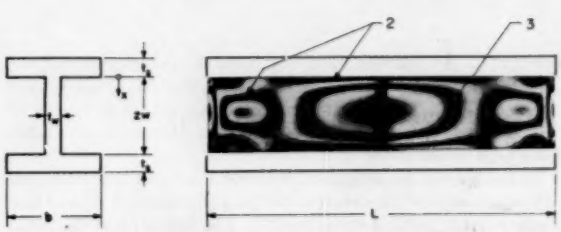

Fig. 2 Fringe pattern of model 2, 4 min after thermal loading was applied. Numbers indicate fringe orders. Dark specks along center line are due to thermocouples.

Evaluation of Test Data

Fringe Patterns. The fringe orders shown in Fig. 2 represented the thermal stresses in the web. It was apparent that the center section was free of end effects and equivalent to a long beam. These conditions therefore allowed the comparison between the fringe orders of the center section and the computed fringe orders obtained from the analysis of a long beam with longitudinal stresses only utilizing the measured temperature data.

Thermal-Stress Analysis. The measured temperature distributions over the model cross section supplied sufficient information to calculate the thermal stresses. The analysis were based on the following assumptions:

(*a*) The beam was considered to be long.

(*b*) The resultant forces and moments over the cross section were zero.

(*c*) The cross section remained plane.

(*d*) Temperature distribution along the longitudinal axis was uniform.

With these assumptions two integral equations containing two unknowns resulted from which the thermal stresses at the center section of the model could be calculated by integrating over the cross-sectional area:

$$\int E(C_1 + C_2 x - \alpha T)\,dx = 0 \tag{2}$$

$$\int E(C_1 + C_2 x - \alpha T)x\,dx = 0 \tag{3}$$

To solve for C_1 and C_2 a numerical method was used in which the integration was replaced by a summation and dx by Δx

Nomenclature

T_f = flange temperature
T_w = web temperature
U, V = temperature functions, Equation (13)
w = one half of height of web, in.
x = distance from inner flange surface, in.
$\bar{x}_f$ = $-x/l_f$
$\bar{x}_w$ = x/w
X = temperature function depending on distance, Equation (14)
Y = temperature function depending on time, Equation (14)
α = thermal-expansion coefficient, microinch/in-deg F
β = constant, Equation (10)
θ = Fourier number, $\theta = D\tau/l_f^2$
ρ = density, pci
σ = stress, psi
$\bar{\sigma}$ = dimensionless stress, $\bar{\sigma} = \sigma/\alpha E(T_{sw} - T_i)$
τ = time, hr

$$C_1 = \alpha \frac{(\Sigma ETt\Delta x)(\Sigma Etx^2\Delta x) - (\Sigma ETtx\Delta x)(\Sigma Etx\Delta x)}{(Et\Delta x)(\Sigma Etx^2\Delta x) - (\Sigma Etx\Delta x)^2} \quad (4)$$

$$C_2 = \alpha \frac{(\Sigma ETt\Delta x)(\Sigma Etx\Delta x) - (\Sigma ETtx\Delta x)(\Sigma Et\Delta x)}{(\Sigma Etx\Delta x)^2 - (\Sigma Etx^2\Delta x)(Et\Delta x)} \quad (5)$$

With these two constants known the thermal stress was obtained from

$$\sigma = E(C_1 + C_2 x - \alpha T) \quad (6)$$

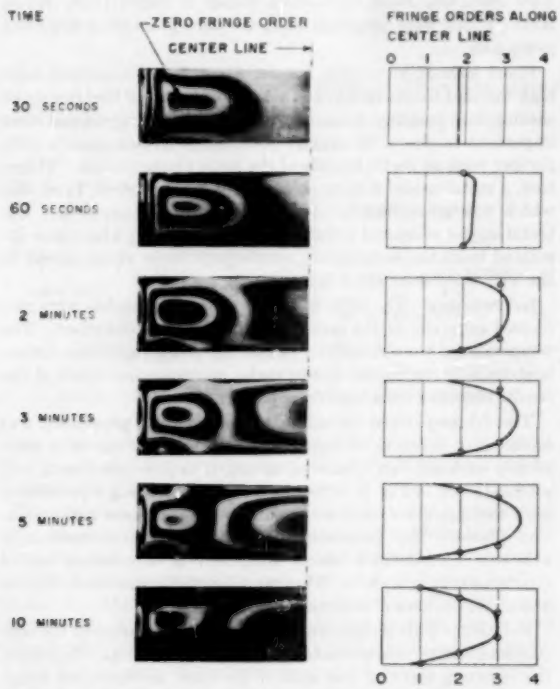

Fig. 3 Photothermoelastic study of I-beam 2. Points indicate observed fringe orders and solid line was computed from measured temperature distribution.

For each time interval, a tabular scheme was used to compute the constants C_1 and C_2. The tabulation was identical for the first three models because they all were narrow flanged and had essentially uniform temperature distribution along the flange width. Model 4, having twice the flange width of the other models, indicated temperature variations up to 25 deg F along the inner flange surfaces. This required temperature measurements at additional points along the flange and modification of the analysis. The material properties used in the calculations were already known because the test specimens of reference [2] and the I-beam models were machined from the same batch of material.

Test Results. For best demonstration of the results, the calculated thermal stresses of the I-beams were first transformed into equivalent fringe orders. Then, they were correlated with the fringe orders which were observed in the models and produced by the same temperature distribution. These results are presented in Fig. 3 for model 2. The results of the other models were equivalent and were therefore omitted. The figure shows time-sequence photographs of one half of the fringe patterns which are all symmetrical with respect to the center line. Associated with each fringe pattern are the corresponding theoretical results in relation to the observed fringe orders. The values of both methods are always well within 10 per cent.

The experimental results obtained on all models are summarized in conventional nondimensional form in Fig. 4. The maximum thermal stresses of both methods which occurred for all models at the center of the web were nondimensionalized by the factor $1/E\alpha(T_{av} - T_s)$ and are plotted versus the nondimensional time which was transformed by the factor $h/c\rho t_s$. Again, the agreement between the calculated and experimentally observed thermal stresses is satisfactory and is considered as proof of the reliability of the photothermoelastic method as applied to models of complex geometric configurations.

2 IDEALIZED WING MODELS

In the study of thermal stresses arising from aerodynamic heating, several of the published theories are based on the same idealized geometrical configurations of wing structures, having the same boundary and initial conditions, and differing from each other only through the simplifying assumptions. Therefore, all of these thermal-stress theories were candidates for experimental evaluations by the same models and the same test arrangements

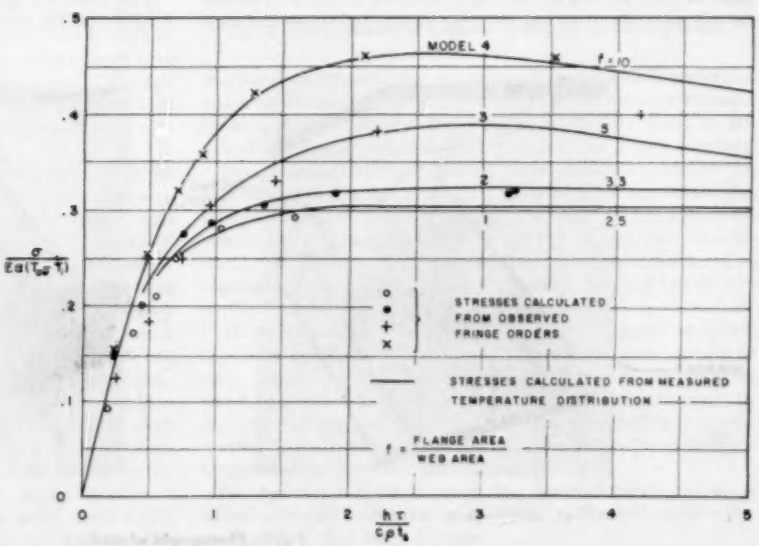

Fig. 4 Experimental results of maximum thermal stresses at center of web for all four models

Table 2 Model dimensions, in.

Model	Width of single cell	Flange thickness	Height	Web thickness	Beam length	Flange area / Web area
5	$1^1/_4$	$^1/_4$	$1^1/_2$	$^1/_8$	5	5
6	$1^1/_4$	$^1/_4$	$1^1/_2$	$^1/_4$	5	2.5

utilizing the photothermoelastic technique Individual tests not only indicated the degree of correlation between theory and experiments but also indicated the relative significance of the simplifying assumptions utilized in each theory.

Two published theories together with one developed herein were evaluated during the course of this investigation. Hoff and Torda [4] presented the simplest solution in which they replaced a wing by a long I-beam, which was thermally loaded by a sudden change in temperature at time zero. The theory, consisting primarily of a heat-transfer analysis, assumed uniform flange temperatures and no heat flow from the flange to the web. The solution is presented in the Appendix.

Pohle and Oliver [5] retained Hoff's assumptions with the exceptions that heat flow from flange to web was included and that the temperature over the flange width was allowed to vary. The series solution, obtained by Laplace transformations, converges slowly in some cases and therefore may be time-consuming to apply. Schuh [6] solved the same problem by use of numerical methods for a wide range of parameters. The same numerical procedures also were used in the present investigation to calculate the thermal stresses for evaluation of Pohle's theory.

The third theory, included here as an alternate solution to the previous two, was developed as shown in the Appendix. The suggested theory assumes variable temperatures over the flange thickness in contrast to the other theories and no heat flow from the flange to the web. Mathematically, it is not more difficult to handle than Hoff's theory and it gives more accurate results over a much greater range of parameters.

Experimental Techniques

Models. In the I-beam investigatio of Part 1, the inside flange and the web surfaces of the models were exposed to the surrounding atmosphere, which influenced the temperature distributions. Consequently, those model tests did not simulate the boundary conditions associated with the theories to be evaluated and new models were constructed in the form of long multicell beams composed of three I-beam sections each, as shown in Fig. 5. The center cell was completely isolated from outside influences and on it alone were measured the temperature and the stress distributions.

The dimensions of the model cells given in Table 2 were the same as two of the I-beams investigated in Part 1. The models were machined from $^1/_4$-in-thick plates of epoxy resin, Hysol 6000-OP, and were cemented using the same procedures described previously.

Since aircraft structures consist generally of materials with high thermal conductivity, and since the evaluated theories make assumptions pertinent to metal structures, it was considered most important to check the results obtained on plastic models with further tests on metal models of the same configuration. Therefore, a metal model was machined from stainless steel, Type 303, which was geometrically identical with plastic model 5. The metal model consisted only of a single-cell beam which was insulated from the surrounding atmosphere since visual access to the web was not required in this case.

Test Procedure. The experiments of the plastic models were performed generally in the same way as previously described. The temperatures were measured primarily to determine the surface heat-transfer coefficient and to make an occasional check of the results obtained from the fringe patterns.

The fringe-pattern recording technique used previously was modified in order to be applicable to the conditions of a completely enclosed web. Mirrors, arranged as shown in Fig. 5, and schematically in Fig. 6, reflected the light ray along a prescribed path through glass windows built into the front and rear insulation plates. The polariscope consisted of two commercially available 1/32-in-thick sheets composed of a polarizer and a quarter-wave plate each. They were located immediately before, and after, the area of interest in the web.

Relatively wide fringes were observed at the center of the web which tended to reduce the accuracy of the recordings. To reduce the resulting error to less than 4 per cent, multicolored fringe patterns produced with white light were visually observed, and particular colors as they appeared on the center line were tabulated versus time.

The metal model was tested in the same way as the plastic models in so far as the temperature measurements and recordings

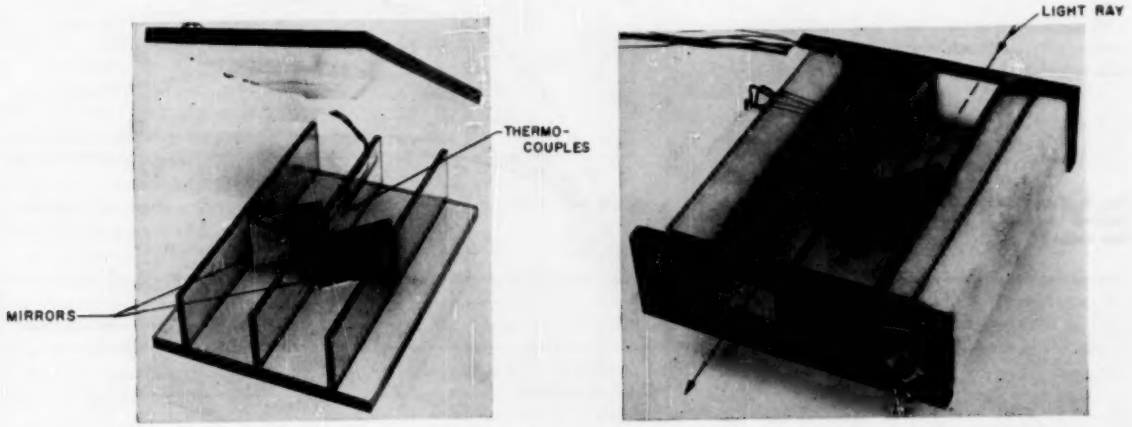

a) ASSEMBLY STAGE b) ASSEMBLED MODEL

Fig. 5 Photographs of model 5

Table 3 Summary of test conditions

	Plastic models		Stainless-steel models	
	5	6	Test 1	Test 2
T_i, deg F	75	75	80	80
T_{aw}, deg F	−110	−110	−95	−100
h_{avg}, Btu/hr-sq ft-deg F	15	15	40	200
k, Btu/hr-sq ft-deg F/in.	1.36	1.36	113	113
D, sq in/hr	0.72	0.72	25	25
α, microin./in-deg F	30.1	30.1	9.6	9.6
E, ksi Temp, deg F				
85	480	480	29000	29000
20	500	500		
−60	540	540		
B	2.70	2.70	0.09	0.45

NOTE: See reference [2] for other physical properties of epoxy resin.

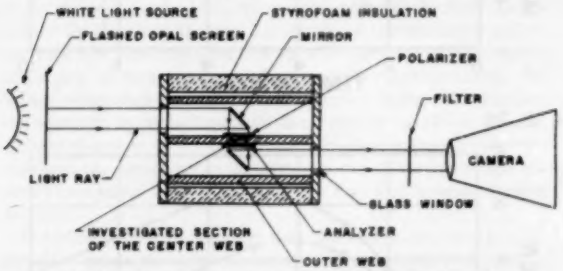

Fig. 6 Fringe-pattern recording arrangement—schematic

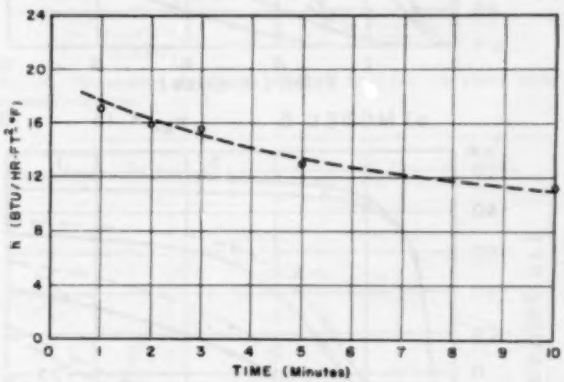

Fig. 7 Typical heat-transfer coefficient observed between dry-ice and plastic models

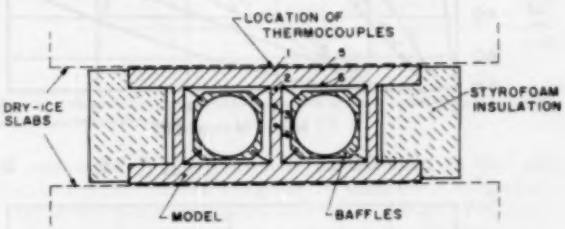

Fig. 8 Cross section of model 5 including convective baffles

were concerned, except that the thermocouples were cemented into the model with a cement of relatively high conductivity (epoxy resin mixed with aluminum powder).

The thermal loading was produced at first with dry ice and later, in order to increase the heat-transfer coefficient, with an alcohol dry-ice mixture. For the latter a fixture was constructed consisting of two containers, each having one vertical side replaced by a thin membrane which was in contact with one model surface. At time zero the alcohol dry-ice mixture was poured through the openings in the top producing the thermal shock. A fairly constant wall temperature and a constant heat-transfer coefficient were observed with this technique.

Heat-Transfer Simulation. The theories to be investigated herein are based on the assumptions of constant material properties, constant adiabatic wall temperature, constant heat-transfer coefficient, and uniform initial temperature. Fortunately, all the material properties of the models were constant or only slightly variable. As shown in reference [2], the greatest change with temperature experienced by any of the properties was in Young's modulus. However, this change affected the results by less than 5 per cent when the correct relationship was replaced by a constant average value.

The convenient application of dry-ice slabs in producing the thermal loading was equivalent to a step-function change in temperature assumed in the theories and at the same time insured constant adiabatic wall temperatures. However, this produced a variable heat-transfer coefficient which made it somewhat difficult to simulate completely the Biot number. Extensive tests indicated that the heat-transfer coefficient always decreased after the dry ice contacted the model surface. Fig. 7 shows a typical time-dependent heat-transfer coefficient which was obtained from the measured temperature distribution using Equation (1). The experiments were therefore limited to the immediate range after the dry-ice application. The range was large enough however to include the maximum thermal stress and still allow the substitution of the variable heat-transfer coefficient by its arithmetic average without introducing any significant error.

The alcohol dry-ice mixture method applied to the metal model indicated that with further development a constant heat-transfer coefficient together with a constant adiabatic wall temperature could be obtained. In addition, by choosing the correct membrane material, different heat-transfer coefficients could be obtained allowing experiments with a large range of Biot numbers.

In conducting the experiments it was necessary to consider the heat transferred inside the model by convective currents. The theories neglect convective heat transfer because they have been developed for structures made of materials of high thermal conductivity. The plastic models, on the other hand, consisted of materials of low thermal conductivity where the heat transferred by the convective currents was not negligible.

Therefore, the evaluations of the particular theories were best conducted by effectively reducing the convective heat transfer to zero. This was accomplished experimentally by the use of baffles which prevented the currents from circulating from the flange to the web. As shown in Fig. 8, the baffles were hollow and subdivided the cell cross section into a series of smaller cells effectively isolating the web from the flange.

Test Results. For convenience, the thermal conditions associated with each test are listed in Table 3. Also included are the pertinent physical property data.

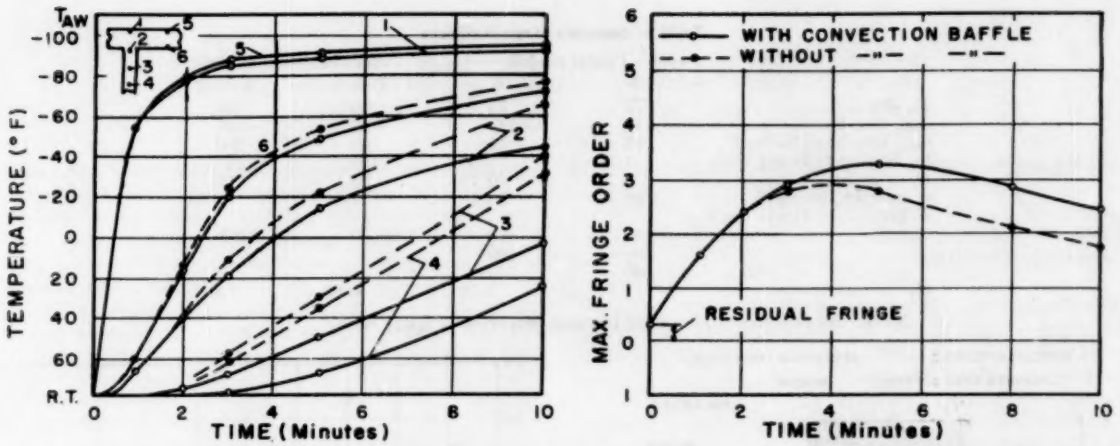

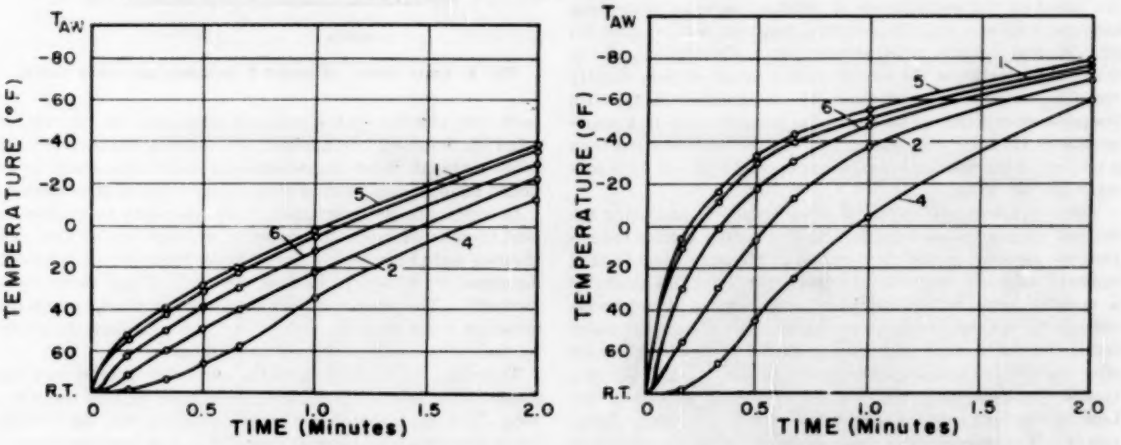

Fig. 9 Recorded temperature distributions and maximum fringe orders at center of web of models

The experiments yielded results composed of recorded fringe patterns and temperature distributions. Fig. 9 gives all the test values, especially indicating the effect of the convective baffles. The heat transferred from flange to the web by the convective currents changed the temperature distribution within the web considerably and thus reduced the maximum thermal stresses at the center of the web as indicated by the fringe orders for the two cases.

Correlation of Tests and Theory

The temperature distributions of the geometrically identical stainless-steel and plastic models are shown in Fig. 10 in nondimensional form. Three graphs classified by the Biot and Fourier numbers are presented, two for the stainless-steel and one for the plastic model. Each shows the temperature distributions as calculated by the three theories in relation to the measured values. For very low Biot numbers, the theories agreed with the experiments only to deviate more and more as its value increased. No change, other than the one expected due to a higher Biot number, was observed by transition from the metal to the plastic models. It could therefore be concluded that the plastic models correctly represent the temperature distribution which would be also observed in a metal model, provided the Biot and Fourier number coincide.

The fringe patterns, together with the known physical properties of the model material of reference [2] were used to determine the thermal stresses. The theories were then evaluated by plotting the maximum thermal stresses from the fringe patterns versus time together with the theoretical results in nondimensional form as shown in Fig. 11. The curves show the result for one particular Biot number associated with dry-ice loading. Consequently, the conclusions apply primarily to this specific region of the theories.

Hoff and Pohle's theories are shown by the same curves since no significant difference could be detected between the two. Both differed 30 per cent from the experimental values at their maximum values. The third theory which was developed in the Appendix approached the test values within 15 per cent but still indicated the necessity for a more accurate theory for investigating the thermal stresses at higher Biot numbers. It appears that a major improvement in the theory would result from a two-dimensional conduction analysis for the flange. All of the theories considered in this investigation treat the flange by a one-dimensional conduction analysis which is apparently inadequate for the Biot numbers studied.

Conclusions

The experiments demonstrated the applicability of the photothermoelastic method in evaluating transient thermal-stress theories of aircraft wing structures. They led to the following conclusions in so far as the evaluated theories were concerned.

(*a*) If the Biot number and the ratio of web thickness to flange thickness are low, Hoff's theory will give satisfactory results.

(*b*) If the Biot number becomes greater, the gradient over the flange thickness must be considered. The theory presented herein may be applied, provided the thickness ratio of web to flange is small.

(*c*) If the Biot number and the thickness ratio of web to flange are in the range of values involved in the experimental studies, then none of the one-dimensional conduction analyses of the flange will give accurate results. For these cases, a two-dimensional conduction treatment of the flange is apparently required.

The continued development of the photothermoelastic technique for application in evaluating thermal-stress theories resulted in the following additional conclusions:

(*d*) Structures of high as well as of low thermal conductivity can be represented by plastic models, provided that the Biot and Fourier numbers coincide and geometric similitude is maintained.

(*e*) Baffles inside the plastic models are effective in reducing the convective heat transfer to a level which is negligible in comparison to the conductive heat transfer.

(*f*) The experiments conducted without convection baffles indicated that the thermal stresses in structures of low thermal diffusivity will be considerably reduced by the convective heat transfer within the structure.

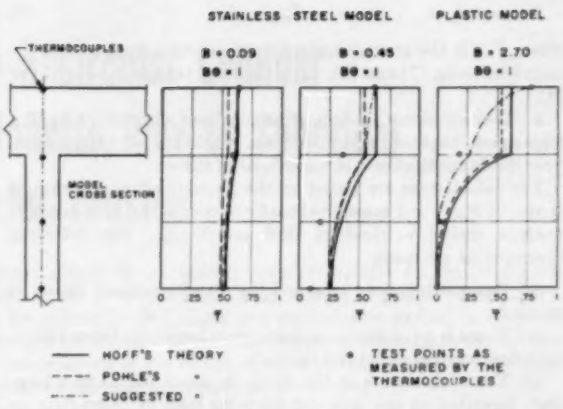

Fig. 10 Temperature distribution predicted by theory correlated with experimental data

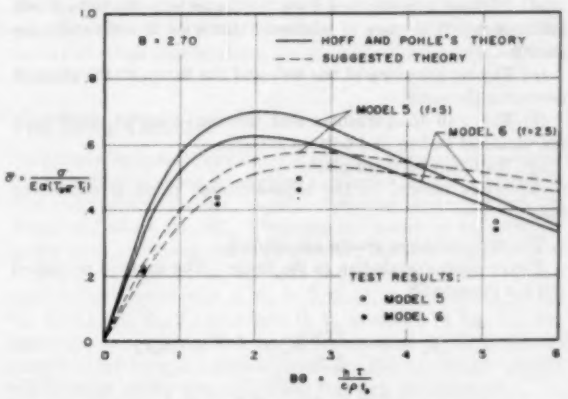

Fig. 11 Maximum thermal stress at center of web correlating theoretical and experimental results

APPENDIX

1 Solutions of heat transfer and thermal-stress analysis of an idealized wing structure of a high-speed airplane as worked out by Hoff and Torda are presented in nondimensional form:

Temperature distribution in the flange

$$\bar{T}_f = 1 - e^{-B\theta} \tag{7}$$

Temperature distribution in the web

$$\bar{T}_w = 1 - e^{-B\theta}\left[\cos\frac{\sqrt{B}}{a}\bar{x}_w + \tan\frac{\sqrt{B}}{a}\sin\frac{\sqrt{B}}{a}\bar{x}_w\right] + \frac{4}{\pi}\sum_{n=1}^{\infty}\frac{\frac{4}{\pi^2}\frac{B}{a^2}e^{-\frac{\pi^2}{4}a^2(2n-1)^2\theta}}{\left[(2n-1)^2 - \frac{4}{\pi^2}\frac{B}{a^2}\right](2n-1)}\sin\frac{\pi}{2}(2n-1)\bar{x}_w \tag{8}$$

Thermal stress $$\sigma = T_{avg} - T \tag{9}$$

where T_{avg} is the average temperature over the cross section obtained by using (7) and (8). T is the local temperature of (7) or (8).

2 Thermal-stress analysis of an idealized wing structure of a high-speed airplane which includes variation of temperature over the flange thickness is worked out as follows:

The calculations are based on the geometrical configurations shown in Fig. 1 and consist primarily of conductive heat-transfer analysis similar to those of Hoff and Torda. The following assumptions are made:

(*a*) Beam is infinitely long and the one-dimensional theory is applied.

(*b*) There is no radiation or convection inside the beam and no heat flow to other structural elements.

(*c*) The temperature of the flange is calculated as in a large slab, insulated on one side and receiving heat by convection on the other. The environmental temperature and heat-transfer coefficient and all the material properties are constant.

(*d*) No heat is conducted from the flange into the web, which for most practical cases of relatively thin webs is sufficiently accurate.

(*e*) The temperature of the web and the flange at the place of contact is the same.

(*f*) The wall temperatures and the heat-transfer coefficients are identical on top and bottom surfaces.

(*g*) No buckling takes place.

(*h*) Stress normal to the cross-sectional plane is considered only.

The dimensionless groups are applied.

Temperature distribution in the flange. The solution is worked out in reference [7]

$$T_* = 1 - \sum_{m=1}^{\infty} K_m e^{-\beta_m^2 \theta} \cos \beta_m \bar{x}_* \tag{10}$$

$$0 \leq \theta \leq \infty, \qquad 0 \leq \bar{x}_* \leq 1$$

where for convenience of expression

$$K_m = \frac{2B}{\beta_m^2 + B + B^2} \frac{1}{\cos \beta_m}$$

and β_m is obtained from the transcendental equation

$$\beta_m \tan \beta_m = B \tag{11}$$

Temperature distribution in the web. The differential equation of heat conduction through the web is in dimensionless form

$$\frac{\partial^2 T}{\partial \bar{x}_w^2} = \frac{1}{a^2} \frac{\partial T}{\partial \theta} \tag{12}$$

To simplify the solution new variables are introduced

$$T_w(\bar{x}_w, \theta) = U(\bar{x}_w, \theta) + \sum_{m=1}^{\infty} V_m(\bar{x}_w, \theta) + 1 \tag{13}$$

where

$$\begin{aligned} U(\bar{x}_w, \theta) &= X(\bar{x}_w) Y(\theta) \\ V_m(\bar{x}_w, \theta) &= X_m(\bar{x}_w) Y_m(\theta) \end{aligned} \tag{14}$$

The boundary and initial conditions then read

$$\text{i)} \quad U(0, \theta) = 0, \quad V_m(0, \theta) = -K_m e^{-\beta_m^2 \theta}$$

$$\text{ii)} \quad \frac{\partial U(1, \theta)}{\partial \bar{x}_w} = 0, \quad \frac{\partial V_m(1, \theta)}{\partial \bar{x}_w} = 0 \tag{15}$$

$$\text{iii)} \quad U(\bar{x}_w, 0) + \sum_{m=1}^{\infty} V_m(\bar{x}_w, 0) = -1$$

The complete solution is obtained by assuming

$$Y_m(\theta) = -K_m e^{-\beta_m^2 \theta} \tag{16}$$

and by inserting the new variables of Equations (13) and (14) into Equation (12) and by applying the boundary and initial conditions of Equation (15)

$$T_w(\bar{x}_w, \theta) = 1 - \sum_{m=1}^{\infty} K_m e^{-\beta_m^2 \theta} \left[\cos \frac{\beta_m}{a} \bar{x}_w + \tan \frac{\beta_m}{a} \sin \frac{\beta_m}{a} \bar{x}_w \right]$$

$$+ \frac{4}{\pi} \sum_{n=1}^{\infty} e^{-\frac{\pi^2}{4} a^2 (2n-1)^2 \theta} \left\{ \frac{\frac{4}{\pi^2} \frac{\beta_1^2}{a^2} - (1 - K_1)(2n-1)^2}{\left[(2n-1)^2 - \frac{4}{\pi^2} \frac{\beta_1^2}{a^2} \right] (2n-1)} \right. \tag{17}$$

$$\left. + \sum_{m=2}^{\infty} K_m \frac{2n-1}{(2n-1)^2 - \frac{4}{\pi^2} \frac{\beta_m^2}{a^2}} \right\} \sin (2n-1) \frac{\pi}{2} \bar{x}_w$$

This solution is composed of two rapidly converging series which for most applications can be simplified greatly. The second root of (11) is already greater than π, making it possible to neglect all the m-terms after the first, provided θ is larger than one half and an error of 1 per cent is permitted. Equations (10) and (16) have then the much simpler form which is comparable with Hoff's solution (7) and (8) as far as its applicability to numerical problems is concerned:

$$T_* = 1 - K e^{-\beta^2 \theta} \cos \beta \bar{x}_* \tag{18}$$

$$T_w = 1 - K e^{-\beta^2 \theta} \left[\cos \frac{\beta}{a} \bar{x}_w + \tan \frac{\beta}{a} \sin \frac{\beta}{a} \bar{x}_w \right]$$

$$+ \frac{4}{\pi} \sum_{n=1}^{\infty} e^{-\frac{\pi^2}{4} a^2 (2n-1)^2 \theta} \frac{\frac{4}{\pi^2} \frac{\beta^2}{a^2} - (1 - K)(2n-1)^2}{\left[(2n-1)^2 - \frac{4}{\pi^2} \frac{\beta^2}{a^2} \right] (2n-1)} \tag{19}$$

$$\sin \frac{\pi}{2} (2n-1) \bar{x}_w$$

where β is the first root of Equation (11).

The thermal stress is again expressed by Equation (9) where T_{avg} is now obtained from Equations (18) and (19) and T by Equation (18) or (19).

References

1 G. Gerard and A. C. Gilbert, "Photothermoelasticity: An Exploratory Study," JOURNAL OF APPLIED MECHANICS, vol. 24, TRANS. ASME, vol. 79, 1957, pp. 355–360.

2 H. Tramposch and G. Gerard, "Physical Properties of Plastics for Photothermoelastic Investigations," JOURNAL OF APPLIED MECHANICS, vol. 25, TRANS. ASME, vol. 80, 1958, pp. 525–528.

3 H. Tramposch, R. Papirno, and G. Gerard, "A Rapid Scanning System for Recording Thermocouple Outputs," *ASTM Bulletin* No. 238, May, 1959, pp. 41–43.

4 N. J. Hoff, "Structural Problems of Future Aircraft," Proceedings of the Third Anglo-American Aeronautical Conference, Brighton, England, September, 1951.

5 F. V. Pohle and H. Oliver, "Temperature Distribution and Thermal Stresses in a Model of a Supersonic Wing," *Journal of the Aeronautical Sciences*, vol. 21, 1954, pp. 8–16.

6 H. Schuh, "Transient Temperature Distributions and Thermal Stresses in a Skin-Shear Web Configuration at High-Speed Flight for a Wide Range of Parameters," *Journal of the Aeronautical Sciences*, vol. 22, 1955, pp. 829–836.

7 H. S. Carslaw and T. C. Jaeger, "Conduction of Heat in Solids," Oxford University Press, England, 1950.

Stresses in a Circular Cylinder Having an Infinite Row of Spherical Cavities Under Tension

AKIRA ATSUMI
Assistant Professor of Mechanical Engineering, Tohoku University, Sendai, Japan

A problem of finding the stresses in an infinite circular cylinder having an infinite row of spherical cavities of the same size under axial tension is studied theoretically. Maximum stresses in the cylinder are calculated by a perturbation method, in each case the radius of the cavity and the distance between the centers of the neighboring cavities being varied. From consideration of the results obtained, some conclusions are made regarding the effects of the surface and the cavities on the stresses.

THE stresses in elastic bodies having a spherical cavity or a flaw have been investigated by many authors under various loading conditions. Even if the loading condition is confined to uniform axial tension, the stresses have been investigated by several authors [1–4].[1] However, the problem presented by the stresses in a region containing a number of spherical cavities has only received attention by Sternberg and Sadowsky [5] and Miyamoto [6]. In dealing with these problems the elastic body is commonly assumed to be unlimited so that the presence of the surface produces no effect on the stresses in the neighborhood of the cavity. For consideration of the effect of the surface, the stresses have been given by Ling [7] for an infinite circular cylinder having a spherical cavity under axial tension.

In the present paper, to consider further the influence of the presence of many cavities on the stresses, a solution for an infinite circular cylinder having an infinite row of spherical cavities under axial tension will be given by means of a stress function. The factors of stress concentration are calculated and compared with those available.

[1] Numbers in brackets designate References at end of paper.

Presented at the West Coast Conference of the Applied Mechanics Division, Stanford, Calif., September 9–11, 1959, of THE AMERICAN SOCIETY OF MECHANICAL ENGINEERS.

Discussion of this paper should be addressed to the Secretary, ASME, 29 West 39th Street, New York, N. Y., and will be accepted until April 10, 1960, for publication at a later date. Discussion received after the closing date will be returned.

NOTE: Statements and opinions advanced in papers are to be understood as individual expressions of their authors and not those of the Society. Manuscript received at ASME Applied Mechanics Division, January 12, 1959. Paper No. 59—APMW-9.

Two Sets of Functions

Consider an infinite circular cylinder of radius a having an infinite number of spherical cavities and under an axial tension T. The radii of the cavities and the distances between them are designated as $a\lambda$ and $a\beta$. Denoting the center of an arbitrary cavity as O, and the center at an arbitrary distance of $qa\beta$ ($q = \pm 1, \pm 2, \ldots$) from O, O_q, we take rectangular, cylindrical, and spherical co-ordinates (x, y, z), (r, θ, z), (ρ, ϕ, θ), and (x_q, y_q, z_q), (r_q, θ_q, z_q), $(\rho_q, \phi_q, \theta_q)$ at origins O, O_q as shown in Fig. 1. For convenience, x, y, z, r, and ρ will be regarded as dimensionless quantities referring to a typical length a. The axis of the cylinder will be taken as the axis of z. Then they are connected by

$$x = x_q, \quad y = y_q, \quad z = z_q + q\beta \tag{1}$$

$$z_q = \rho_q \cos \phi_q, \quad r_q = \rho_q \sin \phi_q \tag{2}$$

Following the method of Ling for solving the problem of a circular cylinder under axial tension and containing a spherical cavity, we will first construct two series of biharmonic functions. These series of functions can be derived by differentiation from the stress functions for a circular cylinder without any cavity

Nomenclature

a = radius of circular cylinder
$a\lambda$ = radius of spherical cavity
$a\beta$ = center distance of cavities
q = arbitrary integer
O = center of standard cavity
O_q = center of cavity at an arbitrary distance of $qa\beta$ from O
(x, y, z), (r, θ, z), (ρ, ϕ, θ) = dimensionless rectangular, cylindrical, and spherical co-ordinates designated as origin O (corresponding co-ordinates with subscript q are also used)
$\chi_{2n}', \chi_{2n}', \chi_{2n}, \chi_{2n}$, $\chi_{2n}, \chi_{2n}', \chi$ = biharmonic functions
μ, μ_q = $\cos \phi$, $\cos \phi_q$, respectively
T = applied axial tension per unit area
ν = Poisson's ratio
I_n, K_n = modified Bessel functions of first and second kind of order n, respectively
P_n = Legendre functions of first kind of order n
${}^{2n}\alpha_{2s}, {}^{2n}\gamma_{2s}, {}^{2n}\beta_{2s}, {}^{2n}\delta_{2s}$ = expansion coefficients of χ_{2s}, χ_{2s}', respectively
${}^{n}\psi_m(k), {}^{n}f_m(k)$ = factors involved in ${}^{2n}\alpha_{2s}$, ${}^{2n}\gamma_{2s}$, ${}^{2n}\beta_{2s}$, and ${}^{2n}\delta_{2s}$ defined by Equations (19) and (20)
A_{2n}, B_{2n} = parametric coefficients involved in solution (subscript s is also used)
C_{2n}, D_{2n} = functions of A_{2n}, B_{2n} defined by Equation (26)
γ_n, δ_n, η_{n+1}, μ_{n+1} = n-dependent coefficients defined by Equation (30)
$A_{2n}^{(p)}, B_{2n}^{(p)}$ = expansion coefficients of A_{2n}, B_{2n} (subscript s is also used)
$C_{2n}^{(p)}, D_{2n}^{(p)}$ = functions of $A_{2n}^{(p)}$, $B_{2n}^{(p)}$ defined by Equation (33)
σ, τ = normal and shear stresses, respectively
K = stress-concentration factor

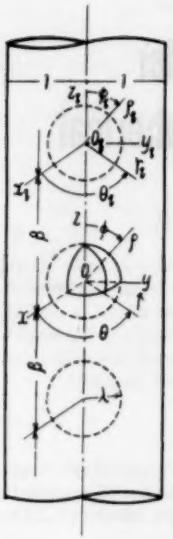

Fig. 1 Reference co-ordinates

under concentrated (a) radial, or (b) axial force acting at each of the infinite number of origins. These two fundamental stress functions are as follows [7]:

$$(a)\quad \chi_a' = \sum_{q=-\infty}^{\infty} \left\{ \frac{a^2}{2} \log \frac{1+\mu_q}{1-\mu_q} + a^2 \int_0^\infty [\psi_1(k) I_0(kr) + \psi_3(k) kr I_1(kr)] \sin kz_q dk \right\} \quad (3)$$

$$(b)\quad \chi_b' = \sum_{q=-\infty}^{\infty} \left\{ a^2 \rho_q + a^2 \int_0^\infty [\psi_3(k) I_0(kr) + \psi_4(k) kr I_1(kr)] \cos kz_q dk \right\} \quad (4)$$

where (x, y, z), (r, θ, z), and (ρ, ϕ, θ) will be used in place of (x_0, y_0, z_0), (r_0, θ_0, z_0), and $(\rho_0, \phi_0, \theta_0)$, and

$$\mu_q = \cos \phi_q \quad (5)$$

$$\left.\begin{aligned} \psi_1(k) &= -\frac{2}{\pi} \frac{kI_0(k)K_0(k) + [k^2 + 2(1-\nu)]I_1(k)K_1(k)/k}{k^2 I_0^2(k) - [k^2 + 2(1-\nu)]I_1^2(k)} - 2(1-\nu)\psi_3(k) \\ \psi_2(k) &= \frac{2}{\pi} \frac{I_0(k)K_1(k) + I_1(k)K_0(k)}{k^2 I_0^2(k) - [k^2 + 2(1-\nu)]I_1^2(k)} \\ \psi_3(k) &= [k^2 - 2(1-\nu)(1-2\nu)]\psi_2(k)/k \\ \psi_4(k) &= [\psi_1(k) + 4(1-\nu)\psi_2(k)]/k \end{aligned}\right\} \quad (6)$$

where ν is Poisson's ratio, and I_n are modified Bessel functions of the first kind of order n.

With these values of ψ_n, it appears that each of the integrals in (3) and (4) becomes divergent at the lower limit. However, each divergence can be removed by modifying the corresponding integral as follows:

$$(a)\quad \chi_a = \sum_{q=-\infty}^{\infty} \frac{a^2}{2} \log \frac{1+\mu_q}{1-\mu_q} + a^2 \int_0^\infty \{ [\psi_1(k) I_0(kr) + \psi_3(k) krI_1(kr)] \sin kz(1 + 2\sum_{q=1}^{\infty} \cos kq\beta) + f_1(k)(1 + 2\sum_{q=1}^{\infty} \cos kq\beta) z \} dk \quad (7)$$

$$(b)\quad \chi_b = \sum_{q=-\infty}^{\infty} a^2 \rho_q + a^2 \int_0^\infty \{ [\psi_3(k) I_0(kr) + \psi_4(k) krI_1(kr)] \cos kz(1 + 2\sum_{q=1}^{\infty} \cos kq\beta) + [f_2(k) r^2 + f_3(k)(1 - \tfrac{1}{2}k^2 z^2)](1 + 2\sum_{q=1}^{\infty} \cos kq\beta) \} dk \quad (8)$$

where

$$\left.\begin{aligned} f_1(k) &= \frac{.4}{\pi(1+\nu)} \left[(2-\nu)K_0(k) + \frac{3(1-\nu)}{k} K_1(k) \right] \\ f_2(k) &= \frac{2}{\pi(1+\nu)} \left[\nu K_0(k) - \frac{1-\nu}{k} K_1(k) \right] \\ f_3(k) &= \frac{4(1-\nu)(1-2\nu)}{\pi(1+\nu)k^2} \left[K_0(k) + \frac{2}{k} K_1(k) \right] \end{aligned}\right\} \quad (9)$$

and K_n are modified Bessel functions of the second kind of order n.

We take as the series of biharmonic functions, which are odd in z, as required by symmetry, and which give no stresses on the surface as well as at infinity of the cylinder, the following:

$$\left.\begin{aligned} \chi_0 &= -\chi_a, \quad \chi_{2s} = -\frac{1}{(2s)!} \frac{\partial^{2s}}{\partial z^{2s}} \chi_a (s \geq 1) \\ \chi_{2s}' &= -\frac{1}{(2s+1)!} \frac{\partial^{2s+1}}{\partial z^{2s+1}} \chi_b (s \geq 0) \end{aligned}\right\} \quad (10)$$

Then each function, constructed with two parts such that one is in spherical harmonics and the other is in cylindrical harmonics, is required to be expressed in terms of spherical co-ordinates at origin O. The first part of the functions χ_{2s} and χ_{2s}' can be expressed with the aid of the equations [8]. In case of $q > 0$, $q\beta > (\rho, \rho_q) > 0$,

$$\left.\begin{aligned} \frac{P_s(\mu_q)}{\rho_q^{s+1}} &= \sum_{n=0}^{\infty} (-1)^s \frac{(n+s)!}{n!s!(q\beta)^{n+s+1}} \rho^n P_n(\mu) \\ \frac{P_s(\mu)}{\rho^{s+1}} &= \sum_{n=0}^{\infty} (-1)^n \frac{(n+s)!}{n!s!(q\beta)^{n+s+1}} \rho_q^n P_n(\mu_q) \end{aligned}\right\} \quad (11)$$

and, besides

$$\sum_{q=-\infty}^{\infty} \left(\mu \frac{\partial}{\partial \rho} + \frac{1-\mu^2}{\rho} \frac{\partial}{\partial \mu} \right) \left(\frac{1}{2} \log \frac{1+\mu_q}{1-\mu_q} \right) = \frac{1}{\rho} + \sum_{q=1}^{\infty} \{ [\rho^2 - 2\rho\mu q\beta + (q\beta)^2]^{-1/2} + [\rho^2 + 2\rho\mu q\beta + (q\beta)^2]^{-1/2} \} = \frac{1}{\rho} + 2\sum_{n=0}^{\infty} \sum_{q=1}^{\infty} \frac{\rho^{2n} P_{2n}(\mu)}{(q\beta)^{2n+1}} \quad (12)$$

where P_n are Legendre functions of the first kind of order n. The final results are given as follows:

$$
\begin{aligned}
\sum_{q=-\infty}^{\infty} \frac{-a^2}{2} \log \frac{1+\mu_q}{1-\mu_q} &= -\frac{a^2}{2} \log \frac{1+\mu}{1-\mu} \\
&\quad - \sum_{q=1}^{\infty} \sum_{n=0}^{\infty} \frac{2a^2 \rho^{2n+1} P_{2n+1}(\mu)}{(2n+1)(q\beta)^{2n+1}} \\
\sum_{q=-\infty}^{\infty} \frac{a^{2s} P_{2s-1}(\mu_q)}{2s \rho_q^{2s}} &= \frac{a^{2s} P_{2s-1}(\mu)}{2s \rho^{2s}} \\
&\quad - \sum_{q=1}^{\infty} \sum_{n=0}^{\infty} \frac{2a^{2s}(2s+2n)! \rho^{2n+1} P_{2n+1}(\mu)}{(2s)!(2n+1)!(q\beta)^{2n+2s+1}} \\
\sum_{q=-\infty}^{\infty} -a^3 P_1(\mu_q) &= -a^3 P_1(\mu) \\
&\quad + \sum_{q=1}^{\infty} \sum_{n=0}^{\infty} a^3 \left[\frac{4n}{(4n+1)(q\beta)^{2n+1}} \right. \\
&\quad \left. - \frac{(4n+4)\rho^2}{(4n+5)(q\beta)^{2n+3}} \right] \rho^{2n+1} P_{2n+1}(\mu) \\
\sum_{q=-\infty}^{\infty} \frac{a^2}{4s+1} \left[\frac{P_{2s-1}(\mu_q) - P_{2s+1}(\mu_q)}{\rho_q^{2s}} \right] &= \frac{a^2}{4s+1} \frac{P_{2s-1}(\mu) - P_{2s+1}(\mu)}{\rho^{2s}} \\
&\quad + \sum_{q=1}^{\infty} \sum_{n=0}^{\infty} \frac{2a^2}{(2s+1)!} \left[\frac{(2n+2s)!}{(2n-1)!(4n+1)(q\beta)^{2n+2s+1}} \right. \\
&\quad \left. - \frac{(2n+2s+2)!\rho^2}{(2n+1)!(4n+5)(q\beta)^{2n+2s+3}} \right] \rho^{2n+1} P_{2n+1}(\mu)
\end{aligned}
\tag{13}
$$

For the second part the following relations will be used [9]:

$$
\begin{aligned}
I_0(kr) \sin kz &= \sum_{n=0}^{\infty} (-1)^n \frac{(k\rho)^{2n+1}}{(2n+1)!} P_{2n+1}(\mu) \\
krI_1(kr) \sin kz &= \sum_{n=0}^{\infty} (-1)^n \frac{(k\rho)^{2n+1}}{(2n+1)!} \\
&\quad \left[\frac{2n(2n+1)}{4n+1} + \frac{(k\rho)^2}{4n+5} \right] P_{2n+1}(\mu) \\
\frac{\partial^{2s}}{\partial z^{2s}} \log \frac{1+\mu}{1-\mu} &= -\frac{2(2s-1)!}{\rho^{2s}} P_{2s-1}(\mu) \\
\frac{\partial^{2s+1} \rho}{\partial z^{2s+1}} &= -\frac{(2s+1)!}{(4s+1)\rho^{2s}} [P_{2s-1}(\mu) - P_{2s+1}(\mu)] \\
\frac{\partial \rho}{\partial z} &= P_1(\mu)
\end{aligned}
\tag{14}
$$

Consequently we obtain the following expressions in spherical co-ordinates at origin O:

$$
\begin{aligned}
\chi_0 &= -\frac{a^2}{2} \log \frac{1+\mu}{1-\mu} \\
&\quad + a^2 \sum_{n=0}^{\infty} ({}^{2n}\alpha_0 + {}^{2n}\gamma_0 \rho^2) \rho^{2n+1} P_{2n+1}(\mu) \\
\chi_{2s} &= \frac{a^{2s} P_{2s-1}(\mu)}{2s \rho^{2s}} \\
&\quad + a^2 \sum_{n=0}^{\infty} ({}^{2n}\alpha_{2s} + {}^{2n}\gamma_{2s} \rho^2) \rho^{2n+1} P_{2n+1}(\mu)
\end{aligned}
\tag{15}
$$

$$
\begin{aligned}
\chi_0' &= -a^2 P_1(\mu) + a^2 \sum_{n=0}^{\infty} ({}^{2n}\beta_0 + {}^{2n}\delta_0 \rho^2) \rho^{2n+1} P_{2n+1}(\mu) \\
\chi_{2s}' &= \frac{a^{2s}}{(4s+1)} \frac{[P_{2s-1}(\mu) - P_{2s+1}(\mu)]}{\rho^{2s}} \\
&\quad + a^2 \sum_{n=0}^{\infty} ({}^{2n}\beta_{2s} + {}^{2n}\delta_{2s} \rho^2) \rho^{2n+1} P_{2n+1}(\mu)
\end{aligned}
\tag{13}
$$

where

$$
\begin{aligned}
{}^{2n}\alpha_0 &= \frac{(-1)^{n+1}}{(2n)!} \left[\frac{{}^{2n+1}\psi_1(k)}{(2n+1)} + \frac{2n^{2n+1}\psi_2(k)}{(4n+1)} \right] \\
&\quad - \sum_{q=1}^{\infty} \frac{2}{(2n+1)(q\beta)^{2n+1}} \\
{}^{2n}\gamma_0 &= \frac{(-1)^{n+1}}{(2n+1)!(4n+5)} {}^{2n+3}\psi_3(k) \\
{}^{2n}\alpha_{2s} &= \frac{(-1)^{n+s+1}}{(2n)!(2s)!} \left[\frac{{}^{2n+2s+1}\psi_1(k)}{(2n+1)} + \frac{2n^{2n+2s+1}\psi_2(k)}{(4n+1)} \right] \\
&\quad - \sum_{q=1}^{\infty} \frac{2(2s+2)!}{(2s)!(2n+1)!(q\beta)^{2n+2s+1}} \\
{}^{2n}\gamma_{2s} &= \frac{(-1)^{n+s+1}}{(2n+1)!(2s)!(4n+5)} {}^{2n+2s+3}\psi_3(k) \\
{}^{2n}\beta_0 &= \frac{(-1)^n}{(2n)!} \left[\frac{{}^{2n+2}\psi_3(k)}{(2n+1)} + \frac{2n^{2n+2}\psi_4(k)}{(4n+1)} \right] \\
&\quad + \sum_{q=1}^{\infty} \frac{4n}{(4n+1)(q\beta)^{2n+1}} \\
{}^{2n}\delta_0 &= \frac{(-1)^n}{(2n+1)!(4n+5)} {}^{2n+4}\psi_4(k) \\
&\quad - \sum_{q=1}^{\infty} \frac{4n+4}{(4n+5)(q\beta)^{2n+3}} \\
{}^{2n}\beta_{2s} &= \frac{(-1)^{n+s}}{(2s+1)!(2n)!} \left[\frac{{}^{2n+2s+2}\psi_3(k)}{(2n+1)} \right. \\
&\quad \left. + \frac{2n^{2n+2s+2}\psi_4(k)}{(4n+1)} \right] \\
&\quad + \sum_{q=1}^{\infty} \frac{2(2n+2s)!}{(2s+1)!(2n-1)!(4n+1)(q\beta)^{2n+2s+1}} \\
{}^{2n}\delta_{2s} &= \frac{(-1)^{n+s}}{(2s+1)!(2n+1)!(4n+5)} {}^{2n+2s+4}\psi_4(k) \\
&\quad - \sum_{q=1}^{\infty} \frac{2(2n+2s+2)!}{(2s+1)!(2n+1)!(4n+5)(q\beta)^{2n+2s+3}}
\end{aligned}
\tag{16}
$$

and in particular

$$
\begin{aligned}
{}^0\alpha_0 &= -\{{}^1\psi_1(k) + {}^0f_1(k)\} - \sum_{q=1}^{\infty} \frac{2}{q\beta} \\
{}^0\beta_0 &= \{{}^3\psi_3(k) + {}^0f_3(k)\}
\end{aligned}
\tag{17}
$$

where

$$
\begin{aligned}
{}^n\psi_m(k) &= \int_0^{\infty} \psi_m(\kappa) k^n (1 + 2 \sum_{q=1}^{\infty} \cos kq\beta) dk, \\
&\qquad (m = 1, 2, 3, 4) \\
{}^nf_m(k) &= \int_0^{\infty} f_m(k) k^n (1 + 2 \sum_{q=1}^{\infty} \cos kq\beta) dk, \ (m = 1, 3)
\end{aligned}
\tag{18}
$$

By using Dirichlet's second integral [10], ${}^n\psi_m(k)$ and ${}^nf_m(k)$ may be written

$$\left.\begin{aligned} {}^n\psi_m(k) &= \lim_{q\to\infty}\int_0^\infty \left(\frac{2}{\beta}\right)^{n+1} k^n\ \psi_m\left(\frac{2k}{\beta}\right)\frac{\sin(2q+1)k}{\sin k}\,dk \\ &= \frac{\pi}{2}\,[f(0)+2f(\pi)+2f(2\pi)+\ldots] \\ {}^nf_m(k) &= \frac{\pi}{2}\,[f'(0)+2f'(\pi)+2f'(2\pi)+\ldots] \end{aligned}\right\} \quad (19)$$

where

$$\left.\begin{aligned} f(k) &= \left(\frac{2}{\beta}\right)^{n+1} k^n\ \ \psi_m\left(\frac{2k}{\beta}\right) \\ f'(k) &= \left(\frac{2}{\beta}\right)^{n+1} k^n\ \ f_m\left(\frac{2k}{\beta}\right) \end{aligned}\right\} \quad (20)$$

The Stress Function

When a solid of revolution is in the state of symmetrical strain, all the quantities such as the displacements, strains, and stresses are derivable from a stress function χ which satisfies the biharmonic equation

$$\nabla^4\chi = 0 \quad (21)$$

In the absence of any cavity, a uniform axial tension of T per unit area would be given by

$$\chi_{00} = \frac{Ta^2}{6(1+\nu)}\,[3\nu r^2 z + (1-2\nu)z^3] \quad (22)$$

which produces throughout the solid the only stress

$$\sigma_z = T \quad (23)$$

The method of satisfying the conditions when the cavities are present is to add an infinite set of functions χ_{2s} and χ_{2s}' to χ_{00} and then satisfy the boundary conditions on the surface of one of the cavities by adjusting the parametric coefficients attached to the functions. Thus the required stress function may be constructed in the form

$$\chi = \chi_{00} + T\sum_{s=0}^{\infty}(A_{2s}\chi_{2s} + B_{2s}\chi_{2s}') \quad (24)$$

Expressing the equation in spherical co-ordinates, we readily find

$$\begin{aligned} \chi = {} & \frac{Ta^2\rho^2}{30(1+\nu)}\,[3P_1(\mu)+2(1-5\nu)P_3(\mu)] - {}^1/_2 Ta^2 A_0 \\ & \log\frac{1+\mu}{1-\mu} + Ta^2\sum_{n=1}^{\infty}\left(\frac{A_{2n}}{2n} + \frac{B_{2n}}{4n+1} - \frac{B_{2n-2}}{4n-3}\rho^2\right) \\ & \frac{P_{2n-1}(\mu)}{\rho^{2n}} + Ta^2\sum_{n=0}^{\infty}(C_{2n}+D_{2n}\rho^2)\rho^{2n+1}P_{2n+1}(\mu) \end{aligned} \quad (25)$$

where

$$\left.\begin{aligned} C_{2n} &= \sum_{s=0}^{\infty}({}^{2n}\alpha_{2s}A_{2s} + {}^{2n}\beta_{2s}B_{2s}) \\ D_{2n} &= \sum_{s=0}^{\infty}({}^{2n}\gamma_{2s}A_{2s} + {}^{2n}\delta_{2s}B_{2s}) \end{aligned}\right\} \quad (26)$$

A_{2n} and B_{2n} are parametric coefficients to be determined from the remaining boundary conditions on the surface of the cavity, that is, at $\rho = \lambda$,

$$\left.\begin{aligned} \sigma_\rho &= \frac{1}{a^3}\left[(2-\nu)\mu\frac{\partial}{\partial\rho} + \frac{\nu(1-\mu^2)}{\rho}\frac{\partial}{\partial\mu}\right]\nabla^2\chi \\ &\quad - \frac{1}{a^3}\frac{\partial^2}{\partial\rho^2}\left(\mu\frac{\partial}{\partial\rho} + \frac{1-\mu^2}{\rho}\frac{\partial}{\partial\mu}\right)\chi = 0 \\ \tau_{\rho\phi} &= \frac{(1-\mu^2)^{1/2}}{a^3}\left[-(1-\nu)\left(\frac{\partial}{\partial\rho} + \frac{\mu}{\rho}\frac{\partial}{\partial\mu}\right)\nabla^2\chi\right. \\ &\quad \left. + \frac{\partial}{\partial\rho}\left(\frac{1}{\rho}\frac{\partial}{\partial\mu}\right)\left(\mu\frac{\partial}{\partial\rho} + \frac{1-\mu^2}{\rho}\frac{\partial}{\partial\mu}\right)\chi\right] = 0 \end{aligned}\right\} \quad (27)$$

Note that in spherical co-ordinates,

$$\nabla^2 = \frac{1}{\rho^2}\frac{\partial}{\partial\rho}\left(\rho^2\frac{\partial}{\partial\rho}\right) + \frac{1}{\rho^2}\frac{\partial}{\partial\mu}\left[(1-\mu^2)\frac{\partial}{\partial\mu}\right] \quad (28)$$

The expressions for the stresses are obtained by using (25) and are replaced by setting $\rho = \lambda$. It is found that the resulting equations contain terms of Legendre functions even in μ or its derivatives only. Equating the coefficient of each term to zero, we obtain a system of linear equations. The system of equations may be replaced by the following system:

$$\left.\begin{aligned} &\frac{(1-5\nu)\lambda^2}{14-10\nu} = A_0 + \frac{15(2-4\nu)C_2\lambda^2}{14-10\nu} \\ &\quad - \frac{30(1-5\nu)(1-\nu)D_0\lambda^2}{14-10\nu} + \frac{27(2-4\nu)D_2\lambda^5}{14-10\nu} \\ &\frac{5\lambda^2}{14-10\nu} = B_0 + [45C_2 - 20(4-5\nu)D_0]\frac{\lambda^2}{14-10\nu} \\ &\quad + \frac{81D_2\lambda^5}{14-10\nu} \\ &A_{2n} + 2n\gamma_n D_{2n-2}\lambda^{4n+1} - n(4n-1)\delta_n C_{2n}\lambda^{4n+1} \\ &\quad - \left[\frac{(4n+5)(2n-2+4\nu)}{4n+3}\gamma_{n+1}\right. \\ &\quad \left. + \frac{4n+5}{4n+3}\eta_{n+1}\right]D_{2n}\lambda^{4n+3} + (n-1+2\nu) \\ &\quad (4n+5)\delta_{n+1}C_{2n+2}\lambda^{4n+3} \\ &\quad - (2n-2+4\nu)\mu_{n+1}D_{2n+2}\lambda^{4n+5} = 0, \quad (n \geqslant 1) \\ &B_{2n} - \left[\frac{(4n+5)(4n+3)}{2}\delta_{n+1}C_{2n+2}\right. \\ &\quad \left. - (4n+5)\gamma_{n+1}D_{2n}\right]\lambda^{4n+3} \\ &\quad + (4n+3)\mu_{n+1}D_{2n+3}\lambda^{4n+5} = 0, \quad (n \geqslant 1) \end{aligned}\right\} \quad (29)$$

where

$$\left.\begin{aligned} \gamma_n &= \frac{(4n-2)(3n-4n\nu+1-\nu)}{(-4n^2+4n\nu-2n-1+\nu)} \\ \delta_n &= \frac{(2n-1)(2n+1)}{(-4n^2+4n\nu-2n-1+\nu)} \\ \eta_{n+1} &= \frac{(4n+2)(2n^2-n-1-\nu)(2n^2-1+\nu)}{+\,2n(4n^2+4n-1+2\nu)(2n^2+3n-\nu)} \\ &\quad \frac{}{(2n+2)(-4n^2+4n\nu-2n-1+\nu)} \\ \mu_{n+1} &= \frac{(2n+3)(4n+9)(8n^2+18n+7)}{(4n+7)(8n^2+20n-8n\nu-10\nu+14)} \end{aligned}\right\} \quad (30)$$

These equations for the biharmonic stress function and boundary conditions remain invariant even if the equations are

expressed in terms of spherical co-ordinates associated with any other one of the cavities. Then, if the boundary conditions on one of the cavities are satisfied, the corresponding conditions on the other cavities are automatically satisfied.

A formal solution by successive approximations can be obtained easily. But, since this method is rather laborious, a perturbation method in which λ is the perturbation parameter, is introduced here.

A Perturbation Method

Assuming that A_{2n} and B_{2n} can be expanded in powers of λ when λ is small, the expansions may be obtained from (29) as follows:

$$\left.\begin{aligned} A_{2n} &= \sum_{p=0}^{\infty} A_{2n}^{(p+4n+1)}\lambda^{p+4n+1} \\ B_{2n} &= \sum_{p=0}^{\infty} B_{2n}^{(p+4n+3)}\lambda^{p+4n+3} \end{aligned}\right\} \tag{31}$$

where $A_{2n}^{(p+4n+1)}$ and $B_{2n}^{(p+4n+3)}$ are independent of λ. Equating the terms of the same order of λ in both sides after substituting (31) into (29),

$$\left.\begin{aligned} A_0^{(1)} &= \frac{1-5\nu}{14-10\nu}, \quad B_0^{(1)} = \frac{5}{14-10\nu}, \quad A_2^{(1)} = \frac{1}{7-5\nu} \\ A_0^{(p+4)} &= -\frac{15(2-4\nu)C_2^{(p+3)}}{14-10\nu} + \frac{30(1-5\nu)(1-\nu)D_0^{(p+3)}}{14-10\nu} - \frac{27(2-4\nu)D_2^{(p)}}{14-10\nu} \\ B_0^{(p+5)} &= -\frac{45C_2^{(p+3)}}{14-10\nu} + \frac{20(4-5\nu)D_0^{(p+3)}}{14-10\nu} - \frac{81D_2^{(p)}}{14-10\nu} \\ A_2^{(p+7)} &= -\frac{9C_2^{(p+3)}}{7-5\nu} + \frac{4(4-5\nu)D_0^{(p+3)}}{7-5\nu} + \frac{180\nu C_4^{(p)}}{14-6\nu} \\ &\quad - \frac{9[16(7-9\nu)\nu(7-5\nu)+5(7-\nu^2)(7-3\nu)]D_2^{(p)}}{7(14-6\nu)(7-5\nu)} + \frac{260\nu D_4^{(p-3)}}{14-6\nu} \\ A_{2n}^{(p+4n+1)} &= -2n\gamma_n D_{2n-2}^{(p)} + n(4n-1)\delta_n C_{2n}^{(p)} + \left[\frac{(4n+5)(2n-2+4\nu)}{4n+3}\gamma_{n+1} + \frac{4n+5}{4n+3}\eta_{n+1}\right]D_{2n}^{(p-2)} \\ &\quad - (4n+5)(n-1+2\nu)\delta_{n+1}C_{2n+2}^{(p-2)} + (2n-2+4\nu)\mu_{n+1}D_{2n+2}^{(p-4)}, \quad (n \geqslant 2) \\ B_{2n}^{(p+4n+3)} &= \frac{(4n+5)(4n+3)}{2}\delta_{n+1}C_{2n+2}^{(p)} - (4n+5)\gamma_{n+1}D_{2n}^{(p)} - (4n+3)\mu_{n+1}D_{2n+2}^{(p-2)}, \quad (n \geqslant 1) \end{aligned}\right\} \tag{32}$$

where

$$\left.\begin{aligned} C_{2n}^{(p)} &= \sum_{s=0}^{\infty}\left({}^{2n}\alpha_{2s}A_{2s}^{(p)} + {}^{2n}\beta_{2s}B_{2s}^{(p)}\right) \\ D_{2n}^{(p)} &= \sum_{s=0}^{\infty}\left({}^{2n}\gamma_{2s}A_{2s}^{(p)} + {}^{2n}\delta_{2s}B_{2s}^{(p)}\right) \end{aligned}\right\} \tag{33}$$

Setting in turn $p = 0, 1, 2, \ldots$ in (32), we can obtain the series of the coefficients of Equations (31) as far as required.

We can now compute the stress at any point in the cylinder. The most important one, however, is the maximum stress occurring at the surface of the cavity across the minimum section where $(\rho, \mu) = (\lambda, 0)$. This stress is given by

$$\begin{aligned} \max \sigma_\phi = T - T\sum_{n=0}^{\infty}\sum_{p=0}^{\infty}\Big\{ &(2n+1)A_{2n}^{(p+4n+1)}\lambda^{p+2n-1} \\ &+ (2n-1+2\nu)B_{2n}'^{(p+4n+3)}\lambda^{p+2n} \\ &- 4n^2\sum_{s=0}^{\infty}[{}^{2n}\alpha_{2s}A_{2s}^{(p+4s+1)}\lambda^{p+4s+2n-1} \\ &+ {}^{2n}\beta_{2s}B_{2s}^{(p+4s+3)}\lambda^{p+4s+2n+1}] - 2(2n^2+8n-4n\nu+7-5\nu) \\ &\sum_{s=0}^{\infty}[{}^{2n}\gamma_{2s}A_{2s}^{(p+4s+1)}\lambda^{p+4s+2n+1} \\ &+ {}^{2n}\delta_{2s}B_{2s}^{(p+4s+3)}\lambda^{p+4s+2n+3}]\Big\}P_{2n+1}'(0) \end{aligned} \tag{34}$$

where

$$P_{2n+1}'(0) = (-1)^n\binom{2n}{n}\frac{2n+1}{2^{2n}} \tag{35}$$

From (34) and (32) the numerical formula for $\max \sigma_\phi/T$ can be obtained for any given value of β. When $\lambda = 0$, the results are equivalent to the value $(27-15\nu)/(14-10\nu)$ which is the known result for an infinitely large tension member having a spherical cavity [4]. When $\lambda \neq 0$ it is necessary to prove convergence of the series, though this is usually difficult. However, it may be seen later in the numerical equations that this method gives results to any required degree of approximation for the case of $\lambda < \beta/4$.

Numerical Calculations and Results

The numerical calculations have been carried out for the cases $\beta = \pi/4$, $\pi/3$, and $\pi/2$ by taking $\nu = 0.3$. The numerical equations are consequently as follows:

$$\begin{aligned} \max \sigma_\phi(\beta = \pi/4) = {} & 2.04545 - 2.63522 \times 10\lambda^3 + 3.07380 \times 10^2\lambda^5 + 2.62098 \times 10^2\lambda^6 - 1.83183 \times 10^3\lambda^7 \\ & - 5.39145 \times 10^3\lambda^8 + 2.81299 \times 10^3\lambda^9 + 5.22079 \times 10^4\lambda^{10} + 6.18008 \times 10^4\lambda^{11} - 4.89116 \times 10^5\lambda^{12} \\ & - 1.04424 \times 10^6\lambda^{13} + 3.84775 \times 10^6\lambda^{14} + 1.25804 \times 10^7\lambda^{15} \ldots \end{aligned} \tag{36}$$

$$\begin{aligned} \max \sigma_\phi(\beta = \pi/3) = {} & 2.04545 - 8.67753\lambda^3 + 6.98689 \times 10\lambda^5 + 4.11870 \times 10\lambda^6 - 2.45277 \times 10^2\lambda^7 - 4.14287 \times 10^2\lambda^8 + 3.96708 \times 10^2\lambda^9 \\ & + 2.64220 \times 10^3\lambda^{10} + 1.14567 \times 10^3\lambda^{11} - 1.62560 \times 10^4\lambda^{12} - 1.82880 \times 10^4\lambda^{13} + 8.15367 \times 10^4\lambda^{14} \\ & + 1.49185 \times 10^5\lambda^{15} \ldots \end{aligned} \tag{37}$$

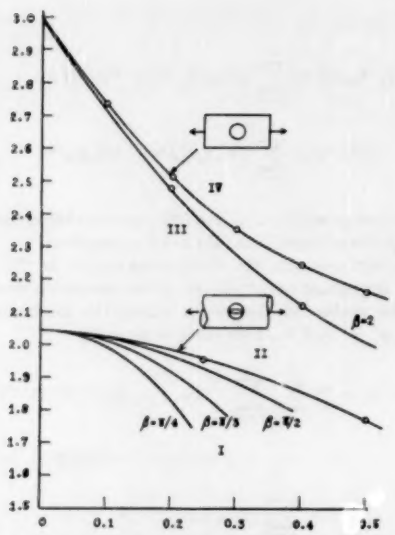

Fig. 2 Stress-concentration factor. I—results for present problem; II—results for a spherical cavity; III—results for an infinite row of circular holes; IV—results for a circular hole.

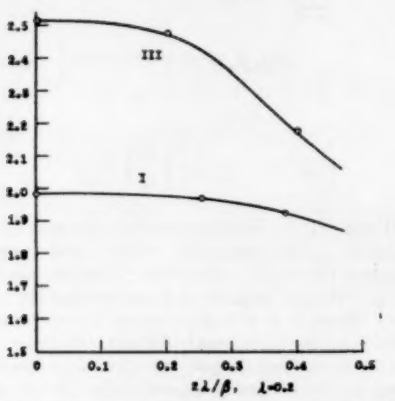

Fig. 3 Stress-concentration factor in case of $\lambda = 0.2$ and β being varied. I—results for resent pproblem; III—results for an infinite row of circular holes.

$$\max \sigma_\phi(\beta = \pi/2) = 2.04545 + 9.72949 \times 10^{-2}\lambda^3 + 1.08001 \times 10\lambda^5 + 6.31907 \times 10^{-2}\lambda^6 - 1.77453 \times 10\lambda^7 + 5.50120 \times 10^{-1}\lambda^8 + 1.45030 \times 10\lambda^9 + 3.13601 \times 10\lambda^{10} - 1.18668 \times 10\lambda^{11} - 1.24253 \times 10^2\lambda^{12} + 1.07925 \times 10\lambda^{13} + 4.04178 \times 10^2\lambda^{14} + 2.02680 \times 10^2\lambda^{15} \ldots \quad (38)$$

In Table 1, the values of $\max \sigma_\phi/T$ calculated from the foregoing equations are shown and are compared with those given by Ling [7]. In Fig. 2, the values of stress-concentration factor $K = (1 - \lambda^2)T^{-1}(\max \sigma_\phi)$ calculated from the values in Table 1 are given and compared. It may be shown that, as the neighboring cavities come close together, the values of stress-concentration factor decrease. Further, in this figure, to compare the decreasing

Table 1 Values of $\max \sigma_\phi/T$ for cases $\beta = \pi/4, \pi/3, \pi/2; \nu = 0.3$

λ	$\beta = \pi/4$	$\beta = \pi/3$	$\beta = \pi/2$	$\beta = \infty$
0	2.045	2.045	2.045	2.045
0.05	2.042	2.044	2.045	
0.10	2.022	2.037	2.046	
0.15	1.979	2.021	2.047	
0.175	1.950	2.010	2.048	
0.20		1.997	2.049	
0.25		1.970	2.057	2.081
0.30			2.071	
0.35			2.097	
0.50				2.359

NOTE: Values for $\beta = \infty$ are as calculated by Ling for a circular cylinder having a spherical cavity under tension.

of stress-concentration factor to that given for the case of an infinite strip under tension, the corresponding values of stress-concentration factor $K = (1 - \lambda)T^{-1}\sigma_{max}$ of an infinite strip containing an infinite row of holes [11] and those calculated by Howland for a circular hole [12] are presented. In Fig. 3, the values of stress-concentration factor, in case of $\lambda = 0.2$ and β being varied, are given for two cases of an infinite row of cavities and holes. From this figure, it becomes clear that the decrease of stress-concentration factor given for the present problem may be somewhat smaller than that given for the case of an infinite strip under tension.

Acknowledgment

In conclusion the author wishes to express his thanks to Professor Emeritus S. Higuchi for his kind advice during the course of the present work.

References

1 R. V. Southwell and H. J. Gough, "Concentration of Stress in the Neighborhood of a Small Spherical Flaw, etc.," *Philosophical Magazine*, series 7, vol. 1, 1926, pp. 71–97.

2 J. N. Goodier, "Concentration of Stress Around Spherical and Cylindrical Inclusions and Flaws," TRANS. ASME, vol. 55, 1933, pp. 39–44.

3 H. Neuber, "Theory of Notch Stresses," Edwards Brothers, 1946, English translation, pp. 102–104.

4 C. B. Ling and K. L. Yang, "On Symmetrical Strain in Solids of Revolution in Spherical Co-ordinates," JOURNAL OF APPLIED MECHANICS, vol. 18, TRANS. ASME, vol. 73, 1951, pp. 367–371.

5 E. Sternberg and M. A. Sadowsky, "On the Axisymmetric Problem of the Theory of Elasticity for an Infinite Region Containing Two Spherical Cavities," JOURNAL OF APPLIED MECHANICS, vol. 19, TRANS. ASME, vol. 74, 1952, pp. 19–27.

6 H. Miyamoto, "On the Problem of the Theory of Elasticity for a Region Containing More Than Two Spherical Cavities," *Transactions of The Japan Society of Mechanical Engineers*, vol. 23, 1957, pp. 431–443.

7 Chih-Bing Ling, "Stresses in a Circular Cylinder Having a Spherical Cavity Under Tension," *Quarterly of Applied Mathematics*, vol. 13, 1956, pp. 381–391.

8 E. W. Hobson, "The Theory of Spherical and Ellipsoidal Harmonics," Cambridge University Press, 1931, p. 139.

9 T. M. MacRobert, "Spherical Harmonics," 2nd edition, 1947, Methuen, p. 362. E. T. Whittaker and G. N. Watson, "Modern Analysis," Cambridge University Press, 1927, p. 332.

10 T. J. I'A. Bromwich, "Introduction to the Theory of Infinite Series," 2nd edition, The Macmillan Company, New York, N. Y., 1926, p. 492.

11 C. B. Biezeno, "Survey of Papers on Elasticity Published in Holland 1940–1946," *Advances in Applied Mechanics*, vol. 1, 1948, pp. 105–170.

12 R. C. J. Howland, "On the Stresses in the Neighborhood of a Circular Hole in a Strip Under Tension," *Philosophical Transactions of the Royal Society of London*, England, series A, vol. 229, 1930, pp. 49–86.

Transient Thermal Stresses in a Semi-Infinite Slab[1]

W. JAUNZEMIS
Assistant Professor,
Department of Engineering Mechanics,
The Pennsylvania State University,
University Park, Pa.

E. STERNBERG
Professor of Mechanics,
Division of Applied Mathematics,
Brown University,
Providence, R. I.
Assoc. Mem. ASME

This investigation is concerned with the transient temperature and thermal-stress distribution generated in a semi-infinite slab if a finite segment of its edge is subjected to a sudden uniform change in temperature. The slab is supposed to be free from external loads and its faces are assumed to be insulated. Exact solutions in series form are obtained both for the heat-conduction problem and for the associated thermoelastic problem. The latter is treated quasi-statically within the classical two-dimensional theory of elasticity. The thermal stresses appropriate to the generalized plane-stress solution vanish identically in the limit as time tends to infinity. The space and time dependence of these stresses is examined in some detail with a view toward tracing the evolution of this well-known, steady-state degeneracy. Finally, the results corresponding to an instantaneous heating or cooling of a portion of the boundary are used to study the effect upon the stresses of gradual changes in the surface temperature.

1 Statement of the Heat-Conduction Problem. Integral and Series Representation of the Temperature Field

Let (x, y, z) be Cartesian co-ordinates and consider a semi-infinite slab of uniform thickness $2h$ occupying the region D defined by $-\infty < x < \infty$, $0 \leq y < \infty$, $-h \leq z \leq h$, Fig. 1. Let $T(x, y, z, t)$ denote the temperature distribution within the solid, t being the time.

We assume that the entire body is initially at zero temperature so that

$$T = 0 \text{ for } (x, y, z) \text{ in } D, \qquad t = 0 \tag{1}$$

Suppose that a segment of length $2a$ of the edge $y = 0$ is suddenly brought to the constant temperature T_0 which is steadily maintained thereafter, while the remaining part of the edge is kept at zero temperature. Then,

$$T = \left\{ \begin{array}{l} T_0 \text{ for } 0 \leq |x| < a, \quad y = 0, \quad 0 \leq |z| \leq h, \\ \qquad\qquad\qquad\qquad\qquad\qquad 0 < t < \infty \\ 0 \text{ for } a < |x| < \infty, \quad y = 0, \quad 0 \leq |z| \leq h, \\ \qquad\qquad\qquad\qquad\qquad\qquad 0 < t < \infty, \end{array} \right\} \tag{2}$$

while

$$\frac{\partial T}{\partial z} = 0 \text{ for } 0 \leq |x| < \infty, \quad 0 \leq y < \infty, \qquad z = \pm h, \qquad 0 < t < \infty \tag{3}$$

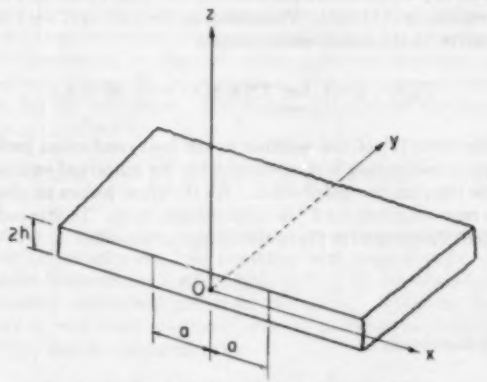

Fig. 1 Semi-infinite slab and Cartesian co-ordinates

insures that the faces of the slab are permanently insulated. Finally, the temperature is to vanish at infinity, or

$$T \to 0 \text{ as } r^2 = x^2 + y^2 \to \infty \text{ for } 0 < t < \infty \tag{4}$$

If the material is homogeneous and isotropic with regard to its thermal response, and in the absence of internal heat sources, the temperature throughout the interior of D must satisfy the heat-conduction equation in the form

$$\nabla^2 T = \frac{1}{\kappa} \frac{\partial T}{\partial t}, \tag{5}$$

provided thermomechanical coupling is disregarded. Here ∇^2 is the Laplacian operator while κ designates the constant[2] thermal diffusivity of the solid.

An integral representation of the solution to the heat-conduction problem governed by (5) subject to the initial condition (1), the boundary conditions (2), (3), and the regularity condition (4), is easily derived with the aid of the available Green's function[3]

---

[1] A major part of the work underlying this investigation was carried out at Illinois Institute of Technology. The paper was prepared under Contract Nonr 562 (25) of Brown University with the Office of Naval Research in Washington, D. C.

Contributed by the Applied Mechanics Division and presented at the Annual Meeting, Atlantic City, N. J., November 29–December 4, 1959 of The American Society of Mechanical Engineers.

Discussion of this paper should be addressed to the Secretary, ASME, 29 West 39th Street, New York, N. Y., and will be accepted until April 10, 1960, for publication at a later date. Discussion received after the closing date will be returned.

Note: Statements and opinions advanced in papers are to be understood as individual expressions of their authors and not those of the Society. Manuscript received by ASME Applied Mechanics Division, January 27, 1959. Paper No. 59—A-63.

[2] Thus, in particular, κ is taken to be independent of the temperature.

[3] See, for example [1], p. 230. Numbers in brackets designate References at end of paper.

appropriate to this problem. Before citing the result thus obtained we introduce the auxiliary position parameters

$$\left.\begin{aligned} R^2 &= (x-s)^2 + y^2, \quad \theta = \arctan\frac{y}{x-s}, \\ R_1^2 &= (x+a)^2 + y^2, \quad \theta_1 = \arctan\frac{y}{x+a}, \\ R_2^2 &= (x-a)^2 + y^2, \quad \theta_2 = \arctan\frac{y}{x-a}, \end{aligned}\right\} \tag{6}$$

where $0 \leq \theta \leq \pi$, $0 \leq \theta_1 \leq \pi$, $0 \leq \theta_2 \leq \pi$. Evidently (R, θ), (R_1, θ_1), and (R_2, θ_2) are plane polar co-ordinates in the half-plane $-\infty < x < \infty$, $0 \leq y < \infty$, $z = 0$, referred to the respective origins $Q(s, 0)$, $Q_1(-a, 0)$, and $Q_2, (a,0)$, as indicated in Fig. 2. The desired temperature field, which is independent of z, is now given by

$$T^*(x, y, t) = \frac{y}{\pi}\int_{-a}^{a} \frac{\psi(R, t)}{R^2}\, ds, \quad T^* = T/T_0, \tag{7}$$

where T^* is a dimensionless temperature and

$$\psi(R, t) = \exp(-R^2/4\kappa t). \tag{8}$$

It is readily verified that the temperature field (7) actually satisfies equations (1) to (5). Proceeding to the limit in (7) as $t \to \infty$, we arrive at the steady-state solution

$$T_\infty^*(x, y) \equiv \lim_{t\to\infty} T^*(x, y, t) = \frac{1}{\pi}(\theta_2 - \theta_1). \tag{9}$$

The form (7) of the solution to the heat-conduction problem under consideration is inconvenient for the numerical evaluation of the temperature distribution. We therefore deduce an alternative representation for T^* in infinite-series form. To this end, we subject the integral in (7) to the change of variable

$$u = \frac{x-s}{2(\kappa t)^{1/2}} \tag{10}$$

and thus obtain

$$T^*(x, y, t) = \frac{1}{\pi}\,[I(\zeta_1, m_1) - I(\zeta_2, m_2)] \quad (|x| \neq a), \tag{11}$$

in which

$$\left.\begin{aligned} I(\zeta, m) &= m\zeta \exp(-m^2\zeta^2)\int_0^\zeta \frac{\exp(-u^2)du}{u^2 + m^2\zeta^2}, \\ \zeta_1 &= \frac{x+a}{2(\kappa t)^{1/2}}, \quad \zeta_2 = \frac{x-a}{2(\kappa t)^{1/2}} \\ m_1 &= \tan\theta_1 = \frac{y}{x+a}, \quad m_2 = \tan\theta_2 = \frac{y}{x-a} \end{aligned}\right\} \tag{12}$$

According to a theorem of Rosser,[4] the definite integral $I(\zeta, m)$ is related to the iterated error integral

$$\Phi(\zeta, m) = \int_0^\zeta \exp(-m^2v^2)\int_0^v \exp(-u^2)du\, dv \tag{13}$$

by means of

$$I(\zeta, m) = \frac{\pi}{2} - \arctan m - 2m\Phi(\zeta, m) \tag{14}$$[5]

and (11), (14), in view of (9), (12), imply

[4] See [2], p. 107.

[5] Here, as well as in subsequent equations, $0 \leq \arctan m \leq \pi$.

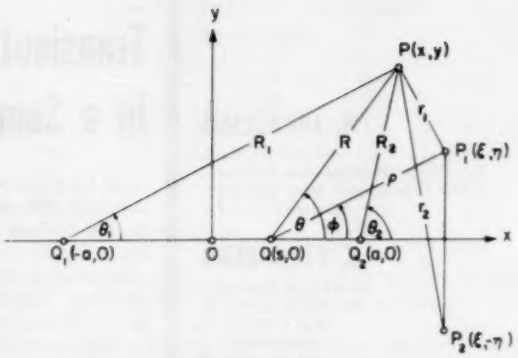

Fig. 2 Auxiliary position parameters

$$T^*(x, y, t) = \frac{2}{\pi}\,[m_2\Phi(\zeta_2, m_2) - m_1\Phi(\zeta_1, m_1)] + T_\infty^*(x, y) \quad (|x| \neq a). \tag{15}$$

When $|x| = a$, either m_1 or m_2 is undefined. In this instance valid formulas for T^*, analogous to (15), are obtained from (15) by passing to the limit as $x \to a$ or $x \to -a$. Consequently,

$$\left.\begin{aligned} T^*(a, y, t) = T^*(-a, y, t) &= -\frac{2}{\pi}\,m_1\Phi(\zeta_1, m_1) + T_\infty(a, y), \\ \text{with} \qquad \zeta_1 &= \frac{a}{(\kappa t)^{1/2}}, \quad m_1 = \frac{y}{2a}. \end{aligned}\right\} \tag{16}$$

The function $\Phi(\zeta, m)$ was studied extensively by Rosser [2]. We record presently certain properties of Φ. From (13) follows

$$\Phi(-\zeta, m) = \Phi(\zeta, -m) = \Phi(\zeta, m), \tag{17}$$

as well as

$$\Phi(\zeta, 0) = \frac{\sqrt{\pi}\,\zeta}{2}\,H(\zeta) + \frac{1}{2}\exp(-\zeta^2) - 1/2, \quad \Phi(0, m) = 0, \tag{18}$$

$$\Phi(\zeta, 1) = \Phi(\zeta, -1) = \frac{\pi}{8}\,H^2(\zeta), \tag{19}$$

$$\Phi(\zeta, m) \to \frac{\pi}{4m} - \frac{1}{2m}\arctan m \quad \text{as} \quad \zeta \to \infty, \tag{20}$$

provided $H(\zeta)$ is the normalized error function; i.e.,

$$H(\zeta) = \operatorname{erf}(\zeta) = \frac{2}{\sqrt{\pi}}\int_0^\zeta \exp(-u^2)du \tag{21}$$

Next, we recall Rosser's expansions[6]

$$\left.\begin{aligned} \Phi(\zeta, m) &= \frac{\pi}{4m}\,H(\zeta)H(m\zeta) - \frac{1}{2m}\arctan m \\ &+ \frac{\sqrt{\pi}}{4}\exp(-\zeta^2)\sum_{n=0}^{\infty}(-m^2)^n g_{2n}(m\zeta) \quad (0 < |m| \leq 1), \\ \Phi(\zeta, m) &= \frac{\pi}{4m} - \frac{1}{2m}\arctan m \\ &- \frac{\sqrt{\pi}}{4m^2}\exp(-m^2\zeta^2)\sum_{n=0}^{\infty}(-m^2)^{-n} g_{2n}(\zeta) \\ &\qquad (1 \leq |m| < \infty), \end{aligned}\right\} \tag{22}$$[7]

[6] See [2], section 17, p. 133 et seq. Recall footnote 5.

[7] Note that $|m| = 1$ is also accounted for by (19).

where

$$g_n(\zeta) = \frac{2}{\sqrt{\pi}} \int_0^1 u^n \exp(-\zeta^2 u^2) du \quad (n = 0, 1, 2, \ldots). \quad (23)^9$$

Equations (15), (16), together with (19), (21), (22), and (23), constitute the desired series representation of the temperature field (7). This representation involves only elementary functions, with the exception of the error function H and the functions $g_{2n}(n = 0, 1, 2, \ldots)$. The functions g_{2n}, which will be found to play an important part throughout the present investigation, are related to the incomplete gamma function; they are also expressible in terms of H and elementary functions. We postpone until later[9] a discussion of certain relevant properties of g_{2n}.

2 Formulation of Associated Thermal-Stress Problem. Integral Representation of Stresses

We turn next to the associated thermal-stress problem, which is to be treated within the classical two-dimensional theory of elasticity. Thus we seek the stresses generated throughout the slab by the temperature distribution established in the preceding section, in the absence of external loads. For the time being, however, we shall not restrict the stress-inducing temperature field to any particular form. We assume merely that $T = T(x, y, t)$ is twice continuously differentiable with respect to (x, y) in the half-plane $\Pi(-\infty < x < \infty, 0 < y < \infty)$ and that

$$T(x, y, t) = O(r^{-3}) \quad \text{as} \quad r^2 = x^2 + y^2 \to \infty. \quad (24)$$

The quasi-static treatment[10] of the plane problem at hand, within the theory of generalized plane stress, is characterized by the equations of equilibrium

$$\frac{\partial \tau_{xx}}{\partial x} + \frac{\partial \tau_{xy}}{\partial y} = 0, \quad \frac{\partial \tau_{xy}}{\partial x} + \frac{\partial \tau_{yy}}{\partial y} = 0 \quad (25)$$

and the compatibility condition

$$\nabla^2(\tau_{xx} + \tau_{yy}) = -E\alpha\nabla^2 T. \quad (26)$$

The stresses governed by these field equations, which must hold in Π for $0 < t < \infty$, are subject to the boundary conditions

$$\tau_{yy}(x, 0, t) = \tau_{xy}(x, 0, t) = 0 \text{ for } -\infty < x < \infty, 0 < t < \infty, \quad (27)$$

and to the regularity requirement

$$\tau_{xx}, \tau_{xy}, \tau_{yy} \to 0 \quad \text{as} \quad r \to \infty \quad \text{for} \quad 0 < t < \infty. \quad (28)$$

Here $\tau_{xx}, \tau_{xy}, \tau_{yy}$ designate the thickness averages of the components of stress,[11] while E and α stand for the modulus of elasticity and the coefficient of thermal expansion, both of which are considered to be independent of the temperature.

The general solution of (25) may be written as

$$\tau_{xx} = \frac{\partial^2 F}{\partial y^2}, \quad \tau_{yy} = \frac{\partial^2 F}{\partial x^2}, \quad \tau_{xy} = -\frac{\partial^2 F}{\partial x \partial y}, \quad (29)$$

in which $F(x, y, t)$ is the Airy function, t playing the role of a parameter. In view of (29), the compatibility condition (26) becomes

$$\nabla^4 F = -E\alpha\nabla^2 T, \quad (30)$$

while (27) are implied by

$$F(x, 0, t) = \left.\frac{\partial F}{\partial y}\right|_{(x,0,t)} = 0 \text{ for } -\infty < x < \infty, 0 < t < \infty. \quad (31)$$

The determination of the thermal stresses therefore reduces to the determination of the Airy function $F(x, y, t)$ that satisfies (30) in Π for $0 < t < \infty$, meets (31), and is such that the stresses (29) conform to (28).

The foregoing characterization remains valid for the corresponding stresses of the plane-strain solution,[12] which are henceforth denoted by $\dagger_{xx}, \dagger_{yy}, \dagger_{xy}$, provided the right-hand member in (30) is replaced with $-E\alpha\nabla^2 T/(1 - \nu)$. The complete stress field belonging to the plane-strain solution is thus given by

$$\left.\begin{aligned} \dagger_{xx} &= \frac{\tau_{xx}}{1-\nu}, \quad \dagger_{yy} = \frac{\tau_{yy}}{1-\nu}, \quad \dagger_{xy} = \frac{\tau_{xy}}{1-\nu} \\ \dagger_{xz} &= \dagger_{yz} = 0, \quad \dagger_{zz} = \frac{\nu}{1-\nu}(\tau_{xx} + \tau_{yy}) - E\alpha T \end{aligned}\right\} \quad (32)$$

Consequently, we may confine the following analysis to the case of generalized plane stress.

In attacking the present temperature-stress problem we follow Goodier's [4] method of integration of the (uncoupled) thermoelastic field equations and adopt a procedure that is, in essence, the two-dimensional counterpart of the approach employed by Mindlin and Cheng [5] in connection with the thermoelastic problem for the half-space. Accordingly, we consider the function $F(x, y, t)$ defined by

$$F(x, y, t) = \iint_\Pi T(\xi, \eta, t) f(x, y, \xi, \eta) d\xi d\eta, \quad (33)$$

in which $f(x, y, \xi, \eta)$ is the Airy function appropriate to the stress field that (a) satisfies the field equations with respect to (x, y) throughout Π except for a singularity at $P_1(\xi, \eta)$ corresponding to a suitably normalized center of dilatation; (b) clears the boundary $y = 0$ from tractions; and (c) vanishes at infinity. Explicitly, f has the elementary form

$$f(x, y, \xi, \eta) = -\frac{\alpha E}{2\pi}\left[\log \frac{r_1}{r_2} + \frac{2y(y + \eta)}{r_2^2}\right], \quad (34)$$

where

$$r_1 = [(x - \xi)^2 + (y - \eta)^2]^{1/2}, \quad r_2 = [(x - \xi)^2 + (y + \eta)^2]^{1/2}, \quad (35)$$

so that r_1 and r_2 are the distances from the point $P(x, y)$ to the points $P_1(\xi, \eta)$ and $P_2(\xi, -\eta)$, respectively, Fig. 2.

It is easily confirmed with the aid of known properties of the logarithmic potential that $F(x, y, t)$, as defined by (33), (34), (35), is the desired Airy function which was previously characterized through (28) to (31). To verify this, we use an argument which yields at the same time an alternative form of (33) that will be useful later on. In accordance with (34), f may be written as

$$f(x, y, \xi, \eta) = \frac{\alpha E}{2\pi}\left[\log r_2 - \log r_1 - 2y \frac{\partial}{\partial y} \log r_2\right]. \quad (36)$$

Now let

$$U_k(x, y, t) = \frac{\alpha E}{2\pi} \iint_\Pi T(\xi, \eta, t) \log r_k d\xi d\eta \quad (k = 1, 2) \quad (37)$$

---

[9] The relation between g_n and Rosser's [2] function ϕ_n is given by

$$g_{2n}(\zeta) = \frac{2}{\sqrt{\pi}} \exp(-\zeta^2)\phi_n(\zeta).$$

[9] See section 4 of this paper.

[10] See, for example [3], p. 761. Inertia effects are not taken into account in the present investigation.

[11] Within the context of the generalized plane-stress solution we shall use the terms "stress" and "thickness average of stress" synonymously.

[12] See [3], p. 755.

By virtue of (24) and of the assumed smoothness of $T(x, y, t)$, the improper integrals (37) are convergent.[13] Accordingly, and by (36), Equation (33) is equivalent to

$$F(x, y, t) = U_2 - U_1 - 2y \frac{\partial U_2}{\partial y}. \tag{38}$$

In view of (37), (35), $U_1(x, y, t)$ is the logarithmic potential of a mass distribution over Π of density $\alpha E T(x, y, t)/2\pi$, while

$$U_2(x, y, t) = U_1(x, -y, t). \tag{39}$$

Consequently, $U_1(x, y, t)$ has continuous space derivatives up to the second order in Π, whereas $U_2(x, y, t)$ is analytic in that domain. Also,

$$\nabla^2 U_1 = \alpha E T, \quad \nabla^2 U_2 = 0 \quad \text{for} \quad (x, y) \text{ in } \Pi. \tag{40}$$

It follows that $F(x, y, t)$ in (38) is twice continuously differentiable in Π and satisfies (30). Further, from (38), (39) we conclude that the boundary conditions (31) are also fulfilled.[14] Finally, the second space derivatives of $F(x, y, t)$ in (38) tend to zero[15] as $x^2 + y^2 \to \infty$, so that the stresses (29) vanish at infinity, as required by (28). Equation (38) thus supplies a representation of the thermal stresses produced by the general temperature field $T(x, y, t)$ in terms of derivatives of the logarithmic potentials (37).

3 Series Representation of the Solution to the Thermal-Stress Problem

At this point we return to the specific temperature field (7) and deduce an explicit series representation for the corresponding thermal stresses. To this end, we insert (7) in (37) and formally[16] interchange the order of the surface integration and of the integration with respect to the parameter s. At the same time, we refer the surface integration to the auxiliary polar co-ordinates (ρ, φ), Fig. 2, defined by

$$\rho^2 = (\xi - s)^2 + \eta^2, \quad \varphi = \arctan \frac{\eta}{\xi - s}, \tag{41}$$

where $0 \leq \varphi \leq \pi$. Proceeding in this manner we reach the iterated triple integrals

$$U_k(x, y, t) = \frac{E\alpha T_0}{2\pi^2} \int_{-a}^{a} \int_0^{\infty} \int_0^{\pi} \psi(\rho, t) \sin \varphi \log r_k \, d\varphi \, d\rho \, ds \qquad (k = 1, 2), \tag{42}$$

in which $\psi(\rho, t)$ is accounted for through (8), while by (35), (6), (41),

$$r_{1,2}^2 = R^2 + \rho^2 - 2R\rho \cos(\theta \mp \varphi), \tag{43}$$

as is immediate from Fig. 2.

By virtue of (43), we have the expansions

$$\left.\begin{aligned} \log r_{1,2} &= \log R - \sum_{n=1}^{\infty} \frac{1}{n} \left(\frac{\rho}{R}\right)^n \cos n(\theta \mp \varphi) \qquad (0 \leq \rho < R), \\ \log r_{1,2} &= \log \rho - \sum_{n=1}^{\infty} \frac{1}{n} \left(\frac{R}{\rho}\right)^n \cos n(\theta \mp \varphi) \qquad (R < \rho < \infty). \end{aligned}\right\} \tag{44}$$

[13] Note that the region of integration Π is unbounded. The integrand in U_1 has a logarithmic singularity at $r_1 = 0$, while that in U_2 is analytic for all (x, y) in Π.

[14] Recall from potential theory that U_1 and U_2, together with their first and second space derivatives, remain bounded in the limit as $y \to 0$.

[15] Recall (24).

[16] Since the validity of the final results will be verified independently in Section 5, we may proceed formally for the present.

Substituting (44) in (42), performing the φ-integration termwise, and introducing the new variable of integration

$$\sigma = x - s, \tag{45}$$

we finally arrive at

$$\left.\begin{aligned} U_k(x, y, t) = \frac{E\alpha T_0}{2\pi^{3/2}} \int_{x-a}^{x+a} R \Bigg[& c_{-1} + C_{-1} \\ & + \frac{(-1)^k \pi}{4} (c_1 + C_1) \sin\theta \\ & + \sum_{n=1}^{\infty} (c_{2n} + C_{2n}) \frac{\cos 2n\theta}{2n(4n^2 - 1)} \Bigg] d\sigma \quad (k = 1, 2). \end{aligned}\right\} \tag{46}$$

Here, because of (45) and the first of (6),

$$R^2 = \sigma^2 + y^2, \quad \theta = \arctan y/\sigma, \tag{47}$$

and c_n, C_n $(n = -1, 0, 1, 2, \ldots)$ are auxiliary functions of R and t, given by

$$\left.\begin{aligned} c_{-1} &= \frac{2}{\sqrt{\pi} R} \int_0^R \psi \log R \, d\rho, \\ c_n &= \frac{2}{\sqrt{\pi} R} \int_0^R \psi \left(\frac{\rho}{R}\right)^n d\rho \quad (n = 0, 1, 2, \ldots), \\ C_{-1} &= \frac{2}{\sqrt{\pi} R} \int_R^{\infty} \psi \log \rho \, d\rho, \\ C_n &= \frac{2}{\sqrt{\pi} R} \int_R^{\infty} \psi \left(\frac{R}{\rho}\right)^n d\rho \quad (n = 0, 1, 2, \ldots), \\ \psi &= \psi(\rho, t) = \exp(-\rho^2/4\kappa t). \end{aligned}\right\} \tag{48}$$

Substitution from (46) into (38) yields for the Airy function

$$F(x, y, t) = \frac{E\alpha T_0 y}{\pi^{3/2}} \int_{x-a}^{x+a} \left[\frac{\pi}{2} c_1 \sin^2\theta + \sum_{n=0}^{\infty} c_{2n} \frac{\sin(2n+1)\theta}{4n^2 - 1} + \sum_{n=1}^{\infty} C_{2n} \frac{\sin(2n-1)\theta}{4n^2 - 1} \right] d\sigma. \tag{49}$$

The stresses may now be computed from (49) by recourse to (29). Bearing in mind (47), (48), we observe that the integrand in (49) is a function of σ, y, and t, and is independent of x. Hence, a single differentiation of $F(x, y, t)$ with respect to x removes the σ-integration appearing in (49). For this reason, (29) lead directly to infinite-series representations for τ_{yy} and τ_{xy} but fail to furnish a convenient form of $\tau_{xx} = \partial^2 F/\partial y^2$. To overcome this difficulty we note from (29), (38), (40) that

$$\tau_{xx} = \nabla^2 F - \tau_{yy} = 4 \frac{\partial^2 U_2}{\partial x^2} - E\alpha T - \tau_{yy}, \tag{50}$$

compute $\partial^2 U_2/\partial x^2$ from (46), and use (50) to represent τ_{xx}.

The results of the very lengthy but straightforward computations outlined in what preceded may be simplified with the aid of the trigonometric expansion

$$\sin\theta = \frac{2}{\pi} - \frac{4}{\pi} \sum_{n=1}^{\infty} \frac{\cos 2n\theta}{4n^2 - 1} \quad (0 \leq \theta \leq \pi) \tag{51}$$

Also, it is expedient to set

$$p = R/2(\kappa t)^{1/2}, \quad p_k = R_k/2(\kappa t)^{1/2} \quad (k = 1, 2), \tag{52}$$

where R and R_k $(k = 1, 2)$ retain their previous definitions given in (47) and (6), respectively.[17] According to (52) and (48),

[17] Note that R is now regarded as a function of σ and y.

$$\left.\begin{aligned} c_n = g_n(p) &= \frac{2}{\sqrt{\pi}} \int_0^1 u^n \exp(-p^2u^2)du, \\ &\qquad (n = 0, 1, 2, \ldots), \\ C_n = G_n(p) &= \frac{2}{\sqrt{\pi}} \int_1^\infty u^{-n} \exp(-p^2u^2)du \\ &\qquad (n = 0, 1, 2, \ldots). \end{aligned}\right\} \quad (53)$$

Using $T^* = T/T_0$, introduced earlier in (7), and letting τ_{xx}^* τ_{yy}^*, τ_{xy}^* denote the dimensionless stresses

$$\tau_{xx}^* = \tau_{xx}/E\alpha T_0, \quad \tau_{yy}^* = \tau_{yy}/E\alpha T_0, \quad \tau_{xy}^* = \tau_{xy}/E\alpha T_0, \quad (54)$$

we ultimately arrive at the following results for the stresses of the generalized plane-stress solution:

$$\left.\begin{aligned} \tau_{xx}^*(x, y, t) &= S(p_2, \theta_2) - S(p_1, \theta_1) - T^*(x, y, t) \\ &\qquad - \tau_{yy}^*(x, y, t), \\ \tau_{yy}^*(x, y, t) &= S_{yy}(p_2, \theta_2) - S_{yy}(p_1, \theta_1), \\ \tau_{xy}^*(x, y, t) &= S_{xy}(p_2, \theta_2) - S_{xy}(p_1, \theta_1), \end{aligned}\right\} \quad (55)$$

where $p_k, \theta_k\,(k = 1, 2)$ are defined through (52) and (6), $T^*(x, y, t)$ is given by (7) or (15), (16), while

$$S(p, \theta) = 2\pi^{-1/2}\left[\frac{\pi}{4} g_1(p) \sin 2\theta + \sum_{n=0}^{\infty} \frac{g_{2n}(p)}{4n^2 - 1} \cos(2n + 1)\theta - \sum_{n=1}^{\infty} \frac{G_{2n}(p)}{4n^2 - 1} \cos(2n - 1)\theta\right], \quad (56)$$

$$S_{yy}(p, \theta) = \pi^{-1/2} \sin\theta\left[\pi g_1(p) \sin\theta \sin 2\theta + \sum_{n=0}^{\infty} \frac{g_{2n}(p)}{2n - 1} \sin 2(n + 1)\theta - \sum_{n=2}^{\infty} \frac{G_{2n}(p)}{2n + 1} \sin 2(n - 1)\theta\right], \quad (57)$$

$$S_{xy}(p, \theta) = \pi^{-1/2}\left\{\frac{\pi}{2} g_1(p) \sin^2\theta(3 - 4\sin^2\theta) + \sum_{n=0}^{\infty} \frac{g_{2n}(p)}{2n - 1}\left[\frac{\sin(2n + 1)\theta}{2n + 1} + \sin\theta \cos 2(n + 1)\theta\right] + \sum_{n=1}^{\infty} \frac{G_{2n}(p)}{2n + 1}\left[\frac{\sin(2n - 1)\theta}{2n - 1} + \sin\theta \cos 2(n - 1)\theta\right]\right\}. \quad (58)$$

This completes the formal solution in series form to the thermal-stress problem under consideration. An inspection of (55) to (58) reveals that the stress series involve merely elementary functions in addition to the functions g_1, g_{2n}, G_{2n} $(n = 0, 1, 2, \ldots)$ given by (53). Referring to (23) we note that g_{2n} was encountered previously in connection with the heat-conduction problem. We now establish certain properties of g_n and G_n that are essential to the further analysis.

4 The Functions g_n and G_n

The definitions

$$\left.\begin{aligned} g_n(p) &= \frac{2}{\sqrt{\pi}} \int_0^1 u^n \exp(-p^2u^2)du \quad (n = 0, 1, 2, \ldots), \\ G_n(p) &= \frac{2}{\sqrt{\pi}} \int_1^\infty u^{-n} \exp(-p^2u^2)du \quad (n = 0, 1, 2, \ldots) \end{aligned}\right\} \quad (59)$$

are evidently equivalent to

$$\left.\begin{aligned} g_n(p) &= \frac{2}{\sqrt{\pi}} p^{-n-1} \int_0^p u^n \exp(-u^2)du, \\ G_n(p) &= \frac{2}{\sqrt{\pi}} p^{n-1} \int_p^\infty u^{-n} \exp(-u^2)du \end{aligned}\right\} \quad (60)$$

Further, if $\gamma(n, p)$ and $\Gamma(n, p)$ are the ordinary and the complementary incomplete gamma functions[18] defined by

$$\gamma(n, p) = \int_0^p u^{n-1} \exp(-u)du, \qquad \Gamma(n, p) = \int_p^\infty u^{n-1} \exp(-u)du, \quad (61)$$

(60) imply the relations

$$\left.\begin{aligned} g_n(p) &= \frac{1}{\sqrt{\pi}} p^{-n-1} \gamma\left(\frac{1 + n}{2}, p^2\right) \\ G_n(p) &= \frac{1}{\sqrt{\pi}} p^{n-1} \Gamma\left(\frac{1 - n}{2}, p^2\right) \end{aligned}\right\} \quad (62)$$

From (59), with aid of integration by parts, follow the recursion relations

$$\left.\begin{aligned} 2p^2 g_{2n+2}(p) &= (2n + 1)g_{2n}(p) - \frac{2}{\sqrt{\pi}} \exp(-p^2), \\ (2n + 1)G_{2n+2}(p) &= -2p^2 G_{2n}(p) + \frac{2}{\sqrt{\pi}} \exp(-p^2), \end{aligned}\right\} \quad (63)$$

while (60) at once lead to

$$g_0(p) = \frac{H(p)}{p}, \quad G_0(p) = \frac{1}{p}[1 - H(p)], \quad (64)$$

if $H(p)$ is again the normalized error function given by (21). As is clear from (63), (64), $g_{2n}(p)$ and $G_{2n}(p)$ $(n = 0, 1, 2, \ldots)$ are expressible in terms of $H(p)$ and elementary functions. In addition to g_{2n} and G_{2n} $(n = 0, 1, 2, \ldots)$ we require merely $g_1(p)$ which, by (59), has the elementary form

$$g_1(p) = \frac{1}{\sqrt{\pi}\, p^2}[1 - \exp(-p^2)]. \quad (65)$$

Next, we shall have occasion to use the power series

$$g_n(p) = \frac{2}{\sqrt{\pi}} \sum_{k=0}^{\infty} \frac{(-1)^k p^{2k}}{(2k + n + 1)\underline{|k}} \quad (n = 0, 1, 2, \ldots), \quad (66)$$

which is derivable directly from the first of (59) and yields in particular

$$g_n(0) = \frac{2}{\sqrt{\pi}(n + 1)} \quad (n = 0, 1, 2, \ldots). \quad (67)$$

The behavior of $G_{2n}(p)$ at $p = 0$ is given by

$$\left.\begin{aligned} G_0(p) &= \frac{1}{p} - \frac{2}{\sqrt{\pi}} + o(p^2) \quad \text{as} \quad p \to 0, \\ G_{2n}(0) &= \frac{2}{\sqrt{\pi}(2n - 1)} \quad (n = 1, 2, \ldots). \end{aligned}\right\} \quad (68)$$

Equations (65) are readily obtainable from the second of (59).

The asymptotic behavior of $g_{2n}(p)$ and $G_{2n}(p)$ for large p and fixed n may be described by

[18] See [6], vol. I, p. 266.

$$\left.\begin{aligned} g_0(p) &= \frac{1}{p} + O[p^{-3}\exp(-p^2)] \quad \text{as} \quad p \to \infty, \\ g_{2n}(p) &= \frac{|2n}{2^{2n}\overline{|n}p^{2n+1}} + O[p^{-3}\exp(-p^2)] \\ &\qquad \text{as} \quad p \to \infty \quad (n = 1, 2, \ldots), \end{aligned}\right\} \tag{69}$$

$$G_{2n}(p) = O[p^{-2}\exp(-p^2)] \text{ as } p \to \infty \quad (n = 0, 1, 2, \ldots) \tag{70}$$

The first of (69) follows from (64) and the asymptotic expansion of the error function,[19] whereas the second of (69) is reached from the first by recourse to (63) and induction. The estimate (70) is most conveniently confirmed on the basis of (59) with the aid of integration by parts. Finally, we cite the uniform bounds, valid for $0 \leq p < \infty$,

$$\left.\begin{aligned} 0 \leq g_{2n}(p) &\leq \frac{2}{\sqrt{\pi}(2n+1)} \quad (n, = 0, 1, 2, \ldots), \\ 0 \leq G_{2n}(p) &\leq \frac{2}{\sqrt{\pi}(2n-1)} \quad (n = 1, 2, \ldots). \end{aligned}\right\} \tag{71}$$

These bounds are also an immediate consequence of the definitions (59).

5 Alternative Stress Series. Convergence Considerations. Verification of Series Solution for Thermal Stresses

We return here to the series representation for the thermal stresses established in Section 3. The convergence of the infinite series (56), (57), (58), for $0 \leq p < \infty$ and $0 \leq \theta \leq \pi$, is assured by (71). It is apparent from the definitions (59) that $g_n(p)$ and $G_n(p)$, for $0 < p < \infty$, $n = 0, 1, 2, \ldots$, are monotone decreasing functions of both p and n. Hence the convergence of the series entering (55) is slowest in the neighborhood of $p_1 = p_2 = 0$ which, according to (52), corresponds to large values of the time t. In fact, as can be gathered from (67), (68), the series (56) for $S(p, \theta)$, as $t \to \infty$ $(p \to 0)$, converges as $1/n^2$, while the series (57), (58), which represent $S_{yy}(p, \theta)$ and $S_{xy}(p, \theta)$, converge merely as $1/n^3$ at $p = 0$.

It is, therefore, desirable to derive infinite series for the thermal stresses which are more rapidly convergent at large values of t. This can be accomplished by summing in closed form portions of the series (56), (57), (58) that slow down their convergence at $p = 0$. To this end, we express $g_{2n}(p)$ and $G_{2n}(p)$ in (56), (57), (58) in terms of $g_{2n+2}(p)$ and $G_{2n-2}(p)$, respectively, by means of the recursion relations (63). The resulting transformed series may be partly summed with the aid of (51) and of the additional trigonometric expansions

$$\left.\begin{aligned} \theta &= \frac{\pi}{2} - \frac{4}{\pi}\sum_{n=0}^{\infty}\frac{\cos(2n+1)\theta}{(2n+1)^2} \quad (0 \leq \theta \leq \pi), \\ \sin 2\theta &= -\frac{8}{\pi}\sum_{n=0}^{\infty}\frac{\cos(2n+1)\theta}{(2n-1)(2n+3)} \quad (0 \leq \theta \leq \pi), \\ \sin^2\theta &= -\frac{8}{\pi}\sum_{n=0}^{\infty}\frac{\sin(2n+1)\theta}{(4n^2-1)(2n+3)} \quad (0 \leq \theta \leq \pi). \end{aligned}\right\} \tag{72}$$

In this manner one is led to the following alternative series representations for S, S_{yy}, and S_{xy}:

$$S(p, \theta) = \frac{1}{2\pi^{1/2}}\left[\pi g_1(p)\sin 2\theta + \sqrt{\pi}\exp(-p^2)(2\theta - \pi - \sin 2\theta) + 8p^2\sum_{n=0}^{\infty}\frac{g_{2n+2}(p)}{(4n^2-1)(2n+1)}\cos(2n+1)\theta + 8p^2\sum_{n=1}^{\infty}\frac{G_{2n-2}(p)}{(4n^2-1)(2n-1)}\cos(2n-1)\theta\right], \tag{73}$$

$$S_{yy}(p, \theta) = \frac{1}{\pi^{1/2}}\sin\theta\left\{[\pi g_1(p) - \sqrt{\pi}\exp(-p^2)]\sin\theta\sin 2\theta + 2p^2\sum_{n=0}^{\infty}\frac{g_{2n+2}(p)}{4n^2-1}\sin 2(n+1)\theta + 2p^2\sum_{n=1}^{\infty}\frac{G_{2n-2}(p)}{4n^2-1}\sin 2(n-1)\theta\right\}, \tag{74}$$

$$S_{xy}(p, \theta) = \frac{1}{2\pi^{1/2}}\left\{[\pi g_1(p) - \sqrt{\pi}\exp(-p^2)]\sin^2\theta(3 - 4\sin^2\theta) + 4p^2\sum_{n=0}^{\infty}\frac{g_{2n+2}(p)}{4n^2-1}\left[\frac{\sin(2n+1)\theta}{2n+1} + \sin\theta\cos 2(n+1)\theta\right] - 4p^2\sum_{n=1}^{\infty}\frac{G_{2n-2}(p)}{4n^2-1}\left[\frac{\sin(2n-1)\theta}{2n-1} + \sin\theta\cos 2(n-1)\theta\right]\right\}. \tag{75}$$

Equations (71) guarantee the absolute and uniform convergence of the transformed series (73), (74), (75) in the domain $0 \leq p < \infty$, $0 \leq \theta \leq \pi$. The new series for $S(p, \theta)$ evidently converges at least as $1/n^4$, while the transformed series appropriate to $S_{yy}(p, \theta)$ and $S_{xy}(p, \theta)$ are seen to converge at least as $1/n^3$. This reflects the improved convergence of the series (73), (74), (75), as compared to the original series[20] (56), (57), (58). Also, if the series (73) is termwise differentiated *twice* with respect to p or θ (or once with respect to p and once with respect to θ), the derived series clearly remain absolutely and uniformly convergent for $0 \leq p < \infty$, $0 \leq \theta \leq \pi$. The same is true of the series generated by a *single* termwise differentiation with respect to p or θ of the expansions (74) and (75) for $S_{yy}(p, \theta)$ and $S_{xy}(p, \theta)$.

We are now in a position to verify the validity[18] of the series solution to the thermal-stress problem governed by (25) to (28) if the temperature field is the solution of the heat-conduction problem characterized by (1) to (5). For this purpose, we employ the series representations (73), (74), (75) for S, S_{yy}, S_{xy} in conjunction with (55). In order to verify the satisfaction of the compatibility condition (26) we need merely show that

$$\nabla^2[S(p_2, \theta_2) - S(p_1, \theta_1)] = 0 \quad \text{in} \quad \Pi. \tag{76}$$

This equation may be confirmed directly by substituting for $S(p, \theta)$ the series (73). In view of the convergence properties just established, the required differentiations may be performed termwise. Similarly, the equilibrium equations (25) are found to hold on substitution from (55), (73), (74), (75). In this connection the temperature field $T^*(x, y, t)$ is most conveniently taken in the form (7).

The boundary conditions (27) are met since $S_{yy}(p, \theta)$ and $S_{xy}(p, \theta)$ both vanish when $\theta = 0$ or $\theta = \pi$. To show that the regularity conditions (28) hold, we note from (52) that $p_k \to \infty$ as $R_k \to \infty$ $(k = 1, 2)$ and refer to (69), (70). This completes the verification of the series solution (55), (73), (74), (75) to the thermal-stress problem.

Finally, we consider the limit of the stress field (55) as $t \to \infty$

[19] See [6], vol. II, p. 147.

[20] The convergence of the stress series can be further accelerated by repeating the process that led from (56), (57), (58) to (73), (74), (75). Such additional improvements are, however, quite superfluous.

which, by (52), corresponds to $p_k \to 0\ (k = 1, 2)$. Making use of (67), (68), we find from (73), (74), (75) that

$$S(0, \theta) = \frac{1}{\pi}\left(\theta - \frac{\pi}{2}\right), \quad S_{xy}(0, \theta) = S_{yy}(0, \theta) = 0, \quad (77)$$

whence (55) and (9) imply

$$\tau_{xx}^*(x, y, t), \quad \tau_{yy}^*(x, y, t), \quad \tau_{xy}^*(x, y, t) \to 0 \quad \text{as} \quad t \to \infty, \quad (78)$$

so that the stresses vanish identically in the steady state. This result is in agreement with a well-known elementary theorem in two-dimensional thermoelasticity[21] concerning steady-state temperature stresses in simply connected bodies. It follows from (78) and (32) that the stresses belonging to the corresponding plane-strain solution also vanish in the steady state, with the exception of t_{xx}. Bearing in mind (7) and (9), and setting $t_{xx}^* = t_{xx}/E\alpha T_0$, we obtain

$$t_{xx}^*(x, y, t) \to -T_\infty^*(x, y) = \frac{1}{\pi}(\theta_1 - \theta_2) \quad \text{as} \quad t \to \infty. \quad (79)$$

The foregoing steady-state plane-strain solution was reached in a different context in [8].

6 Gradual Heating of Boundary. Influence of Rate of Heating

The foregoing analysis rests on the assumption that the surface temperature of the slab obeys the boundary condition (2) and thus is a step-function of time within the segment $-a < x < a$ of the edge. Such an instantaneous heating of the boundary is, of course, physically unrealistic. It is therefore of interest to examine the modifications arising in the results if a portion of the edge is heated (or cooled) gradually, and to study the effect upon the ensuing thermal stresses of the rate at which the surface temperature is altered.

With this objective in mind, we replace the boundary condition (2) with

$$T = \begin{cases} T_0\phi(t) & \text{for} \quad 0 \le |x| < a, \ y = 0, \\ & \qquad 0 \le |x| \le h, \ 0 < t < \infty \\ 0 & \text{for} \quad a < |x| < \infty, \ y = 0, \\ & \qquad 0 \le |x| \le h, \quad 0 < t < \infty, \end{cases} \quad (80)$$

$$\phi(t) = 1 - \exp(-\lambda^2 t),$$

where λ is a parameter governing the rate of heating.[22] Let $T(x, y, t)$ be the solution to the modified heat-conduction problem and suppose that τ_{xx}, τ_{yy}, and τ_{xy} designate the corresponding thermal stresses. According to Duhamel's theorem we then have

$$T^*(x, y, t) = \frac{\partial}{\partial t}\int_0^t \phi(t - u)T^*(x, y, u)du,$$

$$\tau_{xx}^*(x, y, t) = \frac{\partial}{\partial t}\int_0^t \phi(t - u)\tau_{xx}^*(x, y, u)du, \ldots, \ldots \quad (81)$$

provided

$$T^* = T/T_0, \quad \tau_{xx}^* = \tau_{xx}/E\alpha T_0, \ldots, \ldots \quad (82)$$

On substitution for $\phi(t)$ from (80), Equations (81) become

$$T^*(x, y, t) = \lambda^2 \exp(-\lambda^2 t)\int_0^t \exp(\lambda^2 u)T^*(x, y, u)\,du,$$

$$\tau_{xx}^*(x, y, t) = \lambda^2 \exp(-\lambda^2 t)\int_0^t \exp(\lambda^2 u)\tau_{xx}^*(x, y, u)du, \ldots, \ldots \quad (83)$$

[21] See, for example [7], art. 139.

[22] Note that (80) coincides with (2) in the limit as $\lambda \to \infty$.

For the sake of simplicity we shall pursue only the determination of τ_{xx}^* at the origin. From (55), (56), (27), and (52),

$$\tau_{xx}^*(0, 0, t) = -1 - \frac{4}{\pi^{3/2}}\left[\sum_{n=0}^{\infty}\frac{\varphi_{2n}(p_0)}{4n^2 - 1} - \sum_{n=1}^{\infty}\frac{G_{2n}(p_0)}{4n^2 - 1}\right], \quad p_0 = \frac{a}{2(\kappa t)^{1/2}}. \quad (84)$$

The second of (83) now yields

$$\tau_{xx}^*(0, 0, t) = \exp(-\lambda^2 t) - 1 - \frac{4}{\pi^{3/2}}\left[\sum_{n=0}^{\infty}\frac{\beta_{2n}(t, \lambda)}{4n^2 - 1} - \sum_{n=1}^{\infty}\frac{\bar{G}_{2n}(t, \lambda)}{4n^2 - 1}\right], \quad (85)$$

where

$$\beta_{2n}(t, \lambda) = \lambda^2 \exp(-\lambda^2 t)\int_0^t \exp(\lambda^2 u)\varphi_{2n}(q_0)du,$$

$$\bar{G}_{2n}(t, \lambda) = \lambda^2 \exp(-\lambda^2 t)\int_0^t \exp(\lambda^2 u)G_{2n}(q_0)du, \quad (86)$$

and

$$q_0 = \frac{a}{2(\kappa u)^{1/2}}. \quad (87)$$

Bearing in mind (59), we observe that the new functions β_{2n} and $\bar{G}_{2n}$ involve iterated integrals of the type

$$\int_0^t\int_0^1 v^{2n}\exp\left(\lambda^2 u - \frac{a^2v^2}{4\kappa u}\right)dv\,du,$$

$$\int_0^t\int_1^\infty v^{-2n}\exp\left(\lambda^2 u - \frac{a^2v^2}{4\kappa u}\right)dv\,du, \quad (88)$$

the evaluation of which, for arbitrary values of t, presents considerable difficulties. Our main interest in the modified thermoelastic problem, however, concerns the initial period of time during which the thermal stresses appropriate to (80) are bound to depart most appreciably from those corresponding to (2). This leads us to approximate $\beta_{2n}(t, \lambda)$ and $\bar{G}_{2n}(t, \lambda)$ asymptotically in a neighborhood of $t = 0$.

Making use of the asymptotic formulas (69), (70) for $\varphi_{2n}(p)$ and $G_{2n}(p)$ at large values of p, one obtains from (86), (87) after elementary manipulations,

$$\beta_{2n}(t, \lambda) = \bar{h}_{2n}(t, \lambda) + O[t^3\exp(-1/t)],$$

$$\bar{G}_{2n}(t, \lambda) = O[t^3\exp(-1/t)] \quad \text{as} \quad t \to 0 \quad (n = 0, 1, 2, \ldots), \quad (89)$$

if the auxiliary functions $\bar{h}_{2n}$ are defined through

$$\bar{h}_0(t, \lambda) = \frac{1}{\lambda_*}\beta_0(w),$$

$$\bar{h}_{2n}(t, \lambda) = \frac{|2n}{2^{2n}|n\lambda_*^{2n+1}}\beta_{2n}(w) \quad (n = 1, 2, \ldots), \quad (90)$$

$$w = \frac{2\lambda_*}{a}(\kappa t)^{1/2}, \quad \lambda_* = \frac{a\lambda}{2\sqrt{\kappa}},$$

while

$$\beta_{2n}(w) = 2\exp(-w^2)\int_0^w \exp(u^2)u^{2n+2}du \quad (n = 0, 1, 2, \ldots) \quad (91)$$

The functions β_{2n}, in turn, are expressible in terms of the tabulated function[23]

[23] See, for example [2], p. 190.

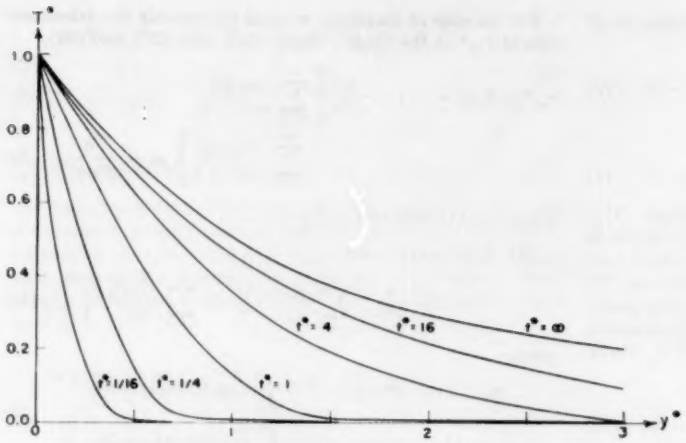

Fig. 3 Variation of T along the y-axis

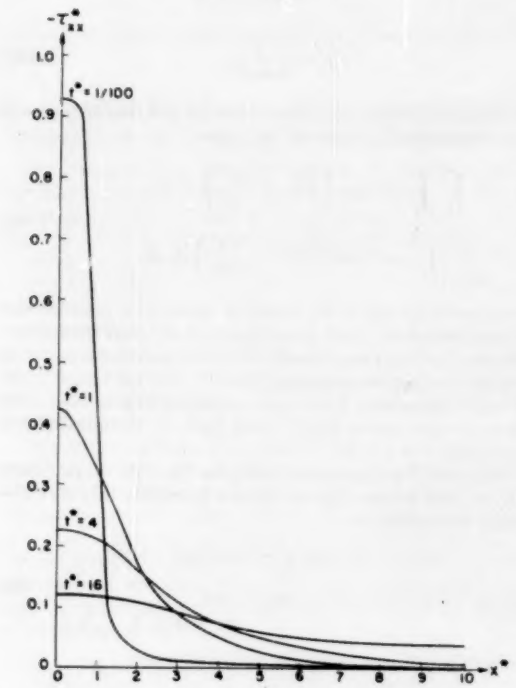

Fig. 4 Variation of τ_{xx} along the x-axis

$$K(w) = \exp(-w^2)\int_0^w \exp(u^2)du \equiv \frac{\sqrt{\pi}}{2}\exp(-w^2)\mathrm{erfi}(w) \quad (92)$$

since (91) gives

$$\beta_0(w) = w - K(w) \quad (93)$$

and implies the recursion relations

$$\beta_{2n} = w^{2n+1} - \frac{2n+1}{2}\beta_{2n-1} \quad (n = 1, 2, \ldots). \quad (94)$$

In the numerical computations to be discussed subsequently $\bar{\tau}_{xx}^*(0, 0, t)$ for small values of t, was approximated by taking the first three terms in the series (85) and by omitting in (89) the terms of order $t^3 \exp(-1/t)$. Thus $\bar{g}_{2n}(t, \lambda)$ was replaced with $\bar{h}_{2n}(t, \lambda)$ and $\bar{G}_{2n}(t, \lambda)$ was replaced with zero. The numerical results obtained in this manner indicate the adequacy of such an approximation.

7 Numerical Results. Discussion

The series solutions established in this paper involve, in addition to elementary functions, the functions H, g_{2n}, G_{2n}, and β_{2n} ($n = 0, 1, 2, \ldots$) defined by (21), (59), and (91). Extensive tabulations of the error function H are to be found in [9]. The numerical values of g_{2n} and G_{2n} are most conveniently determined with the aid of the recursion formulas (63).[24] For small values of the argument p, however, this method of computation leads to a rapid loss of significant figures in $g_{2n}(p)$ and the use of the power series (66) becomes advantageous. The functions β_{2n} are computable on the basis of the recursion relations (94) with the aid of the tabulation of K given in [2].

We take up first certain illustrative numerical results corresponding to the case of an instantaneous change in the temperature of the edge of the slab, represented by the boundary condition (2). These results, as far as the temperature field is concerned, were obtained through evaluation of the series (15), (22). The computations pertaining to the associated thermal stresses, for small values of p_k (i.e., large time-values), were based on the series solution (55), (73), (74), (75). On the other hand, for large values of p_k (i.e., in a neighborhood of $t = 0$) the representation (55), (56), (57), (58) was found to be more advantageous since the functions $g_n(p)$ and $G_n(p)$ decrease rapidly with increasing n if p is sufficiently large. Because of the speedy convergence of the temperature and stress series just mentioned, no more than the leading six terms had to be taken into account even in the most unfavorable circumstances.

The graphs about to be discussed refer to the previously introduced[25] dimensionless temperature and stresses

$$T^* = T/T_0, \quad \tau_{xx}^* = \tau_{xx}/E\alpha T_0, \ldots, \ldots, \quad (95)$$

as well as to the dimensionless Cartesian co-ordinates and time

$$x^* = x/a, \quad y^* = y/a, \quad t^* = 4\kappa t/a^2. \quad (96)$$

Table 1 gives approximate values of the physical units of time and stress corresponding to the units of t^* and τ_{xx}^*, τ_{yy}^*, τ_{xy}^*,

[24] Recourse to (62) and to existing tables of incomplete gamma functions necessitates cumbersome interpolations.

[25] See (7) and (54).

for $a = 1$ in., $T_0 = 1$ deg F, and several actual materials. This information should be helpful in connection with the physical interpretation of the dimensionless diagrams presented later.

Table 1 Units of time and stress for various materials

Material	Unit of time, sec	Unit of stress, psi
Aluminum	2.05	133
Brass	4.36	177
Mild steel	13.44	195
Cast iron	13.44	165

The variation of the temperature T^* along the y-axis, at various times, is shown in Fig. 3. Evidently, $T^*(0, y^*, t^*)$ is a steadily decreasing function of y^* at fixed t^*. Fig. 4 displays the dependence on x^* of the stress τ_{xx}^* along the edge $y^* = 0$, corresponding to several choices of t^*. As $t^* \to 0$ these curves approach the limiting distribution given by

$$\lim_{t^* \to 0} \tau_{xx}^*(x^*, 0, t^*) = \begin{cases} -1 & \text{for } 0 \leq |x^*| < 1, \\ -1/2 & \text{for } |x^*| = 1, \\ 0 & \text{for } 1 < |x^*| < \infty. \end{cases} \quad (97)$$

On the other hand, $\tau_{xx}^*(x^*, 0, 0) = 0$. This discontinuous behavior of the boundary values of τ_{xx}^* at $t^* = 0$ reflects the analogous discontinuity inherent in the temperature field and is induced by the initial and boundary conditions (1), (2). According to (95), (96), (97),

$$\lim_{t \to 0} \tau_{xx}(x, 0, t) = -E\alpha T_0 \quad (-a < x < a). \quad (98)$$

The limiting value given by (98) coincides with the thermal stress produced in a bar by a temperature change T_0 if the bar is fully constrained against expansion or contraction. Consequently, the stress in the heated (or cooled) segment of the edge—regarded as a separate fiber—at $t = 0+$ may be attributed to a momentary complete prevention of thermal deformations. With increasing time a gradual relaxation of this boundary segment takes place, and as the temperature stress τ_{xx} is communicated to the outlying portions of the boundary its maximum magnitude at the origin steadily diminishes.

The variation of τ_{xx}^* and τ_{yy}^* along the y-axis, at several instants, is illustrated in Figs. 5 and 6. It is interesting to note that $\tau_{xx}^*(0, y^*, t^*)$ takes on both tensile and compressive values; its limiting behavior as $t^* \to 0$ is characterized by

$$\lim_{t^* \to 0} \tau_{xx}^*(0, y^*, t^*) = \begin{cases} -1 & \text{for } y^* = 0, \\ 0 & \text{for } 0 < y^* < \infty. \end{cases} \quad (99)$$

The stress $\tau_{yy}^*(0, y^*, t^*)$, which corresponds to pure tension if $T_0 > 0$, attains its maximum approximately at $y^* = 1.4$ and $t^* = 0.56$. This maximum value of τ_{yy}^* is about 0.054 and is thus small compared to the maximum magnitude of τ_{xx}^*, which is unity.

The time dependence of the temperature and stresses at $x^* = 0$, $y^* = 1$, and $x^* = y^* = 1$ is displayed in Fig. 7 and Fig. 8, respectively. The most important observation to be made in this connection is that τ_{xx}^* in Fig. 7, and τ_{xx}^*, τ_{zz}^* in Fig. 8, undergo one complete oscillation, involving a reversal of sign, before monotonically approaching their common steady-state value of zero. In contrast, τ_{yy}^* in both cases rises to a maximum value

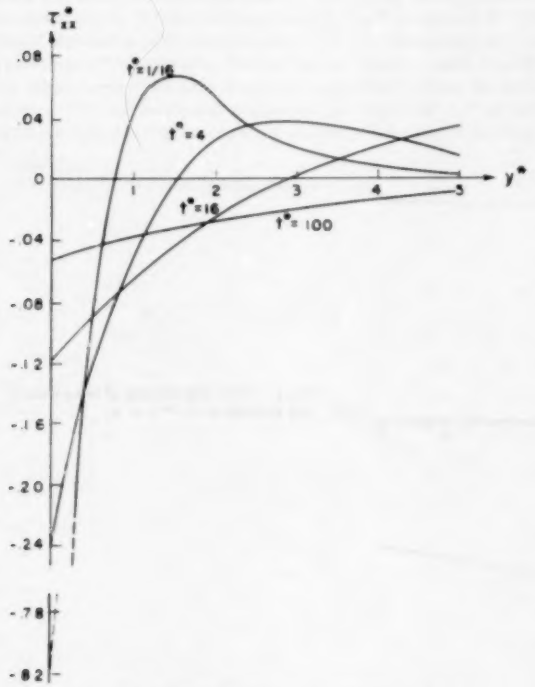

Fig. 5 Variation of τ_{xx} along the y-axis

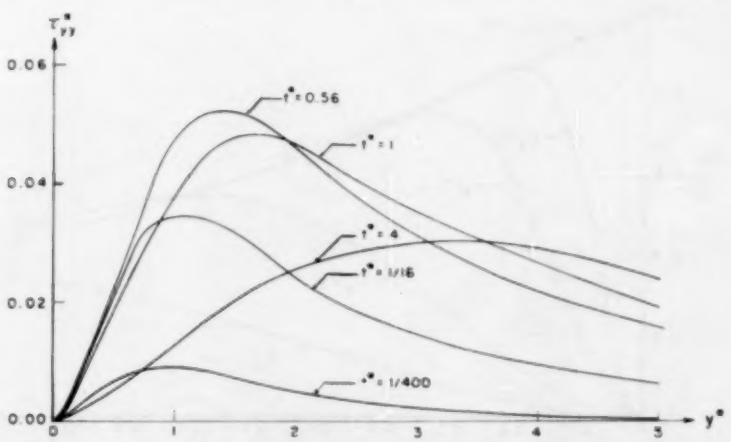

Fig. 6 Variation of τ_{yy} along the y-axis

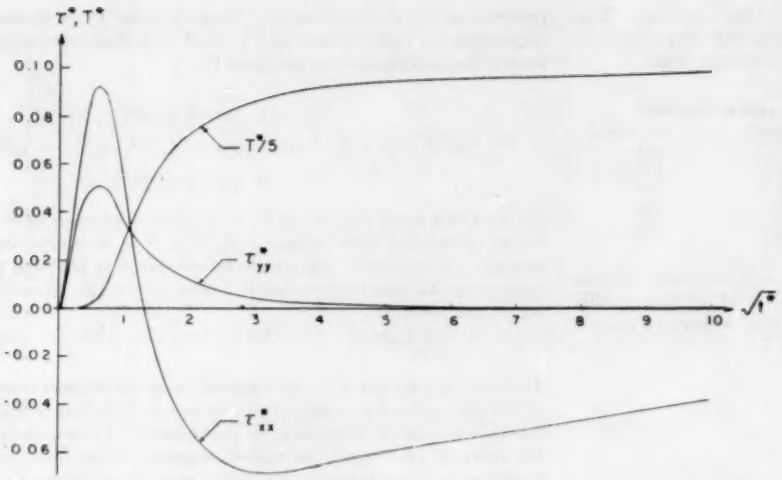

Fig. 7 Time dependence of temperature and stresses at $x = 0$, $y = a$

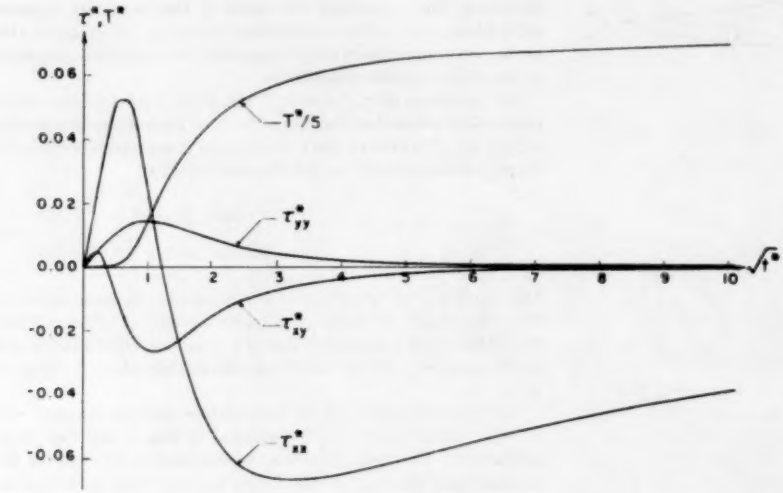

Fig. 8 Time dependence of temperature and stresses at $x = y = a$

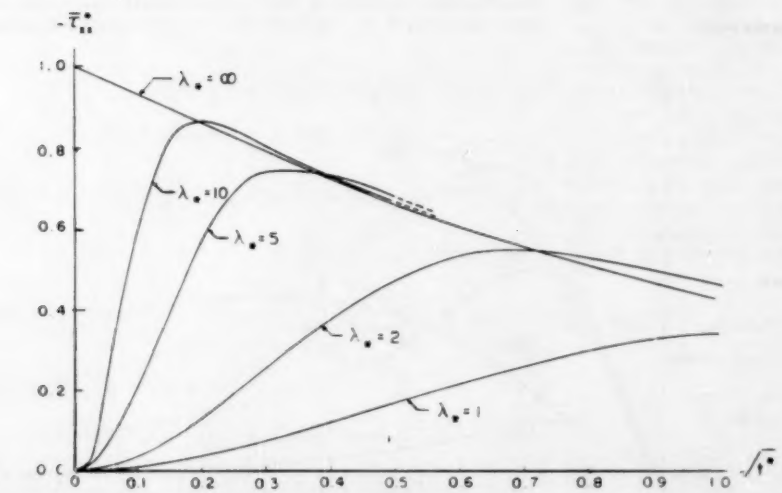

Fig. 9 Time dependence of τ_{xx} at $x = y = 0$ for various rates of heating

and thereafter steadily declines to zero without experiencing a sign reversal.

Fig. 9 refers to the influence of a finite time-rate of heating of the boundary and, for $t^* < 1/4$, is based on the asymptotic approximation deduced in Section 6. The portions of the graphs that belong to values of t^* exceeding 1/4 were established through numerical evaluation of the integrals (88). The figure depicts the time dependence of the dimensionless stress[36] $\bar{\tau}_{zz}^*$ at the origin for various values of the dimensionless "rate-of-heating parameter" λ_* defined by (80), (90). The curve labeled "$\lambda_* = \infty$" represents the previously discussed limiting case in which the temperature of the edge of the slab is altered instantaneously; accordingly, this curve exhibits a jump discontinuity at $t^* = 0$. The remaining curves rise continuously from the initial value of zero to a maximum that lies near the curve for $\lambda_* = \infty$ and then follow the latter curve rather closely. Evidently, the stress relief accompanying a *gradual* heating or cooling of a segment of the edge of the slab is quite considerable. If $\lambda_* = 2$ and the material is aluminum,[37] for example, the temperature at the origin attains over 90 per cent of its final maximum magnitude within the first 1.3 sec. The corresponding maximum magnitude of $\bar{\tau}_{zz}^*$ at the origin is reached in approximately 1 sec and is less than 55 per cent of the maximum τ_{zz}^* induced by an *instantaneous* change of the boundary temperature.

[36] See (82).

[37] Cf. Table 1. We assume here that $a = 1$ in.

References

1 H. S. Carslaw and J. C. Jaeger, "Conduction of Heat in Solids," Oxford University Press, 1947.

2 J. B. Rosser, "Theory and Application of $\int_0^z e^{-x^2}dx$ and $\int_0^z e^{-y^2}dy \int_0^y e^{-x^2}dx$," Mapleton House, Brooklyn, N. Y., 1948.

3 M. Hetényi, editor, "Handbook of Experimental Stress Analysis," John Wiley and Sons, New York, N. Y., 1950.

4 J. N. Goodier, "On the Integration of the Thermo-Elastic Equations," *Philosophical Magazine*, vol. 23, 1937, p. 1017.

5 R. D. Mindlin and D. H. Cheng, "Thermoelastic Stress in the Semi-Infinite Solid," *Journal of Applied Physics*, vol. 21, 1950, p. 931.

6 A. Erdélyi, editor "Higher Transcendental Functions," vols. 1 and 2, McGraw-Hill Book Company, Inc., New York, N. Y., 1953.

7 S. Timoshenko and J. N. Goodier, "Theory of Elasticity," second edition, McGraw-Hill Book Company, Inc., New York, N. Y., 1951.

8 E. Sternberg and E. L. McDowell, "On the Steady-State Thermoelastic Problem for the Half-Space," *Quarterly of Applied Mathematics*, vol. 14, 1957, p. 381.

9 "Tables of Probability Functions," vol. 1, WPA. New York, N. Y., 1941.

J. K. KNOWLES
Assistant Professor of Applied Mechanics, Division of Engineering, California Institute of Technology, Pasadena, Calif.

ERIC REISSNER
Professor of Mathematics, Massachusetts Institute of Technology, Cambridge, Mass. Mem. ASME

On Stress-Strain Relations and Strain-Energy Expressions in the Theory of Thin Elastic Shells[1]

The stress-strain relations of Flügge and Byrne for thin elastic shells are inverted to express strain quantities, and therewith the strain energy, in terms of stress resultants and couples. In this form, and upon omission of terms which are small of order h^2/R^2, the stress-strain relations and the strain-energy expression are shown to be simply related to corresponding results of Trefftz. The strain-energy formula of Trefftz is generalized to arbitrary orthogonal middle surface co-ordinates.

In the following we are primarily concerned with expressions for strain energy in the theory of thin elastic shells, expressed in terms of stress resultants and stress couples. The very simplest of such expressions, that of Love's first-approximation theory, may be set down as a straightforward generalization of corresponding expressions for bending and stretching of flat plates. Our interest in less simple expressions arises from certain inadequacies of Love's first-approximation theory which we have discussed elsewhere.[2]

It is convenient for our purposes to use as a starting point a system of stress-strain relations given by Flügge[3] and Byrne.[4] Our first result is that upon inverting this system it becomes possible to show that, when terms are omitted which are small of a well-defined order, the system reduces to one given by Trefftz.[5]

Our second result is a strain-energy expression in terms of stress resultants and couples for the relations of Flügge and Byrne. From this we obtain by systematic omission of certain terms which are recognizably small of higher order a simplified expression which is again equivalent to Trefftz' improvement of Love's first-approximation theory.

Trefftz' formula is for the case of lines-of-curvature co-ordinates and our third result is a generalization of this formula to the case of arbitrary orthogonal middle surface co-ordinates.

The Flügge-Byrne Stress-Strain Relations

These relations, given by Flügge for circular cylindrical shells and by Byrne for general shells referred to lines of curvature co-ordinates ξ_1, ξ_2, may be written as follows[2] in terms of strain quantities ϵ, γ, κ^*, and τ^*

$$N_{11} = \frac{Eh}{1-\nu^2}(\epsilon_1 + \nu\epsilon_2) + \frac{Eh^3}{12(1-\nu^2)}\left(\frac{1}{R_{22}} - \frac{1}{R_{11}}\right)\kappa_1^*$$
$$N_{22} = \frac{Eh}{1-\nu^2}(\epsilon_2 + \nu\epsilon_1) + \frac{Eh^3}{12(1-\nu^2)}\left(\frac{1}{R_{11}} - \frac{1}{R_{22}}\right)\kappa_2^* \tag{1}$$

$$N_{12} = \frac{Eh}{2(1+\nu)}\gamma_{12} + \frac{Eh^3}{48(1+\nu)}\left(\frac{1}{R_{22}} - \frac{1}{R_{11}}\right)\left[\tau^* + \left(\frac{1}{R_{22}} - \frac{1}{R_{11}}\right)\gamma_{12}\right] \tag{2}$$

$$N_{21} = \frac{Eh}{2(1+\nu)}\gamma_{12} + \frac{Eh^3}{48(1+\nu)}\left(\frac{1}{R_{11}} - \frac{1}{R_{22}}\right)\left[\tau^* + \left(\frac{1}{R_{11}} - \frac{1}{R_{22}}\right)\gamma_{12}\right]$$

$$M_{11} = \frac{Eh^3}{12(1-\nu^2)}\left[\kappa_1^* + \nu\kappa_2^* + \frac{1}{R_{22}}(\epsilon_1 + \nu\epsilon_2)\right]$$
$$M_{22} = \frac{Eh^3}{12(1-\nu^2)}\left[\kappa_2^* + \nu\kappa_1^* + \frac{1}{R_{11}}(\epsilon_2 + \nu\epsilon_1)\right] \tag{3}$$

$$M_{12} = \frac{Eh^3}{24(1+\nu)}\left(\tau^* + \frac{\gamma_{12}}{R_{22}}\right)$$
$$M_{21} = \frac{Eh^3}{24(1+\nu)}\left(\tau^* + \frac{\gamma_{12}}{R_{11}}\right) \tag{4}$$

Equations (1) to (4) may be written in the inverted form

$$\epsilon_1 = \frac{1}{\Delta}\left\{\frac{N_{11}}{Eh}\left[1 + \frac{1}{12}\frac{h}{R_{22}}\left(\frac{h}{R_{22}} - \frac{h}{R_{11}}\right) - \frac{1}{12(1-\nu^2)}\left(\frac{h}{R_{22}} - \frac{h}{R_{11}}\right)^2\right] - \frac{\nu N_{22}}{Eh}\left[1 - \frac{1}{12(1-\nu^2)}\left(\frac{h}{R_{22}} - \frac{h}{R_{11}}\right)^2\right] - \frac{M_{11}}{Eh}\left(\frac{1}{R_{22}} - \frac{1}{R_{11}}\right)\left[1 + \frac{1}{12(1-\nu^2)}\frac{h}{R_{11}}\left(\frac{h}{R_{22}} - \frac{h}{R_{11}}\right)\right] + \frac{\nu M_{22}}{Eh}\frac{1}{12(1-\nu^2)}\frac{1}{R_{22}}\left(\frac{h}{R_{22}} - \frac{h}{R_{11}}\right)^2\right\} \tag{5}$$

---

[1] A report on work carried out under the terms of an Office of Naval Research Contract with the Massachusetts Institute of Technology.

[2] J. K. Knowles and E. Reissner, "Note on Stress Strain Relations for Thin Elastic Shells," *Journal of Mathematics and Physics*, vol. 37, 1958, pp. 269–282.

[3] W. Flügge, "Statik und Dynamik der Schalen," Berlin, 1934.

[4] R. Byrne, "Theory of Small Deformations of Thin Elastic Shells," University of California Publication in Mathematics, NS 2, 1944, pp. 103–152.

[5] E. Trefftz, "Ableitung der Schalenbiegungsgleichungen mit dem Castigilianoschen Prinzip," *Zeitschrift für angewandte Mathematik und Mechanik*, vol. 15, 1935, pp. 101–108.

Presented at the West Coast Conference of the Applied Mechanics Division, Stanford, Calif., September 9–11, 1959, of THE AMERICAN SOCIETY OF MECHANICAL ENGINEERS.

Discussion of this paper should be addressed to the Secretary, ASME, 29 West 39th Street, New York, N. Y., and will be accepted until April 10, 1960, for publication at a later date. Discussion received after the closing date will be returned.

NOTE: Statements and opinions advanced in papers are to be understood as individual expressions of their authors and not those of the Society. Manuscript received at ASME Applied Mechanics Division, November 21, 1958. Paper No. 59—APMW-13.

$$\epsilon_1 = \frac{1}{\Delta}\left\{\frac{N_{11}}{Eh}\left[1 - \frac{1}{12}\frac{h}{R_{11}}\left(\frac{h}{R_{22}} - \frac{h}{R_{11}}\right) - \frac{1}{12(1-\nu^2)}\left(\frac{h}{R_{22}} - \frac{h}{R_{11}}\right)^2\right] - \frac{\nu N_{11}}{Eh}\left[1 - \frac{1}{12(1-\nu^2)}\left(\frac{h}{R_{22}} - \frac{h}{R_{11}}\right)^2\right] + \frac{M_{11}}{Eh}\left(\frac{1}{R_{11}} - \frac{1}{R_{11}}\right)\left[1 - \frac{1}{12(1-\nu^2)}\frac{h}{R_{11}}\left(\frac{h}{R_{22}} - \frac{h}{R_{11}}\right)\right] + \frac{\nu M_{11}}{Eh}\frac{1}{12(1-\nu^2)}\frac{1}{R_{11}}\left(\frac{h}{R_{22}} - \frac{h}{R_{11}}\right)^2\right\} \quad (5)\ \textit{cont.}$$

$$\gamma_{12} = \frac{N_{12} + N_{21}}{Eh/(1+\nu)}\left[1 + \frac{1}{24}\left(\frac{h}{R_{22}} - \frac{h}{R_{11}}\right)^2\right]^{-1} \quad (6)$$

$$\kappa_1^* = \frac{1}{\Delta}\left\{\frac{12M_{11}}{Eh^3}\left[1 + \frac{1}{12}\frac{h}{R_{11}}\left(\frac{h}{R_{22}} - \frac{h}{R_{11}}\right)\right] - \frac{12\nu M_{22}}{Eh^3} - \frac{N_{11}}{Eh}\frac{1}{R_{22}}\left[1 + \frac{1}{12}\frac{h}{R_{11}}\left(\frac{h}{R_{22}} - \frac{h}{R_{11}}\right)\right] + \frac{\nu N_{22}}{Eh}\frac{1}{R_{11}}\right\} \quad (7)$$

$$\kappa_2^* = \frac{1}{\Delta}\left\{\frac{12M_{22}}{Eh^3}\left[1 - \frac{1}{12}\frac{h}{R_{22}}\left(\frac{h}{R_{22}} - \frac{h}{R_{11}}\right)\right] - \frac{12\nu M_{11}}{Eh^3} - \frac{N_{22}}{Eh}\frac{1}{R_{11}}\left[1 - \frac{1}{12}\frac{h}{R_{22}}\left(\frac{h}{R_{22}} - \frac{h}{R_{11}}\right)\right] + \frac{\nu N_{11}}{Eh}\frac{1}{R_{22}}\right\} \quad (7)$$

$$\tau^* = \frac{12(M_{12} + M_{21})}{Eh^3/12(1+\nu)} - \frac{1}{2}\left(\frac{1}{R_{11}} + \frac{1}{R_{22}}\right)\frac{N_{12} + N_{21}}{Eh/(1+\nu)}\left[1 + \frac{1}{24}\left(\frac{h}{R_{22}} - \frac{h}{R_{11}}\right)^2\right]^{-1} \quad (8)$$

where

$$\Delta = 1 - \frac{1}{12(1-\nu^2)}\left(\frac{h}{R_{22}} - \frac{h}{R_{11}}\right)^2 - \frac{1}{144(1-\nu^2)}\frac{h}{R_{11}}\frac{h}{R_{22}}\left(\frac{h}{R_{22}} - \frac{h}{R_{11}}\right)^2 \quad (9)$$

When the stress-strain relations (1) to (4) are written in the form (5) to (8), certain simplifications suggest themselves. If terms of order h^2/R^2 are neglected in comparison with unity, the following simplified system results:

$$\epsilon_1 = \frac{N_{11} - \nu N_{22}}{Eh} + \left(\frac{1}{R_{11}} - \frac{1}{R_{22}}\right)\frac{M_{11}}{Eh} \quad (10)$$

$$\epsilon_2 = \frac{N_{22} - \nu N_{11}}{Eh} + \left(\frac{1}{R_{22}} - \frac{1}{R_{11}}\right)\frac{M_{22}}{Eh} \quad (11)$$

$$\gamma_{12} = \frac{N_{12} + N_{21}}{Eh/(1+\nu)} \quad (12)$$

$$\kappa_1^* = \frac{M_{11} - \nu M_{22}}{Eh^3/12} - \frac{1}{Eh}\left(\frac{N_{11}}{R_{22}} - \frac{\nu N_{22}}{R_{11}}\right) \quad (13)$$

$$\kappa_2^* = \frac{M_{22} - \nu M_{11}}{Eh^3/12} - \frac{1}{Eh}\left(\frac{N_{22}}{R_{11}} - \frac{\nu N_{11}}{R_{22}}\right) \quad (14)$$

$$\tau^* = \frac{M_{12} + M_{21}}{Eh^3/12(1+\nu)} - \left(\frac{1}{R_{11}} + \frac{1}{R_{22}}\right)\frac{N_{12} + N_{21}}{2Eh/(1+\nu)} \quad (15)$$

Equations (10) and (11) are identical with equations given by Trefftz.[5] Equations (13) and (14) reduce to corresponding formulas of Trefftz if we write $\kappa = \kappa^* + (\epsilon/R)$, take ϵ from (10) and (11) and again neglect terms of order h^2/R^2 in comparison with unity. Equation (15) becomes identical with a corresponding equation of Trefftz if in it we express $N_{12} + N_{21}$ in terms of γ_{12} according to equation (12). Finally, it is possible to show that γ_{12} in (12) differs from a corresponding expression of Trefftz by terms of relative order h^2/R^2.

Strain Energy in Terms of Stress Resultants and Couples

An expression for the strain-energy density in terms of strains for lines of curvature co-ordinates has been given by Byrne.[4] It may be written in the form

$$\Pi = \frac{Eh}{2(1-\nu^2)}\left(\epsilon_1^2 + \epsilon_2^2 + 2\nu\epsilon_1\epsilon_2 + \frac{1-\nu}{2}\gamma_{12}^2\right) + \frac{Eh^3}{24(1-\nu^2)}\left[\kappa_1^{*2} + \kappa_2^{*2} + 2\nu\kappa_1^*\kappa_2^* + \frac{1-\nu}{2}\tau^{*2} + \frac{1}{R_{11}R_{22}}(\epsilon_1^2 + \epsilon_2^2 + 2\nu\epsilon_1\epsilon_2) + \frac{2}{R_{22}}(\epsilon_1\kappa_1^* + \nu\epsilon_2\kappa_1^*) + \frac{2}{R_{11}}(\epsilon_2\kappa_2^* + \nu\epsilon_1\kappa_2^*) + \frac{1-\nu}{2}\left(\frac{1}{R_{11}} + \frac{1}{R_{22}}\right)\gamma_{12}\tau^* + \frac{1-\nu}{2}\left(\frac{1}{R_{11}^2} + \frac{1}{R_{22}^2} - \frac{1}{R_{11}R_{22}}\right)\gamma_{12}^2\right] \quad (16)$$

Using the stress-strain relations (1) to (4) it is readily shown that (16) is equivalent to

$$\Pi = \frac{1}{2}\left[N_{11}\epsilon_1 + N_{22}\epsilon_2 + \frac{1}{2}(N_{12} + N_{21})\gamma_{12} + M_{11}\left(\kappa_1^* + \frac{\epsilon_1}{R_{11}}\right) + M_{22}\left(\kappa_2^* + \frac{\epsilon_2}{R_{22}}\right) + \frac{1}{2}M_{12}\left(\tau^* + \frac{\gamma_{12}}{R_{22}}\right) + \frac{1}{2}M_{21}\left(\tau^* + \frac{\gamma_{12}}{R_{11}}\right)\right] \quad (17)$$

If the expressions (5) to (8) are substituted into (17), we obtain the strain-energy density in terms of resultants and couples as follows:

$$\Pi = \frac{1}{2Eh\Delta}\left\{N_{11}^2\left[1 + \frac{1}{12}\frac{h}{R_{22}}\left(\frac{h}{R_{22}} - \frac{h}{R_{11}}\right) - \frac{1}{12(1-\nu^2)}\left(\frac{h}{R_{22}} - \frac{h}{R_{11}}\right)^2\right] + N_{22}^2\left[1 - \frac{1}{12}\frac{h}{R_{11}}\left(\frac{h}{R_{22}} - \frac{h}{R_{11}}\right) - \frac{1}{12(1-\nu^2)}\left(\frac{h}{R_{22}} - \frac{h}{R_{11}}\right)^2\right] - 2\nu N_{11}N_{22}\left[1 - \frac{1}{12(1-\nu^2)}\left(\frac{h}{R_{22}} - \frac{h}{R_{11}}\right)^2\right]\right\} + \frac{1}{Eh^3\Delta/6}\left\{M_{11}^2\left[1 - \frac{1}{144}\frac{h^2}{R_{11}^2}\left(\frac{h}{R_{22}} - \frac{h}{R_{11}}\right)^2\right] + M_{22}^2\left[1 - \frac{1}{144}\frac{h^2}{R_{22}^2}\left(\frac{h}{R_{22}} - \frac{h}{R_{11}}\right)^2\right] - 2\nu M_{11}M_{22}\left[1 - \frac{1}{144}\frac{h}{R_{11}}\frac{h}{R_{22}}\left(\frac{h}{R_{22}} - \frac{h}{R_{11}}\right)^2\right]\right\}$$

$$+\frac{(N_{12}+N_{21})^2}{8Gh}\left[1+\frac{1}{24}\left(\frac{h}{R_{22}}-\frac{h}{R_{11}}\right)^2\right]^{-1}$$
$$+\left(\frac{1}{R_{22}}-\frac{1}{R_{11}}\right)\left\{\frac{(N_{12}+N_{21})(M_{12}-M_{21})}{16Gh}\left[1+\frac{1}{24}\left(\frac{h}{R_{22}}-\frac{h}{R_{11}}\right)^2\right]^{-1}\right.$$
$$+\frac{N_{22}M_{22}}{Eh\Delta}\left[1-\frac{1}{12(1-\nu^2)}\frac{h}{R_{22}}\left(\frac{h}{R_{22}}-\frac{h}{R_{11}}\right)\right]$$
$$-\frac{N_{11}M_{11}}{Eh\Delta}\left[1+\frac{1}{12(1-\nu^2)}\frac{h}{R_{11}}\left(\frac{h}{R_{22}}-\frac{h}{R_{11}}\right)\right]$$
$$\left.+\frac{\nu}{12(1-\nu^2)}\left(\frac{h}{R_{22}}-\frac{h}{R_{11}}\right)\left(\frac{N_{22}M_{11}}{Eh\Delta}\frac{h}{R_{11}}+\frac{N_{11}M_{22}}{Eh\Delta}\frac{h}{R_{22}}\right)\right\}$$
$$+\frac{(M_{12}+M_{21})^2}{2Gh^3/3} \quad (18)$$

If in this expression we neglect terms of relative order of magnitude h^2/R^2, we find the following simpler expression:

$$\Pi=\frac{1}{2Eh}\left[N_{11}^2+N_{22}^2-2\nu N_{11}N_{22}+2\left(\frac{1}{R_{22}}-\frac{1}{R_{11}}\right)(N_{22}M_{22}-N_{11}M_{11})\right]$$
$$+\frac{6}{Eh^3}(M_{11}^2+M_{22}^2-2\nu M_{11}M_{22})+\frac{1}{2Gh}\left(\frac{N_{12}+N_{21}}{2}\right)^2+\frac{6}{Gh^3}\left(\frac{M_{12}+M_{21}}{2}\right)^2$$
$$+\frac{1}{8Gh}\left(\frac{1}{R_{22}}-\frac{1}{R_{11}}\right)(M_{12}-M_{21})\frac{N_{12}+N_{21}}{2} \quad (19)$$

A further simplification becomes possible by observing that the stress-strain relations (2) and (4) imply the identities

$$N_{12}-N_{21}=\frac{M_{21}}{R_{22}}-\frac{M_{12}}{R_{11}} \quad (20)$$

$$M_{12}-M_{21}=\frac{h^2}{24}\left(\frac{1}{R_{22}}-\frac{1}{R_{11}}\right)(N_{12}+N_{21})\left[1+\frac{1}{24}\left(\frac{h}{R_{22}}-\frac{h}{R_{11}}\right)^2\right]^{-1} \quad (21)$$

Equation (21) and the assumption $h^2/R^2 \ll 1$ combine to show that the last term in (19) may be neglected in comparison with the term $(1/2Gh)\,[(N_{12}+N_{21})/2]^2$. If the last term in (19) is thus omitted, what remains is the formula

$$\Pi=\frac{1}{2Eh}(N_{11}^2+N_{22}^2-2\nu N_{11}N_{22})+\frac{1+\nu}{Eh}\left(\frac{N_{12}+N_{21}}{2}\right)^2$$
$$+\frac{6}{Eh^3}(M_{11}^2+M_{22}^2-2\nu M_{11}M_{22})+\frac{1+\nu}{Eh^3/12}\left(\frac{M_{12}+M_{21}}{2}\right)^2$$
$$+\frac{1}{Eh}\left(\frac{1}{R_{22}}-\frac{1}{R_{11}}\right)(N_{22}M_{22}-N_{11}M_{11}) \quad (22)$$

To obtain from (22) the corresponding expression for Love's first-approximation theory, it must be assumed that the order-of-magnitude relations $M = O(hN)$ hold and that h/R (not merely h^2/R^2) is negligible in comparison with unity. The identities (20) and (21) become, to this degree of approximation $N_{12} = N_{21}$, $M_{12} = M_{21}$, and the N-M coupling terms in the last line of (22) become negligible in comparison with the remaining terms.

Equation (22) is identical with the second of two strain-energy expressions given by Trefftz[3] and used by him in conjunction with the Lagrange multiplier method in order to obtain the system of stress-strain relations to which we have referred previously. The first of the two strain-energy expressions which Trefftz used is that leading to Love's first-approximation theory.

Strain-Energy Density for Arbitrary Orthogonal Co-ordinates

We finally give the form assumed by the strain-energy expression (22) when the curvilinear middle-surface co-ordinates ξ_1, ξ_2, are orthogonal but do not necessarily coincide with the lines of curvature of the middle surface.

By applying transformation formulas of the type discussed by the authors[2] for the quantities N, M and $1/R$, the strain-energy density of (22) may be written in terms of quantities referring to such an arbitrary orthogonal system. There results, in the notation of the earlier paper,[2] the following expression:

$$\Pi=\frac{1}{2Eh}(N_{11}^2+N_{22}^2-2\nu N_{11}N_{22})+\frac{1+\nu}{Eh}\left(\frac{N_{12}+N_{21}}{2}\right)^2$$
$$+\frac{6}{Eh^3}(M_{11}^2+M_{22}^2-2\nu M_{11}M_{22})+\frac{1+\nu}{Eh^3/12}\left(\frac{M_{12}+M_{21}}{2}\right)^2$$
$$+\frac{1}{Eh}\left[\left(\frac{1}{R_{22}}-\frac{1}{R_{11}}\right)(N_{22}M_{22}-N_{11}M_{11})+\frac{1}{R_{12}}(N_{11}+N_{22})(M_{12}+M_{21})+\frac{1}{R_{12}}(N_{12}+N_{21})(M_{11}+M_{22})\right] \quad (23)$$

Equation (23) reduces to (22) when $1/R_{12} = 0$.

B. KARUNES
Department of Applied Physics,
University of Calcutta,
Calcutta, India.
Mem. ASME

E. T. ONAT
Associate Professor,
Division of Engineering,
Brown University,
Providence, R. I.
Assoc. Mem. ASME

On the Effect of Shear on Plastic Deformation of Beams Under Transverse Impact Loading[1]

The impact problem for a rigid-plastic beam is formulated by using an interaction curve relating shearing force and bending moment for fully plastic action, and allowing for shear and rotary inertia effects. Using a simplified interaction diagram, the problem of point-impact loading is solved for a special case. The analysis shows that the shear effects are of considerable importance when the parameter $\mu_0 = 2Q_0l/M_0$ is less than 20 where Q_0 and M_0 are plastic-carrying capacities of the cross section for pure shear and bending, respectively, and $2l$ is the length of the beam.

In a recent paper Bleich and Shaw [1][2] have shown that all beams, even those which are statically much stronger in shear than in bending, will begin to yield in shear before yielding in bending, if subjected to sufficiently high initial velocity distributions. This conclusion is drawn from an elastic approach based on the well-known differential equations for the Timoshenko beam.

On the other hand, after the completion of the present note the authors' attention was drawn to a paper by Salvadori and Weidlinger [2] where a simply supported rigid-plastic beam was considered under uniformly distributed blast pressure. These authors showed that the beam may deform plastically by developing plastic slides at the supports in addition to the assumed single-hinge rotation at the mid-section due to yielding in bending. For certain values of the relevant parameters only shear action occurs, while for other values shearing and bending take place simultaneously. Among other things the paper indicates that, on the basis of rigid-plastic theory, yielding in shear will occur if the beam under static loads is either of about equal strength in shear and in bending, or weaker in shear than in bending.

In the present paper a free-free, rigid, ideally plastic beam is considered which is subjected to point impact at the mid-point, the impact velocity being kept constant for subsequent times. In the early stages of the ensuing motion both shear and bending effects are important at the point of impact so that plastic interaction of shearing force Q with the bending moment M must be included into the analysis of the plastic deformations of the beam. It is well known [3] that an interaction curve relating shearing force and bending moment for fully plastic action does not really exist because the geometry and loading of the entire beam are important, not the properties of the section alone. Nevertheless, in view of the fact that very few two or three-dimensional solutions are available, it seemed worth while to use approximate interaction curves for Q and M in the formulation of the present problem.

In the following section a typical interaction curve and the associated flow rule are discussed. Various approximations are suggested for the interaction curve in order to simplify the resulting mathematical problem. Timoshenko's equations for rotary and translatory motion of a beam element are then supplemented by two linear equations obtained from a linearized interaction curve and the associated flow rule. Finally, the impact problem is discussed in detail for the case of the square interaction diagram. The mathematical analysis is comparatively simple in this case and can be based on previous work by Symonds [4], and Symonds and Leth [5].

Interaction Curve for Shear and Bending—the Flow Rule

Various interaction curves for rigid-plastic beams have been proposed [3], [6–10] by several authors. Among these, mention will be made of the simplified curve suggested by Drucker [3] for rectangular cross sections which is given by the equation

$$\left|\frac{M}{M_0}\right| = 1 - \left(\frac{Q}{Q_0}\right)^4 \tag{1}$$

where M_0 and Q_0 are the carrying capacities of the cross section for pure bending and pure shear, respectively. The curve is composed of two arcs, FHL and FNL, as shown in Fig. 1. The nondimensional stress resultants, Q/Q_0 and M/M_0, may be thought

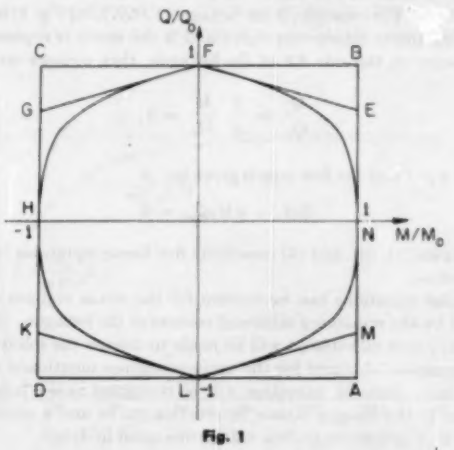

Fig. 1

[1] The results presented in this paper were obtained in the course of research conducted under Contract Nonr 562(10) by the Office of Naval Research and Brown University.

[2] Numbers in brackets designate References at end of paper.

Presented at the West Coast Conference of the Applied Mechanics Division, Stanford, Calif., September 9–11, 1959, of The American Society of Mechanical Engineers.

Discussion of this paper should be addressed to the Secretary, ASME, 29 West 39th Street, New York, N. Y., and will be accepted until April 10, 1960, for publication at a later date. Discussion received after the closing date will be returned.

Note: Statements and opinions advanced in papers are to be understood as individual expressions of their authors and not those of the Society. Manuscript received by ASME Applied Mechanics, December 8, 1958. Paper 59—APMW-7.

of as defining a stress point in Fig. 1. The physical meaning of the curve *FHLN* is as follows: If the stress point associated with a generic element of the beam falls within the area bounded by this curve, then no plastic action takes place at this element. On the other hand, if the stress point is situated on the interaction curve the element may deform plastically. The nature of the plastic deformation is determined from the flow rule. Following previous work on arches [11], where interaction of bending moment with axial force was studied, we shall assume the following flow rule: The vector with the components $M_0\dot{\kappa}$, $Q_0\dot{\beta}$ is normal to the interaction curve at the stress point considered. Here $\dot{\kappa}$ is the rate of change of curvature and $\dot{\beta}$ is the rate of change of shear slope at the plastically deforming element. For a corner state of stress such as F the vector $(M_0\dot{\kappa}, Q_0\dot{\beta})$ is not uniquely determined; it must lie between the normals drawn to the adjacent arcs at the corner point considered.

For mathematical convenience it is customary to approximate the interaction curve by a polygon such as the hexagon shown in Fig. 1.

In sandwich beams or I-sections, bending and shear rigidity are provided by two essentially distinct means so that the use of the square interaction diagrams *ABCD* in Fig. 1 may be quite adequate for the discussion of the plastic deformations of such beams.

Basic Equations

The equations of motion for the Timoshenko beam may be adopted for the present discussion. These equations incorporate shear and rotary inertia effects and with the notation and sign conventions introduced in Fig. 2(*d*) they can be written as

$$\begin{aligned} M_x - Q &= -\rho I_0 \psi_{tt} \\ Q_x &= \rho A_0 y_{tt} \\ y_x &= \psi + \beta \end{aligned} \tag{2}$$

where ψ, β, and y_x are the flexural, shear, and total slope of the neutral axis, respectively, ρ is the density of the material, I_0 is the moment of inertia of the cross section, A_0 is the cross-sectional area, and subscripts denote partial differentiation.

Two additional equations relating the five unknowns ψ, β, y, Q, and M are required. For elastic beams, the familiar relations $Q = kA_0G\beta$ and $M = -EI\psi_x$ provide two more equations. For rigidly moving portions of a rigid-plastic beam, the two additional equations are $\beta_t = 0$ and $\psi_{xt} = 0$. On the other hand, for plastically deforming portions of the beam, the interaction diagram and the associated flow rule must be used to obtain additional information. For example, if the hexagon *EFGKLM*, Fig. 1, is used as approximate interaction curve and if the stress is represented by a point on the side *EF* of the hexagon, then stresses satisfy

$$\frac{Q}{Q_0} + \frac{1}{a}\frac{M}{M_0} = 1 \tag{3}$$

where $a > 1$ and the flow rule is given by

$$Q_0\beta_t + aM_0\psi_{xt} = 0 \tag{4}$$

Equations (2), (3), and (4) constitute five linear equations for five unknowns.

Similar equations can be written for the stress regimes represented by the remaining sides and corners of the hexagon. In the present paper no attempt will be made to discuss the solutions of the equations obtained for the various regimes mentioned in the foregoing. Instead, attention will be restricted in the following section to the simpler square interaction curve and a particular problem of impulsive motion will be discussed in detail.

Square Interaction Diagram

We consider the problem of a uniform beam whose mid-point is suddenly moved with the velocity V which is normal to the beam axis. The mid-point velocity is kept at the constant value V for subsequent times. The beam has the square interaction diagram shown in Fig. 1, has mass per unit length m, and length $2l$. The ends are unconstrained. We are interested in the plastic deformations produced by the impact loading as described.

The following analysis shows that for all values of the relevant parameter $\mu_0 = 2Q_0l/M_0$, the plastic action takes place in discrete sections, so that equations of motion of rigidly moving portions may be used instead of Timoshenko equations (2).

It is easily verified that for $\mu_0 < 4$ the plastic deformation occurs as shear slides which develop immediately to right and left of the mid-section, Fig. 2(*a*). It is found that $|M| < M_0$ everywhere, so that no bending action occurs, but sliding continues until the whole beam has the velocity V. When the parameter μ_0 satisfies the inequality $4 < \mu_0 < 22.8$, the sliding at the point of impact is accompanied by the development of yield hinges to the right and left of impact point in the early stages of motion, Fig. 2(*b*). It is easily seen that the stress point corresponding to the combined slide and hinge to the right of mid-point is at the point C, while the stress points corresponding to the remaining section of the right half-beam fall within the square *ABCD* in Fig. 1. At a certain time after the impact sliding, velocity becomes zero and the further plastic deformation occurs simply as hinge action, and finally the rotation stops when the beam has the uniform velocity V.

For $\mu_0 = 22.8$ the bending moment at the cross sections whose distance from the mid-point is $0.404l$ in each half of the beam reaches the value M_0 at the first phase of motion. This observation indicates the fact that for $\mu_0 > 22.8$ two additional hinges must be expected to develop. The following analysis of the case $\mu_0 > 22.8$ follows closely the previous work by Symonds [4] and Symonds and Leth [5]. The generic mode of deformations of the right-hand half-beam is shown in Fig. 2(*c*). The co-ordinate axes x, y move with the impact point; s is the amount of sliding caused by the shear action; ξ_l denotes the distance of the lateral

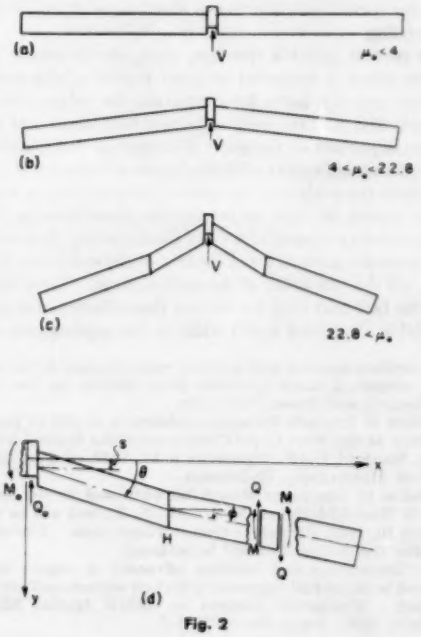

Fig. 2

hinge H from the mid-point; θ and φ are angular deformations of the segments to left and to right of the hinge H, respectively. A dimensionless time η is defined as $\eta = t/\tau$ and dimensionless angular and sliding velocity quantities are introduced as follows:

$$\Omega = \frac{ml^2}{M_0\tau}\dot{\theta}, \quad \psi = \frac{ml^2}{M_0\tau}\dot{\varphi}, \quad S = \frac{ml^2}{M_0\tau}\dot{s}$$

First phase of motion following the impact is characterized by the hinge and slide action at the root of the beam ($Q = Q_0$, $M = -M_0$) with an additional bending hinge occurring at $H(Q = 0, M = M_0)$. Under these conditions the three dynamical equations for the two segments of length ξl and $(1 - \xi)l$ are as follows:

$$\frac{dS}{d\eta} = -\frac{2\mu_0}{\xi} + \frac{12}{\xi^2}$$

$$\frac{d\Omega}{d\eta} = \frac{3\mu_0}{\xi^2} - \frac{24}{\xi^3} \tag{5}$$

$$\frac{d\psi}{d\eta} = \frac{12}{(1-\xi)^3}$$

An additional equation is provided by the relation expressing the amount of the jump in angular velocities Ω and ψ [4]·

$$\mu_0\xi + \frac{6\xi^2}{(1-\xi^3)} - 12 = -(\Omega - \psi)\xi^2\frac{d\xi}{d\eta} \tag{6}$$

It can be verified easily that Equations (5) and (6) are all satisfied with ξ equal to a constant, say ξ_0, related to μ_0 by the expression

$$\mu_0\xi_0 + \frac{6\xi_0^2}{(1-\xi_0)^2} - 12 = 0$$

Since the accelerations are all constant the Ω, ψ, and S are found by simple integrations using the initial conditions $\Omega = \psi = 0$ and $S = ml^2V/M_0\tau$ at $\eta = 0$. If τ is chosen as

$$\tau = \frac{ml^2V}{M_0}\left(\frac{2\mu_0}{\xi_0} + \frac{12}{\xi_0^2}\right)^{-1}$$

then it is found that the dimensionless shear velocity S becomes zero when $\eta = 1$. At this instant dimensionless angular velocities are

$$\Omega_1 = \frac{3\mu_0}{\xi_0^2} - \frac{24}{\xi_0^3}, \quad \psi_1 = \frac{12}{(1-\xi_0)^2} \tag{7}$$

and the rotation angle of the first hinge is given by

$$\theta_1 = \frac{M_0\tau^2}{2ml^2}\left(\frac{3\mu_0}{\xi_0} - \frac{24}{\xi_0^3}\right) \tag{8}$$

For $\eta > 1$ no further sliding action takes place at the root of the beam. The shearing force Q at the mid-section remains smaller than Q_0 and must now be determined by the equations of motion. The equations governing this phase of motion are obtained from (5) and (6) by putting $dS/d\eta = 0$ and replacing μ_0 by $\mu = 2Ql/M_0$.

The integrations of the modified equations are best carried out by eliminating ψ and Ω from (5) and (6) and by integrating the remaining equation once to obtain [5]

$$\frac{d\xi}{d\eta} = \frac{1}{A} = e^{\xi/2}\frac{(1-2\xi)^{1/4}}{\xi} \tag{9}$$

where A is a constant. A is found using the values of Ω and ψ at $\eta = 1$, Equations (7), and is given by

$$A = e^{\xi_0/2}\frac{[(1-\xi_0)^2(3\mu_0\xi_0 - 24) - 12\xi_0^3]}{6\xi_0^2(1-\xi_0)(1-2\xi_0)^{3/4}}$$

As seen from (9), the hinge H moves out during this second phase of motion. Moreover, Equations (6) and (9) show that at the instant when the hinge H reaches the location $\xi = 0.5$,

$$\frac{d\xi}{d\eta} = \Omega - \psi = 0 \tag{10}$$

This equation suggests that during the further motion of the beam, the bending hinge at H will disappear. The angular velocity $\Omega(\eta)$ and the hinge rotation θ_2 at the instant when $\xi = 0.5$ are easily obtained by using the relation $d\Omega/d\eta = (d\Omega/d\xi)(d\xi/d\eta)$ and are given by

$$\Omega = \Omega_1 - 6A\int_0^{\xi} \frac{e^{-z/2}z^{-2}}{(1-2z)^{1/4}}\,dz \tag{11}$$

and

$$\theta_2 = \theta_1 + \frac{M_0\tau^2}{ml^2}A\int_{\xi_0}^{0.5}\frac{\Omega(z)ze^{-z/2}}{(1-2z)^{1/4}}\,dz \tag{12}$$

where Ω_1 and θ_1 are defined by (7) and (8). We note that integrations in (11) and (12) can be carried conveniently by numerical methods.

In the final phase of deformation the complete half of the beam behaves as a rigid body with a single bending hinge occurring at the root of the half-beam. The equation of motion for this phase is simply

$$\frac{d\Omega}{d\eta} = -3 \tag{13}$$

The relative motion of the half-beam with respect to x, y co-ordinate system moving with the impact point stops when Ω becomes zero. The final angle of rotation θ_f at the center hinge is found from (13)

$$\theta_f = \theta_2 + \frac{M_0\tau^2}{ml^2}\frac{\Omega_2^2}{6} \tag{14}$$

where θ_2 and Ω_2 are given by (11) and (12).

It is to be noted here that the bending-moment and shear-force distribution over the half-beam are investigated during each phase described in the foregoing to verify that (except at the critical sections included in the analysis) the stress point falls within the square interaction diagram shown in Fig. 1.

Discussion of Results

The dimensionless final hinge rotation $M_0\theta_f/mlV^2$ and dimensionless shear sliding M_0s/ml^2V^2 at the root of the half-beam are computed using the analysis described in the previous section as functions of the relevant parameter $\mu_0 = 2Q_0l/M_0$ and shown in Fig. 3.

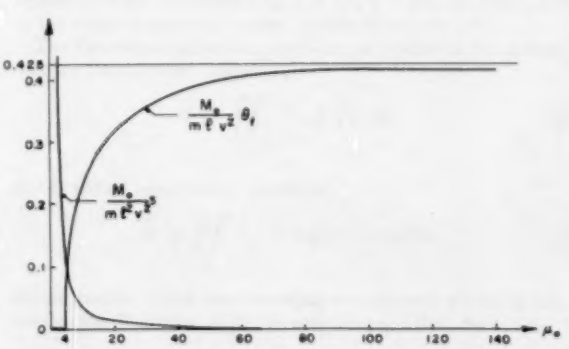

Fig. 3

It is seen from Fig. 3 that for large values of the parameter μ_0 the final angle of rotation approaches the value obtained from the analysis which neglects the shear effects altogether [5]. However, for smaller values of μ_0, say less than 30, the final angle of rotation is reduced appreciably, while for $\mu_0 < 4$ no rotation takes place. For beams of rectangular cross section composed of ideally plastic material obeying Tresca's yield condition, $Q_0 = \sigma_0 hb/2$ and $M_0 = \sigma_0 h^2 b$, where σ_0 is the yield stress in pure tension, b is the width, and h is the height of the beam. Hence for such beams the parameter $\mu_0 = 2Q_0 l/M_0 = 4l/h$. On the other hand, for I-beams the cross-sectional shear area is much smaller compared with the corresponding full rectangular cross section, while bending strength is not affected appreciably. Thus for I-beams a fraction of $4l/h$, say $0.5l/h$, may be taken as a representative value for μ_0. For comparatively long I-beams, say $l/h \leq 40$, μ_0 is less than 20 and, according to Fig. 3, shear effects are quite important and they reduce the final angle of rotation θ_f, while also causing appreciable shear sliding at the root. On the other hand, the influence of the shear forces for the beams of rectangular cross section is comparatively small. Within the framework of the present theory this influence becomes of importance only for $l/h \leq 5$ ($\mu_0 = 20$). It is to be noted, however, that, in static loading, the shear effects become appreciable for much smaller values of l/h compared with the afore-mentioned values for I-beams and for beams of rectangular cross section.

References

1 H. H. Bleich and R. Shaw, "Dominance of Shear Stresses in Early Stages of Impulsive Motion of Beams," Columbia University Technical Report No. 20 to Office of Naval Research, Project NR 360.002, October, 1957.

2 M. G. Salvadori and P. Weidlinger, "On the Dynamic Strength of Rigid-Plastic Beams Under Blast Loads," *Proceedings of ASCE, Journal of the Engineering Mechanics Division*, EM 4, Paper No. 1389, vol. 83, 1957.

3 D. C. Drucker, "The Effect of Shear on the Plastic Bending of Beams," JOURNAL OF APPLIED MECHANICS, vol. 23, TRANS. ASME, vol. 78, 1956, pp. 509–514.

4 P. S. Symonds, "Dynamic Load Characteristics in Plastic Bending of Beams," JOURNAL OF APPLIED MECHANICS, vol. 20, TRANS. ASME, vol. 75, 1953, pp. 475–481.

5 P. S. Symonds and C. F. A. Leth, "Impact of Finite Beams of Ductile Metal," *Journal of Mechanics and Physics of Solids*, vol. 2, 1954, pp. 92–102.

6 M. [illegible] Horne, "The Plastic Theory of Bending of Mild Steel Beams With Particular Reference to the Effect of Shear Forces," *Proceedings of the Royal Society of London*, series A, vol. 207, 1951, p. 216.

7 E. T. Onat and R. T. Shield, "The Influence of Shearing Forces on the Plastic Bending of Wide Beams," Proceedings of the Second U. S. National Congress of Applied Mechanics, University of Michigan, Ann Arbor, Mich., 1954, pp. 535–537.

8 A. P. Green, "A Theory of Plastic Yielding Due to Bending of Cantilevers and Fixed End Beams," *Journal of the Mechanics and Physics of Solids*, vol. 3, 1954, part I, pp. 1–15, part II, pp. 143–155.

9 C. F. A. Leth, "The Effect of Shear Stresses on the Carrying Capacity of I-Beams," DAM Report No. A11-107, Brown University, Providence, R. I., 1954.

10 P. G. Hodge, Jr., "Interaction Curves for Shear and Bending of Plastic Beams," JOURNAL OF APPLIED MECHANICS, vol. 24, TRANS. ASME, vol. 79, 1957, pp. 453–456.

11 E. T. Onat and W. Prager, "Limit Analysis of Arches," *Journal of the Mechanics and Physics of Solids*, vol. 1, 1953, p. 77.

The Half-Space Under Pressure Distributed Over an Elliptical Portion of Its Plane Boundary[1]

H. DERESIEWICZ
Associate Professor,
Department of Mechanical Engineering,
Columbia University, New York, N. Y.
Mem. ASME

In determining the safety of foundations the assumption is usually made that the pressure distribution on the ground, in general unknown, is closely approximated by a constant one. Mathematically, the problem is thereby reduced to finding the components of stress and displacement in a half-space due to a uniform pressure on a portion of its plane boundary. The present paper contains an investigation of this problem for the case of loading over an area bounded by an ellipse. Two of the results are: (a) On the normal to the loading area through its center, the two principal stresses in planes parallel to the undeformed surface, compressive on and near the surface, become tensile within a depth smaller than the length of the corresponding principal axis of the loading area; (b) the normal deflection of the surface is greater at the extremity of the minor axis of the loading area than at the extremity of the major axis, the difference between the two values increasing with the ellipticity of the bounding curve.

THE problem of determining the components of displacement and stress in a semi-infinite solid, arising from the application of normal traction arbitrarily distributed over a finite portion of the bounding plane, was first solved by Lamé and Clapeyron [1].[2,3] The result, however, was expressed in terms of quadruple infinite integrals which did not lend themselves readily to further evaluation. Subsequently, a much more manageable general solution was obtained by Boussinesq[4] in terms of potential functions, and employed by him in the analysis of effects of a variety of particular load distributions.

Still another method of solution, in terms of integrals of Bessel functions, but valid only for cases of axially symmetric loading, was devised by Lamb [2] and employed by Terazawa [3] to find the stress and displacement due to, in particular, a constant pressure distributed over a circular area. The method of potentials was extended further by Love [4], and applied to derive Terazawa's solution and the solution for the case of constant pressure over a rectangular area.

These problems are of considerable importance in determining the safety of foundations, the assumption being made that the pressure distribution on the ground (the half-space), which in general is not known, does not differ sensibly from a uniform one. In the present paper, Boussinesq's potentials are used to study the effect of such a distribution of pressure over an elliptic area. Displacement and stress are determined on the surface of the half-space and on the normal to the surface through the centroid of the loading area; the inherent great mathematical complexity precludes, however, finding a solution in closed form for an arbitrary point in the body. Among other results, it is found that the component of displacement normal to the undeformed surface is always greater at the extremity of the minor axis of the loading area than at the corresponding point of the major axis, this difference increasing with increasing ellipticity of the boundary. Another interesting outcome of the investigation is the fact that, on the centroidal normal to the area of loading, the two principal stresses in planes parallel to the undeformed surface decrease, with distance into the interior, from their respective maximum compressive values at the surface, change sign within a depth smaller than the length of the corresponding principal axis of the loading area, reach their maximum tensile value a short distance below this point, and then decrease monotonically and asymptotically to zero.

The Potential Functions

We choose a set of Cartesian axes such that the plane $z = 0$ coincides with the boundary of the solid, the z-axis being directed into the interior. If x, y, z denote the co-ordinates of an arbitrary point within the body, and $\xi, \eta, 0$ those of a point on the boundary, then

$$r = [(\xi - x)^2 + (\eta - y)^2 + z^2]^{1/2} \tag{1}$$

represents the distance between the two points. In general, the applied pressure is a function of ξ, η, i.e., $q = q(\xi, \eta)$, with $q = 0$ in the region exterior to a given simple closed curve $\mathfrak{C}$.

The Boussinesq potentials which are of interest in the present case are the "inverse" potential,[5]

$$V = \iint_{\mathfrak{D}} \frac{1}{r} q(\xi, \eta) d\xi d\eta, \tag{2}$$

and the "first logarithmic" potential,

$$\Psi = \iint_{\mathfrak{D}} q(\xi, \eta) \log (r + z) d\xi d\eta, \tag{3}$$

the integration in each case extending over the area of loading, i.e., the domain $\mathfrak{D}$ interior to $\mathfrak{C}$. It may be noted that, for $z > 0$,

[1] This investigation was supported by the Office of Naval Research under Contract Nonr-266(09) with Columbia University.

[2] Numbers in brackets designate References at end of paper.

[3] Reference [1], vol. 1, pp. 552–553.

[4] Ibid., vol. 2, part 2, p. 243, et seq.

Contributed by the Applied Mechanics Division and presented at the Annual Meeting, Atlantic City, N. J., November 29–December 4, 1959, of THE AMERICAN SOCIETY OF MECHANICAL ENGINEERS.

Discussion on this paper should be addressed to the Secretary, ASME, 29 West 39th Street, New York, N. Y., and will be accepted until April 10, 1960, for publication at a later date. Discussion received after the closing date will be returned.

NOTE: Statements and opinions advanced in papers are to be understood as individual expressions of their authors and not those of the Society. Manuscript received by ASME Applied Mechanics Division, December 19, 1958. Paper No. 59—A-17.

[5] This represents the Newtonian potential of a uniplanar distribution of mass of density q.

$$\nabla^2 V = 0, \quad \nabla^2 \Psi = 0, \quad \frac{\partial \Psi}{\partial z} = V \tag{4}$$

The pressure q applied on the loading region produces, in the absence of applied shearing stresses, a displacement and stress, at the point x, y, z, whose components are, respectively,[6]

$$u = -\frac{1}{4\pi\mu}\left[(1-2\nu)\frac{\partial \Psi}{\partial x} + z\frac{\partial V}{\partial x}\right]$$

$$v = -\frac{1}{4\pi\mu}\left[(1-2\nu)\frac{\partial \Psi}{\partial y} + z\frac{\partial V}{\partial y}\right] \tag{5}$$

$$w = \frac{1}{4\pi\mu}\left[2(1-\nu)V - z\frac{\partial V}{\partial z}\right]$$

and

$$\sigma_x = \frac{1}{2\pi}\left[2\nu\frac{\partial V}{\partial z} - (1-2\nu)\frac{\partial^2 \Psi}{\partial x^2} - z\frac{\partial^2 V}{\partial x^2}\right]$$

$$\sigma_y = \frac{1}{2\pi}\left[2\nu\frac{\partial V}{\partial z} - (1-2\nu)\frac{\partial^2 \Psi}{\partial y^2} - z\frac{\partial^2 V}{\partial y^2}\right]$$

$$\sigma_z = \frac{1}{2\pi}\left(\frac{\partial V}{\partial z} - z\frac{\partial^2 V}{\partial z^2}\right) \tag{6}$$

$$\tau_{yz} = -\frac{z}{2\pi}\frac{\partial^2 V}{\partial y \partial z}, \quad \tau_{xz} = -\frac{z}{2\pi}\frac{\partial^2 V}{\partial x \partial z}$$

$$\tau_{xy} = -\frac{1}{2\pi}\left[(1-2\nu)\frac{\partial^2 \Psi}{\partial x \partial y} + z\frac{\partial^2 V}{\partial x \partial y}\right]$$

where μ is the shear modulus and ν is Poisson's ratio.

Displacement and Stress on the Surface (z = 0)

At an Interior Point of the Loading Area. It is convenient to introduce the following auxiliary co-ordinates: with $Q(\xi, \eta)$ denoting a source point and $M(x, y)$ a field point, let r_0 represent the distance $\overline{MQ}$ and φ the angle between $\overline{MQ}$ and the positive x-direction. Then

$$\xi - x = r_0 \cos\varphi$$
$$\eta - y = r_0 \sin\varphi \tag{7}$$

and r_0 is given by the positive root of

$$r_0^2 = (\xi - x)^2 + (\eta - y)^2 \tag{8}$$

In addition, the co-ordinates of the field point may be expressed in terms of the usual polar co-ordinates, viz.,

$$x = \rho\cos\theta, \quad y = \rho\sin\theta \tag{9}$$

To determine the limits of integration in (2) and (3), we note that, if the boundary curve $\mathfrak{C}$ of the loading area $\mathfrak{D}$ is an ellipse, then, on this curve,

$$\frac{\xi^2}{a^2} + \frac{\eta^2}{b^2} - 1 = 0 \tag{10}$$

Hence the distance, R, from a field point $M(x, y)$ to a point on $\mathfrak{C}$, obtained from (7) and (10), is given by a root of

$$\left(\frac{x + R\cos\varphi}{a}\right)^2 + \left(\frac{y + R\sin\varphi}{b}\right)^2 - 1 = 0 \tag{11}$$

Choosing the positive sign on the radical, we get

$$R = [-B + (B^2 - AC)^{1/2}]/A, \tag{12}$$

where

$$A = b^2\cos^2\varphi + a^2\sin^2\varphi$$
$$B = b^2 x\cos\varphi + a^2 y\sin\varphi \tag{13}$$
$$C = b^2x^2 + a^2y^2 - a^2b^2$$

Thus the inverse potential, (2), for the interior of the loading area, i.e., $z = 0$, $C < 0$, may be written

$$V = \int_0^{2\pi}\int_0^R q(r_0, \varphi) dr_0 d\varphi \tag{14}$$

For the case of uniform pressure, of magnitude q_0, (14) reduces to[7]

$$V = q_0 \int_0^{2\pi} R d\varphi \tag{15}$$

where R is given by (12) and (13).

The symmetry properties of the function $f(\varphi) = B/A$, appearing in (12), are such that its integral over the interval $0 \leq \varphi \leq 2\pi$ vanishes identically. After some algebraic manipulation, the remaining part of (15) may be put in the form

$$V = q_0 a \int_0^{2\pi} \frac{(1 - e^2\sin^2\varphi - k^2\sin^2\psi)^{1/2}}{1 - e^2\sin^2\varphi} d\varphi \tag{16}$$

where[8]

$$\psi = \varphi - \theta,$$
$$0 \leq k = \rho/b < 1, \quad \text{subject to } C < 0, \tag{17}$$
$$0 \leq e = (1 - a^2/b^2)^{1/2} \leq 1,$$

e being the eccentricity[9] of the elliptic boundary.

Two exact solutions can be extracted immediately from (16): the potential at the center of the elliptic loading area ($k = 0$),

$$V_c = 4q_0 a\mathbf{K}(e), \tag{18}$$

and the potential at any point of a circular loading area ($e = 0$),

$$V_{\text{circle}} = 4q_0 a\mathbf{E}(k), \tag{19}$$

where $\mathbf{K}$ and $\mathbf{E}$ denote the complete elliptic integrals of the first and second kind, respectively.

An analytical evaluation of (16), for arbitrary values of k and e, does not appear feasible. As a consequence, we content ourselves with two sets of approximate solutions: one for elliptical boundaries which do not deviate radically from circular shape, and the other for field points near the center of arbitrarily shaped elliptic loading areas.

(a) Let us first take up the case of small ellipticity; i.e., $e \ll 1$. We may then expand (16) in a series of ascending powers of e^2, k remaining arbitrary in its interval of validity. With the independent variable changed to ψ, and the notation $\delta \equiv (1 - k^2\sin^2\psi)^{1/2}$, the initial terms of the expansion read[10]

$$V/q_0 a = \int_{-\theta}^{2\pi-\theta} \delta d\psi + e^2\left[\sin^2\theta\int_{-\theta}^{2\pi-\theta}(\delta - 1/2\delta)d\psi + \cos 2\theta\int_{-\theta}^{2\pi-\theta}(\delta - 1/2\delta)\sin^2\psi d\psi\right] +$$

[6] The form of these expressions is, in effect, due to Hertz [5].

[7] This expression represents the potential of a homogeneous elliptic disk at one of its points. An alternative expression, for an arbitrary point in space, was first given, in terms of quadrature, by Cayley [6].

[8] It should be noted that θ is constant in this integration.

[9] We have chosen b to denote the length of the major axis.

[10] We have omitted from (20) all terms having antisymmetric integrands, since they vanish identically upon integration between the indicated limits.

$$+ e^4\left[\sin^4\theta\int_{-\theta}^{2\pi-\theta}(\delta - 1/2\delta - 1/8\delta^3)d\psi + (\cos 2\theta - \cos 4\theta)\int_{-\theta}^{2\pi-\theta}(\delta - 1/2\delta - 1/8\delta^3)\sin^2\psi d\psi + \cos 4\theta\int_{-\theta}^{2\pi-\theta}(\delta - 1/2\delta - 1/8\delta^3)\sin^4\psi d\psi\right] \quad (20)$$

Accordingly, the normal component of displacement at a point of the loaded portion, obtained from (5) and (20), is given by[11]

$$[w]_{\substack{z=0\\C<0}} = \frac{1-\nu}{2\pi\mu}[V]_{\substack{z=0\\C<0}} \cong \frac{2(1-\nu)q_0a}{\pi\mu}\left[\mathbf{E}(k) + \frac{1}{12k^2}(a_1 + a_2\cos 2\theta)e^2 + \frac{(1-k^2)^{-1}}{240k^4}(b_1 + b_2\cos 2\theta + b_3\cos 4\theta)e^4\right], \quad (21)$$

where

$$\left.\begin{aligned} a_1 &= 3k^2(2\mathbf{E} - \mathbf{K})\\ a_2 &= 2(1+k^2)\mathbf{E} - (2+k^2)\mathbf{K}\\ b_1 &= 45k^4[(7/4 - 2k^2)\mathbf{E} - (1-k^2)\mathbf{K}]\\ b_2 &= 5k^2[(2 + 3k^2 - 8k^4)\mathbf{E} - 2(1 + k^2 - 2k^4)\mathbf{K}]\\ b_3 &= (12 - 10k^2 - k^4 - k^6)\mathbf{K} - (12 - 4k^2 - 9k^4/4 - 2k^6)\mathbf{E}\end{aligned}\right\} \quad (22)$$

and the elliptic integrals are functions of the modulus k.

Equation (21) yields as its first approximation (i.e., for $e = 0$) the expression

$$w = \frac{2(1-\nu)q_0a}{\pi\mu}\mathbf{E}(k); \quad (23)$$

this is the exact value of w corresponding to a circular loading area and is derivable from the potential in (19). On the other hand, at the center of the ellipse of loading (i.e., for $k = 0$), (21) reduces to

$$w = \frac{(1-\nu)q_0a}{\mu}\left(1 + \frac{e^2}{4} + \frac{9e^4}{64}\right); \quad (24)$$

this represents a displacement equivalent to one derived from a three-term expansion of the potential in (18).

(*b*) Now let us investigate the case of arbitrary eccentricity of the bounding ellipse, with our attention confined to field points in the vicinity of the center; i.e, $k \ll 1$. This time, the approximation to (16) is accomplished by expanding in powers of k^2. With $\Delta \equiv (1 - e^2\sin^2\varphi)^{1/2}$, the first three terms of the expansion are

$$V/q_0a = \int_0^{2\pi}\Delta^{-1}d\varphi - (k^2/2)\left[\sin^2\theta\int_0^{2\pi}\Delta^{-3}d\varphi + \cos 2\theta\int_0^{2\pi}\Delta^{-3}\sin^2\varphi d\varphi\right] - (k^4/8)\left[\sin^4\theta\int_0^{2\pi}\Delta^{-5}d\varphi + (\cos 2\theta - \cos 4\theta)\int_0^{2\pi}\Delta^{-5}\sin^2\varphi d\varphi + \cos 4\theta\int_0^{2\pi}\Delta^{-5}\sin^4\varphi d\varphi\right] \quad (25)$$

Accordingly, the normal displacement becomes

$$[w]_{\substack{z=0\\k^2<<1}} \cong \frac{2(1-\nu)q_0a}{\pi\mu}\left[\mathbf{K}(e) - \frac{(1-e^2)^{-1}}{4e^2}(\alpha_1 + \alpha_2\cos 2\theta)k^2 - \frac{(1-e^2)^{-2}}{192e^4}(\beta_1 + \beta_2\cos 2\theta + \beta_3\cos 4\theta)k^4\right] \quad (26)$$

where

$$\left.\begin{aligned} \alpha_1 &= e^2\mathbf{E}\\ \alpha_2 &= (2-e^2)\mathbf{E} - 2(1-e^2)\mathbf{K}\\ \beta_1 &= 3e^4[2(2-e^2)\mathbf{E} - (1-e^2)\mathbf{K}]\\ \beta_2 &= 4e^2[2(1-e^2+e^4)\mathbf{E} - (2-3e^2+e^4)\mathbf{K}]\\ \beta_3 &= (1-e^2)(16 - 16e^2 - e^4)\mathbf{K} - (16 - 24e^2 + 4e^4 + e^6)\mathbf{E}\end{aligned}\right\} \quad (27)$$

In these expressions the elliptic integrals are functions of the eccentricity, e.

The first approximation to (26),

$$w = \frac{2(1-\nu)q_0a}{\pi\mu}\mathbf{K}(e), \quad (28)$$

represents the exact displacement at the center, for which an approximate expression was derived in (24). On the other hand, for $e = 0$, (26) yields

$$w = \frac{(1-\nu)q_0a}{\mu}\left(1 - \frac{k^2}{4} - \frac{3k^4}{64}\right), \quad (29)$$

which is an approximation to the exact expression, (23).

We now turn our attention to the remaining components of displacement in the loading region. By (5), these are proportional to the corresponding first derivatives of the logarithmic potential (3) on $z = 0$, which, for a uniform pressure, are given by

$$\frac{1}{q_0}\left[\frac{\partial\Psi}{\partial x}\right]_{\substack{z=0\\C<0}} = -\iint_{\mathfrak{D}}\frac{\cos\varphi}{r_0}d\xi d\eta = -\int_0^{2\pi}R\cos\varphi d\varphi$$
$$\frac{1}{q_0}\left[\frac{\partial\Psi}{\partial y}\right]_{\substack{z=0\\C<0}} = -\iint_{\mathfrak{D}}\frac{\sin\varphi}{r_0}d\xi d\eta = -\int_0^{2\pi}R\sin\varphi d\varphi \quad (30)$$

With R expressed by (12), each of the integrals in (30) may be split into two parts. One part, involving $(B^2 - AC)^{1/2}$, vanishes identically by virtue of the antisymmetry of the integrand. The remaining part is easily integrated, with the result[12]

$$[u]_{\substack{z=0\\C<0}} = -\frac{(1-2\nu)q_0x}{2\mu(1+a/b)}$$
$$[v]_{\substack{z=0\\C<0}} = -\frac{(1-2\nu)q_0y}{2\mu(1+b/a)} \quad (31)$$

The displacement components (31) were previously obtained by Way [9], who noted that the resultant displacement in the plane $z = 0$, $(u^2 + v^2)^{1/2}$, is constant around ellipses homothetic with, and interior to, the bounding ellipse $\mathfrak{C}$. Way also computed the components of stress on the surface, which we list[13] (for $C < 0$) in the interest of completeness:

$$\frac{\sigma_x}{q_0} = -\frac{1 + 2\nu(1-e^2)^{1/2}}{1 + (1-e^2)^{1/2}}$$
$$\frac{\sigma_y}{q_0} = -\frac{2\nu + (1-e^2)^{1/2}}{1 + (1-e^2)^{1/2}} \quad (32)$$

[11] In evaluating the various integrals, the tables by Gröbner and Hofreiter [7] were found to be very useful.

[12] It is of interest that these formulas may be extracted from the expressions for the components of Newtonian attraction at an interior point of a homogeneous elliptic cylinder; see p. 71 of [8].

[13] Way's expressions are here written for the case $b \geq a$.

$$\frac{\sigma_z}{q_0} = -1, \quad \tau_{xy} = \tau_{xz} = \tau_{yz} = 0 \qquad (32\ cont.)$$

Thus the components of stress have constant values within the loading area and the principal directions are parallel to the co-ordinate axes.

At an Exterior Point of the Loading Area. If the field point $M(x, y)$ is located outside the loading area $\mathfrak{D}$, then the limits of integration in (14) are

$$V = \int_{\varphi_1}^{\varphi_2} \int_{R_1}^{R} q(r_0, \varphi) dr_0 d\varphi, \qquad (33)$$

where R is given by (12) and R_1 is obtained from (12) by changing the algebraic sign of the radical.

The limiting angles φ_1 and φ_2 represent the angles which the lines passing through M and tangent to the bounding ellipse $\mathfrak{C}$ form with the x-axis. Thus if T denotes such a point of tangency, its co-ordinates $(\bar{\xi}, \bar{\eta})$ must satisfy the equation of the ellipse,

$$\frac{\bar{\xi}^2}{a^2} + \frac{\bar{\eta}^2}{b^2} - 1 = 0, \qquad (34)$$

and the equation of the line $\overline{MT}$,

$$\frac{\bar{\xi} - x}{\bar{\eta} - y} = \tan \varphi = \frac{d\bar{\eta}}{d\bar{\xi}} \qquad (35)$$

Now, from (34), we find

$$\frac{d\bar{\eta}}{d\bar{\xi}} = -\frac{b^2\bar{\xi}}{a^2\bar{\eta}}, \qquad (36)$$

so that the equation of the tangent line (35) becomes

$$\frac{\bar{\xi}x}{a^2} + \frac{\bar{\eta}y}{b^2} - 1 = 0. \qquad (37)$$

The values of $\bar{\xi}$ and $\bar{\eta}$ in terms of x and y may now be computed from (34) and (37), and the result inserted in (35) to yield an expression for $\tan \varphi$. The two values of φ arrived at in this manner are

$$\varphi_1 = \tan^{-1}\left(\frac{\tan\theta - (b/a)\tan\psi'}{1 + (a/b)\tan\theta\tan\psi'}\right)$$
$$\varphi_2 = \tan^{-1}\left(\frac{\tan\theta + (b/a)\tan\psi'}{1 - (a/b)\tan\theta\tan\psi'}\right) \qquad (38)$$

where $\tan\theta = y/x$, and $\tan\psi' = (x^2/a^2 + y^2/b^2 - 1)^{-1/2}$.

In the case of loading distributed over a circular area, $b = a$, so that (38) reduce to

$$\varphi_1 = \tan^{-1}\{\tan(\theta - \psi')\} = \pi + \theta - \psi'$$
$$\varphi_2 = \tan^{-1}\{\tan(\theta + \psi')\} = \pi + \theta + \psi' \qquad (39)$$

where, now,

$$\psi' = \tan^{-1}\{a(\rho^2 - a^2)^{-1/2}\} = \sin^{-1}(a/\rho)$$

Accordingly, we may write the initial terms in the series expression for the normal displacement, these being obtained in the manner which led to (21). In the evaluation of the elliptic integrals it is necessary, however, to distinguish between field points exterior to the bounding ellipse but interior to the circle $\rho = b$, and those exterior to this circle. Thus in the former region, $C > 0$ and $k < 1$, so that

$$[w]_{\substack{z=0\\C>0\\k<1}} = \frac{1-\nu}{2\pi\mu}\,[V]_{\substack{z=0\\C>0\\k<1}}$$

$$\cong \frac{(1-\nu)q_0 a}{\pi\mu}\left[E(\psi, k) + \frac{e^2}{12k^2}(\gamma_1 + \gamma_2\cos 2\theta + \gamma_3 \sin 2\theta)\right]_{\psi=\varphi_1-\theta}^{\psi=\varphi_2-\theta} \qquad (40)$$

where

$$\gamma_1 = 3k^2[2E(\psi, k) - F(\psi, k)]$$
$$\gamma_2 = 2(1 + k^2)E(\psi, k) - (2 + k^2)F(\psi, k) - 4k^2 \sin\psi\cos\psi(1 - k^2\sin^2\psi)^{1/2} \qquad (41)$$
$$\gamma_3 = 2(1 - 2k^2\sin^2\psi)(1 - k^2\sin^2\psi)^{1/2}$$

and $F(\psi, k)$, $E(\psi, k)$ denote incomplete elliptic integrals of the first and second kind, respectively, of argument ψ and modulus k.

On the other hand, in the region $C > 0$, $k > 1$,

$$[w]_{\substack{z=0\\C>0\\k>1}} \cong \frac{(1-\nu)q_0 a}{\pi\mu k}\left[\bar{\gamma} + \frac{e^2}{12}(\bar{\gamma}_1 + \bar{\gamma}_2\cos 2\theta + k^{-1}\gamma_3 \sin 2\theta)\right]_{\psi=\varphi_1-\theta}^{\psi=\varphi_2-\theta} \qquad (42)$$

where

$$\bar{\gamma} = k^2E - (k^2 - 1)F$$
$$\bar{\gamma}_1 = 3[2k^2E - (2k^2 - 1)F] \qquad (43)$$
$$\bar{\gamma}_2 = 2(1 + k^2)E - (1 + 2k^2)F - 4k\sin\psi\cos\psi(1 - k^2\sin^2\psi)^{1/2}$$

and the elliptic integrals are functions of argument $\beta = \arcsin(k\sin\psi)$ and modulus k^{-1}.

To determine the remaining components of displacement in the region exterior to the boundary of the loading area, we may avail ourselves of the results of the Theory of Attractions:[12]

$$[u]_{\substack{z=0\\C>0}} = -\frac{1-2\nu}{2\mu}\,\frac{q_0 abx}{a^2 + \kappa + [(a^2+\kappa)(b^2+\kappa)]^{1/2}}$$
$$[v]_{\substack{z=0\\C>0}} = -\frac{1-2\nu}{2\mu}\,\frac{q_0 aby}{b^2 + \kappa + [(a^2+\kappa)(b^2+\kappa)]^{1/2}} \qquad (44)$$

where κ is the positive root of

$$\frac{x^2}{a^2+\kappa} + \frac{y^2}{b^2+\kappa} - 1 = 0. \qquad (45)$$

An alternative expression for these two components is given by Way [9]:[13]

$$[u]_{\substack{z=0\\C>0}} = -\frac{1-2\nu}{2\mu}\,\frac{q_0 abx/\gamma}{1 + (1 + c^2/\gamma)^{1/2}}$$
$$[v]_{\substack{z=0\\C>0}} = -\frac{1-2\nu}{2\mu}\,\frac{q_0 aby/\gamma}{(1 + c^2/\gamma)^{1/2}[1 + (1 + c^2/\gamma)^{1/2}]} \qquad (46)$$

where $c^2 = b^2 - a^2 = b^2e^2$ and γ is the positive root of

$$\frac{x^2}{\gamma} + \frac{y^2}{c^2+\gamma} - 1 = 0. \qquad (47)$$

The components of stress in this region are [9][13]

$$-\frac{[\sigma_x]_{\substack{z=0\\C>0}}}{q_0} = \frac{[\sigma_y]_{\substack{z=0\\C>0}}}{q_0} = \frac{(1-2\nu)(1-e^2)^{1/2}}{e^2}\left[\frac{(1 + c^2/\gamma)^{1/2}}{1 + x^2c^2/\gamma^2} - 1\right]$$

$$\frac{[\tau_{xy}]_{\substack{z=0\\C>0}}}{q_0} = \frac{(1-2\nu)(1-e^2)^{1/2}}{e^2}\,\frac{xyc^2/\gamma^2}{(1+x^2c^2/\gamma^2)(1+c^2/\gamma)^{1/2}} \quad (48)$$

At the Boundary of the Loading Area. The Newtonian potential of a uniform elliptical disk at a point of its edge is expressible in terms of elementary functions.[14] The normal displacement may, accordingly, be written

$$[w]_{\substack{z=0\\C=0}} = \frac{2(1-\nu)q_0a}{\pi\mu e}\left\{\cos\theta_1 \tanh^{-1}\left[\frac{e\cos\theta_1}{(1-e^2\sin^2\theta_1)^{1/2}}\right] + \sin\theta_1 \tan^{-1}\left[\frac{e\sin\theta_1}{(1-e^2\sin^2\theta_1)^{1/2}}\right]\right\} \quad (49)$$

where

$$\theta_1 = \cos^{-1}(x/a) = \sin^{-1}(y/b)$$

The corresponding expression for a circular boundary may be obtained from (49) by passing to the limit as $e \to 0$. Since

$$\lim_{e\to 0}\left(\frac{\tan^{-1}\alpha e}{e}\right) = \alpha, \quad \lim_{e\to 0}\left(\frac{\tanh^{-1}\beta e}{e}\right) = \beta,$$

(49) reduces to

$$[w]_{\substack{\text{circle}\\z=0\\\rho=a}} = \frac{2(1-\nu)q_0a}{\pi\mu} \quad (50)$$

It should be noted that the components of displacement are continuous across the bounding curve $C = 0$ of the loading area, the expressions (44) reducing to (31) for $\kappa = 0$. Reduction of the alternative form, (46), is accomplished by setting $\gamma = a^2$. The components of stress, however, are discontinuous across the bounding curve, their value, approached from the outside, (48), being

$$-[\sigma_z]_{\substack{z=0\\C=0}} = [\sigma_y]_{\substack{z=0\\C=0}} = \frac{(1-2\nu)(1-e^2)^{1/2}}{e^2}\left[\frac{(1-e^2)^{1/2}}{1-e^2y^2/b^2}-1\right]q_0 \quad (51)$$

$$[\tau_{xy}]_{\substack{z=0\\C=0}} = (1-2\nu)(1-e^2)^{1/2}\left(\frac{xy/ab}{1-e^2y^2/b^2}\right)q_0$$

This discontinuity in the stress is, of course, due to the discontinuity in the applied traction. A discussion of this phenomenon is given by Love [4] who suggests that the difficulty may be obviated by specifying that the applied pressure drop rapidly, in the neighborhood of the boundary, from its constant value to zero (at the boundary).

Displacement and Stress at a Point on Normal Through Centroid of Loading Area ($\rho = 0$)

To obtain the value of the direct potential (2) at a point on the z-axis, we write

$$V = \int_0^{2\pi}\int_0^R q_0(r_0^2+z^2)^{-1/2}r_0\,dr_0\,d\varphi = q_0\int_0^{2\pi}[(R^2+z^2)^{1/2}-z]\,d\varphi \quad (52)$$

where r_0 and R are given by (8) and (12), respectively, with $x = y = 0$. Thus $R = a(1-e^2\sin^2\varphi)^{-1/2}$, so that (52) becomes

$$\frac{1}{q_0a}[V]_{\rho=0} = 4(1+\zeta^2)\int_0^{\pi/2}\left(\frac{1-f^2\sin^2\varphi}{1-e^2\sin^2\varphi}\right)^{1/2}d\varphi - 2\pi\zeta \quad (53)$$

where

$$f^2 = e^2/(1+\zeta^{-2}) \le e^2, \quad (54)$$

$$\zeta = z/a, \quad (55)$$

and e is given by the third of (17).

The integral appearing in (53) is expressible in terms of the complete elliptic integral of the third kind,[15]

$$\int_0^{\pi/2}\left(\frac{1-f^2\sin^2\varphi}{1-e^2\sin^2\varphi}\right)^{1/2}d\varphi = (1-f^2)^{-1/2}\Pi(\alpha^2,\bar{k}), \quad (56)$$

where the parameter, α, and the modulus, $\bar{k}$, are given by

$$\alpha^2 = -f^2/(1-f^2) = -e^2\zeta^2[1+(1-e^2)\zeta^2]^{-1},$$
$$\bar{k}^2 = (e^2-f^2)/(1-f^2) = e^2[1+(1-e^2)\zeta^2]^{-1}, \quad (57)$$

the expressions on the right following by virtue of (54). $\Pi(\alpha^2,\bar{k})$, in turn, is expressible in terms of the complete and incomplete elliptic integrals of the first and second kind.[16] Thus finally,

$$\frac{1}{q_0a}[V]_{\rho=0} = 4[1+(1-e^2)\zeta^2]^{-1/2}\mathbf{K}(\bar{k}) + 2\pi\zeta[\Lambda_0(\bar{\psi},\bar{k})-1] \quad (58)$$

where

$$\Lambda_0(\bar{\psi},\bar{k}) = (2/\pi)\{\mathbf{K}(\bar{k})E(\bar{\psi},\bar{k}') - [\mathbf{K}(\bar{k})-\mathbf{E}(\bar{k})]F(\bar{\psi},\bar{k}')\},$$
$$\bar{\psi} = \sin^{-1}[\alpha^2/(\alpha^2-\bar{k}^2)]^{1/2} = \sin^{-1}[\zeta(1+\zeta^2)^{-1/2}], \quad (59)$$
$$\bar{k}'^2 = 1-\bar{k}^2 = (1-e^2)(1+\zeta^2)[1+(1-e^2)\zeta^2]^{-1}$$

Further, we find that

$$\frac{1}{q_0}\left[\frac{\partial V}{\partial z}\right]_{\rho=0} = \frac{4\zeta^2}{(1+\zeta^2)^{1/2}}\int_0^{\pi/2}\left(\frac{1-e^2\sin^2\varphi}{1-f^2\sin^2\varphi}\right)^{1/2}d\varphi - 2\pi = 2\pi[\Lambda_0(\bar{\psi},\bar{k})-1]. \quad (60)[17]$$

Upon inserting (58) and (60) in the third of (5), we obtain the component of displacement normal to the undeformed bounding plane at a point on the normal to this plane through the centroid of the loading area:

$$[w]_{\rho=0} = \frac{2(1-\nu)q_0a}{\pi\mu}\left\{\frac{\mathbf{K}(\bar{k})}{[1+(1-e^2)\zeta^2]^{1/2}} + \frac{\pi(1-2\nu)}{4(1-\nu)}\zeta[\Lambda_0(\bar{\psi},\bar{k})-1]\right\}. \quad (61)$$

We note that at the centroid itself, $\zeta = \bar{\psi} = 0$, $\Lambda_0(0,\bar{k}) = 0$, and $\bar{k} = e$, so that (51) reduces to (28).

The corresponding formula for the circular loading area may be obtained by setting $e = 0$. In this case, the second of (57) yields $\bar{k} = 0$; moreover, $\mathbf{K}(0) = \pi/2$ and[18]

$$\Lambda_0(\bar{\psi},0) = \sin\bar{\psi} = \zeta(1+\zeta^2)^{-1/2}.$$

Consequently, (61) reduces to

$$[w]_{\substack{\text{circle}\\\rho=0}} = \frac{(1-\nu)q_0a}{\mu(1+\zeta^2)^{1/2}}\left\{1-\frac{1-2\nu}{2(1-\nu)}\zeta[(1+\zeta^2)^{1/2}-\zeta]\right\}. \quad (62)$$

[14] Its value is given on page 95 of [8] (where the semiaxes have been taken such that $a > b$).

[15] Reference [10], p. 166, no. 284.02.

[16] Ibid., p. 225, no. 410.01.

[17] Ibid., p. 166, no. 284.00; p. 167, no. 284.09; p. 225, no. 410.02.

[18] Ibid., p. 36, no. 151.01.

The remaining components of displacement, i.e., those parallel to the undeformed boundary, are easily shown to vanish at all points of the z-axis.

We now turn our attention to the stress component σ_z, for the evaluation of which we require the value of $\partial^2 V/\partial z^2$. We find

$$\frac{1}{q_0}\left[\frac{\partial^2 V}{\partial z^2}\right]_{\rho=0} = \frac{4}{a(1+\zeta^2)^{1/2}}\int_0^{\pi/2}\frac{(1-e^2\sin^2\varphi)^{1/2}}{(1-f^2\sin^2\varphi)^{3/2}}\,d\varphi$$

$$= \frac{4\mathbf{E}(\bar{k})}{a(1+\zeta^2)^{3/2}(1-f^2)^{1/2}}. \quad (63)^{19}$$

Thus upon inserting (60) and (63) in the third of (6), and using (55), we obtain

$$\frac{[\sigma_z]_{\rho=0}}{q_0} = \Lambda_0(\bar{\psi},\bar{k}) - 1 - \frac{2}{\pi}\frac{\zeta\mathbf{E}(\bar{k})}{(1+\zeta^2)[1+(1-e^2)\zeta^2]^{1/2}} \quad (64)$$

On the surface of the solid, $\zeta = 0$, and, since $\Lambda_0(0, 0) = 0$, (64) reduces to

$$[\sigma_z]_{\substack{z=0\\ \rho=0}} = -q_0, \quad (65)$$

which is a prescribed boundary condition. For a circular loading area, (64) becomes

$$[\sigma_z]_{\substack{\text{circle}\\ \rho=0}} = q_0[-1+\zeta^3(1+\zeta^2)^{-3/2}]. \quad (66)$$

The evaluation of the components σ_x and σ_y is considerably more involved, and will be presented here only in outline. Thus from (1) and (2) we find (for our case of $q = q_0$)

$$\frac{\partial^2 V}{\partial x^2} = q_0\iint_{\mathfrak{D}}\frac{3(\xi-x)^2-r^2}{r^5}\,d\xi d\eta, \quad (67)$$

which, for $x = y = 0$, becomes (upon changing variables to r_0 and φ and integrating with respect to the former)

$$\frac{a(1+\zeta^2)^{1/2}}{4q_0}\left[\frac{\partial^2 V}{\partial x^2}\right]_{\rho=0}$$

$$= \int_0^{\pi/2}(1-2\cos^2\varphi)\left(\frac{1-e^2\sin^2\varphi}{1-f^2\sin^2\varphi}\right)^{1/2}d\varphi$$

$$-(1+\zeta^2)^{-1}\int_0^{\pi/2}\frac{\cos^2\varphi}{1-f^2\sin^2\varphi}\left(\frac{1-e^2\sin^2\varphi}{1-f^2\sin^2\varphi}\right)^{1/2}d\varphi$$

$$= e^{-2}(1-f^2)^{-1/2}[(1-e^2)\mathbf{K}(\bar{k}) - (1-f^2)\mathbf{E}(\bar{k})] \quad (68)^{17,\,20}$$

From the first of (4) we see that

$$\frac{\partial^2 V}{\partial^2 y} = -\left(\frac{\partial^2 V}{\partial x^2} + \frac{\partial^2 V}{\partial z^2}\right), \quad (69)$$

so that, with the aid of (63) and (68), we obtain

$$\left[\frac{\partial^2 V}{\partial y^2}\right]_{\rho=0} = \frac{-4q_0(1-e^2)}{ae^2[(1+\zeta^2)(1-f^2)]^{1/2}}[\mathbf{K}(\bar{k}) - \mathbf{E}(\bar{k})]. \quad (70)$$

Further, from (3), we find

$$\frac{\partial^2\Psi}{\partial x^2} = q_0\iint_{\mathfrak{D}}\left[\frac{1}{r(z+r)} - \frac{(\xi-x)^2(z+2r)}{r^3(z+r)^2}\right]d\xi d\eta$$

$$= \frac{q_0}{z}\iint_{\mathfrak{D}}\left(\frac{\sin^2\varphi}{r} + \frac{r-z}{r_0^2}\cos 2\varphi - \frac{r_0^2}{r^3}\cos^2\varphi\right)r_0 dr_0 d\varphi \quad (71)$$

In evaluating this expression for $x = y = 0$, the integration of the first and third terms may be accomplished with the aid of formulas listed in the preceding footnotes in this section. Integration of the second term leads, in addition to terms encountered previously, to the integrals

$$\int_0^{\pi/2}\cos 2\varphi\,\log(1-e^2\sin^2\varphi)^{1/2}d\varphi$$

and

$$\int_0^{\pi/2}\cos 2\varphi\,\log[(\zeta^{-2}+1-e^2\sin^2\varphi)^{1/2} + (1-e^2\sin^2\varphi)^{1/2}]d\varphi,$$

of which the former is listed in Bierens de Haan [11] and the latter reduces, upon integration by parts, to integrals treated previously. Accordingly, (71) becomes

$$\frac{1}{4q_0}\left[\frac{\partial^2\Psi}{\partial x^2}\right]_{\rho=0} = \frac{\pi/2}{1+(1-e^2)^{1/2}} + \frac{\zeta}{(1+\zeta^2)^{1/2}}\left[\frac{1-e^2}{e^2(1-f^2)^{1/2}}\mathbf{K}(\bar{k}) - \frac{\pi/2}{ef}\Lambda_0(\bar{\psi},\bar{k})\right] \quad (72)$$

In addition, by virtue of the second and third of (4),

$$\frac{\partial^2\Psi}{\partial y^2} = -\left(\frac{\partial^2\Psi}{\partial x^2} + \frac{\partial V}{\partial z}\right), \quad (73)$$

which, with the aid of (60) and (72), results in

$$\frac{1}{4q_0}\left[\frac{\partial^2\Psi}{\partial y^2}\right]_{\rho=0} = \frac{(\pi/2)(1-e^2)^{1/2}}{1+(1-e^2)^{1/2}} + \frac{1-e^2}{e^2}\left\{\frac{\pi}{2}\Lambda_0(\bar{\psi},\bar{k}) - \frac{\zeta\mathbf{K}(\bar{k})}{[(1+\zeta^2)(1-f^2)]^{1/2}}\right\} \quad (74)$$

Thus, finally, on inserting (60), (68) and (72) in the first of (6), and (60), (70) and (74) in the second of (6), and taking account of (54) and (55), we obtain

$$\frac{[\sigma_x]_{\rho=0}}{q_0} = -\frac{1+2\nu(1-e^2)^{1/2}}{1+(1-e^2)^{1/2}} + \frac{1}{e^2}[1-2\nu(1-e^2)]\Lambda_0(\bar{\psi},\bar{k}) - \frac{(2/\pi)\zeta}{e^2[1+(1-e^2)\zeta^2]^{1/2}}\left[2(1-\nu)(1-e^2)\mathbf{K}(\bar{k}) - \frac{1+(1-e^2)\zeta^2}{1+\zeta^2}\mathbf{E}(\bar{k})\right] \quad (75)$$

$$\frac{[\sigma_y]_{\rho=0}}{q_0} = -\frac{2\nu+(1-e^2)^{1/2}}{1+(1-e^2)^{1/2}} - \frac{1-e^2-2\nu}{e^2}\Lambda_0(\bar{\psi},\bar{k}) + \frac{(2/\pi)\zeta(1-e^2)}{e^2[1+(1-e^2)\zeta^2]^{1/2}}[2(1-\nu)\mathbf{K}(\bar{k}) - \mathbf{E}(\bar{k})] \quad (76)$$

Passage to the limit, as $\zeta \to 0$, of these two expressions results in the value of σ_x and σ_y at the center of the loading area, in agreement with Way's computations (32). Evaluation of the limiting case of loading over a circular area entails more effort. We note that

$$\lim_{\epsilon\to 0}\Lambda_0(\bar{\psi},\bar{k}) = \frac{\zeta}{(1+\zeta^2)^{1/2}}\left[1 - \frac{1+2\zeta^2}{1+(1-e^2)\zeta^2}\frac{e^2}{4}\right] + O(e^4), \quad (77)^{18,\,21}$$

$$\lim_{\epsilon\to 0}\mathbf{K}(\bar{k}) = \frac{\pi}{2}\left\{1+\frac{e^2}{4[1+(1-e^2)\zeta^2]}\right\} + O(e^4), \quad (78)$$

[19] Reference [10], p. 166, no. 284.01.

[20] Ibid., p. 167, no. 284.08; p. 225, no. 410.03; p. 226, no. 410.08; p. 106, no. 252.28; p. 218, no. 362.12.

[21] Reference [10], p. 302, no. 906.05.

$$\lim_{e\to 0} \mathbf{E}(\bar{k}) = \frac{\pi}{2}\left\{1 - \frac{e^2}{4[1 + (1 - e^2)\zeta^2]}\right\} + O(e^4). \quad (79)$$

When account is taken of these limiting forms, the expressions for the components of stress in (75) and (76) reduce to

$$[\sigma_x]_{\substack{\text{circle}\\ \rho=0}} = [\sigma_y]_{\substack{\text{circle}\\ \rho=0}} = q_0\left\{\frac{1+2\nu}{2}\left[-1 + \frac{\zeta}{(1+\zeta^2)^{1/2}}\right] + \frac{\zeta}{2(1+\zeta^2)^{3/2}}\right\}. \quad (80)$$

The shearing components of stress on the z-axis are easily shown to vanish, as is to be expected from the symmetry of the problem. Accordingly, the normal components of stress given by (64), (75), and (76) represent the principal stresses at any point on the line $x = y = 0$.

Numerical Results[22]

The variation of the ratio of the normal displacement on the edge of the loading area, (49), to that at the center, (28), with position along the boundary is shown, for various values of the eccentricity, in Fig. 1; a more accurate set of values is given in Table 1. It is curious that, in the vicinity of $\theta_1 = 47$ deg, the value of this ratio is essentially independent of the shape of the boundary. In Fig. 2 the displacement ratio at the extremities of the principal axes of the bounding ellipse is depicted as a function of the eccentricity, with a list of numerical values presented in Table 2. It appears that the deflection at the end of the minor

[22] In the computations described in this section the values of the complete elliptic integrals and of the function A_0 were taken from the tables compiled by Heuman [12]. All numerical work pertains to a material for which Poisson's ratio has the value $\nu = 0.3$.

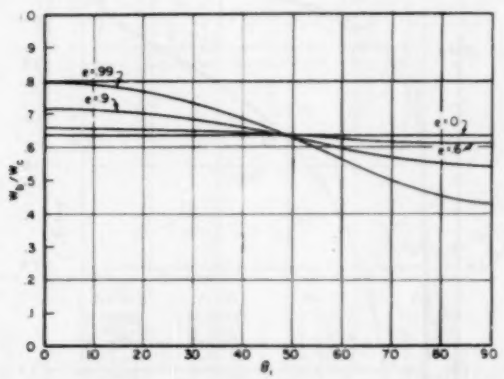

Fig. 1 Variation of ratio of normal displacement at boundary (w_b) to that at center (w_c) of elliptic area of loading with position along boundary (θ_1) for various values of eccentricity (e)

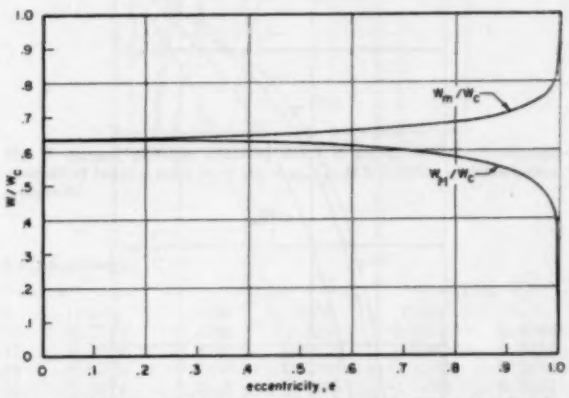

Fig. 2 Variation of ratio of normal displacement at extremity of major axis (w_M) and minor axis (w_m) of area of loading to that at center (w_c) with eccentricity (e)

Table 1 w_b/w_c versus θ_1

e θ_1 deg →	0	10	20	30	40	50	60	70	80	90
0	0.6366	0.6366	0.6366	0.6366	0.6366	0.6366	0.6366	0.6366	0.6366	0.6366
0.3	0.6416	0.6413	0.6405	0.6392	0.6375	0.6358	0.6342	0.6325	0.6319	0.6316
0.6	0.6598	0.6585	0.6546	0.6486	0.6410	0.6329	0.6256	0.6184	0.6141	0.6126
0.9	0.7173	0.7133	0.7007	0.6811	0.6557	0.6268	0.5974	0.5710	0.5525	0.5456
0.99	0.7965	0.7892	0.7666	0.7308	0.6829	0.6263	0.5647	0.5037	0.4528	0.4301

Table 2 $[w_b/w_c]_{\theta_1=0°,\,90°}$ versus e

e	0	0.1	0.2	0.3	0.4	0.5	0.6	0.7	0.8	0.9	0.99	1.0
w_M/w_c	0.6366	0.6361	0.6345	0.6316	0.6274	0.6211	0.6126	0.6001	0.5809	0.5456	0.4301	0
w_m/w_c	0.6366	0.6372	0.6388	0.6416	0.6458	0.6517	0.6598	0.6712	0.6882	0.7173	0.7965	1

Table 3 w/w_c and σ_z/q_0 versus ζ

e →	0		0.3		0.6		0.9		0.99	
ζ	w/w_c	σ_z/q_0	w/w_c	σ_z/q_0	w/w_c	σ_z/q_0	w/w_c	σ_z/q_0	w/w_c	σ_z/q_0
0	1.0000	1.0000	1.0000	1.0000	1.0000	1.0000	1.0000	1.0000	1.0000	1.0000
0.1	0.9693	0.9990	0.9701	0.9991	0.9725	0.9993	0.9790	0.9995	0.9860	0.9996
0.2	0.9346	0.9925	0.9364	0.9929	0.9419	0.9943	0.9524	0.9950	0.9707	0.9967
0.4	0.8567	0.9488	0.8605	0.9518	0.8733	0.9604	0.9032	0.9732	0.9365	0.9859
0.7	0.7339	0.8114	0.7404	0.8201	0.7629	0.8470	0.8211	0.8932	0.8823	0.9087
1.0	0.6234	0.6464	0.6313	0.6587	0.6598	0.6995	0.7392	0.7820	0.8286	0.8150
1.5	0.4827	0.4240	0.4909	0.4365	0.5217	0.4816	0.6201	0.5978	0.7466	0.6624
2	0.3869	0.2845	0.3944	0.2947	0.4234	0.3333	0.5274	0.4529	0.6782	0.5390
3	0.2722	0.1462	0.2781	0.1524	0.3014	0.1767	0.3957	0.2704	0.5708	0.3773
4	0.2084	0.0869	0.2131	0.0908	0.2319	0.1065	0.3126	0.1739	0.4914	0.2804
5	0.1684	0.0549	0.1722	0.0556	0.1879	0.0705	0.2568	0.1194	0.4300	0.2169
10	0.0853	0.0148	0.0872	0.0156	0.0955	0.0185	0.1335	0.0331	0.2578	0.0824

axis is always greater than at the corresponding point of the major axis, and that this difference increases with increasing eccentricity.

Table 3 contains the values of the ratio of the axial component of displacement at points along the z-axis, (61), and of the corresponding (compressive) component of stress, (64), to their respective values at the surface, (28) and (65). As expected, each of these quantities decreases monotonically from its maximum at the surface. The variation is shown in Fig. 3 and by the appropriate curves in Figs. 4(a, b, c, d).

The situation is different with the other two principal stresses along the z-axis. A tabulation, in Table 4, of the values of the ratio of each of these, (75) and (76), respectively, to the value of the applied pressure reveals that, in each case, these principal stresses decrease from their largest compressive value, attained at the surface, reverse sign[23] at a depth smaller than the length of the corresponding principal axis of the area of loading, attain a relatively small maximum tensile value a short distance below, and diminish monotonically thenceforth. The value of the maximum (compressive) principal stress parallel to the minor axis increases, that of the corresponding stress parallel to the major axis decreases, with increasing eccentricity of the loading area.

[23] A similar phenomenon occurs in the Hertz theory of normal contact between two elastic solids [13].

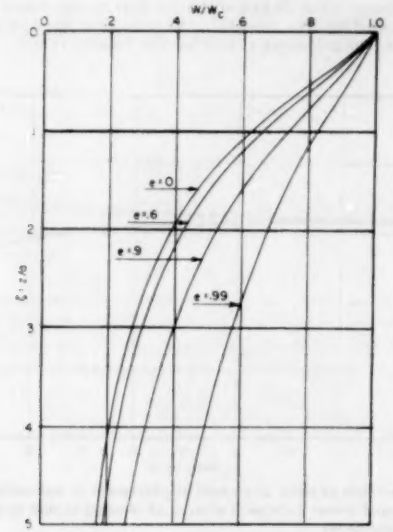

Fig. 3 Normal displacement at points on normal through centroid of loading area (w) as a function of depth below surface (z)

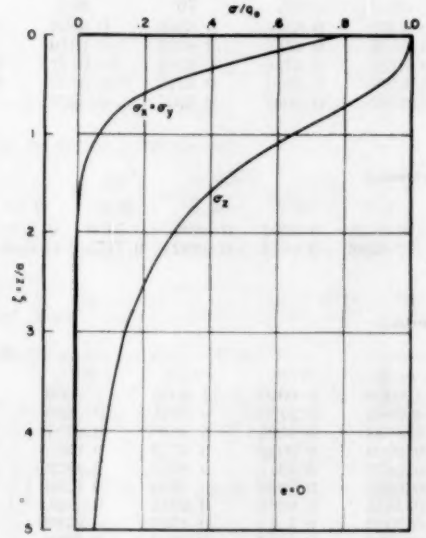

4(a)

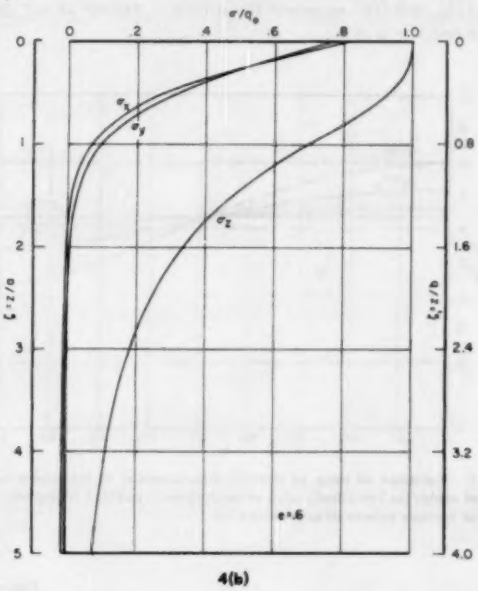

4(b)

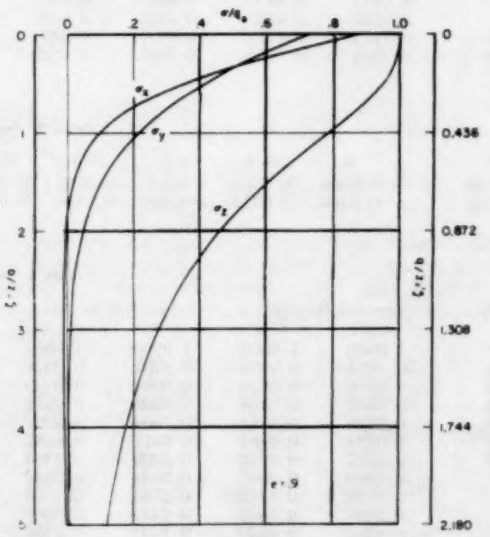

4(c)

Fig. 4 Compressive principal stresses at points on normal through centroid of loading area (σ_x, σ_y, σ_z) as functions of depth below surface (z)

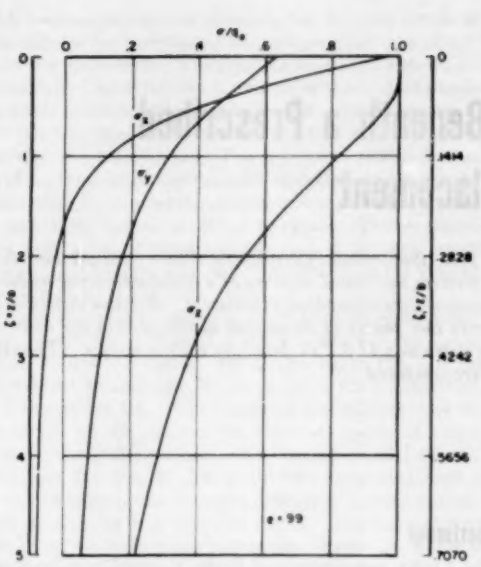

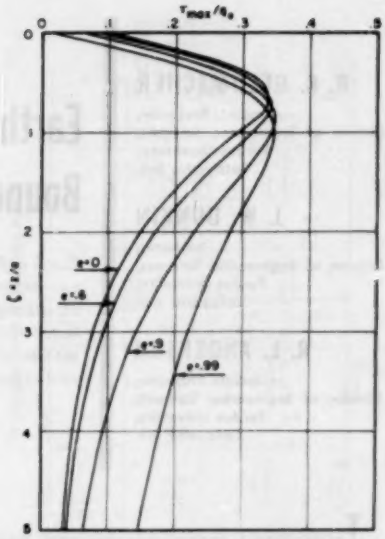

Fig. 5 Largest principal shearing stress at points on normal through centroid of loading area [$\tau = (\sigma_z - \sigma_x)/2$] as a function of depth below surface (z)

Table 4* σ_x/q_0 and σ_y/q_0 versus ζ

$\epsilon \rightarrow$	0		0.3		0.6		0.9		0.99	
ζ	σ_x/q_0	σ_y/q_0	σ_x/q_0	σ_y/q_0	σ_x/q_0	σ_y/q_0	σ_x/q_0	σ_y/q_0	σ_x/q_0	σ_y/q_0
0	0.8000	0.8000	0.8047	0.7953	0.8222	0.7778	0.8786	0.7214	0.9636	0.6364
0.05	0.7351	0.7351	0.7404	0.7330	0.7585	0.7244	0.8157	0.6875	0.8987	0.6158
0.1	0.6711	0.6711	0.6765	0.6716	0.6954	0.6716	0.7535	0.6538	0.8343	0.5954
0.2	0.5488	0.5488	0.5542	0.5542	0.5744	0.5694	0.6338	0.5875	0.7100	0.5551
0.4	0.3428	0.3428	0.3488	0.3531	0.3681	0.3894	0.4236	0.4647	0.5003	0.4849
0.7	0.1488	0.1488	0.1524	0.1599	0.1668	0.1999	0.2094	0.3137	0.2587	0.3839
1.0	0.0575	0.0575	0.0600	0.0648	0.0673	0.0949	0.0928	0.2060	0.1235	0.3105
1.5	0.0064	0.0064	0.0067	0.0090	0.0086	0.0229	0.0134	0.0997	0.0179	0.2270
2	0.0050	0.0050	0.0051	0.0037	0.0055	0.0017	0.0050	0.0457	0.0277	0.1721
3	0.0064	0.0064	0.0062	0.0067	0.0078	0.0054	0.0115	0.0080	0.0604	0.1095
4	0.0046	0.0046	0.0030	0.0064	0.0058	0.0046	0.0092	0.0011	0.0723	0.0761
5	0.0033	0.0033	0.0019	0.0050	0.0038	0.0040	0.0069	0.0030	0.0783	0.0566
10	0.0009	0.0009	0.0015	0.0001	0.0010	0.0013	0.0021	0.0018	0.0898	0.0252

* Numbers above horizontal lines denote compressive values; those below the line, tensile values.

The variation of these stresses with depth below the surface is shown in Figs. 4(a, b, c, d). Finally, the largest principal shearing stress, $\tau = (\sigma_z - \sigma_x)/2$, is plotted in Fig. 5.

Acknowledgment

It is a pleasure to express my thanks to Miss Barbara Wei for performing the numerical work.

References

1 I. Todhunter and K. Pearson, "A History of the Theory of Elasticity," Cambridge University Press, England, vol. 1, 1886, vol. 2, 1893.

2 H. Lamb, "On Boussinesq's Problem," *Proceedings of the London Mathematical Society*, vol. 34, 1902, pp. 276–284.

3 K. Terazawa, "On the Elastic Equilibrium of a Semi-Infinite Solid. . .," *Journal of the College of Science*, University of Tokyo, Tokyo, Japan, vol. 37, 1916, Article 7.

4 A. E. H. Love, "The Stress Produced in a Semi-Infinite Solid by Pressure on Part of the Boundary," *Philosophical Transactions of the Royal Society of London*, England, series A, vol. 228, 1929, pp. 377–420.

5 H. Hertz, "Über die Berührung fester elastischer Körper," *Journal für die reine und angewandte Mathematik* (Crelle), vol. 92, 1882, pp. 156–171.

6 A. Cayley, "On the Potential of the Ellipse and the Circle," *Proceedings of the London Mathematical Society*, vol. 6, 1875, pp. 38–58.

7 W. Gröbner and N. Hofreiter, "Integraltafel," Springer-Verlag, Wien, vol. 1, 1949.

8 W. D. McMillan, "The Theory of the Potential," McGraw-Hill Book Company, Inc., New York, N. Y., 1930.

9 S. Way, "Some Observations on the Theory of Contact Pressures," JOURNAL OF APPLIED MECHANICS, vol. 7, TRANS. ASME, vol. 62, 1940, pp. 147–157.

10 P. F. Byrd and M. D. Friedman, "Handbook of Elliptic Integrals for Engineers and Physicists," Springer-Verlag, Berlin, 1954.

11 D. Bierens de Haan, "Nouvelles Tables d'Intégrales Définies," Stechert and Company, New York, N. Y., 1939, Table 309, No. 16.

12 C. Heuman, "Tables of Complete Elliptic Integrals," *Journal of Mathematics and Physics*, Massachusetts Institute of Technology, Cambridge, Mass., vol. 20, 1941, pp. 127–206, 336.

13 A. E. H. Love, "A Treatise on the Mathematical Theory of Elasticity," Cambridge University Press, England, fourth edition, 1927, p. 198.

R. C. GELDMACHER
Associate Professor,
Division of Engineering Sciences,
Purdue University,
Lafayette, Ind.

J. W. DUNKIN
Instructor,
Division of Engineering Sciences,
Purdue University,
Lafayette, Ind.

R. L. ANDERSON
Associate Professor,
Division of Engineering Sciences,
Purdue University,
Lafayette, Ind.

Earth Motion Beneath a Prescribed Boundary Displacement

Earth deflections beneath a prescribed boundary displacement were obtained theoretically and experimentally. The problem was stated in terms of a two-dimensional model and an attempt was made to design a corresponding experiment. Relative deflections between the surface of the earth and points of increasing depths within the earth were measured. The maximum depth was 42 ft 7 in. below the earth's surface. Theoretical and experimental results were compared.

THE MATERIAL presented in this paper is the result of a theoretical and experimental study of earth motion beneath a prescribed boundary deformation done as a phase of an investigation of the support characteristics of subbase treatments beneath rigid pavements.[1] It should be of interest to anyone planning to attempt to validate a rational analysis of earth motion beneath a prescribed boundary displacement or to anyone engaged in measuring the absolute deflection of a highway, landing strip, or similar structure by means of a device that requires a reference point in the earth.

The purpose of this study was to formulate and to validate experimentally a rational analysis of the motion of the earth beneath a prescribed boundary displacement.

The study was prompted by the results of a series of exploratory measurements of earth motion beneath a pavement deflected by vehicular loads. These measurements were made in an attempt to establish the errors involved in measuring rigid pavement deflections by means of rods anchored at various depths in the earth, and suggested that a rational analysis of the movement of the earth beneath a prescribed boundary displacement and an experiment planned in terms of such an analysis might be fruitful.

It was decided to formulate the problem in terms of a linear plane-strain model because of the simplicity of the theory in comparison to that of a three-dimensional model. Boundary conditions were chosen in terms of displacement. In this way the earth was separated from the pavement and could be treated as a separate simpler problem, obviating the need for such information as tire pressure, tire contact area, pavement geometry, and pavement properties. Difficulties developed, however, in trying to design a two-dimensional experiment and it is the opinion of the authors that any subsequent treatment of the problem should be three-dimensional.

[1] R. C. Geldmacher, R. L. Anderson, J. W. Dunkin, G. R. Partridge, et al., "Subgrade Support Characteristics," Report No. 38, Joint Highway Research Project, Purdue University, Lafayette, Ind., December, 1956.

Contributed by the Applied Mechanics Division and presented at the Annual Meeting, Atlantic City, N. J., November 29–December 4, 1959, of THE AMERICAN SOCIETY OF MECHANICAL ENGINEERS.

Discussion of this paper should be addressed to the Secretary, ASME, 29 West 39th Street, New York, N. Y., and will be accepted until April 10, 1960, for publication at a later date. Discussion received after the closing date will be returned.

NOTE: Statements and opinions advanced in papers are to be understood as individual expressions of their authors and not those of the Society. Manuscript received by ASME Applied Mechanics Division, February 3, 1958. Paper No. 59—A-3.

Experiment

For a truly two-dimensional model, it would have been necessary to have a transverse load extending infinitely far in each transverse direction. Such a load could be visualized as consisting of many equal, concentrated loads closely spaced at equal increments along an infinitely long line. The resulting deflection would be an infinitely long transverse trough.

Two methods for approximating a load which would give the desired result were considered. One was to obtain a vehicle, or vehicles, sufficiently wide and with wheels closely spaced; the other was to superpose the deflections produced by successive laterally spaced passes of a single vehicle in such a way that the resultant superposed deflections would sum to form the desired transverse trough. Of the two methods considered, the second was chosen because it could be more easily realized.

The experimental measurements were made on a section of U. S. Highway 52. The section chosen was relatively new, had no visible cracks, was approximately 50 ft long, and was comprised of two lanes of the four-lane highway. It was placed on upland glacial till, silty clay to clay, of relatively uniform composition down to the depths measured. The vehicle used was an especially prepared one belonging to the State of Indiana. The distance from its front axle to a point midway between its rear tandem dual wheels was 14 ft, and the total load carried by the rear axles was 19,330 lb.

Preliminary measurements had shown that, when a test vehicle was near the center of the section, the range of significant influence did not extend to the ends and, hence, the slab could be regarded as extending infinitely far to the front and rear. It was reasoned, therefore, that the time-dependent deflections of the middle of the section, for slowly moving loads, could, after an appropriate correlation of time and longitudinal distance, be used as the instantaneous profile of the top surface in the longitudinal direction.

Differential transformers were used as deflection transducers.[1,2] Six transformers were placed 1 ft apart in a longitudinal row in a manner which measured the relative motion between the pavement and positions in the earth 1 ft 10 in., 5 ft 4 in., 9 ft 5 in., 14 ft 11 in., 27 ft, and 42 ft 7 in. beneath the bottom of the pavement.

The positions of the transducers in the pavement and the

[2] R. C. Geldmacher, R. L. Anderson, J. W. Dunkin, G. R. Partridge, et al., "Subgrade Support Characteristics as Indicated by Measurements of Deflection and Strain," *Proceedings, Highway Research Board*, vol. 36, 1957, pp. 479–496.

vehicle loading pattern are shown in Fig. 1. The arrows in the figure indicate the positions of the mid-points of each of the rear tires of the test vehicle. The symbols associated with the arrows (for example, L1 and R1) identify left or right rear dual wheels and the vehicle position. Thus, when in position 1, the center of the outer left rear dual of the vehicle was 0.76 ft from the line of centers of the transducers. The successive positions were arranged so that, after algebraically summing, the resultant deflection consisted of a regular distribution of deflections caused by left rear duals spaced at $2^1/_2$-ft intervals. Twelve successive passes were made at creep speed at each of the nine prescribed positions. Deflections were not detectable when the vehicle was at position 8 or beyond.

The method used in summing the deflections of the nine runs was as follows: run 1 + run 2 + run 3 + run 4 − run 5 − run 6 − run 7 + run 8 + run 9. Thus, referring to Fig. 1, it can be observed that L5 cancelled R1, L6 cancelled R2, L7 cancelled R3, and L8 cancelled R5. The remaining deflection is thus due to loads at L1, L2, L3, L4, and L9 which are spaced at $2^1/_2$-ft intervals. Since deflections caused by loads beyond L8 could not be detected, R4, R6, R7, R8, and R9 were neglected in the sum.

A reproduction of the recorded deflections for one pass of the vehicle at position 1 is shown in Fig. 2. The stepped pattern at the left of the records is a calibration. Each step corresponds to 0.0025 in.

An estimate of the distribution of the twelve measurements made at each vehicle position may be inferred from Table 1, which gives the deflections occurring when the vehicle passed along position 1.

The measured motion of the pavement with respect to the earth for the six depths chosen is shown in Fig. 3. Each point of this curve represents the proper superposition of the means of the deflections resulting from the twelve passes of the vehicle over the prescribed nine separate paths.

Theory

The theoretical model was chosen as a semi-infinite, homogeneous, isotropic, elastic medium with its upper surface displaced in the form of an infinitely long trench, thereby providing a condition of plane strain. The analysis is that found in the works of Muskhelishvili.[2]

To find the horizontal displacement u and the vertical displacement v of a point inside such a system, the following boundary-value problem must be solved:

$$(\lambda + \mu)\frac{\partial \theta}{\partial x} + \mu \Delta u = 0 \qquad (1)$$

$$(\lambda + \mu)\frac{\partial \theta}{\partial y} + \mu \Delta v = 0 \qquad (2)$$

under the boundary conditions:

(i) u, v tend to 0 as x approaches $\pm \infty$ and y approaches $-\infty$;
(ii) $v(x, 0)$ and $u(x, 0)$ are specified functions;

where λ and μ are the Lamé constants, $\theta = (\partial u/\partial x) + (\partial v/\partial y)$, and Δ is the Laplacian operator.

The complex-variable solution presented by Muskhelishvili employs the complex co-ordinates shown in Fig. 4. For $y = 0$, the complex displacement $u + iv$ reduces to the boundary condition:

$$2\mu[u(x, 0) + iv(x, 0)] = 2\mu[g_1(t) + ig_2(t)] \qquad (3)$$

where t represents the distance along the boundary; $g_1(t)$ is the horizontal displacement of the boundary surface; and $g_2(t)$ is the vertical displacement of the boundary surface.

[2] N. I. Muskhelishvili, "Some Basic Problems in the Mathematical Theory of Elasticity," P. Noordhoff, Groningen, Holland, 1953.

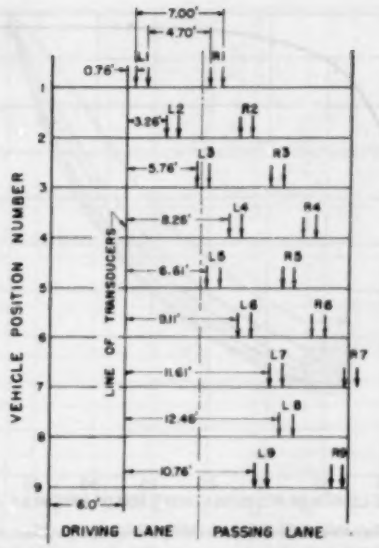

Fig. 1 Relative position of transducer row and left and right sets of rear duals of vehicle (arrow)

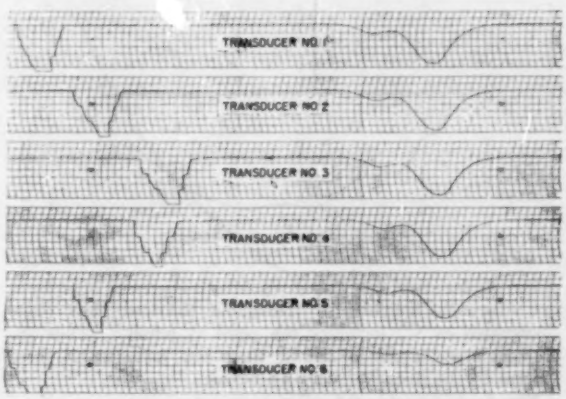

Fig. 2 Relative deflection between earth and pavement versus time for six earth depths. Run No. 6, vehicle traveling at creep speed. Chart speed: 5 mm per sec.

Table 1 Deflection of pavement in milli-in. with respect to six depths in earth for twelve runs at vehicle position 1

Run no.	Transducer number and depth, ft-in. 1 (42-7)	2 (27-0)	3 (14-11)	4 (9-5)	5 (5-4)	6 (1-10)
1	6.8	6.8	6.6	6.3	5.6	2.1
2	6.6	6.6	6.1	5.9	5.0	1.9
3	6.4	6.6	6.2	5.9	5.8	1.9
4	6.7	6.7	6.2	6.0	5.6	2.1
5	6.4	6.6	6.2	5.8	5.3	1.9
6	6.3	6.4	6.1	5.8	5.4	1.8
7	6.5	6.5	6.1	6.0	5.5	2.0
8	6.2	6.4	6.1	5.8	5.4	1.9
9	6.5	6.6	6.1	5.8	5.2	2.0
10	6.1	6.9	6.1	6.0	5.3	1.9
11	6.6	6.8	6.2	5.7	5.3	2.0
12	6.2	6.5	6.1	5.8	5.4	2.1
Average	6.44	6.62	6.17	5.90	5.40	1.98

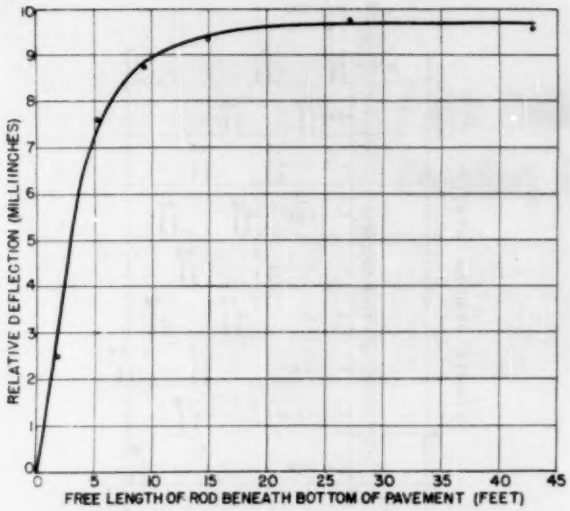

Fig. 3 Relative deflections resulting from superposition procedure

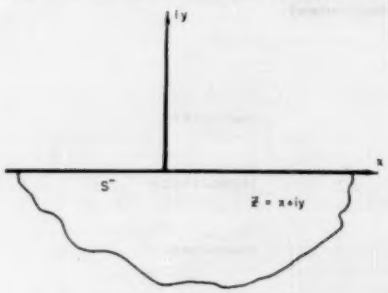

Fig. 4 Complex co-ordinates

The displacement $(u + iv)$ of a point z is expressed in terms of two functions, holomorphic throughout the lower half plane (designated as S^-) including the point at infinity. Thus the problem becomes that of finding these two holomorphic functions under the given boundary conditions.

The displacement is defined as

$$2\mu(u + iv) = \kappa\varphi(z) - z\overline{\varphi'(z)} - \overline{\psi(z)} \tag{4}$$

where $\kappa = (\lambda + 3\mu)/(\lambda + \mu)$, $\varphi(z)$ and $\psi(z)$ are the two holomorphic functions, $\varphi'(z)$ is the derivative of $\varphi(z)$, and $\overline{\varphi'(z)}$ and $\overline{\psi(z)}$ are the complex conjugates of $\varphi'(z)$ and $\psi(z)$.

The functions $\varphi(z)$ and $\psi(z)$ may be expressed in terms of the boundary conditions as:

$$\kappa\varphi(z) = -\frac{\mu}{\pi i}\int_{-\infty}^{\infty}\frac{g_1 + ig_2}{t - z}\,dt \tag{5}$$

$$\psi(z) = \frac{\mu}{\pi i}\int_{-\infty}^{\infty}\frac{g_1 - ig_2}{t - z}\,dt - z\varphi'(z) \tag{6}$$

Using (5) and the Cauchy integral relation for $\varphi'(z)$,

$$\varphi'(z) = -\frac{\mu}{\kappa\pi i}\int_{-\infty}^{\infty}\frac{g_1 + ig_2}{(t - z)^2}\,dt \tag{7}$$

and from (4), (5), (6), and (7),

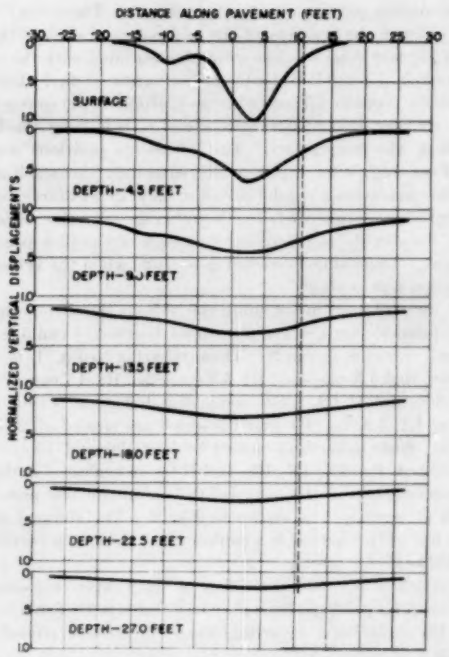

Fig. 5 Deflection of earth predicted by two-dimensional theory

$$u + iv = \frac{1}{2\pi}\int_{-\infty}^{\infty}\frac{g_2 - ig_1}{(t - z)}\,dt + \frac{1}{2\pi}\int_{-\infty}^{\infty}\frac{g_2 - ig_1}{(t - \bar{z})}\,dt - \frac{y}{\kappa\pi}\int_{-\infty}^{\infty}\frac{g_1 - ig_2}{(t - \bar{z})^2}\,dt \tag{8}$$

After separating into real and imaginary parts,

$$u = -\frac{1}{\pi}\int_{-\infty}^{\infty}\frac{yg_1}{(t - x)^2 + y^2}\,dt - \frac{y}{\kappa\pi}\int_{-\infty}^{\infty}\frac{[(t - x)^2 - y^2]g_1 - 2y(t - x)g_2}{[(t - x)^2 + y^2]^2}\,dt \tag{9}$$

$$v = -\frac{1}{\pi}\int_{-\infty}^{\infty}\frac{yg_2}{(t - x)^2 + y^2}\,dt - \frac{y}{\kappa\pi}\int_{-\infty}^{\infty}\frac{[y^2 - (t - x)^2]g_2 - 2y(t - x)g_1}{[(t - x)^2 + y^2]^2}\,dt \tag{10}$$

Relations (9) and (10) give u and v for a point (x, y) in terms of the boundary deformations $g_1(t)$ and $g_2(t)$. It can be seen that no great trouble will be involved in using measured values of g_1 and g_2 and numerically performing the integrations indicated in (9) and (10).

Application of Theory

Since only the vertical component of deflection was measured, it was necessary to assume the boundary function $g_1(t)$ in relations (9) and (10). This function was chosen to be identically zero.

In order to throw some light on the significance of this choice, one may examine the vertical component of displacement due to $g_1(t)$. From (10), it is found to be

$$v_{g_1} = \frac{2y^2}{\kappa\pi}\int_{-\infty}^{\infty}\frac{(t - x)g_1(t)}{[(t - x)^2 + y^2]^2}\,dt \tag{11}$$

For $x = 0$, this relation will be positive for odd functions of $g_1(t)$ which are non-negative in the interval $t > 0$ and negative for odd functions of $g_1(t)$ which are non-negative in the interval $t < 0$. It can be seen that functions of the first kind will be associated with an outward horizontal movement of the surface while functions of the second kind will be associated with an inward horizontal movement of the surface. Of the two functions, the first would seem to be the more realistic for the case under consideration and, as a consequence, the deflection obtained from (10) would be less in magnitude than if $g_1(t)$ were identically zero. This observation is of importance in interpreting the results obtained.

After setting $g_1(t) = 0$, relations (9) and (10) become

$$u = \frac{y}{\kappa\pi} \int_{-\infty}^{\infty} \frac{2y(t-x)g_2(t)}{[(t-x)^2 + y^2]^2}\, dt \tag{12}$$

$$v = -\frac{1}{\pi} \int_{-\infty}^{\infty} \frac{yg_2(t)}{[(t-x)^2 + y^2]}\, dt - \frac{y}{\kappa\pi} \int_{-\infty}^{\infty} \frac{[y^2 - (t-x)^2]g_2(t)}{[(t-x)^2 + y^2]^2}\, dt \tag{13}$$

The measured function $g_2(t)$ is the top curve in Fig. 5. The integration of (12) and (13) was performed numerically using Simpson's rule. The integrand was evaluated at intervals of approximately 2.25 ft and the values were appropriately summed. Computations were made for positions defined by values of $x = 0$, $\pm a/4$, $\pm 2a/4$, . . ., $\pm 6a/4$ and values of $y = 0$, $-a/4$, $-2a/4$, . . ., $-6a/4$ (where $2a$ equals the length of the surface indentation, in this case 36 ft.) The results are shown in Fig. 6.

It should be noted that Poisson's ratio is contained in the deflection relations. The effect of selected values of Poisson's ratio is shown in Fig. 6. The value used in the computation of deflections shown in Fig. 7 was 0.25.

Discussion of Results

A comparison of the measured and theoretical results may be made by referring to Figs. 3 and 7. Here the theoretical results are presented for the earth deflections immediately below the point of maximum deflection of the boundary and are normalized to this deflection at the boundary. The experimental results have not been put in normalized form because no way was found to obtain a measure of the absolute motion of the earth.

One might suppose that the flatness of the relative motion curve (experimental curve) at large depths would indicate that the absolute motion is zero here. However, such a conclusion could be in error since the theoretical curve suggests that, even though the slope of the curve may be quite small, a significant absolute deflection may be present. Furthermore, to obtain the slope of the relative deflection curve accurately at greater depths, it would be necessary to measure small differences occurring in large relative deflections; such differences are on the order of 1 per cent and fall outside the precision of the instrument used.[4]

A great deal of effort was expended in an attempt to obtain an absolute reference but with no success. Several attempts were made to construct a long bridge across the pavement for this purpose, but the instability of the structures (motion on the order of a few ten thousandths of an inch could not be tolerated) made the scheme unworkable. However, had the structures been stable, the validity of the measurements would still have been uncertain since it was subsequently observed that the bridge supports could have experienced significant motion. The establishment of a suitable reference remains a major problem in work of this sort.

[4] G. R. Partridge, J. W. Dunkin, R. L. Anderson, and R. C. Geldmacher, "A 14-Channel Displacement Measuring Device Utilising Magnetic and Paper Tape Recording," *Communications and Electronics*, Part I of *AIEE Transactions*, vol. 76, 1957, pp. 461–467.

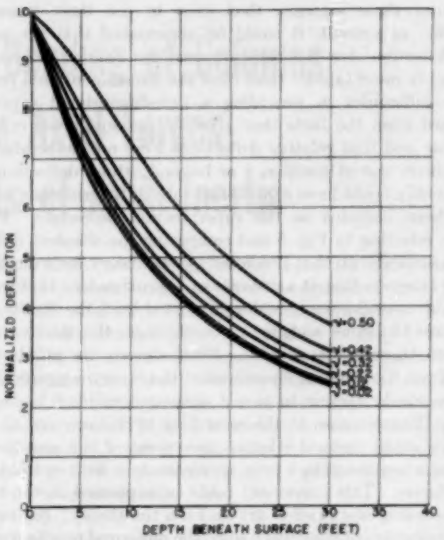

Fig. 6 Effect of Poisson's ratio upon earth deflection beneath point of maximum boundary deflection

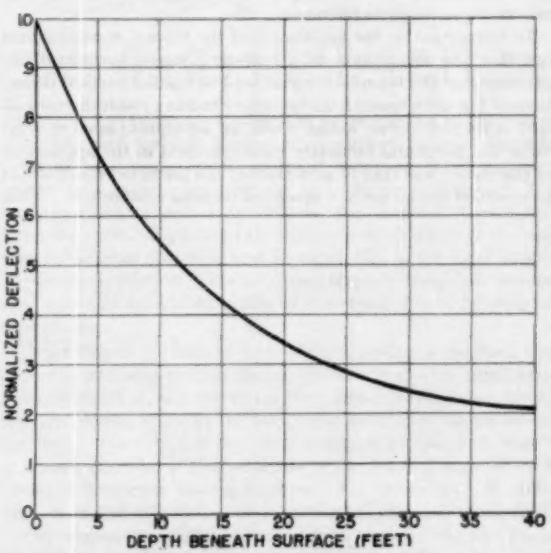

Fig. 7 Theoretical deflection versus depth for points beneath point of maximum boundary deflection

A significant difference between the experimental and theoretical results is that the experimental curve approaches an asymptote much more rapidly than does the theoretical. This difference is thought to be due to one or more of the following conditions:

1 The use of a two-dimensional theory and the subsequent inability to provide an experiment that was truly two-dimensional.

2 The assumption in the application of the theory that the horizontal deflection was zero.

3 Lack of knowledge of the magnitude of Poisson's ratio.

4 System is not linear enough to permit linear analysis.

The two-dimensional theory does not bring in stresses, in

particular shear stresses, that exist in the three-dimensional problem; as a result, it could be anticipated that the normalized deflections for the three-dimensional case would reach an asymptote more rapidly than does the two-dimensional result.

The difficulties in providing a two-dimensional experiment stemmed from the facts that absolute measurements could not be made and that relative deflections were not detectable when the vehicle was at position 8 or beyond; thus, deflections that conceivably could have summed to substantial amounts may not have been included in the superposition procedure. For example, referring to Fig. 5 and comparing the absolute deflection at the surface with that predicted by the theory for a depth of 18 ft, one observes that at a distance of approximately 11 ft from the origin of co-ordinates (position of dotted line) the elastic deflections are the same and, as a consequence, the relative motion between these points is zero. Furthermore, for points farther away from the origin of co-ordinates, the theory suggests that the surface would appear to rise if measured relative to the 18-ft depth. Examination of the record for transducer no. 1, Fig. 2, shows a small upward relative movement of the pavement beginning when the vehicle was approximately 56 ft in front of the transducers. This movement could be explained on the basis of the preceding observation drawn from the theory; however, the relationship is not conclusive since the measured results were used as boundary conditions to obtain the theoretical deflections, and it is thus conceivable that the pavement actually moved upward relative to an absolute reference.

In the section on the application of the theory, it was pointed out that the assumption of a realistic nonzero horizontal displacement of the boundary would lead to smaller vertical deflections of the earth beneath the boundary and as a result the normalized deflection curve would reach an asymptote more rapidly. Since the horizontal boundary condition used in the application of the theory was that of zero motion, the predicted result would be modified by the use of a measured boundary deflection. Thus a significant refinement might result if the horizontal displacement of the boundary was measured and introduced into the integrals from which the earth deflection is computed.

Conclusions

The experimental results obtained have the general character of the theoretical results. However, the plotted experimental data approach an asymptote much more rapidly than do the theoretical.

The theory predicts that, even though the slope of the normalized displacement curve may be quite small, a significant absolute deflection may be present. The experimental verification of this deflection remains to be obtained.

The theory predicts that the magnitude of Poisson's ratio has a strong influence on the deflections, smaller values of Poisson's ratio causing the deflection curve to become asymptotic more rapidly.

A significant refinement in the application of the theory might result if the horizontal deflection of the boundary was obtained and introduced into the integrals from which the vertical deflection was computed.

An important experimental problem to be solved is that of making an absolute measurement of earth displacement.

In order to provide a more valid basis for comparing theory and experiment, effort should be directed toward solving the three-dimensional theoretical problem, thus bringing an accompanying simplification in the experiment.

Acknowledgments

The work described in this paper was supported by the Joint Highway Research Project of the School of Civil Engineering, Purdue University, and by the Division of Engineering Sciences, Purdue University.

On the Elastic Bending of Columns Due to Dynamic Axial Forces Including Effects of Axial Inertia

EUGENE SEVIN
Senior Research Engineer,
Division of Mechanical Engineering Research,
Armour Research Foundation,
Illinois Institute of Technology,
Chicago, Ill.
Mem. ASME

This study is concerned with the influence of axial inertia upon the elastic bending motion of initially slightly curved columns acted on by time-dependent axial forces. The equations of motion include both axial inertia and nonlinear strain terms. Numerical solutions were obtained for a similar problem previously studied by Hoff [1][1] but in which axial-inertia effects were neglected; i.e., the problem of a simply supported column initially bent in the shape of a half sine wave and loaded by displacing one end axially at a constant rate. The range of solutions pertains to conventional structural compression members (slenderness ratios less than 150), and to minimum rates of loading compatible with elastic response of common engineering materials. This study suggests that axial-inertia effects are of secondary importance in so far as the gross elastic response of conventional structural columns is concerned.

THE LITERATURE concerned with the bending of columns under dynamically applied axial loads, though dating from 1934, cannot be considered extensive. This fact is attributed to the complexity of the governing equations which do not admit of an analytical solution. Existing analyses therefore have involved additional simplifying assumptions for, without the aid of modern high-speed computers, even numerical solutions are impractical.

The following equations, subject to suitable boundary and initial conditions, represent a complete system of equations for determining the three unknown space and time-dependent quantities which characterize the column motion; i.e, the lateral deflection y, the axial displacement u, and the axial force P:

$$EI\frac{\partial^4}{\partial x^4}(y - y_0) + \frac{\partial}{\partial x}\left(P\frac{\partial y}{\partial x}\right) + \rho A\frac{\partial^2 y}{\partial t^2} = 0 \qquad (1a)$$

$$-\frac{\partial P}{\partial x} = \rho A\frac{\partial^2 u}{\partial t^2} \qquad (1b)$$

$$-\frac{P}{AE} = \frac{\partial u}{\partial x} + \frac{1}{2}\left[\left(\frac{\partial y}{\partial x}\right)^2 - \left(\frac{\partial y_0}{\partial x}\right)^2\right] \qquad (1c)$$

Equation [1a] expresses equilibrium of the column in the lateral direction, and involves the usual strength-of-material assumptions as to linearly elastic material behavior, small displacements, and uniform geometrical and physical properties, but neglects rotatory inertia and effects due to shear strains and Poisson's ratio. Equation (1b) expresses equilibrium of the column in the axial direction, and Equation (1c) is the axial strain-displacement relation. The nonlinear terms in the latter expression represent axial components of the strain due to bending of the column.

Depending on the form of the boundary conditions specified, two classes of problems may be distinguished. In one, the axial force P is prescribed at, say, one end of the column; in the other, either the axial displacement or the velocity of one end of the column is specified. The latter is the usual situation in so-called impact problems, and also is characteristic of the loading imposed by a constant-strain-rate testing machine. For either class of problems an analytical solution of Equation (1) appears impractical.

The original investigators seem to have been Koning and Taub [2] (1934) who dealt with a simplified form of Equation (1) in which a constant axial force P was specified; other investigators

[1] Numbers in brackets designate References at end of paper.

Contributed by the Applied Mechanics Division and presented at the Annual Meeting, Atlantic City, N. J., November 29–December 4, 1959, of THE AMERICAN SOCIETY OF MECHANICAL ENGINEERS.
Discussion of this paper should be addressed to the Secretary, ASME, 29 West 39th Street, New York, N. Y., and will be accepted until April 10, 1960, for publication at a later date. Discussion received after the closing date will be returned.
NOTE: Statements and opinions advanced in papers are to be understood as individual expressions of their authors and not those of the Society. Manuscript received by ASME Applied Mechanics Division, December 15, 1958. Paper No. 59—A-25.

Nomenclature

- L = column length (actually, initial distance between ends of column measured along the x-axis)
- A = cross-sectional area of column
- I = principal moment of inertia of column cross section with respect to direction of bending
- $r = (I/A)^{1/2}$ = principal radius of gyration
- E = Young's modulus for column material
- ρ = mass per unit volume of column material
- $c = (E/\rho)^{1/2}$ = "speed of sound" in column material
- x = axial co-ordinate
- t = time
- $y = y(x, t)$ = total lateral deflection of column
- $Y = Y(t)$ = total lateral center deflection of column
- $y_0 = y_0(x)$ = initial lateral deflection of column
- Y_0 = initial lateral center deflection of column (maximum value of y_0 for cases considered)
- $u = u(x, t)$ = axial displacement of column (positive u corresponds to extension of column)
- V = forcing velocity; i.e., specified constant rate of axial displacement at $u(L, t)$
- $P = P(x, t)$ = axial force (positive P corresponds to a compressive force)
- Ω = Hoff's dynamic similarity number

have since considered the column problem on essentially the same basis [3–10]. All neglected axial inertia, and the nonlinear axial strains appear to have been retained only in the work of Hoff [1] and Davidson [10]. Hoff (1950) seems to have been the first to consider the bending of a column in a testing machine as a dynamic problem. Here the loading is due to one end of the column being displaced at a constant rate of speed. Following Koning and Taub, Hoff took the column to be simply supported and with an initial shape in the form of a half sine wave. He assumed a solution of the type,

$$y(x, t) = Y(t) \sin (\pi x/L) \tag{2}$$

where

$$y(x, 0) = y_0(x) = Y_0 \sin (\pi x/L) \tag{3}$$

The resulting equation for $Y(t)$ is nonlinear with time-dependent coefficients, and Hoff obtained a solution in terms of a power series.

This paper is an extension of Hoff's work in which the effect of axial inertia is retained. Equation (1) was solved numerically for the case of a simply supported column having an initial deflected shape in the form of a half sine wave and loaded by displacing one end at a constant rate. However, the rates of loading considered herein are greater than those specifically considered by Hoff and encountered in ordinary compression tests.

Formulation of the Problem

The governing column equations, Equations (1), differ from the more usual strength-of-materials approach to the bending of slender columns under time-dependent axial loads only in that axial displacements are considered explicitly. Inasmuch as these equations have been utilized before, they need not be derived here.

Equation (1) can be put into the following convenient nondimensional form:

$$\mathfrak{y}^{iv} + \bar{P}'\mathfrak{y}' + \bar{P}\mathfrak{y}'' + \ddot{\mathfrak{y}} = \mathfrak{y}_0{}^{iv} \tag{4a}$$

$$-\bar{P}' = \ddot{\bar{u}} \tag{4b}$$

$$-\bar{P} = \bar{u}' + {}^1/_2[(\mathfrak{y}')^2 - (\mathfrak{y}_0')^2] \tag{4c}$$

where it is understood that

$$\mathfrak{y} = \mathfrak{y}(\bar{x}, \bar{t}); \quad \bar{u} = \bar{u}(\bar{x}, \bar{t}); \quad \bar{P} = \bar{P}(\bar{x}, \bar{t}); \quad \mathfrak{y}_0 = \mathfrak{y}_0(x)$$

and that the primes and dots refer to differentiation with respect to $\bar{x}$ and $\bar{t}$, respectively. The nondimensional variables are defined by

$$\mathfrak{y} = y/r, \quad \bar{x} = x/r, \quad \bar{u} = u/r, \quad \bar{t} = ct/r,$$
$$\bar{P} = P/AE, \quad \bar{L} = L/r \tag{5}$$

The boundary and initial conditions corresponding to the statement of Hoff's problem are

$$\mathfrak{y}(\bar{x}, 0) = \mathfrak{y}_0(\bar{x}) = \bar{Y}_0 \sin (\pi\bar{x}/L)$$
$$\mathfrak{y}(0, \bar{t}) = \mathfrak{y}(\bar{L}, \bar{t}) = \mathfrak{y}''(0, \bar{t}) = \mathfrak{y}''(\bar{L}, \bar{t}) = \dot{\mathfrak{y}}(\bar{x}, 0) = 0 \tag{6a}$$

$$\bar{u}(\bar{x}, 0) = \dot{\bar{u}}(\bar{x}, 0) = \bar{u}(0, \bar{t}) = 0$$
$$\bar{u}(\bar{L}, \bar{t}) = -\bar{V}\bar{t} \tag{6b}$$

where $\bar{V} = V/c$ is the nondimensional "forcing velocity," and $\bar{Y}_0 = Y_0/r$ is the nondimensional amplitude of the initial deflected shape of the column.

For later reference we quote Hoff's column equation; namely,

$$\frac{d^2\bar{Y}}{d\tau^2} + \Omega\{\bar{Y} - \bar{Y}_0 - \bar{Y}[\tau - (1/4)(\bar{Y}^2 - \bar{Y}_0{}^2)]\} = 0$$

where τ is a nondimensional time parameter, and $\Omega = \pi^2/\bar{V}^2\bar{L}^2$ is referred to by Hoff as the dynamic similarity number. Hoff's average axial force is, in the present nondimensional notation,

$$\bar{P} = \frac{\bar{V}\bar{t}}{\bar{L}} - \frac{\pi^2}{4\bar{L}^2}(\bar{Y}^2 - \bar{Y}_0) \tag{7}$$

Hoff's equation depends on only two parameters Ω and $\bar{Y}_0$, whereas the general column equations involve three parameters $\bar{V}$, $\bar{L}$, $\bar{Y}_0$. For sufficiently slow rates of loading, where it becomes reasonable to neglect the effects of axial inertia, Hoff's equation can be expected to yield the same numerical results as the more exact equations. Even in this situation, however, it would not be evident from the general column equations that the results do not depend explicitly on $\bar{V}$ and $\bar{L}$, but rather on a combination of these parameters.

Analytical Considerations

It has not been possible to find an analytical solution to the general column equation. However, some information of general interest can be obtained. The axial force $\bar{P}$ may be eliminated from Equations (1*b*) and (1*c*) to yield

$$\ddot{\bar{u}} - \bar{u}'' = f'(\bar{x}, \bar{t}) \tag{8a}$$

where

$$f(\bar{x}, \bar{t}) = (1/2)[(\mathfrak{y}')^2 - (\mathfrak{y}_0')^2] \tag{8b}$$

This is recognized as a nonhomogeneous wave equation for $\bar{u}$, subject to the nonhomogeneous boundary conditions of Equation (6*b*). A formal solution of Equation (8) can be obtained as the sum of the solutions to two intermediate problems: (*a*) The homogeneous wave equation subject to the nonhomogeneous boundary conditions; and (*b*) the nonhomogeneous wave equation subject to homogeneous boundary conditions. That is,

$$\bar{u} = \bar{u}_H + \bar{u}_P$$

where $\bar{u}_H$ satisfies

$$\ddot{\bar{u}}_H - \bar{u}_H'' = 0$$
$$\bar{u}_H(\bar{x}, 0) = \dot{\bar{u}}_H(\bar{x}, 0) = \bar{u}_H(0, \bar{t}) = 0 \tag{9a}$$
$$\bar{u}_H(\bar{L}, \bar{t}) = -\bar{V}\bar{t}$$

and $\bar{u}_P$ satisfies:

$$\ddot{\bar{u}}_P - \bar{u}_P'' = f'(\bar{x}, \bar{t})$$
$$\bar{u}_P(\bar{x}, 0) = \dot{\bar{u}}_P(\bar{x}, 0) = \bar{u}_P(0, \bar{t}) = \bar{u}_P(\bar{L}, \bar{t}) = 0 \tag{9b}$$

The appropriate solutions are found to be[2]

$$-\bar{u}_H(\bar{x}, \bar{t}) = \frac{\bar{V}\bar{x}\bar{t}}{\bar{L}} + \frac{2\bar{V}\bar{L}}{\pi^2}\sum_{n=1}^{\infty}\frac{(-1)^n}{n^2}\sin\left(\frac{n\pi\bar{x}}{\bar{L}}\right)\sin\left(\frac{n\pi\bar{t}}{\bar{L}}\right) \tag{10a}$$

$$-\bar{u}_P(\bar{x}, \bar{t}) = \frac{2}{\bar{L}}\sin\frac{n\pi\bar{x}}{\bar{L}}\int_0^{\bar{t}}\sum_{n=1}^{\infty}\left[\int_0^{\bar{L}} f(\bar{x}, \bar{t}) \cos\frac{n\pi\bar{x}}{\bar{L}}\,dx\right]\sin\frac{n\pi}{\bar{L}}(\bar{t} - \tau)d\tau \tag{10b}$$

[2] Note that Equation (10*a*) is not an ordinary solution to Equation (8*a*) since $\ddot{\bar{u}}_H$ does not exist. Inasmuch as $\ddot{\bar{u}}$ appears explicitly in Equation (4*a*), this situation may be circumvented either by considering only a finite number of terms in the series for u_H, or by suitably modifying the boundary condition on $\bar{u}_H$ at $x = L$ so as to remove the discontinuity in $\dot{\bar{u}}_H(\bar{L}, 0)$. The theory of generalized solutions to hyperbolic equations provides the basis for either approach [11].

The corresponding expressions for the axial force

$$\bar{P} = \bar{P}_H + \bar{P}_P$$

are

$$\bar{P}_H(\bar{x}, \bar{t}) = \frac{\bar{V}\bar{t}}{\bar{L}} + \frac{2\bar{V}}{\pi} \sum_{n=1} \frac{(-1)^n}{n} \cos \frac{n\pi\bar{x}}{\bar{L}} \sin \frac{n\pi\bar{t}}{\bar{L}} \quad (11a)$$

and

$$\bar{P}_P(\bar{x}, \bar{t}) = \frac{2\pi}{\bar{L}^2} \cos \frac{2\pi\bar{x}}{\bar{L}} \int_0^{\bar{t}} \left\{ \sum_{n=1}^{\infty} n \left[\int_0^{\bar{L}} f(\bar{x}, \tau) \cos \frac{n\pi\bar{x}}{\bar{L}} d\bar{x} \right] \sin \frac{n\pi}{\bar{L}} (\bar{t} - \tau) d\tau \right\} - f(\bar{x}, \bar{t}) \quad (11b)$$

Equation (11*a*) represents the axial force as determined by the homogeneous wave equation, and by proper evaluation of the series provides the well-known result that the force builds up in stepwise fashion upon reflection of the stress wave from either end of the column. The magnitude of each step is given by $\bar{V}$.

We consider now the implication of Hoff's assumption as to the deflected shape of the column given by Equation (3). Upon substituting this relation into Equation (8*b*) for $f(\bar{x}, \bar{t})$ and integrating Equation (11*b*) by parts, there results

$$\bar{P}_P(\bar{x}, \bar{t}) = -\frac{\pi^2}{4\bar{L}^2} [\bar{V}(\bar{t})^2 - \bar{V}_0^2] + \frac{\pi^2}{4\bar{L}^2} \cos \frac{2\pi\bar{x}}{\bar{L}} \int_0^{\bar{t}} \frac{d}{d\tau} \bar{V}(\tau)^2 \cos \frac{2\pi}{\bar{L}} (\bar{t} - \tau) d\tau \quad (12)$$

Comparing this result with Equation (7), we see that, except for the jump[2] in $\bar{P}_H$, the integral term in Equation (12) represents the correction to Hoff's average force. The magnitude of this correction is time-dependent and varies as $\cos 2\pi\bar{x}/\bar{L}$ over the column. This result is a consequence only of the assumption regarding the shape of the deflected column given by Equation (3). We conclude, therefore, that this assumption is not compatible with neglecting the axial inertia terms in Equation (4); i.e., that the axial force is not constant along the column at each instant of time.

For conventional engineering materials, $\bar{V}$ must be less than about 0.005 for the column to remain elastic during the initial traverse of the axial stress wave; $\bar{V}$ would have to be less than about 0.001 for the assumptions of small strains and elastic behavior to apply up to the time of maximum $\bar{P}$. The latter value of $\bar{V}$ is also compatible with the tacit assumption that the displacement of the moving end of the column remains small compared to L. It is of interest to contrast this value of $\bar{V}$ with what would correspond to the usual column compression test considered by Hoff. The speed of sound in steel or aluminum is about 2×10^5 ips. The loading-head velocity in a testing machine probably would not exceed 0.02 ips, which corresponds to a value of $\bar{V} = 10^{-7}$ for a steel or aluminum column. Thus a value of $\bar{V} = 10^{-4}$ represents a rate of loading ten thousand times as rapid as in an ordinary column test.

Numerical Solution of the Column Equations

Consider now the numerical solution of the general column equations for the conditions of Hoff's problem, Equations (4) and (6). This was accomplished by writing finite-difference equivalents for the derivatives, and solving the resulting difference equations in relation to a rectangular network, or mesh, of points p_{ij} whose separation $\Delta\bar{x}$ and $\Delta\bar{t}$ is uniform in the $\bar{x}(i)$ and $\bar{t}(j)$ directions, respectively. Introduce the notation

$$g(i\Delta\bar{x}, j\Delta\bar{t}) = g_{i,j}$$

Based on an equally divided mesh,[4] i.e., $\Delta\bar{x} = \Delta\bar{t}$, the finite-difference equations yield the following explicit recurrence formulas for $g_{i,j+1}$, $\bar{u}_{i,j+1}$:

$$g_{i,j+1} = 2g_{i,j} - \bar{P}_{i,j}(g_{i+1,j} - 2g_{i,j} + g_{i-1,j}) + (\bar{u}_{i,j+1} - 2\bar{u}_{i,j} + \bar{u}_{i,j-1})g'_{i,j} + (\Delta\bar{x})^2 g_0^{iv} - (g_{i+2,j} - 4g_{i+1,j} + 6g_{i,j} - 4g_{i-1,j} + g_{i-2,j})/(\Delta\bar{x})^2 \quad (13a)$$

$$\bar{u}_{i,j+1} = \bar{u}_{i-1,j} + \bar{u}_{i,j} - \bar{u}_{i,j-1} - (\Delta\bar{x})^2 g_0' g_0'' + (g_{i+1,j} - 2g_{i,j} + g_{i-1,j})g'_{i,j} \quad (13b)$$

where

$$g'_{i,j} = (g_{i+1,j} - g_{i-1,j})/2\Delta\bar{x} \quad (13c)$$

$$\bar{P}_{i,j} = (\bar{u}_{i+1,j} - \bar{u}_{i-1,j})/2\Delta\bar{x} + (g'_{i,j})^2/2 - (g_0')^2/2 \quad (13d)$$

All derivatives are approximated with a truncation error of order $(\Delta\bar{x})^3$.

The boundary and initial conditions of Equation (6) require

$$g_{i,0} = g_0(i\Delta\bar{x})$$

$$g_{0,j} = g_{m,j} = 0$$

$$g_{i,j} = -g_{-i,j};\ g_{m+i,j} = -g_{m-i,j}$$

$$g_{i,j} = g_{i-1}$$

$$\bar{u}_{i,0} = \bar{u}_{0,j} = 0$$

$$\bar{u}_{i,1} = \bar{u}_{i-1}$$

$$\bar{u}_{m,j} = -j(\bar{V}\Delta\bar{t})$$

where m is the number of mesh divisions in the $\bar{x}$-direction; i.e., $m\Delta\bar{x} = \bar{L}$.

If the $\bar{u}$ are known, Equation (13*a*) yields a value for g at a point in the $j + 1$ row in terms of already known values in the $j - 1$ and j-rows. Thus, the entire g-mesh can be computed. Similarly, if the g are known throughout the $\bar{u}$-mesh, Equation (13*b*) permits the unknown $\bar{u}$ to be determined. It will be noted from these equations that $\bar{u}_{i,j+1}$ involves only values of $\bar{u}$ and g in the j and $j - 1$ row, whereas $g_{i,j+1}$ involves $\bar{u}_{i,j+1}$ as well. Thus, the solution can be generated one row at a time starting with the $\bar{u}$, and requires only that a 3 by m-mesh be retained for both $\bar{u}$ and g. Were it not for this fact the solution would have to be of an iterative type [12].

Discussion of Results

The finite-difference equations for g, $\bar{u}$, and $\bar{P}$ were solved on an IBM-650 digital computer. Solutions were obtained for both a six and sixteen-point mesh; i.e., $\Delta\bar{x} = \Delta\bar{t} = \bar{L}/6$ and $\bar{L}/16$. Inasmuch as the finite-difference formulation has not been shown to lead necessarily to meaningful results, the adequacy of the method has been studied from an empirical point of view. The following three "confidence" checks were employed:

1 If the coupling terms in the equation for $\bar{u}$ are neglected, the numerical results for $\bar{u}$ and $\bar{P}$ can be compared directly with known solutions to the homogeneous wave equation. This will always be the case for sufficiently early times in the motion.

2 For sufficiently small $\bar{V}$ the numerical solutions should agree generally with Hoff's results.

[2] Recall that the quantity $\bar{P}_H$ is uniform along the column except at the wave front where it exhibits a jump of magnitude $\bar{V}$. At times when the wave is at either end of the column, $\bar{P}_H = \bar{V}\bar{t}/\bar{L}$.

[4] Reference [12] contains a detailed discussion of the numerical method. A formulation leading to implicit recurrence formulas was not practical for the available computer.

3 Whenever Hoff's assumption as to the half sine shape of the deflection curve is verified, the analytical results for $\bar{u}$ and $\bar{P}$ presented earlier apply.

Each of these confidence checks was applied successfully to the computer solutions where applicable. With reference to the first, a solution to the homogeneous wave equation for $\bar{u}$ and $\bar{P}$ was obtained for the parameter values $\bar{L} = 66$, $V = 0.00022556$. The resulting values of $\bar{u}$ and $\bar{P}$ were correct to eight decimal places over the entire range of the solution; i.e., 45 traverses of the wave. The numerical solution, of course, does not properly represent the discontinuity in $\bar{P}$ at the wave front. Here the solution is found to yield precisely one half the magnitude of the jump. The correct value is then obtained at the end of the next time interval. The results for $\bar{u}$ were correct at each point throughout the solution since this quantity is continuous everywhere.

Computer solutions were obtained for four sets of parameter values and are summarized in Table 1. The values of Hoff's dynamic similarity number are also indicated. These solutions cover the range of interest in so far as conventional structural compression members are concerned (slenderness ratios less than 150). Hoff's equation was solved on the IBM-650 computer by numerical integration in a manner which insured that the results were correct to four significant figures.

With reference to Problem I, consider first the results for transverse displacements $\bar{y}(\bar{x}, \bar{t})$.

The deflection curve was symmetrical to at least three significant figures and did not deviate from the sine curve by more than 2 per cent. This result permits the confidence checks to be applied to the computer solution for $\bar{P}$ and $\bar{u}$.

The mid-span deflection of the column is compared with Hoff's results in Fig. 1. The two curves are essentially identical for the

Table 1 Summary of computer solutions

Problem	Slenderness ratio, $\bar{L}$	Nondimensional forcing velocity, $\bar{V}$	Dynamic similarity number, Ω	Remarks
I	66	0.00023	2.25	Solution obtained for 45 wave traverses using six-point mesh. In agreement with Hoff's results. Elastic range exceeded at max $\bar{P}$ for most materials.
II	24	0.0047	2.25	Same as Problem I except solution obtained for 15 wave traverses. Not a "structural" column.
III	144	0.0001	0.106	Same as Problem I except elastic range would not be exceeded for some materials at max $\bar{P}$.
IV	144	0.001	0.00106	Solution obtained for 20 wave traverses using 16-point mesh. Not in agreement with Hoff's results beyond max $\bar{P}$. Elastic range exceeded prior to max $\bar{P}$ for most materials.

$Y_0 = 0.25$ for all problems.

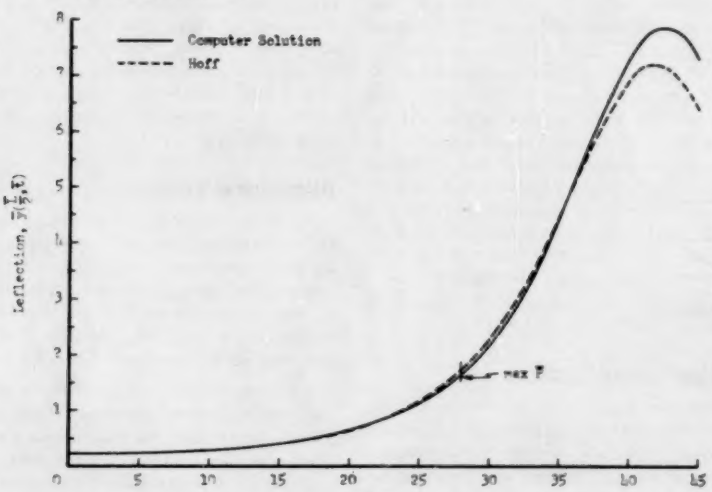

Fig. 1 Mid-span deflection, Problem I

first 25 traverses of the stress wave. Hoff's curve then appears to oscillate about the computer solution, being low at the point of maximum deflection by about 8 per cent.

Fig. 2 shows the time variation of axial force $\bar{P}$ (actually strain) at two column stations. Also shown are Hoff's results which, by assumption, are equally applicable to every column station.

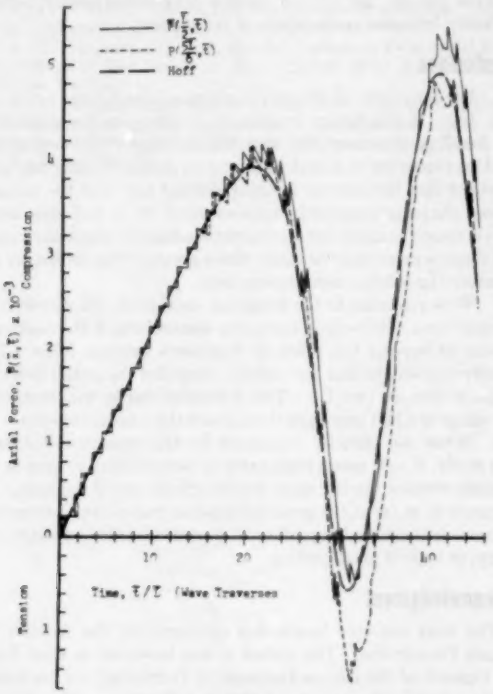

Fig. 2 Axial force, Problem I

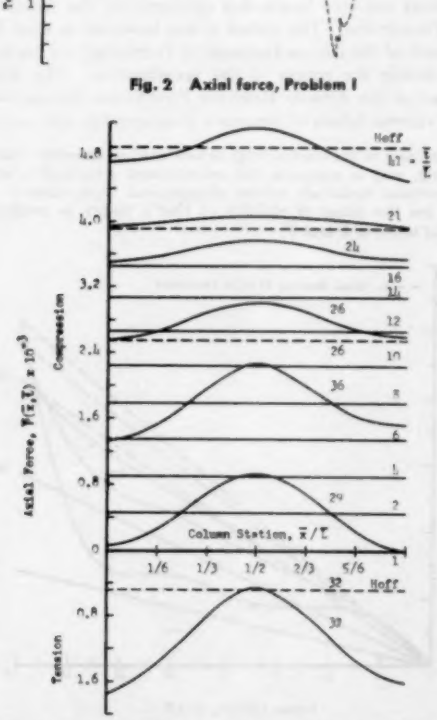

Fig. 3 Spanwise distribution of axial force, Problem I

As is observed from Fig. 2, $\bar{P}$ exhibits the same general behavior as Hoff's average force. The principal difference, aside from the stepwise variation, is the fact that $\bar{P}$ does not remain constant behind the wave front. This behavior is clearly indicated in Fig. 3 where the spanwise distribution of force is shown at times where the wave front is at an end of the column. (Hoff's results are given by the horizontal dashed lines.) The distribution of $\bar{P}$ beyond about the 23rd traverse is essentially that of a cosine curve. This behavior agrees with the sine shape of $\mathcal{G}$ and thus amounts to a consistency check on the computer solution.

A slight asymmetry in the force distribution can be observed in Fig. 3. The nature of this asymmetry agrees with the position of the wave front; i.e., the force is greater at the end of the column corresponding to the position of the wave front at that time. Where this occurs, it indicates a measurable relief in compressive strain due to bending during a single transit of the stress wave.

The axial force as determined from the computer solution exceeds Hoff's values up to about the time of the first minimum in $\bar{P}$. The average difference amounts to about 3 per cent at the maximum value of the force. Locally, the maximum difference is about 5 per cent as a result of the jump in force at the wave front. According to the numerical values shown in Fig. 3, the axial stress would exceed the yield stress for ordinary engineering materials at about the 14th traverse of the wave (the maximum in $\bar{P}$ occurs at about the 21st traverse). The elastic range would actually be exceeded somewhat prior to this time owing to the additive bending stresses.[5] The (first) maximum value of $\bar{P}$ corresponds to a force which exceeds the Euler load for the column by about 80 per cent.

The spanwise distribution of axial displacement $\bar{u}$, at times when the wave is at an end of the column, is shown in Fig. 4. The (dashed) straight lines represent $\bar{u}$ as determined from the

[5] The combined strain at a distance r (the radius of gyration) above the neutral axis of the column, in nondimensional notation, is

$$e = \bar{P} + (\bar{y}'' - \bar{y}w'')$$

At the 14th traverse the bending strain is 18 per cent of the axial strain; at the 21st traverse this strain amounts to 53 per cent of the axial strain.

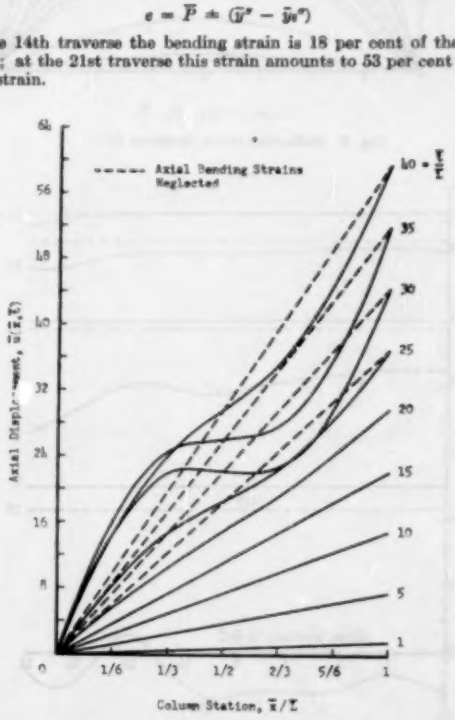

Fig. 4 Axial displacement, Problem I

homogeneous wave equation. The fact that the two values of $\bar{u}$ agree very closely at the center of the column is also in accordance with the analytical results discussed earlier.

The results for Problems II and III show the same general behavior as compared to the corresponding solutions to Hoff's equation. Problem IV treats the same column parameters considered in Problem III, but involves a tenfold more rapid rate of loading. The results of this computation, based on the 16-point mesh, are shown in Figs. 5 through 7. It is observed that the solution compares closely with Hoff's results up to the 10th traverse, but deviates markedly in all respects at later times.

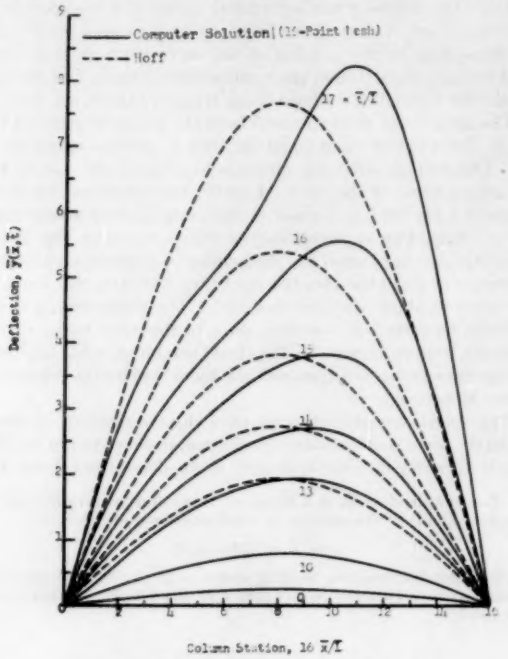

Fig. 5 Deflection curve, Problem IV

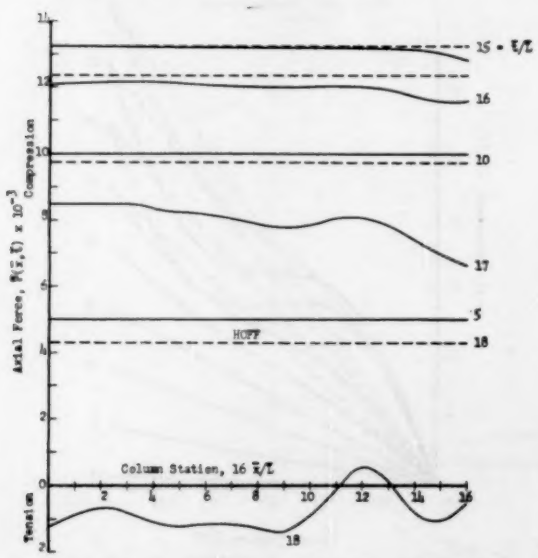

Fig. 6 Spanwise distribution of axial force, Problem IV

The fact that Hoff's equation eventually breaks down for $\Omega = 0.001$ does not necessarily mean that this value of the dynamic similarity number (for $\bar{Y}_0 = 0.25$) represents an upper bound to the validity of the theory. In fact, it is unlikely that such a criterion can be found in terms of Ω alone, but rather will involve $\bar{L}$ and $\bar{V}$ explicitly. Some work has been carried out in this direction and the indications are that Hoff's value of max $\bar{P}$ is reasonable even though the column motion may subsequently deviate markedly from the assumptions of the theory.

Conclusions

1 For conventional structural columns (slenderness ratios less than 150), Hoff's theory is completely adequate for predicting the bending displacements and the average (time-dependent) axial load recorded in a rigid, constant-strain-rate testing machine, provided that the column remains elastic,[6] and that the initially curved shape is reasonably approximated by a half sine wave. This is meant to apply for equivalent loadings in which the rate of end displacement may be many times greater than ordinarily encountered in column compression tests.

2 With reference to the foregoing conclusion, the distribution of axial force will become markedly nonuniform if the loading is continued beyond the point of maximum average force. This distribution will be like $\cos(2\pi x/L)$ provided the initial deflected shape is like $\sin(\pi x/L)$. The deflection curve will remain in the shape of a half sine wave throughout the (elastic) motion.

3 While not directly supported by the numerical results of this study, it now seems reasonable to assume that so long as the column remains elastic, axial inertia effects are of negligible importance in so far as the gross behavior of conventional structural columns is concerned regardless of the initial deflected shape, end fixity, or type of axial loading.

Acknowledgment

The work reported herein was sponsored by the Armour Research Foundation. The author is also indebted to Prof. Lloyd H. Donnell of the Illinois Institute of Technology for his helpful advice during the course of the investigation. Mr. Thomas Englehart of the Armour Research Foundation was responsible for the various details of computer programming and operation.

[6] Restriction to the elastic range is here used as an index of the rate of loading, and is adequate for conventional structural materials. For structural materials whose proportional limit exceeds about 200,000 psi the range of validity of Hoff's theory is properly expressed in terms of $\bar{L}$ and $\bar{V}$.

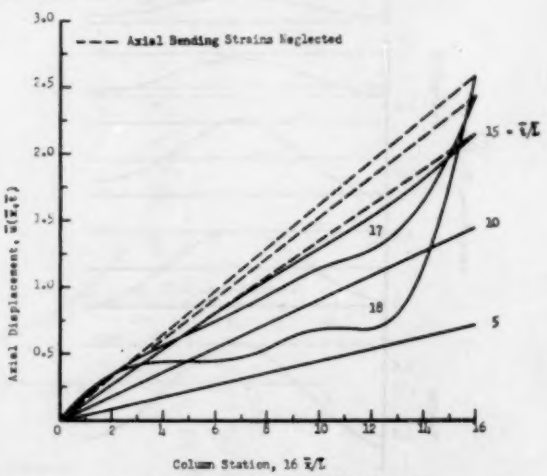

Fig. 7 Axial displacement, Problem IV

References

1 N. J. Hoff, "The Dynamics of the Buckling of Elastic Columns," JOURNAL OF APPLIED MECHANICS, vol. 18, TRANS. ASME, vol. 73, 1951, pp. 68–74.

2 C. Koning and J. Taub, "Impact Buckling of Thin Bars in the Elastic Range Hinged at Both Ends," NACA TM 748, June, 1934.

3 J. Taub, "Impact Buckling of Thin Bars in the Elastic Range for Any End Condition," NACA TM 749, July, 1934.

4 J. H. Meier, "On the Dynamics of Elastic Buckling," *Journal of the Aeronautical Sciences*, vol. 12, 1945, pp. 433–440.

5 T. Davidson and J. H. Meier, "Impact on Prismatical Bars," *Proceedings of The Society for Experimental Stress Analysis*, vol. 4, 1947, pp 88–111.

6 M. A. Lavrentiev and A. U. Ishlinsky, "Dynamic Forms of Loss of Stability of Elastic Systems" (in Russian), *Notes of the Academy of Science USSR*, Doklady Akademiya Nauk USSR, vol. 64, 1949, pp. 779–782.

7 T. H. H. Pian and J. N. Siddall, "Dynamic Buckling of Slender Struts," Massachusetts Institute of Technology, Report to ONR, May, 1950.

8 N. J. Hoff, S. V. Nardo, and B. Erickson, "The Maximum Load Supported by an Elastic Column in a Rapid Compression Test," Proceedings of the First U. S. National Congress of Applied Mechanics, 1951, pp. 419–423.

9 J. P. Chawla, "Numerical Analysis of the Process of Buckling of Elastic and Inelastic Columns," Proceedings of the First U. S. National Congress of Applied Mechanics, 1951, pp. 435–441.

10 J. F. Davidson, "Buckling of Struts Under Dynamic Loading," *Journal of the Mechanics and Physics of Solids*, vol. 2, 1953, pp. 54–66.

11 I. G. Petrovsky, "Lectures on Partial Differential Equations," Interscience Publishers, Inc., New York, N. Y., 1954, Chapters I and II.

12 E. Sevin, "On the Elastic Bending of Columns Due to Dynamic Axial Forces Including Effects of Axial Inertia," Doctoral thesis, Illinois Institute of Technology, June, 1958.

H. H. BLEICH
Professor of Civil Engineering,
Director,
Institute of Flight Structures,
Columbia University,
New York, N. Y.
Mem. ASME

R. SHAW
Research Assistant,
Institute of Flight Structures,
Columbia University,
New York, N. Y.

Dominance of Shear Stresses in Early Stages of Impulsive Motion of Beams[1]

In order to compare the magnitude of bending stresses and shear stresses in beams under the action of impulsive forces, the values of these stresses are determined from the known differential equations for the Timoshenko beam. It is found that in the early stages, soon after the initiation of the motion, the shear stresses are of much larger magnitude than the bending stresses. This result indicates that for sufficiently large initial velocities first yielding will be in shear, a matter of consequence in plastic analysis.

1 Introduction

A RECENT paper[2] has recognized the necessity of studying the dynamic response of beams in which yielding in shear is possible. Based on a rigid-plastic approach, earlier theories which allowed for yielding in bending only are extended, showing that for certain parameters yielding in shear alone, or in shear and bending simultaneously, is to be expected. Among other things the paper indicates that, on the basis of rigid-plastic theory, yielding in shear will occur if the beam under static loads is either of about equal strength in shear and in bending, or weaker in shear than in bending.

It is generally known from studies of the propagation of waves in beams that at high frequencies the effects of shear and rotatory inertia cannot be neglected. It is therefore to be expected that in case of impulsive motion shear stresses will be important—to say the least—during a short period after initiation of the motion. The situation during this period cannot be studied by a rigid-plastic theory.

It is the purpose of this paper to show that all beams, even those which are statically much stronger in shear than in bending, will begin to yield in shear before yielding in bending, if subjected to sufficiently high initial velocity distributions. This conclusion is drawn from an elastic approach allowing for shear and rotary inertia effects, based on the well-known differential equations for the Timoshenko beam. The yielding in shear found occurs a very short time after the initiation of the motion; it is an additional case of yielding in shear which does not occur in the rigid-plastic analysis.

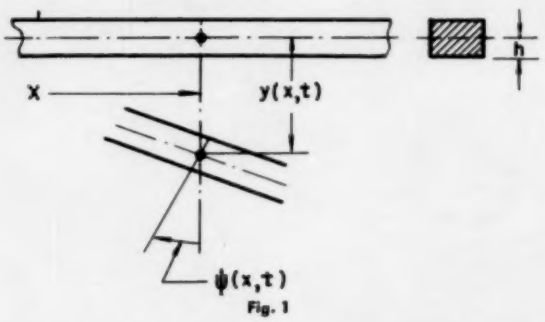

Fig. 1

No attempt is made to extend existing elastoplastic theories;[3,4] it will be shown solely that for sufficiently large initial velocities yield stress in shear will always be reached first. For this purpose it is sufficient to consider the elastic response of a Timoshenko beam which is governed by the differential equations

$$kG(y'' - \psi') - \rho\ddot{y} = 0$$
$$Er^2\psi'' + kG(y' - \psi) - \rho r^2\ddot{\psi} = 0 \qquad (1)$$

[1] This paper is the result of research sponsored by the Office of Naval Research under Contract Nonr 266-08.

[2] M. G. Salvadori and P. Weidlinger, "On the Dynamic Strength of Rigid-Plastic Beams Under Blast Loads," *Proc. ASCE, Journal of the Engineering Mechanics Division*, EM 4, October, 1957.

Contributed by the Applied Mechanics Division and presented at the Annual Meeting, Atlantic City, N. J., November 29–December 4, 1959, of THE AMERICAN SOCIETY OF MECHANICAL ENGINEERS.

Discussion of this paper should be addressed to the Secretary, ASME, 29 West 39th Street, New York, N. Y., and will be accepted until April 10, 1960, for publication at a later date. Discussion received after the closing date will be returned.

NOTE: Statements and opinions advanced in papers are to be understood as individual expressions of their authors and not those of the Society. Manuscript received by ASME Applied Mechanics Division, December 30, 1958. Paper No. 59—A-60.

[3] H. H. Bleich and M. G. Salvadori, "Impulsive Motion of Elastoplastic Beams," *Trans. ASCE*, vol. 120, 1955, p. 499.

[4] H. H. Bleich, "Response of Elastoplastic Structures to Transient Loads," Trans. New York Academy of Sciences, series II, vol. 18, 1955, p. 135.

Nomenclature

A = cross-sectional area of beam
$c \equiv (kG/\rho)^{1/2}$ = quantity of the order of velocity of shear waves
E, G = Young's modulus, modulus of rigidity, respectively
k = constant in Equation (1), k = 5/6 for rectangular cross section
k_1 = constant in Equation (2), k_1 = 3/2 for rectangular cross section
$\kappa \equiv kk_1$
l = span of simple beam; half length of free-free beam; reference length
M = bending moment
Q = shear force
r = radius of gyration of cross section
s = variable in Laplace transform
t = time
x = co-ordinate
$y(x, t)$ = displacement of beam
$\bar{y}(x, s)$ = transform of $y(x, t)$
$V_0(x/l)$ = initial velocity
V_0 = amplitude of $V_0(x/l) = V_0 \sin \pi x/l$ in case of simple beam
$\alpha \equiv (\rho/kG)^{1/2}$, $\beta \equiv (\rho/E)^{1/2}$, $\delta \equiv \pi/\alpha l$, $\lambda \equiv \pi/\beta l$ } constants
ρ = specific mass of material of beam
σ, τ = bending and shear stress, respectively
ψ = rotation of cross section
ω_1, ω_2 = frequencies of simple beam

where y and ψ are the displacement and rotation of the cross section, Fig. 1, respectively. (The other symbols are defined in the nomenclature.) The bending moment M, the shear force Q, and the stresses σ, τ are

$$\left.\begin{aligned} M &= -EAr^2\psi' \qquad & Q &= kAG(y' - \psi) \\ \sigma &= \frac{Mh}{Ar^2} = -Eh\psi' \qquad & \tau &= \frac{k_1 Q}{A} = \bar{k}G(y' - \psi) \end{aligned}\right\} \quad (2)$$

where $\bar{k} = kk_1$.

The case of the simply supported beam under a sinusoidal initial velocity permits a closed solution and is treated in Section 2. This case gives an understanding of the situation with a minimum of mathematical manipulations; it shows that the shear stresses are predominant during a very short time after initiation of the motion. For other boundary conditions or initial velocity distributions, it appears therefore sufficient to obtain a solution valid for small values of the time; such a solution can be obtained in closed form by Laplace transform methods. This is shown in the case of a free-free beam in Section 3 and in the case of discontinuities in Section 4.

In the final Section 5, the question is considered whether the solutions presented are applicable to cases of motion due to shock or impact; it is found that this is not the case, because the short time required for external forces—of however short duration—to establish a uniform velocity in each element of the bar is of the same order as the short time during which the shear stresses are dominant. The concept of the Timoshenko beam in shock and impact problems is therefore not sufficient to determine shear stresses during the very early period of interest. During this period stresses at right angles to the beam axis are of the same importance as the shear stresses and a higher approximation than the Timoshenko beam theory is required. The present paper applies, therefore, only to the rather academic case of the response of beams having prescribed initial velocities.

2 Response of a Simple Beam Due to an Initial Velocity $V_0 \sin \pi x/l$.

For the simple beam shown in Fig. 2 we have the boundary conditions $y = 0$, $M = 0$ at $x = 0$ and $x = l$ for all values of the time t; giving

$$y(0, t) = y(l, t) = \psi'(0, t) = \psi'(l, t) = 0 \quad (3)$$

The initial conditions are obtained from the fact that at $t = 0$ the displacement y, the rotation ψ and the corresponding velocity $\dot{\psi}$ must vanish, while the velocity y must equal the initial one,

$$\begin{aligned} y(x, 0) &= \psi(x, 0) = \dot{\psi}(x, 0) = 0 \\ \dot{y}(x, 0) &= V_0 \sin \pi x/l \end{aligned} \quad (4)$$

This problem lends itself to solution by the mode approach because the displacement components of the modes for the simply supported Timoshenko beam are proportional to $\sin (n\pi x/l)$; due to the second boundary condition (4) modes with $n \neq 1$ will not be excited, such that a closed solution containing only the two modes for $n = 1$ is obtained.

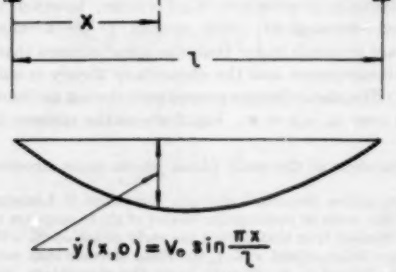

Fig. 2

A suitable expression for the modes for $n = 1$ is

$$y = e^{\pm i\omega t} \sin \pi x/l \qquad \psi = \mu_i e^{\pm i\omega t} \cos \pi x/l \quad (5)$$

which satisfies Equations (3). Substitution in Equations (1) furnishes the frequency equation

$$(\omega_i^2 - \delta^2)(\lambda^2 - \omega_i^2) + \frac{l^2}{\pi^2 r^2}\omega_i^2\delta^2 = 0 \quad (6)$$

where

$$\delta^2 = \frac{\pi^2}{l^2}\frac{kG}{\rho}; \quad \lambda^2 = \frac{\pi^2}{l^2}\frac{E}{\rho} \quad (7)$$

Equation (6) leads to two frequencies ω_1 and ω_2. The corresponding ratios μ_i are

$$\mu_i = -\frac{\pi}{l}\left(\frac{\omega_i^2}{\delta^2} - 1\right) \quad (8)$$

The generalized forces vanish in the present case of impulsive loading such that the differential equations for the generalized co-ordinates q_i, $(i = 1, 2)$

$$\ddot{q}_i + \omega_i^2 q_i = 0 \quad (9)$$

have the general solutions

$$q_i = C_i \sin (\omega_i t + \alpha_i) \quad (10)$$

The first two initial conditions (4) give immediately $\alpha_1 = \alpha_2 = 0$, while the remaining two equations give

$$\begin{aligned} C_1 &= -\frac{\omega_2^2 - \delta^2}{\omega_1(\omega_1^2 - \omega_2^2)} V_0 \\ C_2 &= \frac{\omega_1^2 - \delta^2}{\omega_2(\omega_1^2 - \omega_2^2)} V_0 \end{aligned} \quad (11)$$

Substitution of the solutions

$$\begin{aligned} y &= (C_1 \sin \omega_1 t + C_2 \sin \omega_2 t) \sin \frac{\pi x}{l} \\ \psi &= (\mu_1 C_1 \sin \omega_1 t + \mu_2 C_2 \sin \omega_2 t) \cos \frac{\pi x}{l} \end{aligned} \quad (12)$$

into Equations (2) leads finally to the following expressions for the bending and shear stresses:

$$\begin{aligned} \sigma = -Eh\psi' &= \frac{\pi^2 Eh}{l^2} V_0 \frac{(\delta^2 - \omega_1^2)(\omega_2^2 - \delta^2)}{\delta^2(\omega_2^2 - \omega_1^2)} \\ &\quad \times \left[\frac{\sin \omega_1 t}{\omega_1} - \frac{\sin \omega_2 t}{\omega_2}\right] \sin \frac{\pi x}{l} \\ \tau = \bar{k}G(y' - \psi) &= \frac{\pi \bar{k}G}{l} V_0 \frac{1}{\delta^2(\omega_2^2 - \omega_1^2)} \\ &\quad \times \left[(\omega_2^2 - \delta^2)\omega_1 \sin \omega_1 t + (\delta^2 - \omega_1^2)\omega_2 \sin \omega_2 t\right] \cos \frac{\pi x}{l} \end{aligned} \quad (13)$$

In order to interpret this result, let ω_1 be the smaller of the frequencies; inspection of Equation (6) shows then

$$\delta^2 - \omega_1^2 > 0, \quad \omega_2^2 - \delta^2 > 0 \quad (14)$$

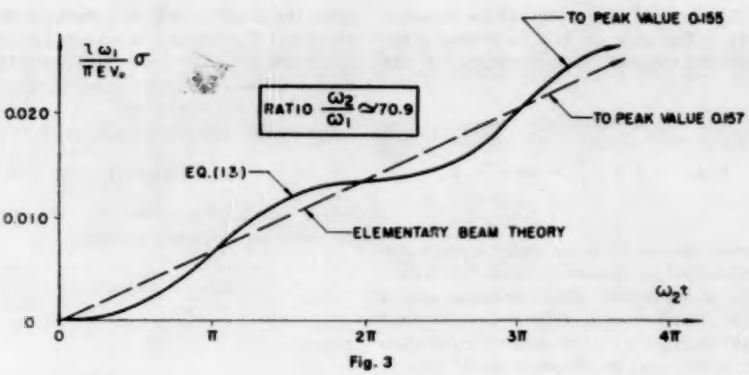

Fig. 3

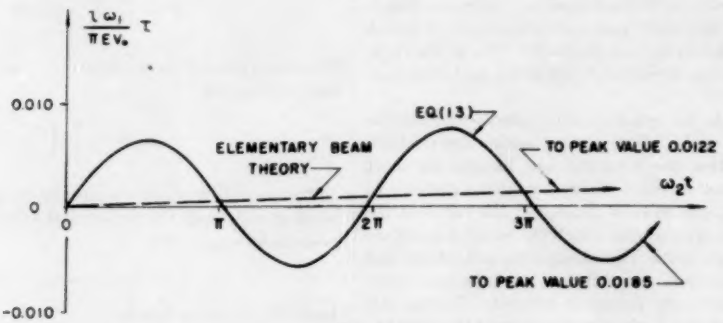

Fig. 4

The various differences $\delta^2 - \omega_1^2$, and so on, in Equation (13) are therefore all positive numbers and the time dependency is given by the combination of the terms sin $\omega_1 t$ and sin $\omega_2 t$ with their respective positive coefficients. It may be noted that when $l^2/\pi^2 r^2$ is much larger than unity ω_2^2 is much larger than δ^2, while ω_1^2 is very much smaller than δ^2.

A typical plot of the bending stress σ at mid-span is shown in Fig. 3. The diagram has a horizontal tangent at $t = 0$, and the moment remains small for a fraction of the period of the faster mode; i.e., for $\omega_2 t \ll \pi$. To obtain the behavior in this range the sines in the equation for σ can be replaced by the first two terms of their expansion sin $\omega t \simeq \omega t - \omega^3 t^3/6$, with the result

$$\sigma \simeq \frac{\pi^2 Eh}{l^2} V_0 \frac{(\delta^2 - \omega_1^2)(\omega_2^2 - \delta^2)}{6\delta^2\omega_2^2} (\omega_2 t)^3 \sin \frac{\pi x}{l} \qquad (15)$$

Fig. 4 shows a typical plot of the shear stress τ, where the coefficient of sin $\omega_1 t$ is larger than that of sin $\omega_2 t$ and has the same sign such that the τ-curve does not have a horizontal tangent at $t = 0$ as the σ-curve has. For small values of the time $t \ll \pi/\omega_2$ one finds similarly (using also the fact $\omega_2^2 \gg \delta^2 \gg \omega_1^2$)

$$\tau \simeq \frac{\pi G V_0}{l\omega_2} \bar{k} \left[\omega_2 t - \frac{1}{6} (\omega_2 t)^3 \right] \cos \frac{\pi x}{l} \qquad (16)$$

The error in the approximations remains below 5 per cent as long as $\omega_2 t < 1$.

To be able to compare the order of magnitude of the stresses σ and τ, Equation (15) can be approximated for long beams $l/h \gg 1$; in such cases $\omega_2^2 \gg \delta^2$, while $\omega_1^2 \ll \delta^2$, such that $(\delta^2 - \omega_1^2)(\omega_2^2 - \delta^2) \simeq \delta^2\omega_2^2$. Equation (15) may then be written

$$\sigma \simeq \frac{\pi G V_0}{l\omega_2} \frac{\pi E h}{6Gl} \sin \frac{\pi x}{l} (\omega_2 t)^3 \simeq \frac{\pi G V_0}{l\omega_2} \frac{h}{l} (\omega_2 t)^3 \sin \frac{\pi x}{l} \qquad (15a)$$

where $\pi E/6G \simeq 1$.

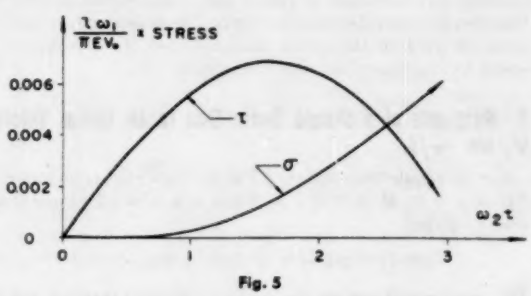

Fig. 5

The ratio h/l being much smaller than unity, while in Equation (16) $\bar{k} > 1$, the shear stress will be much larger than the bending stress for the entire range of validity of Equations (15), (16), $\omega_2 t < 1$. If the initial velocity is made large enough the shear stress (16) will exceed the yield stress at a time $\omega_2 t < 1$ and yield will occur in shear prior to yield in bending.

Figs. 3 and 4 show also the stresses from the elementary beam theory. It is apparent that the latter gives shear stresses which are substantially in error even if $\omega_2 t$ is large; however, in the case considered—rectangular cross section $l \gg h$—the bending stresses are so much larger than the shear stresses that the error is of no consequence and the elementary theory is sufficient for $\omega_2 t \geq \pi$. The shear stresses prevail only during an "early phase," which is over at $\omega_2 t = \pi$; Fig. 5 shows the stresses during this stage.[5]

The duration of the early phase where shear stresses are para-

[5] The situation described changes somewhat if I-beams with extremely thin webs or rectangular beams of short span are considered. While it remains true that during the early phase $\omega_2 t \ll \pi$ the bending stresses are unimportant $\sigma \ll \tau$, the shear stresses may remain dominant even for $\omega_2 t > \pi$; in such cases the elementary beam theory gives only a crude approximation of the stresses (see Section 5).

mount is defined by $\omega_0 t \approx 1$ and it is useful to have a simple estimate for this time. Provided $l/2h$ is not too small, say, >2, the term $l^2/\pi^2 r^2$ in the frequency Equation (6) is large. In this case $\omega_0^2 \gg \lambda^2 > \delta^2$ such that the first term in Equation (6) is approximately $-\omega_0^4$, and one finds

$$\omega_0^2 = \frac{l^2}{\pi^2 r^2}\,\delta^2 = \frac{kG}{r^2\rho} \equiv \frac{c^2}{r^2} \tag{17}$$

where

$$c = (kG/\rho)^{1/2} \tag{17a}$$

The duration of the early phase is

$$t \simeq r/c \tag{18}$$

where the radius of gyration r is a fraction of the beam depth. For rectangular sections $k \simeq 1$, and c is of the order of the velocity of shear waves; for I-sections with thin webs k may be much smaller than unity such that c is only a fraction of the velocity of shear waves. The early phase is in either case quite short. It does not depend on the length of the beam as long as $l/2h > 2$; this indicates that the duration of the early phase is the same for other initial velocity distributions because the result applies to each term of an expansion

$$V_0 = \Sigma a_n \sin \frac{n\pi x}{l}$$

In this short time the effect of boundary conditions cannot affect parts of the beam at distances far from the support such that the result also ought to apply to other boundary conditions. That this is so can be shown in the following quite elementary manner.

Consider an element of a beam of length dx under the action of the not discontinuous initial velocity $V_0(x/l)$, Fig. 6. After a very short time, while the elastic forces are still small, the displacement must be $y = tV_0(x/l)$, such that there is a differential deflection of the two faces of the element

$$y' = \frac{t}{l}\,V_0'\left(\frac{x}{l}\right)$$

The element may also have rotated by the angle ψ, the total change of shape of the element being

$$\left[\frac{1}{l}\,V_0'\left(\frac{x}{l}\right)t - \psi\right]$$

The shear force is therefore

$$Q = k\,AG\left[\frac{1}{l}\,V_0' t - \psi\right]$$

These forces Q being the only ones acting on the element considered, the angular acceleration is $\rho A r^2 \ddot{\psi} = Q$, or

$$\frac{\pi^2 r^2}{l^2\delta^2}\,\ddot{\psi} + \psi = \frac{1}{l}\,V_0'\left(\frac{x}{l}\right)t \tag{19}$$

Using the leading terms of a power series for ψ to solve (19) and noting $\psi(0) = \dot{\psi}(0) = 0$ one obtains

$$\psi = \frac{l\delta^2}{\pi^2 r^2}\,V_0\left(\frac{x}{l}\right)\frac{t^3}{6} + \cdots$$

The bending stress is

$$\sigma = -Eh\psi' = -\frac{Eh\delta^2}{6\pi^2 r^2}\,V_0''\left(\frac{x}{l}\right)t^3 \tag{20}$$

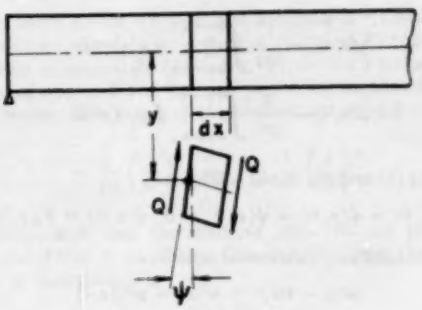

Fig. 6

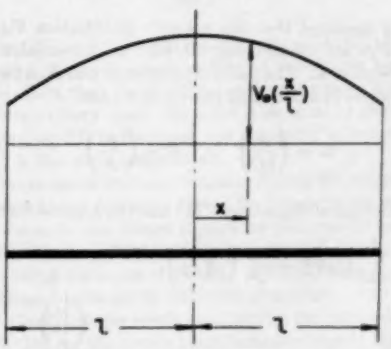

Fig. 7

and the shear stress is

$$\tau = \frac{kG}{l}\,V_0'\left(\frac{x}{l}\right)t \tag{21}$$

where a t^3-term was omitted. These results agree with Equations (15a), (16) for $V_0(x/l) = \sin \pi x/l$ if appropriate approximations due to $\omega_0^2 \gg \delta^2 \gg \omega_1^2$ are made.

This consideration is not valid for points near the support or in case of discontinuous initial velocity $V_0(x/l)$. The latter case can be treated by Laplace-transform methods as shown in Section 3.

3 Response of a Free-Free Beam

The simplicity of the analysis of the response of the simple beam is due to the fact that the displacements y in the various modes are proportional to $\sin n\pi x/l$; if the initial velocity $V_0(x/l)$ is expanded in a Fourier series, each of its terms will therefore excite only the two modes having the same mode number n. In case of other boundary conditions for the beam it is no longer possible to expand $V_0(x/l)$ in any series of orthogonal functions such that each term will excite only two modes, and solutions in closed form are no longer possible except for trivial initial velocity distributions. Approximate expressions valid for small values of the time can be obtained, however, even in the general case by solving Equations (1) by Laplace-transform methods and expanding the solutions in power series in t.

As a representative example, the case of a free-free beam of length $2l$, Fig. 7, will be treated, while other cases are only briefly considered.

Using the reciprocal relationships

$$\bar{y}(x, s) = \int_0^\infty y(x, t)e^{-st}dt$$
$$\bar{\psi}(x, s) = \int_0^\infty \psi(x, t)e^{-st}dt \tag{22}$$

and

$$y(x,t) = \frac{1}{2\pi i}\int_{-i\infty+\epsilon}^{i\infty+\epsilon} \bar{y}(x,s)e^{st}ds$$
$$\psi(x,t) = \frac{1}{2\pi i}\int_{-i\infty+\epsilon}^{i\infty+\epsilon} \bar{\psi}(x,s)e^{st}ds \tag{23}$$

Equations (1) and the initial conditions

$$y(x,0) = \dot{\psi}(x,0) = \psi(x,0) = 0 \quad \dot{y}(x,0) = V_0(x/l) \tag{24}$$

furnish two ordinary differential equations

$$\rho s^2\bar{y} - kG\bar{y}'' + kG\bar{\psi}' = \rho V_0(x/l)$$
$$Er^2\bar{\psi}'' + kG\bar{y}' - kG\bar{\psi} - \rho r^2 s^2\bar{\psi} = 0 \tag{25}$$

It is now assumed that the velocity distribution $V_0(x/l)$ and its derivatives are continuous, the case of discontinuities to be treated in Section 4. The particular solution can then formally be written as series in descending powers of s. Let

$$\alpha = \left(\frac{\rho}{kG}\right)^{1/2} \qquad \beta = \left(\frac{\rho}{E}\right)^{1/2} \tag{26}$$

and the solution of Equations (25) has the general form

$$y(x,s) = \sum_{i=1}^{4} C_i e^{p_i x} + \frac{1}{s^2}V_0\left(\frac{x}{l}\right) + \frac{1}{s^4}\frac{V_0''\left(\frac{x}{l}\right)}{\alpha^2 l^2} + \dots$$
$$\bar{\psi}(x,s) = \sum_{i=1}^{4} \mu_i C_i e^{p_i x} + \frac{1}{s^4}\frac{V_0'\left(\frac{x}{l}\right)}{\alpha^2 r^2 l} - \frac{1}{s^6}\frac{V_0'\left(\frac{x}{l}\right)}{\alpha^4 r^4 l} + \frac{1}{s^6}\frac{V_0'''\left(\frac{x}{l}\right)}{\alpha^4 r^4 l^3}\left(\frac{\alpha^2}{\beta^2}+1\right) + \dots \tag{27}$$

where $V_0'(z) = dV_0/dz$ and the exponents p_i are the roots of the characteristic equation

$$(\alpha^2 s^2 - p^2)(\beta^2 s^2 - p^2) + \frac{\beta^2}{r^2}s^2 = 0 \tag{28}$$

The further treatment is restricted to the determination of the solutions for small values of the time t; to obtain such solutions it is sufficient to determine the functions $\bar{y}$ and $\bar{\psi}$ approximately for large values of the variable s. The solutions p_i of the characteristic equations are then

$$p_{1,2}^2 = \alpha^2 s^2 - \frac{\beta^2}{r^2(\alpha^2-\beta^2)} + \frac{1}{s^2}(\dots) + \dots$$
$$p_{3,4}^2 = \beta^2 s^2 - \frac{\beta^2}{r^2(\beta^2-\alpha^2)} + \frac{1}{s^2}(\dots) + \dots \tag{29}$$

The corresponding values of the coefficients μ_i are

$$\mu_{1,2} = \frac{1}{s}\frac{\beta^2}{r^2\alpha(\beta^2-\alpha^2)} + \frac{1}{s^3}(\dots) + \dots$$
$$\mu_{3,4} = s\frac{\beta^2-\alpha^2}{\beta} + \frac{1}{s}\frac{\beta^2+\alpha^2}{2r^2\beta(\beta^2-\alpha^2)} + \dots \tag{30}$$

Using only the leading terms of the expansions in Equations (27), (29), (30) and assuming for simplicity that the initial velocity distribution is symmetric, $V_0(z) = V_0(-z)$, the solution may be written

$$\bar{y}(x,s) = \frac{1}{s^3}V_0\left(\frac{x}{l}\right) + C_1\cosh\alpha sx + C_2\cosh\beta sx$$
$$\bar{\psi}(x,s) = \frac{1}{s^4\alpha^2 r^2 l}V_0'\left(\frac{x}{l}\right) + \frac{C_1\beta^2\sinh\alpha sx}{sr^2\alpha(\beta^2-\alpha^2)} + \frac{C_2(\beta^2-\alpha^2)s}{\beta}\sinh\beta sx \tag{31}$$

The boundary conditions for a free-free beam at $x = l$ require $\psi' = 0$, $y' - \psi = 0$, such that

$$\bar{y}'(l,s) - \bar{\psi}(l,s) = 0$$
$$\bar{\psi}'(l,s) = 0 \tag{32}$$

Substituting Equations (31) the constants C_1 and C_2 can be determined

$$C_1 = \frac{V_0''(1)}{s^6 r^2 l^2\alpha\beta(\beta^2-\alpha^2)}\frac{\operatorname{tgh}\beta sl}{\sinh\alpha sl} - \frac{V_0'(1)}{l\alpha s^3}\frac{1}{\sinh\alpha sl} + \dots$$
$$C_2 = \frac{-V_0''(1)}{s^6 r^2 l^2\alpha^2(\beta^2-\alpha^2)}\frac{1}{\cosh\beta sl} + \frac{V_0'(1)\beta^2}{s^6 r^2 l\alpha(\beta^2-\alpha^2)^2}\frac{\operatorname{ctgh}\alpha sl}{\cosh\beta sl} + \dots \tag{33}$$

The transforms of the bending and shear stresses are

$$\frac{1}{Eh}\bar{\sigma}(x,s) \equiv -\bar{\psi}'(x,s) = -\frac{V_0''\left(\frac{x}{l}\right)}{s^4\alpha^2 r^2 l^2} + \frac{V_0''(1)}{s^4 r^2 l^2\alpha^2}\frac{\cosh\beta sx}{\cosh\beta sl} - \frac{\beta^2 V_0'(1)}{s^3 r^2 l\alpha(\beta^2-\alpha^2)}\left[\frac{\operatorname{ctgh}\alpha s\, l\cosh\beta sx}{\cosh\beta sl} - \frac{\cosh\alpha sx}{\sinh\alpha s\, l}\right] \tag{34}$$

$$\frac{1}{kG}\bar{\tau}(x,s) \equiv \bar{y}' - \bar{\psi} = \frac{V_0'\left(\frac{x}{l}\right)}{s^2 l} + \frac{V_0''(1)}{s^6 r^2 l^2\beta(\beta^2-\alpha^2)}\left[\frac{\operatorname{tgh}\beta sl\sinh\alpha sx}{\sinh\alpha sl} - \frac{\sinh\beta sx}{\cosh\beta sl}\right] - \frac{V_0'(1)\sinh\alpha sx}{s^2 l\sinh\alpha sl} + \dots \tag{35}$$

where only the leading terms in each of the $V_0'(x/l)$, $V_0''(x/l)$, $V_0'(1)$ and $V_0''(1)$ were retained.

Before inversion the terms containing hyperbolic functions can be simplified due to the fact that s is assumed to be large. Consider the coefficient of $V_0''(1)$ in Equation (34) as example. Noting that βsl is large, the expression

$$\frac{1}{\cosh\beta sl} = 2e^{-\beta sl}(1+e^{-2\beta sl})^{-1} = 2e^{-\beta sl}(1 - e^{-2\beta sl} + e^{-4\beta sl}\dots) \tag{36}$$

has rapidly decreasing terms which lead in $\bar{\sigma}$ to terms of the general form $s^{-n}e^{-\beta ds}$, where $d = l \pm x$, $3l \pm x$, is some distance. The respective inversion integral is

$$\frac{1}{2\pi i}\int_{-i\infty+\epsilon}^{i\infty+\epsilon}\frac{e^{s(t-\beta d)}}{s^n}ds = \begin{cases} 0 & \text{if } t < \beta d \\ \dfrac{(t-\beta d)^{n-1}}{(n-1)} & \text{if } t > \beta d \end{cases} \tag{37}$$

Each such term represents therefore a wave arriving at a time $t = \beta d$ after the motion starts. The successive terms in (36) begin at successive time intervals $2\beta l$, and interpreting $1/\beta$ as a velocity, the interval represents the time required for a wave of this velocity to return to the original position after reflection at both ends of the beam.

The present study will allow only for the earliest arriving term of each of the velocities $1/\alpha$, $1/\beta$, because other approximations made restrict the solution in time so severely that further terms do not contribute. The solution being symmetric in x, Equations (34), (35) need only be written for $x \geq 0$.

$$\frac{\vartheta(x,s)}{Eh} = \frac{-V_0''\left(\frac{x}{l}\right)}{\alpha^2 r^2 l^2 s^4} + \frac{V_0'(1)}{\alpha^2 r^2 l^2 s^4} e^{-\beta s(l-x)} + \frac{V_0'(1)\beta^2}{s^5 r^2 l \alpha(\beta^2-\alpha^2)}\left[e^{-\alpha s(l-x)} - e^{-\beta s(l-x)}\right] + \dots \tag{38}$$

$$\frac{\bar{\tau}(x,s)}{kG} = \frac{V_0'\left(\frac{x}{l}\right)}{ls^3} - \frac{V_0'(1)}{ls^3} e^{-\alpha s(l-x)} + \frac{V_0''(1)}{s^5 r^2 l \beta(\beta^2-\alpha^2)}\left[e^{-\alpha s(l-x)} - e^{-\beta s(l-x)}\right] + \dots$$

and after inversion and rearrangement

$$\frac{r^2}{Ehl}\sigma(x,t) = -\frac{\alpha}{6} V_0''\left(\frac{x}{l}\right)\left(\frac{t}{\alpha l}\right)^3 + \frac{\beta^3}{6\alpha^2} V_0''(1)\left[\frac{t}{\beta l} - \left(1-\frac{x}{l}\right)\right]^3 - \frac{\beta^4}{2\alpha(\beta^2-\alpha^2)} V_0'(1)\left[\frac{t}{\beta l} - \left(1-\frac{x}{l}\right)\right]^2 + \frac{\beta^3\alpha}{2(\beta^2-\alpha^2)} V_0'(1)\left\{\frac{t}{\alpha l} - \left(1-\frac{x}{l}\right)\right\}^2 \tag{39}$$

$$\frac{\tau(x,t)}{kG} = \alpha V_0'\left(\frac{x}{l}\right)\frac{t}{\alpha l} - \alpha V_0'(1)\left\{\frac{t}{\alpha l} - \left(1-\frac{x}{l}\right)\right\} + \frac{\alpha^4 r^2 V_0''(1)}{24\beta(\beta^2-\alpha^2)r^2}\left\{\frac{t}{\alpha l} - \left(1-\frac{x}{l}\right)\right\}^4 - \frac{\beta^3 r^2 V_0''(1)}{24(\beta^2-\alpha^2)r^2}\left[\frac{t}{\beta l} - \left(1-\frac{x}{l}\right)\right]^4 \tag{40}$$

In this equation the terms in parentheses, $\{\dots\}$ and $[\dots]$, are zero until $t > \alpha(l-x)$ and $t > \beta(l-x)$, respectively. In any specific application the terms containing higher powers of t can be neglected versus lower-order terms; these terms have been retained here to cover cases where $V_0'(1)$ or $V_0''(1)$ vanish.

Refined Solution. Range of Validity of Solutions (39) and (40). The short-term solutions just obtained are essentially the leading terms of power series and information on their range of validity can be obtained by finding subsequent terms. If all the terms indicated in Equations (27) are retained, refined expressions for σ and τ result:

$$\frac{r^2}{Ehl}\sigma(x,t) = -\frac{\alpha}{6} V_0''\left(\frac{x}{l}\right)\left(\frac{t}{\alpha l}\right)^3 + \frac{\alpha}{120} V_0''\left(\frac{x}{l}\right)\left(\frac{l}{r}\right)^2\left(\frac{t}{\alpha l}\right)^5 - \frac{\alpha(\alpha^2+\beta^2)}{120\beta^2} V_0^{iv}\left(\frac{x}{l}\right)\left(\frac{t}{\alpha l}\right)^5 + \dots + \text{wave terms}$$

$$\frac{\tau(x,t)}{kG} = \alpha V_0'\left(\frac{x}{l}\right)\frac{t}{\alpha l} - \frac{\alpha}{6} V_0'\left(\frac{x}{l}\right)\left(\frac{l}{r}\right)^2\left(\frac{t}{\alpha l}\right)^3 + \frac{\alpha}{6} V_0'''\left(\frac{x}{l}\right)\left(\frac{t}{\alpha l}\right)^3 + \text{wave terms} \tag{41}$$

If the beam is long $l/r \gg 1$, and assuming a "well-behaved" initial velocity distribution, such that V_0''' and V_0^{iv} are of the same order of magnitude as V_0 and V_0', the third terms in (41) become unimportant and the corrections are expressed by the second terms. The ratios of the leading and second terms are

$$-\frac{1}{20}\left(\frac{t}{\alpha r}\right)^2 \quad \text{and} \quad -\frac{1}{6}\left(\frac{t}{\alpha r}\right)^2$$

respectively, such that the solutions (39), (40) are physically meaningful if $t/\alpha r < 1$. Noting Equation (26) for α, the time of validity of the solutions is

$$t < r\left(\frac{\rho}{kG}\right)^{1/2} = \frac{r}{c} \tag{42}$$

where $c = (kG/\rho)^{1/2}$. This is exactly the result (18) obtained for the length of the early phase in case of the simple beam. This time is so short that the wave terms in (39) and (40) can only reach points at very small distances (less than h) from the ends of the beam, and it is therefore not necessary to investigate the correction in the wave terms at all.

As the wave terms do not contribute during the range for which the solution found is valid, except for points in the extreme vicinity of the ends, the refined Equations (41) can be used to find the stresses σ and τ, obtaining a better approximation. Further terms exceeding the range of validity of the solution could also be found without fundamental difficulty, if desired.

The similarity of the result (41) and of the expansions Equations (15), (16) for the simple beam indicates clearly that the conclusions concerning the magnitude of shear and bending stresses in case of the simple beam are fully applicable for the free-free beam and no further discussion on this point is required.

Other Boundary Conditions. If beams with other modes of support, say, clamped or cantilever beams, are investigated the solutions must necessarily contain the identical leading terms found in Equations (39), (40), the different method of support affecting only the wave terms. Similarly, the refined result, Equations (41), where the wave terms have not been spelled out in detail, is valid for any method of support. There is no difficulty in applying the approach used in this section to find the wave terms near a clamped or even an elastically supported end if desired. As the wave terms only affect minute portions of the beam near the ends, their knowledge is of little practical interest.

4 Effect of a Discontinuity in the Initial Velocity Distribution $V_0(x/l)$

Within the time of validity of the approximate solutions the effect of the boundary conditions of the beam is restricted to very short distances near the ends of the beam. To study the effect of a discontinuity in the initial velocity V_0 at a point in the interior of the beam, say, at $x = 0$, it is therefore sufficient to analyze a beam of infinite length, eliminating all end effects.

Consider the infinite beam, Fig. 7, subjected to an initial velocity distribution

$$V_0 = 0 \qquad x < 0$$
$$V_0 = V_0(x/l) \qquad x \geq 0 \tag{43}$$

where l is an arbitrary reference length.

Using essentially the approach of the preceding section, the discontinuity in V_0 now requires the use of separate expressions for the solutions $\bar{y}$ and $\bar{\psi}$ for $x \gtrless 0$. The solutions for $x > 0$ are given by Equation (27), while those for $x < 0$ are similar but the terms with V_0, V_0', and so on, do not appear. Continuity of the displacements, and the conditions $y, \psi \to 0$ for $x = \infty$, permit the determination of the various constants. Retaining only the respective leading terms the following short-time expressions for the stresses σ and τ were found for $x < 0$:

$$\frac{r^2}{Ehl}\,\sigma(x,t) = -\frac{\alpha\beta^3 V_0(0)}{2(\alpha^2-\beta^2)}\left\{\frac{t}{\alpha l}+\frac{x}{l}\right\} + \frac{\beta^3 V_0(0)}{2(\alpha^2-\beta^2)}\left[\frac{t}{\beta l}+\frac{x}{l}\right] - \frac{\alpha\beta^3 V_0'(0)}{4(\alpha^2-\beta^2)}\left\{\frac{t}{\alpha l}+\frac{x}{l}\right\}^2 + \frac{\beta^3 V_0'(0)}{4(\alpha^2-\beta^2)}\left[\frac{t}{\beta l}+\frac{x}{l}\right]^2 \tag{44}$$

$$\frac{\tau(x,t)}{kG} = -\frac{1}{2}\left\{\alpha V_0(0)\right\} - \frac{\alpha}{2}\,V_0'(0)\left\{\frac{t}{\alpha l}+\frac{x}{l}\right\}$$

where the expressions in the parentheses, $\{\ldots\}$, $[\ldots]$ are zero until $t \geq -\alpha x$, $t \geq -\beta x$, respectively. The stresses for $x > 0$ are

$$\frac{r^2}{Ehl}\,\sigma(x,t) = \frac{\alpha}{6}\,V_0''\left(\frac{x}{l}\right)\left(\frac{t}{\alpha l}\right)^3 + \text{wave terms}$$
$$\frac{\tau(x,t)}{kG} = \alpha V_0'\left(\frac{x}{l}\right)\frac{t}{\alpha l} + \text{wave terms} \tag{45}$$

The wave terms in (45) are not of interest unless V_0' or V_0'' vanish; in this case the values for $x > 0$ can be obtained from (44) by noting that the effect of a discontinuity $V_0(0)$ is antisymmetric, while a discontinuity $V_0'(0)$ produces a symmetric stress pattern.

The leading terms for $x > 0$ are exactly those found in the previous section and the validity of the solution is as a result restricted to the early time given by Equation (42).

The effect of the discontinuity is expressed by the wave terms which affect at early times only points in the vicinity of the discontinuity, similar to the wave terms originating from the ends of a beam. It is interesting to note that, even in the part $x < 0$ of the beam where the stresses are solely due to the wave terms, shear stresses remain during the early phase much larger than the bending stresses; this can be seen from Equations (44) where the respective terms depending on V_0 and V_0' are—after arrival—of smaller magnitude in σ than in τ. The general conclusion that shear stresses dominate during the early phase, defined by Equation (42), is therefore valid even in case of discontinuities in the initial velocity distribution.

5 Conclusion. Applicability to Impact or Explosion Problems

The analysis presented in Sections 2 to 4 indicates that as expected for sufficiently high initial velocities the shear stresses will exceed bending stresses during an early phase after initiation of the motion, regardless of the conditions of support of the beam. The duration of this early phase is approximately independent of the type of beam, and even of its length, provided l/h is large enough to justify calling the structure a beam; this early phase is of the approximate duration

$$t \simeq r\left(\frac{\rho}{kG}\right)^{1/2} \tag{46}$$

It depends not on the length l, but on the radius of gyration r, i.e., on the depth of the beam. $(kG/\rho)^{1/2}$ being of the order of the velocity of shear waves, the duration of the early phase is very short, it is only of the order of the time required for shear waves to traverse a distance which is a fraction of the depth of the beam. The shortness of this time has an important consequence.

The concept of impulsive motion is widely used in case of impact or high-pressure explosion problems where the forces are of very short duration producing within a short time an initial velocity in each element of the beam. Obviously, the stresses due to an instantaneously imposed initial velocity will not and cannot agree with those produced by surface forces during an early phase which must be, from considerations of wave propagation, equal to several times the thickness of the beam divided by $(E/\rho)^{1/2}$. The time required to establish the initial velocities, while short, is however considerably longer than the time (46) during which shear stresses dominate. The analysis presented in this paper is therefore not applicable to impact or explosion problems, because the early phase during which shear stresses are important lies entirely within the short time where the initial velocity is not established.

This, of course, does not mean that high shear stresses do not occur at early times, but indicates that high shear stresses occur simultaneously with even higher transverse (or pinching) stresses[6] which the Timoshenko Beam Theory does not consider. A determination of high stresses at early times must therefore be found on the basis of the theory of elasticity, or at least from a higher-order approximation than the Timoshenko Beam Theory.

Use of Elementary Beam Theory. The results of this paper may be used to draw useful conclusions on the accuracy of the elementary beam theory combined with the initial velocity approximation in high-pressure explosion problems. The time t_i required for the initial velocity distribution to become fairly uniform being longer than the duration of the early phase (46), the initial velocity concept may be used only if $t > t_i$. For such values of $t > t_i \gg \pi/\omega_2$, Figs. 3 and 4 indicate that the stresses σ and τ are at least crudely approximated by the elementary beam theory; the deviations are mostly due to the high-frequency component of the response, the low-frequency part agreeing quite closely to the elementary solution. The damping in actual structures is likely to reduce the high-frequency component quickly, such that the elementary solution in the case of rectangular (or other solid) cross sections should give good results for practical applications. In order to see if this situation also applies for I-beams the stresses for a typical case[7] $l/2h = 10$, $k = 0.25$ are given in Table 1, where $\omega_2/\omega_1 \simeq 18.5$.

The frequency ω_E from elementary theory differs only minutely from ω_1 but the stresses found by the elementary theory exceed the low-frequency components of the refined solution by about 20 per cent.

Table 1

	Timoshenko beam	Elementary theory
$\frac{l\omega_1}{\pi E V_0}\,\sigma\left(\frac{l}{2}\right) =$	$0.1278 \sin \omega_1 t - 0.0060 \sin \omega_2 t$	$0.157 \sin \omega_E t$
$\frac{l\omega_1}{\pi E V_0}\,\tau(0) =$	$0.0364 \sin \omega_1 t + 0.0172 \sin \omega_2 t$	$0.082 \sin \omega_E t$

[6] The magnitude of the transverse stresses may be estimated by computing the stress σ_y required to accelerate an element of the beam, if considered rigid, from velocity 0 to V_0 in the time (46). One finds

$$\sigma_y = \frac{\pi G V_0}{l\omega_2}\,\frac{klh}{\pi r^2}$$

which is quite large compared to the value of the shear stresses τ, given by Equation (16).

[7] The value $k = 0.25$ indicates that the web of the beam represents about 25 per cent of the total area.

The Elastic-Plastic Response of Thin Spherical Shells to Internal Blast Loading

W. E. BAKER
Physicist,
Terminal Ballistics Laboratory,
Ballistic Research Laboratories,
Aberdeen Proving Ground, Md.
Mem. ASME

In this paper, the theory is developed for the elastic-plastic response of a thin spherical shell to spherically symmetric internal transient pressure loading. Analytic solutions are obtained to the linear, small-deflection equations of motion for shell materials which exhibit various degrees of strain-hardening. Numerical solutions obtained by digital computer are also presented for the equations for large deflections obtained by acccounting for shell thinning and increase in radius during deformation. The theory is compared with experiment, and is shown to be in good agreement.

In several fields of engineering and science, there are requirements for gastight structures which must be able to withstand the effects of internally applied transient pressures. Examples of such structures include:

1 Blast chambers, within which the effects of explosives or propellants can be studied under controlled atmospheric conditions.

2 Safety chambers, for proof testing of small pressure vessels.

3 Nuclear-reactor containment structures designed to contain the effects of accidental runaway of the reactors which they house.

Because these structures may have to withstand static as well as transient pressures, they are usually constructed in the form of large-sized, thin-walled pressure vessels, such as spherical shells or cylinders with hemispherical or ellipsoidal end caps.

In designing such structures, one must not rely solely on static-pressure design criteria, but must also consider dynamic response to the expected internal transient pressure.

The simplest analytical problem relating to design of these structures is that of the response of a spherical shell to a spherically symmetric transient pressure pulse on its inner surface. In a recent paper, Baker and Allen [1][1] considered the elastic response of a spherical shell of any thickness to such a pressure pulse. They showed that the elastic response of even a relatively thick shell could be adequately described by an approximate "thin-shell" equation of motion.

In this paper, the author will extend the thin-shell equation to include plastic deformation and the nonlinear effects of shell thinning and increase in radius, obtain solutions to these equations, and compare predicted response with results of experiments which were conducted for comparison with theory.

Theory

General. In so far as the author has been able to determine, no one has yet attempted to predict the response of an elastic-plastic spherical shell to either internal or external transient pressures. Chiarulli [2] has discussed the response of a spherical cap to an external shock wave, but assumes a rigid-plastic mathematical model for the structure. Hunter [3] has considered the dynamic response of an infinite medium to transient pressure pulses

Contributed by the Applied Mechanics Division and presented at the Annual Meeting, Atlantic City, N. J., November 29–December 4, 1959, of The American Society of Mechanical Engineers.

Discussion of this paper should be addressed to the Secretary, ASME, 29 West 39th Street, New York, N. Y., and will be accepted until April 10, 1960, for publication at a later date. Discussion received after the closing date will be returned.

Note: Statements and opinions advanced in papers are to be understood as individual expressions of their authors and not those of the Society. Manuscript received by ASME Applied Mechanics Division, February 4, 1959. Paper No. 59—A-95.

[1] Numbers in brackets designate References at end of paper.

Nomenclature

u_r = radial displacement
u_{ry} = radial displacement at time of yielding
$\dot{u}_{ry}$ = radial velocity at time of yielding
u_{rs} = permanent displacement of plastically deformed shell
t = time
t_y = time of yielding
ϵ = normal strain
ϵ_y = yield strain
ϵ_s = permanent strain of plastically deformed shell
σ_θ, σ_ϕ, σ = normal stresses
σ_y = yield normal stress
τ_{max} = maximum shearing stress
S = slope of plastic portion of stress-strain curve
E = Young's modulus
ν = Poisson's ratio
a = shell radius
a_0 = initial shell radius
a_y = shell radius at time of yielding
h = shell thickness
ρ = density of shell material
g = acceleration of gravity
$p(t)$ = transient pressure
P = peak overpressure of blast wave
T = duration of blast wave
ω = circular vibration frequency, elastic shell
ω_p = circular vibration frequency, plastic shell
K, A, B = constants in solution of elastic-response equation
C_1, C_2, C_3 = constants in equations for plastic deformation of shell

applied at the surface of a spherical cavity, including both the elastic and plastic properties of the medium, but has made no attempt to solve the problem for a shell.

In this section, the author will develop the theory of elastic-plastic response of a thin spherical shell to spherically symmetric internal blast loading. The elastic phase of the motion will be assumed to be governed by the approximate thin-shell equation cited in [1]. During plastic deformation, both perfectly plastic and strain-hardening materials will be considered. Solutions will be obtained for the linear equations of motion which result from assuming that thinning and increase in radius of the shell occurring during plastic deformation are negligible, and for the nonlinear equations obtained by accounting for thinning and assuming that the shell material is incompressible.

Elastic Phase of Motion. The equation of motion in the radial direction of the element in Fig. 1 is

$$h(\sigma_\theta + \sigma_\phi) + \rho h a \frac{d^2u_r}{dt^2} = ap(t) \tag{1}$$

where ρ is density of the shell material, h is shell thickness, and all other quantities are defined in the figure.

Now, $\sigma_\theta = \sigma_\phi = \sigma$, because of spherical symmetry. In the elastic phase, the shell material is assumed to obey Hooke's law, so that

$$\sigma = \frac{E}{1-\nu}\,e = \frac{E}{1-\nu}\,\frac{u_r}{a} \tag{2}$$

where E is Young's modulus and ν is Poisson's ratio. Then, equation (1) can be written as

$$\frac{d^2u_r}{dt^2} + \omega^2 u_r = \frac{p(t)}{\rho h} \tag{3}$$

with the circular frequency ω given by

$$\omega^2 = \frac{2E}{\rho a^2(1-\nu)} \tag{4}$$

Let us assume that the transient pressure $p(t)$ is given by

$$\begin{aligned} p(t) &= P(1 - t/T), \qquad 0 < t \leq T \\ p(t) &= 0, \qquad\qquad t \geq T \end{aligned} \tag{5}$$

where P is the peak overpressure and T the duration of the shock wave. The solution to equation (3) can be obtained readily by Laplace transform techniques. For the shell initially at rest, the solution is

$$u_r = K\left(1 - t/T - \cos\omega t + \frac{\sin\omega t}{\omega T}\right), \qquad 0 < t \leq T \tag{6}$$

$$u_r = A\cos\omega(t-T) + B\sin\omega(t-T), \qquad t \geq T \tag{7}$$

where

$$\left.\begin{aligned} K &= P/\omega^2\rho h \\ A &= K\left(\frac{\sin\omega T}{\omega T} - \cos\omega T\right) \\ B &= K\left(\sin\omega T + \frac{\cos\omega T}{\omega T} - 1/\omega T\right) \end{aligned}\right\} \tag{8}$$

Note that during this phase of the motion the deflections are assumed to be so small that the radius, a, does not change appreciably. The natural frequency ω is therefore constant and we have only to solve a linear differential equation, equation (3).

Plastic Response Phase of Motion, Neglecting Shell Thinning and Variation of Shell Radius. The solution given by equations (6) through (8) applies until the stress reaches yield, σ_y.[2] The shell material is then assumed to obey the linear strain-hardening stress-strain law shown in Fig. 2. Or, for $\sigma \geq \sigma_y$, the stress is given by

$$\sigma = \sigma_y + S(e - e_y) \tag{9}$$

where S is the slope of the plastic portion of the stress-strain curve. The equation of motion (1) can then be written as

$$\frac{d^2u_r}{dt^2} + \frac{2S}{\rho a^2}\,u_r = \frac{p(t)}{\rho h} - \frac{2(\sigma_y - Se_y)}{\rho a}, \qquad t \geq t_y \tag{10}$$

This equation is similar to equation (3), and can be solved in like manner. The shell exhibits a radial vibration frequency defined by

[2] For this problem, where two of the normal stress components are equal and the third is zero, the yield stress would be given as $\sigma_y = \sqrt{3}\,\tau_{max}$ by the Mises yield condition and as $\sigma_y = 2\tau_{max}$ by the Tresca yield condition.

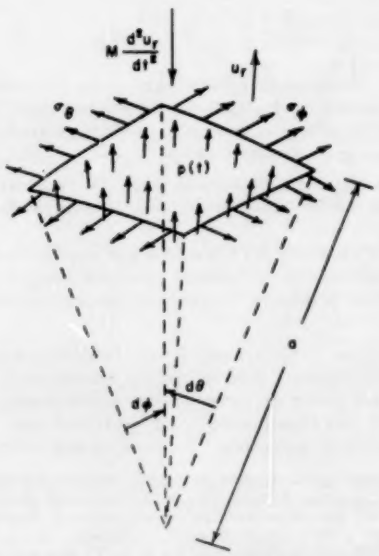

Fig. 1 Element of spherical shell

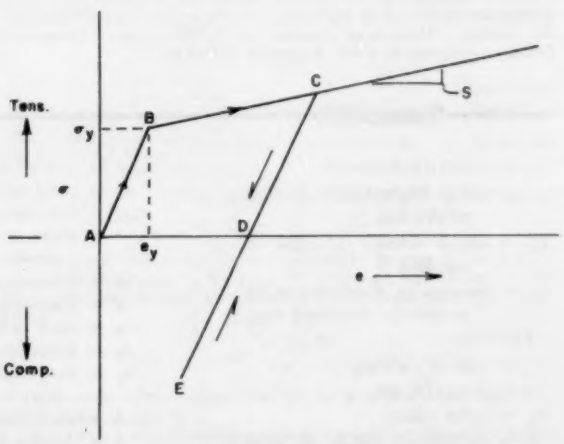

Fig. 2 Stress-strain law

$$\omega_p^2 = \frac{2S}{\rho a^2} \tag{11}$$

which is lower than the elastic frequency.

The solution for (10), for pressure transient defined by (5), is

$$u_r = u_{ry}\cos\omega_p(t-t_y) + \dot{u}_{ry}\frac{\sin\omega_p(t-t_y)}{\omega_p} - \frac{2(\sigma_y - Se_y)}{\rho a\omega_p^2}[1-\cos\omega_p(t-t_y)] + \frac{P}{\rho h\omega_p^2}\left\{(1-t/T)[1-\cos\omega_p(t-t_y)] + \frac{1}{\omega_p T}[\sin\omega_p(t-t_y) - \omega_p(t-t_y)\cos\omega_p(t-t_y)]\right\}$$

$$\text{for} \quad t_y \le t \le T \tag{12}$$

and

$$u_r = u_{ry}\cos\omega_p(t-t_y) + \dot{u}_{ry}\frac{\sin\omega_p(t-t_y)}{\omega_p} - \frac{2(\sigma_y - Se_y)}{\rho a\omega_p^2}[1-\cos\omega_p(t-t_y)] \quad \text{for} \quad t_y \ge T \tag{13}$$

If yielding occurs during the pressure pulse, equation (12) applies until $t = T$, and can be modified to give displacement after the pulse by substituting $t = T$ in the last term. Equation (13) applies if yielding occurs after the the pulse: i.e., if $t_y \ge T$.

The solution holds until velocity $\dot{u}_r$ is zero, at which time elastic motion resumes. In the sequence of events occurring during the shell motion, the material has followed the stress-strain path *A-B-C-D-E-C* in Fig. 2.

For a perfectly plastic material, the slope S of the stress-strain curve is zero and the equation of motion (10) is simplified to

$$\frac{d^2u_r}{dt^2} = \frac{p(t)}{\rho h} - \frac{2\sigma_y}{\rho a} \tag{10a}$$

for $t \ge t_y$. This equation is directly integrable, yielding

$$u_r = \frac{P}{\rho h}[t^3/2 - t^3/6T + (t_y^3/2T - t_y)t + t_y^3/2 - t_y^3/3T] - \frac{2\sigma_y}{\rho a}(t-t_y)^2/2 + \dot{u}_{ry}(t-t_y) + u_{ry} \tag{12a}$$

for $t_y \le t \le T$

and

$$u_r = -\frac{\sigma_y}{\rho a}(t-t_y)^2 + \dot{u}_{ry}(t-t_y) + u_{ry} \tag{13a}$$

$$\text{for} \quad t_y \ge T$$

The conditions noted previously for equations (12) and (13) also apply to equations (12*a*) and (13*a*).

Plastic Response Phase of Motion, Considering Shell Thinning and Variation of Shell Radius. For relatively brittle materials, rupture will occur for strains which are small ($e \ll 1$) and the foregoing analysis should adequately describe the motion. If the shell material is ductile, strains as large as 0.5 can occur before rupture. The shell can, therefore, both be thinned and increase in diameter appreciably. These effects will now be considered.

If one assumes that the shell material is incompressible during plastic deformation,[3] then

$$ha^2 = h_0a_0^2 \tag{14}$$

[3] See Drucker, reference [4], pp. 11–17.

where the thickness, h, and radius, a, are functions of t and subscripts zero denote initial dimensions. Equation (1) still describes the motion. Using (14) to eliminate h and substituting the stress-strain law (9), we get from (1)

$$\frac{d^2u_r}{dt^2} + \frac{2[\sigma_y + S(e-e_y)]}{\rho a} = \frac{p(t)a^2}{\rho a_0^2h_0} \tag{1a}$$

But

$$e = a/a_0 - 1, \quad \frac{d^2u_r}{dt^2} = \frac{d^2a}{dt^2},$$

and (1*a*) becomes

$$\frac{d^2a}{dt^2} + \frac{C_1}{a} + C_2 = C_3a^2p(t) \tag{15}$$

where

$$C_1 = \frac{2[\sigma_y - S(1+e_y)]}{\rho}, \quad C_2 = \frac{2S}{\rho a_0}, \quad C_3 = \frac{1}{\rho a_0^2h_0} \tag{16}$$

Equation (15) is nonlinear, and cannot be solved by Laplace transform or similar techniques. Its solution has been obtained for specific values of the various constants and for specific blast loadings, $p(t)$, by digital computer.

For a perfectly plastic material, the constant C_2 is zero and equation (15) is somewhat simplified. However, it is still nonlinear and must be solved numerically.

Predictions of Response From Theory

To compare theory with experiment, one must compute displacement and strain-time histories of spherical shells whose response to internal blast loading has been measured. Predictions are made here of the response of a small steel shell to loading from several weights of explosive charge detonated at the center of the shell.

The intensity P and duration T of the blast waves are predicted from past experimental data on normally reflected blast waves obtained by Hoffman and Mills [5]. The shell material is assumed to have Young's modulus $E = 30 \times 10^6$ psi, Poisson's ratio $\nu = 1/3$, and $\rho g = 0.283$ lb/in^3. The yield stress $\sigma_y = 40{,}000$ psi, with the corresponding yield displacement $u_{ry} = 13.11 \times 10^{-3}$ in. The initial shell dimensions are $a_0 = 15$ in., $h_0 = 1/16$ in.

Response was first computed from the solutions to the linear (small-deflection) equations for blast loading from 1/64-lb, 1/8-lb, and 1/4-lb spherical Pentolite explosive charges. The first of these produced a maximum displacement below yield, so that equations (6) through (8) could be used to compute the entire motion. These equations were also used to compute the initial phase of motion for the two larger charge weights. The loading from both of these charges was sufficiently intense to cause plastic flow to start before the blast pulse was over. The velocity $\dot{u}_{ry}$ and the displacement u_{ry} then formed the initial conditions for the plastic phase of the motion. Plastic response was computed from equation (12*a*) for no strain-hardening, and from equation (12) for

$$S = {}^1/_2E/(1-\nu)$$

The blast-loading and shell-response parameters are presented in Table 1, while the complete displacement-time histories are shown graphically in Fig. 3.

No solution can be obtained in analytical form to the nonlinear equations for motion obtained when shell thinning and increase in radius are accounted for. However, the Computing Laboratory, Ballistic Research Laboratories, has obtained numerical

solutions on the ORDVAC digital computer to equation (15) for the small steel shell subjected to the blast loading from 1/8-lb and 1/4-lb charges shown in Table 1. The solutions were obtained for several values of the parameter S. Table 2 and Figs. 4 and 5 show the results of these computations. One can see that the effect of considering shell thinning and increase in radius is quite appreciable.

Some insight into the effects of nonlinearity can be inferred from (15). The second term on the left indicates that, as the shell increases in radius, its plastic resistance to motion decreases as $1/a$. The right-hand side, however, shows that the loading is increasing as a^2. The relatively large effect of the nonlinearity is probably primarily due to the "loading term" in the equation.

Strain-time histories can be obtained from the displacement-time histories in Figs. 3 through 5 by merely dividing by the initial shell radius, $a_0 = 15$ in.

Although the predictions of response were made for a specific small shell to several specific blast loads, they can be somewhat generalized by use of model laws for structural response [6]. These laws state that, if geometrical similarity of the structure and explosive loading source is maintained, the displacement-time history of one structure is similar to the history of another, with time and displacement being multiplied by the scale factor.

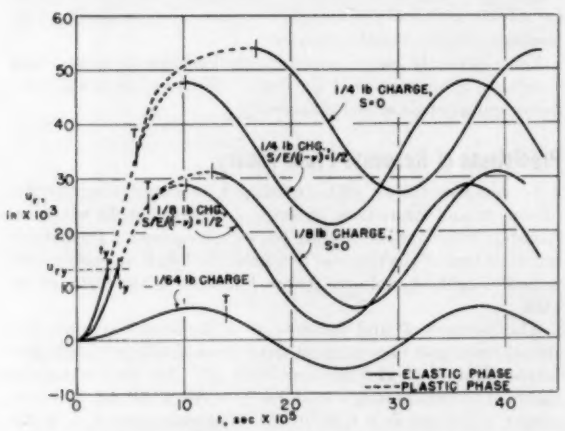

Fig. 3 Displacement-time histories of 1/16-in-thick, 15-in-radius steel shell, linear theory

Table 1 Elastic and elastic-plastic response of thin steel shell from linear theory

Pentolite chg wt, lb	1/64	1/8	1/4
Peak pressure, P, psi	120	1000	1770
Duration, T, sec $\times 10^5$	13.8	6.65	5.54
t_y, sec $\times 10^5$	...	4.10	2.96
u_{ry}, in $\times 10^3$	...	13.33	13.33
$\dot{u}_{ry}$, in per sec	...	510	766
Max u_r, in. $\times 10^3$ (no strain-hard)	5.85	32.2	53.8
Max u_r, in. $\times 10^3$ (with strain-hard)	...	28.7	47.9

Experiments on Shell Response

Description of Experiments. The responses of two sizes of thin steel shells to blast loading from small, centrally located explosive charges were measured for comparison with theory. The shells were fabricated from sheet steel by forming segments and welding them into spheres which were complete save for a small hole which would pass the explosive charges. The smaller size shell (15-in. radius) had the material properties and dimensions assumed for the predictions of response in the preceding section of this paper, while the larger shell (30-in. radius) was a model of the small shell made of the same material and scaled up by a factor of two in all dimensions.

The response of each shell was measured by sixteen SR-4 resistance wire strain gages (type C-10) mounted at nine locations to the shell. To record the two tangential-strain components, the gages were mounted in pairs at right angles to each other in all but two of the locations. Fig. 6 shows schematically the location of all gages on the 15-in-radius shell. The outputs of the strain gages were recorded on a commercial oscillograph recorder.

No attempt was made to measure the loading on the inner surface of the shells, because blast gages having the frequency response requisite for measuring the short duration waves en-

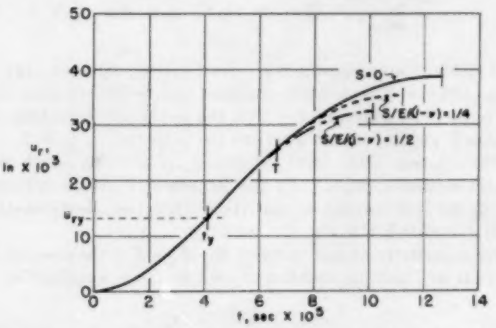

Fig. 4 Response of 1/16-in-thick, 15-in-radius steel shell to 1/8-lb Pentolite charge, nonlinear theory

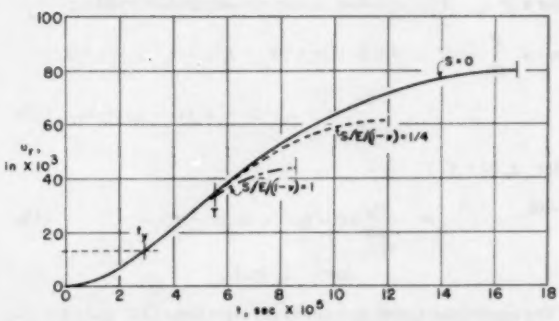

Fig. 5 Response of 1/16-in-thick, 15-in-radius steel shell to 1/4-lb Pentolite charge, nonlinear theory

Table 2 Elastic-plastic response of thin shell from numerical solution to equations which account for thinning and increase in radius[a]

Ratio, $\frac{S}{E/(1-\nu)}$	1/8-lb charge 0	1/8-lb charge 1/4	1/8-lb charge 1/2	1/4-lb charge 0	1/4-lb charge 1/4	1/4-lb charge 1[b]
Max u_r, in $\times 10^3$	38.7	35.4	32.5	80.1	61.3	43.8
Time for max u_r, sec $\times 10^5$	12.61	11.20	10.10	16.80	12.00	8.57

[a] Blast loading parameters, t_y, u_{ry}, and $\dot{u}_{ry}$ are given in Table 1.

[b] The value $S = 1$ was chosen here to simulate the maximum possible resistance to motion of the shell material. The computed values then apply to a shell made of steel with a much higher elastic limit than that assumed for the remainder of the computations.

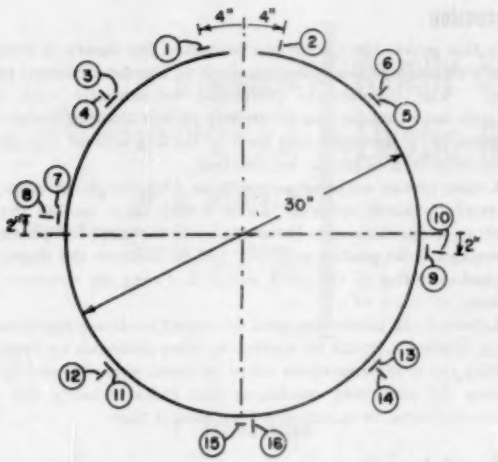

Fig. 6 Location of gages on shell. Numbers indicate channel of recording equipment to which gage is attached.

countered here are quite massive [5], and would seriously alter the response of such thin shells.

The experiments were conducted with the shells suspended in a light rope sling to simulate an unsupported shell. The first small shell was subjected to blast from four 0.016-lb Tetryl explosive charges to compare with predictions of elastic response. A 1/8-lb Pentolite explosive charge was then detonated within the shell to obtain its plastic response. The shell ruptured, failing at a weld. A second small shell also was subjected to blast from a 1/8-lb charge, and ruptured in much the same manner as the first shell. For comparison with the elastic response of the small shell, a single test of a large shell was made, with a 1/8-lb Pentolite charge being detonated within the shell.

Experimental Results. Acceptable strain-time histories were obtained from most of the recording channels during the elastic-response tests. The shells responded initially in a single frequency vibration which persisted for several cycles until arrival of the second shock wave, which was formed by reflection of the initial shock from the inner surface of the shell. The response then became quite erratic, with considerable variation in the records of different strain gages and excitation of additional modes of vibration.[4] For comparison with theory, however, only the portion of the records between the first and second shocks need be considered. Each record could then be characterized by a vibration frequency and a strain amplitude. The data for the four elastic-response experiments on the small shell and the single experiment on the large shell are given in Table 3. One can see from these data that the maximum strains vary considerably from point to point on the shell, but that their average values do not differ significantly from one experiment to another. The average value for the maximum strain measured during the experiment on the larger shell agrees well with the values obtained from experiments on the small shell. The variation of the measured vibration frequencies from their mean values can be seen to be considerably smaller than the variation of maximum strains.

During the plastic response experiments, both small shells ruptured when subjected to the blast from 1/8-lb charges. However, maximum strains were recorded on most of the recording channels before failure of the gage leads. On the first such experiment, the strain-time histories were recorded on some channels for a time long enough to allow measurement of permanent set after maximum deformation. The data from these two experiments are given in Table 4. Because the variations in maximum strains of the first shell are much larger than those of the second shell, the best estimate of maximum strain is probably obtained by using only the data for the second shell.

[4] A possible cause of erratic records after the second shock could be that this shock was not spherical after passing twice through the hot, turbulent detonation products near the shell center.

Table 3 Measured elastic response of thin, steel, spherical shells to internal blast loading from centrally located explosives

(A) Response of 15-in-radius, $^1/_{16}$-in-thick shell to 0.016 lb Tetryl charges

Chan'l No.	Max strains × 10^6 for given test no. 1	2	3	4	Vibration frequency, cps
1	560	780	590	570	3500
2	560	620	480	440	3700
3	410	460	450	400	4000
4	420	420	430	390	3600
5	400	460	400	520	4000
6	...	...	...	450	3500
7	400	...	...	...	3500
8	520	380	340	330	3400
9	410	390	450	...	3500
10	280	270	330	300	3600
11	420	490	550	490	
12	600	600	460	540	Mean 3630
13	480	380	330	300	Std. dev. ±200
14	580	720	...	520	
15	420	500	360	350	
16	420	380	350	...	
Mean	460	490	430	430	
Std. dev.	±80	±140	±80	±90	

NOTES:

1 Channel numbers correspond to gage locations of Fig. 6.

2 Dashes in table indicate malfunction of recording equipment or strain gages.

3 The standard deviations are sample standard deviations.

(B) Response of 30-in-radius, $^1/_8$-in-thick shell to $^1/_8$-lb Pentolite charge

Chan'l No.	Max. strain × 10^6	Chan'l No.	Max strain × 10^6	Chan'l No.	Max strain × 10^6
1	430	7	...	13	350
2	570	8	500	14	390
3	370	9	260	15	430
4	360	10	380	16	570
5	520	11	380	Mean	420
6	510	12	320	Std. Dev.	±90
Vib. freq., cps	1750	1800	1800	Mean...1790	
	1850	1800	1750	Std. dev ±30	

Table 4[5] Measured elastic-plastic response of 15-in-radius steel spherical shells to internal blast loading from $^1/_8$-lb Pentolite charges

Chan'l No.	Strains × 10^6 — Test 1 — Maximum strain	Test 1 — Permanent strain	Test 2 — Maximum strain
1	2170	1360	2980
2	3030	1040	...
3	2440	...	2470
4	1580	...	4240
5	2440	...	3420
6	2300	...	3780
7	5700	...	...
8	1250	...	2400
9	4080	...	...
10	1460	...	2210
11	2720	1360	4440
12	1570	...	2900
13	2720	1360	4070
14	2150	...	3100
15	...	...	4210
16	1360	...	2720
Mean	2460	1280	3300
Std. dev.	±1130	±140	±750

[5] Notes for Table 3 apply also to this table.

Comparison of Theory with Experiment

The elastic response of the small shell to 1/64-lb charges predicted in Table 1 and Fig. 3 can be compared with the measured time histories of tangential strain by merely dividing the predicted displacement by the initial shell radius. The strain-time history obtained in this manner also applies to the response of the large shell to the 1/8-lb charge, if the time scale is multiplied by 2. The general form of measured responses is similar to that predicted from theory. The quantitative agreement between measured and predicted response is also quite good, as can be seen from the comparison of vibration frequencies[5] and maximum strains given in Table 5.

Table 5 Comparison of predicted and measured elastic response of thin steel shells

	1/64-lb charge versus 15-in-rad, 1/16-in-thick shell		1/8-lb charge versus 30-in-rad 1/8-in-thick shell	
	Predicted	Measured	Predicted	Measured
Vibration frequency, cps	3720	3630 ± 200	1860	1790 ± 30
Max strain, × 10^6	390	450 ± 100	390	420 ± 90

[a] The "confidence limits" given are ±one standard deviation of the individual measurements.

The predicted strain-time histories for elastic-plastic responses of the small shells to 1/8-lb charges can be obtained from Tables 1 and 2 and Figs. 3 and 4 by dividing the displacements by the initial shell radius. The general form of the comparable measured responses agrees with the predicted form. The measured maximum strains and permanent strains are compared in Table 6 with strains predicted both from the approximate linear theory and from the more exact nonlinear theory for a material with no strain-hardening.

One can see that the general quantitative agreement of experiment with theory is good.

Table 6 Comparison of predicted and measured elastic-plastic response of 15-in-radius, 1/16-in-thick steel shell to blast from 1/8-lb Pentolite charge

	Predicted (no strain-hardening)		
	Linear theory	Nonlinear theory	Measured
Max strain × 10^6	2100	2580	3300 ± 750
Perm strain × 10^6	1270	1690	1280 ± 140

[5] Predicted frequencies calculated from equation (4).

Discussion

In this paper, the author has presented the theory of elastic-plastic response of thin spherical shells to transient internal pressures. The experiments performed concurrently with the analysis show that one can adequately predict from the theory the response of a thin spherical shell to loading intense enough to cause considerable plastic deformation.

A more precise set of experiments on dynamic-plastic response of carefully made spherical shells would allow one to decide whether to use the simple linear theory or the more complex nonlinear theory to predict response, and to measure the degree of strain-hardening of the shell material during its dynamic response.

Although the theory has been developed for linear strain-hardening materials, it can be applied to other materials by approximating the true stress-strain curve by linear segments and by invoking the continuity conditions that radial velocity and displacement must be continuous functions of time.

Acknowledgments

The financial support of the Division of Reactor Development, U. S. Atomic Energy Commision, for whom this work was performed, is gratefully acknowledged. The author also wishes to acknowledge the able assistance of Mr. W. O. Ewing, Jr., in performing the experiments, and of personnel of the Computing Laboratory, Ballistic Research Laboratories, for obtaining numerical solutions to the nonlinear equations in the paper.

References

1 W. E. Baker and F. J. Allen, "The Response of Elastic Spherical Shells to Spherically Symmetric Internal Blast Loading," Proceedings of the Third U.S. National Congress of Applied Mechanics, ASME, New York, 1958, p. 79.

2 P. Chiarulli, "Plastic Response of a Thin Spherical Cap to a Plane Shock Wave," Technical Report No. 6, Division of Applied Mathematics, Brown University, May, 1955.

3 S. C. Hunter, "Spherically Symmetric Waves and the Dynamic Response of an Infinite Medium to Transient Pressure Pulses at an Internal Boundary," Armament Research Establishment Report 49/54, December, 1954.

4 D. C. Drucker, "Stress-Strain Relations in the Plastic Range—a Survey of Theory and Experiment," Report A11 S1, Graduate Division of Applied Mathematics, Brown University, December, 1950.

5 A. J. Hoffman and S. N. Mills, Jr., "Air Blast Measurements About Explosive Charges at Side-on and Normal Incidence," Ballistic Research Laboratories Report No. 988, July, 1956.

6 W. E. Baker, W. O. Ewing, Jr., and J. W. Hanna, "Laws for Large Elastic Response and Permanent Deformation of Model Structures Subjected to Blast Loading," Ballistic Research Laboratories Report No. 1060, December, 1958.

R. D. MINDLIN
Professor of Civil Engineering, Columbia University, New York, N. Y. Mem. ASME

H. D. McNIVEN
Associate Professor of Civil Engineering, University of California, Berkeley, Calif.

Axially Symmetric Waves in Elastic Rods[1]

A system of approximate, one-dimensional equations is derived for axially symmetric motions of an elastic rod of circular cross section. The equations take into account the coupling between longitudinal, axial shear, and radial modes. The spectrum of frequencies for real, imaginary, and complex wave numbers in an infinite rod is explored in detail and compared with the analogous solution of the three-dimensional equations.

1 Introduction

In a previous paper [1],[2] a derivation was given of approximate equations of motion that take into account the coupling between longitudinal and radial modes of axially symmetric vibration of elastic rods. The frequency of the radial mode depends on Poisson's ratio, ν; the frequency increasing with increasing ν. When $\nu > 0.2833$, the frequency of the radial mode is higher than the frequency, independent of ν, of the lowest axial shear mode. In the latter the displacement is parallel to the axis of the rod and has one circular node. The possibility of such a displacement was not taken into account in the previous paper. In the range of Poisson's ratios commonly encountered, both the axial shear and the radial modes can couple with the longitudinal mode and with each other. This circumstance has a marked influence on phase and group velocities of waves and on the frequencies and shapes of high-frequency vibrational modes.

In the present paper a derivation is given of approximate equations of motion which includes the effects of the additional mode. The approximation is based on expansions of the displacements in series of Jacobi polynomials in the radial co-ordinate, retaining only the earliest terms representative of axial, radial, and axial shear deformation. To offset the error introduced by omission of the terms of higher order, four compensating factors are introduced and chosen in such a way that the behavior of the first three branches of the Pochhammer frequency spectrum is reproduced at long wave lengths. Of particular interest is the approximate reproduction of the complex segments and frequency minima of the second and third branches.

2 Expansion in Infinite Series

The rod is bounded by the cylindrical surface $r = a$ and the planes $z = \pm c$ in a cylindrical co-ordinate system r, θ, z. The circumferential component of displacement u_θ is taken as zero and the radial and axial components are expressed in series of Jacobi polynomials in the radial co-ordinate:

$$u_r = \sum_{n=0}^{\infty} \mathfrak{U}_n(\alpha) u_n(z, t) \tag{1}$$

$$u_z = \sum_{n=0}^{\infty} \mathfrak{W}_n(\alpha) w_n(z, t) \tag{2}$$

where

$$\alpha = r/a$$

and [2][3]

$$\mathfrak{U}_0(\alpha) = \alpha, \quad \mathfrak{U}_1(\alpha) = \alpha - \frac{3}{2}\alpha^3, \ldots$$
$$\ldots \mathfrak{U}_n(\alpha) = \alpha + \sum_{k=1}^{n} (-1)^k \binom{n}{k} \frac{(n+2)_k}{(k+1)!} \alpha^{2k+1} \tag{3}$$

$$\mathfrak{W}_0(\alpha) = 1, \quad \mathfrak{W}_1(\alpha) = 1 - 2\alpha^2, \ldots$$
$$\ldots \mathfrak{W}_n(\alpha) = 1 + \sum_{k=1}^{n} (-1)^k \binom{n}{k} \frac{(n+1)_k}{k!} \alpha^{2k} \tag{4}$$

in which

$$\binom{n}{k} = \frac{n(n-1)(n-2)\ldots(n-k+1)}{k!} \tag{5}$$

$$(\beta)_k = \beta(\beta+1)(\beta+2)\ldots(\beta+k-1), \quad (\beta)_0 = 1 \tag{6}$$

The polynomials $\mathfrak{U}_n$ and $\mathfrak{W}_n$ have the properties

$$4(n+1)^2 \int_0^1 \alpha \mathfrak{U}_m \mathfrak{U}_n d\alpha = \begin{cases} 0, & m \neq n \\ 1, & m = n \end{cases} \tag{7}$$

$$2(2n+1) \int_0^1 \alpha \mathfrak{W}_m \mathfrak{W}_n d\alpha = \begin{cases} 0, & m \neq n \\ 1, & m = n \end{cases} \tag{8}$$

$$d\mathfrak{W}_n/d\alpha = \sum_{k=0}^{n-1} C_{nk} \mathfrak{U}_k, \quad C_{nk} = 4(k+1)^2(-1)^{n+k} \tag{9}$$

Stress Equations of Motion. The series expressions (1) and (2) are substituted in the equations

[1] This investigation was supported by the Office of Naval Research under a contract with Columbia University.

[2] Numbers in brackets designate References at end of paper.

Presented at the West Coast Conference of the Applied Mechanics Division, Stanford, Calif., September 9–11, 1959, of The American Society of Mechanical Engineers.

Discussion of this paper should be addressed to the Secretary, ASME, 29 West 39th Street, New York, N. Y., and will be accepted until April 10, 1960, for publication at a later date. Discussion received after the closing date will be returned.

Note: Statements and opinions advanced in papers are to be understood as individual expressions of their authors and not those of the Society. Manuscript received by ASME Applied Mechanics Division, November 17, 1958. Paper No. 59—APMW-2.

[3] In the notation of reference [2],

$$\mathfrak{U}_n(x) = x\mathfrak{F}_n(2, 2, x^2)$$
$$\mathfrak{W}_n(x) = \mathfrak{F}_n(1, 1, x^2)$$

Note, also, that

$$\mathfrak{U}_n(1) = (-1)^n/n!$$
$$\mathfrak{W}_n(1) = (-1)^n$$

$$\int_{-c}^{c}\int_{0}^{a}\left(\frac{\partial\sigma_r}{\partial r}+\frac{\partial\tau_{rz}}{\partial z}+\frac{\sigma_r-\sigma_\theta}{r}-\rho\frac{\partial^2 u_r}{\partial t^2}\right)\delta u_r\,r\,dr\,dz=0 \quad (10)$$

$$\int_{-c}^{c}\int_{0}^{a}\left(\frac{\partial\tau_{rz}}{\partial r}+\frac{\partial\sigma_z}{\partial z}+\frac{\tau_{rz}}{r}-\rho\frac{\partial^2 u_z}{\partial t^2}\right)\delta u_z\,r\,dr\,dz=0$$

which are obtained from the variational equations of motion [3]. In (10), σ_r, σ_θ, σ_z, τ_{rz} are components of stress derivable from a strain-energy-function U by differentiation with respect to components of strain ϵ_r, ϵ_θ, ϵ_z, γ_{rz} respectively. By substituting (1) and (2) into (10), performing the integrations with respect to r and setting the coefficients of δu_n and δw_n equal to zero, we obtain stress equations of motion of order n:

$$\left.\begin{aligned}\frac{dQ_n}{dz}-\frac{P_n}{a}+\frac{(-1)^n}{n+1}\frac{R}{a}&=\frac{\rho}{4(n+1)^2}\frac{\partial^2 u_n}{\partial t^2}\\ \frac{dF_n}{dz}-\sum_{k=0}^{n-1}C_{nk}\frac{Q_k}{a}+(-1)^n\frac{Z}{a}&=\frac{\rho}{2(2n+1)}\frac{\partial^2 w_n}{\partial t^2}\end{aligned}\right\} \quad (11)$$

where

$$\left.\begin{aligned}P_n&=\int_0^1(\sigma_\theta\mathfrak{U}_n+\sigma_r\alpha d\mathfrak{U}_n/d\alpha)d\alpha\\ Q_n&=\int_0^1\tau_{rz}\mathfrak{U}_n\alpha d\alpha\\ F_n&=\int_0^1\sigma_z\mathfrak{W}_n\alpha d\alpha,\end{aligned}\right\} \quad (12)$$

$$R=[\sigma_r]_{r=a},\quad Z=[\tau_{rz}]_{r=a} \quad (13)$$

Components of Strain. Upon substituting the expansions (1) and (2) in the usual strain-displacement relations, we obtain

$$\left.\begin{aligned}\epsilon_r&=\frac{\partial u_r}{\partial r}=\sum_{n=0}^{\infty}\frac{\partial\mathfrak{U}_n}{\partial\alpha}\frac{u_n}{a}\\ \epsilon_\theta&=\frac{u_r}{r}=\sum_{n=0}^{\infty}\frac{\mathfrak{U}_n}{\alpha}\frac{u_n}{a}\\ \epsilon_z&=\frac{\partial u_z}{\partial z}=\sum_{n=0}^{\infty}\mathfrak{W}_n\frac{\partial w_n}{\partial z}\\ \gamma_{rz}&=\frac{\partial u_r}{\partial z}+\frac{\partial u_z}{\partial r}=\sum_{n=0}^{\infty}\left(\mathfrak{U}_n\frac{\partial u_n}{\partial z}+\frac{\partial\mathfrak{W}_n}{\partial\alpha}\frac{w_n}{a}\right)\end{aligned}\right\} \quad (14)$$

Stress-Strain-Displacement Relations. If the strain-displacement relations (14) are substituted in the stress-strain relations

$$\left.\begin{aligned}\sigma_r&=\partial U/\partial\epsilon_r=\lambda(\epsilon_r+\epsilon_\theta+\epsilon_z)+2\mu\epsilon_r\\ \sigma_\theta&=\partial U/\partial\epsilon_\theta=\lambda(\epsilon_r+\epsilon_\theta+\epsilon_z)+2\mu\epsilon_\theta\\ \sigma_z&=\partial U/\partial\epsilon_z=\lambda(\epsilon_r+\epsilon_\theta+\epsilon_z)+2\mu\epsilon_z\\ \tau_{rz}&=\partial U/\partial\gamma_{rz}=\mu\gamma_{rz}\end{aligned}\right\} \quad (15)$$

and these, in turn, substituted in (12), we obtain, after using (14) and performing the integrations, relations between the components of stress of order n (P_n, Q_n, F_n) and the displacement amplitudes u_n, w_n of order n. The first few relations are

$$\left.\begin{aligned}P_0&=2(\lambda+\mu)\frac{u_0}{a}+\lambda\frac{\partial w_0}{\partial z}+\dots\\ Q_0&=\frac{\mu}{4}\left(\frac{\partial u_0}{\partial z}-\frac{4w_1}{a}\right)+\dots\\ F_0&=\frac{\lambda+2\mu}{2}\frac{\partial w_0}{\partial z}+\lambda\frac{u_0}{a}+\dots\\ F_1&=\frac{\lambda+2\mu}{6}\frac{\partial w_1}{\partial z}+\dots\end{aligned}\right\} \quad (16)$$

(cont.)

where the terms represented by dots contain amplitudes u_n of order higher than $n=0$ and w_n of order higher than $n=1$.

Energy-Densities. From the strain-energy-density of the three-dimensional theory:

$$U=\tfrac{1}{2}[\lambda(\epsilon_r+\epsilon_\theta+\epsilon_z)^2+2\mu(\epsilon_r^2+\epsilon_\theta^2+\epsilon_z^2+\tfrac{1}{2}\gamma_{rz}^2)]$$
$$=\tfrac{1}{2}(\sigma_r\epsilon_r+\sigma_\theta\epsilon_\theta+\sigma_z\epsilon_z+\tau_{rz}\gamma_{rz}) \quad (17)$$

we define an energy-density

$$\bar{U}=\int_0^1 U\alpha\,d\alpha$$
$$=\frac{1}{2}\left[P_0\frac{u_0}{a}+\dots+F_0\frac{\partial w_0}{\partial z}+F_1\frac{\partial w_1}{\partial z}+\dots+Q_0\left(\frac{\partial u_0}{\partial z}-\frac{4w_1}{a}\right)+\dots\right] \quad (18)$$

Similarly, from the kinetic-energy-density

$$K=\frac{\rho}{2}\left[\left(\frac{\partial u_r}{\partial t}\right)^2+\left(\frac{\partial u_z}{\partial t}\right)^2\right] \quad (19)$$

we define an energy-density

$$\bar{K}=\int_0^1 K\alpha\,d\alpha$$
$$=\frac{\rho}{2}\left[\tfrac{1}{4}\left(\frac{\partial u_0}{\partial t}\right)^2+\tfrac{1}{2}\left(\frac{\partial w_0}{\partial t}\right)^2+\tfrac{1}{6}\left(\frac{\partial w_1}{\partial t}\right)^2+\dots\right] \quad (20)$$

3 Second-Order Approximation

We retain only the terms associated with displacement amplitudes u_0, w_0, and w_1. To simplify the notation, let

$$u=u_0,\quad w=w_0,\quad \psi=w_1 \quad (21)$$

$$\left.\begin{aligned}P_r=P_\theta&=\int_0^1(\sigma_r+\sigma_\theta)\alpha d\alpha\\ P_z=P_0&=\int_0^1\sigma_z\alpha d\alpha\\ P_\psi=F_1&=\int_0^1\sigma_z(1-2\alpha^2)\alpha d\alpha\\ P_{rz}=Q_0&=\int_0^1\tau_{rz}\alpha^2 d\alpha\end{aligned}\right\} \quad (22)$$

$$\left.\begin{aligned}\Gamma_r&=u/a & \Gamma_z&=\partial w/\partial z\\ \Gamma_\psi&=\partial\psi/\partial z & \Gamma_{rz}&=\partial u/\partial z-4\psi/a\end{aligned}\right\} \quad (23)$$

The components of displacement, strain, stress, and surface, traction are illustrated in Fig. 1. It may be observed that w, u and ψ are the amplitudes of uniform, linear, and quadratic distributions of axial (w, ψ) and radial (u) displacements along a radius of the rod.[4]

[4] Thus the three-dimensional displacements are represented in the second-order approximation by

$$u_r\approx\alpha u(z,t),\quad u_z\approx w(z,t)+(1-2\alpha^2)\psi(z,t)$$

and the strains by

$$\epsilon_r=\epsilon_\theta\approx\Gamma_r,\quad \epsilon_z\approx\Gamma_z+(1-2\alpha^2)\Gamma_\psi,\quad \gamma_{rz}\approx\alpha\Gamma_{rz}$$

Omission of the higher-order terms limits the applicability, of what is left, to relatively long wave lengths. In this range, the uniform distribution of axial displacement, whose amplitude is w, is a good approximation to the distribution of u_z found in the lowest mode of the exact solution for waves in an infinite rod. In fact, the latter distribution approaches uniformity as the wave length approaches infinity. The linear and quadratic distributions of the other two displacements, i.e., those with amplitudes u and ψ, are not as good approximations to the Bessel-function distributions found in the second and third modes of the exact solution, even at very long wave lengths, as shown by the dotted lines in the diagrams for u and ψ in Fig. 1. It is advisable, therefore, to introduce means for compensating, as well as is possible with the terms retained, for the omission of the polynomials of higher degree. To this end, we replace Γ_r by $\kappa_1\Gamma_r$ and Γ_{rz} by $\kappa_3\Gamma_{rz}$ in the strain-energy-density and $\dot{u}$ by $\kappa_2\dot{u}$ and $\dot{\psi}$ by $\kappa_4\dot{\psi}$ in the kinetic-energy-density, where the κ_i are constants, whose values are determined in Section 5, and the dot indicates differentiation with respect to time. Then the energy-densities of the second-order approximation are

$$U_2 = {}^1/_2[2(\lambda+\mu)\kappa_1^2\Gamma_r^2 + {}^1/_2(\lambda+2\mu)\Gamma_z^2 + 2\lambda\kappa_1\Gamma_r\Gamma_z + {}^1/_4\mu\kappa_3^2\Gamma_{rz}^2 + {}^1/_6(\lambda+2\mu)\Gamma_\psi^2] \quad (24)$$

$$K_2 = {}^1/_2\rho({}^1/_6\kappa_2^2\dot{u}^2 + {}^1/_2\dot{w}^2 + {}^1/_8\kappa_4^2\dot{\psi}^2) \quad (25)$$

The adjusted stress-strain-displacement relations, derived from the strain-energy-density function (24), are

$$\left.\begin{aligned} P_r &= \partial U_2/\partial\Gamma_r = 2(\lambda+\mu)\kappa_1^2\Gamma_r + \lambda\kappa_1\Gamma_z \\ &= [2(\lambda+\mu)\kappa_1^2 u + \lambda\kappa_1 w']a^{-1} \\ P_z &= \partial U_2/\partial\Gamma_z = {}^1/_2(\lambda+2\mu)\Gamma_z + \lambda\kappa_1\Gamma_r \\ &= [{}^1/_2(\lambda+2\mu)w' + \lambda\kappa_1 u]a^{-1} \\ P_{rz} &= \partial U_2/\partial\Gamma_{rz} = {}^1/_4\mu\kappa_3^2\Gamma_{rz} \\ &= {}^1/_4\mu\kappa_3^2(u' - 4\psi)a^{-1} \\ P_\psi &= \partial U_2/\partial\Gamma_\psi = {}^1/_6(\lambda+2\mu)\Gamma_\psi \\ &= {}^1/_6(\lambda+2\mu)\psi' a^{-1} \end{aligned}\right\} \quad (26)$$

where prime indicates differentiation with respect to z/a.

The adjusted stress-equations of motion, derived from the variational equations of motion with the constants κ_3 and κ_4 introduced into the kinetic energy, are

$$\left.\begin{aligned} P_{rz}' - P_r + R &= {}^1/_4\rho a\kappa_2^2\ddot{u} \\ P_z' + Z &= {}^1/_2\rho a\ddot{w} \\ P_\psi' + 4P_{rz} - Z &= {}^1/_6\rho a\kappa_4^2\ddot{\psi} \end{aligned}\right\} \quad (27)$$

and, from (26) and (27), the displacement equations of motion are

$$\left.\begin{aligned} \mu\kappa_3^2(u'' - 4\psi') - 8(\lambda+\mu)\kappa_1^2 u \\ - 4\lambda\kappa_1 w' + 4aR &= \rho a^2\kappa_2^2\ddot{u} \\ (\lambda+2\mu)w'' + 2\lambda\kappa_1 u' + 2aZ &= \rho a^2\ddot{w} \\ (\lambda+2\mu)\psi'' + 6\mu\kappa_3^2(u' - 4\psi) - 6aZ &= \rho a^2\kappa_4^2\ddot{\psi} \end{aligned}\right\} \quad (28)$$

4 Pochhammer Equation

As shown in the next section, the solution of the equations of motion (28) for free vibrations, or waves, in an infinite bar leads to a cubic frequency equation relating the square of the frequency to the square of the wave number, with Poisson's ratio and the coefficients κ_i as parameters. The three branches of this equation should match, as closely as possible, the corresponding branches of Pochhammer's frequency equation [4]

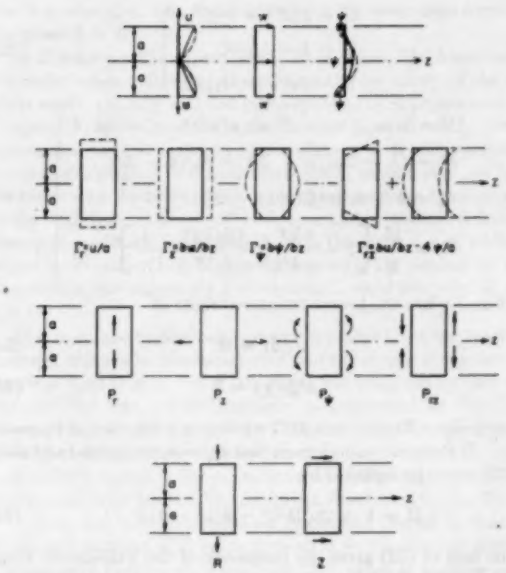

Fig. 1 Displacements, strains, stresses, and surface tractions; second-order approximation

$$(\gamma^2 - \beta^2)\mathcal{J}_1(\alpha a) + 4\gamma^2\alpha^2\mathcal{J}_1(\beta a) = 2(\gamma^2 + \beta^2)\alpha^2 \quad (29)$$

where

$$\alpha^2 = \rho\omega^2/(\lambda+2\mu) - \gamma^2, \quad \beta^2 = \rho\omega^2/\mu - \gamma^2 \quad (30)$$

and $\mathcal{J}_1(x)$ is the Onoe function [5, 6] of the first kind and order unity:

$$\mathcal{J}_1(x) = xJ_0(x)/J_1(x) \quad (31)$$

and $J_n(x)$ is the Bessel function of the first kind. In (29) and (30), the frequency ω must be real; but the wave number along the axis of the bar γ may be real, imaginary, or complex.

The match between the three branches of the cubic equation and the analogous branches of (29) may be adjusted by means of the coefficients κ_i; but, since the κ_i are constants, a perfect match can be made, in general, only at one value of γ for each of them. Now, large enough real γ corresponds to frequencies high enough to enter the frequency range of modes that have not been included in the approximate equations. In general, the applicability of the approximate equations is limited to frequencies below the lowest frequency, for real wave numbers, of the lowest neglected mode and to the correspondingly small wave numbers. This is because, except for infinite trains of sinusoidal waves, there would be coupling of all the Pochhammer modes and their anharmonic overtones wherever they have the same frequency and wave length. There is, then, little advantage to be gained in a choice of the κ_i that makes an approximate branch match the exact one at short wave lengths (large γ) at the expense of a good match at long wave lengths. In fact, we go to the extreme and choose all of the κ_i so that the match is perfect in the neighborhood of $\gamma = 0$. This choice has the advantage of reproducing, in the approximate equations, the intricate behavior which the exact solution has at long wave lengths, as Poisson's ratio varies, while retaining a reasonably good match out to as short wave lengths as the frequency limitation permits.

When γa is small, the three branches of the Pochhammer equation, which correspond to the three branches of the approximation are given by [7]

$$\left.\begin{aligned}\Omega &= \zeta[2(1+\nu)]^{1/2}\\ \Omega &= 1 + {}^1/_2\zeta^2 C_s\\ \Omega &= k\chi/\delta + {}^1/_2\zeta^2 C_r\end{aligned}\right\} \tag{32}$$

where
$$\left.\begin{aligned}&\Omega = \omega/\omega_s,\quad \omega_s = (\delta/a)(\mu/\rho)^{1/2},\quad \zeta = \gamma a/\delta\\ &k^2 = (\lambda+2\mu)/\mu = 2(1-\nu)/(1-2\nu)\\ &C_s = 1 - 8/[k^2\mathcal{J}_1(\delta/k) - 2]\\ &C_r = \frac{k\delta}{\chi}\left[1 + \frac{4[k^2 + 2\mathcal{J}_1(k\chi) - 4]}{k^4\chi^2 - 4(k^2-1)}\right]\end{aligned}\right\} \tag{33}$$

and δ and χ are the lowest (nonzero) roots of

$$J_1(\delta) = 0 \tag{34}$$

$$k^2\mathcal{J}_1(\chi) = 2 \tag{35}$$

respectively. Thus $\delta = 3.8317$ while χ is a function of Poisson's ratio. If Poisson's ratio is such that $k\chi = \delta$, the second and third of (32) are to be replaced by

$$\Omega = 1 \pm 2k\zeta[k^2\delta^2 - 4(k^2-1)]^{-1/2} \tag{36}$$

The first of (32) gives the frequency of the well-known longitudinal mode, which has a limiting phase velocity

$$[2(1+\nu)\mu/\rho]^{1/2} = [E/\rho]^{1/2} \tag{37}$$

where E is Young's modulus. The accompanying distribution of axial displacement u_s is uniform, in the limit as $\zeta \to 0$, and is represented in the approximate equations by w. The second of (32) has a frequency at cutoff (i.e., $\zeta = 0$) of $\omega = \omega_s$ where ω_s is given in (33), and the accompanying displacement is purely axial with one circular node. This mode, the lowest axial shear mode, is represented in the approximate equations by ψ. The mode shape associated with the third of (32), at cutoff, is characterized by a purely radial displacement which is represented in the approximate equations by u. The frequency

$$\left.\begin{aligned}&\omega_r = (\chi/a)[(\lambda+2\mu)/\rho]^{1/2}\\ \text{or}\quad &\Omega_r = \omega_r/\omega_s = k\chi/\delta\end{aligned}\right\} \tag{38}$$

of this radial mode depends on Poisson's ratio whereas ω_s does not. The two are equal when $k\chi = \delta$, i.e., when Poisson's ratio is given by the lowest root of

$$k^2\mathcal{J}_1(\delta/k) = 2,\quad \delta = 3.8317 \tag{39}$$

or, when
$$\nu = \nu_c = 0.2833 \tag{40}$$

The frequency of the radial mode is less than, equal to, or greater than the frequency of the axial shear mode according as Poisson's ratio is less than, equal to, or greater than ν_c. As Poisson's ratio increases above ν_c, the frequency ω_r approaches the frequency of the second axial shear mode, given by

$$\Omega_{2s} = \frac{\delta_2}{\delta} = \frac{7.0156}{3.8317} = 1.8309 \tag{41}$$

where δ_2 is the second root of (34). Now, the second axial shear mode has two circular nodes and such a displacement is not included in the second-order approximation. Hence the approximate equations are limited, in application, to frequencies less than that given by (41) and to the wave lengths associated with such frequencies in the first three branches. Also, the equations are limited to Poisson's ratios less than that for which ω_r is equal to the frequency of the second axial shear mode. This is obtained from the lowest root of

$$k^2\mathcal{J}_1(\delta_2/k) = 2,\quad \delta_2 = 7.0156 \tag{42}$$

from which $\nu = \nu_2 = 0.439$. Actually, the limitation on frequency and Poisson's ratio is probably slightly more severe because of possible coupling with the next higher complex branches in the case of bounded rods or transient waves.

The quantities C_s and C_r in (33) are the curvatures of the two upper branches at $\zeta = 0$. When $\nu < \nu_c$, $C_r < 0$ and $C_s > 0$ and they approach positive and negative infinity, respectively, as $\nu \to \nu_c$ from below. When $\nu_c < \nu < \nu_2$, the signs of the curvatures are reversed. From (32) it may be seen that the slopes of the two upper branches are zero at $\zeta = 0$, in the range $\nu < \nu_2$, except when $\nu = \nu_c$, in which case they can be obtained from (36).

5 The Coefficients κ_i

The intricate behavior of the second and third branches of the exact solution, at $\zeta = 0$, is to be reproduced in the corresponding branches, obtained from the approximate equations, by appropriate choice of the coefficients κ_i as functions of ν. Upon substituting

$$\left.\begin{aligned}u &= A\cos\gamma z\, e^{i\omega t}\\ w &= B\sin\gamma z\, e^{i\omega t}\\ \psi &= C\sin\gamma z\, e^{i\omega t}\\ R &= Z = 0\end{aligned}\right\} \tag{43}$$

in (28) and eliminating the constants A, B, and C, we find, for the cubic equation governing the branches of the approximate equations,

$$\begin{vmatrix} a_{11} & a_{12} & a_{13}\\ a_{12} & a_{22} & 0\\ a_{13} & 0 & a_{33}\end{vmatrix} = 0 \tag{44}$$

where
$$\left.\begin{aligned}a_{11} &= \kappa_2^2\delta^2\zeta^2 + 8(k^2-1)\kappa_1^2 - \kappa_3^2\delta^2\Omega^2\\ a_{22} &= 2\delta^2(k^2\zeta^2 - \Omega^2)\\ a_{33} &= 6(k^2\delta^2\zeta^2 + 24\kappa_2^2 - \kappa_4^2\delta^2\Omega^2)\\ a_{12} &= 4(k^2-2)\kappa_1\delta\zeta\\ a_{13} &= 12\kappa_2^2\delta\zeta\end{aligned}\right\} \tag{45}$$

When $\zeta = 0$, (44) has the three roots

$$\Omega^2 = 0,\quad \frac{24\kappa_2^2}{\delta^2\kappa_4^2},\quad \frac{8(k^2-1)\kappa_1^2}{\delta^2\kappa_3^2} \tag{46}$$

for the longitudinal (w), axial shear (ψ), and radial (u) modes, respectively. To make these frequencies the same as the cutoff frequencies obtained from (32), we set

$$\frac{\kappa_2^2}{\kappa_4^2} = \frac{\delta^2}{24},\quad \frac{\kappa_1^2}{\kappa_3^2} = \frac{k^2\chi^2}{8(k^2-1)} \tag{47}$$

Then, for $\zeta \ll 1$, (44) becomes

$$\left.\begin{aligned}\Omega &= \zeta[2(1+\nu)]^{1/2}\\ \Omega &= 1 + {}^1/_2\zeta^2\bar{C}_s\\ \Omega &= k\chi/\delta + {}^1/_2\zeta^2\bar{C}_r\end{aligned}\right\} \tag{48}$$

where
$$\left.\begin{aligned}\bar{C}_s &= \frac{k^2\delta^2}{24}\left[\frac{1}{\kappa_2^2} - \frac{3\chi^2\kappa_2^2}{\kappa_1^2(k^2-1)(k^2\chi^2-\delta^2)}\right]\\ \bar{C}_r &= \frac{k\chi\delta}{k^2-1}\left[\frac{(k^2-2)^2}{k^2\chi^2} + \frac{\kappa_4^2k^2\chi^2}{8\kappa_1^2(k^2\chi^2-\delta^2)}\right]\end{aligned}\right\} \tag{49}$$

except if $k\chi = \delta$ (i.e., $\nu = \nu_s$) in which case the second and third of (48) are

$$\Omega = 1 \pm \zeta \left[\frac{\delta^2 \kappa_2^2}{32(k^2 - 1)\kappa_1^2} \right]^{1/2} \tag{50}$$

Comparing (48) with (32), we see that the longitudinal mode needs no adjustment, while the others will match if

$$\bar{C}_r = C_r, \quad \bar{C}_s = C_s \tag{51}$$

from which

$$\left.\begin{aligned} \frac{\kappa_2^2}{\kappa_1^2} &= \frac{8(k^2\chi^2 - \delta^2)}{k^2\chi^2} \left[\frac{(k^2 - 1)C_r}{k\chi\delta} - \frac{(k^2 - 2)^2}{k^2\chi^2} \right] \\ \frac{1}{\kappa_2^2} &= \frac{24}{k^2\delta^2} \left[\frac{k^2\chi^2\delta^2\kappa_2^2}{8(k^2 - 1)(k^2\chi^2 - \delta^2)\kappa_1^2} + C_s \right] \end{aligned}\right\} \tag{52}$$

In the case $k\chi = \delta$, we have

$$\lim_{k\chi \to \delta} \frac{\kappa_2^2}{\kappa_1^2} = \frac{128k^2(k^2 - 1)}{\delta^2[k^2\delta^2 - 4(k^2 - 1)]} \tag{53}$$

When this is substituted in (50), that equation becomes identical with (36), as required.

Equations (47) and (52) fix the four coefficients κ_i as functions of Poisson's ratio. With these values, the ordinates, slopes, and curvatures of the three branches from the approximate and exact equations are identical at $\zeta = 0$.

6 Frequency Spectrum

Equation (44) relates Ω^2 to ζ^2 but only real, positive Ω has physical significance. For real, positive Ω, the roots ζ^2 may be three real positive, two real positive, and one real negative or one real positive and two conjugate complex. Hence there are six roots

$$\zeta = \xi + i\eta \tag{54}$$

which occur in two sets of three roots each, distinguished only by reversal of the sign of ζ. In each set, the roots may be three real, or two real and one imaginary, or one real and two conjugate complex. In addition, the character of the spectrum is different according as Poisson's ratio is less than, equal to, or greater than ν_s.

We consider the case $\nu < \nu_s$ first. Then, when $\Omega > 1$, the three branches of (44), corresponding to one set of roots, are real ($\eta = 0$). They are illustrated in Fig. 2(*a*) (for $\nu = 1/4$) by the three dashed curves marked ζ_1, ζ_2, ζ_3 in the plane $\eta = 0$ and the region $\Omega > 1$. As Ω drops below $\Omega = 1$, the largest root ζ_1 approaches zero with asymptotic behavior given by the first of (48); the intermediate branch ζ_2 approaches a frequency minimum at Ω^*, below which there are no real roots other than ζ_1; the smallest root ζ_3 approaches a frequency minimum in the real plane $\eta = 0$, at $\Omega = 1$, $\xi = 0$, with asymptotic behavior given by the second of (48). Continuing with the branch ζ_3, as Ω drops below $\Omega = 1$, the root is imaginary $\xi = 0$ with asymptotic behavior, for small η, given by the second of (48). As Ω approaches Ω_r from above, the branch ζ_3 forms a loop in the imaginary plane ($\xi = 0$) and approaches $\Omega = \Omega_r$, $\eta = 0$, with asymptotic behavior given by the third of (48). As Ω drops below $\Omega = \Omega_r$, the root ζ_3 becomes real with behavior near $\Omega = \Omega_r$, $\zeta = 0$, given by the third of (48), but now ξ is negative. Upon further diminution of Ω, the branch ζ_3 approaches a frequency minimum at $\Omega = \Omega^*$ and negative ξ. The portion of ζ_3 between Ω_r and Ω^* is identified in Fig. 2(*a*) by $[\zeta_3]$, where the brackets indicate that it is the reflection of the branch in the plane $\xi = 0$ that is shown. Finally, when $\Omega < \Omega^*$, the roots ζ_2 and ζ_3 are conjugate complex ($\zeta = \pm\xi + i\eta$). One of them is shown, in Fig. 2(*a*), as the curve ζ_2 below Ω^*. This curve is also $[\zeta_3]$, i.e., the reflection of the conjugate root ζ_3 in the plane $\xi = 0$.

As Poisson's ratio approaches ν_s from below, the frequency of the radial mode increases, approaching the frequency of the axial shear mode; i.e., at $\zeta = 0$, the intercept $\Omega = \Omega_r$ approaches $\Omega = 1$. Conjointly, the curvature of the branch ζ_3 at $\Omega = \Omega_r$, $\zeta = 0$, approaches negative infinity in the plane $\eta = 0$ and positive infinity in the plane $\xi = 0$ while both slopes remain zero, all in accordance with the third of (48). At the same time, the curvature of the branch ζ_3, at $\Omega = 1$, $\zeta = 0$, approaches positive infinity in the plane $\eta = 0$ and negative infinity in the plane $\xi = 0$, while the slopes remain zero, all in accordance with the second of (48). Meanwhile, the imaginary loop shrinks toward the point $\Omega = 1$, $\eta = 0$.

At $\nu = \nu_s$, the axial shear and radial modes have the same frequency; there is no imaginary root and the slopes of the two segments of ζ_3 at $\Omega = 1$, $\zeta = 0$, are equal and are given by (50) with the positive sign. This situation is illustrated in Fig. 2(*b*). Here, again, the portions marked $[\zeta_3]$ are the reflections, in the plane $\xi = 0$, of the actual branches.

When $\nu > \nu_s$, the radial mode has a frequency higher than that of the axial shear mode. The spectrum, illustrated in Fig. 2(*c*) for $\nu = 0.31$, has now undergone an important change in that the imaginary segment of ζ_3 loops up from $\Omega = 1$ instead of down.

Since only powers of ζ^2 occur in (44), there is another set of roots given by the reflections of the curves of Fig. 2 in the planes $\xi = 0$ and $\eta = 0$. These branches correspond to modes in which the sign of the co-ordinate z is reversed.

The shape, along z, of the mode corresponding to a point on any branch can be deduced from the real, imaginary, or complex character of ζ. Real roots correspond to trigonometric shapes; imaginary roots to exponential or hyperbolic shapes; and complex roots to modes whose shapes are given by products of trigonometric and exponential or hyperbolic functions. A striking example of the latter is to be found in the experiments of Oliver [8].

The ratio of the phase velocity (v) and group velocity (v_g) to the velocity of equivoluminal waves $v_2 = (\mu/\rho)^{1/2}$ can be visualized readily from Fig. 2 inasmuch as

$$\frac{v}{v_2} = \frac{\omega}{\gamma v_2} = \frac{\Omega}{\xi} \tag{55}$$

$$\frac{v_g}{v_2} = \frac{d\omega}{v_2 d\gamma} = \frac{d\Omega}{d\xi} \tag{56}$$

Thus the slope of the straight line from the origin to a point on a branch is proportional to the phase velocity, and the slope of the branch is proportional to the group velocity. There are several anomalous velocities in Fig. 2. For example, at the frequency minimum Ω^*, the phase velocity is nonzero and finite while the group velocity is zero; between Ω^* and the lower of the two cutoff frequencies of the third branch, the phase and group velocities have opposite signs; when $\nu = \nu_s$, the point $\Omega = 1$, $\zeta = 0$ corresponds to infinite phase velocity with finite, nonzero group velocity.

The full lines in Fig. 2 are the first three branches of the Pochhammer equation. The approximate branches match the exact ones very well in the neighborhood of $\zeta = 0$; due, of course, to the choice of the κ_i. Without such a choice, the extraordinarily intricate behavior of the exact branches would not be reproduced in the approximate equations based on simple polynomial distributions of displacement. It is, in fact, remarkable that the correspondence is reasonably good for quite large values of ζ and for real, imaginary, and complex portions of the branches; especially since the simple polynomial distributions replace Bessel functions of real, imaginary, and complex arguments.

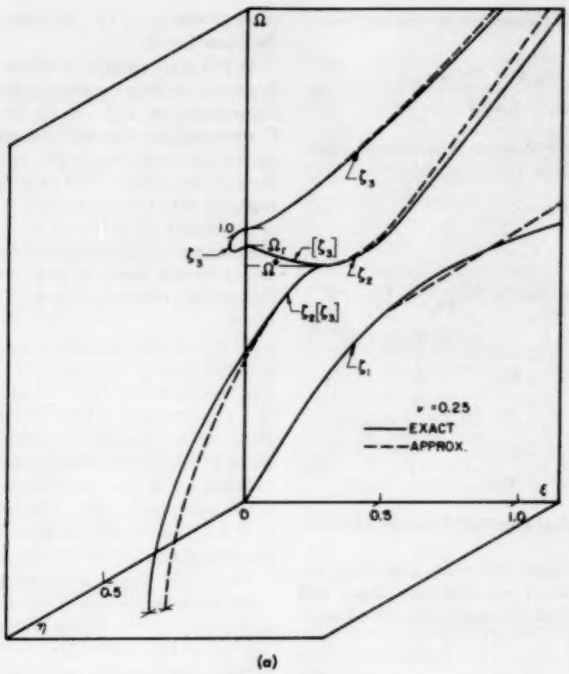

(a)

Fig. 2 Frequency spectrum

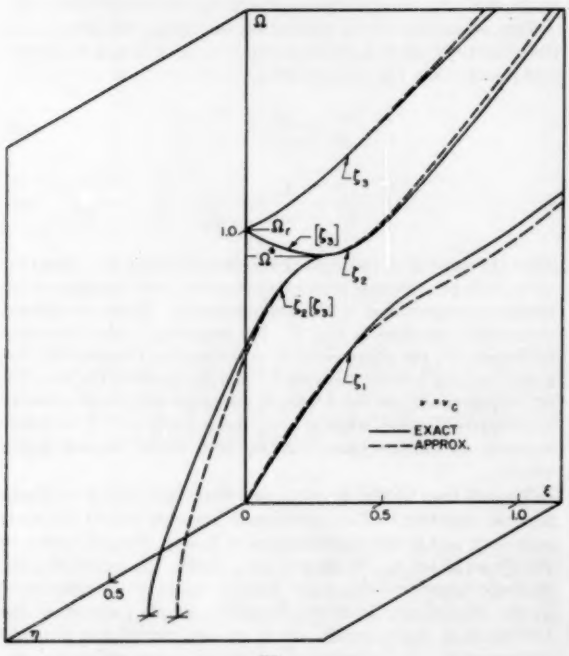

(b)

Fig. 2 Frequency spectrum

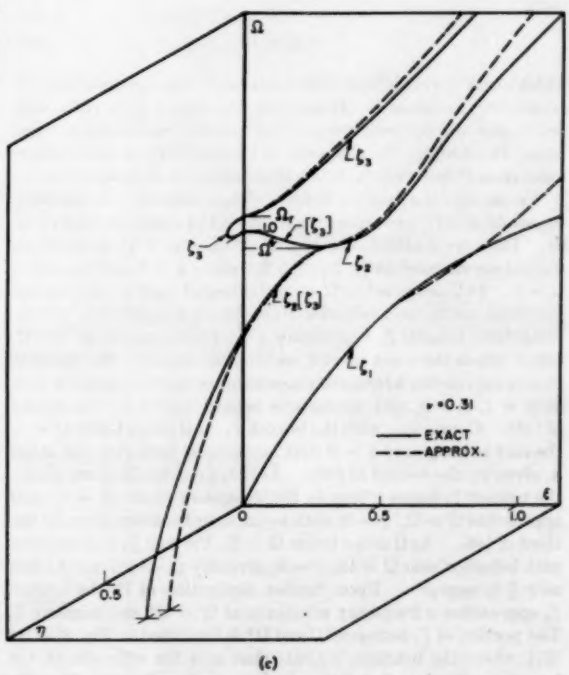

(c)

Fig. 2 Frequency spectrum

7 Uniqueness and Orthogonality

A uniqueness theorem, analogous to Neumann's [9], will establish the initial and boundary conditions appropriate to the second-order equations.

Consider two systems of displacements, strains, and stresses which satisfy the strain-displacement relations (23), the associated compatibility condition

$$\frac{\partial \Gamma_{rz}}{\partial z} + \frac{4}{a}\Gamma_\psi - a\frac{\partial^2 \Gamma_r}{\partial z^2} = 0 \tag{57}$$

the stress-strain relations (26), and the stress equations of motion (27). Let the differences between corresponding components of displacement, strain, and stress constitute a "difference system" of these quantities and let K_2 and U_2 be the kinetic and strain energy densities of the difference system. Then the sum of K_2 and U_2 in a bar of length $2c$ at time t is

$$\mathfrak{K} + \mathfrak{U} = \mathfrak{K}_0 + \mathfrak{U}_0 + \int_0^t dt \int_{-c}^{c} (\dot{K}_2 + \dot{U}_2)dz \tag{58}$$

where $\mathfrak{K}_0$ and $\mathfrak{U}_0$ are the values of $\mathfrak{K}$ and $\mathfrak{U}$ at an initial time $t = 0$.

Now
$$\dot{K}_2 = \rho(^1/_4\kappa_3{}^2\dot{u}\ddot{u} + {}^1/_3\ddot{w}\dot{w} + {}^1/_4\kappa_4{}^2\ddot{\psi}\dot{\psi}) \tag{59}$$

where u, w, and ψ are the displacements of the difference system; and

$$\dot{U}_2 = \frac{\partial U_2}{\partial \Gamma_r}\dot{\Gamma}_r + \frac{\partial U_2}{\partial \Gamma_z}\dot{\Gamma}_z + \frac{\partial U_2}{\partial \Gamma_\psi}\dot{\Gamma}_\psi + \frac{\partial U_2}{\partial \Gamma_{rz}}\dot{\Gamma}_{rz} \tag{60}$$

where the strains are those of the difference system. From (23) and (26), (60) becomes

$$\begin{aligned} a\dot{U}_2 &= P_r\dot{u} + P_z\dot{w}' + P_\psi\dot{\psi}' + P_{rz}(\dot{u}' - 4\dot{\psi}) \\ &= (P_r - P_{rz}')\dot{u} - P_z'\dot{w} - (P_\psi + 4P_{rz})\dot{\psi} \\ &\quad + (P_z\dot{w} + P_\psi\dot{\psi} + P_{rz}\dot{u})' \end{aligned} \tag{61}$$

where prime indicates differentiation with respect to z/a. Hence

$$\begin{aligned} a(\dot{K}_2 + \dot{U}_2) &= -(P_{rz}' - P_r - {}^1/_4\rho a\kappa_3{}^2\ddot{u})\dot{u} \\ &\quad - (P_z' - {}^1/_2\rho a\ddot{w})\dot{w} \\ &\quad - (P_\psi' + 4P_{rz} - {}^1/_4\rho a\kappa_4{}^2\ddot{\psi})\dot{\psi} \\ &\quad + (P_z\dot{w} + P_\psi\dot{\psi} + P_{rz}\dot{u})' \end{aligned} \tag{62}$$

or, using the stress equations of motion (27),

$$a(\dot{K}_2 + \dot{U}_2) = R\dot{u} + Z(\dot{w} - \dot{\psi}) + (P_z\dot{w} + P_\psi\dot{\psi} + P_{rz}\dot{u})' \tag{63}$$

Upon substituting (63) into (58), we have, finally

$$\begin{aligned} \mathfrak{K} + \mathfrak{U} &= \mathfrak{K}_0 + \mathfrak{U}_0 + a^{-1}\int_0^t dt \int_{-c}^{c} [R\dot{u} + Z(\dot{w} - \dot{\psi})]dz \\ &\quad + [P_z\dot{w} + P_\psi\dot{\psi} + P_{rz}\dot{u}]_{-c}^{c} \end{aligned} \tag{64}$$

Then, by the usual argument based on the positive definiteness of K_2 and U_2, the initial and boundary conditions are:

(i) Throughout the rod, the initial values of u, w, ψ and $\dot{u}$, $\dot{w}$, $\dot{\psi}$.

(ii) Throughout the rod, one member of each of the two products Ru and $Z(w - \psi)$.

(iii) At each end of the rod, one member of each of the three products $P_z w$, $P_\psi\psi$, and $P_{rz}u$.

By a closely related procedure, it may be shown that in two solutions

$$\begin{aligned} (u, w, \psi) &= (u_p, w_p, \psi_p)\exp i\omega_p t \\ (u, w, \psi) &= (u_q, w_q, \psi_q)\exp i\omega_q t \end{aligned} \tag{65}$$

of the homogeneous ($R = Z = 0$) stress equations of motion (27), the characteristic functions satisfy the orthogonality condition

$$\int_{-c}^{c}(3\kappa_3{}^2u_pu_q + 6w_pw_q + 2\kappa_4{}^2\psi_p\psi_q)dz = 0 \tag{66}$$

for $\omega_p \neq \omega_q$ and homogeneous end conditions (iii).

8 Helmholtz Equations

In case of free vibrations, or waves, the displacement equations of motion (28) may be reduced to three uncoupled Helmholtz equations. Let

$$\begin{aligned} u &= \varphi\exp i\omega t \\ w &= \sigma\varphi'\exp i\omega t \\ \psi &= \tau\varphi'\exp i\omega t \end{aligned} \tag{67}$$

where σ and τ are coefficients to be determined; φ is a function of z; and prime, as before, indicates differentiation with respect to z/a. Upon substituting (67) in (28), we find that the latter are satisfied if

$$\varphi'' + \delta^2\zeta^2\varphi = 0 \tag{68}$$

provided ζ is one of the three roots of (44) and

$$\begin{aligned} \sigma &= a_{12}/a_{22}\delta\zeta \\ \tau &= 3a_{13}/a_{23}\delta\zeta \end{aligned} \tag{69}$$

Hence

$$\begin{aligned} u &= (\varphi_1 + \varphi_2 + \varphi_3)\exp i\omega t \\ w &= (\sigma_1\varphi_1' + \sigma_2\varphi_2' + \sigma_3\varphi_3')\exp i\omega t \\ \psi &= (\tau_1\varphi_1' + \tau_2\varphi_2' + \tau_3\varphi_3')\exp i\omega t \end{aligned} \tag{70}$$

where

$$\varphi_i'' + \delta^2\zeta_i{}^2\varphi_i = 0, \qquad i = 1, 2, 3 \tag{71}$$

and the σ_i and τ_i are given by (69) with ζ replaced by ζ_i.

References

1 R. D. Mindlin and G. Herrmann, "A One-Dimensional Theory of Compressional Waves in an Elastic Rod," Proceedings of the First U. S. National Congress of Applied Mechanics, 1950, pp. 187–191.

2 W. Magnus and F. Oberhettinger, "Special Functions of Mathematical Physics," Chelsea Publishing Company, New York, N. Y., 1949, p. 83.

3 A. E. H. Love, "A Treatise on the Mathematical Theory of Elasticity," Cambridge University Press, London, England, 1927, p. 167.

4 L. Pochhammer, "Ueber die Fortpflanzungsgeschwindigkeiten Schwingungen in einem unbegrenzten isotropen Kreiscylinder," *Zeitschrift für Mathematik*, vol. 81, 1876, pp. 324–336.

5 M. Onoe, "Formulae and Tables, the Modified Quotients of Cylinder Functions," Report of the Institute of Industrial Science, University of Tokyo, Chiba City, Japan, vol. 4, 1955.

6 M. Onoe, "Tables of Modified Quotients of Bessel Functions of the First Kind for Real and Imaginary Arguments," Columbia University Press, New York, N. Y., 1958.

7 M. Onoe, H. D. McNiven, and R. D. Mindlin, "Dispersion of Axially Symmetric Waves in Elastic Rods," forthcoming.

8 J. Oliver, "Elastic Wave Dispersion in a Cylindrical Rod by a Wide-Band Short-Duration Pulse Technique," *Journal of The Acoustical Society of America*, vol. 29, 1957, pp. 189–194.

9 A. E. H. Love, "A Treatise on the Mathematical Theory of Elasticity," Cambridge University Press, London, England, 1927, p. 176.

R. D. MINDLIN
Professor
of Civil Engineering,
Columbia University,
New York, N. Y.
Mem. ASME

E. A. FOX
Associate Professor
of Mechanics,
Rensselaer Polytechnic Institute,
Troy, N. Y.
Assoc. Mem. ASME

Vibrations and Waves in Elastic Bars of Rectangular Cross Section[1]

An exact solution of the equations of elasticity is found for a family of modes of vibration, or waves, in an infinite bar of rectangular cross section for certain ratios of width to depth. The solution is composed of coupled dilatational and equivoluminal waves and the four faces of the bar are free of traction.

Introduction

SOLUTIONS of the linear equations of elasticity will be described for vibrational modes, or waves, in an isotropic bar, of rectangular cross section and infinite length, with traction-free boundaries. There is a previous solution, by Lamé,[2] which yields a family of modes of equivoluminal distortion that are possible in such a bar. The present solutions involve coupled dilatational (P) and equivoluminal (S) waves.

The results for the bar can be obtained by combining two types of solution that are known for an infinite plate with traction-free faces. One of the solutions for the plate is that given by Rayleigh[3] and Lamb.[4] It is itself composed of a dilatational wave coupled with two equivoluminal waves. The other type of solution contains only equivoluminal deformation and the displacement is parallel to the surfaces of the plate. Two of these modes are required. They are special cases of Love waves[5] and correspond to what are sometimes called SH waves. A property of SH waves, in a plate with traction-free faces, is that the ratio of the thickness of the plate to the distance between nodes, measured through the thickness, is an integer. In combining the three solutions so as to satisfy additional traction-free boundary conditions at a pair of parallel sides of the plate, only those Rayleigh-Lamb modes can be used that have thickness-behavior like that of SH waves. This circumstance restricts the resulting solution to certain frequencies and ratios of width to depth of the cross section. A special property of the modes thus found is that, in addition to the four faces of the bar being traction-free, they remain plane during the motion; i.e., traction-free and mixed boundary conditions are satisfied simultaneously.

For a given, permissible ratio of width to depth, the solution presented gives a set of discrete points on the branches of the frequency spectrum (frequency versus wave-number) of the bar. The complete branches are not known, but their slopes at the discrete points are determined, in Section 9, through the use of the identity of group velocity and velocity of propagation of energy.

In Section 11 it is shown that the five component waves (three in the Rayleigh-Lamb solution and two SH waves) combine into three plane waves. One of the three waves is the original dilatational wave, another is an SH wave whose displacement is parallel to one pair of parallel faces of the bar and the third is an SV wave; i.e., an equivoluminal wave whose displacement is parallel to the other pair of faces of the bar. Each of these waves, in general, progresses along the bar by oblique reflections at all four faces. At each reflection, the angles of incidence and amplitudes of the three waves are so related that the face remains free of traction.

2 Equations of Elasticity

In the linear theory of elasticity, the components of stress in an isotropic body are related to the components of displacement by three equations of the type

$$\sigma_{xx} = \lambda(\partial u/\partial x + \partial v/\partial y + \partial w/\partial z) + 2\mu\partial u/\partial x \quad (1)$$

and three of the type

$$\sigma_{yz} = \mu(\partial w/\partial y + \partial v/\partial z), \quad (2)$$

where λ and μ are Lamé's constants.

Solutions of the displacement-equations of motion for the case of free vibrations, at circular frequency ω, may be expressed in the form

$$\begin{aligned} u &= \partial\varphi/\partial x + \partial H_z/\partial y - \partial H_y/\partial z, \\ v &= \partial\varphi/\partial y + \partial H_x/\partial z - \partial H_z/\partial x, \\ w &= \partial\varphi/\partial z + \partial H_y/\partial x - \partial H_x/\partial y, \end{aligned} \quad (3)$$

if

$$v_1^2\nabla^2\varphi + \omega^2\varphi = 0, \qquad v_1^2 = (\lambda + 2\mu)/\rho, \quad (4)$$

$$v_2^2\nabla^2 H_j + \omega^2 H_j = 0, \qquad v_2^2 = \mu/\rho, \qquad j = x, y, z, \quad (5)$$

where v_1 and v_2 are the velocities of dilatational and equivoluminal waves, respectively, in an infinite medium.

In Equations (3) to (5) and in the sequel, a time-dependent factor $e^{i\omega t}$ is omitted.

3 Rayleigh-Lamb Waves in an Infinite Plate

We consider, first, vibrations or waves in a plate bounded by traction-free surfaces $y = \pm b$. Let $H_y = 0$ and

$$\begin{aligned} \varphi &= -A\zeta \cos \xi x \cos \alpha y \cos \zeta z, \\ H_x &= B\zeta \cos \xi x \sin \beta y \sin \zeta z, \\ H_z &= -B\xi \sin \xi x \cos \beta y \cos \zeta z. \end{aligned} \quad (6)$$

---

[1] This investigation was supported, in part, by the Office of Naval Research under a contract with Columbia University.

[2] G. Lamé, "Leçons sur la théorie mathématique de l'élasticité des corps solides," Gauthier-Villars, Paris, France, second edition, 1866, p. 170.

[3] Lord Rayleigh, "On the Free Vibrations of an Infinite Plate of Homogeneous Isotropic Elastic Matter," *Proceedings of the London Mathematical Society*, England, vol. 20, 1889, pp. 225–234.

[4] H. Lamb, "On Waves in an Elastic Plate," *Proceedings of the Royal Society of London*, England, series A, vol. 93, 1917, pp. 114–128.

[5] A. E. H. Love, "Some Problems in Geodynamics," Cambridge University Press, London, England, 1926, p. 160.

Presented at the West Coast Conference of the Applied Mechanics Division, Stanford, Calif., September 9–11, 1959, of THE AMERICAN SOCIETY OF MECHANICAL ENGINEERS.

Discussion of this paper should be addressed to the Secretary, ASME, 29 West 39th Street, New York, N. Y., and will be accepted until April 10, 1960, for publication at a later date. Discussion received after the closing date will be returned.

NOTE: Statements and opinions advanced in papers are to be understood as individual expressions of their authors and not those of the Society. Manuscript received by ASME Applied Mechanics Division, January 5, 1959. Paper No. 59—APMW-23.

These give modes symmetric with respect to the three co-ordinate planes. The remaining seven symmetries may be obtained by appropriate interchanges of sines and cosines of like argument, as described in Section 5. Equations (6) satisfy Equations (4) and (5) if

$$\alpha^2 + \xi^2 + \zeta^2 = \omega^2/v_1^2, \qquad \beta^2 + \xi^2 + \zeta^2 = \omega^2/v_2^2 \tag{7}$$

For the components of traction on $y = \pm b$ we have

$$\begin{aligned}
\sigma_{xy} &= \mp 2\mu A\xi\alpha\zeta \sin \xi x \sin \alpha b \cos \zeta z \\
&\quad \mp \mu B\xi(\zeta^2 + \xi^2 - \beta^2) \sin \xi x \sin \beta b \cos \zeta z, \\
\sigma_{yy} &= \mu A\zeta(\beta^2 - \xi^2 - \zeta^2) \cos \xi x \cos \alpha b \cos \zeta z \\
&\quad + 2\mu B\beta(\xi^2 + \zeta^2) \cos \xi x \cos \beta b \cos \zeta z, \\
\sigma_{yz} &= \mp 2\mu A\alpha\zeta^2 \cos \xi x \sin \alpha b \sin \zeta z \\
&\quad \mp \mu B\zeta(\xi^2 + \zeta^2 - \beta^2) \cos \xi x \sin \beta b \sin \zeta z.
\end{aligned} \tag{8}$$

The compatibility of the conditions obtained by setting Equations (8) equal to zero requires

$$\frac{B}{A} = \frac{\zeta(\xi^2 + \zeta^2 - \beta^2) \cos \alpha b}{2\beta(\xi^2 + \zeta^2) \cos \beta b} = \frac{2\alpha\zeta \sin \alpha b}{(\beta^2 - \xi^2 - \zeta^2) \sin \beta b}, \tag{9}$$

which are the Rayleigh-Lamb amplitude-ratio and frequency-equation.

In anticipation of a property of SH waves, mentioned in Section 1, we take only the solutions

$$\sin \alpha b = 0, \qquad \sin \beta b = 0 \tag{10}$$

of the frequency equation. Then

$$\alpha = m\pi/2b, \qquad \beta = n\pi/2b, \tag{11}$$

with m and n even integers, and

$$B/A = \zeta(\xi^2 + \zeta^2 - \beta^2)/2\beta(\xi^2 + \zeta^2)(-1)^{(n-m)/2}. \tag{12}$$

From Equations (7) and (11), the allowed frequencies are given by

$$\Omega^2 = k^2(n^2 - m^2)/(k^2 - 1) \tag{13}$$

where

$$\begin{aligned}
\Omega^2 &= 4b^2\omega^2/\pi^2 v_2^2, \\
k^2 &= v_1^2/v_2^2 = (\lambda + 2\mu)/\mu = 2(1 - \nu)/(1 - 2\nu)
\end{aligned} \tag{14}$$

and ν is Poisson's ratio.

The components of traction on planes $x = \pm a$ are

$$\begin{aligned}
\sigma_{xx} &= \mu A\zeta(\beta^2 - 2\alpha^2 + \xi^2 - \zeta^2) \cos \xi a \cos \alpha y \cos \zeta z \\
&\quad - 2\mu B\xi^2\beta \cos \xi a \cos \beta y \cos \zeta z, \\
\sigma_{xy} &= \mp 2\mu A\xi\alpha\zeta \sin \xi a \sin \alpha y \cos \zeta z \\
&\quad \mp \mu B\xi(\xi^2 + \zeta^2 - \beta^2) \sin \xi a \sin \beta y \cos \zeta z, \\
\sigma_{xz} &= \mp 2\mu A\xi\zeta^2 \sin \xi a \cos \alpha y \sin \zeta z \\
&\quad \pm 2\mu B\xi\beta\zeta \sin \xi a \cos \beta y \sin \zeta z.
\end{aligned} \tag{15}$$

4 SH Waves in an Infinite Plate

We consider, now, two SH waves, or vibrations, in a plate bounded by traction-free surfaces $y = \pm b$. Let $\varphi = H_x = H_z = 0$ and

$$H_y = C_1\zeta \sin \eta x \cos \alpha y \sin \zeta z + C_2\zeta \sin \xi x \cos \beta y \sin \zeta z. \tag{16}$$

Equations (5) are satisfied if

$$\omega^2/v_2^2 = \xi^2 + \beta^2 + \zeta^2 = \eta^2 + \alpha^2 + \zeta^2 \tag{17}$$

In this solution $\sigma_{yy} = 0$ everywhere and, on $y = \pm b$, the remaining components of traction are

$$\begin{aligned}
\sigma_{xx} &= \mp \mu C_1\alpha\eta\zeta \cos \eta x \sin \alpha b \sin \zeta z \\
&\quad \mp \mu C_2\beta\xi\zeta \cos \xi x \sin \beta b \sin \zeta z, \\
\sigma_{xy} &= \pm \mu C_1\alpha\zeta^2 \sin \eta x \sin \alpha b \cos \zeta z \\
&\quad \pm \mu C_2\beta\zeta^2 \sin \xi x \sin \beta b \cos \zeta z.
\end{aligned} \tag{18}$$

In view of Equation (11), the surfaces $y = \pm b$ are free of traction. Also, from (17) and (11), we require

$$\eta^2 - \xi^2 = (n^2 - m^2)\pi^2/4b^2 \tag{19}$$

The components of traction on $x = \pm a$ are

$$\begin{aligned}
\sigma_{xx} &= -2\mu C_1\eta\zeta^2 \cos \eta a \cos \alpha y \cos \zeta z \\
&\quad - 2\mu C_2\xi\zeta^2 \cos \xi a \cos \beta y \cos \zeta z, \\
\sigma_{xy} &= \pm \mu C_1\alpha\zeta^2 \sin \eta a \sin \alpha y \cos \zeta z \\
&\quad \pm \mu C_2\beta\zeta^2 \sin \xi a \sin \beta y \cos \zeta z, \\
\sigma_{xz} &= \pm \mu C_1\zeta(\zeta^2 - \eta^2) \sin \eta a \cos \alpha y \sin \zeta z \\
&\quad \pm \mu C_2\zeta(\zeta^2 - \xi^2) \sin \xi a \cos \beta y \sin \zeta z.
\end{aligned} \tag{20}$$

5 Bar of Rectangular Cross Section

The sum of the three solutions, given in Sections 3 and 4, leaves the faces $y = \pm b$ free of traction and the faces $x = \pm a$ with the tractions given in Equations (15) and (20). The tangential components of traction on $x = \pm a$ vanish if

$$\sin \xi a = 0, \qquad \sin \eta a = 0, \tag{21}$$

i.e., if

$$\xi = p\pi/2a, \qquad \eta = q\pi/2a, \tag{22}$$

where p and q are even integers. Then the remaining component of traction vanishes if

$$\begin{aligned}
C_1/A &= (\eta^2 - \alpha^2 - \zeta^2)/2\eta\zeta(-1)^{(q-p)/2}, \\
C_2/A &= \xi(\beta^2 - \xi^2 - \zeta^2)/2\zeta(\xi^2 + \zeta^2)(-1)^{(n-m)/2}.
\end{aligned} \tag{23}$$

From (22) and (19) the allowed ratios of width to depth of the cross section of the bar are given by

$$a^2/b^2 = (q^2 - p^2)/(n^2 - m^2). \tag{24}$$

Thus far we have considered only solutions symmetric with respect to the three co-ordinate planes. A change of symmetry with respect to the plane of x and y is equivalent only to a shift of the origin of co-ordinates along the axis of the bar; but changes of symmetry with respect to the other two co-ordinate planes produce three additional families of modes. To change the symmetry with respect to the plane of y and z or x and z without changing formulas (12) and (23) for the amplitude ratios, it is only necessary to interchange sines and cosines of functions of x or y, change p and q or m and n from even to odd and reverse the sign of u or v. The solutions, in terms of displacements, are then

(i) symmetric-symmetric (m, n even; p, q even)

$$\begin{aligned}
u &= (A\xi \sin \xi x - C_1\zeta \sin \eta x)\zeta \cos \alpha y \cos \zeta z, \\
v &= [A\alpha\zeta \sin \alpha y + B(\xi^2 + \zeta^2) \sin \beta y] \cos \xi x \cos \zeta z, \\
w &= (A\zeta \cos \xi x + C_1\eta \cos \eta x)\zeta \cos \alpha y \sin \zeta z \\
&\quad + (C_2\xi - B\beta)\zeta \cos \xi x \cos \beta y \sin \zeta z;
\end{aligned} \tag{25}$$

(ii) symmetric-antisymmetric (m, n even; p, q odd)

$$\begin{aligned}
u &= -(A\xi \cos \xi x - C_1\zeta \cos \eta x)\zeta \cos \alpha y \cos \zeta z, \\
v &= [A\alpha\zeta \sin \alpha y + B(\xi^2 + \zeta^2) \sin \beta y] \sin \xi x \cos \zeta z, \\
w &= (A\zeta \sin \xi x + C_1\eta \sin \eta x)\zeta \cos \alpha y \sin \zeta z \\
&\quad + (C_2\xi - B\beta)\zeta \sin \xi x \cos \beta y \sin \zeta z;
\end{aligned} \tag{26}$$

(iii) antisymmetric-symmetric (m, n odd; p, q even)

$$\begin{aligned} u &= (A\xi \sin \xi x - C_1\zeta \sin \eta x)\zeta \sin \alpha y \cos \zeta z, \\ v &= -[A\alpha\zeta \cos \alpha y + B(\xi^2 + \zeta^2) \cos \beta y] \cos \xi x \cos \zeta z, \\ w &= (A\zeta \cos \xi x + C_1\eta \cos \eta x)\zeta \sin \alpha y \sin \zeta z \\ &\quad + (C_2\xi - B\beta)\zeta \cos \xi x \sin \beta y \sin \zeta z; \end{aligned} \tag{27}$$

(iv) antisymmetric-antisymmetric (m, n odd; p, q odd)

$$\begin{aligned} u &= -(A\xi \cos \xi x - C_1\zeta \cos \eta x)\zeta \sin \alpha y \cos \zeta z, \\ v &= -[A\alpha\zeta \cos \alpha y + B(\xi^2 + \zeta^2) \cos \beta y] \sin \xi x \cos \zeta z, \\ w &= (A\zeta \sin \xi x + C_1\eta \sin \eta x)\zeta \sin \alpha y \sin \zeta z \\ &\quad + (C_2\xi - B\beta)\zeta \sin \xi x \sin \beta y \sin \zeta z. \end{aligned} \tag{28}$$

In each of the four cases, the amplitude ratios are given by (12) and (23) and the frequency is given by (13).

6 Ratios of Width to Depth

Since Poisson's ratio is restricted to the range $-1 < \nu \leqslant 1/2$ we have, from the last of (14), $(4/3) < k^2 \leqslant \infty$; hence, from (13), we require $n > m$ and, from (24), $q > p$. Now, the difference between the squares of two integers, both even or both odd, is a multiple of four, say $4N$, where N is any integer. Since, by Equation (24), a^2/b^2 is the ratio of two such differences, it may be the ratio of any two integers. Hence, the ratio of width to depth of the bar may be the square root of any positive rational number.

For a given m and n, i.e., for a given frequency, there may be more than one pair of p and q corresponding to the same a/b. Similarly, there may be more than one pair of m and n corresponding to the same frequency. The additional number of pairs is equal to the number of unlike factors of N whose squares are not greater than N. To find all such pairs for any N we write

$$(n_i - m_i)(n_i + m_i) = 4N, \qquad N = 1, 2, 3 \ldots \tag{29}$$

Let

$$n_i = L_i + M_i, \qquad m_i = L_i - M_i, \tag{30}$$

where L_i and M_i are integers and $L_i > M_i$. If L_i and M_i are both even or both odd, n_i and m_i are both even; if one of L_i and M_i is even and the other odd, then n_i and m_i are both odd. From (29) and (30), $L_i = N/M_i$ subject to the restrictions that N/M_i is an integer and $M_i^2 \leqslant N$. Hence

$$\left.\begin{aligned} n_i &= N/M_i + M_i \\ m_i &= N/M_i - M_i \end{aligned}\right\} \begin{cases} N = 1, 2, 3 \ldots \\ M_i = 1, 2, 3 \ldots \leqslant N^{1/2}. \end{cases} \tag{31}$$

The first twenty-five sets of pairs are given in Table 1. The table may be used either for n_i and m_i or q_i and p_i.

7 Frequency Spectrum

The relation between the frequency and the wave length, $\lambda' = 2\pi/\zeta$, along the axis of z, is determined by Equations (7) and (17). In view of (19), the second of (7) and both of (17) are the same and may be written as

$$\Omega^2 = s^2 + \gamma^2, \tag{32}$$

where

$$s^2 = n^2 + p^2b^2/a^2 \tag{33}$$

and

$$\gamma = 2\zeta b/\pi = 4b/\lambda', \tag{34}$$

i.e., γ is the ratio of the depth, $2b$, of the bar, to the half wave length along the axis of z. The remaining expression for the frequency, i.e., the first of (7), can be written as

$$\Omega^2 = k^2(r^2 + \gamma^2) \tag{35}$$

where

$$r^2 = m^2 + p^2b^2/a^2 \tag{36}$$

For real, positive Ω and γ, (32) and (35) are families of hyperbolas in the $\gamma - \Omega$ plane with asymptotes $\Omega = \gamma$ and $\Omega = k\gamma$ and semitransverse axes $\Omega = s$ and $\Omega = kr$, respectively.¶ The curves are illustrated in Fig. 1 for integer-values of r and s and for $\nu = 0.31$. Since both (32) and (35) must be satisfied, permissible combinations of frequency and wave length are given by the intersections of the two families of curves. The co-ordinates of the intersection points are

$$\begin{aligned} \Omega &= [k^2(s^2 - r^2)/(k^2 - 1)]^{1/2}, \\ \gamma &= [(s^2 - k^2r^2)/(k^2 - 1)]^{1/2}. \end{aligned} \tag{37}$$

The parameters r and s need not be integers, but they may not be chosen arbitrarily inasmuch as they must satisfy the relation

Table 1 Pairs of integers $n_i^2 - m_i^2 = 4N$

N	$n_i^2 - m_i^2$	n_1	m_1	n_2	m_2	n_3	m_3	n_4	m_4	n_5	m_5
1	4	2	0								
2	8	3	1								
3	12	4	2								
4	16	5	3	4	0						
5	20	6	4								
6	24	7	5	5	1						
7	28	8	6								
8	32	9	7	6	2						
9	36	10	8			6	0				
10	40	11	9	7	3						
11	44	12	10								
12	48	13	11	8	4	7	1				
13	52	14	12								
14	56	15	13	9	5						
15	60	16	14			8	2				
16	64	17	15	10	6			8	0		
17	68	18	16								
18	72	19	17	11	7	9	3				
19	76	20	18								
20	80	21	19	12	8			9	1		
21	84	22	20			10	4				
22	88	23	21	13	9						
23	92	24	22								
24	96	25	23	14	10	11	5	10	2		
25	100	26	24							10	0

$$s^2 - r^2 = n^2 - m^2 = (q^2 - p^2)b^2/a^2. \tag{38}$$

For real, positive Ω and imaginary, positive γ, (32) are quarter-circles of radii s and (35) are quarter-ellipses of major semiaxes kr and minor semiaxes r. Imaginary values of γ do not pertain to infinite trains of traveling waves but they have significance for vibrations of bars of finite length and for transient motions. Complex values of γ, with real, positive Ω, are permissible in general, but they do not appear in the special solutions described here.

8 Phase-Velocities

The phase-velocity of the coupled waves traveling along the bar is $v = \omega/\zeta$. Hence, from (14), (34), and (37),

$$v/v_2 = [k^2(s^2 - r^2)/(s^2 - k^2r^2)]^{1/2} = \Omega/\gamma. \tag{39}$$

Thus the slope of the straight line connecting an intersection point and the origin, in Fig. 1, gives the ratio of the phase-velocity in the bar to the velocity of equivoluminal waves in an infinite medium. It may be seen that the minimum phase-velocity, of the special waves found here, is the velocity, $v = kv_2 = v_1$, of dilatational waves in an infinite medium. This occurs when $r = 0$, i.e., when m and p are zero and, hence, only in the case of the symmetric-symmetric family of modes.

The maximum phase-velocity can be infinite ($\zeta = 0$), but the character of the solution is then different. There are two groups of modes possible for $\zeta = 0$; the modes in one group do not depend on Poisson's ratio and the modes in the second group exist only for special values of Poisson's ratio.

In the first group there are eight families of simple axial shear modes which may be obtained from equations (25) to (28) by setting $\zeta = 0$ after interchanging $\sin \zeta z$ and $\cos \zeta z$. For example, from (25) we obtain $u = v = 0$ and

$$\begin{aligned} w &= C_1'' \cos \eta x \cos \alpha y, & \Omega^2 &= q^2b^2/a^2 + m^2, \\ w &= C_2'' \cos \xi x \cos \beta y, & \Omega^2 &= p^2b^2/a^2 + n^2. \end{aligned} \tag{40}$$

where C_1'' and C_2'' are unrelated. Similar results are obtained, for the other three symmetries, from equations (26) to (28). The modes of type (40) are those that are independent of Poisson's ratio.

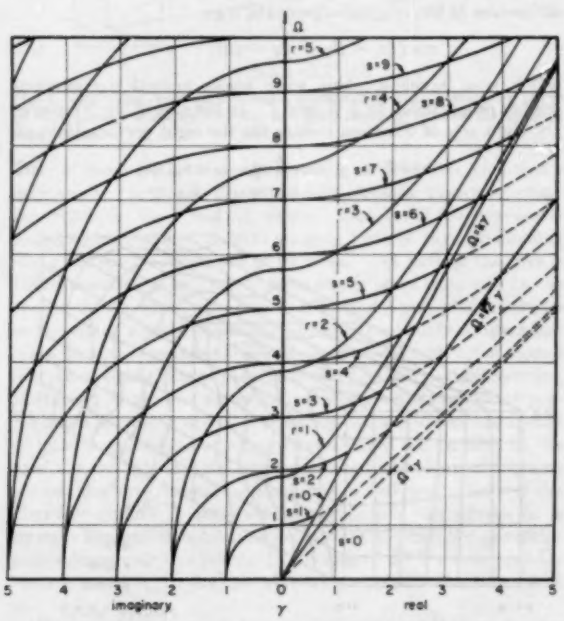

Fig. 1 Spectrum of frequencies and phase velocities

The second group of modes with infinite phase-velocity may be obtained from (25) to (28) by setting

$$\begin{aligned} &\lim_{\zeta \to 0} A\zeta = A^*, & &\lim_{\zeta \to 0} C_1\zeta^2 = C_1^*, \\ &\lim_{\zeta \to 0} C_2\zeta^2 = C_2^*, & &\lim_{\zeta \to 0} (\sin \zeta z)/\zeta = z. \end{aligned} \tag{41}$$

The solution, in the symmetric-symmetric case, then reduces to

$$\begin{aligned} u &= (A^*\xi \sin \xi x - C_1^* \sin \eta x) \cos \alpha y, \\ v &= (A^*\alpha \sin \alpha y + B\xi^2 \sin \beta y) \cos \xi x, \\ w &= z(C_1^*\eta \cos \eta x \cos \alpha y + C_2^*\xi \cos \xi x \cos \beta y), \end{aligned} \tag{42}$$

with

$$\begin{aligned} B/A^* &= (\xi^2 - \beta^2)/2\beta\xi^2(-1)^{(n-m)/2}, \\ C_1^*/A^* &= (\beta^2 - 2\alpha^2 + \xi^2)/2\eta(-1)^{(q-p)/2}, \\ C_2^*/A^* &= (\beta^2 - \xi^2)/2\xi(-1)^{(n-m)/2}. \end{aligned} \tag{43}$$

Corresponding solutions obtain for the remaining three symmetries. These modes exist only for special values of Poisson's ratio. From (32) and (35), with $\gamma = 0$, $\Omega = s = kr$. Hence the modes are possible only for those values of Poisson's ratio satisfying $k = s/r$. In Fig. 1, this means values of k for which there are intersections at $\gamma = 0$.

9 Propagation of Energy

In the case of an infinite train of sinusoidal waves, the velocity of propagation of energy is the group velocity $v_g = d\omega/d\zeta$. Because we have only discrete pairs of ω and ζ, the differentiation cannot be performed. However, the velocity can be obtained from considerations of work and energy.

During a period T, the average rate at which work is done on a right section of the bar is

$$W = T^{-1} \int_0^T dt \int_{-b}^{b} \int_{-a}^{a} (\sigma_{xx}\dot{u} + \sigma_{xy}\dot{v} + \sigma_{xz}\dot{w}) dx dy, \tag{44}$$

where $\dot{u}$, $\dot{v}$, and $\dot{w}$ are the components of velocity. Also, during the period T, the average total energy per unit of length of the bar (E) is twice the average kinetic energy per unit of length, i.e.,

$$E = \rho T^{-1} \int_0^T dt \int_{-b}^{b} \int_{-a}^{a} (\dot{u}^2 + \dot{v}^2 + \dot{w}^2) dx dy. \tag{45}$$

Hence, the velocity at which energy crosses the section is

$$v_g = v_e = W/E. \tag{46}$$

Upon performing the integrations in (44) and (45) and substituting in (46), we find

$$v_g = v_e = (v_2^2/v)(1 + P/Q), \tag{47}$$

where v is, again, the phase-velocity and

$$\begin{aligned} P &= 4n^2(s^2 - m^2)(n^2 - m^2)\gamma^2, \\ Q &= 4n^2(s^2 - m^2)(r^2 + \gamma^2)\gamma^2 \\ &\quad + n^2(s^2 - m^2 + \gamma^2)(s^2 - 2m^2 - \gamma^2)^2 \\ &\quad + (s^2 - m^2)(n^2 + \gamma^2)(s^2 - 2n^2 + \gamma^2)^2. \end{aligned} \tag{48}$$

A case of some interest is that for which $v = v_1$, i.e., when the phase-velocity is the velocity of dilatational waves. For example, the lowest of such modes in a square bar has

$$m, n, p, q = 0, 2, 0, 2$$

Then, for $\nu = 1/4$,

$$v_e = 5v_1/7 = 5v_2\sqrt{3}/7,$$

i.e., the velocity of propagation of energy lies between the velocities of dilatational and equivoluminal waves in an infinite medium.

10 Shapes of Modes

Inspection of Equations (25) to (28) shows that, in view of (11) and (22), $u = 0$ on $x = \pm a$ and $v = 0$ on $y = \pm b$. That is, in addition to these planes being free of traction, they remain plane. The displacement w is zero on $z = 0$ and again at every half wave length, π/ζ, along the z-axis. On these planes of constant z, although the tangential tractions σ_{xz} and σ_{yz} are zero, the normal traction is not. However, since $w = 0$, mixed boundary conditions are satisfied, so that we have solutions for the vibrations of bars of finite length with the four sides free of traction and mixed boundary conditions at the ends. However, the end conditions, although permissible mathematically, are not practical ones.

The displacement u has two wave lengths, $4a/p$ and $4a/q$, along x and one wave length, $4b/m$, along y. The displacement v has two wave lengths, $4b/m$ and $4b/n$, along y and one wave length, $4a/p$, along x. The displacement w has both wave lengths along x and both along y. The integers m and n or p and q are the ratios of the cross-sectional dimensions $2b$ or $2a$ to the half wave lengths in the corresponding directions. All the displacements have the same wave-length, $2\zeta/\pi$, along z. Examples of the mode-shapes for

$m, n, p, q = 0, 2, 0, 2;$ $a = b,$ $\nu = 0.31,$ $\gamma = 1.23,$
$m, n, p, q = 1, 3, 0, 2;$ $a\sqrt{2} = b,$ $\nu = 0.31,$ $\gamma = 1.43,$
$m, n, p, q = 1, 3, 1, 3;$ $a = b,$ $\nu = 0.31,$ $\gamma = 1.02,$

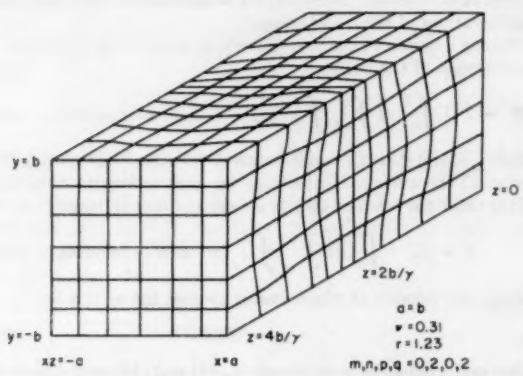

Fig. 2 Mode shape for $m, n, p, q = 0, 2, 0, 2$

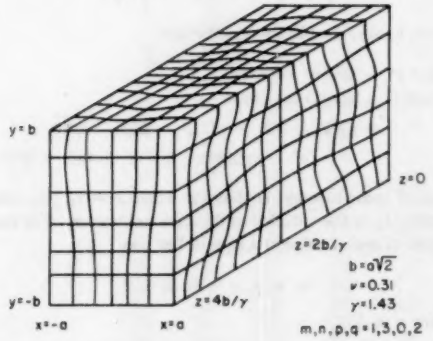

Fig. 3 Mode shape for $m, n, p, q = 1, 3, 0, 2$

are illustrated in Figs. 2, 3, and 4. The first of these is one of the special cases for which the phase-velocity is the velocity of dilatational waves. In these cases a square grid on the cross section becomes a rectangular grid instead of a sinusoidal one.

11 Rays

The solution given in Section 5 was presented as a combination of a Rayleigh-Lamb wave and two SH waves in order to show its relation to known solutions for waves in an infinite plate. The result, however, may be expressed in simpler form. For example, Equations (25) derive from

$$\begin{aligned} \varphi &= -A' \cos \xi x \cos \alpha y \cos \zeta z, \\ H_z &= B' \cos \xi x \sin \beta y \sin \zeta z, \\ H_y &= -C' \sin \eta x \cos \alpha y \sin \zeta z, \end{aligned} \tag{49}$$

where

$$\begin{aligned} A' &= A\zeta, \\ B' &= B(\xi^2 + \zeta^2)/\zeta = A'(\xi^2 + \zeta^2 - \beta^2)/2\beta\zeta(-1)^{(n-m)/2}, \\ C' &= -C_1\zeta = A'(\alpha^2 + \zeta^2 - \eta^2)/2\eta\zeta(-1)^{(q-p)/2}. \end{aligned} \tag{50}$$

Similar forms can be written for the other three symmetries.

The three functions in (49) represent dilatational waves (φ), SV waves (H_z), and SH waves (H_y). The displacement in the SV waves is parallel to planes $x = \text{const}$ and the displacement in the SH waves is parallel to planes $y = \text{const}$. It may be seen, from (49) and (50), that a rotation of 90 deg about the axis of z does not produce another family of solutions. This is not immediately apparent from the form of the solution in Section 5.

Each of the three functions in (49) may be resolved into a set of eight plane waves which progress along the bar by oblique reflections at the faces $x = \pm a$ and $y = \pm b$. The resolution may be effected by expanding the products of four trigonometric functions, for example

$$\cos \xi x \cos \beta y \cos \zeta z \cos \omega t, \tag{51}$$

that appear in Equations (25) to (28), into sums and differences of eight trigonometric functions whose arguments are the sums and differences of the original arguments, e.g.,

$$\cos (\xi x + \beta y + \zeta z - \omega t), \tag{52}$$

which is a traveling, plane wave whose normal has direction cosines proportional to ξ, β, and ζ. In the case of the SV waves, the eight sets of direction cosines are the eight combinations of

$$\pm v_2\xi/\omega, \quad \pm v_2\beta/\omega, \quad \pm v_2\zeta/\omega; \tag{53}$$

or

$$\pm pb/\Omega a, \quad \pm n/\Omega, \quad \pm \gamma/\Omega \tag{54}$$

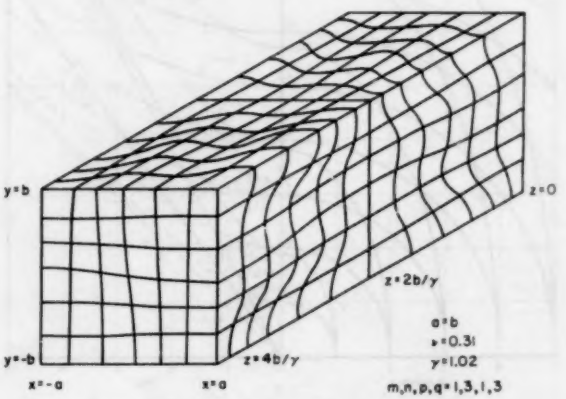

Fig. 4 Mode shape for $m, n, p, q = 1, 3, 1, 3$

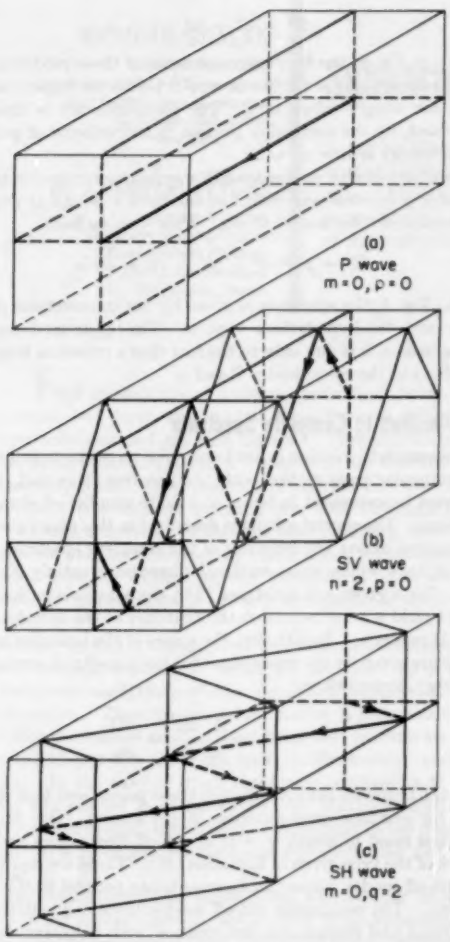

Fig. 5 The three rays for the mode illustrated in Fig. 2; showing paths of rays, planes in which they lie, and projections of rays on the co-ordinate planes

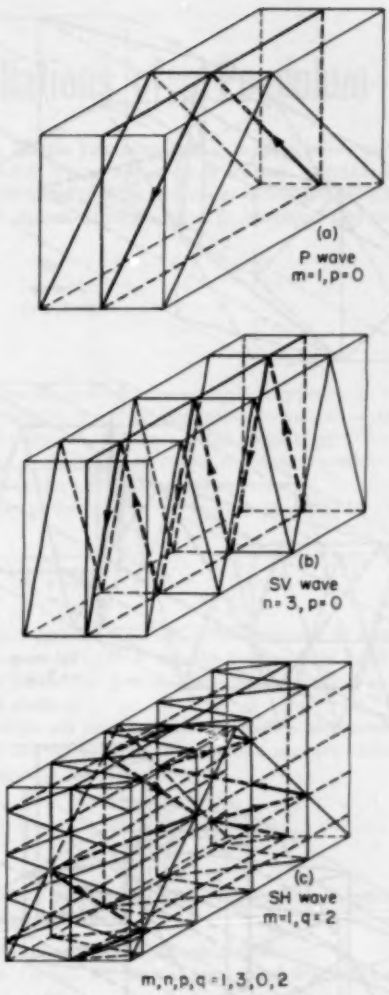

Fig. 6 The three rays for the mode illustrated in Fig. 3; showing paths of rays, planes in which they lie, and projections of rays on the co-ordinate planes

Four of these are for waves progressing in directions such that z increases and four such that z decreases. Similar expressions may be written for the P and SH waves. Each set of four wave-normals can be arranged to form a zigzag path of rays progressing along the bar by reflections at its faces. The path of the rays is the intersection of any two of three sets of plane surfaces. In the case of the SV wave, one of these is a set of zigzag planes parallel to the axis of x and intersecting the faces $x = \pm a$ in a zigzag line whose direction cosines are proportional to $\pm n$ and γ. A second is a set of zigzag planes parallel to the axis of y and intersecting the faces $y = \pm b$ in a zigzag line whose direction cosines are proportional to $\pm pb/a$ and γ. The third set of surfaces is a family of quadrangular prisms whose lateral edges are parallel to the axis of z and whose right sections are equilateral parallelograms whose sides have direction cosines $\pm pb/a$ and $\pm n$. If one of the direction cosines is zero the parallelograms degenerate to a straight line and if both direction cosines are zero the parallelograms degenerate to a point. In the case of the P waves, p and n become p and m; in the case of SH waves p and n become q and m.

The sets of intersecting planes and the paths of the rays for the modes shown in Figs. 2, 3, and 4 are shown in Figs. 5, 6, and 7.

12 Lamé's Equivoluminal Modes

As shown by Lamb[4] the Lamé equivoluminal modes[3] are special cases of the general solution for waves in an infinite plate. One of the four sets may be obtained from (6) by setting

$$A = 0, \quad \xi = 0, \quad \beta = \zeta. \tag{55}$$

The boundary conditions (8) on $y = \pm b$ then reduce to a single condition, on σ_{yy}, which is satisfied by $\cos \beta b = 0$ so that

$$\beta = n\pi/2b \tag{56}$$

where n is now an odd integer instead of the even integer which it was before for the same symmetry. There are no tractions on planes normal to the axis of x so that the result is independent of the ratio a/b. The wave is solely a plane SV wave whose rays are parallel to planes $x = \text{const}$ and reflect at the surfaces $y = \pm b$ at angles of incidence and reflection of 45 deg. For modes antisymmetric with respect to the plane of x and z, n is even.

From (55), (56), and the second of (7),

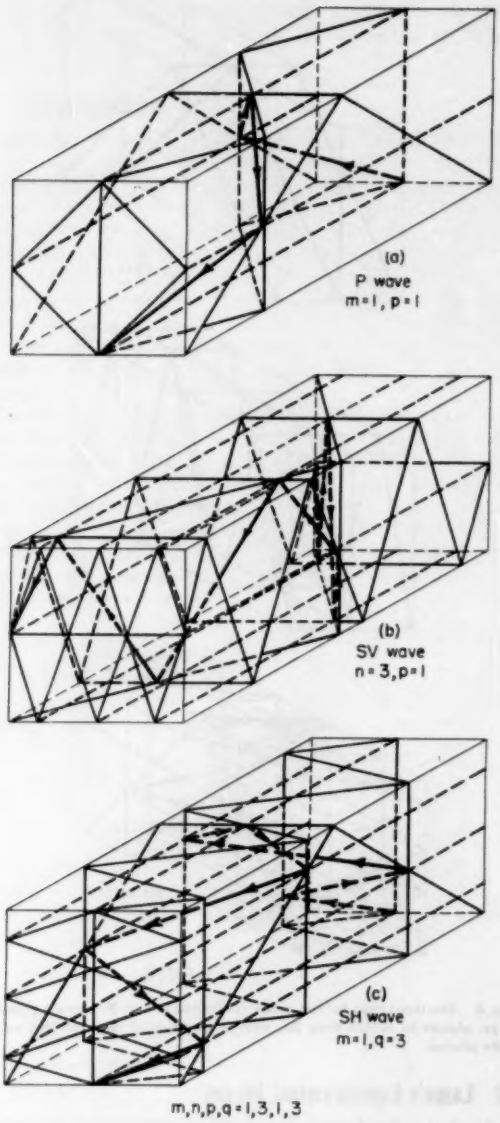

Fig. 7 The three rays for the mode illustrated in Fig. 4; showing paths of rays, planes in which they lie, and projections of rays on the coordinate planes

$$\Omega^2 = n^2 + \gamma^2, \quad \gamma = n \tag{57}$$

so that, in Fig. 1, the frequency spectrum of these modes is given by the intersections of the line $\Omega = \sqrt{2}\,\gamma$ with the hyperbolas $s = \text{const}$, for integer-values of s. The phase-velocity is thus $v = \sqrt{2}\,v_2$ and, by the method of Section 9, the velocity of propagation of energy is $v_e = v_2/\sqrt{2}$.

There are similar modes for SH waves whose rays are parallel to planes $y = \text{const}$ and reflect at the faces $x = \pm a$ at angles of incidence and reflection of 45 deg. This time we have

$$\Omega^2 = p^2b^2/a^2 + \gamma^2, \qquad \gamma = pb/a \tag{58}$$

and, in Fig. 1, the spectrum is given by the intersections of $\Omega = \sqrt{2}\,\gamma$ with the hyperbolas $s = pb/a$. The apparent dependence on the ratio a/b is due only to the fact that a reference length b is contained in the co-ordinates Ω and γ.

13 Relation to Complete Spectrum

The complete solution is not known for waves in an infinite bar of rectangular cross section with traction-free faces and, in fact, it cannot be expressed in terms of a finite number of elementary functions. The special solutions described in this paper give some information about the behavior of the complete spectrum in the case of bars whose cross-sectional dimensions satisfy Equation (24). For a given a/b satisfying (24), the solutions in Sections 5 and 12 yield a set of points on the branches of the complete spectrum Ω versus γ. In addition, the slopes of the branches at these points are given by the expressions for the velocity of propagation of energy, inasmuch as

$$\frac{v_e}{v_2} = \frac{v_g}{v_2} = \frac{1}{v_2}\frac{d\omega}{d\zeta} = \frac{d\Omega}{d\gamma} \tag{59}$$

How the branches behave between these points and how they behave for complex wave-numbers is not known. One family of branches must intersect $\gamma = 0$ at cut-off frequencies and mode shapes of the type given in Equation (40). These are equivoluminal cut-off modes whose displacements are parallel to the axis of the bar. The companion cut-off modes, involving coupled equivoluminal and dilatational deformation with displacements perpendicular to the axis of the bar, are not available. These, along with (*a*) the easily obtainable solutions for a bar with one pair of opposite faces traction-free and the other pair with mixed boundary conditions; and (*b*) the known behavior of the lowest branch at long wave length, could form a basis for establishing the behavior of the complete branches in greater detail. In such a study it would be important to recognize that the special solutions for the rectangular bar, given in Section 5, must be related to the unknown general solution in the same way that the special solutions for the infinite plate, given by Equations (10) to (12), are related to the general solution, Equation (9), for the plate.

RICHARD SKALAK
Associate Professor,
Department of Civil Engineering
and Engineering Mechanics,
Columbia University,
New York, N. Y.

M. I. YARYMOVYCH[1]
Senior Scientist,
Research and Advanced
Development Division,
AVCO Corporation,
Wilmington, Mass.

Subharmonic Oscillations of a Pendulum

Large amplitude oscillations of a simple pendulum whose support moves with a prescribed vertical oscillation are studied by an approximate method. Subharmonics of order 1/2, 1/4, 1/6, and 1/8 are discussed and the theoretical results are compared with experiments. The stability of the theoretical steady states is investigated by the method of Andronow and Witt.

Free oscillations of a simple undamped pendulum, both for small and large amplitudes, have been described by closed form solutions and are well known.[2] Parametrically excited small amplitude oscillations of a pendulum are described by the Mathieu equation. The stability of solutions of the equation, both with and without damping, has been thoroughly explored.[3,4] Large amplitude oscillations with damping, however, are describable only by nonlinear equations which are not amenable to exact solution. Likewise, the stability of steady-state large amplitude parametrically excited oscillations is relatively unknown.

The problem treated in this paper is that of a pendulum executing large amplitude oscillations which are sustained by a prescribed harmonic oscillation of the pendulum support in the vertical direction. Thus the pendulum motion is parametrically excited. For the sake of brevity the term forced oscillations will be used interchangeably with the term parametrically excited oscillations. In the case of small amplitude oscillations of the pendulum, the motion is governed by the Mathieu equation. The consideration of large amplitudes and damping in the present study leads to a more general nonlinear equation with periodic coefficients.

The steady-state pendulum oscillations, which occur as subharmonics of the support motion, are studied by an approximate procedure, and the stability of these oscillations is investigated by the method of Andronow and Witt.[3] It is noteworthy that for the simple physical problem studied some new and interesting results can be obtained. The theoretical results agree very well with experiments.

Equations of Motion and Assumptions

The pendulum is assumed to consist of a weightless rigid rod of length L, pivoted at one end and carrying a point mass M on the other. All results and equations are also applicable to any rigid compound pendulum. The equivalent length L of the compound pendulum is r_0^2/h where r_0 is the radius of gyration and h is the distance of the centroid of the compound pendulum, both measured from the axis of rotation.

The motion of the pendulum, Fig. 1, is governed by the equation

$$\ddot{\theta} + 2K\dot{\theta} + \left(\omega_0^2 + \frac{\ddot{\xi}}{L}\right)\sin\theta = 0 \qquad (1)$$

where the dots indicate time differentiations and K = damping coefficient, $\omega_0 = (g/L)^{1/2}$ = natural frequency of small oscillations of the pendulum, ξ = displacement of pendulum support from a fixed position.

If the motions are periodic with a frequency of pendulum motion $f_p = \omega$ and a frequency of pendulum support motion $f_s = n\omega$, then Equation (1) becomes

$$\theta'' + 2k\theta' + (a - n^2 q\cos nz)\left(\theta - \frac{\theta^3}{6} + \frac{\theta^5}{120} - \ldots\right) = 0 \qquad (2)$$

where the series represents $\sin\theta$, and the equation is expressed in nondimensional form using

$k = K/\omega$ = dimensionless damping coefficient
$(1/a)^{1/2} = (\omega/\omega_0)$ = dimensionless pendulum response frequency
$q = \xi_0/L$ = dimensionless forcing coefficient
ξ_0 = amplitude of pendulum support oscillation
$z = \omega t$ = dimensionless time

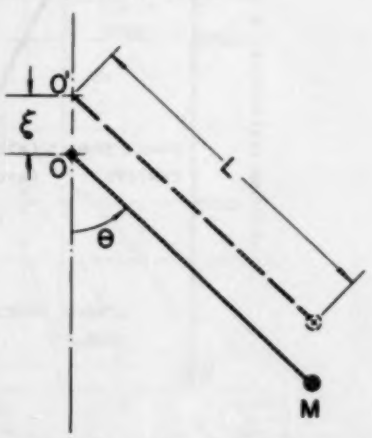

Fig. 1 Simple pendulum with vibrating support

[1] Formerly, Research Assistant, Institute of Flight Structures, Columbia University, New York, N. Y.

[2] N. W. McLachlan, "Ordinary Non-Linear Differential Equations," Oxford at the Clarendon Press, 1956, second edition.

[3] J. J. Stoker, "Non-Linear Vibrations in Mechanical and Electrical Systems," Interscience Publishers, Inc., New York, N. Y., 1950.

[4] K. Klotter, "Technische Schwingungslehre," Springer-Verlag, Berlin, Germany, 1951, second edition.

Contributed by the Applied Mechanics Division and presented at the Annual Meeting, Atlantic City, N. J., November 29–December 4, 1959, of The American Society of Mechanical Engineers.

Discussion of this paper should be addressed to the Secretary, ASME, 29 West 39th Street, New York, N. Y., and will be accepted until April 10, 1960, for publication at a later date. Discussion received after the closing date will be returned.

Note: Statements and opinions advanced in papers are to be understood as individual expressions of their authors and not those of the Society. Manuscript received by ASME Applied Mechanics Division, January 13, 1959. Paper No. 59—A-94.

The primes in Equation (2) indicate differentiation with respect to z. It is assumed that the displacement of the pendulum support in the vertical direction is harmonic: $\xi = \xi_0 \cos n\omega t$. The assumption that the frequency of support motion is $n\omega$ indicates that the solutions anticipated are subharmonics of order $1/n$.

Steady forced oscillations are considered first. The solutions are expressible in the form

$$\theta = \sum_{p=1}^{\infty} (A_p \sin pz + B_p \cos pz), \quad p = 1, 3, 5, \ldots \qquad (3)$$

Odd indexes p are used since only symmetric oscillations are desired. The first type of approximation which will be made consists in retaining only the first terms of the series (3).

A second type of approximation which will be made is the truncation of the series for $\sin \theta$ in Equation (2). Using only the first term of this series will be called the first-order approximation, using two terms, the second-order approximation, and so on.

The general procedure of solution is to substitute the assumed series (3) into Equation (2), and to equate coefficients of $\sin pz$ and $\cos pz$ to zero for each p. It is found convenient and satisfactory to use only the A_1, B_1 terms of the series (3); i.e.,

$$\theta = A_1 \sin z + B_1 \cos z \qquad (4)$$

and to achieve various orders or approximation by using one or more terms of the $\sin \theta$ series in Equation (2). The use of more terms of the Fourier series (3) complicates the computations without a substantial improvement of the results. Both A_1 and B_1 are necessary to allow for the phase shift due to the damping. The total amplitude of the pendulum oscillation will be

$$A = (A_1^2 + B_1^2)^{1/2} \qquad (5)$$

The orders of the subharmonics that a given approximation will exhibit depend on the number of terms of (3) and of the $\sin \theta$ series in (2) that are retained. If (4) is used and m terms of the $\sin \theta$ series are retained, it can be shown that all even-order subharmonics down to $1/2\ m$ will be contained in the approximate solution. Thus the first-order approximation exhibits only the 1/2 subharmonic; the second-order approximation yields the 1/2 and the 1/4 subharmonics; and so on. In the second-order approximation the 1/2 subharmonic response is described more accurately than in the first order, and so on.

Symmetric steady-state oscillations of the pendulum are not possible if the forcing frequency is an odd multiple of the pendulum frequency, including $n = 1$. Hence only $n = 2, 4, 6, \ldots$ are considered.

First-Order Solution

The equation of motion to the first order of approximation is

$$\theta'' + 2k\theta' + (a - n^2 q \cos nz)\,\theta = 0 \qquad (6)$$

This is the Mathieu equation with damping, whose solutions are known.[5] As a demonstration of the approximate method used in this paper, this first-order case is analyzed in detail.

The approximation (4) is substituted into Equation (6). The products of trigonometric functions occurring are expanded into forms involving sums of terms each of which contains either $\sin rz$ or $\cos rz$, $r = 1, 2, 3, \ldots$ Terms with $r > 1$ are neglected and the coefficients of $\sin z$ and of $\cos z$ are each set equal to zero. This procedure has been discussed elsewhere.[2,3,5]

In the first-order approximation, only the 1/2 subharmonic is possible since for $n > 2$ there are no terms with $r = 1$ generated by the last term of Equation (6).

For $n = 2$, the first-order approximation yields two simultaneous equations in A_1 and B_1:

$$\begin{aligned} (a + 2q - 1)A_1 - 2kB_1 &= 0 \\ 2kA_1 + (a - 2q - 1)B_1 &= 0 \end{aligned} \qquad (7)$$

A frequency equation is obtained by setting the determinant of the coefficients of A_1 and B_1 in (7) equal to zero:

$$a = 1 \pm 2(q^2 - k^2)^{1/2} \qquad (8)$$

For any given k and q, Equation (8) yields two steady-state frequencies. Equations (7) determine the ratio A_1/B_1, but the total amplitude is arbitrary. The steady states for $k = 0$ and $k = 0.01$ are shown in Fig. 2. The abscissa in Fig. 2 is a frequency ratio

[5] Lord Rayleigh, "The Theory of Sound," Dover Publications, Inc., New York, N. Y., 1945, second edition, paragraph 68b.

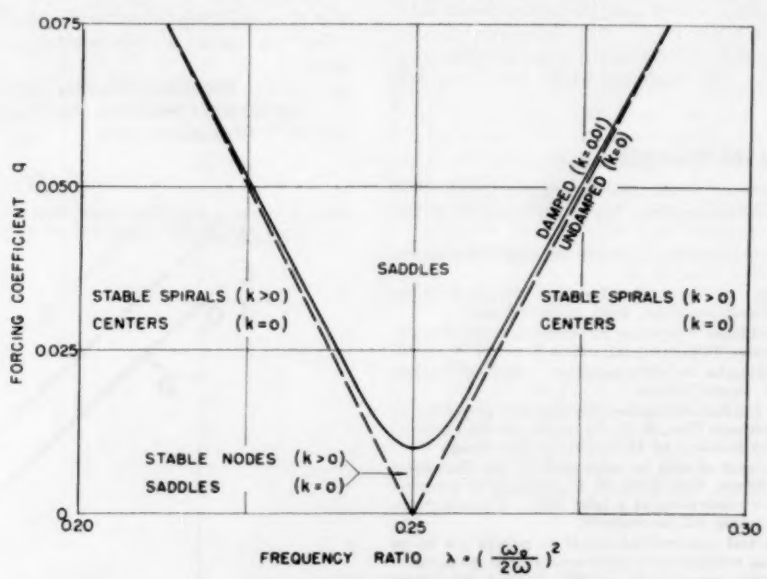

Fig. 2 The 1/2 subharmonic, first-order steady state

$$\lambda = \left(\frac{\omega_0}{2\omega}\right)^2 = \frac{a}{4}$$

The curves are in agreement with results for small values of the forcing q derived by other methods.[3,4]

The curves in Fig. 2 are also known to be boundaries between stable and unstable regions of the q, λ-plane, each point of which is studied with respect to stability of small perturbations about $\theta = 0$. These stability results can also be derived within the present approximation by the method of Andronow and Witt,[3] as follows:

Oscillations in the neighborhood of a steady state are described by considering A_1 and B_1 in (4) to be slowly varying functions of time:

$$\theta = \bar{A}_1(z) \sin z + \bar{B}_1(z) \cos z \tag{9}$$

It is assumed that the derivatives $\bar{A}_1'$ and $\bar{B}_1'$ are small of the order of q and k. The second derivatives $\bar{A}_1''$ and $\bar{B}_1''$ are assumed small of even higher order.

When (9) is substituted into the equation of motion (2) and all but the lowest order terms are neglected, two equations, which may be interpreted as expressions for $\bar{A}_1'$ and $\bar{B}_1'$ in terms of $\bar{A}_1$ and $\bar{B}_1$, are obtained:

$$\begin{aligned} \bar{A}_1' &= -k\bar{A}_1 - \left(\frac{a}{2} - q - \frac{1}{2}\right)\bar{B}_1 \\ \bar{B}_1' &= \left(\frac{a}{2} + q - \frac{1}{2}\right)\bar{A}_1 - k\bar{B}_1 \end{aligned} \tag{10}$$

The path of any pendulum oscillation considered in the $\bar{A}_1$, $\bar{B}_1$-plane may now be studied by the classical method of Poincaré.[3] Any steady-state oscillation is a singular point in the $\bar{A}_1$, $\bar{B}_1$-plane. The classification of a singularity is readily determined by the rules listed by Stoker,[4] and the stability of the steady state is then evident.

All the points in Fig. 2 which do not lie on the curves shown are associated with steady states $\bar{A}_1 = \bar{B}_1 = 0$ only. The stability criteria show the various areas to be stable or unstable as labeled in Fig. 2. These results are in agreement with results obtained by other methods.[4]

The points on the curves in Fig. 2 are singular points in the $\bar{A}_1$, $\bar{B}_1$-plane for all amplitudes A. The usual Poincaré rules do not apply in this case because the determinant of the coefficients of $\bar{A}_1$, $\bar{B}_1$ in (10) is zero for these steady states. However, it may be shown by a direct consideration of paths in the $\bar{A}_1$, $\bar{B}_1$-plane that these steady states are neutrally stable.

Second-Order Solution

In the second-order approximation two subharmonic responses are obtained; namely, the 1/2 and 1/4 subharmonics. It is found that for each subharmonic there are two steady states possible, one stable and one unstable.

(a) The 1/2 Subharmonic. Equation (4) is substituted in Equation (2) where n has been set equal to 2 and the first two terms in the series for $\sin\theta$ have been retained. After expansion of the trigonometric product terms, setting the coefficients of $\sin z$ and of $\cos z$ equal to zero leads to the following equations:

$$\begin{aligned} \left(a - \frac{a}{8}A^2 + 2q - 1\right)A_1 - \frac{q}{3}A_1^3 - 2kB_1 &= 0 \\ \left(a - \frac{a}{8}A^2 - 2q - 1\right)B_1 + \frac{q}{3}B_1^3 + 2kA_1 &= 0 \end{aligned} \tag{11}$$

After a is eliminated from Equations (11), it is possible to obtain a cubic equation in B_1, with A_1 as a parameter:

$$B_1^3 + \frac{6k}{qA_1}B_1^2 - (12 - A_1^2)B_1 + \frac{6kA_1}{q} = 0 \tag{12}$$

There are three roots B_1 for every A_1. To each root B_1 there corresponds a frequency of pendulum response found by calculating a from either of (11). Each root defines a possible steady state, provided that all roots and frequencies are real. In the $n = 2$ case, one of the real roots B_1 always gives an imaginary frequency, so no steady state exists for this root. The other two roots describe the two curves shown in Fig. 3. The phase of the undamped pendulum motion with respect to the support oscillations differs for the upper and lower curves of Fig. 3 by half a period of the support motion. With damping, this phase difference is less than half a period. For very small amplitudes the two steady-state curves approach the first-order steady-state curves, which are the vertical lines in the plot of Fig. 3.

The stability of the steady states is studied by the method described in the preceding section. It is found that the upper curve in Fig. 3 consists of singular points that are stable spiral points and the lower curve consists of saddle points. Thus only

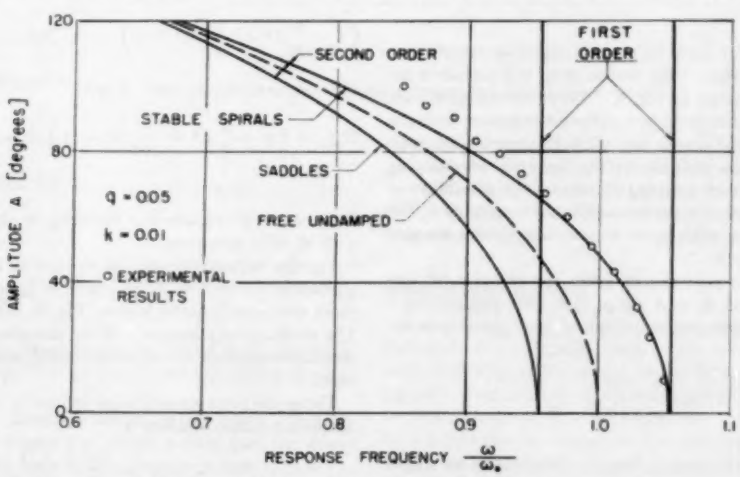

Fig. 3 The 1/2 subharmonic, first and second-order theory and experimental results

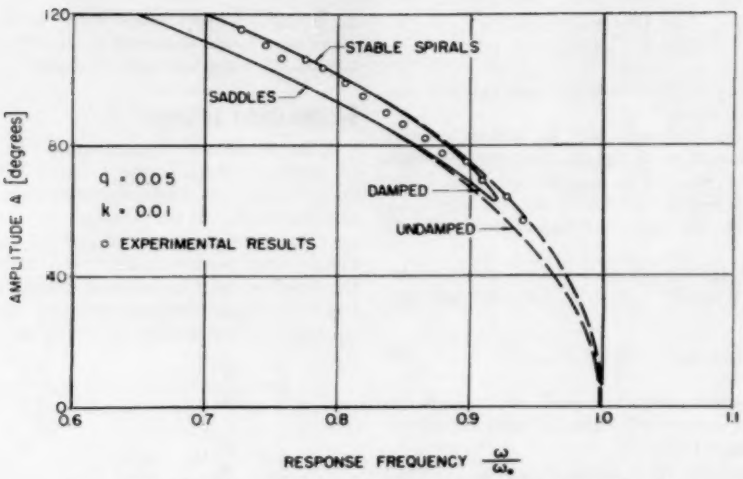

Fig. 4 The 1/4 subharmonic, second-order theory and experimental results

the upper curve represents stable steady states, and hence only the points on the upper curve can be expected to be reproduced experimentally.

The region of small amplitudes is of special interest. According to the first-order theory, any point on the abscissa between the vertical lines in Fig. 3 is an unstable rest state and any perturbation would lead to indefinitely large amplitudes. The second-order theory, however, shows that because of the nonlinearity of the equation of motion there exist finite stable steady states, given by the upper curve in Fig. 3. Thus for any forcing frequency the eventual amplitude is definite and finite. Further, this steady-state response approaches zero amplitude as the upper limiting frequency is approached from below. Experiments confirm this prediction.

(b) The 1/4 Subharmonic. When $n = 4$ in Equation (2), the second-order approximation results in the following set of equations:

$$\left(a - \frac{a}{8}A^2 + \frac{q}{3}A_1^2 - qB_1^2 - 1\right)A_1 - 2kB_1 = 0$$
$$\left(a - \frac{a}{8}A^2 + \frac{q}{3}B_1^2 - qA_1^2 - 1\right)B_1 + 2kA_1 = 0 \qquad (13)$$

Again, elimination of a leads to a cubic algebraic equation in B_1, with A_1 as a parameter. The real roots of this equation describe the two curves shown in Fig. 4. These curves show that the 1/4 subharmonic exhibits quite a different behavior than the 1/2 subharmonic. In the case of the 1/2 subharmonic, arbitrarily small amplitudes are possible in the presence of damping whereas a small amount of damping eliminates the possibility of the 1/4 subharmonic below a definite minimum amplitude. The undamped steady states with $n = 4$ have amplitudes ranging down to zero, as for $n = 2$.

If Equations (13) are rewritten in polar co-ordinates (A, φ), where $A_1 = A\cos\varphi$ and $B_1 = A\sin\varphi$, then after eliminating a, the following relation between amplitude A and phase φ is obtained:

$$A^2 = 6\frac{k}{q}\frac{1}{\sin 4\varphi} \qquad (14)$$

A plot of this function is shown in Fig. 5. The minimum amplitude occurs at the angles

$$\varphi = \tan^{-1}\left(\frac{4m+1}{8}\right)\pi,\ m = 0, 1, 2, 3, \ldots \qquad (15)$$

and the cutoff amplitude is

$$A_{min} = (6)^{1/3}\left(\frac{k}{q}\right)^{1/3} \qquad (16)$$

The stability analysis of the 1/4 subharmonic steady states is performed in the same manner as before. It is found that the upper curve in Fig. 4 consists of singular points that are stable spiral points and the lower curve consists of points that are saddle points. Again, only the upper curve corresponds to stable steady states.

Third-Order Solution

The third-order approximation uses three terms of the series of $\sin\theta$ in Equation (2). The results for the 1/2 and 1/4 subharmonics are refinements of results obtained in the first and second-order approximations and are not recomputed here. The new phenomenon is the 1/6 subharmonic for which the steady states are given by two fifth degree algebraic equations:

$$\left(a - \frac{a}{8}A^2 + \frac{a}{192}A^4 - 1\right)A_1 - 2kB_1 + \frac{3}{320}qA_1(A_1^4 - 10A_1^2B_1^2 + 5B_1^4) = 0$$
$$2kA_1 + \left(a - \frac{a}{8}A^2 + \frac{a}{192}A^4 - 1\right)B_1 - \frac{3}{320}qB_1(B_1^4 - 10A_1^2B_1^2 + 5A_1^4) = 0 \qquad (17)$$

Elimination of a leads to a fifth-degree algebraic equation in B_1, with A_1 as a parameter.

For the undamped case, where $k = 0$, and the response is described by either $\theta = A_1\sin z$ or $\theta = B_1\cos z$, the two equations yield two steady-state curves, Fig. 6, which are similar to the 1/4 subharmonic curves. With damping there is a minimum possible amplitude or amplitude cutoff as in the 1/4 subharmonic case.

Using the polar co-ordinates defined in the previous section the amplitude-phase relation is

$$A^4 = \frac{640}{3}\frac{k}{q}\frac{1}{\sin 6\varphi} \qquad (18)$$

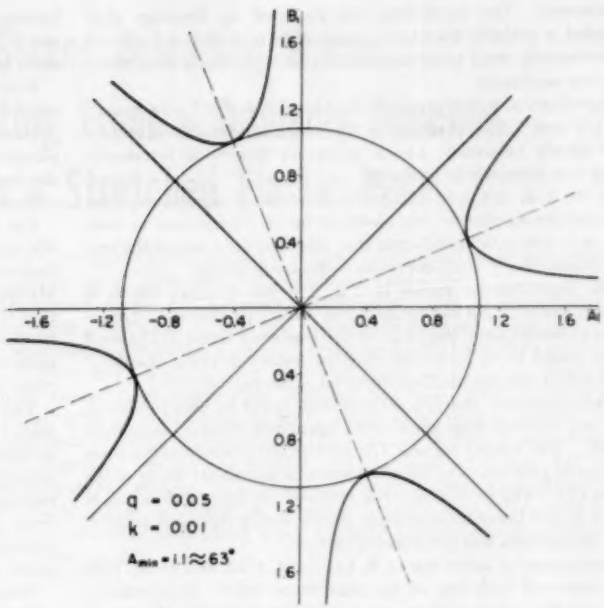

Fig. 5 The 1/4 subharmonic, steady states in A_1, B_1-plane

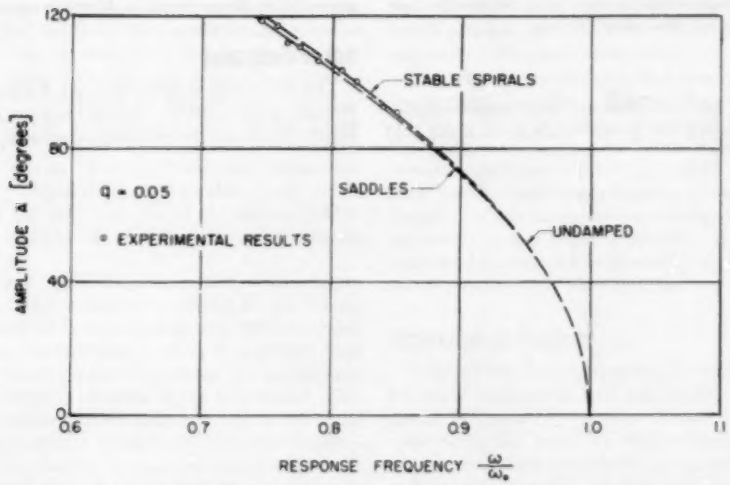

Fig. 6 The 1/6 subharmonic, third-order theory and experimental results

The minimum amplitude occurs at

$$\varphi = \tan^{-1}\left(\frac{4m+1}{12}\right)\pi, \quad m = 0, 1, 2, 3, \ldots \tag{19}$$

and

$$A_{min} = \left(\frac{640}{3}\right)^{1/4}\left(\frac{k}{q}\right)^{1/4} \tag{20}$$

From the original equations it can be found that the cutoff amplitude varies as $(k/q)^{1/n-1}$ for various subharmonics of order $1/n$ $(n > 2)$.

A stability analysis of the steady states for $n = 6$ shows that the upper curve of Fig. 6 consists of stable points and the lower curve consists of unstable points, as in the $n = 4$ case.

It is of interest to compare the parametrically excited oscillations just discussed with the free oscillations of a pendulum without damping. The free undamped oscillations define a curve of amplitude versus frequency which lies between the two steady-state forced oscillation curves in each of Figs. 3, 4, 6 when computed to the same order of approximation.

Experimental Results

Experiments were performed with pendulums of various length mounted on a vibrating table. The pendulums were uniform bars, 2, 6, and 14 in. long, pivoted at one end. The vibration machine used was an electromagnetic vibration exciter with a frequency range of 5 to 2000 cps and a force capacity of 1200 lb. It was possible to determine the pendulum response frequency closely since for steady states it is always an exact submultiple of the forcing frequency which was indicated by the machine's

instruments. The pendulum was mounted on bearings that provided a variable frictional resistance, which was determined approximately from measurements of the logarithmic decrement of a free oscillation.

Experimental points are plotted in Figs. 3, 4, 6. In the case of the 1/4 and 1/6 subharmonics the predicted amplitude cutoffs were clearly exhibited; i.e., a minimum amplitude for steady states was distinctly in evidence.

In the 1/2, 1/4, and 1/6 subharmonic experiments only one steady-state amplitude was observed for any frequency in each case as it was anticipated from that fact that only one of the two theoretical steady-state curves in each case is stable.

The experimental values in Fig. 3 define a curve which is slightly steeper than the second-order theory prediction. This is to be expected since the effect of the neglected terms of the sin θ series would be to make the effective restoring spring "harder." This would steepen the theoretical response curves.

Experimentally the 1/8 subharmonic could be also produced, but only for very large amplitudes, again indicating an amplitude cutoff. The theory for the 1/8 subharmonic would require retention of four terms in the sin θ series or additional terms of the series (3). The numerical work required for the computation of the 1/8 and lower subharmonic steady states increases rapidly, and the analysis was not pursued further.

Subharmonics lower than 1/8, i.e., 1/10, 1/12, and so on, were not observed with any of the pendulums tried. It is possible that for the values of damping and forcing available, the amplitude cutoff for these subharmonics is such that no steady-state oscillation exists with amplitudes below 180 deg.

Conclusions

The theory predicts two steady-state amplitude-frequency curves for each subharmonic for given values of damping and forcing. One of these curves represents stable oscillations in each case. The other represents unstable states. The stable steady-state values agree well with experimental results.

Both theory and experiments show that the lower subharmonics of orders 1/4, 1/6, 1/8, . . ., behave differently from the 1/2 subharmonic in that the lower subharmonics exhibit an amplitude cutoff when damping is present. The cutoff amplitudes are large even for small damping and increase as the order of the subharmonic decreases.

For the 1/2 subharmonic, the first-order solution shows that the rest position of the pendulum is unstable for a certain forcing frequency range. This is also well known from the theory of the Mathieu equation. The higher order solutions show, however, that the nonlinearity of the pendulum equation limits the ultimate amplitude in this range. Moreover, the ultimate steady-state amplitude approaches zero as the forcing frequency approaches the upper limit of the unstable range.

The results for the 1/2 subharmonic can be conveniently presented in a three-dimensional space where the axes are the dimensionless frequency ratio λ, the forcing coefficient q, and the amplitude A. In this space, all possible steady states can be represented as a set of curved surfaces. Fig. 2 would be the trace of these surfaces on the (λ, q)-plane on which $A = 0$. The information in Fig. 3 would be obtained by a plane section, q = const, parallel to the λ, A-plane.

While the present study applies directly to pendulums, the results may be significant for other nonlinear systems which are also governed by the generalized Mathieu equation (2).

Acknowledgment

This study was supported by the National Science Foundation through grant G-4076. The authors are grateful to Prof. H. H. Bleich for his interest and encouragement.

Plane-Stress Unloading Waves Emanating From a Suddenly Punched Hole in a Stretched Elastic Plate[1]

JULIUS MIKLOWITZ[2]
Associate Professor of Applied Mechanics, California Institute of Technology, Pasadena, Calif.
Mem. ASME

The present paper points out that Kromm's [1][3] plane-stress solution, for compressional waves in an infinite elastic plate subjected to radial pressure in a circular hole at its center, has application to still another problem of interest. This is the problem of a stretched elastic plate in which a circular hole is suddenly punched. The plane-stress solution for the tensile circumferential stresses, generated by the unloading mechanism in punching, is given here. This solution is derived independently of Kromm's work in which a rather special Laplace-transform technique was used. The derivation given here also makes use of the Laplace transform but in a more direct manner, employing the inversion integral and a contour integration. It is also shown that the present inversion technique offers important simplifying features over that used by Selberg [3] in the closely related plane-strain problem. The numerical results presented are of interest in fragmentation studies. It is shown that the dynamic circumferential stress field in the vicinity of the punched hole is quite severe, which would be important to the creation and propagation of radial cracks.

THE plane-stress solutions for compressional waves in an infinite elastic plate, subjected to a sudden radial pressure or radial velocity in a circular hole at its center, were recently given by Kromm [1]. One of the purposes of the present paper is to point out that Kromm's solution, for the case of sudden pressure loading in the hole, has application to still another plane-stress problem. This is the problem of a thin elastic plate initially stretched in its plane, and in which a circular hole is suddenly punched at the center. This problem, as formulated here, differs only from Kromm's in the time character of the input function. The solution therefore could be obtained from Kromm's with the aid of a convolution.

Kromm's solutions were derived by using the Laplace-transform method but in a rather special way not employing the inversion integral. Instead, Kromm worked directly with the transformed solution for the displacement, writing it in a form that with the aid of a convolution reduced the problem to a numerical solution of Volterra's integral equation of the first kind.[4] The author has solved the present problem independently of Kromm's work by employing the inversion integral and a contour integration. Presentation of this method of solution, it was felt, would be instructive particularly since the literature gives evidence of the inversion difficulties involved in employing this more direct technique. In this connection the method used here is similar to that employed by Selberg [3], who solved the related plane-strain problem. It will be seen, however, that the present technique offers the greater simplicity.

The stretched-plate, punched-hole problem is of interest in fragmentation studies. It forms the first approximation to the related problem of a large pressurized tank. In these problems the question that arises is on whether the associated fractures produced on punching will remain local to the perforation or propagate, possibly resulting in fragmentation of the medium. The influence of the dynamic stresses, created during punching, might be important in this fracture process. It is with this theme that numerical information is presented here on the in-plane stresses in the punched-hole plate problem.

Statement of Problem

Consider the thin elastic plate shown in Fig. 1. It is infinite in extent, of thickness h, and is stretched so that initially a state of axially symmetric hydrostatic tension exists; i.e., $\sigma_r = \sigma_\theta = \sigma_0$, respectively the radial, circumferential, and initial stress. At $t = 0$, a small flat-nose cylindrical projectile of radius a, traveling with velocity v, strikes the plate and begins to punch out a hole of radius equal to its own.

If one assumes the punching process involved here is that known as "plugging" in armor-perforation studies (removal of a plug of plate material below projectile), a simple boundary condition can be written at the hole for the present in-plane stress problem. Rinehart and Pearson [4] point out that plugging is observed in thin plates when the projectile velocity is high enough (2000 fps and higher). Consistent with the plugging process are the following assumptions that lead to the boundary condition at the punched hole:

1 The plastic flow due to punching is very localized to the neighborhood of the punched section; Rinehart and Pearson [4] give experimental support for this when v is high enough ($v \geq$ 2000 fps).

2 The punching begins instantaneously (at $t = 0$) over the whole punched section; based on a small value of plate thickness h and a large value of impact speed v.

[1] This paper has been abstracted from Ramo-Wooldridge Corp. Reports GM-Tr-259 (October 10, 1957) and GM-TR-0165-00380 (April 24, 1958).

[2] Also Consultant, Space Technology Laboratories, Inc., Los Angeles, Calif.

[3] Numbers in brackets designate References at end of paper.

[4] Goodier and Jahsman [2] have used Kromm's method to solve some related plate plane-stress problems.

Contributed by the Applied Mechanics Division and presented at the Annual Meeting, Atlantic City, N. J., November 29-December 4, 1959, of THE AMERICAN SOCIETY OF MECHANICAL ENGINEERS.

Discussion of this paper should be addressed to the Secretary, ASME, 29 West 39th Street, New York, N. Y., and will be accepted until April 10, 1960, for publication at a later date. Discussion received after the closing date will be returned.

NOTE: Statements and opinions advanced in papers are to be understood as individual expressions of their authors and not those of the Society. Manuscript received by ASME Applied Mechanics Division, September 29, 1958. Paper No. 59—A-46.

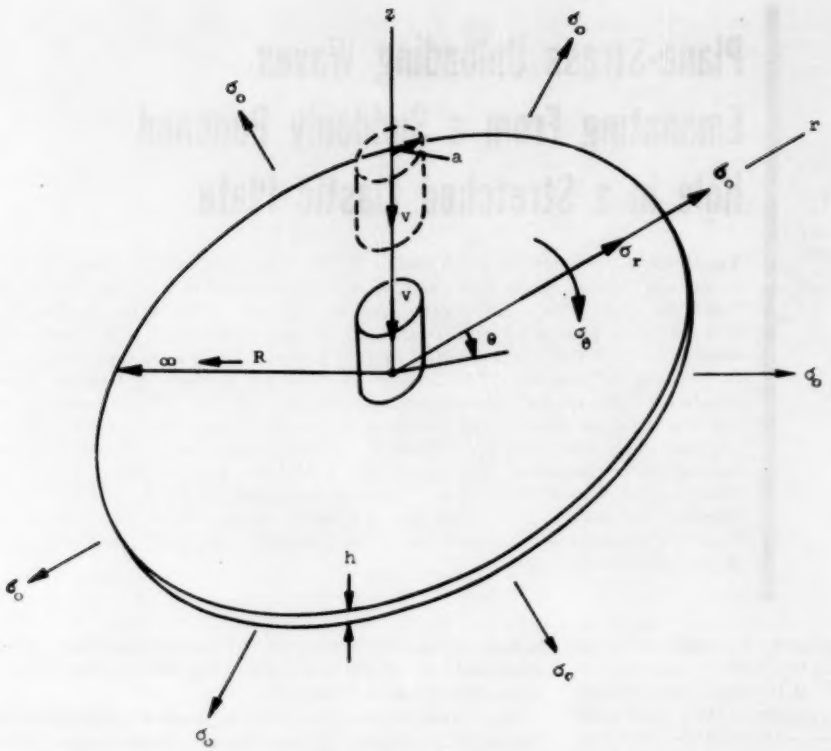

Fig. 1 Elastic plate and projectile at time $t = 0$

3 The punching action takes place at velocity $v/2$, the particle velocity in the compressional wave that develops in both projectile and plate on impact; i.e., the plate material below the projectile is removed as a plug at $v/2$; the corresponding punching time is therefore $2h/v = k$; based on a large ratio of diameter of projectile to plate thickness.

It is clear that the punching process, because of the plate resistance to shear, gives rise to flexural waves as well as the in-plane waves of concern here. Separation of the problem into these component problems, which is inherent in the treatment of the in-plane stress problem given here, should have validity for the far field. For the very thin plate, valid information might be expected reasonably close to the hole.

On the basis of these arguments the following statement for the unloading-wave problem may be made:

$$\nabla^2 u - \frac{u}{r^2} = \frac{1}{c^2}\frac{\partial^2 u}{\partial t^2}, \quad a < r < \infty, \quad t > 0 \tag{1}$$

$$u(r, 0) = \frac{\partial u}{\partial t}(r, 0) = 0, \quad r \geq a \tag{2}$$

$$[\sigma_r(r, t)]_{r=a} = \left[\frac{E}{(1-\nu^2)}\left(\frac{\partial u}{\partial r} + \nu\frac{u}{r}\right)\right]_{r=a} \begin{cases} = 0, & t < 0 \\ = -\dfrac{\sigma_0 t}{k}, & 0 < t < k \\ = -\sigma_0, & t > k \end{cases} \tag{3a}$$

$$\lim_{r\to\infty}[u(r, t)] = 0, \quad t > 0 \tag{3b}$$

Equation (1) is the displacement equation of motion, reflecting the assumption of plane stress in the thin plate, u being the displacement in the r-direction, and $c = [E/(1-\nu^2)\rho]^{1/2}$ the "plate" velocity. E is the modulus of elasticity, ν Poisson's ratio, and ρ the plate material density. Equation (1) can be obtained by first appealing to the equilibrium equation, given by Timoshenko and Goodier [5], which yields the stress equation of motion when the body force is replaced by the inertia force $-\rho(\partial^2 u/\partial t^2)$. Substitution in the stress equation of motion from the stress-displacement equations (5) gives then Equation (1). Equation (2) reflects the state of rest at $t = 0$. Equation (3a) is a statement of the boundary condition at the hole for the dynamic part of the problem, obtained by subtracting off the initial static stress. Adding σ_0 later gives the complete solution. Equation (3b) is consistent in stating that there is no disturbance at infinity. It may be noted that Equations (1), (2), (3a), and (3b), represent the boundary-value problem for an infinite plate, subjected to a sudden pressure loading on the boundary of a small hole at the plate center. Hence, except for the difference in time character of the input, Equation (3a), they form the statement of the problem solved by Kromm (he employed a step input).

It should be pointed out that the displacement equation of motion (1), based on the assumption of plane stress, is the lowest-order approximate theory that might be used in problems such as that treated in Kromm's and this work. Since there are obviously short-wave effects involved in these problems, treatment employing a higher-order theory, taking into account coupling between extensional and thickness modes of motion, would be in order. However, as pointed out in the work of Kane and Mindlin [6], the plane-stress theory yields a good approximation provided the wave lengths involved are long compared to the plate thickness. In this connection the more slowly rising input

function in the present problem can be handled with greater accuracy by the plane-stress theory than the step employed in Kromm's work. The solution given here has been evaluated for two different rise times k. Comparison of these results later throws some light on the short-wave limitations in using the plane-stress theory in the present problem.

Solution of the Problem

The Laplace-transform method of solution is particularly suited to the traveling-wave-type solution of interest here. According to this technique the governing Equation (1), subject to the initial conditions (2), transforms to

$$r^2 \frac{d^2\bar{u}}{dr^2} + r \frac{d\bar{u}}{dr} - \left(\frac{p^2r^2}{c^2} + 1\right)\bar{u} = 0 \tag{4}$$

where $\bar{u}(r, p)$ is the transform of $u(r, t)$ and p is the transformation parameter. Equation (4) may be recognized as Bessel's differential equation. In the case of Equation (4) the general solution is given by

$$\bar{u}(r, p) = A(p)I_1\left(\frac{pr}{c}\right) + B(p)K_1\left(\frac{pr}{c}\right) \tag{5}$$

where I_1 and K_1 are the modified Bessel functions of the first and second kinds, respectively, of order one. Condition (3b) transforms to

$$\lim_{r\to\infty} [\bar{u}(r, p)] = 0. \tag{5a}$$

The leading terms of the asymptotic expansions of I_1 and K_1 given in Erdelyi [7] are

$$I_1 = \left(\frac{c}{2\pi pr}\right)^{1/2} e^{pr/c}, \quad K_1 = \left(\frac{\pi c}{2pr}\right)^{1/2} e^{-pr/c} \tag{5b}$$

Hence condition (5a) is satisfied if $A(p)$ is set $= 0$. The boundary condition at $r = a$, condition (3a), determines $B(p)$. Transforming this condition and applying it to Equation (5) gives

$$\bar{u}(r, p) = \frac{(1 - \nu^2)\sigma_0(1 - e^{-kp})K_1\left(\frac{pr}{c}\right)}{Ekp^2\left[\frac{(1 - \nu)}{a} K_1\left(\frac{pa}{c}\right) + \frac{p}{c} K_0\left(\frac{pa}{c}\right)\right]} \tag{6}$$

for the transformed displacement solution. The circumferential stress-displacement relation [5] and the use of the Mellin inversion theorem given in McLachlan [8] lead to the mathematical statement of the solution for σ_θ/σ_0

$$\frac{\sigma_\theta(r, t)}{\sigma_0} = \frac{1}{k(2\pi i)} \int_{Br_1} \frac{(1 - e^{-kp})\left[\frac{(1 - \nu)}{r} K_1\left(\frac{pr}{c}\right) - \frac{\nu p}{c} K_0\left(\frac{pr}{c}\right)\right] e^{pt} dp}{p^2F(p)} \tag{7}$$

where

$$F(p) = \frac{(1 - \nu)}{a} K_1\left(\frac{pa}{c}\right) + \frac{p}{c} K_0\left(\frac{pa}{c}\right)$$

and where Br_1 is the Bromwich contour in the right half of the p-plane (shown in Fig. 2). Interest in the circumferential stress in the present problem stems from the fact that it is the maximum principal stress and is of tensile character. The possibility of radial cracks in the plate is therefore implied.

The integrand function in Equation (7) has some right half p-plane that is singularity free, stemming from the fact that the governing equation, Equation (1), is hyperbolic. Hence by completing the contour Br_1 with a large circle to the right in Fig. 2, letting $|p| \to \infty$ in Equation (7), and applying Cauchy's theorem and Jordan's lemma to the approximated integrand on this closed path,[6]

$$\frac{\sigma_\theta(r, t)}{\sigma_0} = 0 \quad \text{for} \quad 0 < t < \frac{r - a}{c} \tag{8}$$

results, establishing the expected wave character of the solution. To obtain information for times after the wave-front arrival time $(r - a)/c$, at a particular plate station $r - a$, an integration of Equation (7) must be carried out over some contour Br_2 completed to the left of Br_1 in Fig. 2. This requires further information on possible integrand singularities at other places in the p-plane. It is in this connection that the present integral is difficult to invert, basically due to the difficulty in determining the zeros of the function $F(p)$ in the integrand denominator.[6]

It is clear that there are no zeros of $F(p)$ in the right half of the p-plane (Re $p > 0$) since this would result in residue-type terms in the solution that increase indefinitely with time. Clearly the long-time solution here is bounded since it must be equivalent to the static solution for the infinite plate with uniform radial pressure in a hole at its center. This long-time solution can be derived by imposing small p on the integrand in Equation (7), using the appropriate approximations to the K-functions. The result is

$$\frac{\sigma_\theta}{\sigma_0} = \frac{a^2}{r^2} \tag{9}$$

in agreement with the well-known static result [5]. Support for this argument is given in the work of Erdelyi and Kermack [9] who prove that a general function, of which $F(p)$ is a special case, has no zeros in the right half of the p-plane.

[6] See reference [8], p. 78.
[6] See reference [7], pp. 62–63.

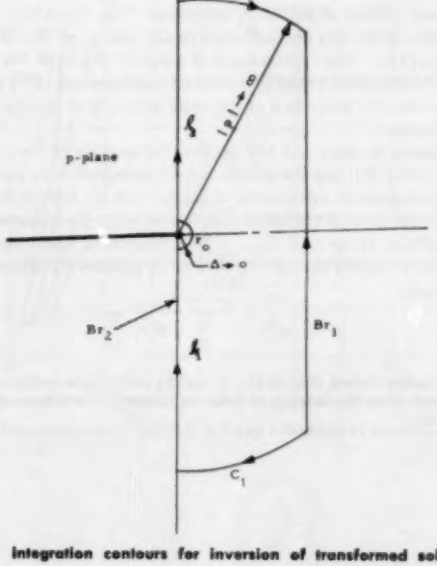

Fig. 2 Integration contours for inversion of transformed solution

The analysis carried out in the Appendix shows that there are no zeros of $F(p)$ along the imaginary axis. On the basis of this, contour Br_2 was chosen as shown in Fig. 2; i.e., along the imaginary axis. This, of course, simplified the analysis considerably, making it unnecessary to seek zeros in the entire left-half plane. Fig. 2 exhibits the only singularity involved in the integration over the chosen contour. It is the common branch point at $p = 0$ of the K-functions, and their combinations in Equation (7), due to their logarithmic behavior there. These functions are regular away from $p = 0$.

In order to obtain a convergent inversion of the integral in Equation (7) it was necessary to rewrite it employing the convolution theorem. According to this theorem the inversion integral is written as

$$\frac{1}{2\pi i}\int_{Br_1}\phi_1(p)\phi_2(p)e^{pt}dp \tag{10a}$$

and has its inverse in

$$\int_0^t f_1(t-\tau)f_2(\tau)d\tau \tag{10b}$$

where ϕ_1 and f_1, ϕ_2 and f_2 are transform pairs. In the present case $\phi_1(p)$ was taken as $1/p$ and $\phi_2(p)$ the rest of the integrand in Equation [7]. Since the inverse $f_1(t-\tau)$ is the unit function, according to Equations (7), (8), and (10), the solution for $\sigma_\theta(r,t)/\sigma_0$ is contained in

$$\frac{\sigma_\theta(r,t)}{\sigma_0} = \frac{1}{k}\int_{\frac{r-a}{c}}^{t} f_2(r,\tau)d\tau \quad \text{for} \quad \frac{r-a}{c} < t < \frac{r-a}{c}+k \tag{11}$$

$$= [\text{RHS of Equation (11)}] - [\text{RHS of Equation (11) with } t \text{ replaced by } (t-k)]$$

$$\text{for } \frac{r-a}{c}+k < t < \infty \tag{12}$$

where

$$f_2(r,\tau) = \frac{1}{2\pi i}\int_{Br_1}\frac{\left[\frac{(1-\nu)}{r}K_1\left(\frac{pr}{c}\right) - \frac{\nu p}{c}K_0\left(\frac{pr}{c}\right)\right]e^{p\tau}dp}{pF(p)} \tag{13}$$

and where neglect of the shift operator e^{-kp} in Equation (13) is taken care of by the second bracket appearing on the RHS of Equation (12). The replacement of contour Br_1 with Br_2 (composed of component paths l_1, r_∞, and l_2), in Equation (13), follows from the Cauchy theorem and the order property of the transform in this integral. [7]

It remains to carry out the contour integration of the integral in Equation (13), and the simple outer τ integration in Equation (11). The contour integration is carried out by first choosing a particular branch of the integrand function on Br_1 to agree with the condition Re $p > 0$ there. This branch is then continued analytically around the contour Br_2. The process is facilitated by first setting

$$p = \omega e^{i\theta}, \quad -\frac{\pi}{2} < \theta < \frac{\pi}{2}$$

[7] It is easily shown that paths C_1 and C_2 contribute nothing to the integration since the integrand behaves as $e^{p\tau}/p$ there (see reference [8], p. 77).

on Br_1. Then a corresponding cut along the negative real axis, Fig. 2, makes the modified Bessel functions in Equation (13) single valued over Br_2. This cut is also in agreement with (which it must be) the asymptotic series for the K_0 and K_1-functions, used in writing Equations (5b) and obtaining Equation (8).

On l_1, $p = -i\omega$, and on l_2, $p = i\omega$, and the integrals on these paths combine to give

$$[f_2(r,\tau)]_{l_1+l_2} = \frac{1}{\pi}\int_0^\infty \text{Re}\left\{\frac{\left[\frac{(1-\nu)}{r}K_1\left(\frac{\omega r}{c}i\right) - \frac{\nu\omega}{c}iK_0\left(\frac{\omega r}{c}i\right)\right]e^{i\omega\tau}}{i\left[\frac{(1-\nu)}{a}K_1\left(\frac{\omega a}{c}i\right) + \frac{\omega}{c}iK_0\left(\frac{\omega a}{c}i\right)\right]}\right\}\frac{d\omega}{\omega} \tag{14}$$

The contribution of path r_0 is found in the usual way by approximating the integrand of Equation (13) for small $|p|$, and obtaining the limiting value of the integral (as $\Delta \to 0$ in Fig. 2). The contribution is found to be

$$[f_2(r,\tau)]_{r_0} = \frac{a^2}{2r^2} \tag{15}$$

The integral in Equation (14) can be reduced to a real integral containing the ordinary Bessel functions by first employing the relation between the modified Bessel and Hankel functions given in Watson [10]

$$K_n(z) = \frac{1}{2}\pi i e^{n\pi i/2}H_n^{(1)}(iz) \tag{16}$$

then the relations between the Hankel and ordinary Bessel functions. The result is

$$[f_2(r,\tau)]_{l_1+l_2} = \frac{1}{\pi}\int_0^\infty \frac{[(A+B)\sin\omega\tau - (C-D)\cos\omega\tau]d\omega}{(F+G)\omega} \tag{17}$$

where

$$A = \alpha_1\alpha_2, \quad B = \alpha_3\alpha_4, \quad C = \alpha_2\alpha_3,$$
$$D = \alpha_1\alpha_4, \quad F = \alpha_2^2, \quad G = \alpha_4^2$$

and

$$\alpha_1 = \frac{(1-\nu)}{r}J_1\left(\frac{\omega r}{c}\right) + \frac{\nu\omega}{c}J_0\left(\frac{\omega r}{c}\right)$$

$$\alpha_2 = \frac{(1-\nu)}{a}J_1\left(\frac{\omega a}{c}\right) - \frac{\omega}{c}J_0\left(\frac{\omega a}{c}\right)$$

$$\alpha_3 = \frac{(1-\nu)}{r}Y_1\left(\frac{\omega r}{c}\right) + \frac{\nu\omega}{c}Y_0\left(\frac{\omega r}{c}\right)$$

$$\alpha_4 = \frac{(1-\nu)}{a}Y_1\left(\frac{\omega a}{c}\right) - \frac{\omega}{c}Y_0\left(\frac{\omega a}{c}\right)$$

Substituting the sum of the results in Equations (15) and (17) in Equation (11), and performing the simple integrations with respect to τ gives the solution for $\sigma_\theta(r,t)/\sigma_0$, as

$$\frac{\sigma_\theta(r,t)}{\sigma_0} = \frac{a^2}{2kr^2}\left(t - \frac{r-a}{c}\right) - \frac{1}{k\pi}\int_0^\infty \left\{\frac{(A+B)\left[\cos\omega t - \cos\omega\left(\frac{r-a}{c}\right)\right] + (C-D)\left[\sin\omega t - \sin\omega\left(\frac{r-a}{c}\right)\right]}{(F+G)\omega^2}\right\} d\omega$$

$$\text{for } \frac{r-a}{c} < t < \frac{r-a}{c} + k \quad (18)$$

= [RHS of Equation (18)] − [RHS of Equation (18) with t replaced by $(t-k)$]

$$\text{for } \frac{r-a}{c} + k < t < \infty \quad (19)$$

The solution given by Equations (18) and (19) was evaluated by numerical integration employing an electronic computer. This required subroutines for the ordinary Bessel functions J_0, J_1, Y_0, and Y_1 but, as in the present case, routines for these oft-used functions usually exist in a modern computing installation. The infinite limit of integration caused no particular problem, since the main contribution to the value of the integral came from the region of small ω. This was due to the oscillatory, but well-behaved, character of the integrand, and the occurrence of ω^2 in the integrand denominator. The integration scheme employed a polynomial representation of the integrand.

Additional simplicity was given the numerical solution through the external checks that existed in the present problem. These were the short-time (after wave-front arrival) and long-time solutions for the problem, written independently of the solution given in Equations (18) and (19). The former is written by imposing large $|p|$ on the integrand in Equation (7), using the asymptotic series for K_0 and K_1. The inversion of terms is simple and can be found in any table of transforms. The result is a power series of the form

$$\left(t - \frac{r-a}{c}\right)^n$$

a few terms of which give a very accurate result for very short times. This series in the present problem appears in a report by the author [11]. The long-time solution has already been discussed and is given by Equation (9).

The related plane-strain problem solved by Selberg [3] generates the same inversion integral for σ_θ/σ_0 as in Equation (7), except for the elastic constants. Selberg inverted this integral by first proving that $F(p)$ has just one root lying in the upper half of the p-plane ($Im\ p \geq 0$), and that this root must be in the interior of the second quadrant. The root is located by successive approximation to seven significant figures. The contour integration that follows, although not stated, was apparently carried out by first rotating the Bromwich contour Br_1 by $\pi/2$ into the upper half plane, and then completing the contour along the real axis to include the pole generated by $F(p)$. Again here a real infinite integral, related to that in Equation (14), is generated in the solution. Selberg evaluates this numerically for $\lambda = \mu$ (the Lamé constants). Comparison of Selberg's inversion technique with that given here points out that the major advantage in the latter lies in the fact that no roots of $F(p)$ have to be determined. It is also clear that the present method is based on relatively simpler arguments.

The curves shown in Figs. 3 and 4 represent the numerical results obtained from Equations (18) and (19) plus one, the static initial stress; i.e., the complete solution for σ_θ/σ_0 in the present problem.[8] The constants employed are given in the box in Fig. 3. They are the basic parameters in the problem, $k = 2h/v$ reflecting the plate thickness, the impact velocity or their ratio (the value in Fig. 3, for instance could represent a $v = 2000$ fps and an $h = 1/32$ in.), the c and ν defining the material (those in Fig. 3 represent steel).

The curves in Fig. 3 represent the tensile circumferential stress σ_θ/σ_0, at particular plate stations $r - a$, as a function of time after the unloading wave front arrives. They bring out the important fact that at each station the maximum dynamic stress is considerably larger than the related static stress given by the right-hand side of Equation (9) plus one.

The most important curve, of course, is that representing the

[8] As mentioned earlier, the accuracy of the present numerical work was checked against results from the independent solution for very short times behind the wave front, given in reference [11]. Excellent agreement was found. For instance, for the curve shown in Fig. 4, ($t = 10k$), the wave-front expansion (δ terms) gave the σ_θ/σ_0 values, 0.9939, 0.9778 and 0.9739 at, respectively, the distances 0.1 ck, 0.5 ck, and ck back of the wave front. The corresponding numbers derived from Equation (18) were 0.9944, 0.9782 and 0.9730.

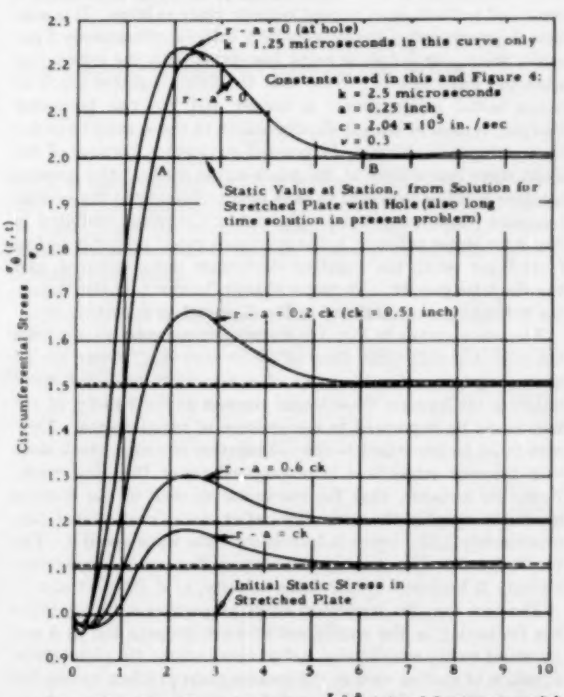
r - a = 0 (at hole)
k = 1.25 microseconds in this curve only
Constants used in this and Figure 4:
k = 2.5 microseconds
a = 0.25 inch
c = 2.04 x 10^5 in./sec
ν = 0.3
r - a = 0
A
B
Static Value at Station, from Solution for Stretched Plate with Hole (also long time solution in present problem)
r - a = 0.2 ck (ck = 0.51 inch)
r - a = 0.6 ck
r - a = ck
Initial Static Stress in Stretched Plate
Circumferential Stress σθ(r,t)/σ0
Time After Wave Front Arrival t - (r - a)/c (k = 2.5 microseconds)

Fig. 3 Circumferential stress $\sigma_\theta(r,t)/\sigma_0$ as a function of time for various stations $r - a$

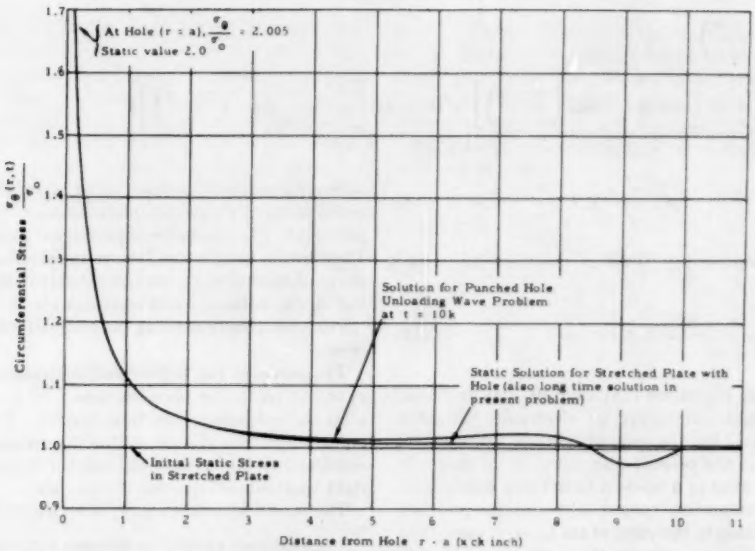
At Hole (r = a), $\frac{\sigma_\theta}{\sigma_0}$ = 2.005
Static value 2.0
Circumferential Stress $\frac{\sigma_\theta(r,t)}{\sigma_0}$
Solution for Punched Hole Unloading Wave Problem at t = 10k
Static Solution for Stretched Plate with Hole (also long time solution in present problem)
Initial Static Stress in Stretched Plate
Distance from Hole r - a (x ck inch)

Fig. 4 Circumferential stress $\sigma_\theta(r, t)/\sigma_0$ as a function of distance from punched hole for fixed time

station at the hole ($r - a = 0$), which involves the largest stresses. The maximum stress σ_θ/σ_0 is approximately 11.5 per cent higher than the static value 2.0. A comparison curve for the hole station with k cut in half is also shown in Fig. 3. This corresponds to a plate half as thick or an impact velocity twice as large. It is seen that the maximum value changes very little (approximately 1 per cent), the major influence being associated with the region just after the wave arrives. Note that the small negative dip (i.e., below initial static stress) is deeper and the rise thereafter sharper, typical of adding shorter waves to the system (k is rise time of input function). As pointed out earlier, because of the short-wave limitations of the plane-stress theory, the present solution could be expected to have greater validity as the k-value increases (slower rise time). Extending the effect exhibited in Fig. 3 for larger values of k, the overshoot would probably be less (<11.5 per cent), the negative short-wave dip eliminated, and the rise time greater. No major change, however, in the character of the response exhibited in Fig. 3, would be expected.

The other curves in Fig. 3 represent various stations out from the hole, but still quite close in (ck = 0.51 in.). They are all similar in form. On the basis of a maximum principal stress criterion for fracture these larger stresses in the vinicity of the hole could be important to the creation of radial cracks. They also could be important to the propagation of such a crack since this dynamic stress field is propagated faster than the crack. Note, for instance, that the maximum at each of the stations occurs at roughly the same time after wave-front arrival (approximately $2.5k$), hence it travels with the wave speed c. The brittle-fracture literature gives evidence that crack-propagation velocity is bounded by the shear velocity, $v_c < (G/\rho)^{1/2} < c$.

The fact that the maximum stress propagates with velocity c has its analog in the nondispersive wave propagation in a rod governed by the one-dimensional wave equation; the plane-stress equation of motion used in the present plate problem having the same character. Other features of the waves also bring out the nondispersive character. Note (a) the general lack of oscillatory character, and (b) the fact that the curve is above the static value for approximately the same time (see A-B in Fig. 3) at each station. The more slowly rising wave for a station farther out may be attributed to the space variable r-distorsion.

The results in Fig. 4 bring out some interesting related points. Fig. 4 is a special plot of the wave for a particular time ($10k$ = 25 μ sec). Note that roughly halfway back of the wave front, dynamic action has ceased; i.e., the static and wave solutions are identical. It is interesting indeed that this situation develops in just 25 μ sec.

The present results are in very good agreement with those in Kromm's and Selberg's work. Comparison can be made with Kromm's Figs. 3 and 6,[9] keeping in mind that one must add σ_0 to his solution and correct for the input-function differences in the two problems. It is clear, of course, that the additional information on u and σ_r, of interest in Kromm's work, could be obtained through inversions similar to that given here for σ_θ. One also could obtain all results from a single inversion on u by making use of the stress-displacement relations [5].

Acknowledgment

The author wishes to acknowledge the numerical evaluation work contributed by Mr. Vilas Henderson and Mr. Frank Meek of the Digital Computing Center of Space Technology Laboratories, Inc.

References

1 A. Kromm, "Zur Ausbreitung von Stosswellen in Kreislochscheiben," *Zeitschrift für angewandte Mathematik und Mechanik*, vol. 28, 1948, pp. 104–114, pp. 297–303.

2 J. N. Goodier and W. E. Jahsman, "Propagation of a Sudden Rotary Disturbance in an Elastic Plate in Plane Stress," JOURNAL OF APPLIED MECHANICS, vol. 23, TRANS. ASME, vol. 78, 1956, pp. 284–286.

3 H. L. Selberg, "Transient Compression Waves from Spherical and Cylindrical Cavities," *Arkiv för Fysik*, vol. 5, 1952, pp. 97–108.

4 J. S. Rinehart and J. Pearson, "Behavior of Metals under Impulsive Loads," American Society for Metals, Cleveland, Ohio, 1954, pp. 159–160.

5 S. Timoshenko and J. N. Goodier, "Theory of Elasticity," McGraw-Hill Book Company, Inc., New York, N. Y., second edition, 1951, p. 58.

6 T. R. Kane and R. D. Mindlin, "High-Frequency Extensional Vibrations of Plates," JOURNAL OF APPLIED MECHANICS, vol. 23, TRANS. ASME, vol. 78, 1956, pp. 277–283.

7 A. Erdelyi, W. Magnus, F. Oberhettinger, and F. G. Tricomi, "High Transcendental Functions, Bateman Project," McGraw-Hill Book Company, Inc., New York, N. Y., 1953, p. 86.

[9] Reference [1], p. 297.

8 N. W. McLachlan, "Complex Variable Theory and Transform Calculus," Cambridge University Press, Cambridge, England, second edition, 1953, p. 135.
9 A. Erdelyi and W. O. Kermack, "Note on the Equation $f(x)K'_n(x) - g(x)K_n(x) = 0$," *Proceedings of The Cambridge Philosophical Society*, vol. 41, 1945, pp. 74–75.
10 G. N. Watson, "Theory of Bessel Functions," Cambridge University Press, Cambridge, England, second edition, 1952, p. 78.
11 J. Miklowitz, "The Dynamic Stresses Emanating from a Suddenly Punched Hole in a Initially Stretched Elastic Plate," Report GM-TR-259, The Ramo-Wooldridge Corporation, Los Angeles, Calif., October 10, 1957, pp. 12–13.
12 M. Onoe, "Formulae and Tables, the Modified Quotients of Cylinder Functions," Report of Institute of Industrial Sciences, University of Tokyo, vol. 4, 1955, p. 223.

APPENDIX

Proof will be given here that $F(p)$ has no zeros on the imaginary axis of the p-plane.

This function may be written as

$$F(p) = \frac{(1-\nu)}{a}\left[K_1\left(\frac{pa}{c}\right) + \frac{pa}{c(1-\nu)}K_0\left(\frac{pa}{c}\right)\right] \tag{20}$$

hence the problem reduces to proving that

$$K_1(z) + \frac{z}{(1-\nu)}K_0(z) = 0 \tag{21}$$

on the imaginary axis cannot be satisfied, where $z = pa/c = \pm i\alpha y(\alpha = a/c)$. Equation (21) may be written as

$$K_1(\pm i\alpha y) \pm i\beta y K_0(\pm i\alpha y) = 0 \tag{22}$$

where $\beta = \alpha/(1-\nu)$.

Now with the aid of Bessel-Hankel function relation, Equation (16), the Hankel-ordinary Bessel function relation, and the relations[10]

$$\left.\begin{aligned} J_n(ze^{m\pi i}) &= e^{mn\pi i}J_n(z) \\ Y_n(ze^{m\pi i}) &= e^{-mn\pi i}Y_n(z) + 2i\sin mn\pi \cot n\pi J_n(z) \end{aligned}\right\} \tag{23}$$

where m, and n are integers, it can be shown that

$$K_1(i\alpha y) = \frac{\pi}{2}\left[-J_1(\alpha y) + iY_1(\alpha y)\right] \tag{24a}$$

and

$$K_0(i\alpha y) = -\frac{\pi}{2}\left[Y_0(\alpha y) + iJ_0(\alpha y)\right] \tag{24b}$$

[10] See reference [10], p. 75.

Equations (24a) and (24b) substituted in Equation (22) reduces the proof to showing that it is not possible to satisfy the two real equations

$$\left.\begin{aligned} J_1(\alpha y) &= \beta y J_0(\alpha y) \\ Y_1(\alpha y) &= \beta y Y_0(\alpha y) \end{aligned}\right\} \tag{25}$$

Letting $x = \alpha y$, these become

$$\frac{xJ_0(x)}{J_1(x)} = \frac{xY_0(x)}{Y_1(x)} = \frac{\alpha}{\beta} \tag{26}$$

The quotient functions appearing in Equation (26) are special cases of the class of functions of concern in the work of M. Onoe [12].[11] He states the general relation connecting the two quotient functions as[12]

$$\phi_\nu = \psi_\nu + \frac{2}{\pi J_\nu(z)Y_\nu(z)} \tag{27}$$

where

$$\phi_\nu = \frac{zY_{\nu-1}(z)}{Y_\nu(z)}$$

and

$$\psi_\nu = \frac{zJ_{\nu-1}(z)}{J_\nu(z)}$$

In these terms Equation (26) becomes

$$\phi_1 = \psi_1$$

which according to Equation (27) would only be true if

$$\frac{2}{\pi J_1(x)Y_1(x)} = 0$$

But it is easily proved that this is never true. Hence Equation (26) is not satisfied and there are no zeros of expression (20) on the upper half of the imaginary axis. The proof for the lower half of the imaginary axis is similar, reducing to consideration of Equations (25) again.

[11] The author is indebted to Prof. R. D. Mindlin of Columbia University for pointing out this paper to him.
[12] This relation can be derived using the Wronskian relation (12), p. 77, reference [10].

Plastic-Wave Propagation Effects in Transverse Impact of Membranes[1]

B. KARUNES[2]
Department of Applied Physics
University of Calcutta
Calcutta, India
Mem. ASME

E. T. ONAT
Associate Professor,
Division of Engineering,
Brown University,
Providence, R. I.
Assoc. Mem. ASME

The paper is concerned with the plane motion of a rigid-strain-hardening membrane attached to two parallel fixed supports. The membrane is subjected to a uniformly distributed transverse impulse and the subsequent motion of the membrane is to be determined with the particular emphasis on the variation of thickness in the final deflected shape. It is first shown that two essentially different initial modes of deformation exist depending on the average rate of hardening. For both modes, the analysis can be based on two types of waves of discontinuity until the moment when the compressive membrane forces occur in the middle region of the membrane. The presence of compressive forces will generally preclude the existence of a unique solution for further motion. The bending rigidity will probably have to be included into the analysis in order to obtain a unique solution. However, for the technically important rates of hardening and velocities, the kinetic energy of the membrane at the moment of occurrence of compressive forces is small compared with the initial energy, so that significant information could be obtained from the present analysis about the variation of thickness and hardening throughout the membrane.

Introduction

EXPERIMENTS on elastoplastic circular membranes subjected to blast loading [1][3] show that the final deformed shape is essentially conical. Taylor [2] predicted the conical shape using the simple argument that the uniform motion of the membrane caused by the blast is gradually stopped by the inward moving transverse wave. The angle which the generators of the dished-out circular "cone" make with the undistorted membrane is, therefore, $\theta = U_0/c$, where U_0 is the initial velocity given to the plate by the impulse and c is the velocity of the transverse wave associated with the membrane biaxially stressed to the yield point. While Taylor's theory explains the over-all situation satisfactorily, it does not provide information about the observed variation of strain along a radius and, especially, the pronounced thinning that occurs in the central portion of the plate [1]. On the other hand, it is well known [3–5] that tests carried out at high speed may be markedly influenced by longitudinal plastic-wave propagation effects which cause a variation of permanent strain along the test specimen.

Therefore, it would seem that a more detailed analysis of the impulsive motion of membranes must take account of the effects of both transverse and longitudinal waves.

In the present paper such an analysis is carried out for a rigid-strain-hardening membrane attached to two long parallel supports subjected to uniform impulse. It is assumed that a uniaxial state of plane strain exists within the plane normal to the supports. The analysis shows that for the technically important rates of hardening and impact speeds, the distribution of strains is nonuniform, greatest straining occurring in the middle portion of the membrane. This result suggests that the variation of permanent strain observed in the impulsive loading of circular or rectangular plates may also be explained satisfactorily by an analysis using the plastic-wave propagation approach employed in this paper.

Transverse and Longitudinal Waves of Discontinuity

Consider the plane motion of a thin, perfectly flexible membrane. We are interested in large deformations of the membrane so that it is permissible to neglect elastic strains and to consider the material as rigid up to the yield point. Furthermore, we assume that the material is strain-hardening and has a piecewise linear force-extension relation shown in Fig. 1. Here f denotes the membrane force within the plane of motion measured per unit length of the membrane normal to that plane; ϵ is the engineering strain, defined as the change in length per unit initial length in the plane of motion; λ is the slope of the strain-hardening line. The straight line BC indicates the unloading behavior. In the case when buckling action is hindered, reloading in compression follows the lines CD and DE where $\overline{CD} = \overline{BC}$.

The material is incompressible so that ϵ can be expressed in terms of initial and current cross-sectional areas, a_0 and a, respectively[4]: $\epsilon = (a_0 - a)/a$. For a membrane which is in the state of plane strain a_0 and a may be interpreted as initial and current thickness.

In the problem of impulsive loading considered in this paper the initial conditions involve discontinuities of velocity at the supports. As first shown by Rahmatulin [6],[5] such discontinuous initial conditions enable one to construct the solution to the problem with the help of waves along which discontinuities in slope or stress propagate.

[1] The results presented in this paper were obtained in the course of research sponsored by Norfolk Naval Shipyard under Contract N189-37083A with Brown University.

[2] Now at the Department of Applied Physics, University of Calcutta, Calcutta, India.

[3] Numbers in brackets designate References at end of paper.

Contributed by the Applied Mechanics Division and presented at the Annual Meeting, Atlantic City, N. J., November 29–December 4, 1959, of THE AMERICAN SOCIETY OF MECHANICAL ENGINEERS.

Discussion of this paper should be addressed to the Secretary, ASME, 29 West 39th Street, New York, N. Y., and will be accepted until April 10, 1960, for publication at a later date. Discussion received after the closing date will be returned.

NOTE: Statements and opinions advanced in papers are to be understood as individual expressions of their authors and not those of the Society. Manuscript received by ASME Applied Mechanics Division, December 8, 1958. Paper No. 59—A-128.

[4] It may be noted that this expression for the engineering strain ϵ follows from the usual definition of ϵ ($\epsilon = \Delta l/l_0$) and from the fact that the material is incompressible. It does not contain any assumption of geometrical nature and thus can be used for strains of arbitrary magnitude.

[5] See also [8]. For a more complete list of references the reader is referred to a recent book by Cristescu [9].

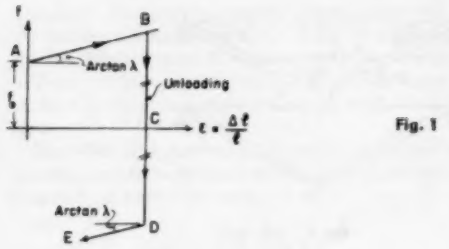

Fig. 1

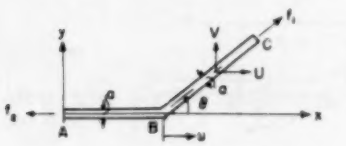

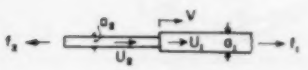

Fig. 2

In the following the equations governing such waves of discontinuity will be reviewed briefly.

Fig. 2(*a*) shows a transverse wave referred to the co-ordinate axes (x, y) which lie within the plane of motion and are attached to AB. The discontinuity in slope is at B and it is moving with the velocity u. The motion of BC consists of rigid-body translation characterized by the velocity components U and V. No plastic action occurs at B and the thickness a remains unchanged as the material is transported from AB to BC or vice versa. The laws of conservation of mass and momentum applied to ABC provide the following equations:

$$f_1 = f_2 = f = \rho a u^2 \tag{1}$$

$$U = u(1 - \cos\theta), \qquad V = -u \sin\theta \tag{2}$$

where ρ is the density of the material and θ is the angle of discontinuity. It is seen from the foregoing relations that the tension has the same value f at both sides of the transverse wave and the transverse wave velocity u is related to the tension by the well-known equation: $u = \pm(f/\rho a)^{1/2}$. A longitudinal wave of stress discontinuity is shown in Fig. 2(*b*). Let the velocity of the plastic-wave front be V and let U_1 and U_2 be the material velocities in front and back of it. The values of the remaining physical quantities are shown in Fig. 2 (*b*). The conservation laws provide the following equations:

$$a_2(U_2 - V) = a_1(U_1 - V) \tag{3}$$

$$f_1 - f_2 = \rho a_1(U_1 - V)(U_1 - U_2) \tag{4}$$

The material just ahead of the wave front is at the yield point. Its yield strength f_1 depends generally on the history of deformation. However, if the previous deformations occurred under tension, then f_1 is related to a_1 by the stress-strain relation

$$f = f_0 + \lambda\epsilon = f_0 + \lambda\frac{a_0 - a}{a} \tag{5}$$

The same equation applies for the membrane element which is just behind the wave front. Hence

$$f_1 - f_2 = \lambda a_0\left(\frac{1}{a_1} - \frac{1}{a_2}\right) \tag{6}$$

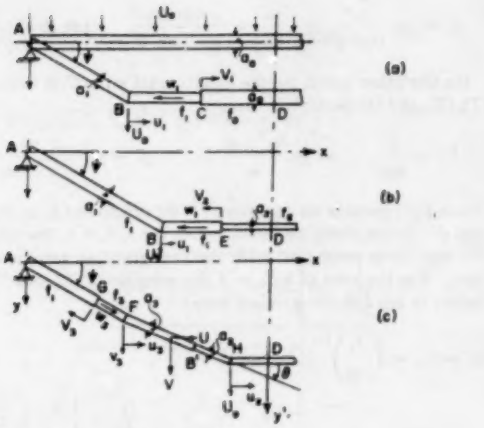

Fig. 3 $\lambda/f_0 > 1$

It follows from (3), (4), and (5) that

$$(U_1 - V)^2 = \frac{\lambda}{\rho a_2}\left(\frac{a_0}{a_1}\right)^2 \tag{7}$$

Note that $(U_1 - V)$ is the wave velocity relative to the material ahead of the wave front. Equation (7) shows that for weak waves the wave velocity may be approximated by the value $(\lambda/\rho a_0)^{1/2}$.

In the next section, the analysis of a specific problem will be based on the foregoing equations.

Membrane Under Uniformly Distributed Transverse Impulse

Consider a membrane of thickness a_0 attached to two parallel fixed supports. The distance between the supports is $2l$ and the length of the membrane in the direction of supports is large compared with l.

Suppose that initially the membrane is unstretched but just taut, and that at time zero a uniformly distributed downward impulsive velocity U_0 is applied to it by the action of blast pressure. Our purpose is to determine the subsequent motion of the membrane, the distribution of thickness and hardening during the motion, and the final deflected shape.

It will be assumed that the state of plane strain exists during the motion within anv plane normal to the supports.

The assumption of neglecting elastic strains implies an infinite velocity of propagation for elastic waves so that the yield force f_0 occurs throughout the plane of motion instantaneously. Moreover, as shown by Rahmatulin in [6] and [7], a longitudinal and a transverse wave will originate from each support.

The following analysis will show that when the nondimensional rate of hardening λ/f_0 satisfies the inequality $\lambda/f_0 > 1$, the longitudinal wave of stress discontinuity C will move ahead of the transverse wave B as shown in Fig. 3(*a*) which represents the state of affairs within the plane of motion. Because of symmetry the cross section of half of the membrane is shown in this figure. The part of membrane which is behind the transverse wave B remains at rest while the part ahead of it moves with uniform velocity U_0. The membrane force ahead of the longitudinal wave C is f_0. The thickness and the membrane force behind C are a_1 and f_1, respectively. Let V_1 be the velocity of the longitudinal wave and w_1 be the horizontal material velocity behind it measured positive in the direction shown in Fig. 3(*a*); u_1 is the horizontal velocity of the transverse wave, and ψ is the angle between AB and the horizontal axis.

By suitable transformation of co-ordinates we obtain from (1) and (2) the following equations for the transverse wave B:

$$f_1 = \rho a_1 \frac{u_1^2}{\cos^2 \psi}, \qquad \frac{u_1}{w_1} = \frac{\cos \psi}{1 - \cos \psi}, \qquad \tan \psi = \frac{U_0}{u_1} \quad (8)$$

On the other hand, for the longitudinal wave C, it follows from (7), (3), and (5) that

$$V_1 = \frac{\lambda}{\rho a_0}, \qquad w_1 = \frac{a_0 - a_1}{a_1} V_1, \qquad f_1 - f_0 = \lambda \frac{a_0 - a_1}{a_1} \quad (9)$$

(8) and (9) provide six equations for six unknowns f_1, a_1, w_1, V_1, u_1, and ψ. It can easily be verified that, for $\lambda/f_0 > 1$, the solution of (8) and (9) is consistent with the configuration assumed in Fig. 3(a). For the case of $\lambda/f_0 = 1$ the solution of (8) and (9) is obtained in the following closed form:

$$u_1 = V_1 = \left(\frac{f_0}{a_0 \rho}\right)^{1/2}, \qquad \tan \psi = \frac{U_0}{V_1},$$

$$\frac{f_1}{f_0} = \left\{1 + \left(\frac{U_0}{V_1}\right)^2\right\}^{1/2}$$

and

$$\frac{a_1}{a_0} = \left\{1 + \left(\frac{U_0}{V_1}\right)^2\right\}^{-1/2}, \qquad \frac{w_1}{V_1} = \left\{1 + \left(\frac{U_0}{V}\right)^2\right\}^{1/2} - 1$$

It is seen that when $\lambda/f_0 = 1$ the transverse wave velocity is equal to the velocity of the longitudinal wave; thus the points B and C coincide as shown in Fig. 4(a).

The foregoing result suggests that the transverse wave must travel ahead of the longitudinal wave when $\lambda/f_0 < 1$ as shown in Fig. 5(a). In view of the dependence of the initial mode of deformation on the rate of hardening λ/f_0, it may be appropriate here to note that for high-tensile steels the average rate of hardening λ/f_0 is greater than 2, whereas for mild steel and up to the strains of the order of 3 per cent λ/f_0 is much smaller than 1. However, in the experiments mentioned in the introduction maximum strains are of the order of 10 per cent and for such high strains considerable hardening occurs in mild steel. It can easily be seen from typical stress-strain curves for mild steel that the average linearized rate of hardening must again be taken greater than 1 if the large deformations are to be analyzed.

The initial mode of deformation was indicated for three different cases in Figs. 3(a), 4(a), and (5a). The following remarks and analysis will concern the subsequent motion of the membrane. For the special case of $\lambda/f_0 = 1$, the configuration in Fig. 4(a) persists throughout the motion. When the composite wave (B, C) reaches the mid-point, the kinetic energy of the system becomes zero and the motion stops. The final deflected wave is composed of two straight portions and the final thickness distribution is uniform, Fig. 4(b). In the case of $\lambda/f_0 < 1$, the first phase of motion, Fig. 5(a), ends when the transverse wave B reaches the mid-point. At this instant, Fig. 5(b), the portions BC and BC' have the longitudinal velocities w_1, directed to the point B. It can be shown that such a velocity distribution will cause *compressive membrane forces* to occur in the neighborhood of the mid-point for subsequent times. On the other hand, it is well known that when the bending rigidity is zero no unique solution can be expected in the presence of compressive forces.

However, a possible mode of motion, Fig. 5(c), may be described briefly in order to obtain some physical insight into the problem. In Fig. 5(c) the membrane element ahead of the longitudinal wave C_1 is in tension and the membrane force gradually decreases along C_1B to reach a certain compressive value[6] immediately ahead of the stationary transverse wave B. Under the joint action of the end forces, the portion C_1B is constantly decelerated. It is easily

[6] It is assumed that the compressive membrane force at B causes no yielding in compression.

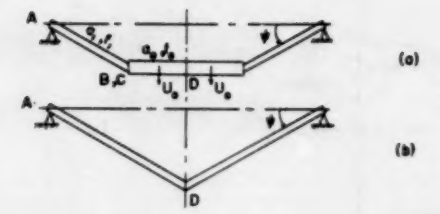

Fig. 4 $\lambda/f_0 = 1$

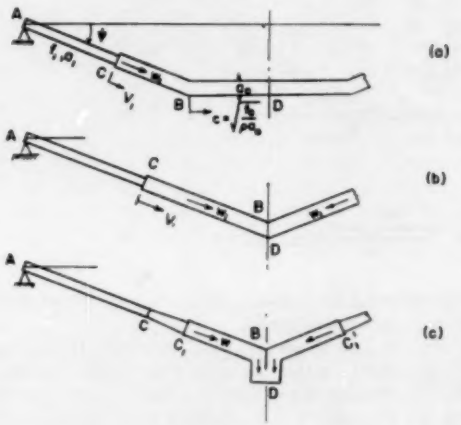

Fig. 5 $\lambda/f_0 < 1$

seen from (3) and (7) that the decrease in the velocity of C_1B is accompanied by an increase of thickness behind the wave front C.

It may be conjectured here that in the case of a membrane having bending rigidity, the broken line C_1BD in Fig. 5(c) will probably be replaced by a smooth curve but the weakening of the longitudinal wave C_1 will take place in a manner similar to the one described previously. Now we consider the case of $\lambda/f_0 > 1$ in further details. Here the second phase of motion begins when the plastic-wave front C meets its symmetrical counterpart at the mid-point. For subsequent times a reflected wave E returns toward the incoming transverse wave B with a velocity V_2, Fig. 3(b). The motion to the left of E remains unchanged, while the membrane force behind E has now a greater value f_2.

Using shock relations (3), (6), and (7) we find V_2, f_2, and the thickness a_2 in terms of previously obtained quantities

$$V_2 = 2w_1 + V_1, \qquad a_2 = \frac{V_1}{V_2} a_0, \qquad f_2 = f_1 + \rho a_0 V_1 w_1 \quad (10)$$

This phase of motion continues until the longitudinal wave E meets the transverse wave B. At this instant BD has the uniform downward velocity U_0 while AB is at rest. In analogy with the first phase of motion it may be expected that such discontinuous distribution of velocity will cause the occurrence of two pairs of waves, each pair being composed of a transverse and longitudinal wave. One of the wave pairs will move toward A, the other one toward the mid-point.

It must be remembered here that due to the passage of the wave front E, the yield strength has a greater value in ED compared with AB. Therefore a longitudinal plastic wave may not develop at all in the portion ED.

Numerical examples discussed at the end of this section indicate that this is indeed the case. The third phase of motion thus involves a longitudinal wave G and two transverse waves F and H,

Fig. 3(c). The physical quantities associated with this phase of motion are defined in Fig. 3(c). Here the longitudinal wave G is weaker than the wave E of the previous phase so that $f_3 < f_2$ and $a_3 > a_2$. At the material point B' where the waves B and E meet there is a permanent discontinuity in thickness as shown in the figure.

The equations governing this phase of motion are again obtained from the basic relations (1), (2) and (3), (6), (7). For the longitudinal wave G we have

$$V_3 = V_1 \frac{a_0}{a_1}, \qquad w_3 = \left(\frac{a_1}{a_3} - 1\right) V_3,$$

$$f_1 - f_3 = \lambda a_0 \left(\frac{1}{a_1} - \frac{1}{a_3}\right) \tag{11}$$

At the transverse wave F, in addition to the obvious geometrical relation,

$$\frac{v_3}{u_3} = \tan \psi \tag{12}$$

we have three equations which follow from (1) and (2) by a suitable transformation of co-ordinates

$$f_3 = \rho a_3 \left(\frac{u_3}{\cos \psi} - w_3\right)^2 \tag{13}$$

$$U = \left(\frac{u_3}{\cos \psi} - w_3\right)(\cos \psi - \cos \theta) + w_3 \cos \psi \tag{14}$$

$$V = \left(\frac{u_3}{\cos \psi} - w_3\right)(\sin \psi - \sin \theta) + w_3 \sin \psi \tag{15}$$

Similarly for the transverse wave H, we have

$$U = u_3(1 - \cos \theta) \tag{16}$$

$$V = U_0 - u_3 \sin \theta \tag{17}$$

$$f_3 = \rho a_3 u_3^2 \tag{18}$$

Equations (11), (12)–(18) provide ten relations for the ten unknowns V_3, w_3, a_3, f_3, u_3, v_3, U, V, θ, and u_3.

This phase of motion ends when the transverse wave reaches the mid-point. At this stage it is appropriate to discuss the results of numerical examples listed in Table 1. In Examples I and II the rate of hardening is $\lambda/f_0 = 1.05$ and the impact velocities U_0 are $0.2c$ and c, respectively, where c is the velocity of the transverse wave in a membrane carrying the yield stress f_0: $c = (f_0/\rho a_0)^{1/2}$. In Example III a higher rate of hardening is considered: $\lambda/f_0 = 4$ and $U_0 = c$. The relevant physical quantities for three phases of motion are determined from (8), (9), and (10)–(18) and listed in Table 1. The cross-sectional shape of the membranes at the end of the third phase of motion is shown in Figs. 7, 8, and 9. Various interesting conclusions can be derived from Table 1 and Figs. 7, 8, 9:

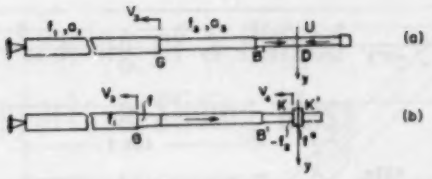

Fig. 6

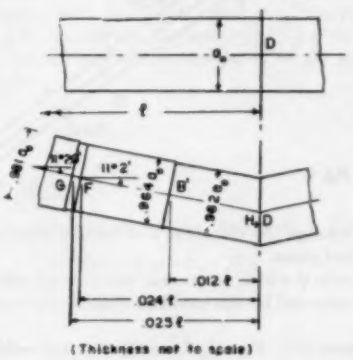

Fig. 7

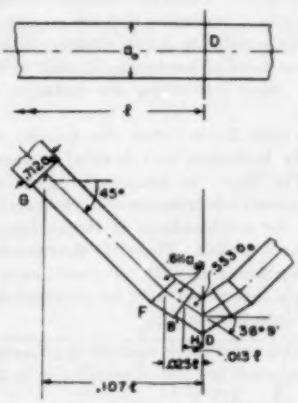

Fig. 8

(a) The kinetic energy E_1 stored in the membrane at the end of the third phase of motion is only a small fraction of the initial energy E_0 imparted by the blast. The ratios E_1/E_0 can easily be computed for the Examples I, II, and III using Table 1, and are found to be 2×10^{-4}, 5×10^{-3}, 7×10^{-2}, respectively. It may therefore be concluded that the further motion will not

Table 1 Physical quantities for three phases of motion

Example	First phase of motion							
	λ/f_0	U_0/c	f_1/f_0	a_1/a_0	u_1/c	V_1/c	w_1/c	ψ
I	1.05	0.2	1.0203	0.9810	1.0000	1.0247	0.0198	11° 20′
II	1.05	1.0	1.4244	0.7121	1.0001	1.0247	0.4142	45°
III	4	1.0	1.7896	0.8351	1.0691	2.0000	0.3948	43° 3′

Example	Second phase of motion			Third phase of motion					
	f_2/f_0	a_2/a_0	V_2/c	f_3/f_0	a_3/a_0	w_3/c	U/c	V/c	θ
I	1.0406	0.9628	1.0643	1.0394	0.9638	0.0186	0.0189	−0.0001	11° 2′
II	1.8489	0.5530	1.8531	1.6680	0.6111	0.2376	0.3341	−0.0250	36° 9′
III	2.5792	0.7170	2.7896	2.2625	0.7601	0.2364	0.3242	−0.0232	35° 10′

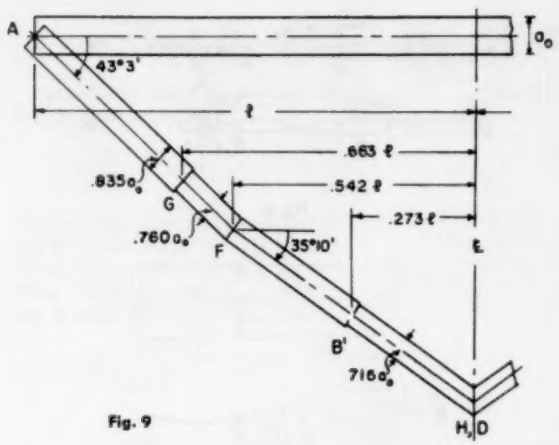

Fig. 9

appreciably change the thickness distribution that exists at the end of the third phase.

(*b*) The angle ψ which determines the over-all deflected shape is well approximated by the modified Taylor's formula, $\tan \psi = U_0/c$.

(*c*) It is seen from Figs. 7, 8, and 9 that the reflection of the longitudinal wave C from the mid-point constitutes the main cause for the occurrence of pronounced thinning in the middle region of the membrane. Since the reflection of the plastic wave occurs only for rates of hardening that are greater than a critical value, it should be possible to devise experiments using materials exhibiting various rates of hardening, in order to verify the conclusions of this paper concerning the variation of permanent strains.

(*d*) It is seen from Table 1 that the velocity of the portion FH is essentially horizontal and directed toward the axis of symmetry y', Fig. 3(*c*). As remarked before for the case of $\lambda/f_0 < 1$, such a velocity distribution will create compressive membrane forces in the neighborhood of the mid-point during the subsequent phase of motion. Therefore the existence of a unique solution for this phase is unlikely. It would seem that a physically significant solution can only be obtained by introducing bending rigidity into the analysis.

To illustrate this point let us consider the Example I. In this case only a very small portion of membrane is still in motion. In view of the small slope of the deflected shape and small transverse velocity, let us neglect the transverse motion altogether and assume further that the membrane has enough bending rigidity so that buckling does not occur.

Under these assumptions, the configuration at the end of the third phase can be simplified as shown in Fig. 6(*a*). The velocity distribution indicated in this figure causes two compressive wave fronts K and K'. During further motion, Fig. 6(*b*), the material between the longitudinal waves G and K moves as a rigid body. The membrane force decreases continuously along GK; it has the value $f(f_1 < f < f_2)$ behind the wave front G and the value $-f_2$ immediately ahead of K. The motion of GK is constantly decelerated by the joint action of the membrane forces f and $-f_2$. This deceleration weakens the waves G and K so that the magnitude of the membrane forces f and f^* decreases. The detailed analysis of this case is similar to the analysis described in [4] and [5] and will not be given here. It suffices to note that the motion stops when K moved out a distance of $0.0002l$, so that the fourth phase of motion hardly changes the shape shown in Fig. 7.

References

1 J. W. Lisanby, J. E. Rasmussen, and H. M. Schauer, "Comparison of Dynamic Yield Effects of Steel," UERD Report 10-57, Underwater Explosions Research Division, Norfolk Naval Shipyard, Portsmouth, Va., June, 1957.

2 G. I. Taylor, "The Distortion Under Pressure of a Diaphragm Which Is Clamped Along its Edge and Stressed Beyond the Elastic Limit," Underwater Explosion Research, vol. 3—The Damage Progress, Office of Naval Research, Department of the Navy.

3 E. H. Lee and H. Wolf, "Plastic-Wave Propagation Effects in High-Speed Testing," JOURNAL OF APPLIED MECHANICS, vol. 18, TRANS. ASME, vol. 73, 1951, pp. 379–386.

4 G. I. Taylor, "The Use of Flat-Ended Projectiles for Determining Dynamic Yield Stress—1. Theoretical Considerations," *Proceedings of the Royal Society*, London, series A, vol. 194, 1948, pp. 289–299.

5 E. H. Lee and S. J. Tupper, "Analysis of Plastic Deformation in a Steel Cylinder Striking a Rigid Target," JOURNAL OF APPLIED MECHANICS, vol. 21, TRANS. ASME, vol. 74, 1954, pp. 63–72.

6 K. A. Rahmatulin, "On the Oblique Impact on an Elastic String at High Speeds in the Presence of Friction," *Prikladnaya Matematika i Mekhanika*, vol. 9, 1945, pp. 449–462 (in Russian).

7 K. A. Rahmatulin, "On the Impact on an Elastic Strand," *Prikladnaya Matematika i Mekhanika*, vol. 11, 1947, pp. 379–382 (in Russian).

8 J. W. Craggs, "Wave Motion in Plastic-Elastic Strings," *Journal of Mechanics and Physics of Solids*, vol. 2, 1954, pp. 286–295.

9 N. Cristescu, "Probleme Dinamice in Teoria Plasticitătii," *Editura Technica*, Bucuresti, 1958.

The Motion and Loading of a Hinged Ramp Which Supports a Sliding Mass

B. SAELMAN
Engineer,
Lockheed Aircraft Corp.
Burbank, Calif.

Equations of motion of a hinged ramp supporting a sliding mass, which moves at constant velocity, are derived; these are shown to have no closed solution when the ramp is spring supported or when the cylinder force is proportional to the square of the velocity. For small velocities of the sliding mass the Coriolis term may be neglected and a good approximation to the solution of the equations is obtained by means of the Madelung transformation. The solutions by special methods are compared to the solutions obtained by standard numerical methods.

Some military cargo aircraft are designed to discharge large pieces of equipment during flight. This is accomplished by extending a large ramp, located at the rear of the airplane, to a horizontal position; then the cargo is moved through the body of the airplane to the end of the ramp, usually by means of the aerodynamic forces acting on a drag chute attached to the mass, and from which it is dropped. This is illustrative of the problem herein considered.

Assumptions

1 The sum total of external forces on the mass parallel to the ramp is zero so that the velocity of the sliding mass on the ramp is constant. Thus in the case of a mass dispatched from a ramp in an air drop the drag chute could be designed so that the resulting aerodynamic forces on the chute would just equal the sliding friction forces. The mass would be accelerated from rest to the design velocity before reaching the ramp-hinge point. The force on the drag chute remains parallel to the ramp.

2 The force at the hydraulic cylinder remains perpendicular to the ramp.

3 The ramp deflections are such that powers greater than unity of the ramp angle can be neglected.

Contributed by the Applied Mechanics Division and presented at the Annual Meeting, Atlantic City, N. J., November 29–December 4, 1959, of The American Society of Mechanical Engineers.

Discussion of this paper should be addressed to the Secretary, ASME, 29 West 39th Street, New York, N. Y., and will be accepted until April 10, 1960, for publication at a later date. Discussion received after the closing date will be returned.

Note: Statements and opinions advanced in papers are to be understood as individual expressions of their authors and not those of the Society. Manuscript received by ASME Applied Mechanics Division, April 14, 1958. Paper No. 59—A-85.

Equations of Motion

The basic equations of motion for the system in Fig. 1 are

$$Mg - P\cos\theta = M\ddot{y} \tag{1}$$

and

$$PVt - Fb = I_R\ddot{\theta} \tag{2}$$

where

$$y = \frac{Vt}{l}\,x \tag{3}$$

Combining Equations (1), (2), and (3), we have

$$\left(\frac{I_R}{l^2} + \frac{MV^2t^2}{l^2}\right)\ddot{x} + \frac{2MV^2t}{l^2}\,\dot{x} + \frac{\beta b^2\dot{x}^2}{l^2} - \frac{MgV}{l}\,t = 0 \tag{4}$$

where

$$F = \frac{\beta b\dot{x}^2}{l}$$

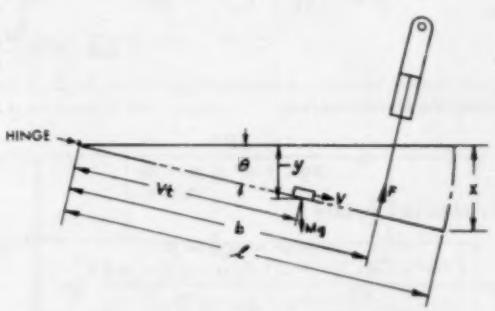

Fig. 1 Ramp supporting a sliding mass

Nomenclature

W = weight of sliding body, lb
M = mass of sliding body, lb/g
V = velocity of sliding body, ips
P = force between ramp and sliding body, lb
F = force in ramp supporting structure, lbs
l = length of ramp, in.
b = distance from ramp hinge to supporting structure, in.
k = spring constant, lb per in.
β = damping constant, lb/(in./sec)^2
I_R = moment of inertia of ramp about its hinge, lb/g-sq in.
T = applied torque about ramp hinge, in-lb
θ = angular deflection of ramp, radians
I = moment of inertia of ramp and sliding mass about ramp hinge, lb/g-sq in.
x = deflection of ramp at its extremity, in.
x_{max} = maximum deflection of ramp at its extremity, in.
y = deflection of ramp at instantaneous location of sliding mass, in.
t = time for traversing distance from hinge to arbitrary point on ramp, sec
g = acceleration of gravity, 386 ips

It was assumed in Equation (4) that the cylinder force is proportional to the square of the velocity. This is true for orifices in a thin plate. However, for viscous (linear) damping such as occurs as a result of flow in a long tube, $F = \beta b^2 \dot{x}/l$ and the solution of the differential equation is

$$x = \int \left\{ \left[\int \frac{et}{a + Bt^2} e^{\int \frac{ct+d}{a+Bt^2} dt} dt + K_1 \right] e^{-\int \frac{ct+d}{a+Bt^2} dt} \right\} dt + K_2 \quad (5)$$

where

$$a = \frac{I_R}{l^2}, \quad B = \frac{MV^2}{l^2}, \quad c = \frac{2MV^2}{l^2}, \quad d = \frac{\beta b^2}{l^2}, \quad e = \frac{MgV}{l}$$

Equation (4) could have been written directly from the fundamental equation

$$\frac{d}{dt}(I\dot{\theta}) - T = 0 \quad (6)$$

where

$$I = I_R + MV^2 t^2$$

and

$$T = MgVt - Fb \quad (7)$$

Reduction of Equation (4) to a Canonical Form and Proof That It Has No Closed Finite Solution

Let us write Equation (4) as

$$\dot{y} + \frac{Ct}{\phi} y + \frac{D}{\phi} y^2 - \frac{Et}{\phi} = 0 \quad (8)$$

where

$$y = \dot{x}, \quad \phi = \frac{I_R}{l^2} + \frac{MV^2 t^2}{l^2}, \quad C = \frac{2MV^2}{l^2}, \quad D = \frac{\beta b^2}{l^2},$$

and $$E = \frac{MgV}{l}$$

Applying the transformation,

$$\dot{y} = \frac{2Et^2}{2t\phi u + ct^2 + \phi - t\dot{\phi}} \quad (9)$$

to Equation (8), we have

$$\dot{u} + u^2 - \psi(t) = 0 \quad (10)$$

where

$$\psi(t) = \frac{3\phi^2 t - 2t^2\phi\dot{\phi} + c^2 t^5 - 2t^3\phi\dot{\phi} + 4DEt^4 - t^3\dot{\phi}^2}{4t^2\phi^2} \quad (11)$$

Then the transformation

$$u = \frac{1}{\sigma}\frac{d\sigma}{dt} \quad (12)$$

reduces Equation (10) to

$$\frac{d^2\sigma}{dt^2} - \psi(t)\sigma = 0 \quad (13)$$

It will now be shown that the special case of Equation (8) given by

$$\dot{y} + Dy^2 = Et, \qquad (D, E \text{ const}) \quad (14)$$

has no solution in finite form; hence Equation (8) has no such solution. Watson[1] shows that the Riccati equation,

$$\dot{y} + Ay^2 = Bt^m, \quad (15)$$

where A and B are constants is integrable in closed finite terms, if and only if

$$m = -2 \text{ or } m = \frac{-4i}{2i \pm 1} \quad (i = 0, 1, 2, 3, \ldots\ldots\ldots) \quad (16)$$

Equation (14) with $m = 1$ is not included in this set of numbers; hence it follows that Equation (14) and, *a fortiori*, Equation (8) has no solution in closed finite form. Of course, for special values of the constants, Equation (8) may have finite solution; e.g., the equation,

$$(c_1 + c_2 t^2)\dot{y} + y^2 + c_3 t = 0 \quad (17)$$

where

$$4c_1c_2^3 - c_3^2 = 0 \quad (18)$$

has the particular solution

$$y = \frac{c_2}{2c_1} - c_3 t \quad (19)$$

But when a particular solution of a Riccati equation is determined, its general solution also exists.

Approximation to the Solution of the Equation of Motion When V Is Small and When the Ramp Is Spring Supported

Substituting $s = Vt$ and $F = kbx/l$ into Equation (4), we have

$$\left(\frac{I_R}{l^2} + \frac{Ms^2}{l^2}\right)\ddot{x} + \frac{2MsV}{l^2}\dot{x} + \frac{kb^2x}{l^2} - \frac{Mgs}{l} = 0 \quad (20)$$

It is obvious that when V is small, the second term, which is due to the Coriolis forces arising from the motion of a body on a carrier, which itself is in rotating motion, can be neglected. We have

$$\left(\frac{I_R}{l^2} + \frac{MV^2t^2}{l^2}\right)\ddot{x} + \frac{kb^2x}{l^2} - \frac{MgV}{l}t = 0 \quad (20a)$$

$$x = 0 \quad \text{when} \quad t = 0$$
$$\dot{x} = 0 \quad \text{when} \quad t = 0$$

The transformation

$$x = cv\tau + y \quad (21)$$

where

$$t = \left(\frac{I_R}{kb^2}\right)^{1/2}\tau, \qquad v = \left(\frac{M}{kb^2}\right)^{1/2}V, \qquad c = \frac{Mgl}{kb^2}\left(\frac{I_R}{M}\right)^{1/2}$$

is applied to Equation (20a). There results

$$(1 + v^2\tau^2)\ddot{y} + y = 0 \quad (22)[2]$$

$$\dot{y} = -cv \quad \text{when} \quad \tau = 0$$
$$y = 0 \quad \text{when} \quad \tau = 0$$

Applying the Madelung transformation,[3] the general solution of

[1] G. N. Watson, "A Treatise On The Theory of Bessel Functions," McGraw-Hill Book Company, Inc., New York, N. Y., 1944, p. 123.

[2] In the following development the derivatives are with respect to τ.

[3] D. R. Hartree, "Numerical Analysis," Oxford University Press, London, England, 1952.

Equation (22) will be written

$$y = A\xi \sin\left\{B + \int \frac{d\tau}{\xi^2}\right\} \tag{23}$$

where ξ has to satisfy the nonlinear differential equation

$$\xi^3\ddot{\xi} = 1 - \frac{\xi^4}{1 + v^2\tau^2} \tag{24}$$

If ξ is a slowly varying function, we may, as a first approximation, neglect the left-hand side of Equation (24), whence

$$\xi \doteqdot (1 + v^2\tau^2)^{1/4} \tag{25}$$

and by Equations (21) and (23) with the appropriate boundary conditions

$$x_{max} \doteqdot c v\tau - cv(1 + v^2\tau^2)^{1/4} \sin\left\{\frac{1}{v} \sinh^{-1} v\tau\right\} \tag{26}$$

The differential equation which Equation (26) satisfies exactly is

$$\frac{1 + v^2\tau^2}{1 - \frac{v^2}{4}\left(\frac{2 - v^2\tau^2}{1 + v^2\tau^2}\right)} \ddot{x} + x = cv\tau \tag{27}$$

It is noted that

$$v^2\tau^2 = \frac{M}{I_R} V^2 t^2 \tag{28}$$

The condition is now imposed that $v\tau$ and v are of such a magnitude that the denominator of Equation (27) is close to unity; then we can write:

$$\left|\frac{v^2}{4} \frac{2 - v^2\tau^2}{1 + v^2\tau^2}\right| < \epsilon \tag{29}$$

where ϵ is a small quantity. A plot[4] of

$$1 - \frac{v^2}{4}\left(\frac{2 - v^2\tau^2}{1 + v^2\tau^2}\right)$$

for $v\tau = 8.68$ is given in Fig. 2. Thus it is seen that Equation (27) closely approximates the differential equation given by Equation (22).

An improved solution is obtained by using Equation (25) as a first approximation. If Equation (25) is a good approximation, it may be used to evaluate the left side of Equation (24). This yields an improved expression for (25)

$$\xi^4 \doteqdot \left(1 - \frac{v^2}{2}\right) + v^2\tau^2\left(1 + \frac{v^2}{4}\right) \tag{30}$$

Then the value of x_{max} becomes

$$x_{max} \doteqdot cv\tau - cv\left(1 - \frac{v^2}{2}\right)^{1/2} \left\{1 + \frac{4 + v^2}{4 - 2v^2} v^2\tau^2\right\}^{1/4} \sin\left\{\frac{2}{v(4 + v^2)^{1/2}} \sinh^{-1} v\tau \left(\frac{4 + v^2}{4 - 2v^2}\right)^{1/2}\right\} \tag{31}$$

As before we find that the equation which (31) satisfies exactly is

$$\frac{1 + v^2\tau^2}{1 + E} \ddot{x} + x = cv\tau \tag{32}$$

where

$$E = \frac{v^2}{16} \frac{-2\left(1 - \frac{v^2}{2}\right) + \left(8 + \frac{5v^2}{4}\right) v^2\tau^2 + \left(1 + \frac{v^2}{4}\right) v^4\tau^4}{\left[1 - \frac{v^2}{2} + \left(1 + \frac{v^2}{4}\right) v^2\tau^2\right]^2}$$

The function, $1 + E$, differs very little from unity for a practical range of the variables, so that (31) is a close approximation to the required solution. The function, $1 + E$, is also given in Fig. 2 for $v\tau = 8.68$. The process of approximation could be continued further by substitution from (30) on the left side of (24), but the result is very unwieldy and the accuracy of (26) is probably quite sufficient.

Considering (26) it is seen that, when $v\tau$ is constant,

$$\lim_{v \to 0} x_{max} = cv\tau \tag{33}$$

and for the physical system,

$$cv\tau = \frac{MgVl}{kb^2} = \frac{Mgl^2}{kb^2} \tag{34}$$

This is the static deflection of the ramp extremity when the mass is at rest at this extreme point, which is as expected for the limiting case indicated above for (26).

Approximation to the Solution of Equation (22) When $v\tau$ Is Large

When $v\tau$ is large compared to unity, Equation (22), expressed in terms of x, can be written

$$v^2\tau^2\ddot{x} + x - cv\tau = 0 \tag{35}$$

This is of the form of Cauchy's linear equation and can be solved by the method of variations of parameters. The exact solution of Equation (35) is

$$x = \begin{cases} cv\tau + G\tau^{1/2} \sin\left\{H + \left(\frac{1}{v^2} - \frac{1}{4}\right)^{1/2} \log \tau\right\}, & v < 2 \\ cv\tau + M\tau^{z_1} + N\tau^{z_2}, & v > 2 \end{cases} \tag{36}$$

where G, H, M, and N are constants of integration and where z_1 and z_2 are roots of the equation,

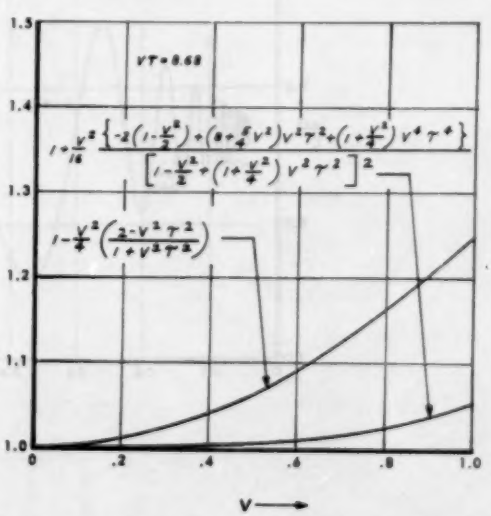

Fig. 2 Denominators of coefficients of $\ddot{x}$ of Equations (27) and (32)

[4] This is based on the values given in the example given later.

$$z^2 - z + \frac{1}{v^2} = 0$$

If v is sufficiently small but $v\tau$ is considerably larger than unity, Equation (31) degenerates to

$$x_{max} \doteq cv\tau - cv \left\{\left(1 - \frac{v^2}{2}\right)\left(1 + \frac{v^2}{4}\right) v^2\right\}^{1/4}$$

$$\tau^{1/2} \sin \left\{\frac{2}{v\,(4 + v^2)^{1/2}} \log\, 2v\tau \left(\frac{4 + v^2}{4 - 2v^2}\right)^{1/2}\right\} \quad (37)$$

The affinity of Equation (37) for Equation (36) is obvious.

Numerical Solutions of the Equations

Equation (4), except with the term, kb^2x/l^2, substituted for $\beta b^2\dot{x}^2/l^2$, is first considered. Assigning the numerical values

$W = 25{,}000$ lb, $k = 20{,}000$ lb per in., $l = 120$ in., $b = 93$ in., $I_R = 1.24 \times 10^4$ lb/g-sq in.

we have:

$$(0.86 + 0.00455V^2t^2)\ddot{x} + 0.00895V^2t\dot{x} + 12{,}000x - 208Vt = 0 \quad (38)$$

Equation (20a), for the same numerical values, reduces to

$$(0.86 + 0.00445V^2t^2)\ddot{x} + 12{,}000x - 208Vt = 0 \quad (39)$$

Using the method of Adams, Equations (38) and (39) (Table 1) are solved, with various values of V, for the deflection, x_{max}. This is accomplished by means of a high-speed computing

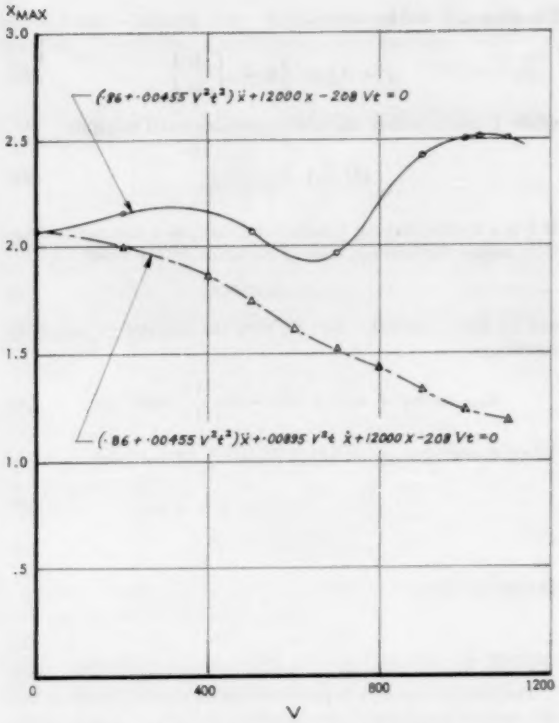

Fig. 3 Solutions of Equations (38) and (39)

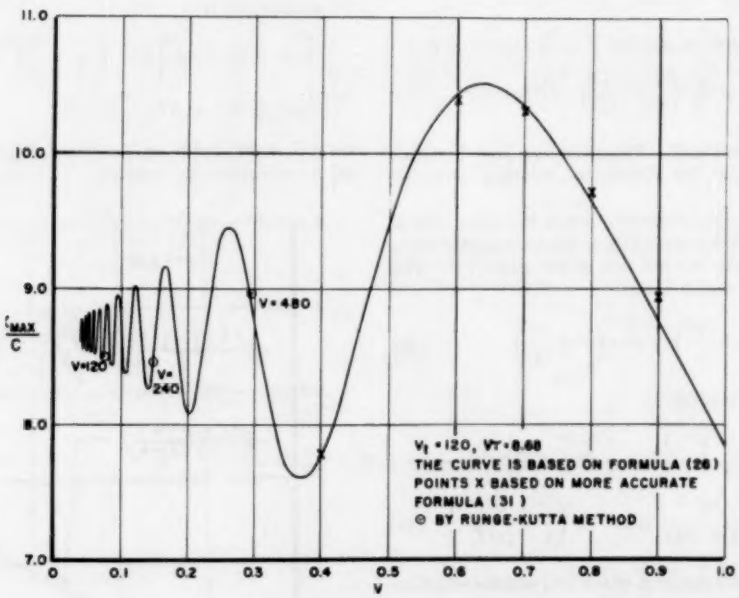

Fig. 4

Table 1 Values plotted in Figs. 3 and 4

	Fig. 3		Fig. 4		
V	x_{max} (Eq. 38)	x_{max} (Eq. 39)	v	x_{max}/c	x_{max}
120	2.04	2.12	0.073	8.51	2.04
240	1.98	2.17	0.147	8.47	2.02
480	1.77	2.10	0.294	8.97	2.15

machine and the results are plotted in Fig. 3. The curves indicate that, for small values of V, the Coriolis term may be, conservatively, neglected, and that, for large values of V, the error in x_{max} may be sizable as a result of neglecting the term due to the Coriolis forces.

The solutions for x_{max} given by Equation (26) and (31) and for three values of V have been computed and are compared with the values obtained from Fig. 3.

By the conditions given with (21) and (28),

$$v = 6.12 \times 10^{-4}V, v_T = 8.68, \text{ and } c = 0.24$$

Assuming that two springs support the ramp, the maximum force in each spring is

$$F = \frac{k}{2}\left(\frac{b}{l}\right)x_{max} = \frac{20{,}000}{2}\left(\frac{93}{120}\right)x_{max} = 7800x_{max}$$

Note that the static deflection, when the mass rests at the ramp extremity, is $x = 2.08$. This value is less than the values for x_{max} in Table 1 as obtained from Equation (39) but greater than the values obtained from Equation (38), which accounts for the Coriolis term.

An Analytical Method for Locating the Burmester Points for Five Infinitesimally Separated Positions of the Coupler Plane of a Four-Bar Mechanism

J. C. WOLFORD
Associate Professor,
Department of Engineering Mechanics,
The University of Nebraska,
Lincoln, Neb.
Assoc. Mem. ASME

A method is developed for analytically locating the Burmester points for the motion of the coupler plane of a four-bar mechanism through five infinitesimally separated positions. The results of an example are compared with the results obtained by the graphical method of Müller for locating the Burmester points. The two methods are found to give essentially identical results.

In the design of six-bar coupler-drive dwell mechanisms such as shown in Fig. 1, point D is located at the center of curvature of the path traced by point C. Then link 6 will dwell when the linkage is in the vicinity of the design position. For a better dwell in the vicinity of the design position, coupler point C is chosen on a curve, associated with the coupler link called the cubic of stationary curvature (in German, Kreisungspunktkurve) [1].[1] This curve applies for a single position of the mechanism, and points on this curve have the property that their point paths have stationary curvature at that instant. That is, the rate of change of the radius of curvature of the point path with respect to distance along the path is momentarily zero for all points of the curve. Four infinitesimally separated positions of each point lie on a circle.

If an even better dwell is required in the vicinity of the design position, it may be possible to choose the coupler point C such that both the first and second derivatives of the radius of curvature of the point path with respect to distance along the path are zero in the design position. Five infinitesimally separated positions of such points lie on a circle. Müller [2] proved that in the case of plane motion of a rigid plane system, there are four points in the moving plane which have this property. He called them Burmester points, since Burmester first noticed their existence. All four may be real, two may be real and two imaginary, or all four may be imaginary. Only the real Burmester points are of interest in linkage design.

[1] Numbers in brackets designate References at end of paper.

Contributed by the Applied Mechanics Division and presented at the Annual Meeting, Atlantic City, N. J., November 29–December 4, 1959, of The American Society of Mechanical Engineers.

Discussion of this paper should be addressed to the Secretary, ASME, 29 West 39th Street, New York, N. Y., and will be accepted until April 10, 1960, for publication at a later date. Discussion received after the closing date will be returned.

Note: Statements and opinions advanced in papers are to be understood as individual expressions of their authors and not those of the Society. Manuscript received by ASME Applied Mechanics Division, November 12, 1958. Paper No. 59—A-11.

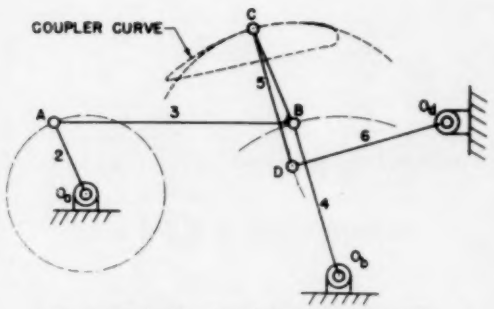

Fig. 1 Six-bar dwell mechanism—design position

Müller [2] made an extensive investigation of the motion of a rigid plane system through five infinitesimally separated positions, and he developed ingenious graphical methods for locating the Burmester points [3, 4].

When it is necessary to locate the Burmester points on the coupler link of a four-bar mechanism with considerable precision, as, for example, when a very precise dwell in the vicinity of the design position is required, an analytical approach may be preferred. A method for analytically locating the Burmester points is given in this paper.[2]

Mathematical Development[3]

The motion of a rigid plane system (a mechanism link, for ex-

[2] Subsequent to the acceptance of this paper by the ASME, the author became aware of the work of Allievi [5] on this problem. He gave an analytical method for locating Burmester points and, although the procedure which he gave is somewhat different than the one given in this paper, it gives identical end results.

[3] The initial portion of the development, up to and including the equation for the first derivative of the radius of curvature of the point path with respect to distance along the polode and the equation for the cubic of stationary curvature, is from "Notes on Kinematics," by A. S. Hall, Jr., Purdue University. It is repeated here because these notes are presently not generally available.

Nomenclature

D = diameter of inflection circle
P = pole or instant center of moving system
R = radius of curvature of moving polode
s = distance along point path
r, α = co-ordinates of points in the moving system. Point P is the origin of the co-ordinate system and angle α is measured from the pole tangent
ρ = radius of curvature of point path of a point in moving plane
σ = distance along moving polode

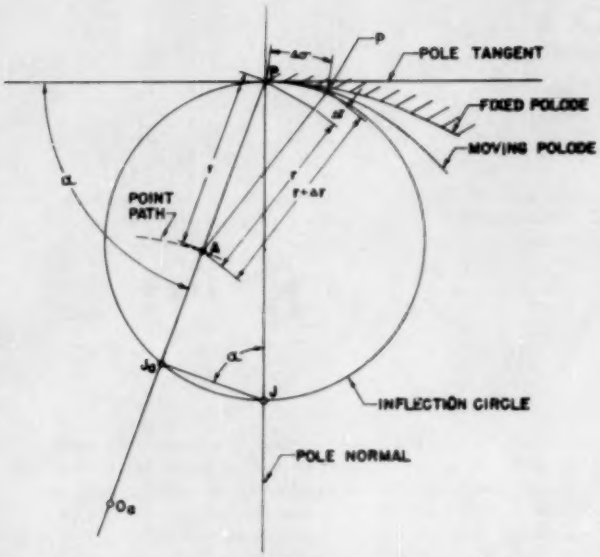

Fig. 2 Motion of rigid plane system represented by rolling of moving polode on fixed polode. (Letter "P" at top should read "P'")

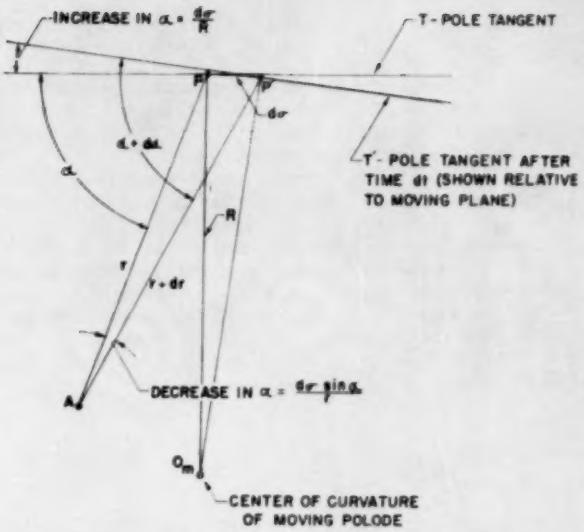
INCREASE IN α = dσ/R
T - POLE TANGENT
T' - POLE TANGENT AFTER TIME dt (SHOWN RELATIVE TO MOVING PLANE)
DECREASE IN α = dr sin α / r
CENTER OF CURVATURE OF MOVING POLODE

Fig. 3 Change in angle α as point of polode contact moves a distance $d\sigma$ along polode

ample) is represented in Fig. 2 by the rolling of the moving polode on the fixed polode. There are some points of the moving plane which are tracing paths such that the first derivative of the radius of curvature of the point path with respect to distance along the path is zero. That is, $d\rho/ds = 0$ at a given instant for some points. The locations of these points may be determined in the following manner:

Let point A, Fig. 2, be a point on the moving plane. Point O_a is the center of curvature of the path traced by point A, and J_a is the point where line PA crosses the inflection circle. The Euler-Savary equation relates distances O_aA, PA, and J_aA as follows:

$$O_aA = \frac{(PA)^2}{J_aA}$$

But $J_aA = PA - PJ \sin \alpha$, so

$$O_aA = \frac{(PA)^2}{PA - PJ \sin \alpha}$$

Letting $PA = r$, $O_aA = \rho$, and $PJ = D$, the equation becomes

$$\rho = \frac{r^2}{r - D \sin \alpha} \tag{1}$$

Since $d\rho/ds = (d\rho/d\sigma)(d\sigma/ds)$ and since $d\sigma/ds$ is not in general zero, $d\rho/ds$ will be zero when $d\rho/d\sigma = 0$. An expression for $d\rho/d\sigma$ is next obtained and equated to zero.

Differentiating Equation (1) gives

$$\frac{d\rho}{d\sigma} = \frac{1}{r - D \sin \alpha} 2r \frac{dr}{d\sigma} - \frac{r^2}{(r - D \sin \alpha)^2} \left[\frac{dr}{d\sigma} - D \cos \alpha \frac{d\alpha}{d\sigma} - \sin \alpha \frac{dD}{d\sigma} \right] \tag{2}$$

In Fig. 2, P is the point on the moving polode which is in contact with the fixed polode. Point P' is the point on the moving polode which will be in contact with the fixed polode after time Δt. The distance along the polode from P to P' is $\Delta\sigma$. Then

$$\lim_{\Delta\sigma \to 0} \frac{\Delta r}{\Delta \sigma} = \cos \alpha$$

Therefore, $dr/d\sigma$ in Equation (2) can be replaced by $\cos \alpha$.

From Fig. 3 it is seen that

$$d\alpha = \frac{d\sigma}{R} - \frac{d\sigma \sin \alpha}{r}$$

Therefore, $d\alpha/d\sigma$ in Equation (2) can be replaced by

$$\frac{1}{R} - \frac{\sin \alpha}{r}$$

Making these substitutions, Equation (2) becomes

$$\frac{d\rho}{d\sigma} = \frac{3r^2 D \sin \alpha \cos \alpha}{(r - D \sin \alpha)^2} \left\{ \frac{1}{\sin \alpha} \frac{1}{3} \left[\frac{1}{D} + \frac{1}{R} \right] + \frac{1}{\cos \alpha} \left[\frac{1}{3D} \frac{dD}{d\sigma} \right] - \frac{1}{r} \right\}$$

The magnitudes of D, R, and $dD/d\sigma$ do not vary with r and α; i.e., they are constant for any given position of the moving system. Letting

$$\frac{1}{3} \left[\frac{1}{D} + \frac{1}{R} \right] = \frac{1}{M} \tag{3}$$

and

$$\frac{1}{3D} \frac{dD}{d\sigma} = \frac{1}{N} \tag{4}$$

the expression for $d\rho/d\sigma$ becomes

$$\frac{d\rho}{d\sigma} = \frac{3r^2 D \sin \alpha \cos \alpha}{(r - D \sin \alpha)^2} \left[\frac{1}{M \sin \alpha} + \frac{1}{N \cos \alpha} - \frac{1}{r} \right] \tag{5}$$

From Equation (5), it is evident that $d\rho/d\sigma = 0$ for points (r, α) such that the expression in brackets is zero, except perhaps for the point where $r = D \sin \alpha$. Thus the locus of points having stationary curvature is given by

$$\frac{1}{r} = \frac{1}{M \sin \alpha} + \frac{1}{N \cos \alpha} \tag{6}$$

This is a third-degree equation defining a curve called the cubic of stationary curvature. The existence of such a curve was apparently first noticed by Burmester [6], and the equation for the curve was apparently first written by Léauté [7].

If Equation (6) is to be written for the coupler plane of a four-bar mechanism, the constants M and N may be determined easily. There are two points on the coupler plane which are known to lie on the curve—the centers of the pin joints at the ends of the cranks. Substituting the values of (r, α) for these two points into Equation (6) gives two equations in the two unknowns M and N. The values of M and N are then determined from these two equations.

Next, the locations of points tracing paths such that $d\rho/ds$ and $d^2\rho/ds^2$ are both zero are to be investigated. Since

$$\frac{d\rho}{ds} = \frac{d\rho}{d\sigma}\frac{d\sigma}{ds}$$

we have

$$\frac{d^2\rho}{ds^2} = \frac{d^2\rho}{d\sigma^2}\left[\frac{d\sigma}{ds}\right]^2 + \frac{d\rho}{d\sigma}\frac{d^2\sigma}{ds^2}$$

The quantities $d\sigma/ds$ and $d^2\sigma/ds^2$ will not in general be equal to zero. However, as previously noted, points for which $d\rho/ds = 0$ will also have $d\rho/d\sigma = 0$. Hence, for points having $d\rho/ds = d^2\rho/ds^2 = 0$, $d^2\rho/d\sigma^2$ must be equal to zero. An expression for $d^2\rho/d\sigma^2$ is next obtained.

Differentiating Equation (5) gives

$$\begin{aligned}\frac{d^3\rho}{d\sigma^2} = {} & \left\{3(r - D\sin\alpha)^2\left[2r\frac{dr}{d\sigma}D\sin\alpha\cos\alpha\right.\right. \\ & + r^2\frac{dD}{d\sigma}\sin\alpha\cos\alpha + r^2D\cos^2\alpha\frac{d\alpha}{d\sigma} - r^2D\sin^2\alpha\frac{d\alpha}{d\sigma}\Big] \\ & - 3r^2D\sin\alpha\cos\alpha\left[2(r - D\sin\alpha)\left(\frac{dr}{d\sigma} - D\cos\alpha\frac{d\alpha}{d\sigma}\right.\right. \\ & \left.\left.\left. - \sin\alpha\frac{dD}{d\alpha}\right)\right]\right\}\left[\frac{1}{(r - D\sin\alpha)^4}\right] \\ & \left[\frac{1}{M\sin\alpha} + \frac{1}{N\cos\alpha} - \frac{1}{r}\right] \\ & + \frac{3r^2D\sin\alpha\cos\alpha}{(r - D\sin\alpha)^2}\left[\frac{-M\cos\alpha\frac{d\alpha}{d\sigma} - \sin\alpha\frac{dM}{d\sigma}}{M^2\sin^2\alpha}\right. \\ & \left. + \frac{N\sin\alpha\frac{d\alpha}{d\sigma} - \cos\alpha\frac{dN}{d\sigma}}{N^2\cos^2\alpha} + \frac{\frac{dr}{d\sigma}}{r^2}\right] \end{aligned} \tag{7}$$

If, in the right-hand side of Equation (7), r is replaced by

$$\frac{NM\sin\alpha\cos\alpha}{N\cos\alpha + M\sin\alpha}$$

from Equation (6), an expression in α results. The roots of the equation obtained by equating the expression to zero give values of α which, along with the corresponding values of r obtained from Equation (6), locate points tracing paths for which $d\rho/d\sigma = d^2\rho/d\sigma^2 = 0$ at the instant.

Making the substitutions

$$r = \frac{NM\sin\alpha\cos\alpha}{N\cos\alpha + M\sin\alpha}$$

$$\frac{dr}{d\sigma} = \cos\alpha$$

and

$$\frac{d\alpha}{d\sigma} = \frac{1}{R} - \frac{\sin\alpha}{r}$$

in Equation (7), collecting and rearranging terms, equating the resulting expression to zero, and dividing through by $-RM^2\cos^4\alpha$ gives

$$\begin{aligned}\tan^4\alpha + \frac{RN - NM}{RM}\tan^3\alpha + \left[\frac{dN}{d\sigma} - 1\right]\tan^2\alpha \\ + \frac{N^2\frac{dM}{d\sigma} - 3NM}{M^2}\tan\alpha + \frac{N^2(M - 2R)}{RM^2} = 0\end{aligned} \tag{8}$$

Since this is a fourth-degree equation, it will have four roots. If we are dealing with the coupler link of a four-bar mechanism O_aABO_b, two of the roots of Equation (8) are known, since the pin joints at the ends of the cranks are tracing paths for which $d\rho/d\sigma = d^2\rho/d\sigma^2 = 0$. These roots are designated $\tan\alpha_a$ and $\tan\alpha_b$. Angles α_a and α_b are the known angles which lines PA and PB form with the pole tangent. The other two roots are designated $\tan\alpha_1$ and $\tan\alpha_2$.

Using a well-known property regarding the roots and coefficients of a quartic equation, we have

$$\tan\alpha_1 + \tan\alpha_2 + \tan\alpha_a + \tan\alpha_b = \frac{N(M - R)}{RM}$$

and

$$(\tan\alpha_1)(\tan\alpha_2)(\tan\alpha_a)(\tan\alpha_b) = \frac{N^2(M - 2R)}{RM^2}$$

or

$$\tan\alpha_1 + \tan\alpha_2 = \frac{N(M - R)}{RM} - \tan\alpha_a - \tan\alpha_b$$

and

$$(\tan\alpha_1)(\tan\alpha_2) = \frac{\frac{N^2(M - 2R)}{RM^2}}{(\tan\alpha_a)(\tan\alpha_b)}$$

Then by consideration of the property regarding the roots and coefficients of a quadratic equation, $\tan\alpha_1$ and $\tan\alpha_2$ are the roots of the quadratic

$$\begin{aligned}\tan^2\alpha + \left[\tan\alpha_a + \tan\alpha_b + \frac{N(R - M)}{RM}\right]\tan\alpha \\ + \frac{\frac{N^2(M - 2R)}{RM^2}}{(\tan\alpha_a)(\tan\alpha_b)} = 0\end{aligned} \tag{9}$$

The values of N and M are found, as previously mentioned, by substituting the known values of r and α for points A and B into Equation (6) and solving the resulting two equations for N and M. The value of R is most easily obtained from Equation (3), and $\tan\alpha_a$ and $\tan\alpha_b$ are known values. Then the unknown roots, $\tan\alpha_1$ and $\tan\alpha_2$, may be found easily. The values of α_1 and α_2 are then determined and the corresponding values of r found from Equation (6). These co-ordinates locate the two unknown Burmester points. If

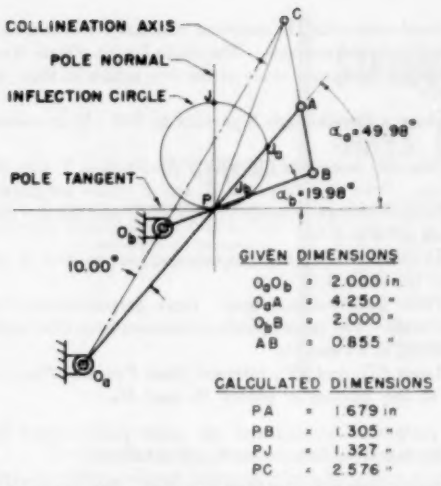

Fig. 4 Given four-bar mechanism for which the Burmester points, M_1 and M_2, are to be determined

$$\left[\tan\alpha_a + \tan\alpha_b + \frac{N(R-M)}{RM}\right]^2 - \frac{\dfrac{4N^2(M-2R)}{RM^2}}{(\tan\alpha_a)(\tan\alpha_b)} < 0$$

the two Burmester points are imaginary.

The method will be illustrated by a numerical example.

Example

A four-bar mechanism O_aABO_b is shown in Fig. 4. The lengths of the links and the position of crank O_aA are specified. The angles α_a and α_b, and the diameter of the inflection circle were determined analytically. Points A and B are two of the Burmester points for five infinitesimally separated positions of the coupler link AB, and it is required to find the other two Burmester points.

Substituting the known values of r and α for points A and B into Equation (6), and solving the two equations for N and M, we get

$$N = 4.269 \text{ in.}$$

$$M = 5.665 \text{ in.}$$

Substituting the known value of D (always positive) into Equation (3), we get

$$R = -4.462 \text{ in.}$$

Substituting the values for N, M, R, α_a, and α_b into Equation (9), we get

$$\tan^2\alpha + 3.265\tan\alpha - 4.288 = 0$$

from which

$$\tan\alpha_1 = +1.005$$

$$\tan\alpha_2 = -4.270$$

and

$$\alpha_1 = +45.15 \text{ deg}$$

$$\alpha_2 = -76.82 \text{ deg}$$

Substituting these values for α into Equation (6) gives

$$r_1 = 1.721 \text{ in.}$$

$$r_2 = 1.181 \text{ in.}$$

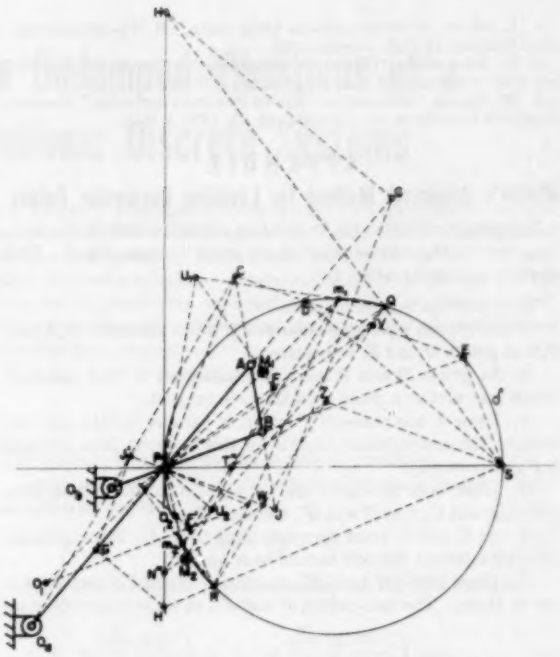

Fig. 5 Burmester points located by Müller's method

The co-ordinates (r_1, α_1) locate the Burmester point M_1 and the co-ordinates (r_2, α_2) locate the Burmester point M_2.

Müller's graphical method is applied to the same four-bar mechanism in Fig. 5 (see Appendix for graphical procedure). The co-ordinates of M_1 and M_2 by the graphical method are

$$\alpha_1 = 44.1 \text{ deg}$$

$$r_1 = 1.72 \text{ in.}$$

$$\alpha_2 = -76.8 \text{ deg}$$

$$r_2 = 1.18 \text{ in.}$$

Conclusion

The method presented can be used to locate the Burmester points, easily and accurately, for the motion of the coupler link of a four-bar mechanism through five infinitesimally separated positions. It can be used in lieu of Müller's graphical method if an analytical approach is preferred, or both methods can be used when a check is desired.

Acknowledgments

The author is indebted to the Engineering Experiment Station and the University Research Council of The University of Nebraska for financial support of this study.

References

1 Kurt Hain, "Angewandte Getriebelehre," Hermann Schroedel Verlag, Hannover, 1952, pp. 302–306.

2 R. Müller, "Ueber die Bewegung eines starren ebenen Systems durch fünf unendlich benachbarte Lagen," *Zeitschrift für Mathematik und Physik*, vol. 37, 1892, pp. 129–150.

3 Ibid., pp. 148–149.

4 R. Müller, "Construction der Burmester'schen Punkte für ein ebenes Gelenkviereck," *Zeitschrift für Mathematik und Physik*, vol. 37, 1892, pp. 211–217.

5 L. Allievi, "Cinematica della biella piana," R. Tipografia Francesco Giannini et Figli, Napoli, 1895.
6 L. Burmester, "Ueber die Geradführung durch das Kurbelgetriebe," *Civilingeneur*, vol. 22, 1876, pp. 598–606.
7 H. Léauté, "Mécanique—Sur les Systèmes Articulés," *Comptes Rendus de l'Académie des Sciences*, vol. 87, 1878, p. 153.

APPENDIX

Müller's Graphical Method for Locating Burmester Points

This graphical method is for locating the two unknown Burmester points on the coupler plane of a four-bar linkage, Fig. 5. The steps in the construction are:

1 Draw the collineation axis PC.

2 At C erect a perpendicular to PC which intersects O_aA and O_bB at points D and E, respectively.

3 At points D and E erect perpendiculars to O_aA and O_bB which intersect at a point S on the pole tangent.

4 Draw a line through P which is parallel to CD, and determine the intersections J and J' of this line with lines AB and O_aO_b, respectively.

5 Draw lines through J and J', parallel to PC. These lines will intersect O_aA at G and G', respectively.

6 At G and G' erect perpendiculars to O_aA. These perpendiculars intersect the pole normal at H and H'.

7 Draw lines SH and SH', and lines PQ and PR perpendicular to them. The mid-points, F and F', of these perpendiculars are the focal centers for the cubics of stationary curvature for the direct and inverted motions. The circle δ with PS as diameter is the mutual osculatory circle of the two cubics at their double point P.

8 Draw a line through S parallel to DE. It intersects RQ at Z.

9 Line RQ intersects DE and PJ at points V and W, respectively. Draw lines through W and Z which are parallel to PV. The line through W intersects PH at N'' and the line through Z intersects PS at T''.

10 Draw line $N''T''$ and get intersections m_1 and m_2 of this line with the circle δ.

11 Draw lines Qm_1 and Qm_2. Draw perpendiculars from P to these lines. The perpendiculars intersect lines Qm_1 and Qm_2, respectively, at U_1 and U_2.

12 Lines FU_1 and FU_2 intersect lines Pm_1 and Pm_2, respectively, at the Burmester points M_1 and M_2.

The centers of curvature of the point paths traced by the points M_1 and M_2 of link AB are found as follows:

1 Draw a perpendicular from P to Rm_1. Join the point at the foot of the perpendicular with F'. This line intersects line Pm_1 at O_1, the center of curvature of the path traced by M_1.

2 Draw a perpendicular from P to Rm_2. Join the point at the foot of the perpendicular with F'. This line intersects line Pm_2 at O_2, the center of curvature of the path traced by M_2.

Steady-State Undamped Vibrations of a Class of Nonlinear Discrete Systems

P. R. SETHNA

Assistant Professor,
Department of Aeronautical Engineering,
University of Minnesota,
Minneapolis, Minn.

Steady-state vibrations of a class of nonlinear discrete systems with an arbitrary number of degrees of freedom are studied. The co-ordinates of the system are first transformed to the principal co-ordinates corresponding to the linear part of the system. A perturbation scheme is used to obtain the solutions. Some special effects of the ratios of the linear natural frequencies on the qualitative nature of the solutions are demonstrated. Solutions are obtained for some specific problems and the results are checked against those obtained from an analog-type computer.

STEADY-state vibrations of multiple-degrees-of-freedom systems with nonlinear restoring forces have been studied in the past by Arnold [1],[1] Klotter [2], Huang [3], Rosenberg [4], Rosenberg and Atkinson [5], the author [6], and others. In most cases the systems are restricted to those of two degrees of freedom and with one of the restoring forces nonlinear. The methods used to obtain the response relationships can often be extended to more general systems but not without a great increase in difficulty in the solution of the resulting higher order algebraic equations.

The method indicated in this investigation is applicable to certain classes of discrete systems with an arbitrary number of degrees of freedom. No restriction is placed on the number of nonlinear restoring forces but they are limited as to the nature of the nonlinear terms.

One feature of the method is that it demonstrates the effect of the ratios of the linear natural frequencies on the qualitative nature of the solutions.

General Theory for N Degrees of Freedom

Consider a discrete dynamical system of N degrees of freedom with potential energy

$$V = V(q_1, q_2, \ldots . q_N) \tag{1}$$

where q_i, $i = 1, 2, \ldots . N$ are the N generalized co-ordinates.[2] The q_i are to be chosen as dimensionless quantities.

Let q_{0i}, $i = 1, 2 \ldots N$ be the values of the co-ordinates at some equilibrium configuration. Let

$$q_i = q_{0i} + \eta_i \tag{2}$$

Then expanding the potential energy in Taylor's expansion

$$V = V_0 + \sum_{i=1}^{N} \left(\frac{\partial V}{\partial q_i}\right)_0 \eta_i + {}^1/_2! \sum_{i,j=1}^{N} \left(\frac{\partial^2 V}{\partial q_i \partial q_j}\right)_0 \eta_i \eta_j + {}^1/_3! \sum_{i,j,k=1}^{N} \left(\frac{\partial^3 V}{\partial q_i \partial q_j \partial q_k}\right)_0 \eta_i \eta_j \eta_k + \ldots$$

where V_0 is a constant immaterial to the problem, which will be assumed zero. For equilibrium

$$\left(\frac{\partial V}{\partial q_i}\right)_0 = 0, i = 1, 2 \ldots N$$

Introduce the notation

$$V_{ij} = \left(\frac{\partial^2 V}{\partial q_i \partial q_j}\right)_0; \quad V_{ijk} = \left(\frac{\partial^3 V}{\partial q_i \partial q_j \partial q_k}\right)_0, \text{ etc.}$$

This study will be restricted to those problems where all the coefficients of the power of η_i are zero except V_{ij} and V_{ijkl}; $i, j, k, = 1, 2 \ldots N$

Thus we have

$$V = 1/2! \sum_{i,j=1}^{N} V_{ij} \eta_i \eta_j + {}^1/_4! \sum_{i,j,k,l=1}^{N} V_{ijkl} \eta_i \eta_j \eta_k \eta_l \tag{3}$$

The kinetic energy will be of the form

$$T = {}^1/_2 \sum_{i,j=1}^{N} T_{ij} \dot{\eta}_i \dot{\eta}_j; \; T_{ij} = T_{ji}, \quad i, j = 1, 2 \ldots N \tag{4}$$

[1] Numbers in brackets designate References at end of paper.

[2] The notation and the underlying linear theory is the same as in [7].

Contributed by the Applied Mechanics Division and presented at the Annual Meeting, Atlantic City, N. J., November 29–December 4, 1959, of THE AMERICAN SOCIETY OF MECHANICAL ENGINEERS.

Discussion of this paper should be addressed to the Secretary, ASME, 29 West 39th Street, New York, N. Y., and will be accepted until April 10, 1960, for publication at a later date. Discussion received after the closing date will be returned.

NOTE: Statements and opinions advanced in papers are to be understood as individual expressions of their authors and not those of the Society. Manuscript received by ASME Applied Mechanics Division, February 5, 1959. Paper No. 59—A-67.

Nomenclature

V = potential energy
q_i = ith generalized co-ordinate
q_{0i} = ith generalized co-ordinate at equilibrium
η_i = ith generalized co-ordinate from equilibrium position
ζ_i = ith principal co-ordinate
T = kinetic energy
Q_i = ith generalized force
a_{ij} = ith component of jth eigenvector
Ω = circular frequency of excitation force
ω_i = ith natural circular frequency
C_i = amplitude of the ith external force
m_i = mass of ith particle
k_i = coefficient of linear term of ith spring
h_i = coefficient of nonlinear term of ith spring
A_i = amplitude of ith principal co-ordinate

where a dot above a variable denotes differentiation with respect to time. For the purpose of this study the T_{ij} will be assumed to be constants.

Using Lagrange's equations we have

$$\frac{d}{dt}\left(\frac{\partial T}{\partial \dot{\eta}_r}\right) - \frac{\partial V}{\partial \eta_r} = Q_r \qquad r = 1, 2 \ldots N \tag{5}$$

where Q_r is the generalized force corresponding to the rth generalized co-ordinate η_r and has the dimension of work.

Using (3) and (4) the equations of motion are

$$\sum_{i=1}^{N} T_{ri}\ddot{\eta}_i + \sum_{i=1}^{N} V_{ri}\eta_i + {}^1/_{3!}\sum_{i,j,k=1}^{N} V_{rijk}\eta_i\eta_j\eta_k = Q_r$$

$$r = 1, 2 \ldots N \tag{6}$$

Let

$$\eta_i = \alpha\xi_i \tag{7}$$

where α is a positive dimensionless parameter.

Using (7) equation (6) becomes

$$\sum_{i=1}^{N} T_{ri}\ddot{\xi}_i + \sum_{i=1}^{N} V_{ri}\xi_i = -\frac{\alpha^2}{3!}\sum_{i,j,k=1}^{N} V_{rijk}\xi_i\xi_j\xi_k + \left(\frac{Q_r}{\alpha}\right) \tag{8}$$

The equations which result from taking the right-hand side of (8) equal to zero are the equations of free linear oscillations of the system. If $\xi_j = a_j e^{i\omega t}$, where $i = \sqrt{-1}$, then the frequency equation for ω is obtained from

$$\begin{vmatrix} V_{11} - \omega^2 T_{11} & V_{12} - \omega^2 T_{12} \ldots V_{1N} - \omega^2 T_{1N} \\ \cdot & \cdot \quad \cdot \quad \cdot \quad \cdot \\ V_{N1} - \omega^2 T_{N1} & V_{N2} - \omega^2 T_{N2} \ldots V_{NN} - \omega^2 T_{NN} \end{vmatrix} = 0 \tag{9}$$

The roots ω_i, $i = 1, 2 \ldots N$ of (9) will be assumed to be simple.

Let ζ_i, $i = 1, 2 \ldots N$ be the principal co-ordinates corresponding to the linear system [7]. Then

$$\xi_i = \sum_{j=1}^{N} a_{ij}\zeta_j \qquad i = 1, 2 \ldots N \tag{10}$$

where a_{ij} is the ith component of the jth eigenvector.

Then from the properties of eigenvectors

$$\sum_{i,j=1}^{N} T_{ij}a_{ik}a_{jl} = 0 \qquad k \neq l$$

$$k, l = 1, 2 \ldots N$$

Let

$$\sum_{i,j=1}^{N} T_{ij}a_{ik}a_{jk} = K_{kk} \qquad k = 1, 2 \ldots N \tag{11}$$

where K_{kk}, $k = 1, 2 \ldots N$ are constants to be chosen such that the largest a_{ij} corresponding to the jth natural frequency will be equal to unity. Note a_{ij} will be dimensionless if K_{kk} has the same dimensions as T.

Consider the terms on the right-hand side of (8) as forces R_j. The force corresponding to the rth principal co-ordinate transforms as follows:

$$N_r = \sum_{j=1}^{N} a_{jr}R_j \qquad r = 1, 2 \ldots N \tag{12}$$

Using (10), (11), and (12) the equations of motion in terms of the principal co-ordinates become

$$\frac{1}{\omega_m^2}\ddot{\zeta}_m + \zeta_m = -\sum_{i,j,k,l,p,q,r=1}^{N} a_{im}a_{jp}a_{ir}a_{kq}\frac{\alpha^2}{3!}\frac{V_{ijkl}}{K_{mm}\omega_m^2}\zeta_p\zeta_q\zeta_r + \sum_{i=1}^{N} a_{im}\frac{Q_i}{\alpha K_{mm}\omega_m^2} \tag{13}$$

where $m = 1, 2 \ldots N$ and ω_m, $m = 1, 2 \ldots N$ are the linear natural frequencies which are the roots of (9).

Examine all the terms $V_{ijkl}/K_{mm}\omega_m^2$, $i, j, k, l, m = 1, 2 \ldots N$ and select one that is a maximum in absolute value, say $V_{abcd}/K_{ff}\omega_f^2$, for some specific values of a, b, c, d, and f.

$$\text{Now let } U_{ijklm} = \frac{V_{ijkl}}{K_{mm}\omega_m^2}\left|\frac{K_{ff}\omega_f^2}{V_{abcd}}\right| \tag{14}$$

where all the U_{ijklm}, $i, j, k, l, m = 1, 2 \ldots N$ will be less than or equal to unity in absolute value. There may be more than one of the U_{ijklm}, $i, j, k, l, m = 1, 2 \ldots N$ having an absolute value equal to unity if more than one of the combinations $V_{ijkl}/K_{mm}\omega_m^2$ have values equal in magnitude to $V_{abcd}/K_{ff}\omega_f^2$.

Introduce the parameter

$$\epsilon = \left|\frac{\alpha^2}{3!}\frac{V_{abcd}}{K_{ff}\omega_f^2}\right| \tag{15}$$

and the notation

$$F_{im} = \frac{Q_i}{\alpha K_{mm}\omega_m^2}\frac{1}{\epsilon}$$

Then (13) can be written as

$$\frac{1}{\omega_m^2}\ddot{\zeta}_m + \zeta_m = -\epsilon\sum_{i,j,k,l,p,q,r=1}^{N} a_{im}a_{jp}a_{kq}a_{lr}U_{ijklm}\zeta_p\zeta_q\zeta_r + \epsilon\sum_{i=1}^{N} a_{im}F_{im} \tag{16}$$

The arbitrary parameter α is now to be adjusted so that the positive quantity ϵ will be much less than one. Using this value of α the generalized forces Q_i, $i = 1, 2 \ldots N$ will be restricted in magnitude so that F_{im}, $i, m = 1, 2 \ldots N$ will be quantities less than or equal to one in magnitude.

Let F_{im} be periodic with least period $2\pi/\Omega$. Let $\Omega t = \theta$ and derivatives with respect to θ be represented by primes. Then (16) becomes

$$\frac{\Omega_m^2}{\omega_m^2}\zeta_m'' + \zeta_m = -\epsilon\sum_{i,j,k,l,p,q,r=1}^{N} a_{im}a_{jp}a_{kq}a_{lr}U_{ijklm}\zeta_p\zeta_q\zeta_r + \epsilon\sum_{i=1}^{N} a_{im}F_{im} \tag{17}$$

where $\Omega_m = \Omega$, $m = 1, 2, 3 \ldots N$ are written in this manner for reasons that will be apparent later.

The following conditions will be imposed on the solutions:

$$\zeta_m(\theta) = \zeta_m(\theta + 2\pi) \qquad m = 1, 2 \ldots N \tag{18a}$$

$$\zeta_m(0) = A_m \qquad m = 1, 2 \ldots N \tag{18b}$$

$$\zeta_m'(0) = 0 \qquad m = 1, 2 \ldots N \tag{18c}$$

Approximate solutions of (17) with conditions (18) can be obtained by any one of several iterative or perturbation methods. The following perturbation scheme will be used.

Let

$$\Omega_i = \Omega_0 + \sum_{u=1}^{\infty}\Omega_{i,u}\epsilon^u \tag{19}$$

$$\zeta_i = \sum_{u=0}^{\infty} \zeta_{i,u}\epsilon^u \qquad i = 1, 2 \ldots N \tag{20}$$

where Ω_0 and $\Omega_{m,u}$ are constants and $\zeta_{i,u} = \zeta_{i,u}(\theta)$.

Substituting in (17) and equating coefficients of powers of ϵ we have:

From ϵ^0

$$\frac{\Omega_0^2}{\omega_m^2}\zeta_{m,0}'' + \zeta_{m,0} = 0 \tag{21}$$

From ϵ'

$$\frac{\Omega_0^2}{\omega_m^2}\zeta_{m,1}'' + \zeta_{m,1} = -\frac{2\Omega_0\Omega_{m,1}}{\omega_m^2}\zeta_{m,0}'' - \sum_{i,j,k,l,p,q,r=1}^{N} a_{im}a_{jp}a_{kq}a_{lr}U_{ijklm}\zeta_{p,0}\zeta_{q,0}\zeta_{r,0} + \sum_{i=1}^{N} a_{im}F_{im} \tag{22}$$

From ϵ^2

$$\frac{\Omega_0^2}{\omega_m^2}\zeta_{m,2}'' + \zeta_{m,2} = -\frac{2\Omega_0\Omega_{m,1}}{\omega_m^2}\zeta_{m,1}'' - \frac{2\Omega_0\Omega_{m,2} + \Omega_{m,1}^2}{\omega_m^2}\zeta_{m,0}'' - 3\sum_{i,j,k,l,p,q,r=1}^{N} a_{im}a_{jp}a_{kq}a_{lr}U_{ijklm}\zeta_{p,0}\zeta_{r,0}\zeta_{r,1} \tag{23}$$

Condition (18*a*) will be satisfied by letting

$$\zeta_{m,u}(\theta) = \zeta_{m,u}(\theta + 2\pi) \qquad m = 1, 2 \ldots N, \quad u = 0, 1 \ldots \infty \tag{24a}$$

As will be apparent later, in order to obtain steady-state solutions only one of the A_m can be prescribed arbitrarily in (18*b*). The remaining A_m are obtained in terms of this one with progressively improved accuracy at each step of perturbation procedure.

Condition (18*b*) will be satisfied by letting

$$\zeta_{m,0}(0) = A_m \qquad m = 1, 2 \ldots N \tag{24b}$$

$$\zeta_{m,u}(0) = 0 \qquad m = 1, 2 \ldots N, \quad u = 1, 2 \ldots \infty$$

Condition (18*c*) will be satisfied by letting

$$\zeta_{m,u}'(0) = 0, \qquad m = 1, 2 \ldots N, \qquad u = 0, 1 \ldots \infty \tag{24c}$$

Terms of Zero Order in ϵ.

$$\frac{\Omega_0^2}{\omega_m^2}\zeta_{m,0}'' + \zeta_{m,0} = 0 \tag{25}$$

$$\zeta_{m,0} = D_{m,0}\cos\frac{\omega_m}{\Omega_0}\theta + E_{m,0}\sin\frac{\omega_m}{\Omega_0}\theta \qquad m = 1, 2 \ldots N \tag{26}$$

where $D_{m,0}$ and $E_{m,0}$ are arbitrary constants. From (24*a*), Ω_0 can be equal to any of the N natural frequencies. Let that frequency be called ω_1, not necessarily the lowest natural frequency. Of the remaining $N - 1$ natural frequencies say $S - 1$ natural frequencies are integral multiples of ω_1, thus

$$\omega_i = n_i\omega_1 \qquad i = 1, 2 \ldots S \tag{27}$$

where n_i, $i = 1, 2 \ldots S$ are positive integers. Arrange these S natural frequencies in ascending order of magnitude $\omega_1, \omega_2 \ldots \omega_s$. The remaining $N - S$ frequencies, some of which are less and some greater in magnitude than ω_1, can now be arranged in ascending order of magnitude. Thus from (24*a*) we have

$$\zeta_{m,0} = D_{m,0}\cos n_m\theta + E_{m,0}\sin n_m\theta, \quad m = 1, 2 \ldots S$$

$$\zeta_{m,0} = 0, \quad m = S + 1, \quad S + 2 \ldots N$$

From (24*c*) we have $E_{m,0} = 0$, $m = 1, 2 \ldots S$ and using (24*b*) the solutions of zero order are

$$\zeta_{m,0} = A_m\cos n_m\theta \qquad m = 1, 2 \ldots S \tag{28}$$

$$\zeta_{m,0} = 0 \qquad m = S + 1, \quad S + 2, \ldots N$$

Furthermore

$$\Omega_0 = \omega_1 \tag{29}$$

The constants A_m, $m = 1, 2, 3 \ldots S$ are arbitrary and $A_m = 0$, $m = S + 1, S + 2 \ldots N$ for solution up to zero order in ϵ.

Terms of First Order in ϵ. Substituting (27), (28), and (29) into the equation for the first approximation (22) we have for $m = 1, 2 \ldots S$

$$\frac{1}{n_m^2}\zeta_{m,1}'' + \zeta_{m,1} = \frac{2\Omega_0\Omega_{m,1}}{\omega_m^2}n_m^2A_m\cos n_m\theta + \sum_{i=1}^{N} a_{im}F_{im} - \sum_{i,j,k,l=1}^{N} a_{im}U_{ijklm}\sum_{p,q,r=1}^{S} a_{jp}a_{kq}a_{lr}A_pA_qA_r \cos n_p\theta\cos n_q\theta\cos n_r\theta \tag{30}$$

This can be written as

$$\frac{1}{n_m^2}\zeta_{m,1}'' + \zeta_{m,1} = \frac{2\Omega_0\Omega_{m,1}}{\omega_m^2}n_m^2A_m\cos n_m\theta + \sum_{i=1}^{N} a_{im}F_{im} - \sum_{i,j,k,l=1}^{N} a_{im}U_{ijklm}\sum_{p,q,r=1}^{S} a_{jp}a_{kq}a_{lr}A_pA_qA_r [3/4\cos(n_p + n_q - n_r)\theta + 1/4\cos(n_p + n_q + n_r)\theta] \tag{31}$$

Denote summation over those p, q, r where $p, q, r = 1, 2 \ldots S$ such that

$$|n_p + n_q - n_r| = n_m \text{ by } \sum_{p,q,r=1}^{S}{}'$$

and summation over those p, q, r where $p, q, r = 1, 2 \ldots S$ such that

$$|n_p + n_q + n_r| = n_m \text{ by } \sum_{p,q,r=1}^{S}{}''$$

and the summation over p, q, r where $p, q, r = 1, 2 \ldots S$ over the remaining combinations of

$$p, q, r \text{ by } \sum_{p,q,r=1}^{S}$$

Equations (31) can then be written as

$$\frac{1}{n_m^2}\zeta_{m,1}'' + \zeta_{m,1} = \frac{2\Omega_0\Omega_1}{\omega_m^2}n_m^2A_m\cos n_m\theta + \sum_{i=1}^{N} a_{im}F_{im} - \sum_{i,j,k,l=1}^{N} a_{im}U_{ijklm}\left\{[3/4\sum_{p,q,r=1}^{S}{}' a_{jp}a_{kq}a_{lr}A_pA_qA_r + 1/4\sum_{p,q,r=1}^{S}{}'' a_{jp}a_{kq}a_{lr}A_pA_qA_r]\cos n_m\theta\right.$$

$$+ \sum_{p,q,r=1}^{S} a_{jp}a_{kq}a_{lr}A_pA_qA_r \left[3/4 \cos (n_p + n_q - n_r)\theta + 1/4 \cos (n_p + n_q + n_r)\theta\right]\Bigg\} \quad (32)$$

Substituting (27), (28), and (29) into (22) we have for $m = S + 1, S + 2 \ldots N$

$$\frac{\omega_1^2}{\omega_m^2}\zeta_{m,1}'' + \zeta_{m,1} = \sum_{i=1}^{N} a_{im}F_{im} - \sum_{i,j,k,l=1}^{N} a_{im}U_{ijklm}\left\{\sum_{p,q,r=1}^{S} a_{jp}a_{kq}a_{lr}A_pA_qA_r \left[3/4 \cos (n_p + n_q - n_r)\theta + 1/4 \cos (n_p + n_q + n_r)\theta\right]\right\} \quad (33)$$

Now we restrict the Q_i, $i = 1, 2 \ldots N$ to functions of time such that

$$Q_i = C_i \cos \Omega t \quad (34)$$

where C_i are constants which can be positive or negative.

Let

$$P_{im} = \frac{C_i}{\alpha K_{mm}\omega_m^2}\frac{1}{\epsilon} \quad (35)$$

so that

$$F_{im} = P_{im} \cos \theta$$

In order that equation (32) will satisfy (24a), the right side must have no terms in $\cos n_m\theta$. Setting the coefficients of $\cos n_m\theta$ equal to zero we have the following secular equations:

When $m = 1$

$$\frac{2\Omega_0\Omega_{1,1}}{\omega_1^2}A_1 + \sum_{i=1}^{N} a_{i1}P_{i1} - \sum_{i,j,k,l=1}^{N} a_{i1}U_{ijkl1} \sum_{p,q,r=1}^{S}{}' 3/4\, a_{jp}a_{kq}a_{lr}A_pA_qA_r = 0 \quad (36)$$

When $m = 2, 3 \ldots S$

$$\frac{2\Omega_0\Omega_{m,1}}{\omega_m^2}n_m^2 A_m - \sum_{i,j,k,l=1}^{N} a_{im}U_{ijklm}\left[3/4 \sum_{p,q,r=1}^{S}{}' a_{jp}a_{kq}a_{lr}A_pA_qA_r + 1/4 \sum_{p,q,r=1}^{S}{}'' a_{jp}a_{kq}a_{lr}A_pA_qA_r\right] = 0 \quad (37)$$

Equations (36) and (37) are S-equations in S-unknowns $2\Omega_0\Omega_{m,1}$, $m = 1, 2 \ldots S$ which can be solved in terms of A_m, $m = 1, 2 \ldots S$ where the A_m are arbitrary constants.

The solutions of (32) when all the conditions (24) are satisfied are as follows:

When $m = 1$

$$\zeta_{1,1} = + \sum_{i,j,k,l=1}^{N} a_{i1}U_{ijkl1} \sum_{p,q,r=1}^{S} a_{jp}a_{kq}a_{lr}A_pA_qA_r \left\{\frac{3/4}{(n_p + n_q - n_r)^2 - 1}\left[-\cos\theta + \cos (n_p + n_q - n_r)\theta\right] + \frac{1/4}{(n_p + n_q + n_r)^2 - 1}\left[-\cos\theta + \cos (n_p + n_q + n_r)\theta\right]\right\} \quad (38)$$

When $m = 2, 3 \ldots S$

$$\zeta_{m,1} = + \sum_{i=1}^{N} \frac{a_{im}P_{im}n_m^2}{n_m^2 - 1}\left[\cos\theta - \cos n_m\theta\right] + \sum_{i,j,k,l=1}^{N} a_{im}U_{ijklm} \sum_{p,q,r=1}^{S} a_{jp}a_{kq}a_{lr}A_pA_qA_r \left\{\frac{3/4\, n_m^2}{(n_p + n_q - n_r)^2 - n_m^2}\left[\cos (n_p + n_q - n_r)\theta - \cos n_m\theta\right] + \frac{1/4 n_m^2}{(n_p + n_q + n_r)^2 - n_m^2}\left[\cos (n_p + n_q + n_r)\theta - \cos n_m\theta\right]\right\} \quad (39)$$

When $m = S + 1, S + 2 \ldots N$

$$\zeta_{m,1} = \frac{\omega_m^2}{\omega_1^2}\sum_{i=1}^{N} \frac{a_{im}P_{im}\cos\theta}{\left(\frac{\omega_m^2}{\omega_1^2} - 1\right)} + \sum_{i,j,k,l=1}^{N} a_{im}U_{ijklm} \sum_{p,q,r=1}^{S} a_{jp}a_{kq}a_{lr}A_pA_qA_r \cdot\left[\frac{3}{4}\frac{\omega_m^2 \cos (n_p + n_q - n_r)\theta}{\omega_1^2(n_p + n_q - n_r)^2 - \omega_m^2} + \frac{1}{4}\frac{\omega_m^2 \cos (n_p + n_q + n_r)\theta}{\omega_1^2(n_p + n_q + n_r)^2 - \omega_m^2}\right] \quad (40)$$

The constants A_m, $m = 1, 2 \ldots S$ in equations (36) to (40) are up to this point arbitrary. If the perturbation procedure is to be terminated to obtain solutions up to an accuracy of ϵ to the first power, the constants A_m are determined by using equation (19) up to the first power in ϵ:

$$\Omega_m^2 = \Omega^2 = \Omega_0^2 + \epsilon 2\Omega_0\Omega_{m,1} \quad m = 1, 2 \ldots S$$

and we get when $m = 1$

$$\Omega^2 = \omega_1^2 - \frac{\epsilon\omega_1^2}{A_1}\sum_{i=1}^{N} a_{i1}P_{i1} + \frac{\epsilon\omega_1^2}{A_1}\sum_{i,j,k,l=1}^{N} a_{i1}U_{ijkl1} \sum_{p,q,r,=1}^{S}{}' 3/4\, a_{jp}a_{kq}a_{lr}A_pA_qA_r \qquad A_1 \neq 0 \quad (41)$$

and when $m = 2, 3 \ldots S$

$$\Omega^2 = \omega_1^2 + \frac{\epsilon\omega_m^2}{n_m^2 A_m}\sum_{i,j,k,l=1}^{N} a_{im}U_{ijklm} \cdot\left[3/4 \sum_{p,q,r=1}^{S}{}' a_{jp}a_{kq}a_{lr}A_pA_qA_r + 1/4 \sum_{p,q,r=1}^{S}{}'' a_{jp}a_{kq}a_{lr}A_pA_qA_r\right] \qquad A_m \neq 0 \quad (42)$$

where values for $2\Omega_0\Omega_{m,1}$, $m = 1, 2 \ldots S$ are substituted from (36) and (37).

Equations (41) and (42) are S-equations in $(S + 1)$ unknowns: A_m, $m = 1, 2 \ldots S$ and Ω which can be solved in terms of any one of the amplitudes A_m. They give relationships between A_m, $m = 1, 2 \ldots S$ and Ω up to an accuracy of ϵ to the first power and these values are to be used in equations (38), (39), and (40). If the perturbation procedure is to be carried on to obtain solution of higher accuracy, the constants A_m, and therefore the

parameters $2\Omega_0\Omega_{m,1}$ are left arbitrary and are determined at a later stage as explained in the following text.

Terms of Second Order in ϵ. Equation (23) for terms of second order in ϵ is

$$\frac{\omega_i^2}{\omega_m^2}\ddot{\zeta}_{m,2} + \zeta_{m,2} = -\frac{2\Omega_0\Omega_{m,1}}{\omega_m^2}\ddot{\zeta}_{m,1} - \frac{2\Omega_0\Omega_{m,2} + \Omega_{m,1}^2}{\omega_m^2}\zeta_{m,0}$$

$$- 3\sum_{i,j,k,l,r=1}^{N} a_{im}a_{lr}U_{ijklm}\zeta_{r,1}\sum_{p,q=1}^{S} a_{jp}a_{kq}\zeta_{p,0}\zeta_{q,0} \quad (43)$$

where the commutative property of the first four suffixes of U_{ijklm} has been utilized.

An explicit statement of the solutions of (43) in the general case is not necessary in order to understand the nature of further calculations. When proper functions $\zeta_{i,0}$, $\zeta_{i,1}$, from (28) and (38), (39) and (40), and for $2\Omega_0\Omega_{1,1}$ and $2\Omega_0\Omega_{i,1}$ from (36) and (37) are substituted in (43) there will arise S secular equations for $m = 1, 2 \ldots S$. These equations will be for quantities $(2\Omega_0\Omega_{m,2} + \Omega_{m,1}^2)$, $m + 1, 2 \ldots S$ and they will be expressed in terms of A_m, $m = 1 \ldots S$, which are arbitrary. If the perturbation procedure is to be terminated to obtain results accurate up to second power in ϵ then (19) is used thus:

$$\Omega^2 = \Omega_0^2 + \epsilon 2\Omega_0\Omega_{m,1} + \epsilon^2(2\Omega_0\Omega_{m,2} + \Omega_{m,1}^2)$$

to obtain S-equations in $S + 1$ unknowns A_m, $m = 1, 2 \ldots S$ and Ω, which can be solved in terms of any one of the A_m. They give relationships between A_m and Ω that are of higher accuracy than those obtained from (41) and (42). The functions $\zeta_{m,2}$, $m = 1, 2 \ldots N$ are obtained in the same manner as $\zeta_{m,1}$, $m = 1, 2 \ldots N$.

Solutions of even higher accuracy are obtained by continuing the procedure as indicated in the foregoing. The results in terms of the generalized co-ordinates η_i, $i = 1, 2 \ldots N$ are obtained by using (10) and (7).

Special Cases of the General Theory

The nature of the response curves will now be examined for different values of S. The examination will be limited to the secular equations obtained from equations corresponding to ϵ up to the first power.

Case When $S = 1$. This occurs when none of the natural frequencies is an integral multiple of the natural frequency in the neighborhood of which is the frequency of the excitation force.

In this case only equation (41) is to be satisfied and it takes the simple form

$$\Omega^2 = \omega_i^2 - \frac{\epsilon\omega_i^2}{A_1}\sum_{i=1}^{N} a_{i1}P_{i1}$$

$$+ \tfrac{3}{4}\epsilon\omega_i^2 A_1^2 \sum_{i,j,k,l=1}^{N} a_{i1}a_{j1}a_{k1}a_{l1}U_{ijkl} \qquad A_1 \neq 0 \quad (44)$$

Equation (44) is in the same form as that for the response curves for Duffing's equation (8). Thus for the case of $S = 1$ the response curves when expressed in terms of amplitude of the principal co-ordinate are simple to interpret. All but one of the principal co-ordinates are small and the response corresponding to the one principal co-ordinate that is not small takes the familiar form for Duffing's equation.

When $S = 2$. In this case there are two secular equations. An examination of (41) and (42) indicates that the system has different properties for the cases when $n_2 \neq 3$ as compared to the case when $n_2 = 3$.

In the case when $n_2 \neq 3$ we have the secular equations

$$\Omega^2 = \omega_i^2 - \frac{\epsilon\omega_i^2}{A_1}\sum_{i=1}^{N} a_{i1}P_{i1}$$

$$+ \frac{\epsilon\omega_i^2}{A_1}\sum_{i,j,k,l=1}^{N} a_{i1}U_{ijkl}[a_{j1}a_{k1}a_{l1}A_1^3 + 2a_{j1}a_{k2}a_{l2}A_1A_2^2]$$

and $A_1 \neq 0$ (45)

$$A_2\Omega^2 = A_2\omega_i^2 + \frac{\epsilon\omega_i^2}{n_2^2}\sum_{i,j,k,l=1}^{N} a_{i2}U_{ijkl}$$

$$[2a_{j1}a_{k2}a_{l1}A_2A_1^2 + a_{j1}a_{k2}a_{l2}A_2^3] \quad (46)$$

It is to be noted that (46) can be satisfied by taking $A_2 = 0$ and in this case (45) becomes the same as (44) and the cases for $S = 1$ and $S = 2$ give the same response curves. Thus in the case $S = 2$ two distinct types of response relationships are possible according as A_2 is or is not taken equal to zero. As is discussed later in the case of one specific example, the assumption $A_2 = 0$ gives stable response relationships. A discussion of the case when $A_2 \neq 0$ requires a separate study.

When $n_2 = 3$ we have the secular equations

$$\Omega^2 = \omega_i^2 - \frac{\epsilon\omega_i^2}{A_1}\sum_{i=1}^{N} a_{i1}P_{i1} + 3/4\,\frac{\epsilon\omega_i^2}{A_1}\sum_{i,j,k,l=1}^{N} a_{i1}U_{ijkl}$$

$$[a_{j1}a_{k1}a_{l1}A_1^3 + a_{j1}a_{k1}a_{l2}A_1^2A_2 + 2a_{j1}a_{k2}a_{l2}A_1A_2^2]$$

$$A_2 \neq 0 \quad (47)$$

and

$$\Omega^2 = \omega_i^2 + \frac{\epsilon\omega_i^2}{9A_2}\,3/4\sum_{i,j,k,l=1}^{N} a_{i2}U_{ijkl}$$

$$[2a_{j1}a_{k2}a_{l1}A_1^2A_2 + a_{j1}a_{k2}a_{l2}A_2^3 + \tfrac{1}{3}a_{j1}a_{k1}a_{l1}A_1^3] \quad (48)$$

It is seen that the form of (47) and (48) differs from (43) and (44) and it is not possible to take $A_2 = 0$.

When $S > 2$. For $S > 2$ a general examination of the secular equations (41) and (42) becomes difficult. The case of $S = 3$ has been examined in some detail and it appears that in some cases, depending on the values of n_2 and n_3, it is possible to satisfy the secular equations by taking $A_2 = 0$ and $A_3 = 0$ and thus reduce the response relationships to the one for $S = 1$. On the other hand there are many cases when this is not possible. For instance, if $n_3 = n_2 + 2$ for any n_2 it is not possible to take A_2 and A_3 equal to zero. It is thus seen that the vibrations can be complicated if several of the linear natural frequencies are integral multiples of the frequency in the neighborhood of which is the exciting frequency. It is in general not possible to ignore the effect of the modes corresponding to these frequencies even if the values of these frequencies are considerably higher than that of the exciting force.

Specific Applications

The theory is applied to four different specific problems. The first three problems are examples of systems with two degrees of freedom and the fourth problem is an example of a system with three degrees of freedom. Fig. 1 is a schematic diagram representing the first three problems and Fig. 2 is a schematic diagram representing the fourth.

The springs are nonlinear, producing a restoring force $(k_i\Delta + h_i\Delta^3)$. Here Δ is the change in length of the spring; k_i, $i = 1, 2, 3, 4$ are positive constants, and h_i, $i = 1, 2, 3, 4$ are positive or negative constants. The equations of motion for the system in Fig. 1 corresponding to (6) are

$$m_1\ddot{\eta}_1 + k_1\eta_1 + h_1\eta_1^3 + k_2(\eta_1 - \eta_2) + h_2(\eta_1 - \eta_2)^3 = C_1\cos\Omega t \quad (49)$$

$$m_2\ddot{\eta}_2 - k_2(\eta_1 - \eta_2) - h_2(\eta_1 - \eta_2)^3 + k_3\eta_2 + h_3\eta_2^3 = C_2 \cos \Omega t \tag{50}$$

and equations of motion for the system in Fig. 2 corresponding to (6) are

$$m_1\ddot{\eta}_1 + k_1\eta_1 + h_1\eta_1^3 + k_2(\eta_1 - \eta_2) + h_2(\eta_1 - \eta_2)^3 = C_1 \cos \Omega t \tag{51}$$

$$m_2\ddot{\eta}_2 - k_2(\eta_1 - \eta_2) - h_2(\eta_1 - \eta_2)^3 + k_3(\eta_2 - \eta_3) + h_3(\eta_2 - \eta_3)^3 = C_2 \cos \Omega t \tag{52}$$

$$m_3\ddot{\eta}_3 - k_3(\eta_2 - \eta_3) - h_3(\eta_2 - \eta_3)^3 + k_4\eta_3 + h_4\eta_3^3 = C_3 \cos \Omega t \tag{53}$$

In Table 1 are given the numerical values of the various constants occurring in (49) to (53) for the four different problems to which the theory was applied. The response curves in terms of the amplitude of the generalized co-ordinate for the different problems are shown in Figs. 3 to 8 and 10. The positive direction of the co-ordinates and the forces are shown in Figs. 1 and 2. The amplitude of a generalized co-ordinate is indicated as positive or negative in Figs. 3 to 8 and 10 according as the motion is in phase or out of phase with the force (forces) on the system with positive amplitude constant (constants) C_i.

The results from the theory are checked against results from an analog-type computer. A discussion of the technique used in the computer work is given in the next section. The computer results are indicated by crosses in Figs. 3 to 8 and 10. The convention for the sign of the amplitude of the computer solution is the same as that for the theory solution as just stated.

Problem I is a case of a system with two degrees of freedom with the higher natural frequency not an integral multiple of the lower natural frequency. All the springs are taken nonlinear with nonlinear coefficients h_1, h_2, and h_3 taken equal to or greater in magnitude than the corresponding linear coefficients k_1, k_2, and k_3. The amplitudes of the external forces are chosen very small as explained in the theory. The response curves in terms of the amplitudes of the principal co-ordinates are obtained up to an accuracy of ϵ at each of the natural frequencies from (44) and by computing $\zeta_2 = 0 + \epsilon\zeta_{2,1}$ from (40).

Then equations (10) and (7) are used to obtain the response curves in terms of the amplitude of the generalized co-ordinates η_1 and η_2. The results are plotted in Figs. 3 and 4 which give the amplitudes of η_1 and η_2, respectively, in the neighborhood of the two natural frequencies. The response curves when plotted in terms of the amplitudes of the principal co-ordinates have the same appearance as that for Duffing's equation. The response curves, however, when plotted in terms of the generalized co-ordinate show some unexpected behavior. In Fig. 3, when the response is in the neighborhood of the higher natural frequency, the positive branch and the negative branch cross at P. The crosses indicate results obtained from an analog-type computer. It was definitely confirmed that the negative branch in the neighborhood of the point P is unstable.

Problem II is a case of a system of two degrees of freedom with the higher natural frequency twice the lower natural frequency. In the neighborhood of the lower natural frequency, (45) and (46) must be satisfied. The amplitude A_2 is taken equal to zero reducing (45) and (46) to (42), and the computations for the response curves are the same as for Problem I. The response curves in terms of the amplitude of η_1 are shown in Fig. 5. This problem has only one nonlinear term and the Ritz-Galerkin procedure for a one-term approximation is easily applicable. Curves from the Ritz-Galerkin procedure are included in Fig. 5 for comparison.

Table 1

Problem	I	II	III	IV
m_1	1	2	2	2
m_2	1	1	1	2
m_3	—	—	—	2
k_1	1	2	2	2
k_2	1	1	$36/146-100\sqrt{1.84}$	2
k_3	3	0	0	1
k_4	—	—	—	1
h_1	3	0.2	0.2	0.2
h_2	−1	0	0	0
h_3	−4	0	0	0.1
h_4	—	—	—	0
c_1	0.02	0.2	0.2	0.1
c_2	0.04	0	0	−0.2
c_3	—	—	—	0

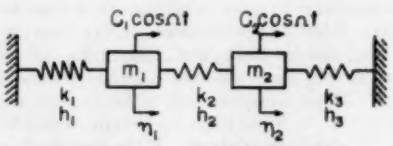

Fig. 1 Schematic diagram of a system with two degrees of freedom

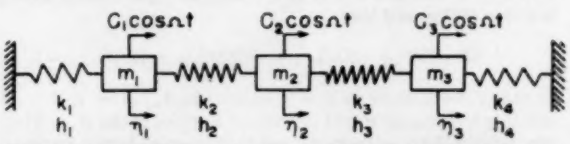

Fig. 2 Schematic diagram of a system with three degrees of freedom

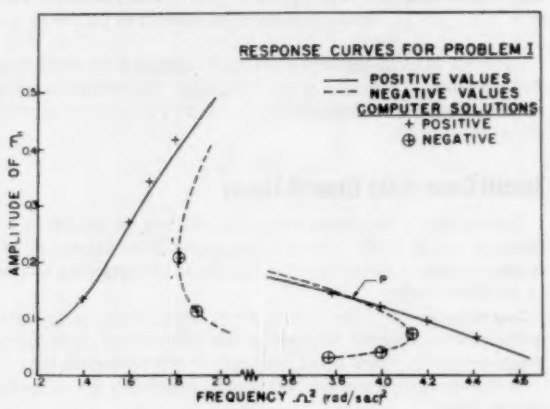

Fig. 3

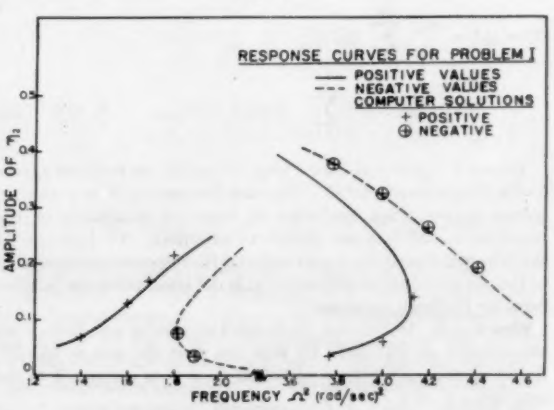

Fig. 4

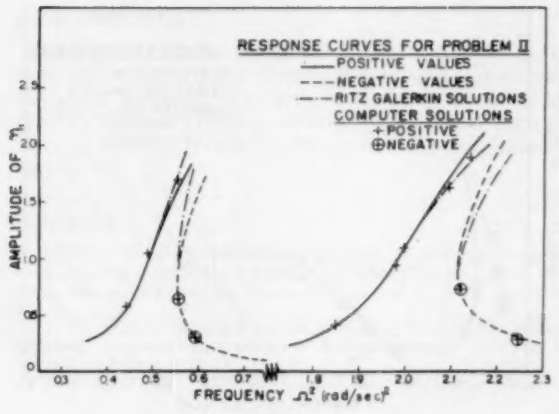

Fig. 5

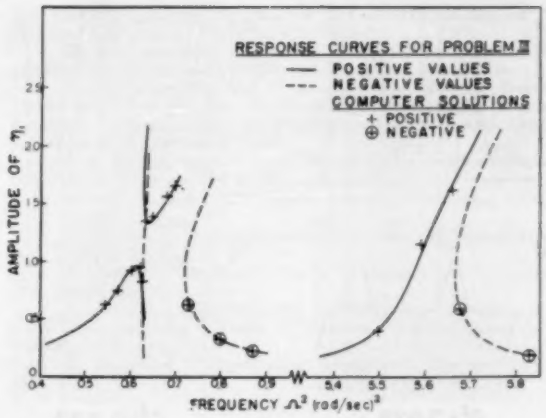

Fig. 6

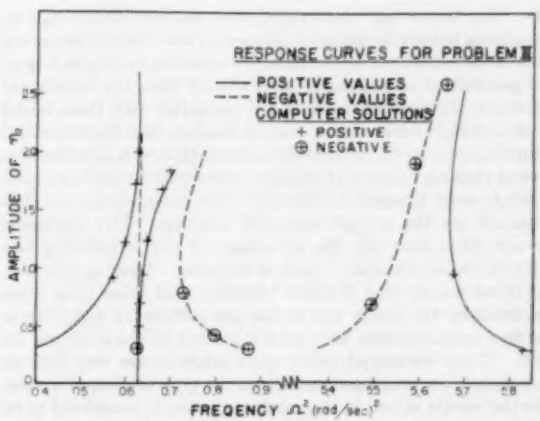

Fig. 7

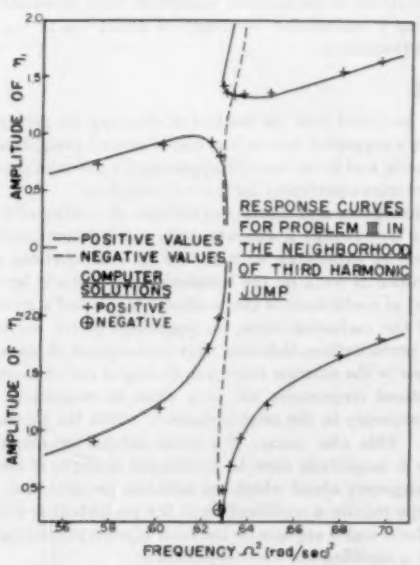

Fig. 8

Problem III is the same as Problem II in all respects except for the constant k_2 which has been changed to get the higher natural frequency exactly three times the lower natural frequency. In the neighborhood of the lower natural frequency (45) and (46) have to be satisfied. The quantity Ω^2 can be eliminated between (45) and (46) and the resulting cubicin A_2 is solved for the real roots for different values of A_1. The resulting pairs of values of A_1 and A_2 are then substituted in (47) to obtain the response curves in terms of the principal co-ordinates. The response curves in terms of the amplitude of the generalized co-ordinates are obtained by using (10) and (7) and are plotted in Figs. 6 and 7. The curves in the neighborhood of the higher natural frequency are obtained in the same manner as in Problem I.

Figs. 6 and 7 show properties that are quite different from those of Problem II although Problem III differs from Problem II only in its values of the linear natural frequencies. When the excitation frequency is very close to the lower linear natural frequency the solution demonstrates a very strong third harmonic. The value of this third harmonic increases as the excitation frequency is increased until at a critical value of the frequency which is still quite close to the linear natural frequency the third harmonic changes phase by π but is still quite strong. As the excitation frequency further increases, the third harmonic gets smaller and does not appear to be much stronger than that obtained in Problem II. On further increase of the excitation frequency the usual "jump" phenomenon is obtained. The nature of the response curves where the resonance phenomenon of the third harmonic occurs has been shown on a larger scale in Fig. 8. The crosses in Figs. 6, 7, and 8 show computer solutions. In Fig. 9 are shown computer traces for Ω near the third-harmonic resonance frequency.

It is to be noted that in Problem II or III when the excitation frequency is near the higher natural frequency no indication of a subharmonic oscillation was observed on the computer.

Problem IV is a problem with three degrees of freedom and is included to demonstrate the applicability of the method to systems with degrees of freedom higher than two. The natural frequencies are chosen so that the higher natural frequencies are not integral multiples of the lower natural frequencies. The computations are similar to those of Problem I and in Fig. 10 are shown the response curves in terms of the amplitude of the generalized coordinate η_1.

Computer Technique

An electronic analog-type computer was used to obtain the computer solutions plotted in Figs. 3 to 10. A novel feature of the computer technique is that the solutions are obtained without the inclusion of any terms corresponding to damping in the sys-

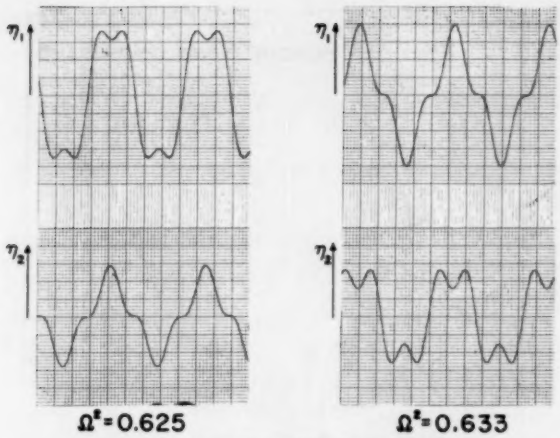

Fig. 9 Third harmonic resonance in problem III

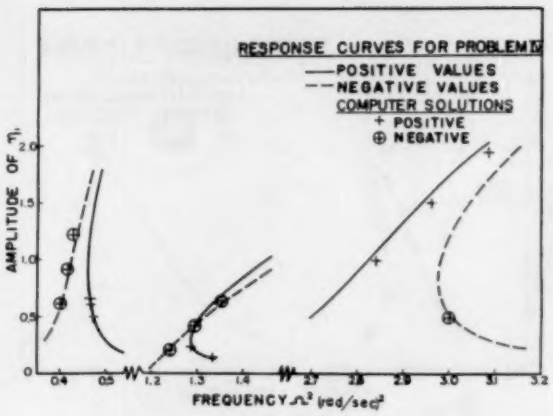

Fig. 10

tem. The theoretical solutions are first obtained and then, corresponding to a given excitation frequency, the computer is started with initial conditions for the different variables, corresponding to the generalized co-ordinates, as obtained from the theoretical solutions. If the solution from the computer with these initial conditions maintains a steady-state oscillation, then the theoretical solutions are correct. If a steady-state oscillation, is not obtained, several runs are taken with slightly varied initial conditions until a steady-state solution is obtained. The initial conditions thus obtained are the correct computer solution. This technique though often slow has the advantage of not introducing any errors in the solutions as a result of damping. There is, however, the disadvantage that if stable branches exist other than those predicted by the theory and if they are sufficiently remote from the theoretical solution they are not located by the computer results. Truly undamped steady-state solutions are very difficult to maintain for prolonged periods on the type of computer used. For the results shown in this work a solution is considered to be close enough to steady-state solution if the amplitude of the solution fluctuates less than 1 per cent about a mean amplitude. The fluctuations in the solution amplitude were invariably very slow, giving a modulation frequency of about $^1/_{20}$ to $^1/_{40}$ of the excitation frequency.

Remarks

It may be noted that the method of choosing the perturbation parameter ϵ suggested here is just one of several possible alternative methods, and in any specific application a different parameter may prove more convenient for the computations.

The convergence and stability of solution of systems of the type considered here require a separate study. A few comments, however, based on experience with the actual computations and on the experimental work on the computer will be made here. For a given set of coefficients of the nonlinear terms and a given magnitude of the excitation force, an inspection of the solutions at different perturbations indicates that convergence of the solution will be slow or the solution may even diverge if one or more of the linear natural frequencies are very close in magnitude to the natural frequency in the neighborhood of which the solutions are obtained. This also occurs if a linear natural frequency of the system is in magnitude close to an integral multiple of the linear natural frequency about which the solutions are obtained. Cases of this type require a modification of the perturbation procedure as given here, and it appears on the basis of some preliminary work that such a modification may be possible.

There is a clear need for a thorough investigation of the stability of the various branches of the response curves. Until questions of stability are settled, it was arbitrarily decided that variations of amplitude of less than 1 per cent as described under "Computer Technique" will be considered a sufficiently close approximation to a stable steady-state solution.

Work is in progress at the present time to extend the procedure given here to systems excited with general periodic forces and to systems having small damping.

The study of vibrations of the simpler nonlinear continuous systems, such as the elastic string or the slender beam with the strain energy a nonlinear function of the displacements,[3] poses interesting questions in view of the present investigation. In these problems the linear natural frequencies are often integral multiples of the lower natural frequencies or are roots of transcendental equations whose higher roots are often close to integral multiples of lower ones. Some preliminary work has been done on these problems.

Conclusions

It has been shown that steady-state vibration solutions of systems with an arbitrary number of degrees of freedom of the type discussed here, can be studied in the neighborhood of each of the linear natural frequencies by obtaining the solutions in separate steps.

The solutions in many cases require simple computations and are obtained in a form that facilitates classifications of the solutions into different types depending on the ratios of the linear natural frequencies.

If none of the natural frequencies is an integral multiple of the natural frequency in the neighborhood of which is the excitation frequency, the solutions present little computational difficulty. The nature of the solution has a simple physical interpretation; the amplitudes of all but one of the principal co-ordinates take small values and the one that is not small varies with frequency in the same manner as in the case of Duffing's equation.

If the foregoing condition on the linear natural frequencies does not hold, the algebraic expressions that give the response relationships in terms of the principal co-ordinates are more complicated. It is, however, possible by inspection of these algebraic expressions to determine which of the principal co-ordinates will have significant amplitudes and which others will have amplitudes that can be ignored for excitations in the neighborhood of a given natural frequency.

The method is restricted to vibrations in the neighborhood of free linear vibrations of the system.

[3] See, for instance, references [9] and [10].

Acknowledgments

The author wishes to express his appreciation to Mr. B. E. Fristedt and Mr. V. G. Harvester for their enthusiastic assistance throughout this work. The author also wishes to express his thanks to Mr. W. J. Trapp under whose general liaison this work was supported by Wright Air Development Center, Materials Laboratory.

References

1 F. R. Arnold, "Steady-State Behavior of Systems Provided with Nonlinear Dynamic Vibration Absorbers," JOURNAL OF APPLIED MECHANICS, vol. 22, TRANS. ASME, vol. 77, 1955, pp. 487–492.

2 K. Klotter, "Steady State Oscillations in Nonlinear Multiloop Circuits," Transactions, Institute of Radio Engineers, CT-1 No. 4, December, 1954, pp. 13–18.

3 T. C. Huang, "Harmonic Oscillations of Nonlinear Two-Degree-Freedom Systems," JOURNAL OF APPLIED MECHANICS, vol. 22, TRANS. ASME, vol. 77, 1955, pp. 107–110.

4 R. M. Rosenberg, Discussion, JOURNAL OF APPLIED MECHANICS, vol. 22, TRANS. ASME, vol. 77, 1955, pp. 602–603.

5 R. M. Rosenberg and C. P. Atkinson, "On the Natural Modes and Their Stability in Nonlinear Two-Degree-of-Freedom Systems," JOURNAL OF APPLIED MECHANICS, vol. 26, TRANS. ASME, vol. 81, series E, 1959, pp. 377–385.

6 P. R. Sethna, "Steady-State Motion of One and Two-Degree-of-Freedom Systems with a Nonlinear Restoring Force," Proceedings of the Second U. S. National Congress of Applied Mechanics, ASME, 1954, pp. 64–78.

7 H. Goldstein, "Classical Mechanics," Addison-Wesley Press, New York, N. Y., 1951.

8 J. J. Stoker, "Nonlinear Vibrations," Interscience Publishers, Inc., New York, N. Y., 1950.

9 R. Grammel, "Nichtlineare Schwingungen mit unendlich vielen Freiheitsgraden," France, Ministère de l'Air Publication S. T. 276–282, 1953.

10 H. Kauderer, "Nichtlineare Mechanik," Springer-Verlag, 1958.

A Unified Criterion for the Degree of Constraint of Plane Kinematic Chains

B. PAUL

Assistant Professor,
Division of Engineering, Brown University,
Providence, R. I.
Assoc. Mem. ASME

The degree of freedom or overconstraint of plane kinematic chains is determined by means of an analysis of independent loops. It is shown how the independent loops of a system may be identified and how they may be used to recognize certain special cases which do not fit into the framework of so-called "general formulas." The independent loops may also be used to systematically formulate the governing kinematic equations of a system. It is shown that the equations so formulated are in general sufficient to solve for all unknown velocities and accelerations.

1 Introduction

THE CRITERIA of constraint for plane kinematic chains have been treated extensively in several textbooks, e.g. [1],[1] and the number of degrees of freedom for both plane and spatial linkages has been discussed by Bottema [2], for the general case. However, in such discussions there are several special, but extremely important, cases which are not covered by the formulas which govern the so-called general cases.

In this paper, a unified point of view is presented which facilitates the analysis for the degrees of freedom of the widest possible class of plane kinematic chains. Only kinematic chains with lower pairing will be considered explicitly since it is well known [3] that chains with higher pairing can be reduced at any instant of time to kinematically equivalent chains with lower pairing only.

The analysis of velocity or acceleration in a plane linkage depends mathematically on the solution of a set of linear simultaneous algebraic equations. The consistency and sufficiency of the set of equations determine the degree of freedom or overconstraint of the physical system.

A straightforward technique for setting up the governing equations for any kinematic chain consists in tracing out all independent closed loops formed by the linkage and thinking of the constituent links of any given loop as directed line segments which form a closed-vector polygon. By separately equating to zero the vector sum of the projections of all links in a given loop, on two orthogonal axes, two scalar equations will be produced for each loop. For example, Fig. 1 shows a fairly general type of system with three loops described by the links. Fig. 2 shows the corresponding vector polygons. The small letters $a, b, \ldots$, and so on, represent the lengths of the individual vectors. These lengths are constant for rotating links but are variable when sliding members are present. For any closed-vector polygon the following two equations are valid:

$$\begin{aligned} \Sigma \text{ projections on } x &= \Sigma k \cos \theta_k = 0 \\ \Sigma \text{ projections on } y &= \Sigma k \sin \theta_k = 0 \end{aligned} \tag{1}$$

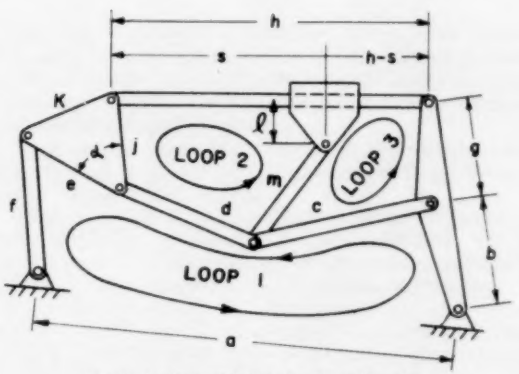

Fig. 1 Linkage with two degrees of freedom

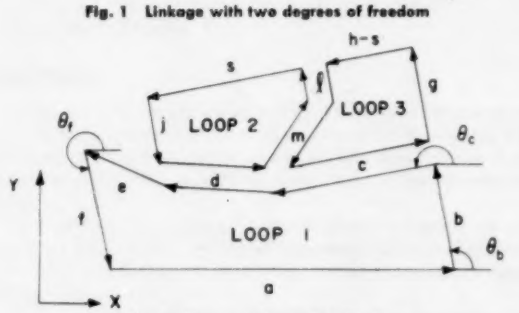

Fig. 2 Vector polygons for Fig. 1

where k designates the length of any link in a given loop, θ_k represents the angle between the link k and the x-axis in the sense shown in Fig. 2, and the summation includes all links included in the given loop. Since two such equations may be written for each loop, it is apparent that in general $2L$ equations can be written if L-loops are described. These equations will be independent if the L-loops are independent in the sense that no loop can be formed by merely superposing several of the other loops. For example, a fourth loop in Fig. 1 can be formed by traversing members a, b, g, h, k, f, but this loop obviously results from the superposition of loops 1, 2, 3 and the resulting equations would merely be the equations derived by adding together the equations found from the other three loops. A systematic technique for identifying the independent loops in a kinematic chain will be developed in Section 2.

Differentiation, with respect to time, of Equations (1) gives the following $2L$ equations for velocities:

[1] Numbers in brackets designate References at end of paper.

Contributed by the Applied Mechanics Division and presented at the Annual Meeting, Atlantic City, N. J., November 29–December 4, 1959, of THE AMERICAN SOCIETY OF MECHANICAL ENGINEERS.

Discussion of this paper should be addressed to the Secretary, ASME, 29 West 39th Street, New York, N. Y., and will be accepted until April 10, 1960, for publication at a later date. Discussion received after the closing date will be returned.

NOTE: Statements and opinions advanced in papers are to be understood as individual expressions of their authors and not those of the Society. Manuscript received by ASME Applied Mechanics Division, December 16, 1958. Paper No. 59—A-34.

$$\Sigma k \cos \theta_k - \dot{\theta}_k \sin \theta_k = 0$$
$$\Sigma k \sin \theta_k + \dot{\theta}_k \cos \theta_k = 0 \qquad (2)$$

where a dot signifies differentiation with respect to time. A second differentiation will give rise to similar equations for the accelerations, if desired.

It is to be observed that terms such as k appear only for those links in contact with sliding members, so that the formulation of the actual equations in any given case is quite simple and can proceed almost automatically as one traverses the given loop on the linkage skeleton.

An alternative approach to the formulation of the governing equations would be to use "independent-position equations" and complex vectors as described by Raven [4].

In either case, there will be twice as many independent equations as there are independent loops in the system. It is to be noted that these governing equations are, as stated, linear in the velocities and accelerations.

In Section 2, a general technique for identifying independent loops and for determining the degree of freedom of a plane system is given. In Section 3, the recognition of certain special cases is discussed, and in Section 4, it is shown that, in general, the number of independent loops associated with any plane closed kinematic chain is mathematically sufficient to solve for all unknown velocities. Conclusions are stated in Section 5.

2 Degrees of Freedom and Loop Independence

The consistency and solvability of the set of equations for velocity depend upon the coefficients of the velocity terms. These coefficients are functions only of the dimensions of the links and their instantaneous position in the plane.

Assuming the set to be solvable, the number of degrees of freedom of the system is generally the difference between the number of unknown velocities and the number of independent equations. In order to find the difference, it is not necessary to actually set up the equations. It is only necessary to draw a set of independent loops, as shown, for example, in Fig. 1, and to subtract from the number of *moving* members twice the number of independent loops.

In Fig. 1, there are three independent loops and eight moving members, giving rise to 8-(2)(3) = 2 degrees of freedom.

In general, the number of independent loops in a linkage may or may not be immediately apparent. For example, in Fig. 1 it is apparent that only three independent loops exist, but Fig. 3 shows a somewhat more complex system where the total number of loops which can be drawn is quite large, and the choice of an independent set of such loops is not obvious. In general, the number of independent loops in a system with *no* crossing links, i.e., mappable on a plane, is equal to the total number of interior loops. This is easily proved since:

(a) Each interior loop contains at least one link not included in any other interior loop and is therefore independent; (b) if each interior loop is traversed in the same sense, e.g., counterclockwise, *any* closed loop in the system may be synthesized by superposing all the interior loops which have a line in common (and pointing in the correct direction) with the desired loop. Thus, if no crossing member is present, the interior loops or any combination thereof may be taken as the independent loops of the system.

If crossing members are present, the method of finding independent loops must be modified slightly. In this case, the linkage may be thought of as consisting of a basic uncrossed tier and several additional uncrossed tiers constructed upon some closed loop in the basic tier. For example, Fig. 3 shows a fairly complex linkage consisting of the basic tier shown in Fig. 3(a) and the two additional tiers shown in Figs. 3(b) and 3(c).

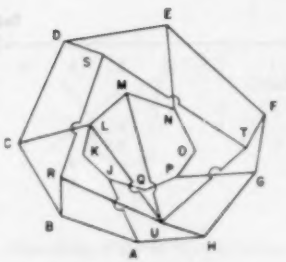

Fig. 3 Crossed kinematic chain

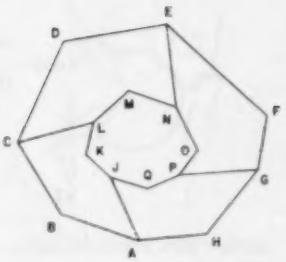

Fig. 3(a) Base tier

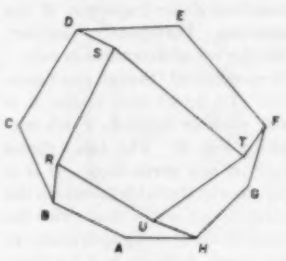

Fig. 3(b) First additional tier

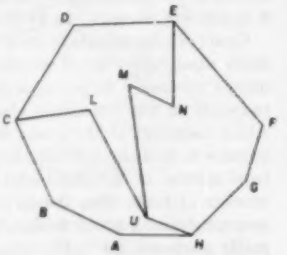

Fig. 3(c) Second additional tier

The total number of independent loops for such a system equals the number of interior loops in the basic tier plus the number of interior loops less one in each additional tier. That is, if L_0 is the number of interior loops in the basic tier and L_i is the number of interior loops in the ith tier, then the total number L of independent loops for the entire system is given by

$$L = L_0 + \sum_i (L_i - 1) \qquad (3)$$

For example, the network shown in Fig. 3 has $L = 5 + 4 + 2 = 11$ independent loops. (It should be noted in passing that if the network consists exclusively of binary links, that is, if each link has only two junction points, the total number of movable members is 29, and the system has $29-(2)(11) = 7$ degrees of freedom. If, on the other hand, multijunction links occur, the number of movable members is reduced. For example, if the central octagon *J-K-L-M-N-O-P-Q* is made up of four bell cranks th[illegible] are only 25 movable members, and the system has three degr[illegible] of freedom, irrespective of which set of alternate vertexes [illegible] the octagon are hinged together.)

The validity of the technique follows from the fact that the basic tier has as many independent loops as interior loops, but each additional tier has one loop (the outer loop in Figs. 3a, b, c) which has already been included in the basic tier. Thus the number of independent loops for each additional tier is one less than the number of interior loops in the tier.

It should be mentioned that other methods for finding the number of independent loops in a network may be found in the electrical-engineering literature. For example, Guillemin [5] describes a technique based on consideration of current flow and the concept of "trees" contained in the "graph" of the network. Such ideas may be used as alternatives to the exclusively topological approach described in the foregoing.

3 Special Cases

There are three special cases where the simple expedient of counting independent loops and members is not adequate. These are (a) when a part of the chain is overconstrained and

Table 1

Loop	Members 1 (fixed)	2	3	4	5	6	7	8	9	10	11	12	13	14
I	x	x	x											
II		x		x	x									
III	x			x		x								
IV					x	x	x		x	x				
V					x		x	x			x			
VI									x	x	x	x	x	x

another part is independently movable; (*b*) when a *permanent* critical form exists in the kinematic chain; (*c*) when one or more movable groups in the chain consist entirely of sliding pairs.

All of these cases require a somewhat closer inspection of the nature of the governing set of equations. Fortunately, however, it is still not necessary to write out the set of equations in full.

Case (*a*) corresponds to an overconstrained (though not necessarily unsolvable) set of equations. To detect such a case, it is merely necessary to set up a table such as Table 1, which corresponds to the kinematic chain in Fig. 4. The table shows which members of the chain occur in any given loop. If it is possible to find any combination of rows in the table for which the total number of movable members included is less than twice the number of rows, then the members in these rows constitute an overconstrained group within the larger linkage, and for kinematic purposes the entire group can be treated as a rigid assemblage; that is, if the number of independent equations exceeds the number of movable members there is a negative degree of freedom or overconstraint.

For example, in Table 1, it is evident that the loops I through III provide six independent equations for five movable members. Therefore all of the members included in the first three rows are part of a rigid assemblage which may be considered the single fixed link of the chain. The remaining three loops provide six equations for eight additional movable members. Obviously then, two of the members 7 through 14 may be thought of as driving links, and the system has two degrees of freedom.

A further advantage of Table 1 is that it also indicates which of the links may be used as driving links. Unlike a single-degree-of-freedom system, the driving members of a multiple-degree-of-freedom system cannot be chosen arbitrarily. For example, if the two driving members in Fig. 4 were chosen from among members 7, 8, 9, 10, 11, loops IV and V provide four equations for the remaining three unknown velocities in the group (see Table 1), thus representing an incompatible motion. Therefore, at least one of the driving members must be chosen from members 12, 13, 14.

Case (*b*) corresponds to a set of velocity equations where the determinant of the coefficients vanishes. If no overconstrained groups (Case *a*) are present and it is indicated by counting independent loops and members that zero degrees of freedom should exist (that is, the kinematic chain is just locked, forming a structure with statically determinate reactions), it is still possible that for certain configurations known as *permanent* critical forms additional degrees of freedom can exist. The presence of such configurations can be detected with the aid of the "zero load test" [6]; that is, if any set of nontrivial self-equilibrating reactions at the joints of the linkage can exist, the linkage is said to be a critical form, but not necessarily a *permanent* critical form. For example, Fig. 5(*a*) shows a linkage with seven potentially movable members and three independent loops (corresponding to six equations). It would appear on the surface that the system has a single degree of freedom; however, analysis of Table 2 shows that loops I and II give rise to four equations involving four potentially movable members and, therefore, the members of this grouping constitute either a structure or a critical form.

It may be shown that no self-equilibrating joint reactions can occur within the group (1, 2, 3, 4) in Fig. 5(*a*) unless bars 3 and 4 intersect somewhere on line *A-B*, as shown for example in Fig. 5(*b*). A possible system of self-equilibrating joint forces, which act on member 1, is shown at point *O*. The same forces act with reversed sense on member 2. It is apparent from Fig. 5(*b*) that infinitesimal rotations of members 3 and 4 can occur about point *O*. However, any finite rotation would tend to destroy the con-

Table 2

Loop	Members 1	2	3	4	5	6	7	8 (Fixed)
I	x	x	x					x
II	x	x	x	x				
III		x			x	x	x	x

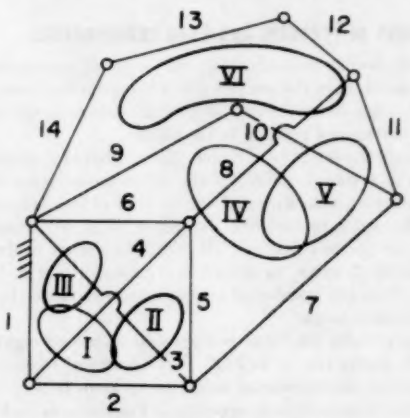

Fig. 4 Partially overconstrained chain

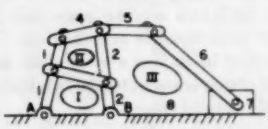

FIG. 5a STRUCTURAL GROUP

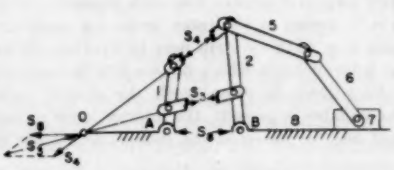

FIG. 5b INSTANTANEOUS CRITICAL FORM

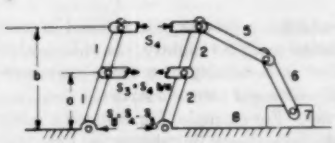

FIG. 5c PERMANENT CRITICAL FORM

Fig. 5 Chain with critical form

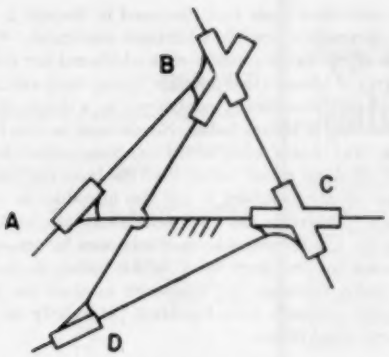

Fig. 6 Sliding-pair chain

currence of members 3, 4, and line *A-B;* finite rotations of these members is therefore impossible. On the other hand, if the point of concurrence remains at infinity, as shown in Fig. 5(*c*), finite rotations can occur. The corresponding joint forces shown in the figure remain self-equilibrated throughout the motion. Critical forms of the type shown in Fig. 5(*b*) will be referred to as instantaneous critical forms; critical forms of the type shown in Fig. 5(*c*) will be referred to as permanent critical forms.

Although only the permanent type of critical form introduces an additional degree of freedom into an ideal system, it should be recognized that for actual linkages with finite elasticity and clearance at the joints undesirably large distortions of instantaneous critical forms may occur.

The third special case (*c*) can be handled by temporarily considering any loop, which consists entirely of sliding members, to be rigid. Then one finds the degree of freedom in the new kinematic chain by the usual method and adds on the degree of freedom for the sliding-pair groups.

To find the number of degrees of freedom in a sliding-pair chain, let n designate the number of members (including fixed members) in a sliding pair chain, such as shown in Fig. 6, and let j_i be a junction where i different members meet. To begin with, each member in the system has three degrees of freedom except for the fixed member. Therefore $3(n-1)$ co-ordinates are necessary to specify the configuration of the system. Since each member of such a chain can only translate, there are $(n-1)$ additional equations of type $\omega_i = 0$, where ω_i is the angular velocity of the ith member. In addition, at each joint one of the members may be thought of as driving the joint with velocity $\mathbf{V}$.

There are then $(i-1)$ equations expressing the fact that the projection of $\mathbf{V}$ on the normal to any bar equals the normal velocity of the bar. The total number of degrees of freedom x for a sliding group (with one fixed member) is therefore

$$x = 3(n-1) - (n-1) - \sum_i (i-1)j_i = 2(n-1) - \sum_i (i-1)j_i \quad (4)$$

The derivation of Equation (4) follows the reasoning of Bottema [2] and a suggestion of Blaschke and Mueller [7]. Applying Equation (4) to Fig. 6, it is found that: $n = 5$, $j_2 = 2$, $j_3 = 2$, therefore

$$x = 2(5-1) - 2 - 2(2) = 2$$

It is to be noted that one of the two degrees of freedom consists merely of a translation of the bar *B-C* parallel to its axis. Such a motion, of course, is completely uncoupled from the motion of the rest of the system and would not show up in a loop equation.

It is to be noted that in the derivation of Equation (4) it was assumed that each joint was driven by one of the members meeting at the joint; therefore, in order to apply the equation when joints such as that shown in Fig. 7(*a*) are present, it is necessary to think of the slider as a member to be included in the term n of Equation (4). This can be visualized by thinking of Fig. 7(*a*) in terms of Fig. 7(*b*), which is its kinematic equivalent and fulfills the postulates upon which Equation (4) is based. Of course, the presence of partial overconstraint or the presence of critical forms (where self-equilibrating joint forces may occur) will necessitate a modification of Equation (4) of the type previously discussed. However, the poor frictional characteristics of closed kinematic chains which consist exclusively of sliding members prevents wide usage of such construction. Therefore, detailed discussion is felt to be unwarrented.

Fig. 7(*a*) Free slider

Fig. 7(*b*) Fixed sliders

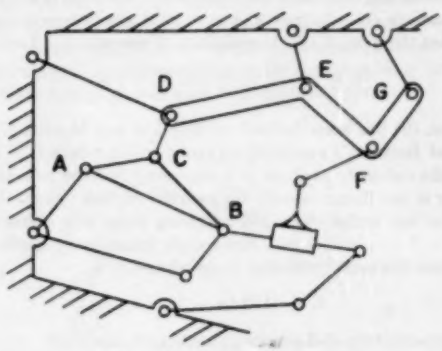

Fig. 8 Uncrossed plane linkage

4 Sufficiency of Loop Equations in Nonsingular Case

It will now be shown in an analytic manner that for plane closed kinematic chains the number of independent loops available is just sufficient to provide the correct number of equations needed to solve for all unknown velocities. This statement, of course, must exclude the three special cases discussed in Section 3. The statement will first be proved for uncrossed chains and then extended to crossed chains.

Fig. 8 shows an arbitrary uncrossed plane linkage with both sliding and turning pairs. Links with more than two joints on them can be considered as combinations of simple trusses, e.g., the link *A-B-C*, or else merely as multiple bell cranks, e.g., link *D-E-F-G*.

Let n_i designate the number of members with i-joints attached, let j_i be the number of joints at which i-members join, and let n and j be the total number of members and joints, respectively.

It is apparent that

$$n = \sum_i n_i, \quad j = \sum_i j_i \quad (5)$$

The total number of lines s connecting the joints in the linkage is

$$s = \sum_k (k-1)n_k \quad (6)$$

It is known [8] that the Euler characteristic C is given by

$$C = L - s + j = 1 \tag{7}$$

where L is the total number of interior (independent) loops in the system.

Upon substitution of Equations (6) and (5) into Equation (7), one obtains

$$L = 1 - j - \sum_k n_k + \sum_k k n_k = 1 - j - n + \sum_k k n_k \tag{8}$$

The number of degrees of freedom x in the system can be obtained by noting that each member except the fixed one requires three position co-ordinates, and at a joint where i-members are connected there are $2(i - 1)$ equations of constraint. Therefore,

$$x = 3(n - 1) - 2 \sum_i (i - 1) j_i \tag{9}$$

Equation (9) has been derived by Blaschke and Mueller [7] who extended Bottema's reasoning to cover joints where $i > 2$.

For the complete analysis it is necessary to know one angular velocity or one linear velocity for each driven link. Since there is one fixed link in the chain and x driving links, it is necessary to find $n - 1 - x$ velocities. Since each vector loop supplies two equations, the total number of loops necessary is

$$L = (1/2)(n - 1 - x) \tag{10}$$

Upon substitution of Equation (9) into (10), one finds

$$L = 1 - n + \sum_i (i - 1) j_i = 1 - n - j + \sum_i i j_i \tag{11}$$

If there are n_k-links with k other links attached, the total number of elements e in the system is

$$e = \sum_k k n_k, \tag{12}$$

where an element is defined to be that part of a link in immediate contact with another link. The number of elements can also be expressed by noting that i-elements join at each of j_i-joints so that

$$e = \sum_i i j_i \tag{13}$$

Therefore,

$$e = \sum_i i j_i = \sum_k k n_k \tag{14}$$

Upon substitution of Equation (14) into Equation (11) one finds that the total number of independent loops required for the system is

$$L = 1 - n + \sum_k k n_k - j,$$

which, according to Equation (8), is precisely the number of independent loops available.

The previous proof applies only to uncrossed (plane mappable) chains. A chain with crossing members can be considered to consist of the uncrossed basic tier, discussed in Section 2, and the additional tiers which provide additional constraint. One may without loss of generality consider each additional tier to be made up exclusively of binary (two-junction) links, since any multiple-junction link is kinematically equivalent to a simple truss consisting exclusively of binary links. Now it may be seen from Fig. 3(*b*) or Fig. 3(*c*) that if each additional independent loop, e.g., loop *B-R-U-H-A*, in a tier (other than the basic tier) introduces m additional binary members, it will also introduce $m - 1$ additional joints. Therefore, for each additional independent loop, L increases by 1, n increases by m, j increases by $(m - 1)$, and $\Sigma k n_k$ increases by $2m$ (since $n_k = n_2$ for binary links). These additions leave Equation (8) unaltered so that the proof for crossed chains proceeds from Equation (8) exactly as does the proof for uncrossed chains.

5 Conclusions

By drawing the independent loops associated with any plane closed kinematic chain, it is possible to extract a great deal of information about the system with a minimum of effort. It has been shown how one may easily identify the independent loops of both crossed and uncrossed chains, and how these loops aid in determining the number of degrees of freedom, and also provide a unifying technique for identifying important special cases.

For multiple-degree-of-freedom systems the choice of driving members is not unrestricted, but the technique described clearly and simply indicates which members may be considered driving members. The independent loops may also be used directly to write out systematically the governing kinematic equations for the system, if so desired.

Finally, it has been shown in the nonsingular case that the number of equations provided by the independent loops is sufficient to solve for all unknown velocities and accelerations.

References

1 N. Rosenauer and A. H. Willis, "Kinematics of Mechanisms," Associated General Publishers, Pty. Ltd., Sydney, Australia, 1953, chapter 11.

2 O. Bottema, "On Grubler's Formulae for Mechanisms," *Applied Scientific Research*, vol. A2, 1950, pp. 162–164.

3 R. T. Hinkle, C. Ip, and J. S. Frame, "Acceleration in Mechanisms," JOURNAL OF APPLIED MECHANICS, vol. 22, TRANS. ASME, vol. 77, 1955, pp. 222–226; also discussion in vol. 23, 1956, pp. 138–143.

4 F. H. Raven, "Velocity and Acceleration Analysis of Plane and Space Mechanisms by Means of Independent-Position Equations," JOURNAL OF APPLIED MECHANICS, vol. 25, TRANS. ASME, vol. 80, 1958, pp. 1–6.

5 E. A. Guillemin, "Introductory Circuit Theory," John Wiley & Sons, Inc., New York, N. Y., 1953, chapter 1.

6 S. Timoshenko and D. H. Young, "Theory of Structures," McGraw-Hill Book Company, Inc., New York, N. Y., 1945, p. 82.

7 W. Blaschke and H. R. Mueller, "Ebene Kinematik," Verlag Von R. Oldenbourg, Munich, Germany, 1956, p. 82.

8 R. Courant and H. Robbins, "What Is Mathematics?" Oxford University Press, New York, N. Y., 1943, chapter 5.

Approximate Synthesis of Spatial Linkages

J. DENAVIT
Department of Mechanical Engineering, Northwestern University, Evanston, Ill.
Assoc. Mem. ASME

R. S. HARTENBERG
Department of Mechanical Engineering, Northwestern University, Evanston, Ill.
Mem. ASME

Freudenstein's approximate synthesis of planar four-bar linkages is generalized to spatial linkages, and the conditions under which this generalization is applicable are expressed. Three cases of synthesis of spatial linkages to generate functions of one variable between nonparallel axes are considered in detail: (a) The spherical four-bar linkage; (b) a variation of the four-bar linkage in which two turning pairs are replaced by ball-and-socket joints, a linkage which may be designed to generate arbitrary functions with up to seven accuracy points; and (c) a second variation of the four-bar linkage where three turning pairs are replaced by cylinder pairs, a linkage capable of being designed to generate a variable-pitch helical motion with three accuracy points.

A LINKAGE is a particular type of mechanism in which the links, assumed rigid, are connected by means of only lower pairs, i.e., pairs allowing surface contact between adjacent links. There are only six lower pairs, the spheric pair or ball-and-socket joint, the planar pair, the cylinder pair whose elements are mating right circular cylinders, the screw pair, the revolute or turning pair, the prism or crosshead. A linkage is thus characterized by the nature and number of the pairs forming its connections, and the parameters defining the relative positions in the pairs in each link. For example, the four-bar linkage in Fig. 1 is characterized by the fact that it has four revolute pairs with parallel axes, the distances between axes being the parameters a_1, a_2, a_3, a_4.

The purpose of a linkage is to transform one motion into another. For example, the slider-crank mechanism transforms the uniform rotation of its crank into the reciprocating translation of its slider; the universal joint (Hooke's joint) transforms rotation around an axis into rotation around another nonparallel but intersecting axis. As a computing mechanism, the four-bar linkage may be designed to generate some functions with remarkable accuracy. The synthesis of four-bar linkages, i.e., the determination of the parameters a_1, a_2, a_3, a_4 that will yield an approximation to a desired function between the input (or crank angle) ϕ and the output (or follower angle) ψ, Fig. 1, has been approached by a number of geometric and, more recently, analytical methods. One method in particular, that of Freudenstein [1],[1] will be discussed here, because it may be generalized to a wide variety of planar and spatial linkages.

This paper presents a general method for the synthesis of spatial linkages and applies the method to three specific cases for which complete solutions are given in the form of tables usable without a detailed knowledge of the derivations. An IBM 650 computer program to perform the synthesis of the linkage taken as the second example is available from the authors.

This method differs from that of Levitskii and Shakvuasian [10] which was concerned with the synthesis of a spatial linkage (the second example which follows), and yields a greater flexibility in design for it leaves some parameters to be chosen by the designer to meet space or force-transmission requirements. Other work on the synthesis of spatial linkages by Woerle [2] made use of graphical considerations and it is believed that the analytical method presented here yields closer approximations to the desired functions.

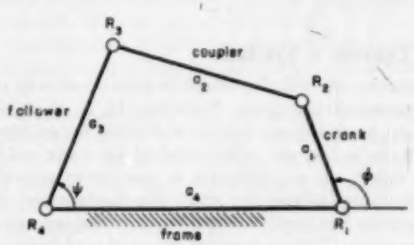

Fig. 1 Four-revolute planar mechanism

Consider the problem of designing a planar four-bar linkage such that to three given positions of the crank, defined by ϕ_1, ϕ_2, and ϕ_3, there correspond three prescribed positions of the follower, ψ_1, ψ_2, and ψ_3. In other words, develop a method to determine the parameters a_1, a_2, a_3, a_4 such that to three values ϕ_1, ϕ_2, ϕ_3 of ϕ there correspond three prescribed values ψ_1, ψ_2, ψ_3 of ψ. Freudenstein's method is based on the following displacement equation relating the crank and follower angles ϕ and ψ, Fig. 1:

$$k_1 \cos \phi - k_2 \cos \psi + k_3 = \cos (\phi - \psi) \qquad (1)$$

where

$$k_1 = \frac{a_4}{a_2}, \quad k_2 = \frac{a_4}{a_1}, \quad k_3 = \frac{a_1^2 - a_2^2 + a_3^2 + a_4^2}{2a_1a_2}.$$

When the foregoing equation is written for the three pairs of values (ϕ_1, ψ_1), (ϕ_2, ψ_2), (ϕ_3, ψ_3), it yields a system of three equations linear in k_1, k_2, k_3,

$$k_1 \cos \phi_1 - k_2 \cos \psi_1 + k_3 = \cos (\phi_1 - \psi_1),$$
$$k_1 \cos \phi_2 - k_2 \cos \psi_2 + k_3 = \cos (\phi_2 - \psi_2),$$
$$k_1 \cos \phi_3 - k_2 \cos \psi_3 + k_3 = \cos (\phi_3 - \psi_3),$$

which may be solved for k_1, k_2, and k_3 from which the parameters of the linkage may be deduced as

$$a_1 = \frac{a_4}{k_2}, \quad a_2 = \frac{a_4}{k_1}, \quad a_3 = (a_1^2 + a_2^2 + a_4^2 - 2a_1a_2k_3)^{1/2}$$

It is noted that the value of the parameter a_4 may be chosen arbitrarily. This parameter determines the scale of the linkage, and thus in the present problem there are only three design parameters, i.e., a_1/a_4, a_2/a_4, and a_3/a_4.

[1] Numbers in brackets designate References at end of paper.

Contributed by the Applied Mechanics Division and presented at the Annual Meeting, Atlantic City, N. J., November 29–December 4, 1959, of THE AMERICAN SOCIETY OF MECHANICAL ENGINEERS.

Discussion of this paper should be addressed to the Secretary, ASME, 29 West 39th Street, New York, N. Y., and will be accepted until April 10, 1960, for publication at a later date. Discussion received after the closing date will be returned.

NOTE: Statements and opinions advanced in papers are to be understood as individual expressions of their authors and not those of the Society. Manuscript received by ASME Applied Mechanics Division, January 30, 1959. Paper No. 59—A-24.

The problem of designing a four-bar linkage having prescribed angular velocities and angular accelerations of the crank and follower for a given configuration may be solved in similar fashion by twice taking the derivative of Equation (1),

$$k_1 \cos \phi - k_2 \cos \psi + k_3 = \cos (\phi - \psi),$$

$$k_1(\omega_\phi \sin \phi) - k_2(\omega_\psi \sin \psi) = (\omega_\phi - \omega_\psi) \sin (\phi - \psi),$$

$$k_1(\alpha_\phi \sin \phi + \omega_\phi^2 \cos \phi) - k_2(\alpha_\psi \sin \psi + \omega_\psi^2 \cos \psi) = (\alpha_\phi - \alpha_\psi) \sin (\phi - \psi) + (\omega_\phi - \omega_\psi)^2 \cos (\phi - \psi),$$

where $\omega_\phi = d\phi/dt$ and $\omega_\psi = d\psi/dt$ are the angular velocities of the crank and follower, and $\alpha_\phi = d^2\phi/dt^2$ and $\alpha_\psi = d^2\psi/dt^2$ are the angular accelerations of the crank and follower. Solution of this system yields k_1, k_2, and k_3 from which the three ratios a_1/a_4, a_2/a_4, a_3/a_4 may be deduced. Freudenstein also developed methods to match four and five positions of the crank and follower of a planar four-bar linkage, but these methods will not be discussed in this paper.

General Equation of Synthesis

The foregoing method of synthesis is made possible by the form of the displacement equation, Equation (1), in which three coefficients k_1, k_2, and k_3 are functions of three design parameters a_1/a_4, a_2/a_4, a_3/a_4 and also independent of the crank and follower angles ϕ and ψ. It will therefore be possible to generalize this method to other linkages for which the displacement equation may be written in a form having essentially the same properties. Consider a general linkage, in which the number of design parameters is n, and for which ϕ and ψ are the input and output variables, analogous to the crank and follower angles in the case of the four-bar linkage. If the displacement equation of the linkage may be written in the form

$$\sum_{i=1}^{n} k_i(n \text{ design parameters})\, G_i(\phi, \psi) = F(\phi, \psi), \qquad (2)$$

then, writing this equation for n pairs of values (ϕ_j, ψ_j), $j = 1, 2, \ldots, n$, there will be n equations linear in $k_1, k_2, \ldots, k_n$,

$$k_1 G_1(\phi_1, \psi_1) + k_2 G_2(\phi_1, \psi_1) + \ldots + k_n G_n(\phi_1, \psi_1) = F(\phi_1, \psi_1),$$

$$k_1 G_1(\phi_2, \psi_2) + k_2 G_2(\phi_2, \psi_2) + \ldots + k_n G_n(\phi_2, \psi_2) = F(\phi_2, \psi_2)$$

$$\ldots\ldots\ldots\ldots\ldots\ldots\ldots\ldots\ldots\ldots\ldots\ldots\ldots\ldots\ldots\ldots\ldots\ldots\ldots\ldots\ldots\ldots$$

$$k_1 G_1(\phi_n, \psi_n) + k_2 G_2(\phi_n, \psi_n) + \ldots + k_n G_n(\phi_n, \psi_n) = F(\phi_n, \psi_n),$$

which may be solved for $k_1, k_2, \ldots, k_n$. Since these coefficients are functions of n design parameters, this leads to a set of n equations that must be solved for these n design parameters.

In summary, the proposed method of synthesis therefore applies to linkages satisfying the following conditions:

(a) A displacement equation relating the input ϕ and output ψ may be written. It must be noted here that this is not always possible; it is, for example, in general impossible to write such a displacement equation for a seven-revolute mechanism.

(b) The displacement equation may be written in the form of Equation (2), where n is the number of design parameters.

The Four-Revolute Spherical Mechanism

Three linkages of four revolutes are known to have motion with one degree of freedom. They are the planar four-revolute mechanism (or four-bar linkage), Fig. 1, where the revolute axes are parallel, the spherical four-revolute mechanism, Fig. 2, where all four axes intersect at one point (Hooke's joint is a special case of this mechanism), and Bennett's mechanism [3], where the axes are skewed, but with prescribed geometric relations.

Earlier papers [4, 5] introduced a method by which linkages

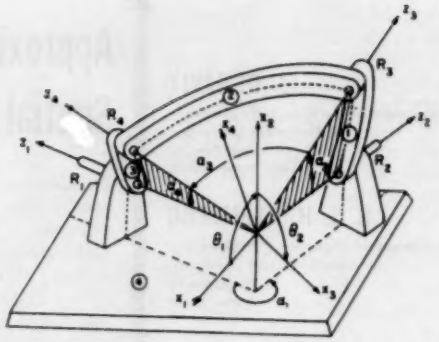

Fig. 2 Four-revolute spherical mechanism

(planar and spatial) could be described in terms of "symbolic equations." These symbolic equations, which may be interpreted in terms of matrices and yield algebraic methods of displacement analysis, characterize linkages by specifying their pairs and the geometric relations existing between the pairs of each link. Thus the symbolic equation for the spherical four-revolute mechanism shown in Fig. 2 may be written as

$$R_1 \begin{vmatrix} 0 \\ \alpha_1 \\ \theta_1 \\ 0 \end{vmatrix} R_2 \begin{vmatrix} 0 \\ \alpha_2 \\ \theta_2 \\ 0 \end{vmatrix} R_3 \begin{vmatrix} 0 \\ \alpha_3 \\ \theta_3 \\ 0 \end{vmatrix} R_4 \begin{vmatrix} 0 \\ \alpha_4 \\ \theta_4 \\ 0 \end{vmatrix} = I$$

in which the four-revolute pairs are indicated as R_1, R_2, R_3, R_4. The relative position of successive pairs in each link is defined by the parameters between verticals; the first parameter refers to the length of the common perpendicular between pair axes. Here these lengths are zero since all revolute axes intersect. The second parameter is the angle between successive pair axes; these parameters α_1, α_2, α_3, α_4 do not vary with the motion of the linkage, but since they define the geometry, become the design parameters. The axis, x_1, Fig. 2, is the common perpendicular to z_4 and z_1, i.e., the perpendicular to the plane of link 1, similarly, x_2, x_3, x_4 are, respectively, perpendicular to z_1 and z_3, z_2 and z_3, z_3 and z_4. The third parameter between verticals is the angle between successive x-axes; it represents the rotation of each revolute pair; θ_1 is the rotation of R_1, θ_2 the rotation of R_2, and so on, each varying with the motion of the linkage. Positive directions for the α and θ are shown in Fig. 2. The last parameter between verticals is the distance between successive x-axes. Here these distances are zero since all axes intersect at the same point. The symbols $= I$ of the equation indicate that the linkage forms a closed chain; this symbolism is justified by the interpretation of the symbolic equation in terms of matrices [4, 5].

Now, if θ_1 is chosen as the input variable of the linkage, and θ_2 as its output variable, a displacement analysis [5] leads to the following equation:

$$\sin \alpha_1 \cot \alpha_2 \cos \theta_1 + \sin \alpha_1 \cot \alpha_4 \cos \theta_2 + \frac{\cos \alpha_3}{\sin \alpha_2 \sin \alpha_4} - \cos \alpha_1 \cot \alpha_2 \cot \alpha_4 = \sin \theta_1 \sin \theta_2 - \cos \alpha_1 \cos \theta_1 \cos \theta_2, \qquad (3)$$

from which the synthesis will be made. If three design parameters are chosen as α_2, α_3, α_4, it is seen that Equation (3) may be put in the form of Equation (2) on setting

$$k_1 = \sin \alpha_1 \cot \alpha_2, \quad k_2 = \sin \alpha_1 \cot \alpha_4,$$

$$k_3 = \frac{\cos \alpha_3}{\sin \alpha_2 \sin \alpha_4} - \cos \alpha_1 \cot \alpha_2 \cot \alpha_4,$$

$$G_1 = \cos\theta_1, \quad G_2 = \cos\theta_2, \quad G_3 = 1,$$

$$F = \sin\theta_1 \sin\theta_2 - \cos\alpha_1 \cos\theta_1 \cos\theta_2,$$

to yield

$$k_1 \cos\theta_1 + k_2 \cos\theta_2 + k_3 = \sin\theta_1 \sin\theta_2 - \cos\alpha_1 \cos\theta_1 \cos\theta_2.$$

To determine the design parameters α_1, α_2, α_4 such that to three values θ_1^1, θ_1^2, θ_1^3 of the input variable θ_1 there correspond three prescribed values θ_2^1, θ_2^2, θ_2^3 of the output variable θ_2, the foregoing equation is written for each pair of values,

$$k_1 \cos\theta_1^i + k_2 \cos\theta_2^i + k_3 = \sin\theta_1^i \sin\theta_2^i - \cos\alpha_1 \cos\theta_1^i \cos\theta_2^i \quad (4)$$

Subtracting the equations corresponding to $i = 2$ and 3 from the equation corresponding to $i = 1$ and solving the resulting system yields k_1 and k_2; from these k_3 may be obtained by means of Equation (4), written for any value of i (1, 2, 3). The angle α_1 is deduced from k_1, α_4 is deduced from k_2, and α_2 from k_3. The computation procedure is summarized in Table 1.

Table 1 Synthesis of four-revolute spherical mechanism for three specified positions of input and output links

Positions of input link: θ_1^i $(i = 1, 2, 3)$
Positions of output link: θ_2^i $(i = 1, 2, 3)$
α_1: specified (different from zero)

$$w_1 = \cos\theta_1^1 - \cos\theta_1^3, \quad w_2 = \cos\theta_2^1 - \cos\theta_2^3,$$

$$w_3 = \cos\theta_1^1 - \cos\theta_1^2, \quad w_4 = \cos\theta_2^1 - \cos\theta_2^2,$$

$$F^i = \sin\theta_1^i \sin\theta_2^i - \cos\alpha_1 \cos\theta_1^i \cos\theta_2^i,$$

$$w_5 = F^1 - F^3, \quad w_6 = F^1 - F^2,$$

$$k_1 = \frac{w_4 w_5 - w_2 w_6}{w_1 w_4 - w_2 w_3}, \quad k_2 = \frac{w_1 w_6 - w_3 w_5}{w_1 w_4 - w_2 w_3},$$

$$k_3 = F^i - k_1 \cos\theta_1^i - k_2 \cos\theta_2^i \quad (\text{with } i = 1, 2 \text{ or } 3)$$

$$\alpha_2 = \text{arc cot}\left(\frac{k_1}{\sin\alpha_1}\right), \quad \alpha_4 = \text{arc cot}\left(\frac{k_2}{\sin\alpha_1}\right),$$

$$\alpha_3 = \text{arc cos}\,(k_3 \sin\alpha_2 \sin\alpha_4 + \cos\alpha_1 \cot\alpha_2 \cot\alpha_4)$$

Example. Design a four-revolute spherical mechanism to generate the function $y = \log_{10} x$ in the interval $1 \leqslant x \leqslant 10$ between two perpendicular shafts. Further specifications are ranges of variation of θ_1 and θ_2 to be $\Delta\theta_1 = 60°$ and $\Delta\theta_2 = 90°$; accuracy points at 1, 3, 10; initial value of θ_1 (corresponding to $x = 1$) equal to 45°; initial value of θ_2 equal to $-45°$. Then

$$\theta_1^1 = 45°, \quad \theta_1^2 = 58°20', \quad \theta_1^3 = 105°$$

$$\theta_2^1 = -45°, \quad \theta_2^2 = -2°6', \quad \theta_2^3 = 45°$$

Table 1, with $\alpha_1 = 90°$ yields $w_1 = 0.182$, $w_2 = -0.292$, $w_3 = 0.966$, $w_4 = 0$, $w_5 = 0.468$, $w_6 = -1.183$ from which $k_1 = -1.225$, $k_2 = 0.842$, $k_3 = -0.230$ and $\alpha_2 = -39°20'$, $\alpha_3 = 83°40'$, $\alpha_4 = 49°50'$. The maximum absolute error, i.e., the maximum difference between $\log_{10} x$ and the value given by the linkage, is $\epsilon = 0.07$, which corresponds to 7 per cent of the range of variation of y.

Two-Revolute, Two-Spheric-Pair Mechanism

The familiar planar four-bar linkage may be modified by replacing the two revolutes connecting the coupler to the crank and follower by spheric pairs. In the resulting mechanism, shown in Fig. 3, the axes z_1 and z_4 of the remaining two revolutes R_1 and R_4 do not have to be parallel and thus their angle α_4 as well as their perpendicular distance a_4 may assume any value. To these parameters and to the crank, coupler, and follower lengths, a_1, a_2, and a_3 two more parameters s_1 and s_4 must now be added, bringing the total number of fixed parameters to seven; s_1 is the distance along z_1 from the axis x_1 to the plane of rotation of the crank, and s_4 is the distance along z_4 from the plane of rotation of the follower to x_1, Fig. 3.

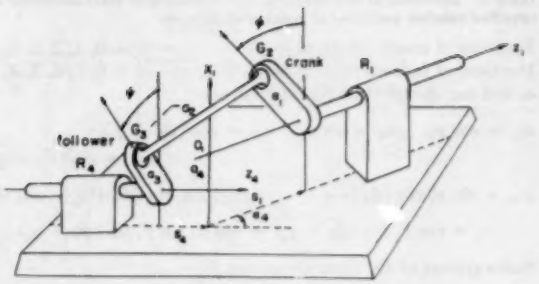

Fig. 3 Two-revolute, two-spheric-pair mechanism (general case)

A displacement analysis of this linkage may be carried out by writing the co-ordinates of the centers of the spheric pairs G_2 and G_3 with respect to the co-ordinate system $o_1x_1y_1z_1$, Fig. 3 (y_1 is chosen to complete the right-handed rectangular system $o_1x_1y_1z_1$), and expressing the fact that the distance between these centers is equal to a_2. Such an analysis yields the relation between crank (or input) angle ϕ and follower (or output) angle ψ:

$$a_1^2 - a_2^2 + a_3^2 + a_4^2 + s_1^2 + s_4^2 + 2s_1s_4 \cos\alpha_4 + 2a_1a_4 \cos\phi + 2a_1s_4 \sin\alpha_4 \sin\phi - \cos\psi(2a_3a_4 + 2a_1a_3 \cos\phi) - \sin\psi(2a_1a_3 \cos\alpha_4 \sin\phi - 2s_1a_3 \sin\alpha_4) = 0 \quad (5)$$

where ϕ is measured counterclockwise around z_1 from x_1 to the axis of the crank, and ψ measured counterclockwise around z_4 from x_1 to the axis of the follower.

The values of a_4 and α_4, which determine the relative position of the input and output shafts will be specified; the remaining five parameters will be used in the synthesis of the linkage. In addition, the angle ϕ_0 of the crank corresponding to the initial position, which was chosen arbitrarily in the preceding example, may now be taken as a design parameter, and $\phi = \phi_0 + p$. The angle ψ_0 of the follower corresponding to the initial position will still be chosen arbitrarily. With the foregoing substitution, the displacement equation may be put in the form of Equation (2) as

$$k_1 \cos p + k_2 \sin p + k_3 \cos\psi + k_4 \sin\psi + k_5(\sin p \cos\psi - \cos\alpha_4 \cos p \sin\psi) + k_6 = \cos p \cos\psi + \cos\alpha_4 \sin p \sin\psi$$

in which

$$k_1 = \frac{a_4 + s_4 \sin\alpha_4 \tan\phi_0}{a_3}, \quad k_4 = \frac{s_1 \sin\alpha_4}{a_1 \cos\phi_0},$$

$$k_2 = \frac{s_4 \sin\alpha_4 - a_4 \tan\phi_0}{a_3}, \quad k_5 = \tan\phi_0,$$

$$k_3 = \frac{-a_4}{a_1 \cos\phi_0},$$

$$k_6 = \frac{a_1^2 - a_2^2 + a_3^2 + a_4^2 + s_1^2 + s_4^2 + 2s_1s_4 \cos\alpha_4}{2a_1a_3 \cos\phi_0},$$

allowing a synthesis for six positions of the input and output shafts in the present case; the computation procedure is summarized in Table 2. A program for use with the IBM 650

Table 2 Synthesis of two-revolute, two-spheric-pair mechanism for six specified relative positions of crank and follower

Positions of crank: $\phi = \phi_0 + p_i$ $(i = 0, 1, 2, 3, 4, 5)$
Positions of follower: $\psi = \psi_0 + q_i$ $(i = 0, 1, 2, 3, 4, 5)$
a_4 and α_4: specified (different from zero)

$$w_{i1} = \cos p_i, \quad w_{i2} = \sin p_i, \quad w_{i3} = \cos(\psi_0 + q_i), \quad w_{i4} = \sin(\psi_0 + q_i),$$

$$w_{i5} = \sin p_i \cos(\psi_0 + q_i) - \cos\alpha_4 \cos p_i \sin(\psi_0 + q_i), \quad w_{i6} = 1$$

$$v_i = \cos p_i \cos(\psi_0 + q_i) + \cos\alpha_4 \sin p_i \sin(\psi_0 + q_i)$$

Solve system of six linear equations [6]

$$\sum_{j=1}^{6} w_{ij} k_j = v_i \qquad (i = 0, 1, 2, 3, 4, 5)$$

to find $k_1, k_2, k_3, k_4, k_5, k_6$.

$$\phi_0 = \arctan k_5 \qquad (-90^\circ < \phi_0 \leqslant +90^\circ)$$

$$a_1 = -\frac{a_4(1 + k_5^2)^{1/2}}{k_3}, \quad s_1 = -\frac{k_4 a_4}{k_3 \sin\alpha_4},$$

$$s_4 = \frac{a_4(k_2 + k_1 k_5)}{\sin\alpha_4(k_1 - k_2 k_5)}, \quad a_3 = \frac{s_4 \sin\alpha_4 - a_4 k_5}{k_2},$$

$$a_2 = \left[a_1^2 + a_3^2 + a_4^2 + s_1^2 + s_4^2 + 2a_1 s_4 \cos\alpha_4 - \frac{2a_1 a_3 k_5}{(1 + k_5^2)^{1/2}}\right]^{1/2}$$

magnetic-drum data-processing machine has been prepared to perform this synthesis. This program is available upon request from the authors. Another program, also available from the authors, will perform the analysis of the mechanism and thus check the results of the synthesis and evaluate the errors between accuracy points.

Example (a). Design a two-revolute, two-spheric-pair mechanism to generate the function $y = \log_{10} x$ in the interval $1 \leqslant x \leqslant 100$ between perpendicular shafts ($\alpha_4 = 90^\circ$) a distance of 1 in. apart ($a_4 = 1$). Further specifications are range of variation of ϕ is 120°, range of variation of ψ is 90°, and initial value of ψ is $\psi_0 = 0$. Six accuracy points are taken with Chebychev spacing [7], thus

$$p_0 = 0, \quad p_1 = 15.5270^\circ, \quad p_2 = 42.4212^\circ, \quad p_3 = 76.4738^\circ, \quad p_4 = 100.3694^\circ, \quad p_5 = 115.8962^\circ$$

$$q_0 = 0, \quad q_1 = 34.240^\circ, \quad q_2 = 51.601^\circ, \quad q_3 = 61.744^\circ, \quad q_4 = 67.617^\circ, \quad q_5 = 70.344^\circ$$

The parameters of the resulting mechanism are

$$a_1 = 2.5171, \quad a_2 = 4.0409, \quad a_3 = 3.8708, \quad a_4 = 1.0$$

$$s_1 = 0.1566, \quad s_4 = -1.3937, \quad \alpha_4 = 90^\circ$$

with the initial value of $\phi: \phi_0 = -63.334^\circ$. The maximum error, i.e., the maximum difference between $\log_{10} x$ and the value given by the linkage is $\epsilon = 0.01$, which corresponds to 1 per cent of the range of variation of y.

Example (b). Generate the function $y = \cos x$ in the interval $0 \leqslant x \leqslant 180^\circ$ with $\alpha_4 = 90^\circ$, range of $\phi = 150^\circ$, range of $\psi = 100^\circ$, initial value of $\psi: \psi_0 = 0$. Taking six accuracy points with Chebychev spacing yields

$$p_0 = 0, \quad p_1 = 19.41^\circ, \quad p_2 = 53.03^\circ, \quad p_3 = 91.85^\circ, \quad p_4 = 125.47^\circ, \quad p_5 = 144.88^\circ$$

$$q_0 = 0, \quad q_1 = -5.125^\circ, \quad q_2 = -30.165^\circ, \quad q_3 = -69.695^\circ, \quad q_4 = -94.735^\circ, \quad q_5 = -99.86^\circ,$$

and the parameters of the resulting mechanism are

$$a_1 = -0.4949, \quad a_2 = 2.7460, \quad a_3 = -1.3158, \quad a_4 = 1.0$$

$$s_1 = -0.8388, \quad s_4 = -2.0749, \quad \alpha_4 = 90^\circ,$$

with $\phi_0 = -40.291^\circ$. In this case the maximum error is $\epsilon = 0.0028$ which corresponds to 0.14 per cent of the range of variation of y.

Example (c). Generate the function $y = x^2$ in the interval $-1 \leqslant x \leqslant +1$. Because of the symmetry of this function in the given interval, a symmetrical mechanism will be chosen here. This may be done by specifying $\alpha_4 = 90^\circ$, $\psi_0 = 0$ and choosing two symmetrical accuracy points as $x = 1$ and $x = -1$. The remaining accuracy points are all chosen between $x = 0$ and $x = 1$, at $x = 0.25$, $x = 0.50$ and $x = 0.75$. In this case, ψ must be chosen as the input representing x, and ϕ as the output representing y, for the mechanism is symmetrical with respect to the plane $x_1 z_4$, Fig. 4. The range of ϕ is taken as 100° while ψ will vary between −100° and +100°. With these assumptions, the six accuracy points are

$$p_0 = 0, \quad p_1 = 6.25^\circ, \quad p_2 = 25.00^\circ, \quad p_3 = 56.25^\circ, \quad p_4 = 100.00^\circ, \quad p_5 = 100.00^\circ$$

$$q_0 = 0, \quad q_1 = 25^\circ, \quad q_2 = 50^\circ, \quad q_3 = 75^\circ, \quad q_4 = 100^\circ, \quad q_5 = -100^\circ$$

and the parameters of the resulting mechanism are

$$a_1 = 0.5171, \quad a_2 = 5.5660, \quad a_3 = -2.4990, \quad a_4 = 1.0$$

$$s_1 = 0, \quad s_4 = 4.5792, \quad \alpha_4 = 90^\circ,$$

with $\phi_0 = -62.172^\circ$. Note that $s_1 = 0$, a required condition to obtain a mechanism which is symmetrical with respect to the plane $x_1 z_4$, Fig. 4; this condition results from the choice of two symmetrical accuracy points. This mechanism fits the function exactly at nine accuracy points: $x = 0, 0.25, 0.50, 0.75, 1.0, -1.0$, as specified, and $x = -0.25, -0.50, -0.75$, because of symmetry. The maximum error is $\epsilon = 0.0013$ which corresponds to 0.13 per cent of the range of variation of y. The magnitude of this error shows that the present mechanism is well suited for the generation of symmetrical functions. In comparison, the optimum planar four-bar linkage in the same interval generates the function $y = x^2$ with an error of 4.47 per cent of the range of variation of y [8].

It may be noted that by repeating the synthesis for a sequence of values of ψ_0, it is possible to obtain a sequence of solutions, among which the most desirable from the standpoint of force transmission or space requirements may be chosen. By the same

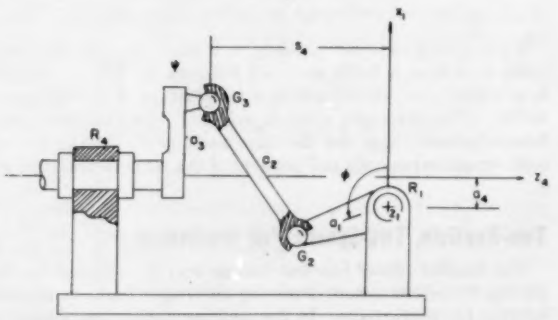

Fig. 4 Symmetrical two-revolute, two-spheric-pair mechanism. (NOTE: Axis x_1 should point down, whence ϕ is 180° larger than shown.)

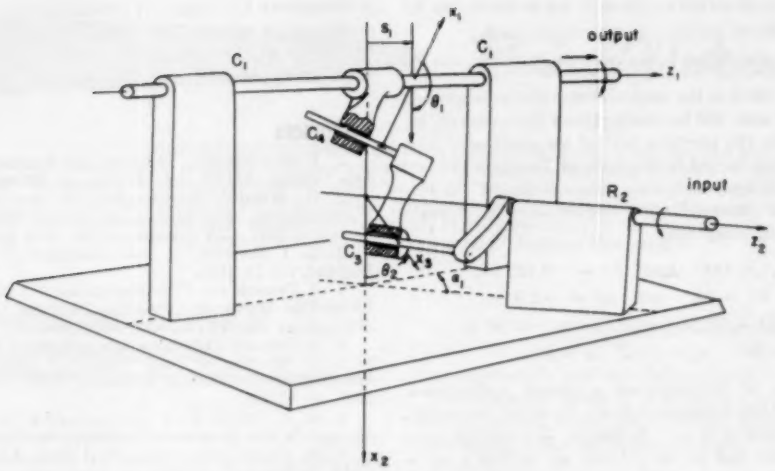

Fig. 5 Three-cylinder, one-revolute mechanism

repeated process it is also possible, in general, to obtain a value of ψ_0 for which a given function will be generated with seven accuracy points.

Three-Cylinder, One-Revolute Mechanism

A cylinder differs from a revolute in that it allows rectilinear translation along its axis as well as rotation around this axis. If, in a four-revolute spherical mechanism, three of the revolutes R_1, R_3, and R_4, for example, are replaced by cylinders, the resulting linkage, Fig. 5, will be movable even when the pair axes do not intersect. A symbolic equation for this linkage is obtained by simply replacing the revolute symbols R_1, R_3, and R_4 by cylinder symbols C_1, C_3, and C_4. Since the pair axes may now assume any relative position, the zeros characterizing the four-revolute spherical mechanism may be replaced by parameters a_1, a_2, a_3, a_4 in the first row and s_1, s_2, s_3, s_4 in the last row to give

$$C_1\begin{vmatrix} a_1 \\ \alpha_1 \\ \theta_1 \\ s_1 \end{vmatrix} R_2\begin{vmatrix} a_2 \\ \alpha_2 \\ \theta_2 \\ s_2 \end{vmatrix} C_3\begin{vmatrix} a_3 \\ \alpha_3 \\ \theta_3 \\ s_3 \end{vmatrix} C_4\begin{vmatrix} a_4 \\ \alpha_4 \\ \theta_4 \\ s_4 \end{vmatrix} = I$$

Since rectilinear translation is now possible along the axes z_1, z_2, and z_4, the parameters s_1, s_2 and s_4 vary with the motion of the mechanism, which thus involves seven variables and nine fixed parameters.

The purpose of this linkage is to transform an input rotation into an output of combined rotation and translation. If θ_2 is the input variable, with θ_1 and s_1 as output variables, the synthesis involves two functions, θ_1 as a function of θ_2, and s_1 as a function of θ_2.

A displacement analysis [5] shows that the equation relating θ_1 and θ_2 in the present linkage is identical to the equation relating θ_1 and θ_2 in the four-revolute spherical mechanism, Equation (3), and is independent of the length parameters a_1, a_2, a_3, a_4, and s_1. Specifying a value for α_1, the determination of the design parameters α_2, α_3, α_4 such that to three given values of θ_2 there correspond three prescribed values of θ_1, will therefore follow the procedure of Table 1.

The remainder of the synthesis is based on the following displacement equation relating s_1 to θ_1 and θ_2 [5], where a_2 is taken equal to zero:

$$s_1(A_0 \cos\theta_1 - B_0 \sin\theta_1) + A_1 \sin\theta_1 + B_1 \cos\theta_1 - C_1 = 0 \quad (6)$$

in which

$$A_0 = \sin\alpha_3 \sin\alpha_4 \sin\theta_2,$$

$$B_0 = -\sin\alpha_4(\sin\alpha_1 \cos\alpha_2 + \cos\alpha_1 \sin\alpha_2 \cos\theta_2),$$

$$A_1 = (a_3 \cos\alpha_2 \sin\alpha_4 + a_4 \sin\alpha_2 \cos\alpha_4)\sin\theta_2,$$

$$B_1 = -a_4 \cos\alpha_4(\sin\alpha_1 \cos\alpha_2 + \cos\alpha_1 \sin\alpha_2 \cos\theta_2) - a_1 \sin\alpha_4(\cos\alpha_1 \cos\alpha_2 - \sin\alpha_1 \sin\alpha_2 \cos\theta_2) - a_2 \sin\alpha_4(-\sin\alpha_1 \sin\alpha_2 + \cos\alpha_1 \cos\alpha_2 \cos\theta_2),$$

Table 3 Synthesis of three-cylinder, one-revolute mechanism for three specified positions of input and output links

Positions of input link: θ_2^i $(i = 1, 2, 3)$
Positions of output link: θ_1^i and s_1^i $(i = 1, 2, 3)$
α_1 and a_1: specified (different from zero),
Determine α_2, α_3, α_4 as in Table 1

$$r_1 = -\cos\alpha_1 \cos\alpha_2 \sin\alpha_4, \quad r_3 = -\cos\alpha_1 \sin\alpha_2 \cos\alpha_4,$$

$$r_2 = -\sin\alpha_1 \cos\alpha_2 \cos\alpha_4, \quad r_4 = \sin\alpha_1 \sin\alpha_2 \sin\alpha_4,$$

$$G_1^i = r_3 + r_1 \cos\theta_1^i + r_3 \cos\theta_2^i + r_4 \cos\theta_1^i \cos\theta_2^i,$$

$$G_2^i = r_3 + r_4 \cos\theta_1^i + r_2 \cos\theta_2^i + r_1 \cos\theta_1^i \cos\theta_2^i + \cos\alpha_3 \sin\alpha_4 \sin\theta_1^i \sin\theta_2^i,$$

$$G_3 = \sin\alpha_3,$$

$$G_4^i = r_1 + r_2 \cos\theta_1^i + r_4 \cos\theta_2^i + r_3 \cos\theta_1^i \cos\theta_2^i + \sin\alpha_3 \cos\alpha_4 \sin\theta_1^i \sin\theta_2^i,$$

$$A_0^i = \sin\alpha_2 \sin\alpha_4 \sin\theta_2^i,$$

$$B_0^i = -\sin\alpha_4(\sin\alpha_1 \cos\alpha_2 + \cos\alpha_1 \sin\alpha_2 \cos\theta_2^i),$$

$$F^i = -a_1 G_1^i - s_1^i(A_0^i \cos\theta_1^i - B_0 \sin\theta_1^i),$$

$$w_1 = G_2^1 - G_2^3, \quad w_2 = G_4^1 - G_4^3, \quad w_3 = G_2^1 - G_2^2, \quad w_4 = G_4^1 - G_4^2, \quad w_5 = F^1 - F^3, \quad w_6 = F^1 - F^2$$

$$a_2 = \frac{w_4 w_5 - w_2 w_6}{w_1 w_4 - w_2 w_3}, \quad a_4 = \frac{w_1 w_6 - w_3 w_5}{w_1 w_4 - w_2 w_3},$$

$$a^3 = \frac{-G_2^i a_2 - G_4^i a_4 + F^i}{G_3} \quad (\text{with } i = 1, 2, \text{or } 3)$$

$$C_1 = -a_3 \sin \alpha_3 + a_4 \sin \alpha_4(\cos \alpha_1 \cos \alpha_2 - \sin \alpha_1 \sin \alpha_2 \cos \theta_2) + a_1 \cos \alpha_4(\sin \alpha_1 \cos \alpha_2 + \cos \alpha_1 \sin \alpha_2 \cos \theta_2) + a_2 \cos \alpha_4(\cos \alpha_1 \sin \alpha_2 + \sin \alpha_1 \cos \alpha_2 \cos \theta_2)$$

The parameter a_1, which is the perpendicular distance between the input and output axes, will be specified, and the angles α_1, α_2, α_3, α_4 are known from the previous part of the synthesis. The foregoing equation may be put in the form of Equation (2) and a three-point synthesis made following the procedure of Table 3.

Example. Design a three-cylinder, one-revolute mechanism satisfying the following conditions:

$$\theta_2^1 = 0 \rightarrow \theta_1^1 = 144^\circ \quad \text{and} \quad s_1^1 = -0.123 \text{ in.},$$
$$\theta_2^2 = 90^\circ \rightarrow \theta_1^2 = 81^\circ \quad \text{and} \quad s_1^2 = -2.10 \text{ in.},$$
$$\theta_2^3 = 180^\circ \rightarrow \theta_1^3 = 83^\circ 30' \quad \text{and} \quad s_1^3 = -0.186 \text{ in.},$$
$$\alpha_1 = 60^\circ, \quad a_1 = 5 \text{ in.}, \quad s_2 = 0$$

From the synthesis of four-revolute spherical mechanisms, Table 1, the values of the angles are known, $\alpha_2 = 30^\circ$, $\alpha_3 = 55^\circ$, $\alpha_4 = 45^\circ$. From Table 3, $r_1 = -0.3062$, $r_2 = -0.5303$, $r_3 = -0.1767$, $r_4 = 0.3062$ and $w_1 = -1.183$, $w_2 = 0.613$, $w_3 = -1.130$, $w_4 = 1.225$, $w_5 = -0.521$, $w_6 = 1.406$, from which $a_2 = 1.982$ in., $a_3 = 4.00$ in., $a_4 = 2.974$ in. A simple model [9] of this mechanism, Fig. 5, was built; it gave an approximate check of these results.

Acknowledgment

The authors are greatly indebted to the Computing Center of Northwestern University for providing computation facilities and programming advice. They wish to express their appreciation to Mr. Peter W. Pakeltis whose skill and enthusiasm made this undertaking possible.

References

1 F. Freudenstein, "Approximate Synthesis of Four-Bar Linkages," TRANS. ASME, vol. 77, 1955, pp. 853–861.

2 H. Woerle, "Kurventafeln für den Entwurf Raeumlicher Kurbelgetriebe," presented at the German Mechanisms Conference, Konstanz, 1957, *VDI Berichte*, vol. 29, 1958, pp. 131–137.

3 G. T. Bennett, "A New Mechanism," *Engineering*, London, England, vol. 76, 1903.

4 J. Denavit and R. S. Hartenberg, "A Kinematic Notation for Lower-Pair Mechanisms Based on Matrices," JOURNAL OF APPLIED MECHANICS, vol. 22, TRANS. ASME, vol. 77, 1955, pp. 215–221.

5 J. Denavit, "Displacement Analysis of Mechanisms Based on (2 × 2) Matrices of Dual Numbers," presented at the German Mechanisms Conference, Konstanz, 1957, *VDI Berichte*, vol. 29, 1958, pp. 81–89.

6 R. A. Frazer, W. J. Duncan, and A. R. Collar, "Elementary Matrices," The Macmillan Company, New York, N. Y., 1947.

7 F. Freudenstein, "Structural Error Analysis in Plane Kinematic Synthesis," *Journal of Engineering for Industry*, TRANS. ASME, series B, vol. 81, February, 1959, pp. 15–22.

8 F. Freudenstein, "Four-Bar Function Generators," *Machine Design*, vol. 30, no. 24, Nov. 27, 1958, pp. 119–123.

9 R. S. Hartenberg, "Die Modellsprache in der Getriebetechnik," presented at the German Mechanisms Conference, Konstanz, 1957, *VDI Berichte*, vol. 29, 1958, pp. 109–113.

10 N. I. Levitskii and K. Ch. Shakvuasian, "Synthesis of Spatial Four-Link Mechanisms With Lower Pairs," *Trudi Seminara Po Teorii Mashin i Mekhanizmov*, vol. 14, no. 54, 1954, pp. 5–24.

Journal of APPLIED MECHANICS

Brief Notes

On the recommendation of the Executive Committee of the ASME Applied Mechanics Division, it was decided to initiate a section devoted to brief notes on technical matters in mechanics. These notes must not be longer than 750 words (about 2½ double-spaced typewritten pages, including figures) and will be subject to the usual review procedure prior to publication. After approval such notes will be published as soon as possible, normally in the next issue of the Journal. The notes should be submitted to the Technical Editors of the Journal of Applied Mechanics.

The Buckling and Deflection of Isosceles-Triangular Plates

L. S. HAN[1]

Consider an isosceles-triangular plate of height a and base $2sa$. The boundaries are defined by $x - a = 0$, $y - sx = 0$, $y + sx = 0$. The plate is acted upon by: (a) a normal compressive thrust N along the boundaries, and (b) a lateral load q (uniform). The governing equation for small deflection is:

$$D\nabla^4 w = q - N\nabla^2 w \tag{1}$$

For simply supported edges, the following boundary conditions apply:

$$w = \nabla^2 w = 0 \tag{2}$$

To solve equation (1) with boundary conditions (2), the Marcus method is used; i.e., to replace equation (1) by

$$-\nabla^2 M = (q + NM)/D \tag{3}$$

$$\nabla^2 w = -M \tag{4}$$

with

$$M = w = 0 \tag{5}$$

on the boundaries.

Each one of equations (3) and (4) may be looked upon as a membrane equation, with equation (3) denoting that of a membrane on a foundation with a negative elastic constant. An approximate solution to each is possible by using the Rayleigh-Ritz method in conjunction with the following deflection function:

$$(M, w) = \sum_n (A_n, B_n)F_n \tag{6}$$

in which A_n and B_n are arbitrary constants for M and w, respectively; and

$$F_n = 2\sin(n\pi x/a)\cos(n\pi y/as) - \sin(2n\pi x/a) \tag{7}$$

Note that

$$\int_A F_n F_m dA = 0, \quad m \neq n$$

and

$$\int_A F_n^2 dA = (3sa^2/2)$$

Furthermore, $F_n = 0$ on the boundaries.

The foregoing function, equation (7), was first introduced and used by Nuttall.[2] According to the Rayleigh-Ritz method, the following integrals are to be minimized:

$$I_m = \int_A [(1/2)(M_x^2 + M_y^2) - M(q/D) - (M^2/2)(N/D)]dA$$

$$I_w = \int_A [(1/2)(w_x^2 + w_y^2) - wM]dA$$

The procedure is therefore to determine the coefficients A_n's from I_m and the B_n's from I_w. In this way, the following coefficients are obtained:

$$A_n = (q/D)(a^2/n^2\pi^2)/[1 + (s^2/3) - (Na^2/D)(1/2n^2\pi^2)] \tag{8}$$

$$B_n = (q/D)(a^4/2n^2\pi^6)/[1 + (s^2/3) - (Na^2/D)(1/2n^2\pi^2)] \tag{9}$$

Equations (6) and (9) therefore define the deflection function for the loading conditions specified. The minimum normal thrust N, before buckling occurs, can be easily identified from equation (9) as

$$(Na^2/D)(1/2n^2\pi^2) = 1 + (s^2/3) \tag{10}$$

from which the smallest N is given by

$$(Na^2/D) = 2\pi^2[1 + (s^2/3)] \tag{11}$$

Equation (11) gives the exact buckling thrust N for an equilateral triangular plate with $s = 1/\sqrt{3}$. In this case,

$$(Na^2/D) = 4\pi^2$$

and the functions in equations (6) and (7) satisfy the Lagrange equation (1) directly, in addition to the boundary conditions (2).

For a right isosceles-triangular plate, equation (11) gives

$$(Na^2/D) = 8\pi^2/3$$

which differs from the exact answer[3] by 6.7 per cent.

An alternate function[3] to equation (7) is

$$F_{m,n} = \cos(\pi(m + n)x/2a)\cos(\pi(m - n)y/2as) - \cos(\pi(m - n)x/2a)\cos(\pi(m + n)y/2as) \tag{12}$$

with

m = odd integers
n = even integers

Taking advantage of the property that

[1] Associate Professor of Mechanical Engineering, The Ohio State University, Columbus, Ohio. Consultant, Janitrol Aircraft Division, Surface Combustion Corporation, Columbus, Ohio.

Discussion of papers in Brief Notes should be addressed to the Secretary, ASME, 29 West 39th Street, New York, N. Y., and will be accepted until April 10, 1960, for publication at a later date. Discussion received after the closing date will be returned.

Note: Statements and opinions advanced in papers are to be understood as individual expressions of their authors and not those of the Society. Manuscript received by Applied Mechanics Division, July 13, 1959.

[2] H. Nuttall, "Torsion of Uniform Rods With Particular Reference to Rods of Triangular Cross Section," Journal of Applied Mechanics, vol. 19, Trans. ASME, vol. 74, 1952, pp. 554–557.

[3] S. Timoshenko, "Theory of Plates and Shells," McGraw-Hill Book Co., Inc., New York, N. Y., 1951, p. 311.

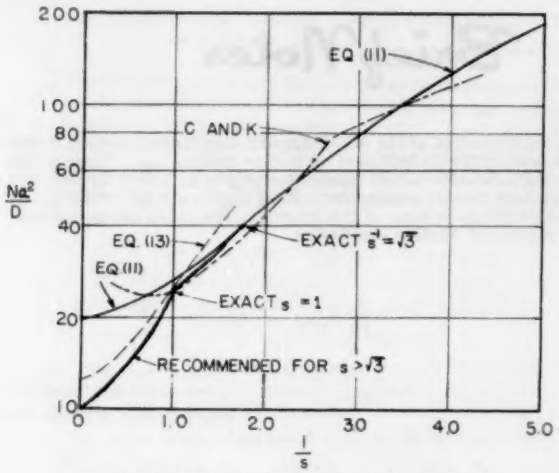

Fig. 1 Buckling thrust N for isosceles-triangular plates

$$\int_A (F_{m,n})(F_{r,p})dA = 0, \quad \text{if} \quad m \neq r, \quad n \neq p$$

and performing identical operations, the buckling thrust N is expressed by

$$(Na^2/D) = 5\pi^2(1 + (1/s^2))/4 \tag{13}$$

which gives the exact buckling strength for $s = 1$.

The buckling loads as given by equations (11) and (13) are plotted in Fig. 1, which also includes the data obtained by Cox and Klein[4] based on the method of collocation. It is apparent therein that in general the data of Cox and Klein agree with those given by equation (11) except a discontinuity in slope in Cox and Klein's data. For large s, the triangular plate approaches a long rectangle; equation (13) seems to give more accurate results than equation (11) and those of Cox and Klein. For $s \to \infty$, i.e., a long rectangle, the exact answer is π^2, while equation (13) yields $1.25\,\pi^2$, a 25 per cent overestimate.

The Creep Deflection of a Rivet in Double Shear

L. N. TAO[1]

In a recent paper[2] the creep deflection of a short, deep, simply supported, and uniformly loaded beam is studied. It is of interest to point out that the solution of the problem may be expressed in closed form by beta functions.

The governing equation of the problem given by Marin[2] is

$$\frac{d^2y}{dx^2} = k_2\left(1 - \frac{4x^2}{L^2}\right)^n + k_3x^{n-1}. \tag{1}$$

With boundary conditions

$$x = 0, \quad y' = 0, \quad y = -\delta;$$
$$x = L/2, \quad y = 0; \tag{2}$$

and the substitution of

$$\xi = 4x^2/L^2,$$

Equation (1) can be integrated as

$$y' = \frac{k_2L}{4}B_\xi\left(\frac{1}{2}, n+1\right) + k_3\frac{x^n}{n} \tag{3}$$

where $B_s(s, t)$ is the incomplete beta function.[3]

Using boundary conditions (2) and integration by parts, we may find

$$y = \frac{k_2L^2}{8}\left[\xi^{1/2}B_\xi\left(\frac{1}{2}, n+1\right) + \frac{(1-\xi)^{n+1}-1}{n+1}\right] + k_3\frac{x^{n+1}}{n(n+1)} - \delta, \tag{4}$$

and

$$\delta = \frac{k_2L^2}{8}\left[B_1\left(\frac{1}{2}, n+1\right) - \frac{1}{n+1}\right] + \frac{k_3}{n(n+1)}\left(\frac{L}{2}\right)^{n+1} \tag{5}$$

where $B_1(s, t)$ is the complete beta function, which is related to gamma functions,

$$B_1(s, t) = \frac{\Gamma(s)\Gamma(t)}{\Gamma(s+t)} \tag{6}$$

Furthermore, the creep deflection factor D and the shear deflection coefficient α_1 of a circular beam[2] may also be expressed in terms of gamma functions,

$$D = \frac{I^n}{kQ_m{}^nr^{n-1}} = \frac{2^n}{k}r^{2n+1}\left[B_1\left(\frac{1}{2n}+1, \frac{3}{2}\right)\right]^n, \tag{7}$$

$$\alpha_1 = \frac{\tau_{max}}{(V/A)} = \frac{\pi}{4}\frac{\Gamma\left(\frac{1}{2n}+\frac{1}{2}\right)\Gamma\left(\frac{1}{2n}+\frac{5}{2}\right)}{\Gamma\left(\frac{1}{2n}+1\right)\Gamma\left(\frac{1}{2n}+2\right)} \tag{8}$$

where

$$Q_m = \frac{I}{2r^4}\left[B_1\left(\frac{1}{2n}+1, \frac{3}{2}\right)\right]^{-1}, \tag{9}$$

$$\tau_{max} = \frac{Vr^2}{2I}Q_mB_1\left(\frac{1}{2n}+\frac{1}{2}, \frac{3}{2}\right). \tag{10}$$

It may be mentioned that the present result is directly reduced to that of the elastic case as the creep exponent n becomes unity.

To apply the present solution to the rivet joint problem, the deflection δ_r of the rivet may be obtained from

$$\delta_r = \left[\frac{kF^nL^{n+2}}{d^{3n+1}}\right]J \tag{11}$$

where

$$J = \frac{B_1\left(\frac{1}{2}, n+1\right) - \frac{1}{n+1}}{2^{2n+1}\left[B_1\left(\frac{1}{2n}+1, \frac{3}{2}\right)\right]^n} + \left(\frac{d}{L}\right)^{n+1}\frac{3^{\frac{n+1}{2}}\alpha_1{}^n}{(n+1)\pi^n}. \tag{12}$$

The numerical calculation is readily obtainable by the use of any tabulation of gamma functions.

[4] H. L. Cox and B. Klein, "The Buckling of Isosceles Triangular Plates," *Journal of the Aeronautical Sciences*, vol. 22, 1955, pp. 312–325.

[1] Associate Professor of Mechanics, Illinois Institute of Technology, Chicago, Ill. Assoc. Mem. ASME.

[2] J. Marin, "Determination of the Creep Deflection of a Rivet in Double Shear," Journal of Applied Mechanics, vol. 26, Trans. ASME, series E, vol. 81, 1959, pp. 285–290.

Manuscript received by ASME Applied Mechanics Division, August 6, 1959.

[3] A. Erdélyi, W. Magnus, F. Oberhettinger, and F. G. Tricomi, "Higher Transcendental Functions, vol. I," McGraw-Hill Book Company, Inc., New York, N. Y., 1953.

Torsion of Prismatical Rods With Isosceles-Triangle and Other Cross Sections

H. D. CONWAY[1]

When calculating the torsional rigidity of prismatical rods having isosceles-triangle cross sections, a satisfactory solution due to Nuttall[2] is available, wherein a Rayleigh-Ritz type solution is used to tabulate the rigidities for a wide range of side ratios. These results are accurate to within 4 per cent.

As is usual with such solutions, the accuracy of the shearing stresses is considerably less than that of the rigidity, and hence it is not surprising that the stress expressions presented are rather crude approximations. Hence it is the object of the present investigation to obtain a closed-form expression whereby the maximum shearing stress can be computed to a good degree of accuracy. It is believed that this expression will augment Nuttall's solution.

Taking the origin at the point O in Fig. 1, combining harmonic functions of the form $r^n \cos n\theta$, and noting that $-G\alpha r^2/2$ is a particular solution of $\nabla^2\phi = -2G\alpha$, a stress function is written in the form:

$$\phi = -G\alpha r^2/2 + Ar\cos\theta + Br^2\cos 2\theta + Cr^3\cos 3\theta + Er^5\cos 5\theta \quad (1)$$

We then write $B = -G\alpha/2$ for ϕ to be zero on $\theta = \pm 90$ deg for all r and obtain

$$\phi = -G\alpha r^2\cos^2\theta + Ar\cos\theta + Cr^3\cos 3\theta + Er^5\cos 5\theta$$
$$= r\cos\theta[-G\alpha r\cos\theta + A + Cr^2(4\cos^2\theta - 3) + Er^4(16\cos^4\theta - 20\cos^2\theta + 5)] \quad (2)$$

To compute appropriate values of A, C, and E, the square bracketed term above is equated to zero for ($r = b$, $\theta = 0$), ($r = a$, $\theta = 90$ deg), and ($r = \left(\sqrt{a^2 + b^2}\right)/2$, $\theta = \arctan a/b$). The stress function so found satisfies $\nabla^2\phi = -2G\alpha$ and is zero at all points on the vertical side of the triangle and at the centers and intersection of the remaining sides. Thus it is expected to yield a good approximation to the true value of the stress at O, the approximation being given by

$$\tau = \frac{G\alpha a^2 b(69a^4 + 50a^2b^2 - 3b^4)}{a^4(81a^2 + 89b^2) + b^4(7a^2 - b^2)} \quad (3)$$

It is interesting to compare this expression with known results; this is done in Table 1.

Table 1 Magnitude of maximum shear stress

a/b	$\tau/G\alpha b$ = const $\tau/G\alpha b$ from Eq. (3)	$\tau/G\alpha b$ exact
$1/\sqrt{3}$	0.500	0.500[3]
1	0.659	0.649[2]
$\sqrt{3}$	0.766	0.767[2] (relaxation)

For the equilateral triangle, Equation (3) is exact and the accuracy for the other cases (apex angles 90 and 120 deg, respectively) is very satisfactory. When a/b is quite a small quantity, it may be that the maximum shearing stress will not occur at the point O in Fig. 1, but rather at points on the equal sides. However, it is thought that Equation (3) will give the maximum shearing stress for most practical sections.

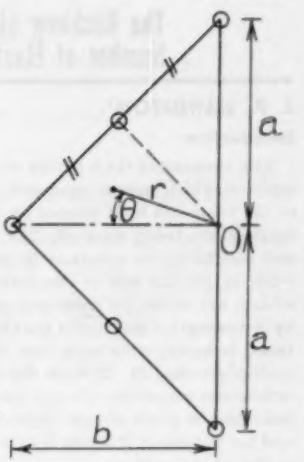

Fig. 1 Geometry of isosceles triangle

Knowing A, C, and E, the torsional rigidity might now be computed. However, the accuracy would not be so great as for the stress and, since Nuttall's results are sufficiently accurate for all practical purposes, this has not been done.

Finally, it is interesting and important to note that the stress function in Equation (2) may be used to analyze other symmetrical sections having a flat edge. Considering, for example, a semicircle of radius a and finding A, C, and E in Equation (2) by equating the square-bracketed term to zero for ($r = a$, $\theta = 0$, 45 deg and 90 deg), gives the stress at point O as

$$\tau = G\alpha a(2 + \sqrt{2})/4 = 0.853G\alpha a \quad (4)$$

This compares very favorably with the exact value of $0.849\,G\alpha a$.[4] No doubt the method will give similar results for the more general problem of the circular segment, which has been discussed by Weigand.[5]

An investigation similar to the foregoing may be made for cross sections bounded partially by a circular arc. The torsion function in this case is

$$-G\alpha r^2/2 + A + B_1 r\cos\theta + C_1 r^2\cos 2\theta + \ldots\ldots + (B_2/r)\cos\theta + (C_2/r^2)\cos 2\theta + \ldots\ldots \quad (5)$$

Writing $A = G\alpha a^2/2$ and combining terms

$$\phi = G\alpha(a^2 - r^2)/2 + A(\cos\theta)(a^2 - r^2)/r + B(\cos 2\theta)(a^4 - r^4)/r^2 + C(\cos 3\theta)(a^6 - r^6)/r^3 - \ldots\ldots$$
$$= (a^2 - r^2)[G\alpha/2 + A(\cos\theta)/r + B(\cos 2\theta)(\ldots + r^2)/r^2 + C(\cos 3\theta)(a^4 + a^2r^2 + r^4)/r^3 + \ldots\ldots] \quad (6)$$

Because of the factor $(a^2 - r^2)$, ϕ is zero on the arc $r = a$.

Appropriate values of A, B, C may then be found by equating the bracketed term to zero for points on the other boundary curve. It may be noted that, if only the first two terms are retained in the square bracket, the solution applies to a boundary formed by two intersecting circular arcs, one having its center on the circumference of the other. This latter solution is due to Weber.[6]

---

[1] Professor of Mechanics, Cornell University, Ithaca, N. Y. Also Julius F. Stone Visiting Professor of Mechanics, The Ohio State University, Columbus, Ohio.

[2] Henry Nuttall, "Torsion of Uniform Rods With Particular Reference to Rods of Triangular Cross Section," Journal of Applied Mechanics, vol. 19, Trans. ASME, vol. 74, 1952, pp. 554–557.

[3] S. Timoshenko and J. N. Goodier, "Theory of Elasticity," McGraw-Hill Book Co., Inc., New York, N. Y., 1951, p. 266.

Manuscript received by ASME Applied Mechanics Division, May 11, 1959.

[4] Reference in footnote 3, p. 279.

[5] A. Weigand, "The Problem of Torsion in Prismatic Members of Circular Segmental Cross Section," NACA Tech. Memo. 1182, 1948.

[6] Reference in footnote 3, p. 268.

The Buckling of a Beam on a Number of Elastic Restraints

J. P. ELLINGTON[1]

Introduction

THE PROBLEM of the buckling of a beam on equally spaced elastic supports which possess resistance to both deflection and rotation of the beam has been treated by several authors, two major investigations being given [1, 2].[2] Both reports treat the same end conditions, in reference [1] an energy method being used, while in [2] the sets of simultaneous equations specifying the system are solved by a suitable multiplication scheme followed by a summation giving the buckling condition. The end conditions, however, were such that the series used in [1] and the multipliers used in [2] were the normal buckling modes whose orthogonal properties allowed the resulting simplifications. No indication is given of how other end conditions may be treated, and the purpose of this note is to indicate a more general approach to the whole problem.

The Difference Equations

Consider a long uniform beam of flexural rigidity EI, subjected to a compressive end load P and resting on point supports which are spaced at equal distances L. The point supports are supposed to be perfectly elastic and of stiffness such that a force λ displaces them unit distance, and a couple μ twists them through unit change of slope.

The deflection and slope of the beam at the rth support are y_r and θ_r, while the bending moments to the left and right of the support are M_r' and M_r''. The corresponding shear forces are R_r' and R_r''.

From reference [3] the following relationships are obtained:

$$M_r' = (EI/L)[s\theta_{r-1} + c\theta_r - (c+s)(\delta_r - \delta_{r-1})]$$

and

$$M_r'' = (EI/L)[-c\theta_r - s\theta_{r+1} + (c+s)(\delta_{r+1} - \delta_r)] \quad (1)$$

where, with $u = (PL^2/EI)$ and $\delta_r = (y_r/L)$ (2)

$$s = \frac{u(u - \sin u)}{2 - 2\cos u - u\sin u} \quad \text{and} \quad c = \frac{u(\sin u - u\cos u)}{2 - 2\cos u - u\sin u} \quad (3)$$

The shear forces are

$$R_{r+1}' = R_r'' = (1/L)(M'_{r+1} - M_r'') + (P/L)(y_{r+1} - y_r) \quad (4)$$

For equilibrium of moments and for vertical equilibrium at the rth support

$$0 = M_r' + \mu\theta_r - M_r''$$

and

$$0 = R_r'' + \lambda y_r - R_r'$$

or, on writing $\mu^* = (\mu L/2EI)$ and $\lambda^* = (\lambda L^3/2EI)$ (5)

$$0 = s\theta_{r+1} + 2(c+\mu^*)\theta_r + s\theta_{r-1} - (c+s)(\delta_{r+1} - \delta_{r-1}) \quad (6)$$

and

$$0 = (c+s)(\theta_{r+1} - \theta_{r-1}) - 2(c + s - u^2/2)(\delta_{r+1} - 2\delta_r + \delta_{r-1}) + 2\lambda^*\delta_r \quad (7)$$

Equations (6) and (7) are a pair of linear difference equations [3], and may be solved by assuming

$$\delta_r = A\exp(\beta r) \quad \text{and} \quad \theta_r = A\alpha\exp(\beta r) \quad (8)$$

where α and β are to be determined. Substituting in (6) and (7) gives

$$\alpha = \frac{(c+s)\sinh\beta}{s\cosh\beta + (c+\mu^*)} = \frac{[2(c+s) - u^2](\cosh\beta - 1) + \lambda^*}{(c+s)\sinh\beta} \quad (9)$$

Eliminating α and using the above equations gives the characteristic equation

$$0 = \cosh^2\beta - a\cosh\beta + b \quad (10)$$

where

$$a = (1 + \cos u) - \lambda^*\frac{(u - \sin u)}{u^3} + \mu^*\frac{\sin u}{u}$$

and

$$b = \cos u + \lambda^*\frac{\sin u - u\cos u}{u^3} + \mu^*\frac{\sin u}{u} + \lambda^*\mu^*\frac{2 - 2\cos u - u\sin\mu}{u^4}$$

There are thus four values of β, $\pm\beta_1$, and $\pm\beta_2$, while from equation (9) there are four corresponding values of α, $\pm\alpha_1$, and $\pm\alpha_2$.

From equation (8) the expressions for the deflections and slopes at the supports become

$$\delta_r = \Sigma A\exp(\beta r) = A_1\cosh\beta_1 r + A_2\cosh\beta_2 r + B_1\sinh\beta_1 r + B_2\sinh\beta_2 r \quad (11)$$

and

$$\theta_r = \Sigma A\alpha\exp(\beta r) = \alpha_1(A_1\sinh\beta_1 r + B_1\cosh\beta_1 r) + \alpha_2(A_2\sinh\beta_2 r + B_2\cosh\beta_2 r) \quad (12)$$

The end conditions considered in references [1] and [2] were akin to those of simple supports. For a beam with N spans there is no deflection at $r = 0$ and N, and the rotational stiffness at the ends is $(\mu/2)$, or half the stiffness of the other supports.

The corresponding equations are

$$0 = \delta_0 = \delta_N$$

and

$$0 = (\mu/2)\theta_0 - M_0'' = (\mu/2)\theta_N + M_N'$$

These equations may be solved, or the beam may be regarded as a portion of a larger beam, the end supports corresponding with nodes. Thus, from symmetry,

$$\delta_1 = -\delta_{-1} \quad \text{and} \quad \theta_1 = \theta_{-1}$$

or

$$0 = A_1\cosh\beta_1 + A_2\cosh\beta_2$$

and

$$0 = A_1\alpha_1\sinh\beta_1 + A_2\alpha_2\sinh\beta_2$$

giving

$$A_1 = A_2 = 0$$

Similarly

$$\delta_{N+1} = -\delta_{N-1} \quad \text{and} \quad \theta_{N+1} = \theta_{N-1}$$

or

$$0 = B_1\cosh\beta_1\sinh\beta_1 N + B_2\cosh\beta_2\sinh\beta_2 N$$

and

$$0 = B_1\alpha_1\sinh\beta_1\sinh\beta_1 N + B_2\alpha_2\sinh\beta_2\sinh\beta_2 N$$

---

[1] United Kingdom Atomic Energy Authority, Development and Engineering Group, Risley, Warrington, Lancs., England.

[2] Numbers in brackets indicate References at end of Note.

Manuscript received by ASME Applied Mechanics Division, July 22, 1959.

A solution is obtained when $B_2 = 0$ and $\sinh \beta_1 N = 0$ giving

$$\beta_1 = (ik\pi/N), \qquad i \equiv \sqrt{(-1)} \tag{13}$$

Permissible values of k are 1, 2, 3 . . $(N-1)$, and from equations (10) the equilibrium equation is

$$0 = \cos^2(k\pi/N) - a\cos(k\pi/N) + b \tag{14}$$

The value $k = N$ in equation (13) represents the case of double roots in the characteristic equation (10) and corresponds with no deflection of the supports. The equilibrium condition is then independent of λ^* and is readily shown to be

$$\mu^* = (-u)/\tan(u/2) \tag{15}$$

Some results from these equations are given in references [1] and [2].

References

1 B. Budiansky, P. Seide, and R. A. Weinberger, "The Buckling of a Column on Equally Spaced Deflectional and Rotational Springs," NACA TN 1519, 1948.

2 C. B. Biezeno and J. J. Koch, "On the Buckling of a Girder, Elastically Supported and Elastically Clamped in a Number of Equidistant Points," *Applied Scientific Research*, vol. A1, 1949, pp. 249–257.

3 F. Bleich, "The Buckling Strength of Metal Structures," McGraw-Hill Book Company, Inc., New York, N. Y., 1952, pp. 211 and 277.

The Second Approximation for Buckling Loads of Tapered Struts

M. M. ABBASSI[1]

THE differential equation $(d^2y/dx^2) + \phi(x)y = 0$ is solved to the second approximation. The solution is applied to find the critical buckling loads for tapered struts, and more accurate results than those given by the same author are obtained.

In a previous paper by the same author,[2] the solution of the differential equation $(d^2y/dx^2) + \phi(x)y = 0$ was carried out to the first approximation by assuming that $\phi(x)$ is slowly varying function of x, and buckling loads were found according to this approximation for some shapes of tapered struts.

In this investigation the method is extended so as to obtain the second approximation for the foregoing differential equation, and more accurate results for critical loads are obtained.

Approximate Solution of the Equation

$$(d^2y/dx^2) + \phi(x)y = 0 \tag{1}$$

As a first approximation, consider the case in which ϕ is a slowly varying function of x which does not vanish in a certain interval (usually the length of the strut). Make the substitution $y = e^{i\int Z dx}$ $(i = \sqrt{-1})$ where Z is a function of x to be determined. We get from (1)

$$Z^2 = \phi(x) + i\frac{dZ}{dx} \tag{2}$$

If $\phi(x)$ is slowly varying as we have assumed, dZ/dx will be small and as a first approximation we have

$$Z = \pm\sqrt{\phi(x)}^{3}$$

Hence the general solution of equation (1) is given by

$$y = A_1 e^{i\int\sqrt{\phi(x)}\,dx} + A_2 e^{-i\int\sqrt{\phi(x)}\,dx}$$

or

$$y = A\cos\left(\int\sqrt{\phi(x)}dx\right) + B\sin\left(\int\sqrt{\phi(x)}\,dx\right) \tag{3}$$

The Second Approximation. If we substitute $Z = \pm\sqrt{\phi(x)}$ in the small term dZ/dx in (2), we get

$$Z^2 = \phi(x) \pm i\frac{\phi'(x)}{2\sqrt{\phi(x)}}$$

where

$$\phi'(x) = \frac{d\phi}{dx}$$

Taking the square root we get

$$Z = \pm\left[\sqrt{\phi(x)} \pm \frac{i}{4}\frac{\phi'(x)}{\phi(x)}\right] \text{ approximately}$$

The general solution of equation (1) is then given by

$$y = A_1 e^{i\int\left[\sqrt{\phi(x)} + \frac{i}{4}\frac{\phi'(x)}{\phi(x)}\right]dx} + A_2 e^{-i\int\left[\sqrt{\phi(x)} - \frac{i}{4}\frac{\phi'(x)}{\phi(x)}\right]dx}$$

Hence the second approximation is given by

$$y = [\phi(x)]^{-1/4}\left[A\cos\left(\int\sqrt{\phi(x)}dx\right) + B\sin\left(\int\sqrt{\phi(x)}dx\right)\right] \tag{4}$$

Application to Struts of Variable Cross Section. Referring to the author's previous paper,[2] the differential equation for buckling of tapered struts shown in Fig. 1 is

$$\frac{d^2y}{dx^2} + n^2\left(\frac{x}{a}\right)^{-m}y = 0 \tag{5}$$

The second approximation to the solution of equation (5) according to the solution (4) is given by

$$y = n^{-1/2}\left(\frac{x}{a}\right)^{\frac{m}{4}}\left[A\cos\left\{\frac{2na}{2-m}\left[\left(\frac{x}{a}\right)^{-\frac{m}{2}+1} - \left(\frac{b}{a}\right)^{-\frac{m}{2}+1}\right]\right\} + B\sin\left\{\frac{2na}{2-m}\left[\left(\frac{x}{a}\right)^{-\frac{m}{2}+1} - \left(\frac{b}{a}\right)^{-\frac{m}{2}+1}\right]\right\}\right]$$

At $x = b$, $y = 0$, this gives $A = 0$, at $x = a$, $dy/dx = 0$, and n is given by

$$\cot\left[\frac{2na}{2-m}\left\{1 - \left(\frac{b}{a}\right)^{-\frac{m}{2}+1}\right\}\right] = -\frac{m}{4an} \tag{6}$$

It is noted that $\frac{I_1}{I_0} = \left(\frac{b}{a}\right)^m = \alpha$, $\quad a = \frac{l}{2(1-\alpha 1/m)}$

Equation (6) can be written in the form

$$f(\theta) \equiv \cot\theta + \frac{mk}{4a\theta} = 0 \tag{7}$$

where

[3] The proof was given in the author's previous paper.[2]

---

[1] Assistant Professor of Mathematics, Faculty of Engineering, Alexandria University, Alexandria, Egypt.

[2] M. M. Abbassi, "Buckling of Struts of Variable Bending Rigidity," JOURNAL OF APPLIED MECHANICS, vol. 25, TRANS. ASME, vol. 80, 1958, pp. 537–540.

Manuscript received by ASME Applied Mechanics Division, November 26, 1958; final draft received July 20, 1959.

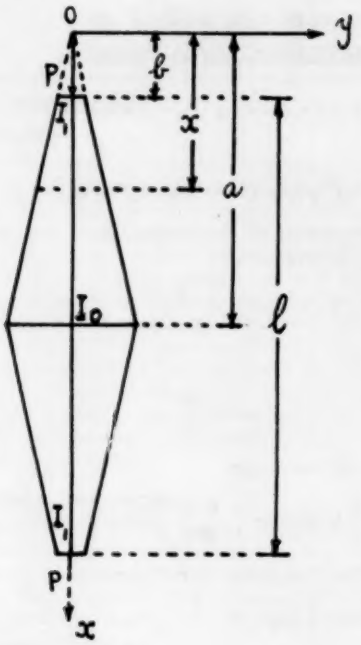

Fig. 1

$$\theta = kn,\ k = \frac{l(1-\alpha^{1/m-1/2})}{(1-\alpha 1/m)(2-m)},\quad n = \sqrt{\frac{P}{EI_0}}$$

The first approximation to the solution of equation (5) gives $\theta = \frac{\pi}{2}$, so that an approximate root of equation (7) according to Newton's method is given by

$$\frac{\pi}{2} - \frac{f\left(\frac{\pi}{2}\right)}{f'\left(\frac{\pi}{2}\right)}$$

Hence

$$\theta = \frac{\pi}{2}\left(1 + \frac{mk}{mk + \pi^2 a}\right) \tag{8}$$

If the strut has a constant thickness in the direction perpendicular to Fig. 1, $m = 1$ and we have

$$a = \frac{l}{2(1-\alpha)},\quad k = \frac{l}{1+\sqrt{\alpha}},\quad \theta = \frac{l}{1+\sqrt{\alpha}}\sqrt{\frac{P}{EI_0}}$$

Relation (8) gives:

$$P = 1/4(1+\sqrt{\alpha})^2\frac{\pi^2 EI_0}{l^2}\left[1 + \frac{2(1-\sqrt{\alpha})}{2(1-\sqrt{\alpha})+\pi^2}\right]^2$$

If the strut consists of two solid cones, $m = 4$ and we have

$$a = \frac{l}{2(1-\alpha^{1/4})},\quad k = \frac{l}{2\alpha^{1/4}},\quad \theta = \frac{l}{2\alpha^{1/4}}\sqrt{\frac{P}{EI_0}}$$

We get:

$$P = \sqrt{\alpha}\,\frac{\pi^2 EI_0}{l^2}\left[1 + \frac{4(\alpha^{-1/4}-1)}{4(\alpha^{-1/4}-1)+\pi^2}\right]^2$$

If the strut consists of four angles connected by lattices, $m = 2$ approximately, the second approximation to the solution of equation (5) is given by:

$$y = \sqrt{\frac{x}{na}}\left[A\cos\left(na\log\frac{x}{b}\right) + B\sin\left(na\log\frac{x}{b}\right)\right]$$

The boundary conditions give $A = 0$ and

$$\cot\left(na\log\frac{a}{b}\right) = -\frac{1}{2na}$$

or

$$\cot\theta - \frac{1}{4\theta}\log\alpha = 0 \tag{9}$$

where

$$\theta = na\log\frac{b}{a},\quad a = \frac{l}{2(1-\sqrt{\alpha})},\quad \log\frac{b}{a} = 1/2\log\alpha$$

The second approximation to the solution of equation (5) gives

$$\theta = \frac{\pi}{2}\left(1 - \frac{\log\alpha}{\pi^2 - \log\alpha}\right)$$

hence,

$$P = 4\left(\frac{1-\sqrt{\alpha}}{\log\alpha}\right)^2\frac{\pi^2 EI_0}{l^2}\left[1 - \frac{\log\alpha}{\pi^2-\log\alpha}\right]^2$$

In all the foregoing cases the second approximation shows clearly the effect of the variation of the cross section on the critical buckling load.

Application To Uniform Struts Under the Action of Varying Axial Forces. This case was treated by the author in his previous paper, and if the solution is carried out to the second approximation we obtain the same value for the critical load as that obtained in the first approximation; hence there is no need to find the second approximation in this case.

Bibliography

1 J. C. Jaeger, "An Introduction to Applied Mathematics," Oxford University Press, 1951, pp. 351–352.

2 S. Timoshenko, "Strength of Materials, Part II," McGraw-Hill Book Co., Inc., New York, N. Y., 1941, pp. 205–207.

3 S. Timoshenko, "Theory of Elastic Stability," McGraw-Hill Book Co., Inc., New York, N. Y., 1936, pp. 115–128.

Some Preliminary Results of Visual Studies of the Flow Model of the Wall Layers of the Turbulent Boundary Layer[1]

P. S. KLEBANOFF.[2] In recent years there has been an increased awareness of the three-dimensional character of phenomena associated with the instability of the laminar boundary layer. The present paper demonstrates the importance of understanding this three-dimensionality, not only for the transition problem, but perhaps also for the turbulent boundary layer as well. The theory of disturbances of finite amplitude even in the case of two-dimensional flow is not too tractable, and it appears that for the present the experimentalist has to lead the way in providing a sound physical model as a basis for theoretical approach. The writer's comments stem from an experimental investigation with just such a purpose being conducted at the National Bureau of Standards under the sponsorship of the National Aeronautics and Space Administration. In this investigation the growth and evolution of Tollmien-Schlichting waves are being studied under controlled conditions using hot-wire methods for the measurements and the vibrating-ribbon technique for the introduction of forced oscillations. It is not possible to go into detail, but briefly stated it has been observed that the wave motions become strongly three-dimensional prior to transition, exhibiting large spanwise variations in wave amplitude.

The development of this three-dimensional pattern is apparently an inherent characteristic of a wave as it leads to transition to turbulence and is of basic importance. Consequently, in the experiment it was decided to control the spanwise variation in wave amplitude in order that the structure and significance of the observed three-dimensionality could be investigated adequately. This was done by placing single strips of scotch tape 0.5 in. long and 0.5 in. apart on the surface beneath the ribbon. The well-controlled spanwise variation in wave amplitude which was obtained is shown by the distribution of u' in Fig. 1 where u' is the root-mean-square value of the longitudinal fluctuation, U_1 is the free-stream velocity, and Z represents the distance in the spanwise direction measured from the edge of the flat plate. The center of the flat plate is at $Z = 25.5$ in., and the scotch-tape spacers under the ribbon extended from the 1 in. to $^1/_2$-in. positions. The measurements shown in the figure were made in the boundary layer at a distance from the surface corresponding to three tenths of the boundary-layer thickness, and at a downstream position from the ribbon where the wave behavior has already departed from that given by linear theory and just upstream from transition to turbulence. Measurements of the spanwise component of mean velocity W were made also at a distance from the wall corresponding to one tenth the boundary-layer thickness, and these are shown by the dashed curve.

The distribution of the root-mean-square value of the spanwise fluctuation w' is also shown. The spanwise fluctuation is highly correlated with the u-fluctuation, has a maximum on each side of the peak in the u'-distribution, and is of the same order as u'. The measurements of the spanwise component of mean velocity are perhaps the most interesting. They exhibit a maximum at each side of the peak in u', and a change in sign from one side to the other, as well as a change in sign across the boundary layer. A positive sign of W indicates that the flow direction is to the left. However, since the measurements indicated by the dashed curve were obtained closer to the surface, the arrows indicating flow direction were arbitrarily changed in the region on the right side of the peak in u' to illustrate that in the spatial configuration the eddies are rotating in a clockwise direction on one side of the peak, and in a counterclockwise direction on the other side. The measurements of the local mean velocity in the boundary layer U show that the distribution of mean velocity is distorted in a manner one would suspect from the superposition of a longitudinal eddy system rotating as shown.

There is little doubt that associated with the three-dimensional wave motions there are present longitudinal vortexes. The general features that are observed by hot-wire methods are in agreement with those observed by the dye techniques. The dye technique marks the fluid particle thus showing the behavior of the mean flow, and not necessarily that of the disturbance. The hot wire, on the other hand, can follow the disturbance and has the decided advantage of yielding quantitative results. Its disadvantage is that it does not give an over-all view and the peiture must be pieced together from many separate measurements.

Measurements are now in progress to map the eddy structure in

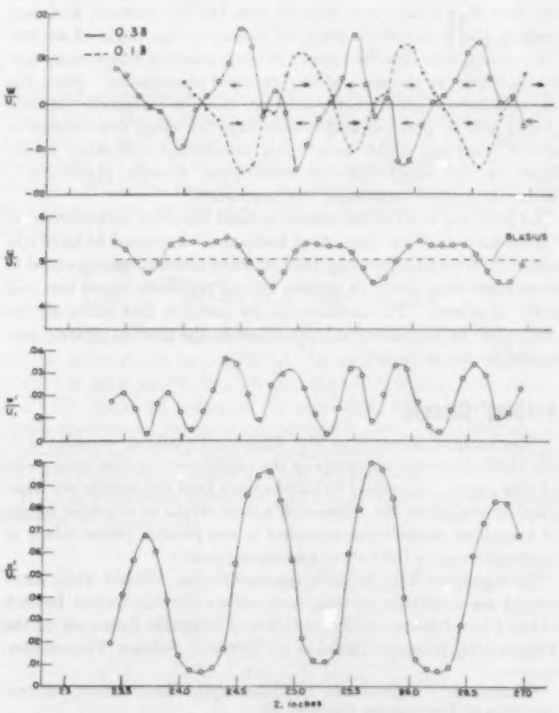

Fig. 1 Spanwise distribution of mean and fluctuating components of velocity in the boundary layer prior to transition

[1] By S. J. Kline and P. W. Runstadler, published in the June, 1959, issue of the JOURNAL OF APPLIED MECHANICS, vol. 26, TRANS. ASME, vol. 81, pp. 166–170.

[2] Fluid Mechanics Section, National Bureau of Standards, U. S. Department of Commerce, Washington, D. C.

detail. A question of immediate interest is the originating mechanism of the observed vortexes. It may well be that the existing theories attempting to deal with the region of finite amplitude will not be adequate and that a new formulation will be required.

J. A. MILLER.[3] The work of the author and his co-workers demonstrates the classical picture of the turbulent boundary layer to be grossly oversimplified, and, in all probability, in need of marked revision before one can hope to make any considerable progress in this field. The flow picture presented also may provide a means for understanding the later stages of transition where the possibility of a mathematical treatment, at least along the lines of classical developments, appears very remote.

It is indeed unfortunate that the rather excellent color motion picture prepared by the authors cannot in some way be published or at least made available to other workers in the field of fluid mechanics since it portrays the observed phenomena far more adequately than the written word.

While the dye-injection techniques employed have proved very successful in this work, there appears to be a fundamental shortcoming in the use of line sources of dye. This is because the simultaneous phenomena occurring at other lengthwise positions on the wall and in particular their interactions with one another are masked. This difficulty might possibly be overcome by constructing the wall of some dye substance which is slowly dissolved in the flow stream and which would provide a two-dimensional injection system by means of which the three-dimensional phenomena of the turbulent boundary layer might be better visualized. Possibly potassium permanganate could be employed.

Two further comments may be made in connection with this work. The first concerns the isolation of the "dynamic history of the fluid" on the observed phenomena of turbulent boundary layers. This isolation might well be accomplished by studying the flow over a flat plate inserted into the flow stream, and controlling the pressure gradient by means of the angle of attack. The second comment concerns the correlation of free-stream turbulence level to the scale of the observed phenomena. Since the use of hot-wire anemometry in water flows is extremely difficult, it may well be possible to introduce into the water flow screens or screen matrices which have been previously calibrated in air flows by the usual hot-wire techniques, thereby producing a stream of known turbulence characteristics.[4]

In his own studies the writer noticed that the distribution of "transitory stall" or "islands of hesitation" appeared to have statistically favored locations; that is, these phenomena appeared to form more frequently at certain lateral positions across the wall than at others. The authors fail to mention this although the writer felt he had observed this effect in the motion picture presented by the authors.

Authors' Closure

The authors appreciate Mr. Klebanoff's added comments of the three-dimensional nature of the phenomena in the later stage of transition. It should be emphasized that the results are complementary, since Mr. Klebanoff's data relate to the later stages of transition while those reported in the present paper relate to various cases of a fully turbulent shear layer.

In regard to Mr. Miller's comments, the colored films mentioned are available on loan from either the Mechanics Branch of the United States Air Force Office of Scientific Research, or the Engineering Sciences Division of National Science Foundation.

Mr. Miller's comments on line sources are correct. Some studies have been done with porous walls, but these tend to make visualization difficult. In regard to Mr. Miller's comments on favored locations, two points should be added. First, Mr. Miller, who did some early work preliminary to that reported in the present paper,[5] used an apparatus designed for diffuser studies, rather than model studies of the wall layers. Later, more careful tests showed that the favorable locations were due to slight irregularities in the wall. When more carefully made walls were employed, favorable locations did not seem to appear. Second, more complete studies show that while some aspects of the streaks of backflow, or small transitory stall, are related to the islands of hesitation, the two are not identical. In a favorable or zero pressure gradient, the islands of hesitation are present, but no streaks of backflow have ever been observed. It is only after an appreciable positive pressure gradient is applied that streaks of backflow appear; upon further increase in adverse pressure gradient, these lead to large transitory stall patterns, as described by Kline.[6]

The authors would like to reiterate the remarks of Mr. Klebanoff and Mr. Miller that further careful experimental data are badly needed, and that these may well lead to a reformulation of the physical picture, not only of the later stages of transition, but also of the fully turbulent shear layer. Experiments of a number of types are needed. Some, but not all, of these are being pursued at Stanford. In particular, current studies are aimed at coupling quantitative measurements with the sort of visualization studies reported in the present paper. These are being carried out by use of hot-film techniques which allow both mean velocity and fluctuation measurements in water.

The writers have also gathered considerable additional corollary evidence relating to the flow model of the fully turbulent layer. In addition to the careful data reported by Mr. Klebanoff, this information covers a wide range of types of data and situations. To date much of it is confirming and none of it is in conflict with the model suggested in the present paper. The writers hope to report both on this additional corollary evidence and on further details of the flow model in the near future.

Influence Coefficients for Edge-Loaded Short, Thin, Conical Frustums[1]

H. E. WILLIAMS.[2] The author's purpose, in the section entitled "An Approximate Solution," seems to be the calculation of a correction to the previous results of Horvay, Linkous, and Born that would be valid for shallow conical frustums. Essentially, this requires an expansion of the pertinent quantities in powers of $(1/\xi)$ with quantities of order $(1/\xi^2)$ considered negligible. In carrying out this procedure, the author chose to approximate the Kelvin functions by neglecting terms of order $(1/\xi)$. Hence the correction proposed by the author of order $(1/\xi)$ is of doubtful validity, and one should consider the results of this paper as only a confirmation of the results of Horvay, Linkous, and Born in the range where $\xi \gg 1$.

[3] Instructor, Department of Mechanical Engineering, Illinois Institute of Technology, Chicago, Ill.

[4] G. B. Schubauer, W. G. Spangenberg, and P. S. Klebanoff, "Aerodynamic Characteristics of Damping Screens," NACA TN 2001, January, 1950.

[5] S. J. Kline, "Some New Conceptions of the Mechanism of Stall in Turbulent Boundary Layers," *Journal of the Aeronautical Sciences*, Readers' Forum, vol. 24, 1957, pp. 470–471.

[6] S. J. Kline, "On the Nature of Stall," *Journal of Basic Engineering*—TRANS. ASME, series D, vol. 81, 1959, pp. 305–319.

[1] By J. H. Baltrukonis, published in the June, 1959, issue of the JOURNAL OF APPLIED MECHANICS, vol. 26, TRANS. ASME, vol. 81, series E, pp. 241–245.

[2] Jet Propulsion Laboratory, California Institute of Technology, Pasadena, Cal.

Analysis of Complex Kinematic Chains With Influence Coefficients[1]

T. P. GOODMAN.[2] By simplifying and systematizing the graphical solutions for velocities and accelerations in mechanisms of higher-order complexity, this paper makes an important contribution to the literature of kinematic analysis. Velocity solutions by superposition have also been discussed by Hain,[3] but the author's use of influence coefficients which are employed again in the acceleration solution is a major step forward.

Since Equations (1) and (8) of the paper were presented without formal derivation or proof, the following derivation, which proves the validity of superposition and discloses the nature of the influence coefficients, may be of interest. Let θ_i be the angle from a line fixed in the machine frame to a line fixed in link i of the mechanism, let s_i be the scalar length of a line segment i joining two points of the mechanism, and let $\mathbf{R}_j$ be a vector drawn from an origin in the machine frame to a point j of the mechanism. If the mechanism has constrained motion (one degree of freedom), these variables are all functions of a single variable, which may be taken as the angular position θ_D of the driving link. Then, as shown in reference [3] of the paper,[4] all velocities in the mechanism can be expressed in terms of the input angular velocity ω_D as

$$\dot{\theta}_i = \omega_i = \frac{d\theta_i}{d\theta_D}\,\omega_D \tag{1}$$

$$\dot{s}_i = V_i = \frac{ds_i}{d\theta_D}\,\omega_D \tag{2}$$

$$\dot{\mathbf{R}}_j = \mathbf{V}_j = \frac{d\mathbf{R}_j}{d\theta_D}\,\omega_D \tag{3}$$

and all accelerations in the mechanism can be expressed in terms of the input angular velocity and acceleration as

$$\dot{\omega}_i = \frac{d^2\theta_i}{d\theta_D{}^2}\,\omega_D{}^2 + \frac{d\theta_i}{d\theta_D}\,\dot{\omega}_D \tag{4}$$

$$\dot{V}_i = \frac{d^2s_i}{d\theta_D{}^2}\,\omega_D{}^2 + \frac{ds_i}{d\theta_D}\,\dot{\omega}_D \tag{5}$$

$$\dot{\mathbf{V}}_j = \frac{d^2\mathbf{R}_j}{d\theta_D{}^2}\,\omega_D{}^2 + \frac{d\mathbf{R}_j}{d\theta_D}\,\dot{\omega}_D \tag{6}$$

All of the derivatives in these six equations can be evaluated from graphical velocity and acceleration solutions using arbitrary values of ω_D and $\dot{\omega}_D$.

If one constraint in the mechanism is now relaxed, yielding a mechanism with two degrees of freedom, then θ_i, s_i, and $\mathbf{R}_j$ are functions of two variables, which may be taken (following the notation of the Conclusions of the paper) as θ_D and θ_F. Thus the other velocities in the mechanism can be expressed in terms of ω_D and ω_F as:

$$\omega_i = \frac{\partial\theta_i}{\partial\theta_D}\,\omega_D + \frac{\partial\theta_i}{\partial\theta_F}\,\omega_F \tag{7}$$

$$V_i = \frac{\partial s_i}{\partial\theta_D}\,\omega_D + \frac{\partial s_i}{\partial\theta_F}\,\omega_F \tag{8}$$

$$\mathbf{V}_j = \frac{\partial\mathbf{R}_j}{\partial\theta_D}\,\omega_D + \frac{\partial\mathbf{R}_j}{\partial\theta_F}\,\omega_F \tag{9}$$

Comparison of Equation (9) with Equation (15) of the paper shows that the influence coefficients $\bar{\mu}_{jD}$ and $\bar{\mu}_{jF}$ are actually the partial derivatives $\partial\mathbf{R}_j/\partial\theta_D$ and $\partial\mathbf{R}_j/\partial\theta_F$, respectively. Since these partial derivatives are purely geometrical properties of the mechanism, depending on its position but not on its velocity, Equations (7) to (9) are linear in ω_D and ω_F. This proves that the total velocity of any point can be found by superposition of solutions with $\omega_F = 0$ and $\omega_D = 0$, respectively.

The constraint which was relaxed in order to write Equations (7) to (9) can now be reintroduced to give the relationship between ω_D and ω_F. In the problem discussed in the paper, the constraint which was relaxed was the fixed distance between the two pivots of link 8. Denoting this distance by s_8, the constraint can be expressed as $V_8 = 0$. Using Equation (8) of this discussion to reintroduce this constraint, we can solve for ω_F in terms of ω_D:

$$\frac{\omega_F}{\omega_D} = \frac{d\theta_F}{d\theta_D} = -\frac{\partial s_8}{\partial\theta_D}\Big/\frac{\partial s_8}{\partial\theta_F} \tag{10}$$

(This, of course, is merely the analytical equivalent of the author's graphical solution in which V_8 is required to be tangential to link 8.)

The accelerations in the mechanism can be expressed in terms of ω_D, ω_F, $\dot{\omega}_D$ and $\dot{\omega}_F$ as

$$\dot{\omega}_i = \frac{\partial^2\theta_i}{\partial\theta_D{}^2}\,\omega_D{}^2 + 2\,\frac{\partial^2\theta_i}{\partial\theta_D\partial\theta_F}\,\omega_D\omega_F + \frac{\partial^2\theta_i}{\partial\theta_F{}^2}\,\omega_F{}^2 + \frac{\partial\theta_i}{\partial\theta_D}\,\dot{\omega}_D + \frac{\partial\theta_i}{\partial\theta_F}\,\dot{\omega}_F \tag{11}$$

with similar equations for $\dot{s}_i$ and $\dot{\mathbf{R}}_j$. This equation is nonlinear in ω_D and ω_F; hence superposition cannot be applied. However, the equation can be made linear in $\omega_D{}^2$, $\dot{\omega}_D$, and $\dot{\omega}_F$ by restricting ω_F (though not $\dot{\omega}_F$) to values which are compatible with the constraint. With this restriction, expressed by Equation (10), the first three terms on the right side of Equation (11) may be rewritten.

$$\left[\frac{\partial^2\theta_i}{\partial\theta_D{}^2} + 2\,\frac{\partial^2\theta_i}{\partial\theta_D\partial\theta_F}\,\frac{d\theta_F}{d\theta_D} + \frac{\partial^2\theta_i}{\partial\theta_F{}^2}\left(\frac{d\theta_F}{d\theta_D}\right)^2\right]\omega_D{}^2$$

In the remainder of this discussion, the expression in the brackets will be abbreviated as $D^2\theta_i/D\theta_D{}^2$; it should be noted that this is not the same as $d^2\theta_i/d\theta_D{}^2$, which can be evaluated from Equation (4). Since all terms of the expression in the brackets are purely geometrical properties of the mechanism, depending on its position but not on its velocity or acceleration, $D^2\theta_i/D\theta_D{}^2$ is also a purely geometrical property of the mechanism.

With this notation Equation (11) can be rewritten as a linear function of $\omega_D{}^2$, $\dot{\omega}_D$, $\dot{\omega}_F$:

$$\dot{\omega}_i = \frac{D^2\theta_i}{D\theta_D{}^2}\,\omega_D{}^2 + \frac{\partial\theta_i}{\partial\theta_D}\,\dot{\omega}_D + \frac{\partial\theta_i}{\partial\theta_F}\,\dot{\omega}_F \tag{12}$$

Similarly,

$$\dot{V}_i = \frac{D^2s_i}{D\theta_D{}^2}\,\omega_D{}^2 + \frac{\partial s_i}{\partial\theta_D}\,\dot{\omega}_D + \frac{\partial s_i}{\partial\theta_F}\,\dot{\omega}_F \tag{13}$$

$$\dot{\mathbf{V}}_j = \frac{D^2\mathbf{R}_j}{D\theta_D{}^2}\,\omega_D{}^2 + \frac{\partial\mathbf{R}_j}{\partial\theta_D}\,\dot{\omega}_D + \frac{\partial\mathbf{R}_j}{\partial\theta_F}\,\dot{\omega}_F \tag{14}$$

---

[1] By J. Modrey, published in the June, 1959, issue of the JOURNAL OF APPLIED MECHANICS, vol. 26, TRANS. ASME, vol. 81, pp. 184–188.

[2] Kinematics Engineer, General Engineering Laboratory, General Electric Company, Schenectady, N. Y. Assoc. Mem. ASME.

[3] K. Hain, "Angewandte Getriebelehre," Hermann Schroedel Verlag, Hannover and Darmstadt, Germany, 1952, pp. 84–87.

[4] The double-subscript notation of reference [3] is not used here, since here the machine frame is always taken as the reference link.

Comparison of Equation (14) with Equations (8), (10), and (16) of the paper shows analytically that the first two acceleration influence coefficients, $\bar{\mu}_{jD}$ and $\bar{\mu}_{jF}$, are the same as the corresponding velocity influence coefficients, since they are the same pair of partial derivatives. Also it is seen that the third acceleration influence coefficient, $\bar{\beta}_{jD}$, is equal to $D^2\mathbf{R}_j/D\theta_D^2$, which is of a different nature from the other influence coefficients, since it gives the effect due to two interrelated inputs [ω_D and ω_F as related by Equation (10)] rather than the effect due to a single input.

As in the velocity solution, these influence coefficients can be evaluated by graphical solutions, and then the constraint which was removed to obtain a second degree of freedom can be reintroduced to evaluate $\dot{\omega}_F$ in terms of ω_D and $\dot{\omega}_D$. For the example in the paper, this can be accomplished analytically by setting $\bar{V}_s = 0$ in Equation (13) of this discussion.

When the velocity influence coefficients are identified as partial derivatives, it is seen that the application of influence coefficients for synthesis of mechanisms by variation, as suggested in the final paragraph of the paper, is similar in principle to the method described by Svoboda,[5] by Nickson,[6] and by Hall and Tao.[7]

A. S. HALL.[8] The writer has always been troubled by the fact that there seemed to be in the literature no method guaranteed to solve the problems of velocity and acceleration analysis in all conceivable plane mechanisms. The paper by Goodman, author's reference [3], was an excellent step in the right direction and probably his method will take care of most practical mechanisms. However, there still remained the (possibly academic) question of whether we could conceive mechanisms which could not be analyzed.

The author has answered the question to the writer's satisfaction. It now appears that suitable use of the suggested superposition ideas should lead to a solution for any plane mechanism.

Author's Closure

The author appreciates the interest taken by Dr. Goodman and Dr. Hall in this paper. Dr. Goodman is especially to be commended for the analytical proof he offers. The author's contribution was primarily heuristic, although he did satisfy himself of the analytical rigor of the method. Unfortunately, the analytical proof used by the author was quite clumsy and would not have added to the discourse.

On the other hand, Dr. Goodman's proof is more incisive; it is a most constructive addition to the paper. Dr. Goodman's proof gains its clarity by exploiting the analytics of entire links, whereas the author's unpublished proof relied on the dynamics of the pivot points.

While an analytical proof is imperative for removing any lingering doubts concerning the rigor of the method, the author nevertheless feels that the use of over-all influence coefficients rather than partial derivative forms, such as the foregoing equation (11), makes for a more workable insight into the relationships involved.

While Dr. Hall concedes that the technique described makes higher-order problems tractable, he casts doubts on the need for methods beyond those sufficient to solve systems of second-order complexity. The author can only point out that the rapid changes in our technology invariably wrest ideas from the academic to the practical domain at phenomenal rates. Furthermore, it should be pointed out that the method described is quite general. Not only does it subdue HOC systems, but it also resolves the more common SOC systems and treats them as simple versions of the general case.

[5] A. Svoboda, "Computing Mechanisms and Linkages," McGraw-Hill Book Company, Inc., New York, N. Y., 1948, pp. 199–206.

[6] P. T. Nickson, "A Simplified Approach to Linkage Design," *Machine Design*, vol. 25, December, 1953, pp. 196–209.

[7] A. S. Hall and D. C. Tao, "Linkage Design—A Note on One Method," TRANS. ASME, vol. 76, 1954, pp. 633–637.

[8] School of Mechanical Engineering, Purdue University, West Lafayette, Ind. Mem. ASME.

Transients in Simple Undamped Oscillators Under Inertial Disturbances[1]

ANDREA CAPELLO.[2] It is interesting to remark how similar results are reached in the case of transients in rotating shafts.

For instance, let us take a circular cross-section shaft, supported at the ends, bearing a disk of mass m in its middle section; no gyroscopic effects therefore need be taken into account. Let us suppose that the disk is eccentrically mounted and let us call e the distance between the center of gravity of the disk and the axis of the shaft, Fig. 1. Let us suppose that the angle φ of rotation of the shaft varies according to a given function of time.

Let us take three fixed orthogonal axes, Fig. 1, with the z-axis through the two supports of the shaft, the x and y-axes in the middle plane of the disk, and let the y-axis, at the time $t = 0$, form an angle φ_0 with the direction of the eccentricity.

Let us call x,y the co-ordinates of point O_1, intersection of the shaft axis with the x,y-plane, and x^*,y^* the co-ordinates of the center of gravity G of the disk.

The equation of equilibrium to the rotation around the z-axis gives a relation between the angular acceleration $\ddot{\varphi}$ of the disk and the moment C that must be applied to the disk in order to obtain that acceleration; if e, x^*, and y^* may be considered small with respect to the inertial radius of the disk, such relation becomes linear.[3]

The equation of equilibrium along the x and y-axes are, if we neglect any dissipative force,

$$\begin{aligned} m\ddot{x}^* + kx &= 0 \\ m\ddot{y}^* + kx &= 0 \end{aligned} \qquad (1)$$

where k is the elastic constant of the shaft.

[1] By Antongiulio Dornig, published in the June, 1959, issue of the JOURNAL OF APPLIED MECHANICS, vol. 26, TRANS. ASME, vol. 81, series E, pp. 217–223.

[2] Assistant, Institute of Applied Mechanics and Machine Design, Polytechnic of Milan, Milan, Italy.

[3] C. B. Biezeno and R. Grammel, "Technische Dynamik," J. Springer Verlag, 1939, p. 775.

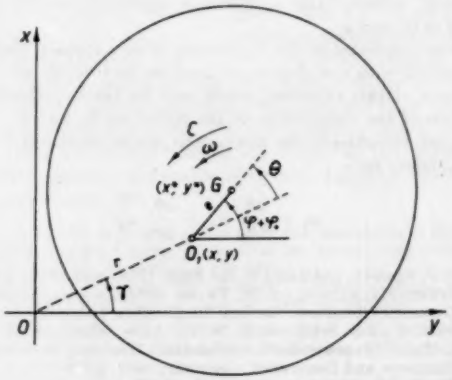

Fig. 1

Dividing by m and observing that

$$x^* = x + e\sin(\varphi + \varphi_0)$$
$$y^* = y + e\cos(\varphi + \varphi_0)$$

we have

$$\ddot{x} + \Omega^2 x = -e\ddot{u} \qquad (2)$$
$$\ddot{y} + \Omega^2 y = -e\ddot{v}$$

where $\Omega = k/m$ is the angular frequency corresponding to the critical speed of the shaft and

$$u = \sin(\varphi + \varphi_0)$$
$$v = \cos(\varphi + \varphi_0)$$

The first equation of system (2) is the same as equation (3) in the paper; from the second equation we can easily obtain the same formulas found for the first one when we substitute $\cos\varphi_0$ and $-\sin\varphi_0$ for $\sin\varphi_0$ and $\cos\varphi_0$, respectively.

As an application let us consider the transients in the starting and stopping of the shaft with a constant acceleration.

(a) Starting From Rest. If we start the shaft from rest with a constant angular acceleration 2λ, putting

$$\xi(\eta) = \frac{x(\eta)}{e} \qquad \zeta(\eta) = \frac{y(\eta)}{e}$$

where $\eta = 2\lambda t/\Omega$, the equations of motions, in dimensionless form, are

$$\xi(\eta) = \frac{\pi}{2}\rho[L'\sin\varphi_0 + N'\cos\varphi_0]$$
$$\qquad (3)$$
$$\zeta(\eta) = \frac{\pi}{2}\rho[L'\cos\varphi_0 - N'\sin\varphi_0]$$

Introducing the deflection $r = (x^2 + y^2)^{1/2}$ or, in dimensionless form, $\nu = (\xi^2 + \zeta^2)^{1/2}$ where $\nu(\eta) = r(\eta)/e$, we have

$$\nu(\eta) = \frac{\pi}{2}\rho(L'^2 + N'^2\eta)^{1/2} \qquad (4)$$

which is identical to equation (14a) in the paper, which gives the envelope of the family of curves $\xi(\eta, \varphi_0)$.

The same result is reached if we consider ξ and ζ as projections of a rotating vector which in our case represents the deflection of the shaft. While the author was concerned only with the study of only one of such projections, it is clear that the formula for the deflection in our case will be the same as the one found by the author for the envelope. The same results found in the paper therefore can be applied in our case.

It is also possible to find the value of the angle γ that the deflection forms with the y-axis. We have

$$\gamma(\eta) = \tan^{-1}\frac{\xi(\eta)}{\zeta(\eta)} \qquad (5)$$

If we let $\varphi_0 = 0$ (y-axis along the eccentricity e at $t = 0$), equation (5) of this discussion becomes

$$\gamma(\eta) = \tan^{-1}\frac{N'}{L'} \qquad (6)$$

The total angle of which the deflection has rotated at the time t is given by

$$\delta(\eta) = \gamma(\eta) + 2\pi n$$

where n can be calculated numerically by tabulating equation (6) at intervals sufficiently small.

Since in our case $\varphi(t) = \lambda t^2$, i.e., $\varphi(\eta) = (\pi/2)\rho^2\eta^2$, the deflection and the eccentricity (i.e., the disk) do not rotate, during the transient, with the same law. Calling

$$\theta(\eta) = \varphi(\eta) - \delta(\eta)$$

the angle that the eccentricity forms with the deflection, we have

$$\theta(\eta) = \frac{\pi}{2}\rho^2\eta^2 - 2\pi n - \tan^{-1}\frac{N'}{L'} \qquad (7)$$

Also the plane of deflection of the shaft is therefore variable in time with the law given by (7).

(b) Stopping. Also in the case of stopping to rest with a constant angular deceleration 2λ from a constant velocity ω_0, we arrive at results similar to those obtained by the author.

In particular we have (with the same notation of the paper)

$$\nu(\eta) = \frac{\pi}{2}\rho(L''^2 + N''\eta)^{1/2} \qquad (4a)$$

$$\gamma(\eta) = \tan^{-1}\frac{N''}{L''} \qquad (6a)$$

$$\theta(\eta) = \frac{\pi}{2}\rho^2\eta^2 - \frac{\omega_0^2}{4\lambda} - 2\pi n - \tan^{-1}\frac{N''}{L''} \qquad (7a)$$

It is interesting to observe that if we take into account some internal viscous damping in the material, the analogy does not hold any longer between our case and that treated in the paper. In fact, in the latter we must introduce a damping force proportional to the velocity, while in the case of the rotating shaft we must introduce a force proportional to the derivative of the deflection vector with respect to a couple of axes rotating with the disk.

MARIO TESSAROTTO.[4] The author begins the development of the proposed study starting from the expression that gives, in permanent state, the value of forced displacement (amplitude) in an undamped, vibrating, single-degree-of-freedom system self-excited by its inertial forces. Such an expression can be expressed as

$$\frac{X}{e} = \frac{-1}{1 - \dfrac{\Omega^2}{\omega_0^2}}$$

where

Ω = angular frequency of mechanical system
ω_0 = angular frequency of self-excitation (in permanent excitation)

Supposing that the ratio

$$\frac{-1}{1 - \dfrac{\Omega^2}{\omega_0^2}} = \frac{(\omega_0/\Omega)^2}{1 - (\omega_0/\Omega)^2}$$

is assumed of convenient value in order to the degree of tranquillity of the machine which must be reached in stationary condition of excitation, the author considers the behavior of vibrating system in possible transient states like those of starting and stopping with constant angular acceleration, or constant angular deceleration, respectively, and supposing of course that the natural frequency of system is conveniently minor than that induced during stationary state. By convenient mathematic development for integration of differential equation of dynamic balance, the author

[4] Professor, Chairman, Department of Applied Mechanics, University of Trieste, Trieste, Italy.

arrives at the determination of greatest excursion in transient condition in function of characteristic data of system.

The functions-answer introduced in analytical development is studied by the author graphically, or with response curves.

Author's Closure

The author is grateful to Professor Tessarotto for bringing the problem so well into focus, and wishes to thank Dr. Capello for his interesting extension of the results of the paper to the problem of transients in rotating shafts. It would certainly be of great interest to further pursue the matter taking into account the internal damping of the material also in order to determine to what degree the results of the author's recent study[5] on the transient behavior of damped simple oscillators can be useful here.

Natural Frequencies of Two Nonlinear Systems Compared With the Pendulum[1]

R. W. SHREEVES.[2] The solution to Equation (1) of this interesting note may be found in terms of known functions, thus eliminating the need for a digital computer.[3]

Let

$$C_1 - 2C_2 = I/M\,a^2,$$
$$C_2 = R(R-a),$$
$$C_3 = g(R-a),$$
$$C_4 = C_1/2C_2$$

Substitute these relations into Equation (1) and let $p = \dot{\theta}$. This yields

$$(C_3/C_2)^{1/2}\tau/4 = \int_0^{\theta_0} \frac{d\theta}{\left(\dfrac{\cos\theta - \cos\theta_0}{C_4 - \cos\theta}\right)^{1/2}}$$

In this equation, let $u = \tan(\theta/2)$. The resulting expression immediately suggests the presence of elliptic integrals. With the aid of some algebraic manipulation and the substitution $u = \tan^2(\theta_0/2)\cos\phi$, the following expression for the square of the period is readily obtained:

$$\tau^2 = \frac{64C_2}{C_3(C_4-1)(1+\cos\theta_0)(1+p^2)}\{(1+C_4)K(k) - (1+\cos\theta_0)\Pi(\nu, k)\}^2$$

where K and Π are complete elliptic functions of the first and third kinds, respectively;

$$p^2 = \tan^2(\theta_0/2)/(C_4^2-1),$$
$$k^2 = [\tan^2(\theta_0/2)]/[\tan^2(\theta_0/2) + (C_4^2-1)],$$

and

$$\nu = (\cos\theta_0 - 1)/2$$

For convenience, the complete elliptic function of the third kind in the foregoing may be expressed in terms of elliptic functions of the first and second kinds.[4] The values of these functions are easily obtained.[5]

Therefore,

$$\tau^2 = \frac{64C_2}{C_3(C_4-1)(1+\cos\theta_0)(1+p^2)}\left\{(C_4 - \cos\theta_0)K(k) - \left(\frac{2(1-\cos^2\theta_0)}{(2k^2-(1-\cos\theta_0)}\right)^{1/2}[K(k)E(\alpha, k) - E(k)F(\alpha, k)]\right\}^2$$

where F and E are incomplete elliptic functions of the first and second kinds, respectively, and α varies from 0 to arc sin $\left(\frac{1}{k}\sin\frac{\theta_0}{2}\right)$.

K. KLOTTER.[6] E. W. Gaylord[1] recently treated the free oscillations of two systems, identified as "cylindrical profile rocker" and "bar rocking on a cylindrical surface," respectively. After having established the differential equations of the two systems, the author shows in a diagram (his Fig. 3) the amplitude-frequency relationships which he obtained by integrating the differential equations numerically (applying the Runge-Kutta method and using a digital computer). The results are given for one specific value of the parameter β of the first system and three specific values of the parameter λ of the second system.

Two remarks may be added to that note:

1 It seems worth mentioning that the differential equations allow exact integration. Using the author's nomenclature and (corrected) abbreviations,

$$\beta = \frac{R(R-a)}{k^2+a^2}\quad,\quad \Omega^2 = \frac{g(R-a)}{k^2+a^2} \tag{1a}$$

and

$$\lambda = \frac{a^2}{l^2/12}\quad,\quad \Omega^2 = \frac{ga}{l^2/12} \tag{1b}$$

respectively, we may write the differential equations as

$$\ddot{\theta}[1 + 2\beta(1-\cos\theta)] + (\beta\dot{\theta}^2 + \Omega^2)\sin\theta = 0 \tag{2a}$$

$$(1+\lambda\theta^2)\ddot{\theta} + (\lambda\dot{\theta}^2 + \Omega^2\cos\theta)\theta = 0. \tag{2b}$$

They can be transformed into the following first-order linear differential equations for $V = \dot{\theta}^2$ as a function of θ:

$$[1 + 2\beta(1-\cos\theta)]V' + 2\beta\sin\theta V = -2\Omega^2\sin\theta \tag{3a}$$

$$[1+\lambda\theta^2]V' + 2\lambda\theta V = -2\Omega^2\theta\cos\theta. \tag{3b}$$

The first step of integration can be carried out immediately; in the second step the variables can be separated, and the q-t relationships appear in the form of quadratures.

2 A rather accurate approximate amplitude-frequency relationship which contains the parameters in general form, not specified, can be obtained by applying the Ritz-Galerkin procedure[7] to Equations (2). Assuming

$$\theta = Q\cos\omega t \tag{4}$$

---

[1] A. Dornig, "Transitorio d'avviamento negli oscillatori semplici smorzati soggetti a perturbazione a caratteristica inerziale," *L'Energia Elettrica*, June, 1959.

[1] By Eber W. Gaylord, published in the March, 1959, issue of the JOURNAL OF APPLIED MECHANICS, vol. 26, TRANS. ASME, series E, vol. 81, pp. 145–146.

[2] Senior Scientist, AVCO Research and Advanced Development Division, Wilmington, Mass.

[3] R. W. Shreeves, "A Trochoidal 'Oscillator,'" *Avco RAD*, 1959.

[4] A. Erdelyi, W. Magnus, F. Oberhettinger, and F. Tricomi, "Higher Transcendental Functions," McGraw-Hill Book Company, Inc., New York, N. Y., 1955, p. 321.

[5] B. O. Peirce, "A Short Table of Integrals," Ginn and Company, New York, N. Y., 1929, pp. 121–123.

[6] Professor of Engineering Mechanics, Stanford University, Stanford, Calif.

[7] K. Klotter, "Nonlinear Vibration Problems Treated by the Averaging Method of W. Ritz," Proceedings of the First U. S. National Congress of Applied Mechanics, ASME, 1952, pp. 125–131.

and replacing the trigonometric functions in (2) by their power-series expansions, retaining terms up to the third order only, we find for the amplitude-frequency relationship

$$\eta^2 = \frac{1 - {}^1/_8 Q^2}{1 + {}^1/_2 \beta Q^2} \tag{5a}$$

$$\eta^2 = \frac{1 - {}^3/_8 Q^2}{1 + {}^1/_2 \lambda Q^2} \tag{5b}$$

respectively; η denotes the ratio ω/Ω. The result for the pendulum, to the same degree of approximation, reads

$$\eta^2 = 1 - {}^1/_8 Q^2; \text{ with } \Omega^2 = g/l. \tag{5c}$$

Numerical values from Equations (5) agree very closely with the author's results for his specific values of the parameters. Equations (5), however, allow comparing the three systems for any other values of the parameters β and λ, without the need for subsequent integration.

The accuracy of the procedure may readily be increased, if need should be, by (*a*) keeping more terms in the expansions mentioned, and/or (*b*) replacing the approximation (4) either by one containing higher (odd) harmonics, or by an appropriate non-sinusoidal function.[8]

Collapse Loads of Rings and Flanges Under Uniform Twisting Moment and Radial Force[1]

N. C. DAHL.[2] The author uses conventional plate-and-ring theory and this implies certain practical restrictions on the ratio of ring thickness to tube radius. The upper limit of this ratio certainly is of the order of $^1/_4$ and thus the upper limit of h/a which is practically of interest is about 0.1. Thus the area of Fig. 13 of the paper, which is of interest, is that region below $h/a = 0.1$. For all practical purposes the restriction on b/a may then be said to be independent of h/a with the result shown in the accompanying Fig. 1, where any combination of α and b/a in the shaded region is consistent with a statically admissible stress field. Consistent with the approximation represented by Fig. 1, it may also be stated that any value of h/a (which is less than 0.1) will result in a statically admissible stress field.

[8] K. Klotter and Phil R. Cobb, "The Use of Nonsinusoidal Approximating Functions for Nonlinear Oscillation Problems," to appear in the JOURNAL OF APPLIED MECHANICS.

[1] By Burton Paul, published in the June, 1959, issue of the JOURNAL OF APPLIED MECHANICS, vol. 26, TRANS. ASME, vol. 81, series E, pp. 265–270.

[2] Professor of Mechanical Engineering, Massachusetts Institute of Technology, Cambridge, Mass.

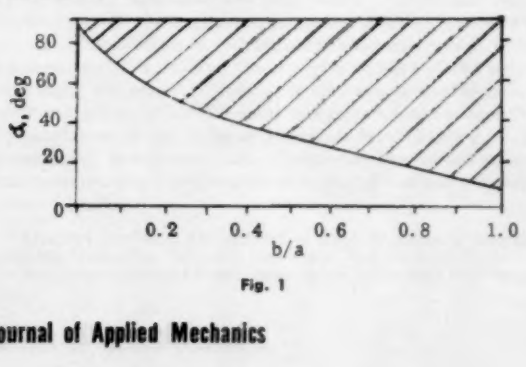

Fig. 1

Author's Closure

The problem of the axially compressed corrugated tube was treated merely to illustrate how a fairly complex problem can be simplified and solved *within the framework* of the given theory of rings. One of the stated assumptions of the theory is that the rings in question have a "small" ratio of depth to diameter. However, no attempt was made to delimit the meaning of the word "small." Professor Dahl suggests that, from a practical point of view, ratios of h/a less than 0.1 are *necessary* in order to apply the given solution. This value seems quite reasonable to the author and does lead, as Professor Dahl shows, to some simplification in the criteria for applicability of the solution.

In the same spirit, one should perhaps require that, in addition, the slant height L of the conical frustrum, depicted in Fig. 12 of the paper, should be somewhat greater (say five times) than the thickness $2h$.

Normal Vibrations of a Uniform Plate Carrying Any Number of Finite Masses[1]

W. H. HOPPMANN, II.[2] The theoretical treatment of the subject by the authors is very interesting and the results should be of value to those who have to analyze the vibrations of flat plates with attached masses. On the other hand, the experimental portion of the work may be criticized because the assumed boundary conditions are not satisfied. In order to obtain any reasonable approximation to simple support of a rectangular plate, positive provision must be made for maintaining zero deflection at each point on the boundary and especially at the vertexes. It is of course well known that, in order to prevent movement of the vertexes, substantial forces must be applied. The method used by the authors does not provide for these requirements. In the past the writer faced somewhat the same problem, and, as a result, introduced the so-called grooved plate for simulating simple support conditions on the boundary.[3,4] The authors are referred to the papers describing the method and it is hoped that they have an opportunity to do further experimental work in connection with the problem.

Authors' Closure

It is certainly true that to obtain the simply supported boundary condition provision must be made to insure zero deflection at all boundary points, and to restrain the corners. In some tests on a 10-in. × 20-in. plate, made after those described in the paper, each corner of the plate was held down with a 5-lb weight. The frequencies were found to be 3 to 7 per cent higher than when the corners were not restrained. Of course, even this provision did not insure that the desired boundary conditions were obtained completely, and the method devised by the discusser would be superior. The authors' interest in the work was primarily with large plates on which fairly large masses were mounted, specifi-

[1] By W. F. Stokey and C. F. Zorowski, published in the June, 1959, issue of the JOURNAL OF APPLIED MECHANICS, vol. 26, TRANS. ASME, vol. 81, series E, pp. 210–216.

[2] Professor of Mechanics, Department of Mechanics, Rensselaer Polytechnic Institute, Troy, N. Y. Mem. ASME.

[3] W. H. Hoppmann, II, and Joshua Greenspon, "An Experimental Device for Obtaining Elastic Rotational Constraint on Boundary of a Plate," Proceedings of the 2nd U. S. National Congress of Applied Mechanics, ASME, 1954, p. 187.

[4] W. H. Hoppmann, II, and W. G. Soper, "Note on the Boundary Conditions for Bending Experiments With Bars and Plates," JOURNAL OF APPLIED MECHANICS, vol. 23, TRANS. ASME, vol. 78, 1956, p. 646.

cally electronic chassis. With such systems, it is believed that the use of the grooved plate would lead to difficulties because of the relatively large deflections that would occur, with the accompanying membrane stresses, which are not accounted for in the analytical solution.

On the Natural Modes and Their Stability in Nonlinear Two-Degree-of-Freedom Systems[1]

C. M. ABLOW.[2] The authors have covered their ground so carefully and completely that it is very difficult to find points for discussion or criticism. A suggestion for extension of the work is therefore offered.

It would seem that some of the results could be established without linearization, even perhaps without specialization to cubic polynomial springs, by an investigation following the phase-plane methods of Poincaré and Liapunov. For example, a periodic solution of either equation (4) of the paper is represented by the arc of a roughly parabolic curve in the upper half of the $(x, \dot{x}^2)$-plane. Half the period of such a solution is obtained by integrating $(1/\dot{x})$ between the points where the curve cuts the x-axis.

Thus solutions of the two equations (4) having the same amplitude and period are represented by arcs which cross the x-axis in the same places and also intersect each other elsewhere. It follows that there are values of abscissa x at which one curve has greater slope than the other and others where it has less. The difference in slopes is then zero somewhere in the range of interest. These slopes being proportional to the right-hand sides of their respective equations, there is a point x_1 at which $F(2x)$ is zero. Since $F(2x)$ is also zero at $x = 0$, its derivative is zero somewhere between x_1 and 0. It follows that the authors' statement "real crossover amplitude can occur only in systems in which the slope of the coupling spring force has a change in sign" is valid in a very general setting.

If other of the authors' results can be similarly extended, the restrictions to small motions can be dropped. The analog verifications can then be scaled to lie in an easily observable range. One may then hope that the few discrepancies between theory and experiment as noted by the authors would disappear.

Authors' Closure

We wish to thank Dr. Ablow for his discussion and compliment him on the lucid manner in which he has used simple and appealing geometrical arguments to generalize one of our results. His idea of comparing the periodic solutions of the uncoupled equations in the phase plan is an excellent suggestion and a welcome addition to the methods available for the discussion of the solutions, even when the system is much more general than that discussed by us. It should prove very useful for examining all properties of the solutions that can be deduced from the uncoupled equations.

However, not all properties of the solutions can be deduced from these, and one of them is the stability of the solutions. Stability questions must be resolved from a study of the coupled equations (3) of the paper. The few discrepancies between theory and experiment, noted in our paper and mentioned by Dr. Ablow, are largely due to the fact that the identification of the stability of the solutions of the dynamical problem with those of a Mathieu equation is the result of a commonly used linearization of the stability problem. When the spring forces are odd, cubic polynomials in the spring deflections, it is actually possible to discuss the stability problem without this linearization because the solutions of the dynamical problem are elliptic functions, and their stability can be identified with that of the solutions of a Lamé equation (rather than a Mathieu equation). However, the problem is now much more complex, and the improved results are probably not worth the added effort because the agreement between experiment and the simpler theory used by us is excellent in nearly every case that was investigated.

[1] By R. M. Rosenberg and C. P. Atkinson, published in the September, 1959, issue of the JOURNAL OF APPLIED MECHANICS, vol. 26, TRANS. ASME, vol. 81, series E, pp. 377–385.

[2] Stanford Research Institute, Menlo Park, Calif.

Structural Engineering

Dynamics of Framed Structures. By Grover L. Rogers. John Wiley & Sons, Inc., New York, N. Y., 1959. Cloth, 9¼ × 6¼ in., xv and 355 pp., illus. $10.25.

REVIEWED BY FRANK L. DIMAGGIO[1]

PRESENT widespread interest in structural design for dynamic loads has created a need for an elementary text on dynamic analysis specifically for structural-engineering students. This excellent book fills that gap.

Primary emphasis is on elastic response, although viscous damping and a short treatment of ideal elastoplastic response of lumped systems are included. There is no material on rigid-plastic analysis or elastoplastic analysis of continuous structures. Trusses are not considered.

The subjects covered, however, are presented clearly. In considering lumped systems, their relation to continuous structures is emphasized and the employment of influence coefficients and matrix techniques is particularly appropriate in the light of increasing utilization of electronic computers. A chapter on beams introduces normal modes and the methods of Rayleigh and Vianello-Stodola. Chapters on continuous beams and rigid frames employ dynamic moment distribution, and one on floor systems emphasizes Bleich's method of complementary systems. Throughout the text, Newton's equations are used to formulate the problems, but a final chapter briefly introduces Lagrange's equations. Many illustrative examples and a collection of problems accompany the text.

A number of minor complaints must be registered. This reviewer would like to have seen some cautionary remarks concerning convergence problems associated with series solutions, a discussion of the requirements to be satisfied by the approximating function so that Rayleigh's method will yield an upper bound, and a consideration of distributed loads which are not product functions of space and time.

Plasticity

Introduction to Plasticity. By William Prager. Addison-Wesley Publishing Co., Reading, Mass., 1959. Cloth, 6 × 9 in., viii and 148 pp., illus. $9.50.

REVIEWED BY B. G. NEAL[2]

THE text presents in a concise manner the theory of plastic behavior of both structures and solid bodies. The author begins with a review of the mechanical properties of plastic solids, illustrating the ideas involved with the aid of kinematic models, which are then used to introduce the powerful concept of the plastic potential. The behavior of plastic structures subjected to various loading programs is then discussed with reference to a geometrical representation of the states of stress produced, leading to the statement of various extremum principles and to the concepts of failure under a single combination of loads and also under variable repeated loading.

With this background, the various theorems of limit analysis are introduced, and their applications to structures such as plane frames, rings, plates, and shells are discussed. The possible influence of changes in the basic geometry of the structural system due to deflections is emphasized and is exemplified by the case of a simply supported circular plate carrying a central concentrated load. The design of both plane frames and plates for minimum weight is also discussed.

Finally, a full discussion of the theory of plane plastic flow in solids, involving finite plastic deformations, is given, and applications to such problems as extrusion, indentation, and drawing are discussed.

The author has assumed a thorough knowledge of the fundamentals of the mechanics of solids and of structural analysis, although no previous acquaintance with the theory of plasticity is required. The material has been selected with considerable care so that the main topics are quickly carried to an advanced level. The result is a delightfully clear and concise presentation of the present position in this field. The book is exceedingly well documented so that topics not dealt with in the text can be followed up in the relevant literature. The usefulness of the book is further enhanced by the provision of examples at the end of each chapter.

This book will be read with great interest by all those who are active in the field, and will also be found invaluable for advanced course work in the subject.

Thermodynamics

Engineering Thermodynamics. By D. B. Spalding and E. H. Cole. E. Arnold, London, and McGraw-Hill Book Co., Inc., New York, N. Y., 1959. (McGraw-Hill Series in Mechanical Engineering.) 375 pp. $8.50.

REVIEWED BY S. J. KLINE[3]

THIS book covers the elements of thermodynamics as a science and as an engineering tool. It follows essentially the rigorous methods of Keenan ("Thermodynamics," Wiley, 1941), but expands and simplifies them into extremely readable form. Emphasis is on fundamentals and understanding, but engineering implications and methodology are discussed in detail in context.

Chapters cover: Brief Historical Survey, Units, Work, Temperature, Heat, First Law, The Pure Substance, First Law for Flow Processes, Properties of the Pure Substance, Second Law, Reversibility, Absolute Temperature, Entropy, Ideal Gases, Gaseous Mixtures, and Fuels and Combustion.

Treatments of these topics are uniformly rigorous, simple, and clear. A good selection of significant, up-to-date examples from a wide range of technology is included. An excellent feature of the work is that it not only discusses rigorous methods but also gives examples showing the more important of the numerous pitfalls in elementary thermodynamics which are avoided by adoption of these methods.

Standards in elementary textbooks in thermodynamics have been advancing at a high rate during the postwar period, and many good texts are presently available. However, this is the first text to appear which the reviewer feels is simultaneously of

[1] Assistant Professor, Department of Civil Engineering and Engineering Mechanics, Columbia University, New York, N. Y.

[2] Professor, Division of Engineering, Brown University, Providence, R. I.

[3] Associate Professor, Department of Mechanical Engineering, Stanford University, Stanford, Calif.

sufficient rigor, coverage, and readability so that a beginner can, with reasonable ease, learn the subject well from the text alone. This book can be wholeheartedly recommended either for a first course or for the engineer who needs to learn or review the subject on his own. As an introductory text, this work should provide a standard of comparison for some years to come.

Heat Transfer

Heat and Mass Transfer. By E. R. G. Eckert and Robert M. Drake, Jr. McGraw Hill Book Co., Inc., N. Y., 1959. 530 pages. $12.50.

REVIEWED BY H. H. SOGIN[4]

THE second edition of the senior author's "Introduction to the Transfer of Heat and Mass" now joins the publisher's textbook Series in Mechanical Engineering. Nearly doubled in content, it may be regarded as "practically a new book," but readers familiar with the first edition will find themselves quite at home in the second. Each of the authors is well known by his published work, much of which is summarized in the text. They have in the main succeeded in Dr. Eckert's expressed rule to explain physical processes and to minimize mathematical manipulations within the constraints of providing essentials to understanding.

After an introductory chapter of miscellany, the text is divided into five parts subdivided by chapters, a great improvement over the first edition. In Part A, about one fourth of the text, Dr. Drake deals with conduction: scalar theory, steady state, unsteady state, and moving sources. The remaining parts of the text, with the exception of an article on rarefied gases, have been written by Dr. Eckert. Part B, nearly half the text, covers heat convection in seven chapters: internal and external fluid flow, laminar transfer, turbulent transfer, immersed surfaces, "special processes," free convection, and boiling and condensation. Part C covers radiation properties and heat exchange. Part D deals with psychrometrics in one chapter and convective mass transfer in a second one. Part E consists of one chapter on steady-state and regenerative heat exchangers. Each part starts with an unnumbered section mainly outlining the treatment and delineating the scope. Examples are discussed, and problems at the end of each chapter exhibit content. References are in the footnotes; there is no attempt at a comprehensive bibliography. Dr. Drake's documented "Appendix of Property Values" is an excellent source of data for practical work as well as the problems.

"Special processes" include aerodynamic heating, rarefied gases, liquid metals, and transpiration and film cooling. It thus appears as a depository of pet topics that could not be conveniently inserted without major revisions. Some other new material, mainly unsteady conduction and boundary-layer theory, is inserted on a "skip" basis. This general allowance for alternative coverage occasionally retards the pace by minor redundancies and by omissions of transition bridging, as does the misguiding usage of the terms chapter, section, and paragraph, and of references to unnumbered equations. The use of e for emissive power is unfortunate. Although the book is addressed to mechanical and aeronautical engineers interested in research, few experimental techniques are discussed. One gets the feeling that we are living in pressing times.

This textbook will hardly assuage the current cries for a return to fundamentals. For certainly they require that in an exposition of this applied science the First Law be given prominent stature rather than a casual sentence in an article devoted to Fourier's "Law." Also, a more thorough treatment of the momentum principle is demanded.

The excellent qualities of this book outweigh the deficiencies that have been mentioned. It will retain its importance for a number of years because much of its newness springs from a rich decade and because students and engineers alike can share a penetrating understanding of the physical processes through lucid explanation under almost every topic covered.

[4] Associate Professor of Engineering, Brown University, Providence, R. I.

Symposium on Plasticity

Brown University, April 5–7, 1960

The Second Symposium on Naval Structural Mechanics will occur at Brown University, Providence, R. I., under the joint sponsorship of the Office of Naval Research and Brown University.

The Symposium, to be held in six sessions, will be devoted exclusively to the field of plasticity. The program will consist of critical surveys in selected areas and of reports on original research, with ample time for discussion.

The organizing committee consists of Professors E. H. Lee and P. S. Symonds (co-chairmen) and Professors D. C. Drucker and W. Prager.

Journal of APPLIED MECHANICS

Information for Authors

• Manuscripts should be submitted in final form to the Technical Editors. Each manuscript must be accompanied by a statement that it has not been published elsewhere nor has it been submitted for publication elsewhere. A paper which would occupy more than five pages of the Journal may be returned to the author for abridgment.

• The author should state his business connection, the title of his position, and his mailing address. A short abstract (50 to 100 words) should be included on the first page immediately preceding the introductory paragraph of the paper.

• Three copies of the manuscript are required. One of these must be a carefully prepared printer's copy, typed in double spacing, on one side of the page only, with wide margins, on $8^1/_2$ by 11-in. opaque white paper. Mimeographed manuscripts, if prepared with exceptional care, can be accepted provided they are completely edited.

• As far as possible, all mathematical expressions should be typewritten. Greek letters and other symbols not available on the typewriter should be carefully inserted in ink. Care should be taken to distinguish between capital and lowercase letters, between zero (0) and the letter (*O*), between the numeral (1) and the letter (*l*), etc. A letter representing a vector cannot be printed with an arrow above or below it. The letter should be underscored with a single wavy line, wherever it appears in the text, to designate boldface type. A list of symbols carefully marked for the use of the editor (thus: κ, Greek l.c. kappa), if it has not been included in the body of the paper, should accompany the manuscript on a separate page.

• Before preparing a manuscript the author should study printed articles in the Journal, with special attention to the form and style of mathematical expressions, tables, footnotes, references, and abstract. Numbers that identify mathematical expressions should be enclosed in parentheses. Numbers that identify references at the end of the paper should be enclosed in brackets. Care should be taken to arrange all tables and mathematical expressions in such a way that they will fit into a single column when set in type. Equations that might extend beyond the width of one column (fractions that should not be broken or long expressions enclosed in parentheses) should be rephrased to go on two or more lines within column width. Fractional powers are preferred to root signs and should always be used in more elaborate formulas. The solidus should be used instead of the horizontal line for fractions wherever possible.

• A normal paper should not exceed five pages in the Journal. It is about 6000 words or twenty to twenty-five double-spaced typewritten pages inclusive of drawings. A Brief Note should not exceed 750 words or about one column in the Journal inclusive of drawings.

• Originals and two copies of figures must accompany the manuscript. Line drawings should not be larger than $8^1/_2 \times 11$ inches and should be planned for reduction to column width. Lettering should be large enough to be clearly legible when the illustration is reduced. The originals of line drawings must be in India ink on white or pale blue tracing paper or tracing cloth. Photographs of equipment or test specimens must be glossy prints and should be used sparingly. Captions for figures should be typed double-spaced and included as the last page of the manuscript. The figure number and author's name should be written in the margin or on the back of each illustration.

• Titles of papers should be brief.

• Authors can obtain copies of the ASME Manual MS-4, "An ASME Paper," from the Technical Editors and are urged to do so before drafting their papers in final form.

• Papers published in the Journal of Applied Mechanics must be presented at a Meeting, either in person or by title. Scheduling of papers is in the hands of the Secretary of the Applied Mechanics Division. Authors should indicate their preference in this respect to the Technical Editors when submitting a paper.

• An author is entitled to 25 preprints free of charge (in the case of two authors, 15 each; three or more authors, 10 each). Larger quantities of preprints or reprints can be ordered from Editorial Department, The American Society of Mechanical Engineers, 29 West 39th Street, New York 18, N. Y. Quotations will be sent on request.

ASME Publications Committee

Please address all communications to:

Technical Editors

Journal of Applied Mechanics, ASME

Division of Engineering

Brown University

Providence 12, R. I.

"Proved" Technical Aids for Engineers

APPLIED MECHANICS REVIEWS

Engineers in all parts of the world rely on **Applied Mechanics Reviews** because it enables them to survey world-wide advances in applied mechanics and related engineering science in a relatively short time . . pinpoint any major development in their fields in seconds . . . .keep abreast of rapidly expanding scientific frontiers . . . and have a constant flow of new ideas, some of which have evolved into money-makers for them and their employers.

To provide this service, the most significant findings are culled from over a thousand sources including 750 engineering periodicals of thirty countries, new books in all languages, and reports of industrial specialists everywhere which are then appraised and evaluated by specialists in the fields involved. Each review bears the signature of the reviewer, thus attesting to the authority of the opinion advanced.

Over 400 reviews are published monthly, highlighted by an article written exclusively for AMR by an established authority to apprise readers of progress in a specialized area. In a year's total AMR publishes 5,000 signed reviews on approximately 600 subjects—conveniently grouped under the following fifty classifications:

General: Analytical Methods in Applied Mechanics. Computing Methods and Computers. Analogies. Kinematics. Rigid Dynamics, and Oscillations. Instrumentation and Automatic Control. Tables, Charts, Dictionaries, etc.

Mechanics of Solids: Elasticity. Viscoelasticity. Plasticity. Rods, Beams, and Strings. Plates, Shells, and Membranes. Buckling. Vibrations of Solids. Wave Motion and Impact in Solids. Soil Mechanics: Fundamental. Soil Mechanics: Applied. Processing of Metals and Other Materials. Fracture (Including Fatigue). Experimental Stress Analysis. Material Test Techniques. Properties of Engineering Materials. Structures: Simple. Structures: Composite. Machine Elements and Machine Design. Fastening and Joining Methods.

Mechanics of Fluids: Rheology. Hydraulics. Incompressible Flow. Compressible Flow (Continuum and Noncontinuum Flow). Boundary Layer. Turbulence. Aerodynamics. Vibration and Wave Motions in Fluids. Fluid Machinery. Flow and Flight Test Techniques and Measurements.

Heat: Thermodynamics. Heat and Mass Transfer. Combustion. Prime Movers and Propulsion Devices.

Combined Fields and Miscellaneous: Magneto-fluid-dynamics. Aeroelasticity. Aeronautics. Astronautics. Ballistics, Explosions. Acoustics. Micromeritics. Porous Media. Geophysics, Hydrology, Oceanography, Meteorology. Naval Architecture and Marine Engineering. Friction, Lubrication, and Wear.

Published monthly. Annual subscription price: $25.00 to nonmembers, $10.00 to ASME members.

STRUCTURAL DAMPING

Provides a wealth of information useful in engineering design

This book discusses such structural damping techniques as interfacial coulomb slip, viscoelastic laminate damping, and coulomb or viscoelastic junction damping. The information has been written by authorities in the field and was presented at the 1959 ASME Annual Meeting.

Contents: Energy Dissipation Mechanisms in Structures, with Particular Reference to Material Damping. A Review of Progress in Analysis of Interfacial Slip Damping. Damping of Plate Flexural Vibrations by Means of Viscoelastic Laminae. Vibrational Energy Dissipation at Structural Support Junctions. Measurement of Damping. Material Design for Resonant Members. Selected Bibliography on Structural Damping.

Published 1959 **$4.25***

MECHANICAL IMPEDANCE METHODS FOR MECHANICAL VIBRATIONS

A reference for engineers specializing in vibration analysis and control

This book shows how impedance methods apply to lumped and continuous systems of simple and moderate complexity, reviews measurement techniques, demonstrates the power of digital computers by comparing the calculated and measured characteristics of a highly symmetrical system of moderate complexity, gives measured values of typical structures of large size and high complexity, discusses the importance of the impedance in influencing shock and vibration spectra measured in field service, indicates how to apply impedance methods to the calculation of vibration isolator effectiveness, treats impedance of some disordered systems, shows how impedance methods may be used to find the response to random excitation, and describes a dynamic stiffness method that has proved useful in predicting critical speeds of steam turbines.

Published 1958 **$5.50***

THERMODYNAMIC AND TRANSPORT PROPERTIES OF GASES, LIQUIDS, AND SOLIDS

A valuable and advanced survey of data and techniques on the thermal properties of important materials engineering

The methods and important experimental findings in this book are based on the work of the foremost authorities in the field. They include a survey of the present theoretical and experimental state of the science, a large amount of new data on current experimental and theoretical techniques, including thermodynamic and transport properties, PVT data and equation of state, some experimental transport properties, and high thermodynamic properties of gases. The forty-two papers in this book were originally presented at a Symposium on Thermal Properties sponsored by the ASME.

Published 1959 **$12.50***

Proceedings, 3rd U. S. NATIONAL CONGRESS OF APPLIED MECHANICS

Presents the findings of original researches and discusses the current approach to problems

Within this 904-page volume are reports of important studies in the fields of dynamics, vibration, elastic waves, elasticity, elastic structures, plasticity, viscoelastic flow, fracture, fluid flow, aerodynamics, and heat transfer. There are also discussions of new concepts and methods, and a large amount of new data which will aid in generating new ideas and new approaches toward solving other problems of the applied mechanics field.

Published 1958 $20.00 to members and nonmembers

***20% discount to ASME members.**

THE AMERICAN SOCIETY OF MECHANICAL ENGINEERS
29 West 39th Street New York 18, N. Y.